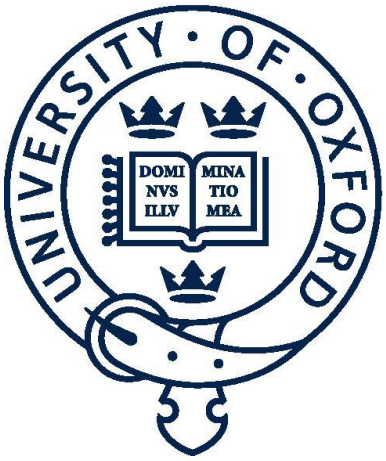
Development of an effective stress model for sand under cyclic loading in the hyperplastic framework



Luc Simonin

Saint Catherine's College

University of Oxford

A thesis submitted for the degree of

Doctor of Philosophy

Hilary Term 2023

Abstract

Offshore wind plays a key role in the world's energy transition from fossil fuels to renewable energy. The rate of growth of offshore wind will depend on the reduction of installed capital costs, with the foundation on which the turbine sits representing up to a third of the cost. The most popular foundation is the monopile, an impact-driven, large diameter, open-ended pile. New design methods have seen markedly improved assessments of ultimate capacity under monotonic or static loading, leading to significant cost reductions. Cyclic loading, from the wind and waves, now represents the main challenge for designers, particularly as the serviceability limit state design becomes critical.

Finite element (FE) calculations are widely used for engineering design, including for monopiles, with calculations for monotonic loading reasonably straightforward. Procedures for cyclic loading still require significant research and development, particularly for granular materials such as sands. This thesis describes a new effective stress constitutive model for sands, HySand_base, which robustly captures their complex behaviour under cyclic loading. HySand_base is developed within the hyperplasticity framework, guaranteeing thermodynamic consistency, mathematical soundness, robustness, and modularity. HySand_base is formulated as a multi-surface model with non-associative plasticity, allowing representation of the small strain and cyclic behaviour of sand. The construction of the model follows a step-by-step process; initially as a purely frictional model, then with anisotropy and density dependent dilation, and finally density dependent consolidation. A robust calibration process for the model's 14 parameters is described, requiring extreme densities of the sand, three isotropic tests, three drained tests, and two cyclic undrained stress-controlled tests. The calibration is complemented by a sensitivity study, exploring the impact of each parameter on model performance.

HySand_base is validated against a wide range of triaxial tests on different sands, with varied densities, pressure conditions, drainage conditions, consolidation, and loading histories. The model performs well for all types of triaxial tests, capturing the observed variations of capacity, stiffness, and volumetric behaviour. HySand_base is a compromise between performance and simplicity, and further options are proposed to improve the model performance, for example to increase the contraction on load reversal. Finally, the thesis presents an implementation of HySand_base in FE software, to explore simple boundary value problems, and demonstrating the value of the model to future design processes.

Acknowledgements

I would first like to thank my supervisors Byron Byrne and Guy Houlsby for their crucial advice and help in defining the contours and intricacies of my thesis. I would especially like to thank Guy for his invaluable scientific guidance on all aspects of soil mechanics, notably in hyperplasticity, and for deeply interesting conversations throughout my DPhil. I would also like to thank Jenny and Guy for most enjoyable times in Barhill. I am highly grateful for Byron's directions to navigate through the different phases of my DPhil and for the group spirit he has injected into the REMS CDT.

I would also like to thank Prof. Wichtmann and Dr Duque for sending me additional data.

I am grateful to Ørsted for funding this DPhil as part of the PICASO project.

I was extremely lucky to be part of the civil engineering group at Oxford, where academics, students and other staff concoct an ideal joyful and peaceful atmosphere for both work and breaks in Jenkin 11, the Wallis room and beyond. I am also very thankful to have been part of the REMS CDT with its enthusiastic atmosphere, stimulating discussions, and mutual assistance, with special thanks to Sarah, Mark, Bohan, Wayne, Emily, Toby, Iona and Russell, as well as Cranfield and Strathclyde students.

I would also like to thank my family and friends from across the Channel, whose support and visits have painted my delightful time in Oxford in even brighter colours. Finally and foremost, I would like to thank Lucile for her invaluable support, as well as her technical and organisational advice which have shaped my thesis.

Contents

Chapter 1 Introduction....1
1.1. The role of offshore wind in the energy mix towards cleaner energy....1
1.2. Foundations of OWTs....2
1.3. Loading of offshore wind turbines and design requirements....3
1.4. Design of a monopile under monotonic loading....4
1.5. Design of a monopile under cyclic loading....6
1.6. The PICASO project....7
1.7. Structure of the thesis....8

Chapter 2 Behaviour of sand and modelling approaches....10
2.1. Background on sand and testing....10
2.1.1. A granular material....10
2.1.2. Drainage....11
2.1.3. Methods to observe the behaviour of sand and modelling scales....12
2.2. The behaviour of sands....13
2.2.1. Triaxial variables....13
2.2.2. General behaviour of monotonic tests....13
2.2.3. Cyclic loading....15
2.2.4. A material with memory: the impact of preloading....19
2.3. Modelling of sand....26
2.3.1. Hypoplastic models....26
2.3.2. Bounding surface models....28
2.3.3. Elasto-plastic models with multiple surfaces....32
2.3.4. Choice of the theory for further developments....34

Chapter 3 Theoretical construction of HySand....39
3.1. Hyperplasticity: a robust and sound theoretical framework....40
3.1.1. Origins and thermodynamical basis....40
3.1.2. From hyperplasticity to plasticity....41
3.1.3. Constraint equations....44
3.1.4. Parallel works....44
3.2. Triaxial construction....45
3.2.1. Benchmark tests by Wichtmann....48
3.2.2. A frictional model with perfect plasticity and no volumetric plasticity....51
3.2.3. Dilation constraint....55
3.2.4. Asymmetrisation of the yield surface....58
3.2.5. Introducing density dependence....61
3.2.6. Anisotropy and its impact on volumetric strain....64
3.2.7. Non-linear elasticity....73
3.2.8. Consolidation plasticity....77
3.2.9. Base monotonic model with updated density dependence....87
3.2.10. General base model: Multi-surface....92
3.2.11. Options for more advanced models....101
3.3. Generalising to 3D....106
3.3.1. Non-linear elasticity in 3D....106
3.3.2. Matusoka-Nakai yield criterion....106
3.3.3. Generalisation of anisotropy....107
3.3.4. Generalisation of dilation....108
3.3.5. Generalisation of consolidation....109
3.3.6. Translation to multi-surface....109
3.3.7. Comparing 2D and 3D results....110
3.4. Numerical implementation....111

Chapter 4 Calibration process for the base model 114
4.1. Sensitivity study: Impact of the variation of parameters 114
4.1.1. Effects of the variation of parameters on monotonic tests 115
4.1.2. Effects of the variation of parameters on cyclic undrained tests 120
4.1.3. Summary 128
4.2. Initialisation of tests 129
4.2.1. Isotropic fabric 129
4.2.2. Anisotropic fabric 129
4.2.3. Overconsolidated sample 129
4.3. Calibration process 130
4.3.1. Characteristic specific volumes: Δ and B 131
4.3.2. Isotropic tests: k_r, m, λ_B, λ_Δ 131
4.3.3. Drained tests: Γ, φ_c, β_{LB}, A_{max} 134
4.3.4. Undrained cyclic tests: g_r, h_0, b and r 137
4.4. Optimisation routine 142
4.4.1. Error function f_{err} 143
4.4.2. Running the optimisation routine 145
4.4.3. Alternative use of the optimisation routine 150
4.5. Conclusion of the calibration process 150

Chapter 5 HySand_base results 151
5.1. Simulation of the Wichtmann database 151
5.1.1. Critical state line 152
5.1.2. Stiffness degradation with strain 152
5.1.3. Isotropic tests 152
5.1.4. Oedometric tests 153
5.1.5. Monotonic drained tests 155
5.1.6. Monotonic undrained tests 157
5.1.7. Cyclic stress controlled tests 160
5.1.8. Cyclic strain controlled tests 169
5.1.9. Drained tests with unloading reloading 173
5.1.10. Special tests 175
5.1.11. Conclusions for Wichtmann data 178
5.2. Adamidis data 179
5.2.1. Initial anisotropy of the samples 179
5.2.2. Calibration 180
5.2.3. Isotropic tests 180
5.2.4. Monotonic drained tests 180
5.2.5. Cyclic stress-controlled tests with no inflow 181
5.2.6. Cyclic stress-controlled tests with inflow 184
5.2.7. Conclusions for Adamidis data 186
5.3. Other qualitative comparisons 187
5.3.1. Hostun sand 187
5.3.2. Fuji river sand 196
5.3.3. Toyoura sand 201
5.4. Characteristic limitations of constitutive models for cyclic loading of sand 205
5.4.1. Overshooting after small unloading/reloading 205
5.4.2. Strain accumulation during cyclic mobility for a symmetric loading 207
5.4.3. Cyclic liquefaction strength curves 208
5.4.4. Dense sample liquefaction in undrained cyclic strain controlled tests 210
5.4.5. Accumulation of strain on small closed loop cycles 211
5.4.6. Oedometric stiffness and over/undershooting 213
5.4.7. Influence of preloading 214
5.4.8. Conclusion 216

5.5. Storm data series 217
5.6. Conclusions on HySand_base performance 218
5.6.1. Tests summary 218
5.6.2. Initial anisotropy 221
5.6.3. Perspectives 221

Chapter 6 Implementation of HySand into finite element codes 222
6.1. Implementation scheme 222
6.1.1. Inputs and outputs 222
6.1.2. Structure of Hyper_FEA 222
6.1.3. Implementation of a specific model 223
6.1.4. Numerical scheme 223
6.1.5. Use in PLAXIS 224
6.2. Triaxial tests in PLAXIS 224
6.2.1. Drained test TMD7 224
6.2.2. Undrained test: TMU2 225
6.3. Cavity expansion 225
6.4. Circular footing 227
6.5. Conclusions on the finite element implementation 228

Chapter 7 Conclusions 229
7.1. Introduction 229
7.2. Key contributions 230
7.3. Implications for design 232
7.4. Future work 233
7.5. Overview 234

Nomenclature

This thesis uses effective stresses. For tensors in index notation, the Einstein summation rule is used.

Latin notation:

A	anisotropy rate parameter
A_0	first approximation of the maximum anisotropy rate development parameter.
a	anisotropy scalar
a_0	initial value of the anisotropy scalar
a_c	acceleration parameter used in the consistency condition
b	power exponent for hardening shear moduli in multi-surface plasticity
C	compliance matrix
C_a	anisotropic constraint
C_c	contraction constraint
C_d	dilation constraint
d	dissipation function, depending on strains and stress and internal variables rates
D	diameter of a monopile, or stiffness matrix
d_r	dilation rate, $d_r = \dot{\alpha_p}/\dot{\alpha_q}$ in triaxial space
D_{r_0}	initial relative density with log definition
e	void ratio
E	Young's modulus
f	free energy function, depending on strain and internal variables: $f(\epsilon, \alpha^{(n)})$
f_0	base natural frequency of an OWT
f_{1p}	rotational frequency
f_{3p}	passing blade frequency
f_a	factor for an hybrid anisotropy law
g	Gibbs energy function, depending on stress and internal variables: $g(\sigma, \alpha^{(n)})$
G	shear modulus (kPa)
G_s	Shear stiffness (kPa)
g_r	dimensionless shear modulus for non-linear elasticity
g_{sec}	secant stiffness
H	shear hardening modulus
H_B	horizontal force at the base of a monopile
H_G	horizontal force at the ground level for a monopile
h_0	base shear hardening factor
h	plastic modulus in bounding surface theory
K	bulk modulus (kPa)
K_0	coefficient of earth pressure at rest
k_r	dimensionless bulk modulus for non-linear elasticity
L	plastic multiplier, or embedded length of a pile
m	pressure power index for non-linear elasticity, or distributed moment along a pile
M	frictional ratio (in compression with a subscript c, in extension with a subscript e)
M_B	moment at the base of a monopile
M_G	moment transmitted to a monopile at the ground level
n	index corresponding to a yield surface/ internal variable
n_{int}	number of state variables in a hyperplastic model
n_y	number of yield surface
N_{liq}	number of cycles to liquefaction

p mean effective pressure, or distributed lateral load in the "$p-y$" method
p_0 initial mean effective stress
p_c consolidation pressure
p_{c0} initial consolidation pressure
$p_{N_{liq}}$ mean effective stress before liquefaction phase
p_r reference pressure (100kPa)
q shear stress, in triaxial condition $q = \sigma_1 - \sigma_3$
Q heat input
q_0 initial shear stress
q_c amplitude of shear stress cycles
S signum function, or entropy in Clausius-Duheim inequality
U internal energy
u pore pressure
$u_{30\%}$ pore pressure after a number of cycles equal to 30% of N_{liq}
v specific volume, $v = 1 + e$
v_0 initial specific volume
w weight for error functions
W work
y yield function, or lateral displacement for the "$p-y$" curves
y_0 current yield value of yield surface

Greek notation:

$\alpha^{(n)}$ n^{th} internal variable
β dilation ratio
β_{LB} lower bound of the maximal dilation ratio
β_c contraction ratio
β_d modified dilation ratio
β_{max} maximum dilation ratio
B loosest specific volume achievable for a given soil
Γ critical specific volume for a given soil
Δ densest specific volume achievable for a given soil
ϵ strain-like variable
ϵ_q^{amp} amplitude of a strain cycle
θ temperature
Λ constraint multiplier (in association with dissipation
λ slope of isotropic plastic compression in $\ln(v) - \ln(p)$ space or $\ln(v) - (p/p_r)^{1-m}$ space
λ_B slope of the loosest state consolidation line
λ_Δ slope of the normal consolidation line for the densest state
μ friction coefficient $\mu = \tan\varphi_c$
ν_{pr} Poisson's ratio
σ stress-like variable
σ_s threshold capacity in hypoplasticity
φ friction angle
φ_c critical state friction angle
ϕ_i functions serving as polynomial factors of hypoplastic constitutive relations
χ,$\bar{\chi}$ generalised stresses

Subscript:

a associated to anisotropy

c associated to contraction

d associated to dilation

err denoting error between data and simulation

H used for strains to designate logarithmic strains

p volumetric (for strains, generalised stresses, and internal variables in triaxial space)

p_c associated to the consolidation pressure

q deviatoric (for strains, generalised stresses, and internal variables in triaxial space)

W used for strains to designate linear strains

0 initial value

1 associated to major direction (for stress and strains in triaxial space)

3 associated to minor direction (for stress and strains in triaxial space)

Superscript:

e elastic

n indicating the association to the number of a yield surface ($y^{(n)}$) or of an internal variable ($\alpha^{(n)}$)

p plastic

Miscellaneous:

$\dot{t}$ the time differential of t

$\boldsymbol{t}$ bold denotes a tensor $\boldsymbol{t} = t_{ij}$

t_{ij}^T denotes the transpose of a tensor

t'_{ij} denotes the deviator of a tensor $t'_{ij} = t_{ij} - \frac{t_{kk}}{3}\delta_{ij}$

Tensor invariants (for tensor $\boldsymbol{t}$):

I_{1t} first invariant: $I_{1t} = \mathrm{tr}(\boldsymbol{t}) = t_{ii}$

I_{2t} second invariant: $I_{2t} = \frac{1}{2}\left(\mathrm{tr}(\boldsymbol{t}^2) - \mathrm{tr}^2(\boldsymbol{t})\right) = \frac{1}{2}\left(t_{ij}t_{ji} - t_{ii}t_{jj}\right)$

I_{3t} third invariant: $I_{3t} = \det(\boldsymbol{t}) = \det(t_{ij})$

J_{2t} second invariant of deviator: $J_{2t} = I_{2t'} = \frac{1}{2}\mathrm{tr}(\boldsymbol{t}'^2) = \frac{1}{2}t'_{ij}t'_{ji}$

Acronyms:

OWT offshore wind turbine

OCR overconsolidation ratio

FE finite element

FEA finite element analysis

FEM finite element method

PICASO PIle Cyclic Analysis project

PISA PIle Soil Analysis project

Wichtmann's test notation:

ISO isotropic test

OE oedometric test

OEC cyclic oedometric test

TCUI undrained cyclic stress-controlled triaxial test with isotropic consolidation

TCUA undrained cyclic stress-controlled triaxial test with anisotropic consolidation

TCUE undrained cyclic strain-controlled triaxial test

TMCD drained triaxial test with unloads and reloads

TMCU undrained monotonic triaxial test and additional cycles

TMD drained monotonic triaxial test

TMU undrained monotonic triaxial test (for air pluviated samples, -MT for moist tamping)

Chapter 1 Introduction

In this introduction, the motivations for the modelling of sand under cyclic loading are explained. The importance of offshore wind in the future global energy mix is first highlighted, then offshore wind turbines (OWTs), their foundations, and the nature of the loadings to which they are submitted are described. Next, recent advances on the design of monopile foundations under monotonic lateral loading in sands and clays are displayed, and, finally, the lack of proper design method for monopiles under cyclic loading in sand is shown.

1.1. The role of offshore wind in the energy mix towards cleaner energy

The necessary transition from fossil fuels to renewable energies to limit global warming motivates the development of new production modes. Offshore wind energy plays a key role in the transition strategy of a number of countries, with ambitions for growing capacities.

In its "British Energy Security Strategy" report of April 2022 (United Kingdom Government (2022)), the objective of the United Kingdom is 50GW of installed capacity by 2030, of which 45GW would be bottom founded structures.

In France, the objective is to produce more than 40% of electricity from renewable sources by 2030. As part of its strategy, the French government aims an installed offshore wind capacity of 2.4GW by 2023, and 5GW by 2028. (Ministère de l'écologie français, 2022)

At the European Union level, in order to reach climate neutrality in 2050, the European Commission estimates it is possible to reach 300GW of installed offshore wind capacity by 2050, requiring 800G€ of investment. (European Commission, 2020)

Cumulative offshore capacity in the European Union currently amounts to 15.6GW, representing 2% of the electricity demand. The cumulative offshore capacity in the UK currently amounts to 12.7GW, representing 12% of the electricity demand. (Wind Europe (2021a)).

In order to reach the targets fixed at the national and community level, the rate of installation of new offshore wind parks needs to increase. This is illustrated for the following years in Europe by the graphic presented in Figure 1.

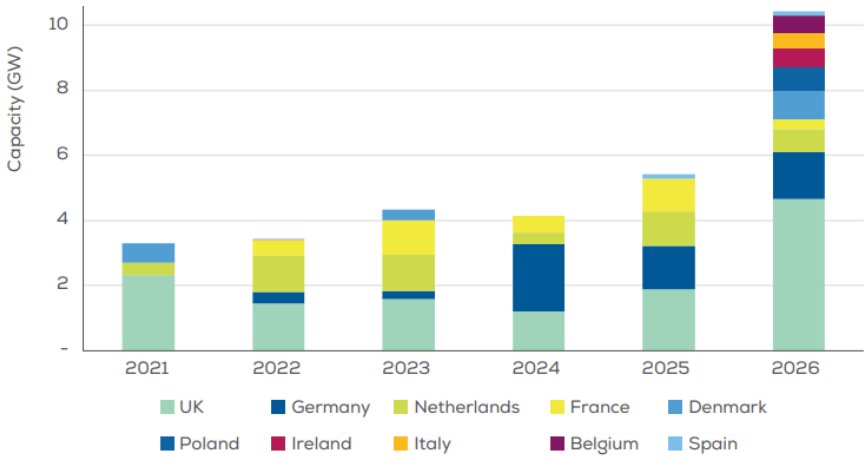


Figure 1 Expectations for new offshore installations per country in Europe over the period 2022-2026, by (Wind Europe (2021))

Offshore wind installation is also rapidly growing outside of Europe, in China, Japan, Taiwan, and the United States of America among others. For example, China has installed 16GW of new offshore wind capacity in 2021, and new bids all along the coast are being developed and awarded (Dutch Ministry of Foreign Affairs, 2022).

1.2. Foundations of OWTs

An OWT is composed of a foundation system, a tower, a nacelle, a rotor, and blades. Figure 2 presents different bottom-fixed foundation types. 81% of bottom-founded OWTs (Wind Europe (2021b)) use a monopile foundation, a large open-ended steel tube usually impact-driven into the ground, although vibratory driving techniques are under study (e.g. Tsetas *et al.* (2023)).

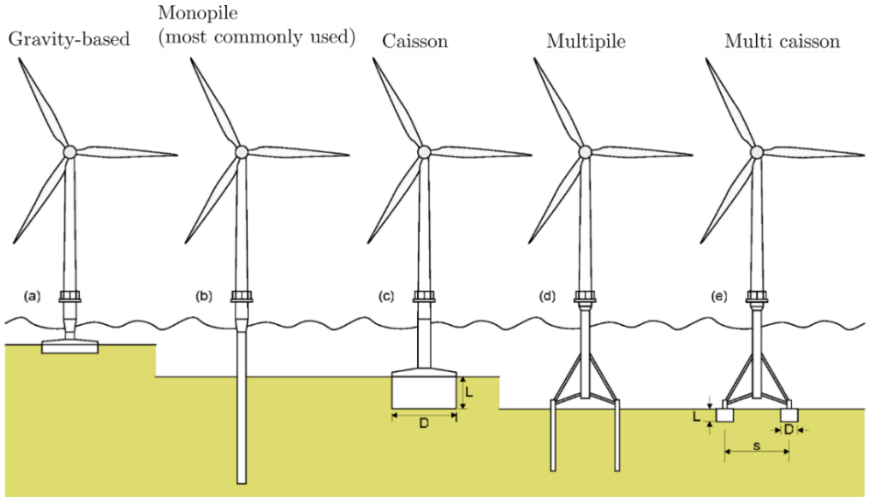


Figure 2 Different types of fixed-bottom foundations of OWTs (from Byrne and Houlsby (2006))

The success of the deployment of offshore wind power resides in the ability to drive down costs and finding adequate sites for new wind farms. Foundations account for up to 35% of the installation cost (Byrne and Houlsby (2004), Bhattacharya (2019)), and optimising their design could thus lead to significant savings.

The size, and thus capacity, of OWTs are increasing in order to harvest more power, and new sites in deeper water are considered. This implies an increase of the diameter and length of monopile foundations, with common dimensions now 8 to 10m in diameter, and 30 to 40m embedded length, and these are bound to increase for the next generation of OWTs in deeper water (Byrne (2020)).

1.3. Loading of offshore wind turbines and design requirements

OWTs sustain a multitude of loadings: their own weight, wind (both on the blades and tower), waves and current, accidental loads, and loads due to their own operation because of the rotation of the blades, rotor and mechanical pieces in the gearbox. This is illustrated in Figure 3.

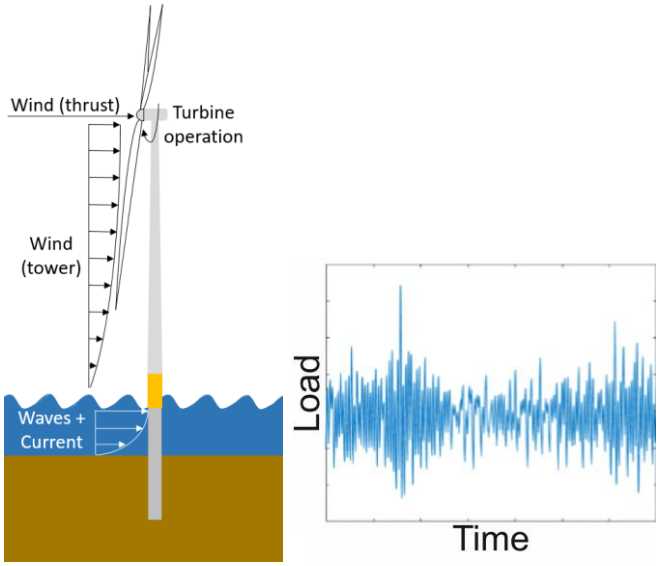


Figure 3 Left: Schematic of the loadings on an OWT; right: pseudo-random distribution of the loading

The horizontal loadings are the drivers of the design of the foundation, contrarily to the oil and gas industry where vertical loading (the weight of the platform) is predominant. The horizontal loading is pseudo-random cyclic, with different frequencies for the waves, the wind, and the rotation of the blades. The OWT system should be designed in order to avoid these frequencies, as illustrated in Figure 4.

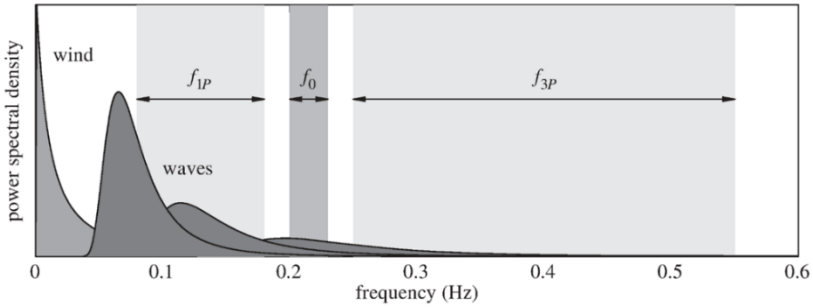


Figure 4 Frequencies of wave and wind loading, superposed with the fundamental frequency of the OWT system (f_0), the rotational frequency (f_{1p}), and the blade-passing frequency (f_{3p}) (from Kallehave et al. (2015))

The prediction of the monopile dynamic response (its stiffness, and its damping) is thus essential. Besides avoiding resonance effects, the design of a monopile should guarantee that the rotation at the mudline does not exceed a conventional value of 2° for Ultimate Limit State (Byrne *et al.* 2017), and a permanent accumulated rotation of 0.25° for Serviceability Limit State (DNVGL (2016)).

1.4. Design of a monopile under monotonic loading

The "$p-y$" method is recommended by design standards (API (2011), DNVGL (2016)) for the design of monopiles under lateral loading. In this method, the system is modelled with the Winkler assumption (assuming that soil reactions only depend on the local displacement and rotation): the monopile is modelled as an elastic beam, while the lateral soil reaction is modelled by a discrete distribution of non-linear springs whose force-displacement relation is defined by "$p-y$" curves. This is pictured in Figure 5.

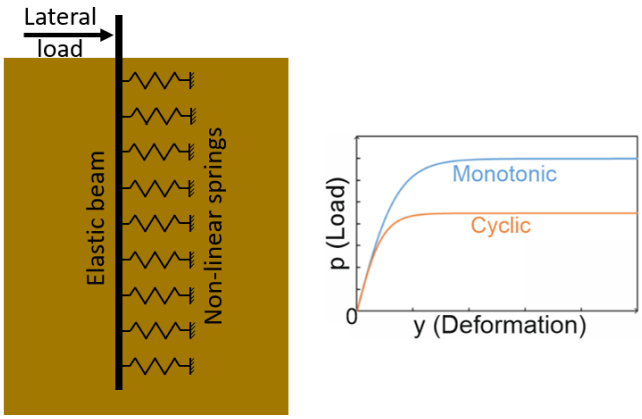


Figure 5 Illustration of the $p-y$ method. Left: spring distribution along an elastic beam; right: typical $p-y$ curves.

This method has its roots in the work by Matlock (1970) and Reese *et al.* (1974) and in field testing conducted by Matlock (1970) and Cox *et al.* (1974) for long slender piles used for the oil and gas industry. Doherty and Gavin (2012) have shown that the "$p-y$" curves designed during these works, and recommended by standard guidelines, are inappropriate for the design of monopiles for the offshore wind industry which present larger diameters, and length to diameter ratio less than 6. This is such that DNVGL (2016) advises to validate conventional "$p-y$" curves with, for example, finite element analyses for monopiles with diameters more than 1m.

The original "$p-y$" method is progressively being supplanted by the PISA design model for OWT monopiles in clays (Byrne *et al.* (2020a)), sand (Burd *et al.* (2020a)), and layered soils (Burd

et al. (2020b)). Like the conventional "$p - y$" method, the PISA design model uses a one-dimensional model with a Winkler assumption, dividing the monopile, modelled with Timoshenko beam theory, into multiple sections. The PISA design model not only considers the lateral soil reaction, but also includes the vertical shear tractions along the pile (modelled as distributed moments in one dimension), the horizontal force and the base moment at the pile base. This is illustrated in Figure 6.

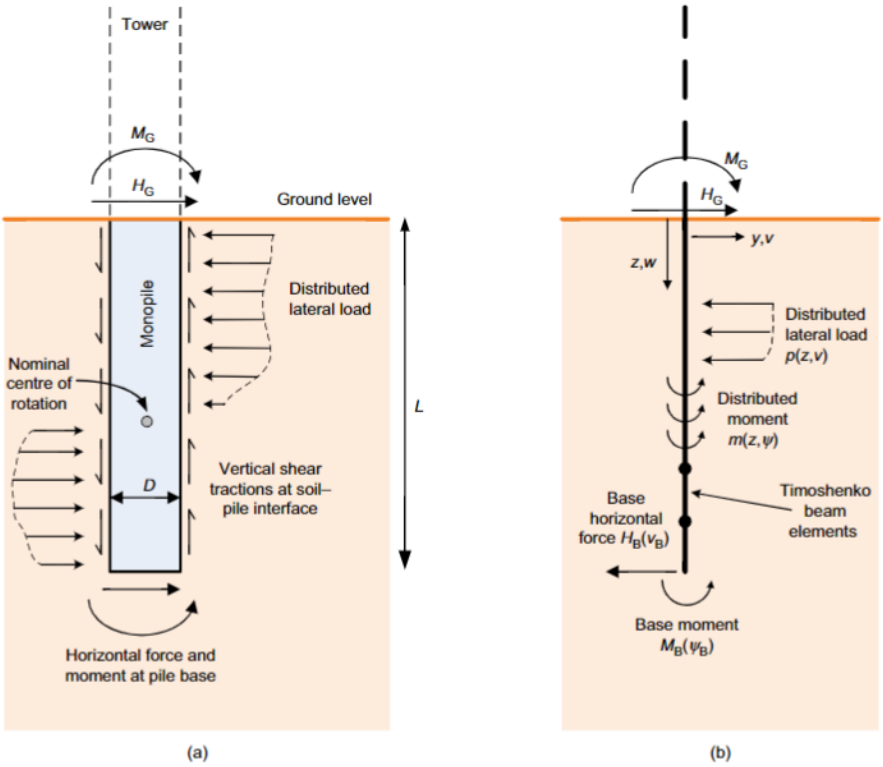


Figure 6 PISA design model from Burd et al. (2020a): (a) idealisation of the soil reaction components on the pile; (b) 1D finite-element implementation of the model showing the soil reactions acting on the pile M_G and H_G are the moment and horizontal load born from the loading of the OWT at the mudline

These four soil reactions are idealised with one type of conic function, defined by four parameters, as shown in Figure 7.

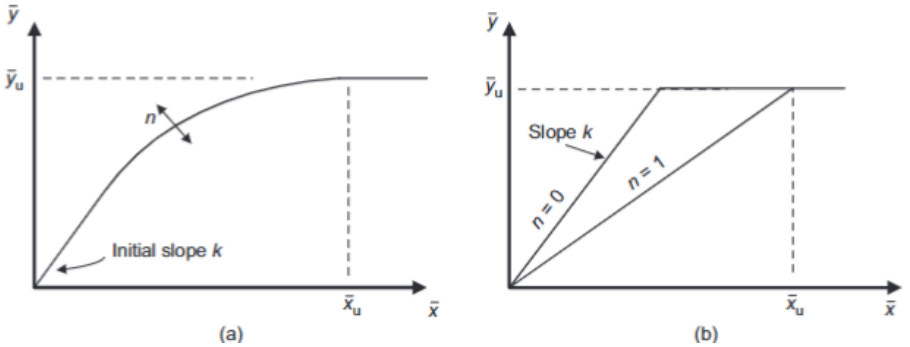


Figure 7 Conic function adopted for the parametric soil reaction curves in the PISA design model: (a) conic form; (b) bilinear form for extreme case $n \in \{0,1\}$ *(from Burd et al. (2020))*

A large number (38 in the case of the original PISA design model for Dunkirk sand, Burd *et al.* (2020a)) of three-dimensional finite element analysis were conducted to cover the whole design space. In the case of Dunkirk sand by Burd *et al.* (2020a), this includes four different initial relative densities (45%, 60%, 75% and 90%), three different diameters (5m, 7.5m and 10m), and two length to diameter ratios (2 and 6). The finite element analyses are presented in Zdravković *et al.* (2020) for clays and in Taborda *et al.* (2020) for sand.

The soil reactions are extracted from these finite element analyses in 30 points along the pile, and at its base. The conic yield functions are then calibrated for each soil reaction obtained from the finite element analysis, and the depth and density dependences of the four conic parameters are established. These dependences are idealised as linear or constant. The four calibrated conic functions so obtained can then be used in the one-dimensional Winkler type model across the design space. The global results from the one-dimensional models are in very good agreement with the global results from the three-dimensional finite element analysis, despite disparities in the local results (Burd *et al.* (2020)).

Once calibrated, the one-dimensional model allows for an optimised and fast design of large wind farms where each turbine encounters location-specific conditions. Manceau *et al.* (2019) have shown that this optimised and fast design method has contributed to significant cost reduction.

In order for the PISA design model to be successful, it is essential that the finite element modelling covers adequately the design space, represents well the foundation system, and also that the adopted constitutive model is capable of representing well the soil behaviour.

1.5. Design of a monopile under cyclic loading

For sand (Burd *et al.* (2020)), the model by Taborda *et al.* (2014) has been estimated to provide an adequate representation of sand behaviour under monotonic loading, but there is no guarantee that this is the case for cyclic loading.

Indeed, the cyclic loading behaviour of sand is complex: it is necessary to capture the changes in stiffness, strength and damping, and to estimate the permanent accumulated deformation. This is illustrated in Figure 8.

In the conventional "$p - y$" method, cyclic loading is only modelled by a homothetic reduction of the "$p - y$" curve, as seen in the right graphic of Figure 5, which is based on little evidence on slender piles by Cox *et al.* (1974), and does not capture the real effects of cyclic loading.

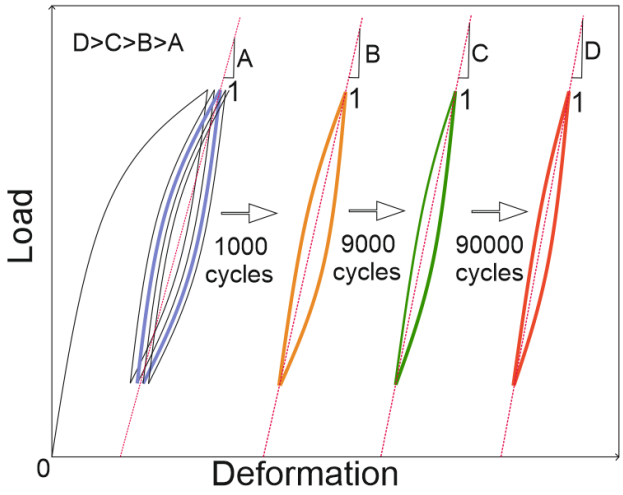


Figure 8 Idealised behaviour of sand under cyclic loading

While the PISA design model has optimised and put confidence in the design of OWTs under monotonic loading for ultimate limit state, no such work has been undertaken for cyclic loading. Because of the optimisation of the design under monotonic loading, the increasing size of OWTs and monopile foundations, and the deeper water they are founded in, serviceability and fatigue limit states have progressively become key drivers of the design of new monopiles. This is such that design under cyclic loading of monopiles has become a crucial gap in the knowledge to fill.

1.6. The PICASO project

The PICASO project (Byrne *et al.* (2020b)), a joint research project between the University of Oxford and Ørsted, has thus been launched to tackle the design of monopiles under cyclic loading. Its objective is to develop a fast and robust method of design of monopiles under cyclic loading.

The focus of the PICASO project is on short ($L/D < 5$), relatively rigid piles under pseudo-random loading. The PICASO project revolves around five work packages:

- Advanced foundation modelling: for an OWT park, finite element analyses should be conducted to cover its design space. New interpolation methods based on machine learning applied to a large number of simulations across the design space are under development to enable a faster and more reliable design process.

- Calibration methods: element testing is essential to calibrate constitutive models for numerical models. The PICASO project aims to fill the gap between cyclic element testing and design methods for cyclic loading, with a focus on ratcheting behaviour. Small-scale model testing is also used to explore the effects of multi-directional loading, as well as rate effects.
- Theoretical developments: the HARM approach (Houlsby *et al.* (2017)), notably able to model the ratcheting of the foundation and to depict its hysteretic behaviour, is under further development. Also, new constitutive models with a focus on cyclic loading are under development. This is the focus of this thesis.
- Medium scale field testing: nine 1.22 m and three 2.05 m diameter piles with $L/D = 3$ and a load application height of $4D$ are being tested at a clay site and a sand site, exploring rate effects, one-way and two-way cyclic loading, varying cycling amplitudes including pseudo-random amplitudes, across a wide range of numbers of cycles. These tests are predicted before the testing to assess the PISA and HARM design approaches.
- Application to design: a new design approach, adapted to the industry, is under development.

This thesis constitutes one part of the PICASO project.

1.7. Structure of the thesis

Because a finite element analysis requires constitutive models able to reproduce the soil behaviour it is trying to model, it is essential for the adopted models to capture the evolution of the soil reaction under cyclic loading. This thesis focuses on the behaviour of sand.

In the second chapter of this thesis, the behaviour of sand will be explained. Different families of constitutive models will be presented, and it will be shown that current advanced constitutive models for sand are not able to capture sand behaviour under cyclic loading and variable initial conditions. A new constitutive model is thus needed. The analysis of the behaviour of sand demonstrates the importance of the memory of this material, and in consequence the theoretical framework adopted for its modelling is multi-surface plasticity.

In the third chapter, after an introduction of hyperplasticity, a thermodynamically based theoretical framework, the progressive build-up in triaxial space of a new hyperplastic

constitutive model, HySand_base, is explained step-by-step. This construction starts from a very simple frictional model, and arrives at a simple 14 parameters multi-surface (capped-cones) model with density dependence (compatible with critical state theory), anisotropy dependent non-associated behaviour, and shear hardening. This model is generalised to three-dimensions, and the numerical scheme used to run simulations for one element is explained.

In a fourth chapter, the sensitivity of the model to the variation of its parameters is studied. Then, the calibration process of HySand_base is explained. It requires the determination of minimal and maximal densities of the sand of interest, and 8 triaxial tests: three isotropic, three drained, and two cyclic stress-controlled undrained.

In a fifth chapter, simulations with HySand_base are compared to numerous triaxial tests for a variety of sands. Results of calibrated HySand_base are compared to the large database of tests by Wichtmann (2021) on Karlsruhe fine sand, as well as tests on Hostun sand with water inflow by Adamidis and Anastasopoulos (2022). A large number of other triaxial tests are modelled without dedicated calibration, to assess qualitatively the capacity of HySand_base to model drained and undrained, monotonic and cyclic tests after various preloadings. Finally, HySand_base is compared to other advanced constitutive models by using the benchmark paper by Duque *et al.* (2022).

In a sixth chapter, the implementation of HySand_base into PLAXIS and Abaqus is explained, and results for simple boundary value problems in PLAXIS are displayed.

In the final chapter, the contribution of this thesis to the design of monopiles under cyclic loading in sand is presented, and perspectives for future work explained.

Chapter 2 Behaviour of sand and modelling approaches

In this chapter, the behaviour of sand at the mesoscale is explained, based on laboratory experiments. Existing constitutive models for sand are then presented, with emphasis on bounding surface, hypoplastic, and multi-surface models.

The limitations of bounding surface and hypoplastic models justify the construction of a new multi-surface constitutive model whose structure builds upon the behaviour described herein. The theoretical background of this model is presented in the following chapter.

2.1. Background on sand and testing

2.1.1. A granular material

Sand is a collection of solid particles with voids that can be partially or fully saturated by water. An idealised sand matrix is pictured in Figure 9.

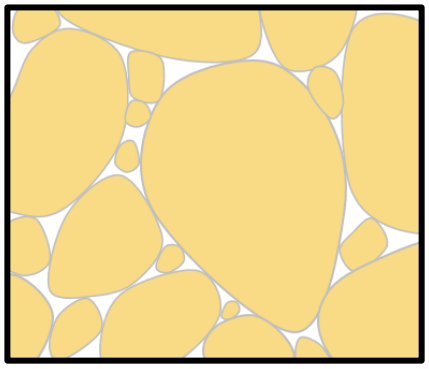


Figure 9 Idealistic representation of clean sand

These grains are characterised by their chemical composition, their sizes (and size distribution), their roundness, their roughness, their brittleness, and the eventual presence of bonding. One should note that these characteristics allow description of a clean sand, but consideration should be given to the presence of other particles (e.g. silt, clay, rocks) when considering a soil.

In this thesis, which focuses on offshore geotechnics applications, only the case of fully saturated sand is considered. The case of carbonate sands with high shell content (as encountered for example in Australia) is not considered, and the sand behaviour described hereafter is that of clean sand.

To describe the behaviour of this ensemble of particles at the mesoscale, continuum mechanics can be adopted. The sand is then treated as a continuous material. However, its granular nature

means that sand is anisotropic, but also that this anisotropy can evolve over time. Sand is a collection of non-spherical grains of diverse sizes, which means that the structure of the particle skeleton (its fabric) depends on how the grains were deposited, and on the stress it currently sustains and has sustained over its history.

The granular nature of sand, its brittleness, the non-roundness of the particles, and the presence of voids result in a complex volumetric behaviour. When a sand sample is subjected to stresses, the particles break up, rotate and roll over each other, filling or enlarging existing and new voids.

2.1.2. Drainage

Three drainage conditions can be encountered in the case of saturated sand: drained conditions where water is free to circulate and pore pressures do not increase; undrained conditions where water cannot circulate and where volumetric changes cannot take place, leading to changes of water pressure in pores; partially drained conditions where water can circulate through the pore matrix and volumetric changes take place, but not fast enough for there to be no change of pore pressures (less than would occur in undrained condition). A fourth condition can be considered in the case of seismic activity for a sand layer topped by a low-permeability soil layer. In this latter case, water can flow from the depth of the soil, but cannot drain through the low-permeability layer, leading to increased water pressures in the upper part of the sand layer (Adamidis and Madabhushi (2018)). In this fourth case, the condition is that of partial drainage, but with water inflow rather than the outflow presented previously.

For geotechnical problems involving sand, slow and small loadings can generally be treated as drained problems, but this is not the case for offshore wind turbine foundation problems. Indeed, Li *et al.* (2018) have shown that conditions can range from drained to undrained, including partially drained, around a monopile foundation of an OWT, depending on the load cases.

This means that a modelling approach for OWT foundations in sand should be able to capture all drainage conditions. This is also true for other problems involving cyclic or rapid loadings, such as earthquakes.

2.1.3. Methods to observe the behaviour of sand and modelling scales

Sand behaviour can be observed at different scales: the contact behaviour between two particles (e.g. Nardelli (2019)); the evolution of the fabric in a laboratory test observed with stereophotogrammetry or X-ray tomography (e.g. Desrues and Viggiani (2004), Andò *et al.* (2013)); the evolution of the strains, stresses, and pore pressure at a laboratory test scale (e.g. Wichtmann and Triantafyllidis (2016a,b)); the evolution of forces/moments and displacements/rotations for small scale models in the laboratory (e.g. Abadie (2015), Richards *et al.* (2019)); the evolution of forces/moments and displacements/rotations for larger scale models tested in the field (e.g. McAdam *et al.*, 2019).

These different testing techniques inform different levels of modelling, from the microscale to the macroscale. The finer the scale, the closer the modelling can be to physical behaviour, but also the more complex and diverse the phenomena are to observe and model, and the more computer intensive the modelling gets.

For these reasons, large scale problems sustaining millions of cycles such as monopile foundations of OWT cannot be modelled down to the microscale using, for example, the discrete element method (Cundall and Strack, 1979). It has been demonstrated through the results of the PISA project (Burd *et al.* 2020a) that a method using finite element analysis is appropriate for the design of monopile foundations under monotonic lateral loading. It is herein assumed that finite element modelling will also be of essence for the design of monopiles under cyclic lateral loading.

Finite element analysis (FEA) requires constitutive laws to model the soil. These laws should be representative of the behaviour of the soil at the element scale in the simulation, and of the stresses and strains experienced by the soil. Laboratory tests such as triaxial, shear, and torsional tests appear to be good candidates to characterise the behaviour of sand at the representative scale of the finer elements of an FEA and for small deformations.

Therefore, the development of the constitutive model in this thesis is based on laboratory tests on sand with a variety of initial conditions, loading directions, drainage conditions, and including cyclic tests.

2.2. The behaviour of sands

The following observations are based on triaxial tests on a variety of sands, with isotropic normal consolidation, unless otherwise stated. The observations are mainly illustrated by tests from the database on Karlsruhe fine sand by Wichtmann (2021).

2.2.1. Triaxial variables

In this thesis, all stress variables refer to effective stresses.

The following triaxial variables are used throughout the thesis:

Effective mean stress: $p = \frac{\sigma_1 + 2\sigma_3}{3}$ *Eq. 1* Deviatoric stress: $q = \sigma_1 - \sigma_3$ *Eq. 2*

Volumetric strain: $\epsilon_p = \epsilon_1 + 2\epsilon_3$ *Eq. 3* Shear strain: $\epsilon_q = \frac{2}{3}(\epsilon_1 - \epsilon_3)$ *Eq. 4*

Volumetric plastic strains: α_p & α_{p_c} Shear plastic strain: α_q

Logarithmic strains are used, such that the specific volume (v) is a function of the volumetric strain (ϵ_p) and of the initial specific volume (v_0):

$$v = v_0 e^{-\epsilon_p} \qquad \textit{Eq. 5}$$

2.2.2. General behaviour of monotonic tests

2.2.2.1. Drained condition

Figure 10 presents a typical drained test on dense sand (TMD17 by Wichtmann, 2021).

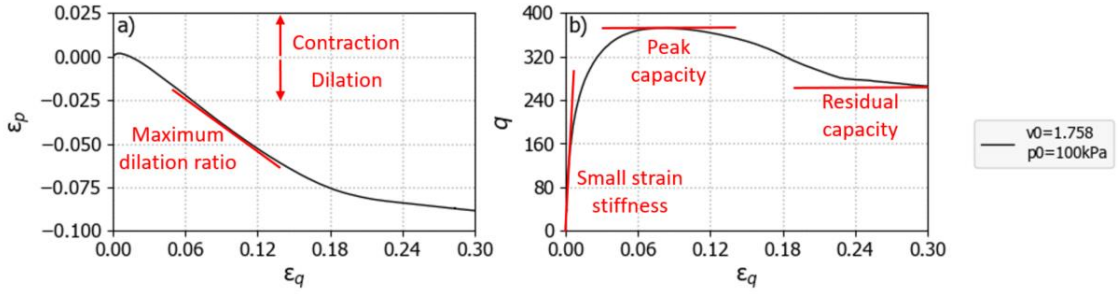


Figure 10 Drained test on a medium dense sand (adapted from Wichtmann, 2016a)

In the left-hand graph, representing the volumetric strain function of shear strain, the test begins with a short contractive phase, followed by a long dilative phase, until a stabilisation. In the right-hand graph, with shear stress function of shear strain, the stiffness progressively decreases until a peak capacity is reached, then softening ensues towards a residual capacity.

2.2.2.2. Undrained condition

Figure 11 presents a typical undrained test on medium dense sand (TMU3 by Wichtmann, 2021).

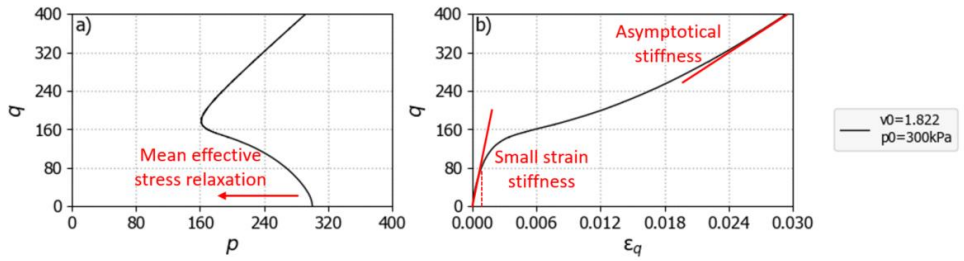


Figure 11 Undrained test on a medium dense sand (adapted from Wichtmann, 2021)

In the left-hand graph, representing the stress path, the test shows an initial phase of mean effective stress reduction: pore pressure builds-up because the sample cannot contract in undrained conditions. A dilative phase follows. In the right-hand graph, the stiffness progressively decreases, before a readjustment to an asymptotical stiffness occurs.

2.2.2.3. Impact of density

The initial density of the packing has a large influence on the behaviour of sand, the denser it is:

- the stiffer the initial response.
- the larger the maximum dilation ratio is, and the more dilation takes place in drained conditions; the less the mean effective stress relaxes under undrained conditions.
- the higher the peak capacity is under drained conditions.
- the steeper the stiffness asymptote is under undrained conditions.

This is illustrated for Karlsruhe fine sand monotonic drained and undrained normally consolidated tests by Wichtmann (2021) in Figure 12 and Figure 13.

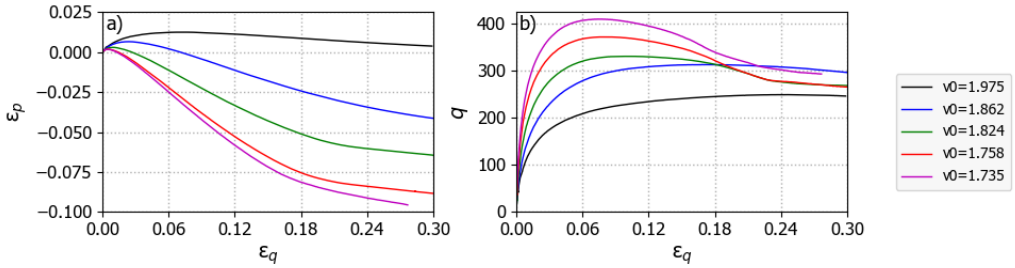


Figure 12 Drained tests on Karlsruhe fine sand by Wichtmann (2021) for different initial densities

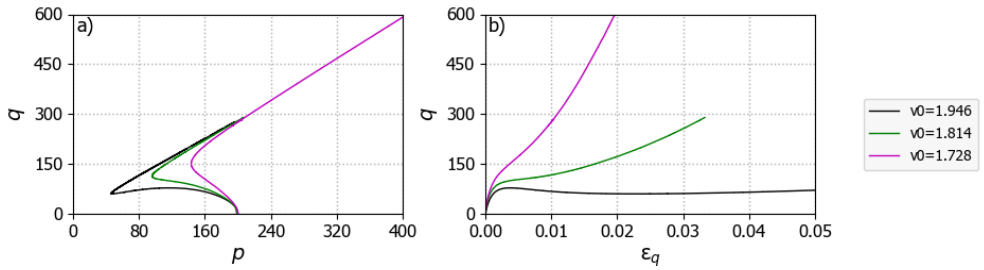


Figure 13 Undrained tests on Karlsruhe fine sand by Wichtmann (2021) for different initial densities

In Figure 14, which represents the same tests as in Figure 12, the convergence towards a similar specific volume and similar residual capacity are evidence of a critical state.

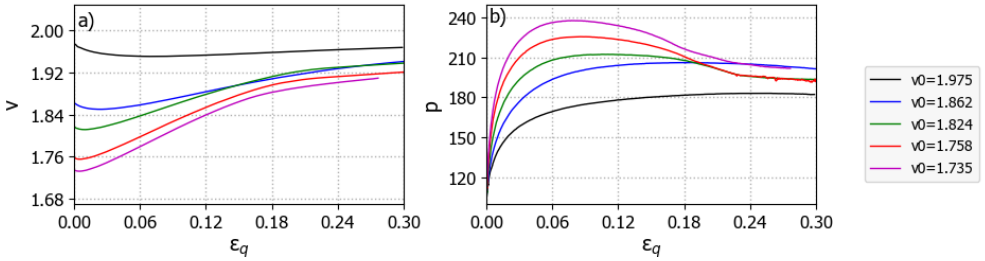


Figure 14 Same drained tests as in Figure 12, but representing the variation of v and p with ϵ_q

2.2.2.4. Impact of pressure

The higher the consolidation pressure is, the higher the stiffness is, and the slower the maximum dilation ratio is reached. The variation of other quantities is less significant. This is shown in Figure 15 and Figure 16 for drained and undrained condition on medium dense Karlsruhe fine sand (from Wichtmann (2021)).

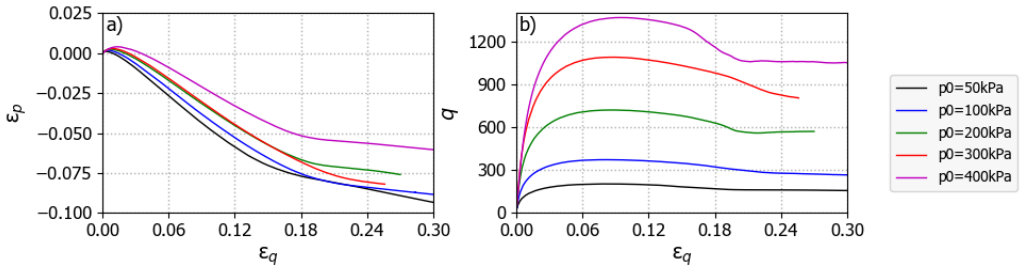


Figure 15 Drained tests on medium dense Karlsruhe fine sand by Wichtmann (2021) for different consolidation pressures

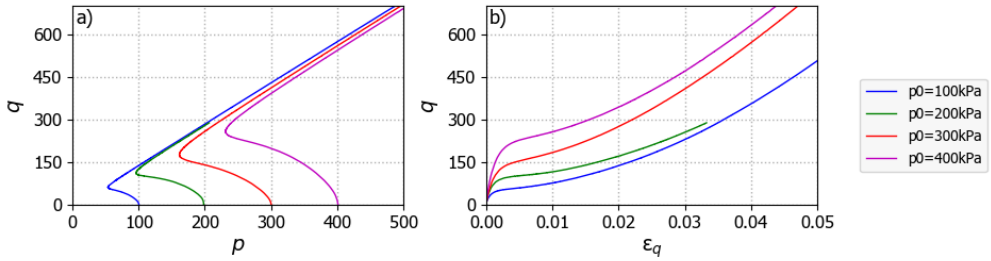


Figure 16 Undrained tests on medium dense Karlsruhe fine sand by Wichtmann (2021)

2.2.3. Cyclic loading

2.2.3.1. Stress-controlled undrained tests

2.2.3.1.1. Isotropic consolidation

An isotropically consolidated cyclic stress-controlled undrained test on medium dense sand (TCUI7 by Wichtmann (2021)) is presented in Figure 17.

In the top left-hand graph, the stress path shows a pattern of mean effective stress reduction common to all stress-controlled test: significant reduction during the first cycle, then reduction per cycle slows down, until it picks up again at lower mean effective stresses. A cyclic mobility phase, with butterfly-shaped stress loops, follows.

In the top right-hand graph, the shear stress-strain relation is pictured, with stiff cycles until large strains develop during the cyclic-mobility phase.

In the bottom graph, a zoom is made on the cycles before the cyclic-mobility phase. These cycles present a growing hysteresis and a lower secant stiffness as cycle number increases.

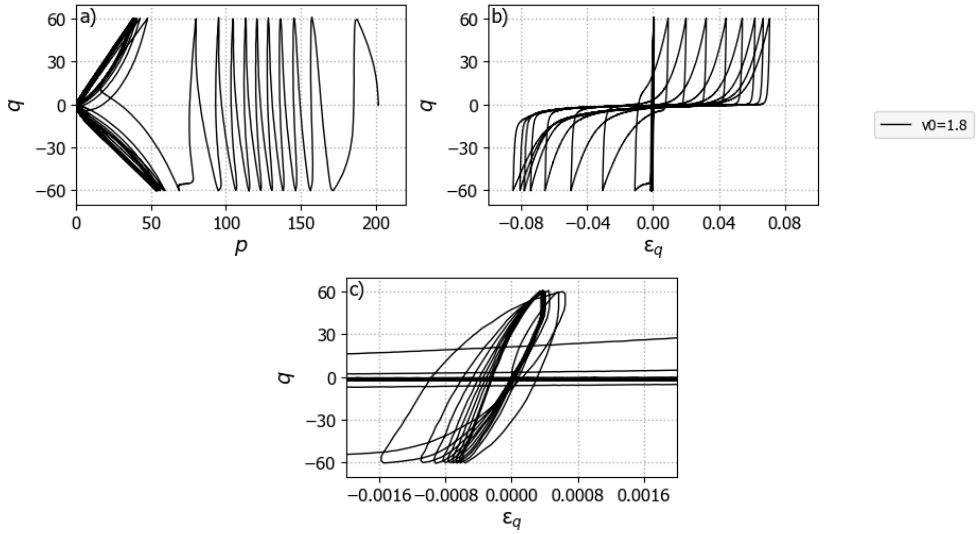


Figure 17 Cyclic undrained stress-controlled test on medium dense sand (by Wichtmann (2021))

For loose samples, such as shown in Figure 18, no cyclic mobility phase is observed.

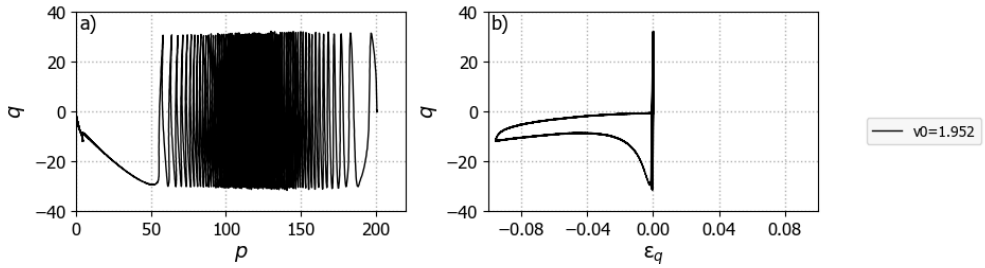


Figure 18 Cyclic undrained stress-controlled test on loose sand (by Wichtmann (2021))

The higher the shear stress amplitude, and the looser the sample, the lower the number of cycles required to reach liquefaction is.

2.2.3.1.2. Asymmetric loading

Figure 19 presents a cyclic stress-controlled one-way test on medium dense sand (TCUA6 by Wichtmann (2021)). The right-hand graph shows shear strain accumulation (ratcheting). The rate of accumulation progressively diminishes but never becomes zero.

In the left-hand graph, similar to two-way cyclic tests, there is initially an important pore pressure build-up, and the rate progressively decreases.

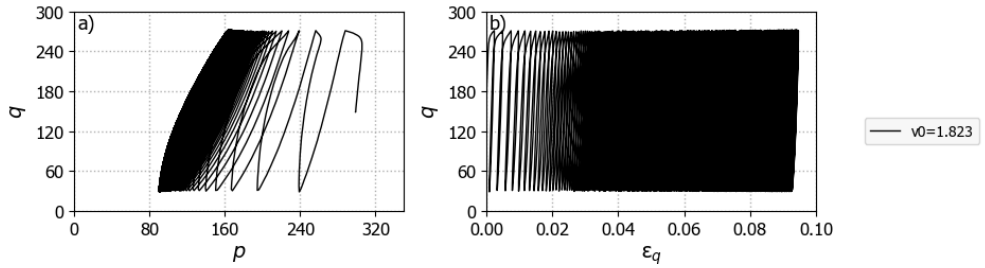


Figure 19 One-way undrained test on anisotropically consolidated medium dense sand (by Wichtmann (2021))

Contrary to two-way cyclic tests, one-way tests do not reach liquefaction, and stress loops stabilise away from $p = 0$, even when the minimum absolute shear ($|q|$) is null. However, partial two-way loadings reach liquefaction, such as TCUA16 shown in Figure 20.

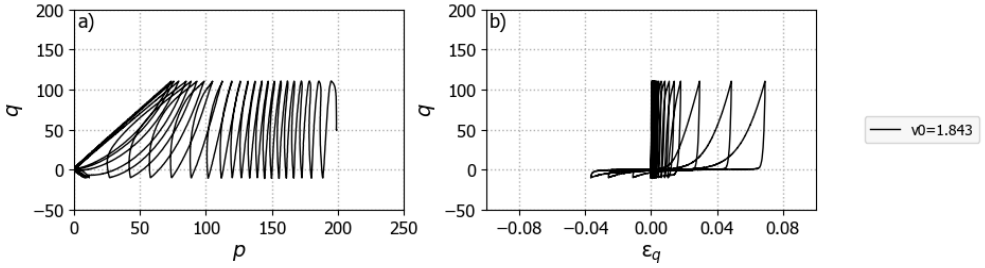


Figure 20 Anisotropically consolidated partial two-way undrained test on medium dense sand (Wichtmann (2021))

As with symmetric tests, this includes a final phase with an acceleration of the pore pressure build-up before reaching liquefaction, as seen in the left-hand graph.

2.2.3.2. Strain-control undrained

Figure 21 presents test TCUE9 by Wichtmann (2021), a strain-controlled isotropically consolidated undrained test on medium dense sand. In the left-hand graph, as with stress-controlled tests, the mean effective stress relaxation per cycle is initially large, before progressively slowing down, but it never becomes null such that liquefaction ($p = 0$) is reached. Interestingly, the shear stress amplitude first increases slightly in the first few cycles, before progressively decreasing with decreasing mean effective stress.

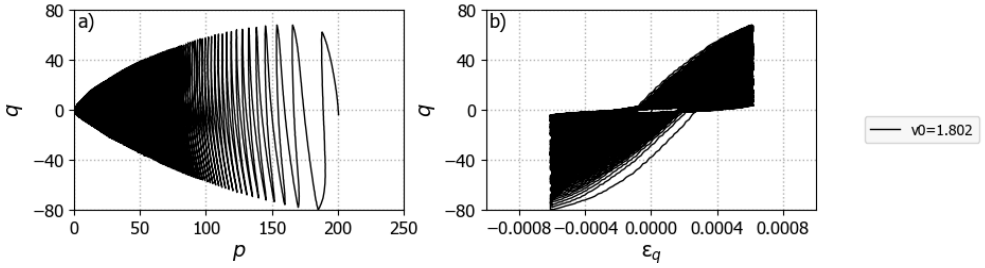


Figure 21 Cyclic undrained strain-controlled test on medium dense sand (by Wichtmann (2021))

As can be seen in test TCUE5 on medium dense sand by Wichtmann (2021) shown in Figure 22, anisotropic consolidation does not change the pattern of pore pressure build-up. The stress path tends to re-centre around $q = 0$ with decreasing mean effective stresses.

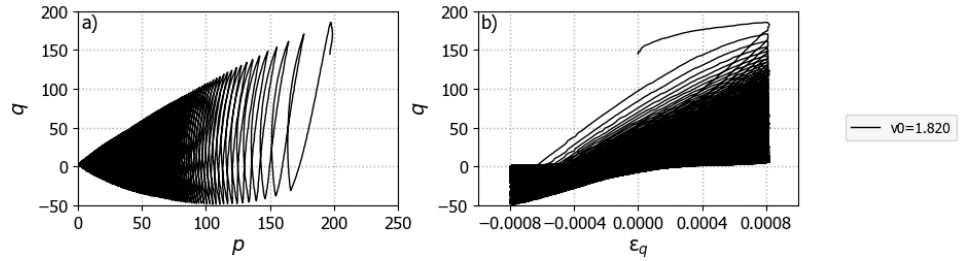


Figure 22 Cyclic strain-controlled test on anisotropically consolidated sand (by Wichtmann (2021))

Test TCUE17 on dense sand by Wichtmann (2021) with larger strains is shown in Figure 23. During each half-cycle, a dilative phase takes place, and on load reversal, an important mean effective stress reduction ensues. This last phenomenon more than compensates the dilative phases so that, even for a dense sample, the test reaches liquefaction.

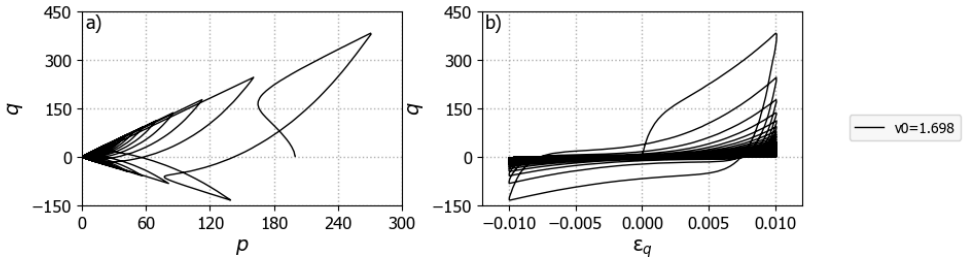


Figure 23 Cyclic strain-controlled test on dense sand with large strains (from Wichtmann (2021))

2.2.3.3. Drained tests

Cyclic drained tests are scarcer in the literature. Pradhan *et al.* (1989) have conducted a variety of cyclic drained tests on Toyoura sand. Figure 24 and Figure 25 present drained cyclic triaxial test with constant mean effective stress for loose and dense sand respectively.

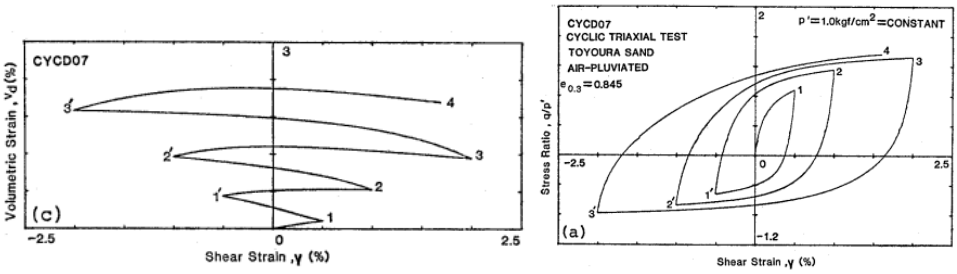


Figure 24 Cyclic drained tests with constant p for loose Toyoura sand (from Pradhan et al., 1989)

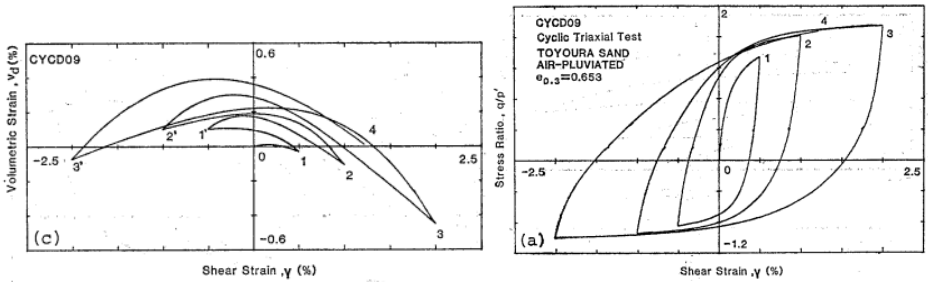


Figure 25 Cyclic drained tests with constant p for dense Toyoura sand (from Pradhan et al., 1989)

In the right-hand graphs, the stiffness upon load reversal is comparable to the initial stiffness, and during each half-cycle, this stiffness progressively decreases.

In the left-hand graph for loose sand (Figure 24), contraction increases cycle after cycle. However, one can observe that the dilation ratio is not constant throughout the half-cycles: when the absolute shear strain increases, the contraction decreases.

For monotonic tests on dense sand, dilation follows the initial contraction. In the left-hand graph of Figure 25, one can observe that an important contractive phase follows the initial dilative phase upon load reversal. In fact, after each load reversal, important contraction takes place, before being progressively compensated and dominated by dilation.

The database by Wichtmann does not comprise two-way cyclic drained tests. However, it does contain seven drained tests to large strains with intermediate unloadings-reloadings, e.g. Figure 26. The general developments of the capacity and dilation broadly follow the results of a monotonic test. Similarly to the test by Pradhan on dense sand, upon unloading, contraction takes place with a higher intensity than the preceding dilation.

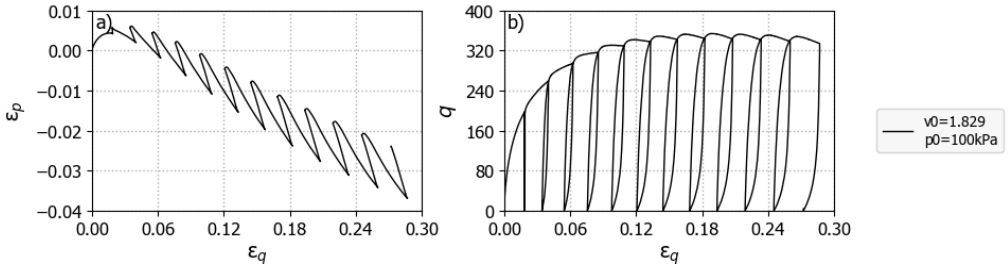


Figure 26 Drained test with unload-reloads on medium dense Karlsruhe fine sand (from Wichtmann (2021))

2.2.4. A material with memory: the impact of preloading

2.2.4.1. Overconsolidation

Figure 27 presents monotonic undrained tests on loose Karlsruhe fine sand by Wichtmann (2016c), for a normally consolidated sample (blue), and for an overconsolidation of OCR=8/3 (red). The initial pore pressure build-up is lower for the overconsolidated sample: the initial stress path curves toward increasing mean effective stresses. As a result, the strength at which the overconsolidated sample softens is higher than for the normally consolidated sample.

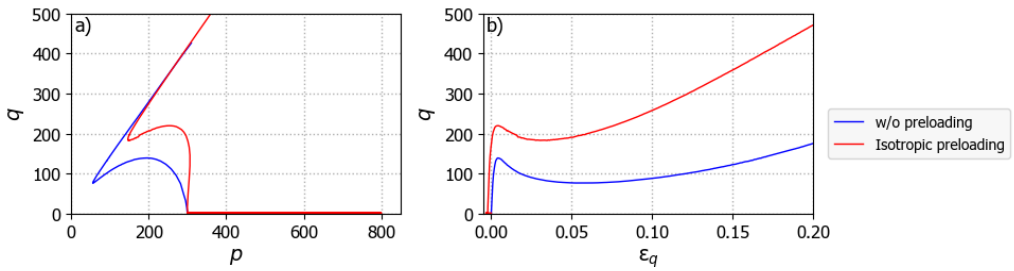


Figure 27 Impact of overconsolidation on monotonic undrained loading of loose sand (by Wichtmann (2016))

This behaviour can also be observed in tests on Fuji river sand by Ishihara and Okada (1978b) (c.f. Figure 28), and for Fontainebleau sand in tests by Dang *et al.* (2020) shown in Figure 29.

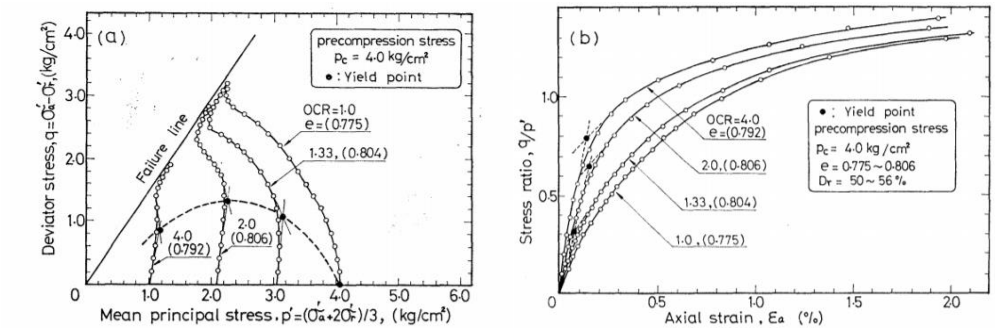


Figure 28 Influence of overconsolidation in undrained test on Fuji river sand by Ishihara and Okada (1978b)

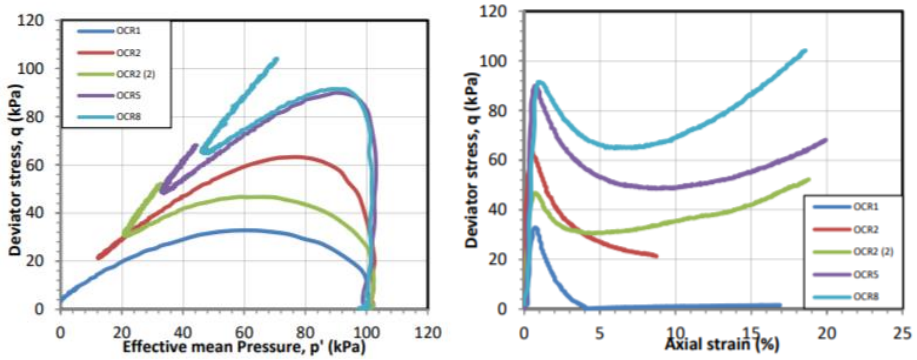


Figure 29 Effect of overconsolidation on loose Fontainebleau sand by Dang et al.

This behaviour also appears in tests conducted by Finge *et al.* (2006) on loose Hostun sand, as shown in Figure 30 for tests with initial mean effective stress of 50kPa and overconsolidation ratio spanning from one to eight. The effect seems to be the same for tests in extension.

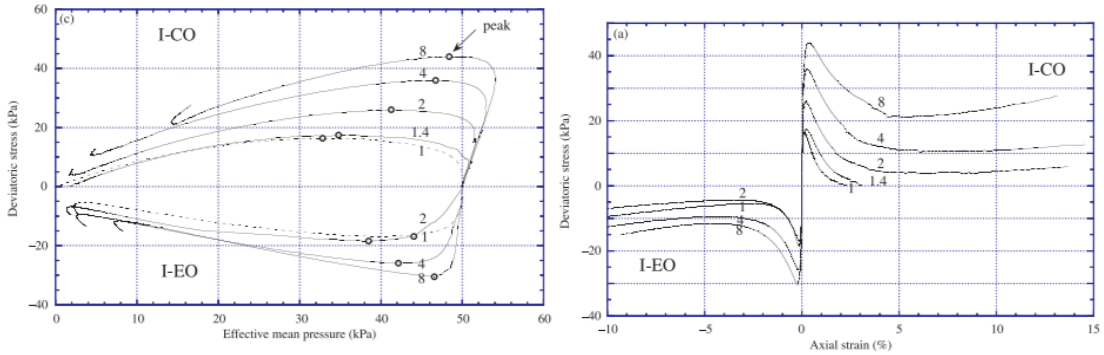


Figure 30 Impact of overconsolidation on undrained tests on loose Hostun sand by Finge et al. (2006)

Finge *et al.* (2006) have also conducted similar test for anisotropically ($K_0 = 0.5$) overconsolidated samples ($OCR \in [1,24]$), shown in Figure 31. All tests were anisotropically consolidated starting from an isotropic consolidation at 20kPa. The impact of the anisotropic overconsolidation on tests in compression is similar to the effect of isotropic consolidation, but with initial reloading curves orientated even more towards higher mean effective stresses. The effect on tests in extension is small and hard to evaluate.

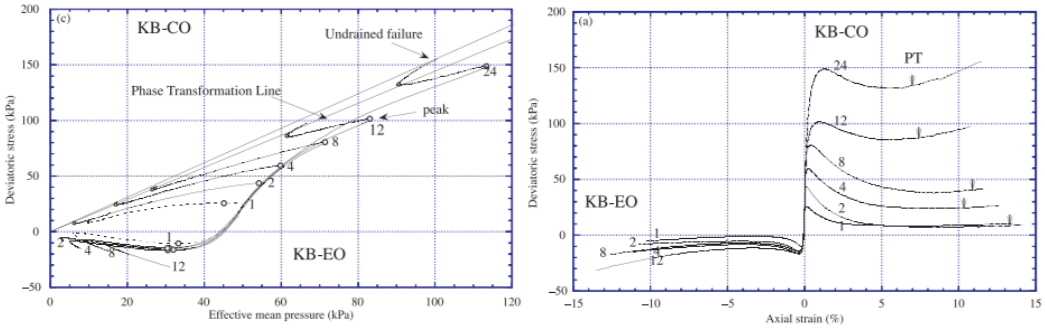


Figure 31 Impact of anisotropic overconsolidation on loose Hostun sand (from Finge et al., 2006)

Overconsolidation also has an important impact on undrained stress-controlled tests. This is shown in Figure 32 for the stress paths of tests on Fuji river sand by Ishihara and Okada (1978a). The larger the OCR, the lower the mean effective stress reduction on each cycle, and, thus, the higher the required number of cycles to liquefaction. Thus, overconsolidation does not only impact monotonic loading/the first half-cycle, but also the subsequent cycles.

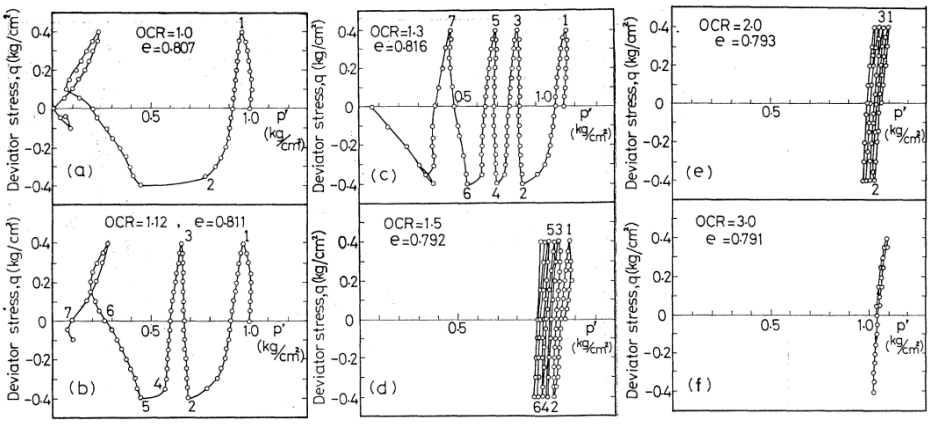


Figure 32 Overconsolidated cyclic undrained stress-controlled tests by Ishihara (1978b)

In summary, overconsolidation reduces the pore pressure build-up during the first monotonic loading as well as during further cycles, and increases the intermediate strength of the sample.

2.2.4.2. Preshearing

Wichtmann (2016) has studied the influence of a large drained preshearing in compression on the subsequent undrained loading in compression, as shown in Figure 33. During reloading, no pore pressure build-up is observed, and stiffness is very high, up to the maximum shear stress encountered during preloading.

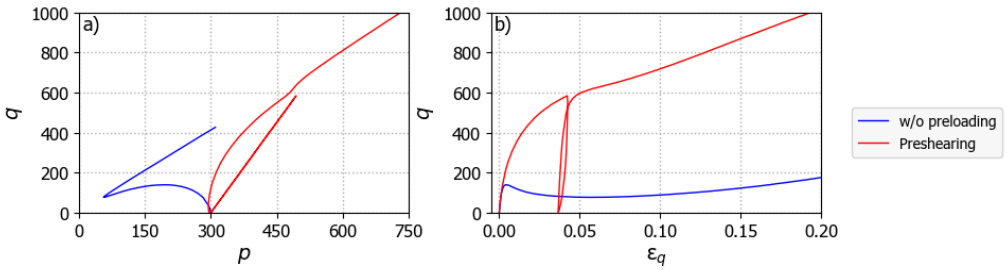


Figure 33 Influence of drained preshearing on undrained test on loose sand by Wichtmann (2016)

Gajo and Piffer (1999) have also studied the influence of drained shear preloading on subsequent undrained loading in compression, but varying the amplitude of the drained preloading, as shown in Figure 34. The larger the amplitude of the drained preloading, the higher and the more towards high mean effective stress the stress path goes.

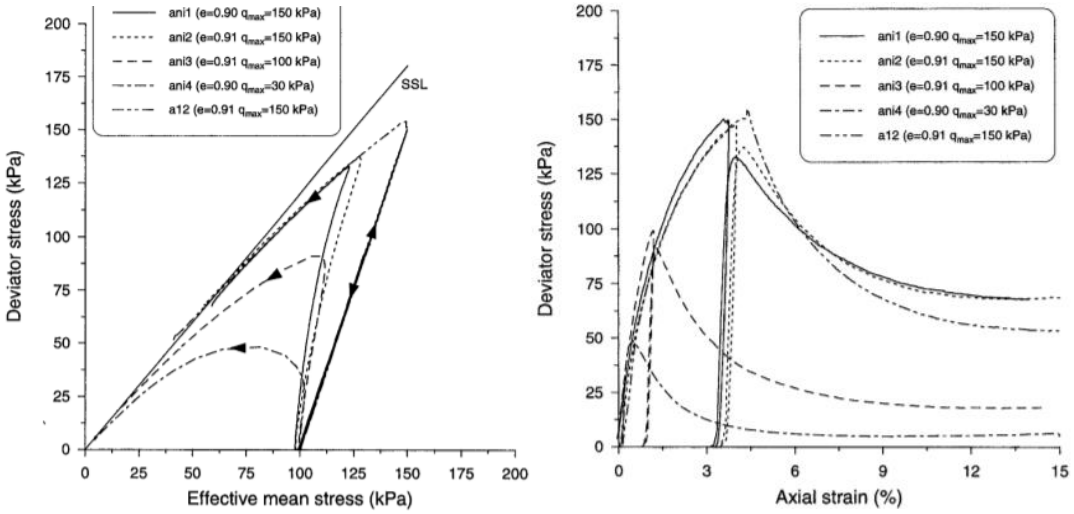


Figure 34 Influence of drained preshearing amplitude on subsequent undrained loading of very loose Hostun sand by Gajo and Piffer (1999)

Interestingly, if a multitude of drained load-unload cycles are conducted rather than a single cycle, the results only vary slightly, as shown in Figure 35 for one and sixteen cycles for very loose Hostun sand samples by Gajo and Piffer (1999).

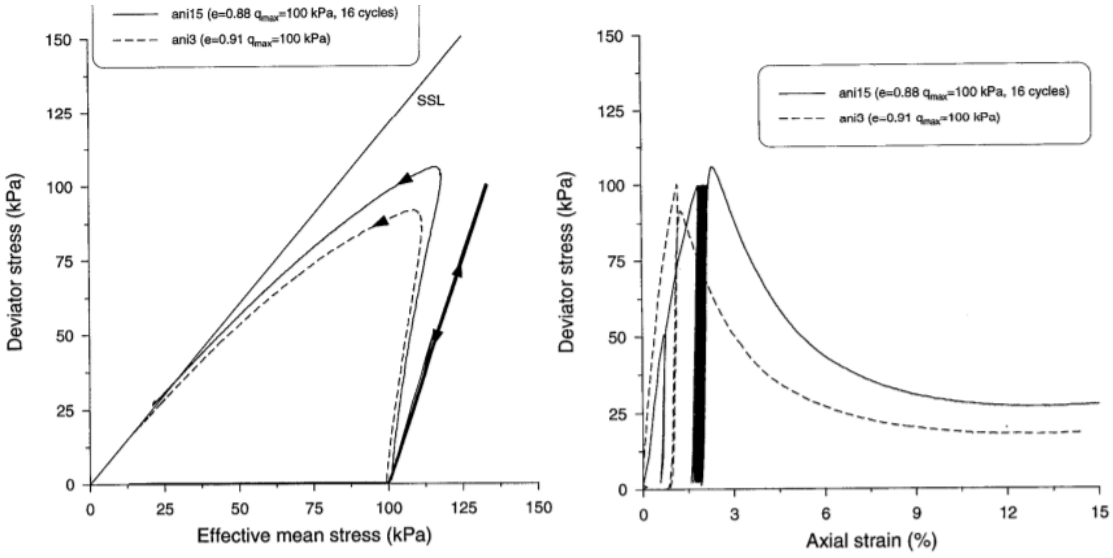


Figure 35 Influence of the number of drained preshearing cycles by Gajo and Piffer (1999)

Gajo and Piffer (1999) have also explored the influence of the direction of the drained preloading, as shown in Figure 36. For an equal stress ratio (q/p) reached during these preloadings, the more the direction is towards higher mean effective stresses, the less the pore pressure increases and the higher the peak capacity is.

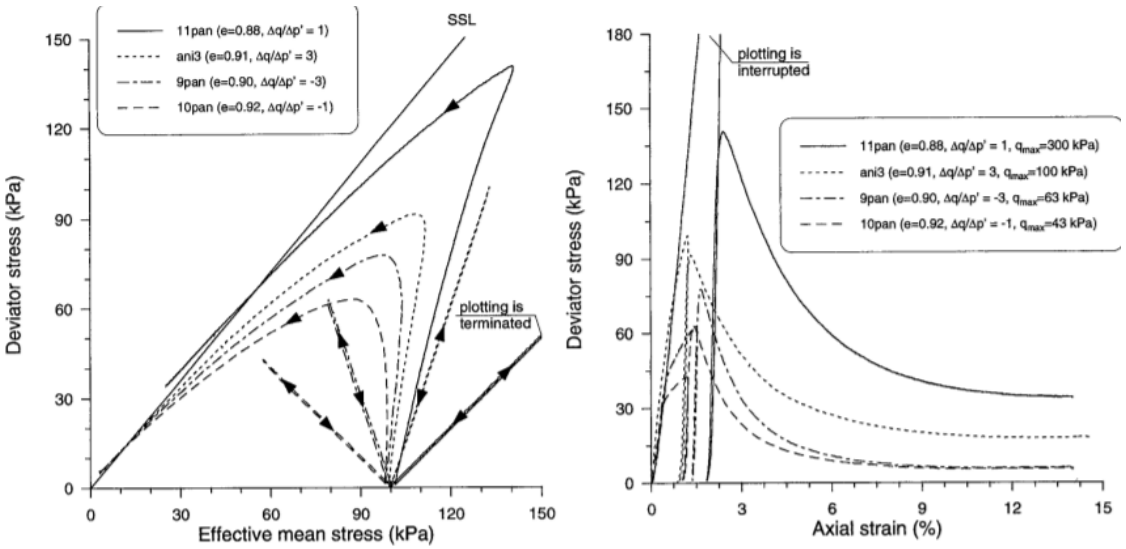


Figure 36 Influence of the direction of drained preloading by Gajo and Piffer (1999)

Gajo and Piffer (1999) have also conducted tests with undrained preshearing in compression before an isotropic reconsolidation, pictured in Figure 37. The undrained preshearing has a similar effect to the drained preshearing on the reloading in compression, with less pore pressure build-up and a higher peak capacity. On the contrary, reloading in extension shows less capacity and faster pore pressure build-up.

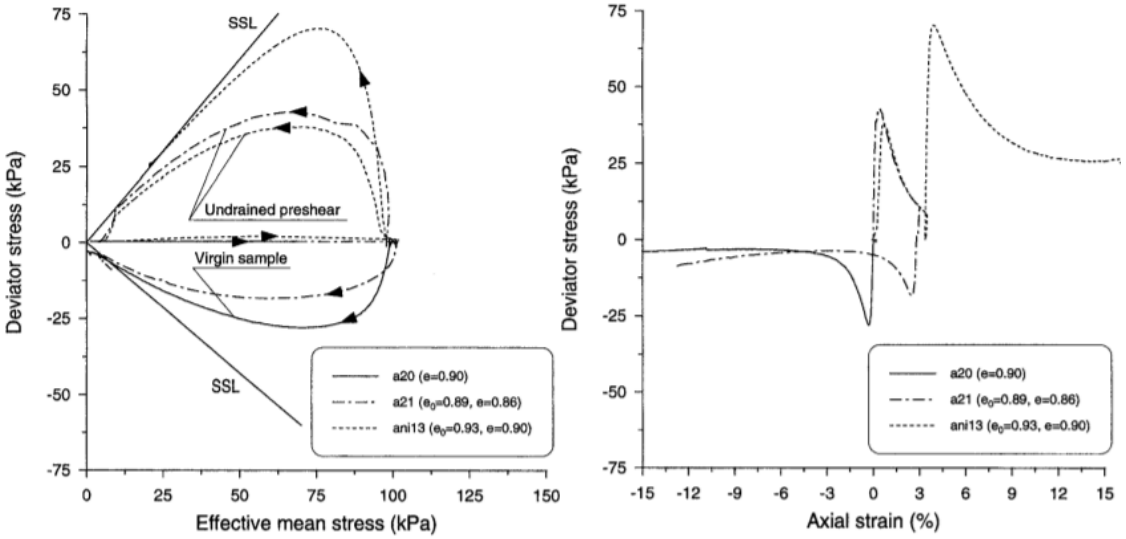


Figure 37 Effect of undrained preshearing by Gajo and Piffer (1999)

The observations on the influence of drained preshearing on pore pressure build-up for subsequent undrained tests in compression and extension are confirmed by the results on Hostun loose sand by Doanh *et al.* (2010), shown in Figure 38.

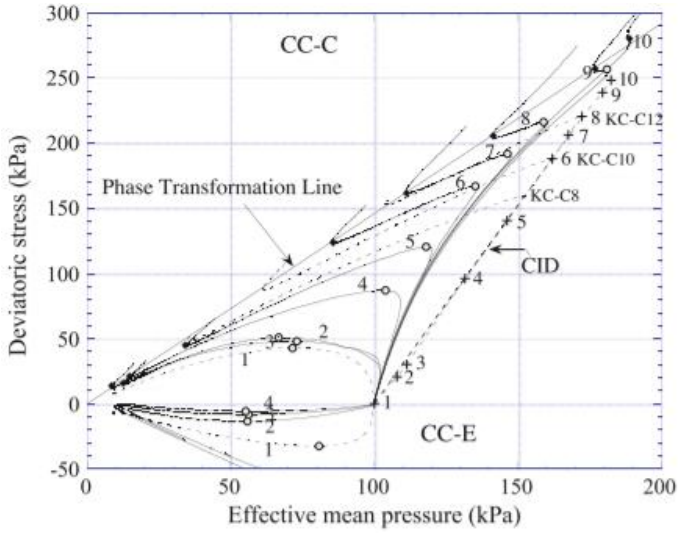


Figure 38 Influence of drained preshearing amplitude on very loose Hostun sand by Doanh et al. (2010)

Ishihara and Okada (1978a) distinguish the influence of small and large preshearing, as shown in Figure 39. In the case of a preloading with symmetric undrained cycles with low stress ratios leading to small shear strains (see graphics on the left of Figure 39), the subsequent undrained loading (after isotropic reconsolidation) shows a decrease of pore pressure build-up in compression and extension, and a diminution of the secant stiffness. However, the behaviour is different for tests with a preloading reaching a high stress ratio leading to large shear strains in one direction (in compression in the right graph of Figure 39): the subsequent reloading (after isotropic reconsolidation) leads to very little pore pressure build-up and a high stiffness in the same direction as the large preshearing, but an increased pore pressure build-up and a decreased stiffness in the opposite direction to the large preshearing.

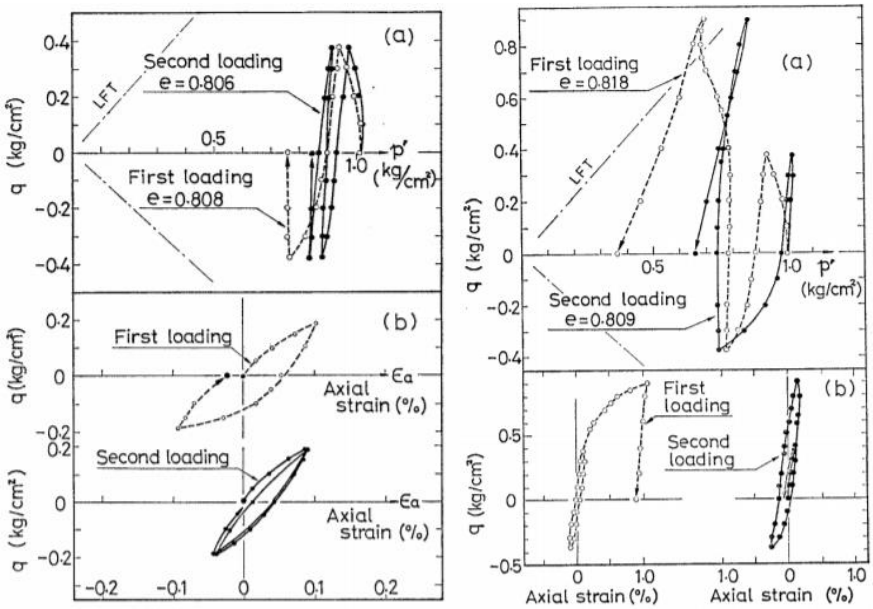


Figure 39 Influence of preshearing (small on the right, large on the left) for Fuji river sand by Ishihara and Okada (1978a)

2.2.4.3. Conclusions on the influence of preloading

The different results presented above show that tests on a sand of the same density and with the same initial conditions of stress will differ greatly depending on the preloading history sustained by the sand. In particular, the volumetric behaviour, the stiffness, and the peak capacities are significantly affected.

Isotropic preloading leads to a diminution of the contractive behaviour of the sand, to an initially stiffer elastic-like response, and to larger capacities.

Small shear preloading has a similar effect to the isotropic loading.

Large shear preloading in one direction has two opposite effects on the following loading, depending on its direction. If the reloading takes place in the same direction, the effects are similar to that of isotropic preloading, but with more intensity. However, if the reloading is in the opposite direction, the reloading becomes more contractive, softer, and shows less strength.

These observations have led authors to speak of the "memory" of the sand and the essential role it holds. This has led researchers working with the tools of plasticity to formulate models with yield functions that attempt to reflect this memory, with, for example, deformation of the yield function in the direction of compression or extension by Yasufuku *et al.* (1991), or a distinctive OCR yield locus and shear yield loci whose presence depends on the overconsolidation of the sample by Ishihara and Okada (1978a) as illustrated in Figure 40.

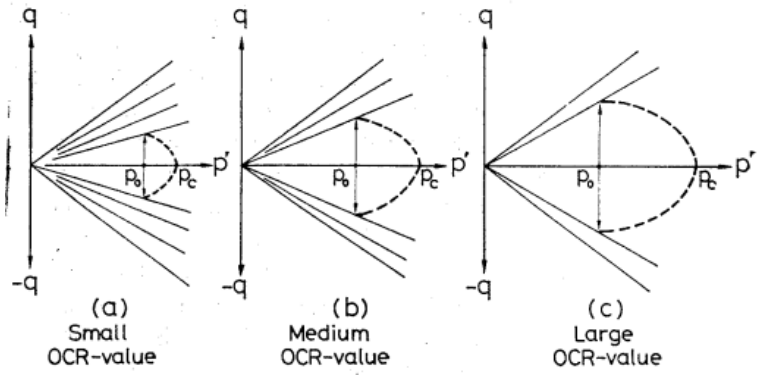


Figure 40 Dependency of yield loci on overconsolidation values in Ishihara and Okada (1978a)

This has also led researchers to develop new theories such as barodesy (Kolymbas (2015)).

2.3. Modelling of sand

As the previous section has shown, sand behaviour is complex. This is such that no consensus has been reached on an ideal constitutive model for sand, and that a variety of constitutive models have been developed during the last decades. The number of proposed constitutive models is so large that a comprehensive review is hard to establish. Among these models, one can list a number of original contributions in the field of elasto-plasticity, with sometimes the introduction of original concepts and complex mechanisms such as the models by Aubry and Hujeux *et al.* (1982), Mroz and Pietruszczak (1983), Pastor *et al.* (1985), Oka *et al.* (1994), Pestana and Whittle (1999) with a unified model for sands and clays, Jefferies (1993) and Jefferies and Shuttle (2005) with the critical state sand model NorSand, NorSand further modified by Imam *et al.* (2005) or Chiaro *et al.* (2011). An interesting overview has been established by Mroz (1998).

Three families of model have particularly thrived, with a focus on cyclic loading: bounding surface models, hypoplastic models, and elasto-plastic models with multiple yield surfaces. The following sections summarise the founding concepts of these families, the latest extensions brought in to address some fundamental issues of the initial concepts and to model cyclic loading, as well as evaluations of these models when available.

2.3.1. Hypoplastic models

2.3.1.1. Theoretical construction

Hypoplasticity has been developed independently in Karlsruhe and Grenoble (cf. Desrues and Chambon (1993)). Here, the explanations relate more closely to the development in Karlsruhe and are mainly based on Kolymbas and Herle (2005).

This theory is separate from elasto-plasticity (e.g. there is no separation of strain into elastic and plastic strain) and finds its origin in the work by Truesdell (1955). The constitutive equations of hypoplasticity relate stress rate directly to stress state and strain rate: $\dot{\sigma} = f(\sigma, \dot{\epsilon})$.

Starting from the common observation that the stress-strain response of a soil is non-linear, hypoplasticity is based on nonlinear equations, such as (for a simplistic example):

$$\dot{\sigma} = E\left(\dot{\epsilon} - \left(\frac{\sigma}{\sigma_s}\right)|\dot{\epsilon}|\right) \qquad \textit{Eq. 6}$$

In this equation, the $E\dot{\epsilon}$ is a linear part while the $E(\sigma/\sigma_s)|\dot{\epsilon}|$ introduces non-linearity with σ_s a threshold capacity value.

In three dimensions, the theory uses a tensorial function $\boldsymbol{H}$: $\dot{\sigma} = \boldsymbol{H}(\sigma, \dot{\epsilon})$ (Eq. 1). A number of restrictions apply to $\boldsymbol{H}$ to fulfill geotechnical observations such as:

- $\boldsymbol{H}$ is positively homogenous of the first order in $\dot{\epsilon}$ to ensure rate independency;
- $\boldsymbol{H}$ is homogenous in σ to ensure pressure sensitivity;
- $\boldsymbol{H}$ must fulfil the requirement of objectivity (no dependence on systems of coordinates)

which leads to $\boldsymbol{H}$ being expressed through the representation theorem, which gives:

$$\dot{\sigma} = \phi_0\mathbf{1} + \phi_1\sigma + \phi_2\dot{\epsilon} + \phi_3\sigma^2 + \phi_4\dot{\epsilon}^2 + \phi_5(\sigma\dot{\epsilon} + \dot{\epsilon}\sigma) + \phi_6(\sigma^2\dot{\epsilon} + \dot{\epsilon}\sigma^2) + \phi_7(\sigma\dot{\epsilon}^2 + \dot{\epsilon}^2\sigma) + \phi_8(\sigma^2\dot{\epsilon}^2 + \dot{\epsilon}^2\sigma^2) \quad \textit{Eq. 7}$$

Where ϕ_i are functions of the invariants and joint invariants of σ and $\dot{\epsilon}$

The assumption is taken that $\boldsymbol{H}$ can be decomposed into linear ($\boldsymbol{L}(\sigma, \dot{\epsilon})$) and non-linear ($\boldsymbol{N_0}(\sigma, \dot{\epsilon})$) tensorial functions, and that the nonlinear part can be simplified, finally giving:

$$\dot{\sigma} = \boldsymbol{L}(\sigma, \dot{\epsilon}) + \boldsymbol{N}(\sigma)\|\dot{\epsilon}\| \quad \textit{Eq. 8}$$

One such constitutive equation is:

$$\dot{\sigma} = \left(c_1\big(\mathrm{tr}(\sigma)\big)\dot{\epsilon} + \frac{c_2(\mathrm{tr}(\sigma\dot{\epsilon})\sigma)}{\mathrm{tr}(\sigma)}\right) + \left(\frac{c_3\sigma^2}{\mathrm{tr}(\sigma)} + \frac{c_4\sigma'^2}{\mathrm{tr}(\sigma)}\right)\|\dot{\epsilon}\| \quad \textit{Eq. 9}$$

where σ' the deviatoric stress.

From its formulation, hypoplasticity produces: a non-linear relation that can be calibrated to tests; cyclic loading responses with hysteresis (c.f. right graph of Figure 41); and an unrealistic ratcheting for small unload-reload loops (which is due to the only dependence of $\boldsymbol{H}$ on the state of stress but not on its path) shown in the left graph of Figure 41. This shortcoming has, for example, been pointed out by Houlsby (1981, and 1985).

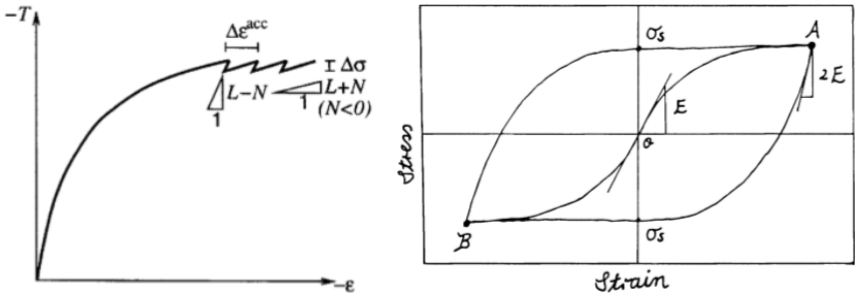


Figure 41 Left: unrealistic ratcheting; Right: Development of the hysteresis (Niemunis and Herle (1997))

Thus, the initial concept of hypoplasticity has focused on capturing the non-linear behaviour of soil, and is capable of representing large symmetric strain loops. However, it does not include any concept of memory in its formulation, which has been seen to be of essence for modelling cyclic loading and preloading in previous observations.

2.3.1.2. Extensions of the original concept

To control the unrealistic ratcheting behaviour, an extension has been proposed: hypoplasticity with "intergranular strain" (Niemunis and Herle (1997)). Here an intergranular strain range is defined in which, when the strain path changes, stiffness increases (in which the value depends on the direction) until the strain reaches the limit of this intergranular strain range after which stiffness decreases. For example, after a small unloading, the reload is ruled by a higher stiffness (avoiding the ratcheting shown in Figure 41). The introduction of intergranular strain introduces an elastic domain defined by a strain amplitude, a concept which strongly resembles a yield surface.

Another extension of the hypoplastic model, with its main focus being the capacity to model cyclic loading, is the ISA model by Fuentes and Triantafyllidis (2015a,b). ISA also adopts the concept of intergranular strains, introducing it as a "yield surface in the intergranular strain space". ISA uses both hypoplastic and bounding surface concepts, and has integrated an extension considering inherent fabric effects.

Other examples of hypoplastic model are the model by Wu and Bauer (1994), and the model by Grandas Tavera *et al.* (2020) which combines hypoplasticity with a historiotropic yield surface.

2.3.2. Bounding surface models

A well-known family of model for sand is SANISAND, developed in Manzari and Dafalias (1997), and which most referenced version is Dafalias and Manzari (2004). SANISAND builds on bounding surface theory with roots in Dafalias and Herrmann (1980). SANISAND is frequently extended, with recent versions such as SANISAND with memory surface (Liu *et al.*, 2018), SANISAND-F with evolving fabric tensor (Petalas *et al.*, 2019), and SANISAND-MSf with memory surface and semi-fluidised states (Yang *et al.*, 2022).

Other bounding surface models developed independently or related to SANISAND are models by Hirai (1987), Wang *et al.* (1990), Papadimitriou and Bouckovalas (2002), Zhang and Wang (2012), Boulanger and Ziotopoulou (2013) with PM4Sand, and Cheng and Detournay (2021).

2.3.2.1. Bounding surface theory

In bounding surface theory, an outmost yield surface which stresses cannot exceed is named the bounding surface. Inside the bounding surface, plastic deformation can take place. For any stress

point inside the bounding surface (P(σ_{ij})), a unique image point (I(σ_{ij})) sits on the bounding surface and is determined by a mapping rule (e.g. radial mapping rule in Figure 42). Through the stress point passes a homothetic image of the bounding surface. The theory defines the evolution of stress and strain in a stress-controlled case as dependent on the direction of the stress increment: if it is directed inward of the homothety of the bounding surface, the behaviour is elastic; if it is directed outward, the behaviour is elastoplastic and the plastic modulus is a function of the distance from the stress point to the image point: $h(\overline{PI})$.

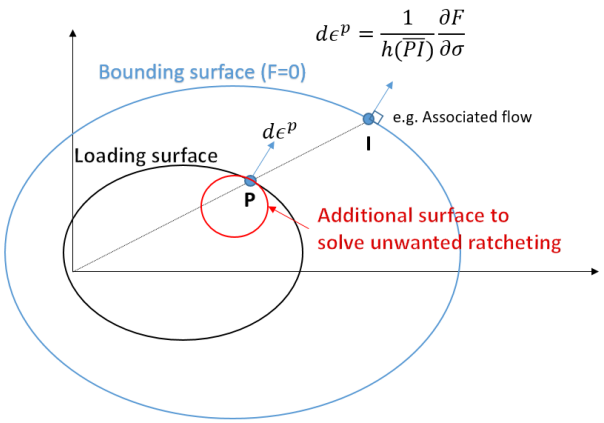


Figure 42 Illustration of a bounding surface model, in red an additional yield surface essential to the remediation of small cycles ratcheting

The main benefit of bounding surface models is that only the definition of the plastic modulus function is necessary, while enabling good agreement with the non-linear loading curves. The bounding surface behaviour is also capable of correctly modelling large unload-reload loops.

However, for small unload-reload loops, bounding surface models demonstrate unrealistic ratcheting: the unloading is always only elastic, while any reloading is elasto-plastic (the same effect as seen in the left graph of Figure 41).

2.3.2.2. SANISAND model

The major difference between the initial bounding surface theory and a SANISAND-type model (e.g. Dafalias and Manzari, 2004), is the introduction of a yield surface (grey wedge in Figure 43). Similarly to the multi-surface model (see section 2.3.3), kinematic hardening is allowed such that the stress point can move across the whole stress space delimited by the bounding surface while dragging along the yield surface. This addition was introduced to remediate the unrealistic ratcheting for small unload-reload loops:

- unloading is initially elastic (inside the yield surface), but if the unloading continues, the stress point meets the yield surface and elastoplastic behaviour ensues;

- on reload, the stress point is strictly inside the yield surface, behaving elastically, until it attains again the yield surface in the opposite direction, then behaving elasto-plastically.

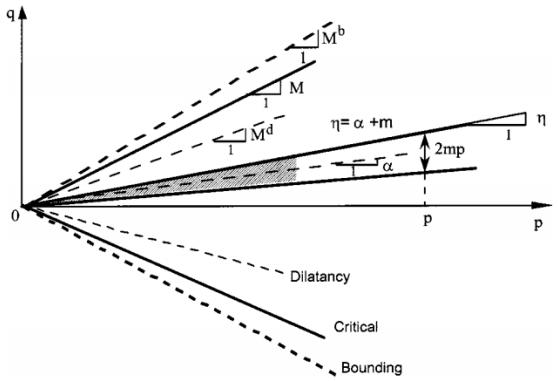


Figure 43 SANISAND in triaxial stress space (from Dafalias and Manzari, 2004)

SANISAND adopts non-linear elasticity with elastic moduli proportional to the square root of the mean effective stress. The yield surface and bounding surface are cone-type surfaces in 3D space, and wedge type in triaxial space. The yield surface hardening can be both kinematic and isotropic. The plastic modulus is linearly dependent on the distance from the bounding surface but also depends on the mean effective stress and the void ratio.

Dilatancy is accounted for in the plastic strain by noting that the volumetric strain is a factor times the absolute value of the shear strain in $q - p'$ space. The dilatancy factor is linearly dependent on the distance between the yield surface and a dilatancy surface: the yield surface can be on either side of the dilation surface leading to contractant or dilatant behaviour. Anisotropy is included by considering asymmetry of the bounding and dilation surfaces in different loading directions with respect to the isotropic axis.

To be consistent with critical state theory, the model adopts an expression for the critical void ratio as a function of the pressure. It also adopts the critical state ratio M and rules the positions of the dilatancy and bounding surfaces relative to the "critical surface" based on a measure of the "distance" of the material state from the critical state. For states denser than critical, this allows the dilatancy surface to be inside the critical surface, which is itself inside the bounding surface; and a reverse ordering for states looser than critical. At critical state, these lines overlap.

2.3.2.3. Addition of a memory surface

In order to address the inability of previous SANISAND versions to capture quantitatively the high-cyclic ratcheting of sand under drained cyclic loading, Liu *et al.* (2018) combined the founding principles of fabric dependent SANISAND (Dafalias and Manzari (2004)) with the

memory surface concept introduced by Stallebrass and Taylor (1997) and used for example by Corti (2016).

The additional memory surface is introduced to keep track of fabric changes, and consequently better predict ratcheting, which was overpredicted by previous versions of SANISAND. The memory surface covers the stress-space that has already sustained plastic loading, and reduces the accumulation of plastic strain within this evolving locus. This additional memory surface is illustrated, along the previously defined yield and bounding surfaces in Figure 44.

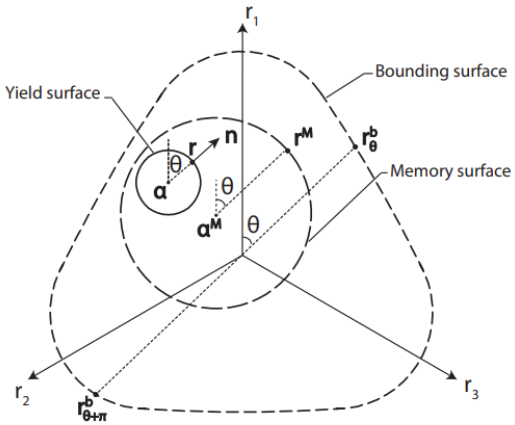


Figure 44 Illustration of the SANISAND model with memory surface in the π plane (from Liu et al. (2018)

The original SANISAND form is resumed if the yield and memory surface are tangent at the point of loading, while the stiffness is increased as a function of the size of the memory surface in other cases. The memory surface kinematically hardens to follow the stress path, and it isotropically hardens in order to obtain the progressive stiffening observed during cyclic loading.

It should be noted that successive developments of bounding surface models to model soil behaviour realistically have involved the introduction of a number of additional surfaces, thus rendering them more and more like multisurface models.

2.3.3. Elasto-plastic models with multiple surfaces

The multiple surface model was proposed by Mroz (1967, 1969) and Iwan (1967) and gained interest for the modelling of cyclic loading of soils with the works of Prevost (1977, 1978a, 1978b). Another example of a multi-surface model is found in Elgamal *et al.* (2002) and Yang *et al.* (2003).

The idea of multiple surface plasticity is to separate the stress space in a number of surfaces, as shown in Figure 45.

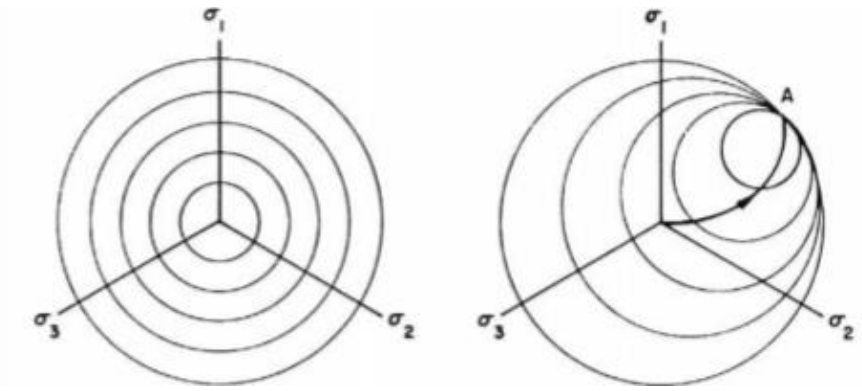


Figure 45 Multiple surfaces in principal values space. Left: initial configuration; Right: after loading with dragged surfaces. From Krabbenhoft (2019)

When the stress reaches one of these surfaces, a plastic strain linked to this surface is created, the surface hardens and moves with the stress point (kinematic hardening and eventually isotropic hardening) until it reaches the next surface where a new plastic strain contribution is created; and so forth. Mapping the stress space with yield surfaces with different properties allows a close depiction of a monotonic loading through the modulation of the plastic properties of each surface (e.g. Prevost (1977)). On unloading, the stress point is found strictly inside all surfaces and thus the model behaves elastically, until it reaches the first surface again, where it develops plasticity, and so on.

Initially, a self-imposed restriction on multi-surface models was to keep the surfaces nested: with only a tangent contact between the surfaces such that they do not intersect (see the right sketch of Figure 45). This constrains the kinematic hardening of the surfaces, and, for example, Mroz (1967) proposed that the translation direction of the surface should be given by the vector linking the points with same normal on the two surfaces (where the point on the activated surface is the current stress point) to keep the surfaces nested. Furthermore, in the presence of isotropic

hardening, further conditions should be satisfied to avoid the intersection of surfaces if one wants to conserve their nested property.

Houlsby and Puzrin (2006) argue that the non-intersection of surfaces does not need to be enforced, which greatly relaxes the conditions on hardening rules.

Taking into account the rejection of the nesting constraint, Table 1 presents advantages and disadvantages of the multi-surface theory.

Advantages	Disadvantages
Monotonic loading can be reproduced with high fidelity.	Properties and plastic laws should be allocated to each surface.
A hysteresis loop develops naturally and obeys, in the case of pure kinematic hardening, the Masing rule (Masing (1926)) (the unloading curve is an image of the loading curve with a scale factor of 2, and as any loading curve reaches one of existent loading curves, follows it).	Handling multiple yiel surfaces has a computational cost, with the solving of larger system of equations than for one surface.
The Bauschinger effect is naturally present (yield stress is reduced in the opposite direction of the direction where it has been plastically loaded).	
This theory is simple compared to other theories tackling cyclic loading.	
The theory has been proven to provide good results for stress-strain responses compared to experiments (Prevost (1982)).	

Table 1 Advantges and disadvantages of multi-surface plasticity

The need to define properties and plastic laws for each surface, can largely be decreased by using basic distributions for properties and plastic laws.

The generalisation to an infinite number of surfaces is the logical extension of such a theory; Houlsby and Puzrin (2006) present its theoretical development.

2.3.4. Choice of the theory for further developments

2.3.4.1. Evaluation of existing constitutive models

The uninterrupted publications of new constitutive models for sand, including recent extensions for hypoplastic models, and very recent extensions for SANISAND models, is a clear sign that no model is yet good enough to model cyclic loading in sand adequately.

To identify better and quantify problems these advanced models face, researchers have evaluated them against the database on Karlsruhe fine sand developed by Wichtmann (2021).

2.3.4.1.1. Wichtmann's inspections of three constitutive models

Wichtmann (2016) has compared to the data, results of several advanced models: SANISAND by Dafalias and Manzari (2004), the hypoplastic model with intergranular strain by Niemunis and Herle (1997) and von Wolffersdorff (1996), and the ISA model by Fuentes and Triantafyllidis (2015a,b).

First, in his conclusions on the comparison of models results with monotonic tests, Wichtmann remarks that each model has different strengths and weaknesses, being able to reproduce some tests well, but not others, and that parameters would need to be varied across tests to obtain better results.

Second, the three models require different sets of parameters to predict optimally the drained monotonic behaviour, on one hand, and the cyclic undrained behaviour, on the other hand.

Third, simulations of cyclic tests appear even more problematic. For undrained cyclic stress-controlled tests with calibrations to fit the observed number of cycles required to reach liquefaction, the changes of rates of pore pressure build-up are not well reproduced. Also, the intergranular strain model (noted Hypo) and SANISAND show unwanted ratcheting, as seen in Figure 46. In particular, the models are not able to capture well the variation in the number of cycles needed to reach liquefaction with the variation in density and amplitude of cyclic loading, as shown in Figure 47.

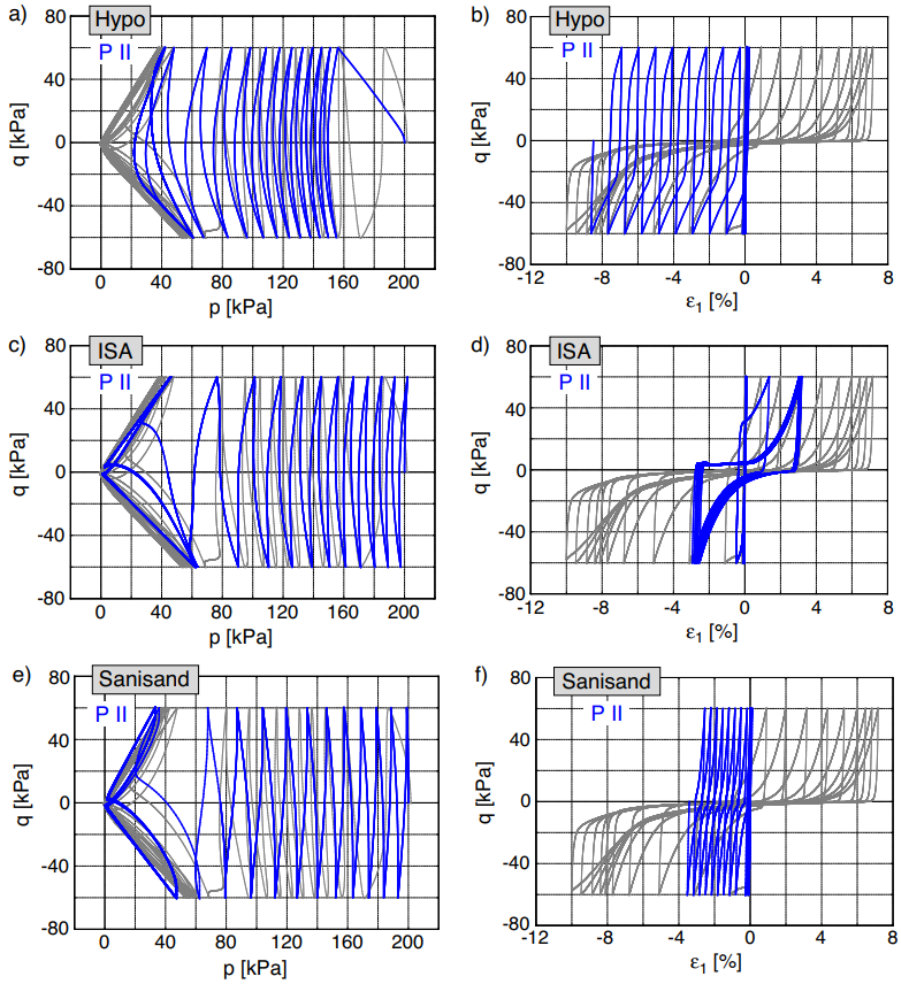


Figure 46 Simulation of test TCUI7 (data in grey) with the hypoplastic model with intergranular strain (a,b), the ISA model (c,d), and SANISAND 2004 (e,f), with calibration for cyclic test (reproduced from Wichtmann (2016)).

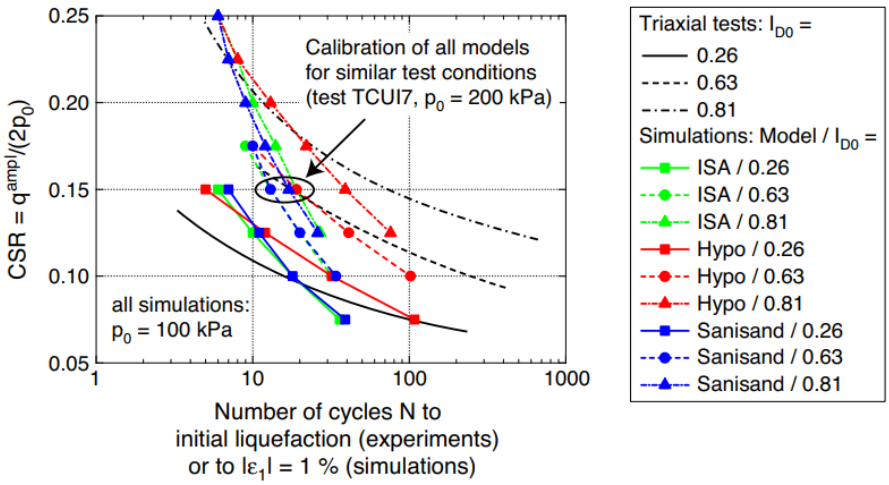


Figure 47 Numbers of cycles required to reach liquefaction as a function of the cyclic stress amplitude for three different range of densities. Data in black, results of the hypoplastic model with intergranular strain in red, of the ISA model in green, and of SANISAND in blue. (Reproduced from Wichtmann (2016)).

For one-way cyclic stress-controlled undrained tests, the three models give very inaccurate predictions of the ratcheting and stress paths as shown in Figure 48.

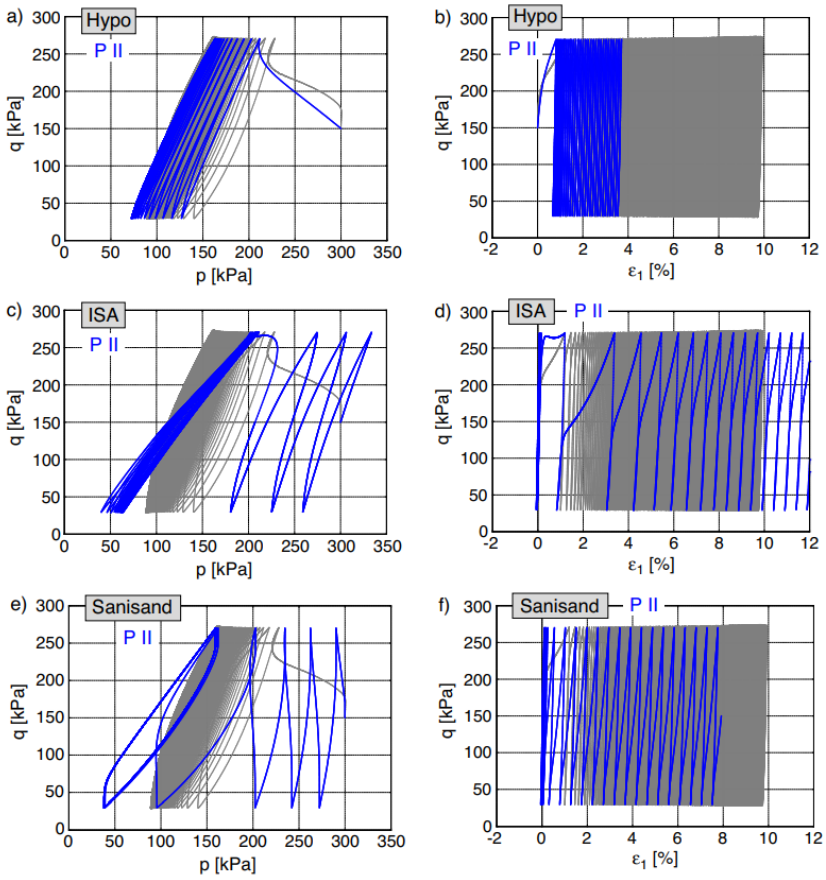


Figure 48 Simulations of test TCUA2 (data in grey) with the hypoplastic model with intergranular strain (a,b), the ISA model (c,d), and SANISAND 2004 (e,f), with calibration for cyclic test (reproduced from Wichtmann (2016)). Simulations in blue, data in grey.

SANISAND and the ISA model also have problems reproducing small strain cyclic strain-controlled tests as shown in Figure 49.

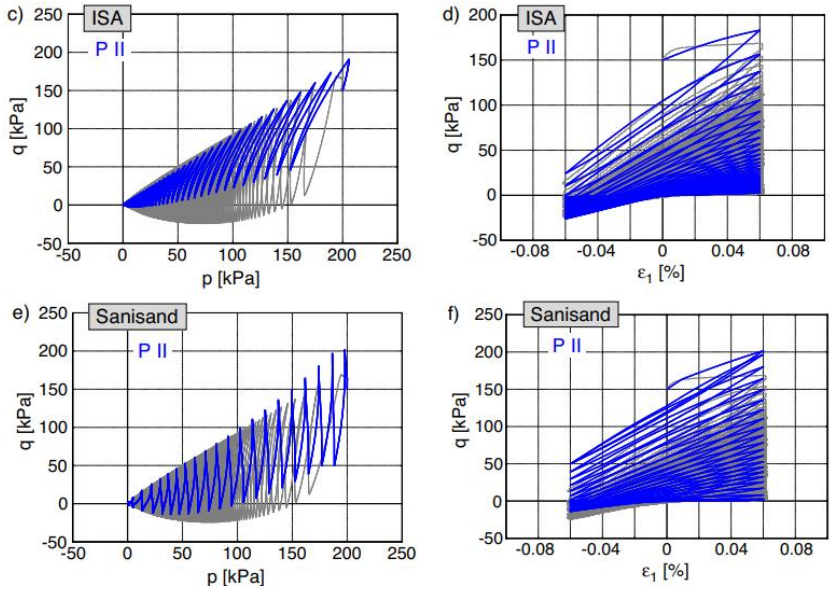


Figure 49 Simulations of test TCUE1 (data in grey) with the ISA model (c,d), and SANISAND 2004 (e,f), with calibration for cyclic test (reproduced from Wichtmann (2016)). Simulations in blue, data in grey.

The three models show great difficulties to capture the large strain cyclic strain-controlled tests on dense sand as shown in Figure 50.

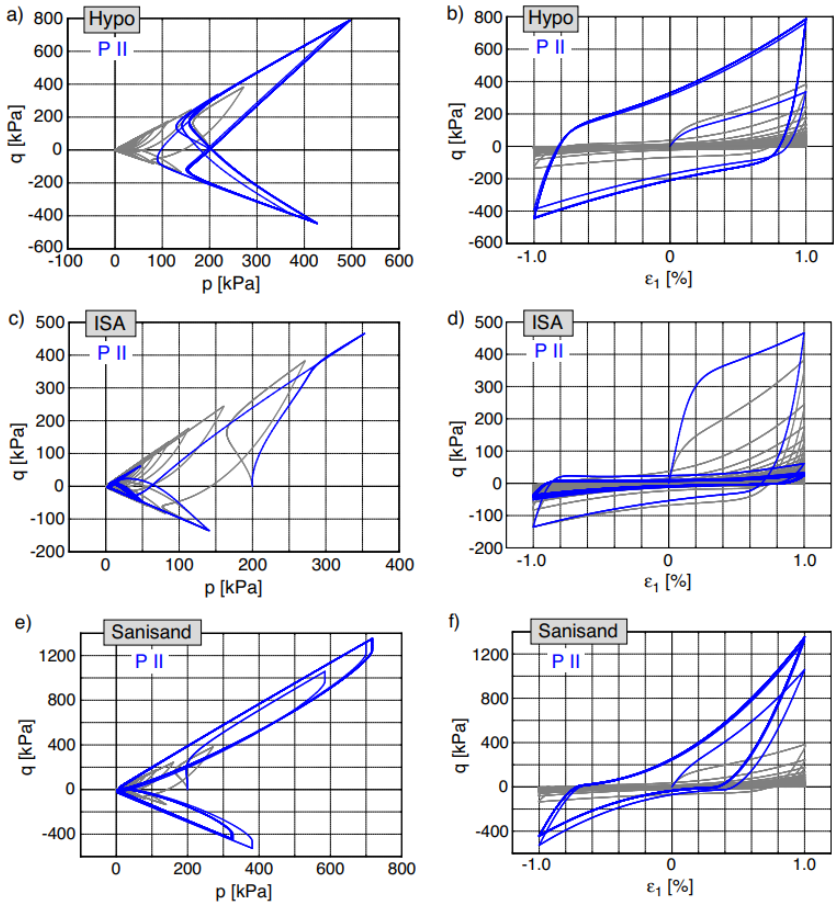


Figure 50 Simulations of test TCUA2 (data in grey) with the hypoplastic model with intergranular strain (a,b), the ISA model (c,d), and SANISAND 2004 (e,f), with calibration for cyclic test (reproduced from Wichtmann (2016)). Simulations in blue, data in grey.

In summary, Wichtmann has shown that the three models are not satisfactory for the modelling of sand under cyclic loading. Models require different set of parameters for monotonic and cyclic tests, which further poses the question of the capacity of modelling irregular cycles with varying amplitudes. Also, the models' inability to model cyclic tests have been shown, with an incapacity to reproduce adequately the pore pressure build-up during undrained tests, with unwanted ratcheting during symmetric tests, and with very poorly predicted strain accumulation in one-way tests.

2.3.4.1.2. Further investigation by Duque

Duque *et al.* (2022) have further evaluated these three models, along with SANISAND with memory surface and the semi-fluidized state model by Yang *et al.* (2022), against the same data by Wichtmann. Duque *et al.* have identified seven common limitations of constitutive models that will be further discussed in 5.4, and which demonstrate the imperfection of existing models.

2.3.4.2. Choice of the theoretical framework

Having acknowledged the necessity to further extend existing constitutive models or to create a new constitutive model, a choice must be made as to which theoretical framework this extension or new model should be developed in.

The theoretical nature of the three main options should be considered, in relation to the nature of sand that is deeply rooted in its memory.

The nature of the hypoplastic model lies in the incremental expression of constitutive relations, which is not consistent with the nature of sand.

Bounding surface models are positional models, where the constitutive behaviour only depends on the relative position in stress space to the bounding surface and on the direction of loading. Bounding surface models have initially almost no records of the history of loading (except for the small yield surface). The mapping of the stress space thus is originally immobile, except at load reversal.

Multi-surface plasticity models are by nature "historiotropic". Like bounding surface models, they map the stress space. But contrarily to bounding surface, this mapping naturally evolves via the hardening of the yield surfaces. Kinematic hardening allows surfaces to go along the direction of loading, and makes this direction "favourable", while unloading in the opposite direction will be "unfavourable". Isotropic hardening changes the domain sizes such that the lesser plastic zones extend, making the material stiffer in these regions.

The fact that extensions of hypoplastic and bounding surface models developed to capture cyclic loading include additional yield surfaces (intergranular strain for hypoplasticity, memory surface for SANISAND) is also an argument in favour of multiple-surface models. Indeed, instead of hybridising theories leading to more complicated models, it seems more interesting to found the constitutive behaviour around what has been shown to be essential: the memory of the material monitored and represented by yield surfaces.

Chapter 3 Theoretical construction of HySand

In developing a constitutive model, the goal is to capture the behaviour of the modelled material in the clearest and simplest way, with a sound, well thought out construction and structure, both physically and mathematically. This will allow the model to withstand its future uses and developments, and users to understand better how the model works.

However, the complexity of sand behaviour and the simplicity of a model pull in two opposite directions. The objective in this chapter is to present a base model that can easily be expressed and understood, and with enough features to represent a broad range of behaviour. This base model is able to model monotonic, cyclic, drained, partially drained, undrained, virgin or preloaded tests for the whole density spectrum of sand, with only two equations and 14 parameters.

This chapter builds up to this base model, starting from a very basic friction model. Furthering this base model, it discusses additional options that would improve the prediction capabilities of the model but were judged too complex for too little improvement to be integrated into the base model. This chapter also highlights options that were explored during its development, and the reason they were discarded, as well as mentioning possibly interesting options that were not studied.

In the first part of this chapter, the hyperplastic framework in which HySand is built is presented. In the second part, the progressive construction of HySand in triaxial space is thoroughly explained, and the effects of the features added along its construction are illustrated. In the third part, the base model built in triaxial space is generalised to three dimensions. Finally, in the fourth part, the numerical framework developed by Houlsby (2023) to run models developed in hyperplasticity is briefly explained.

3.1. Hyperplasticity: a robust and sound theoretical framework

3.1.1. Origins and thermodynamical basis

Hyperplasticity has its roots in the work of Ziegler (1977). From the first two laws of thermodynamics, Ziegler shows that a mechanical system can be fully described by an energy function and a dissipation function. The derivation of the energy and dissipation functions from the laws of thermodynamics can be found in Ziegler (1977) or Houlsby and Puzrin (2006). Table 2 illustrates in a simpler manner the translation of the first and second laws of thermodynamics into the energy and dissipation functions respectively.

First law of Thermodynamics $\dot{U} = \dot{Q} - \dot{W}$ *Eq. 10* In a system, the change in internal Energy ($\dot{U}$) is equal to the heat added ($\dot{Q}$) minus the work done by the system ($\dot{W}$). This expresses the conservation of energy.	Energy Function $f = \cdots$ $g = \cdots$ *Eq. 11* The free energy function (f), or equivalently minus the Gibbs energy function ($-g$), expresses the energy stored by the system.
Second law of Thermodynamics $\dot{S} > \sum_{i=1}^{n} \frac{\dot{Q}_i}{\theta_i}$ *Eq. 12* Here, the Clausius-Duheim inequality: the change of entropy of the system of interest ($\dot{S}$) is superior to the rate of heat input ($\dot{Q}_i$) from n reservoirs that are at temperature θ_i.	Dissipation function $d = \cdots > 0$ *Eq. 13* The dissipation function (d) expresses the energy dissipated by the system.

Table 2 From thermodynamics to hyperplasticity

Hyperplasticity has been developed by Houlsby and others, starting with the application of these concepts to soil (Houlsby (1981)). Collins and Houlsby (1997) re-cast the strain-based theory in terms of stress, with use of the Legendre transform, and demonstrated the formal links between the dissipation and yield function (which is used in the explanation of the triaxial construction of the model). Houlsby and Puzrin (2006) encompass all the preceding advances in the domain, exploring multiple approaches further, and describing continuous hyperplasticity. Houlsby maintains the Hyperplasticity website (Houlsby, 2023) where the content of the book and further works are regularly updated.

One should note that hyperplasticity in its simple "small strain" form uses quantities per unit volume, whereas thermodynamics use quantities per unit mass. To be fully consistent with thermodynamics, the stresses obtained with hyperplastic calculations should be factored by a

reference specific volume such as the critical state specific volume (Γ) divided by the current specific volume (v), while stresses inputted in hyperplastic calculations should be factored by the current specific volume divided by the critical state specific volume.

3.1.2. From hyperplasticity to plasticity

It appears that almost all models expressed in hyperplasticity can be expressed in plastic theory (but the reverse is not true) (Houlsby, 2023). The following paragraphs explain how a reader more familiar with plasticity can extract from a hyperplastic formulation its equivalent plastic formulation.

3.1.2.1. Stress-strain relationship

The essence of a plastic model is to relate stress (σ) and strain ($\epsilon = \epsilon^e + \epsilon^p$), often distinguishing elastic (ϵ^e) and plastic (ϵ^p) strains.

In hyperplasticity, the energy function is expressed in either strain and internal variables (free energy function $f(\epsilon, \alpha)$), or stress and internal variables (Gibbs energy function $g(\sigma, \alpha)$), where internal variables (α) are plastic strains in the simplest case.

Differentiating the free energy function by the strain gives the stress:

$$\frac{\partial f(\epsilon, \alpha)}{\partial \epsilon} = \sigma \qquad \textit{Eq. 14}$$

Complementarily, differentiating the Gibbs energy function by the stress gives minus the strain:

$$-\frac{\partial g(\sigma, \alpha)}{\partial \sigma} = \epsilon \qquad \textit{Eq. 15}$$

In both cases, the stress-strain relationship is obtained.

3.1.2.2. Elastic stiffness matrix and elastic strain

Continuing the differentiation process allows one to obtain the stiffness/compliance matrix.

Differentiating the free energy function by the strain twice gives the elastic stiffness matrix (D^e):

$$\frac{\partial^2 f(\epsilon, \alpha)}{\partial \epsilon^2} = \frac{\partial \sigma}{\partial \epsilon} = D^e \qquad \textit{Eq. 16}$$

Differentiating the Gibbs energy function by the stress twice gives minus the elastic compliance matrix (C^e):

$$-\frac{\partial^2 g(\sigma, \alpha)}{\partial \sigma^2} = \frac{\partial \epsilon}{\partial \sigma} = C^e = D^{e-1} \qquad \textit{Eq. 17}$$

The elastic strains rate are obtained by multiplying the stress rate by the compliance matrix:

$$\dot{\epsilon}^e = C^e \dot{\sigma} \qquad \textit{Eq. 18}$$

3.1.2.3. Generalised stresses

One of the founding principles of hyperplasticity is the use of generalised stresses.

Differentiating the energy function by its internal variables gives the generalised stresses associated to this internal variable:

$$\frac{\partial f(\epsilon,\alpha)}{\partial \alpha} = -\bar{\chi} \qquad or \qquad \frac{\partial g(\sigma,\alpha)}{\partial \alpha} = -\bar{\chi} \qquad \textit{Eq. 19}$$

The dissipation is expressed in terms of the internal variables, their rates, and the strain and stress. The generalised stresses are also obtained by differentiation of the dissipation by the internal variables rates:

$$\frac{\partial d(\epsilon,\sigma,\alpha,\dot{\alpha})}{\partial \dot{\alpha}} = \chi \qquad \textit{Eq. 20}$$

Ziegler (1977) assumed that the generalised stresses obtained from the energy function and the ones obtained from the dissipation function are equal:

$$\bar{\chi} = \chi \qquad \textit{Eq. 21}$$

This orthogonality principle by Ziegler is a key hypothesis used in hyperplasticity: thermodynamics lead to $(\chi - \bar{\chi})\dot{\alpha} = 0$, and Ziegler makes the stronger assumption $\chi - \bar{\chi} = 0$.

3.1.2.4. Yield function

From the generalised stresses expressions, yield functions can be obtained and expressed in terms of stress, strain, internal variables and generalised stress: $y(\epsilon,\sigma,\alpha,\chi)$. Houlsby and Puzrin (2006) and Houlsby (2023) explains that the yield function is a degenerate Legendre transform of the dissipation function, which also provides the plastic flow rule.

3.1.2.5. Direction of plastic flow

In plasticity, the direction of plastic flow is given by the differentiation of a plastic potential by stress. In hyperplasticity, the sole definition of the yield function is sufficient and the plastic flow direction is given by the differentiation of the yield function by the generalised stress $(\partial y/\partial \chi)$.

3.1.2.6. Plastic strain

In hyperplasticty, the plastic strain increments are obtained in the same way as in plasticity: by multiplying the direction of plastic flow by a plastic multiplier (L), but this principle is generalised to all internal variables (α):

$$d\alpha = L\frac{\partial y}{\partial \chi_\alpha} \qquad \textit{Eq. 22}$$

This plastic multiplier is obtained by solving the consistency condition ($dy = 0$). This is explained further in 3.4 (numerical implementation).

3.1.2.7. Summary

A model in hyperplasticity is formulated with a pair of functions, which can either be an energy function (f or g) and the dissipation (d), or an energy function (f or g) and the yield function (y).

The stress-strain relation is obtained by differentiation of the energy function by the strain (free energy: f) or stress (Gibbs energy: g). The elastic stiffness matrix is obtained by double differentiation of the energy function by strain (f) or stress (g). The elastic strain rate is obtained by multiplying the stress rate by the elastic stiffness matrix. The yield function is obtained by manipulation of the generalised stresses obtained from the energy and dissipation functions. Plastic flow direction is obtained by differentiation of the yield function by the generalised stress. The plastic multiplier is obtained by solving the consistency condition. Finally, the plastic strains increments are obtained by multiplying the plastic flow direction by the plastic multiplier. Figure 51 summarises this process.

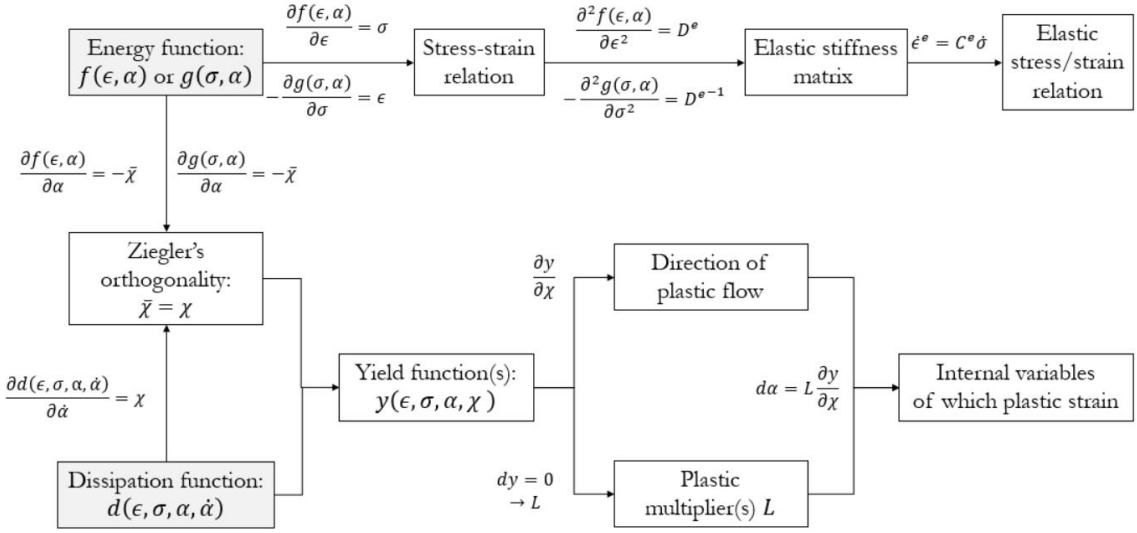


Figure 51 Mechanical behaviour determination in hyperplasticity

The full-mechanical behaviour is derived from only two functions: (1) the energy function and (2) the dissipation or yield function.

To understand this process better, the reader can refer to the examples given in section 3.2 of this chapter, the simplest being in 3.2.2 for a simple frictional model.

3.1.3. Constraint equations

Further to the basic concept explained in the last paragraphs, constraints equations can be used. Constraint equations (C), which are always equal to zero, can be added to the dissipation function with a Lagrange multiplier (Λ):

$$d^*(\epsilon, \sigma, \alpha, \dot{\alpha}) = d(\epsilon, \sigma, \alpha, \dot{\alpha}) + \Lambda\, C(\epsilon, \sigma, \alpha, \dot{\alpha}) > 0 \qquad \textit{Eq. 23}$$

$$C(\epsilon, \sigma, \alpha, \dot{\alpha}) = 0 \qquad \textit{Eq. 24}$$

A constraint equation allows one to constrain the evolution of strain, stress, internal variables or their rates. Generalised stresses are obtained from a modified dissipation equation as follows:

$$\frac{\partial d(\epsilon, \sigma, \alpha, \dot{\alpha})}{\partial \dot{\alpha}} + \Lambda \frac{\partial C(\epsilon, \sigma, \alpha, \dot{\alpha})}{\partial \dot{\alpha}} = \chi \qquad \textit{Eq. 25}$$

In the case of the model presented hereafter, it is especially useful to constrain the plastic volumetric strain, as well as the anisotropy development.

As explained in the previous paragraph, the equality of generalised stresses allows one to obtain yield functions, equivalent to the dissipation function. The constraint equations can be integrated into the yield functions. This is shown for the simplest case in section 3.2.3 which integrates a dilation constraint to the simplest frictional model.

3.1.4. Parallel works

In parallel to the work of Ziegler (1963, 1977), other thermodynamically based mechanical approaches have been developed such as the works of Coleman (1964). Based on Ziegler (1963), Moreau (1970, 1971) has worked on the existence of a dissipation potential, which has then given rise to the "matériaux standards" (Halphen *et al.*, 1975) developed in France and taught in engineering schools (e.g. course based on Suquet's work at ENSTA ParisTech). Hyperplasticity and matériaux standards appear to have developed independently but arrive at the same structure, although with different terminology.

The conclusion on the advantages of these thermo-mechanical theories by Germain *et al.* (1983), agreed by Houlsby *et al.* (2017), is that "all the constitutive equations of the material can be recast in two non-negative closed functions", namely the energy function and the dissipation function. Hyperplasticity guarantees a thermo-mechanical consistency and a sound mathematical foundation, and allows an additive and progressive construction of models as will be demonstrated in the following for HySand.

3.2. Triaxial construction

HySand has first been developed in triaxial space. The well-stocked triaxial test database by Wichtmann and Triantafyllidis (2016a, 2016b) synthesised and made available by Wichtmann (2021), as well as data on Hostun sand (Gajo (1999), Doanh (1997, 2006, 2010)), Fuji river sand (Ishihara (1978a,b, 1982), and Aio sand (Yasufuku (1991)) allow the model and its modifications to be tested against a wide range of tests and conditions. Further to the availability of data, the ease of modification of a triaxial model compared to a three-dimensional model, the distinction between volumetric and deviatoric behaviour, as well as the reduced calculation time, explain the choice of working first in triaxial space.

The development of HySand has roots in the models developed by Houlsby (1992) and Houlsby and Mortara (2004). HySand preserves three key principles of these models:

- the frictional base of the model;
- the plastic dilation is a function of anisotropy and density;
- the necessity to transit to a multi-surface model to capture cyclic and small strain behaviour.

HySand differs from these models in its theory:

- a Matsuoka-Nakai formulation for the yield surface;
- the pressure dependence of a consolidation based contraction;
- normal consolidation slopes varying with density;
- the implementation of non-linear elasticity;
- a new anisotropy law;
- a new hardening process;
- its generalisation to 3D.

HySand also differs in the way it was developed: in close relation to a large database, while the former models were developed within a more general phenomenological approach.

Figure 52 is a brief overview of the paragraphs that follow. It displays the different model components as well as the key effects they have on the modelled mechanical behaviour.

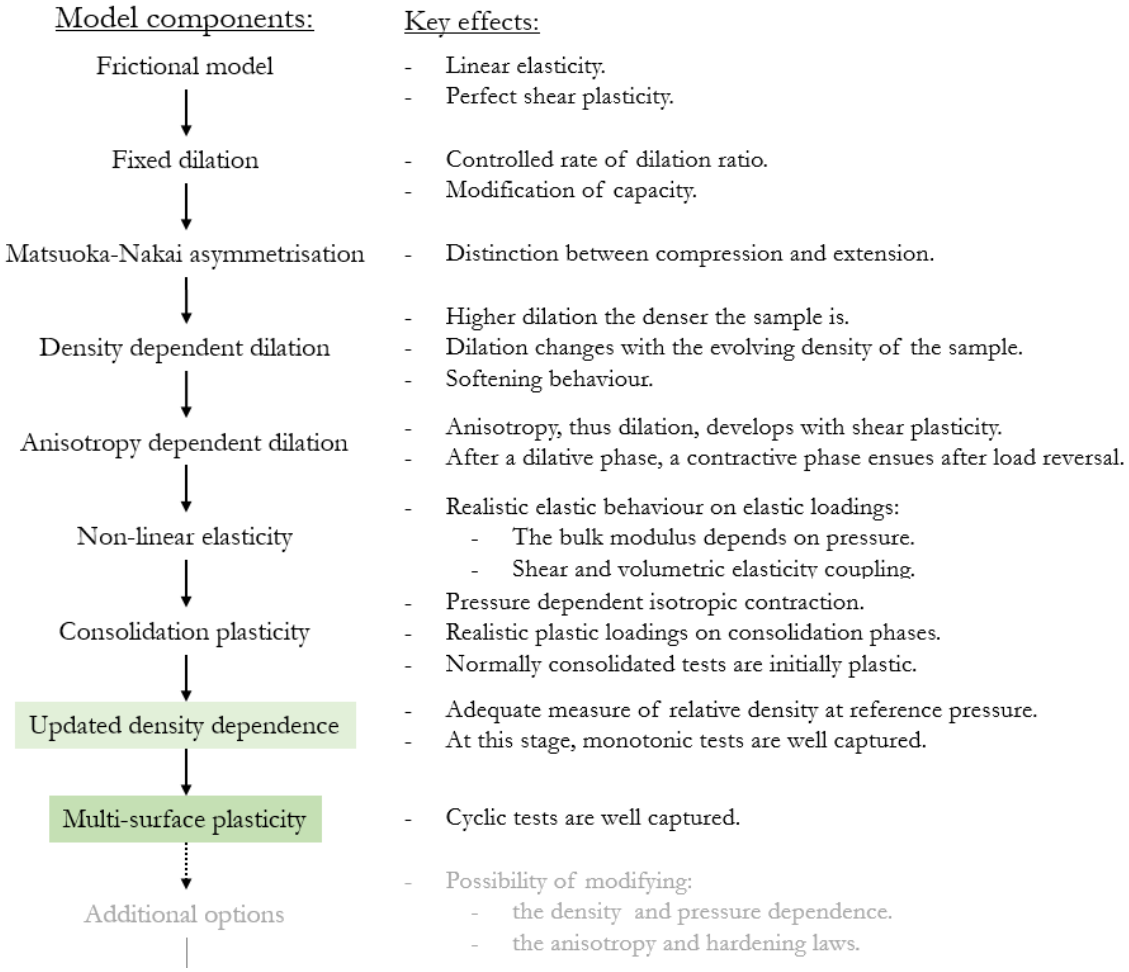


Figure 52 Summary of the progressive construction of the triaxial base model

Figure 53 illustrates the evolution of the simulation of a monotonic drained test and of a cyclic stress-controlled undrained test (only stress path) with the progressive addition of the different components of the model that is presented hereafter.

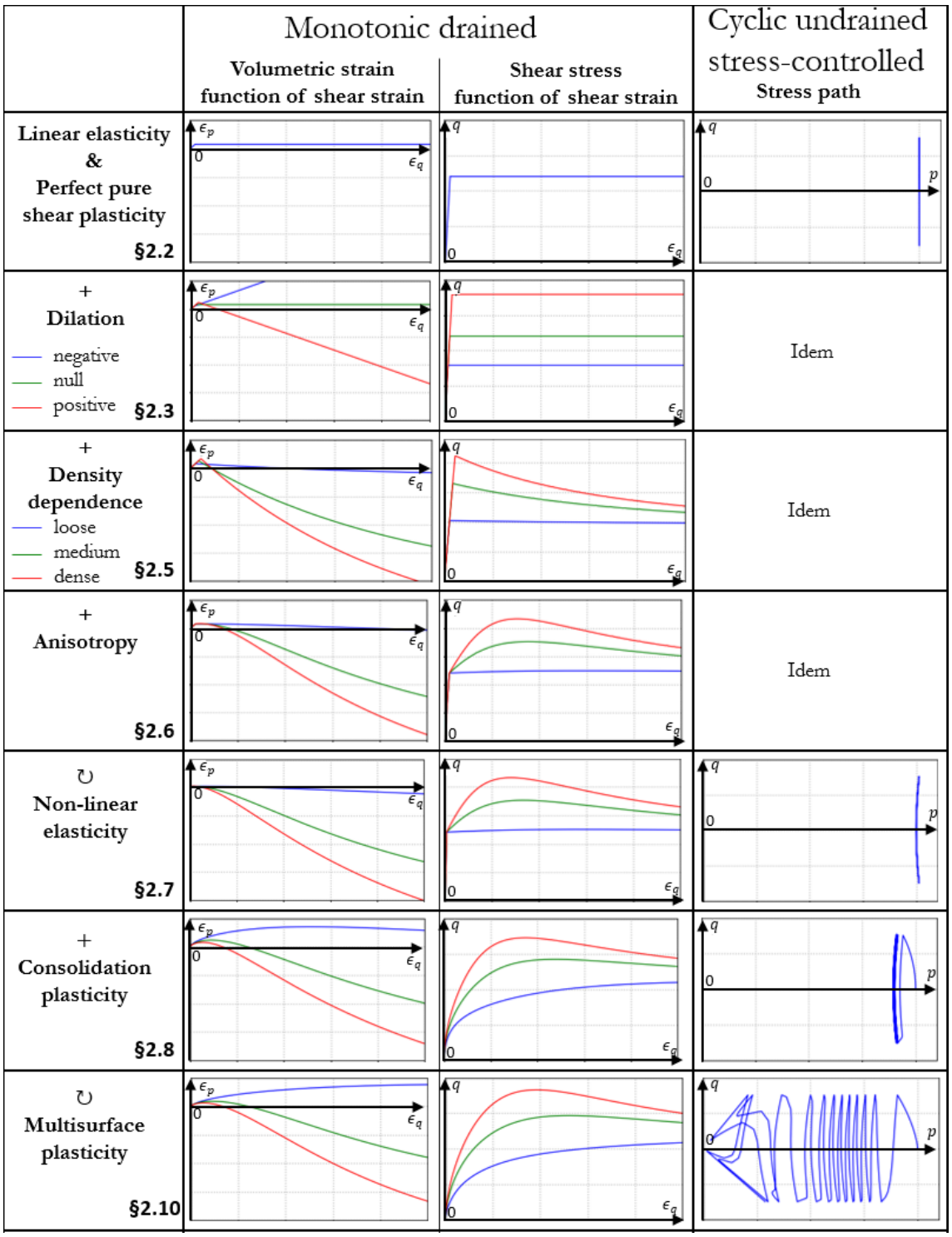


Figure 53 Simulated monotonic drained test and stress path of a cyclic stress-controlled undrained test: evolution of the simulations with the progressive addition of the components of the model

3.2.1. Benchmark tests by Wichtmann

Wichtmann (2016, 2021) has conducted a large campaign of triaxial tests on Karlsruhe fine sand that have been partially presented in Chapter 2. In order to illustrate the effects of progressive modifications to the model, a series of tests are simulated at each construction step, and can be compared to the test data presented here.

The strains measured by Wichtmann are linear strains. In order to compare the results by Wichtmann to the results produced by hyperplastic models, the linear strains provided by Wichtmann have been converted to logarithmic strains. Eq. 26 to Eq. 29 show how to convert Wichtmann linear strains (denoted by the subscript W) to logarithmic strains (denoted by the subscript H to denote their compatibility with hyperplasticity):

$$\epsilon_{p_H} = -\ln\left(1-\epsilon_{p_W}\right) \quad \textit{Eq. 26}$$

$$\epsilon_{1_H} = -\ln\left(1-\epsilon_{1_W}\right) \quad \textit{Eq. 27}$$

$$\epsilon_{3_H} = \ln\sqrt{\frac{1-\epsilon_{1_W}}{1-\epsilon_{p_W}}} \quad \textit{Eq. 28}$$

$$\epsilon_{q_H} = \ln\left(\frac{\sqrt[3]{1-\epsilon_{p_W}}}{1-\epsilon_{1_W}}\right) \quad \textit{Eq. 29}$$

Figure 54 presents three drained monotonic tests at an initial $p_0 = 200kPa$ at different densities: TMD3 (blue curve, loose sand $v_0 = 1.975$), TMD13 (green curve, medium dense $v_0 = 1.824$), and TMD18 (red curve, dense sand $v_0 = 1.748$).

Three key characteristics are:

- the volumetric behaviour is initially contractive for all tests, but only the loose sand continues to contract, while dilation ensues for the medium dense sample, and the dense sample in a larger magnitude.
- the three tests seem to converge towards a similar shear capacity, however, the medium dense, and to a larger extent the dense sample, exhibit an extra capacity at lower strains.
- the secant shear stiffness increases the denser the sample is.

Figure 55 presents monotonic undrained normally consolidated tests at 200kPa for different densities: TMU5 (blue curve, loose sand $v_0 = 1.946$), TMU2 (green curve, medium dense sand $v_0 = 1.814$), and TMU6 (red curve, dense sand $v_0 = 1.728$).

Three key characteristics are:

- the asymptotes of the stress paths collapse on a similar line, the critical stress ratio line.
- the stress path to reach this critical ratio show more mean effective stress (p) relaxation (more pore pressure build-up) the looser the sample is.
- the asymptotes of the shear stress against shear strain curves have steeper slopes the denser the sample is.

Figure 56 displays test TCUI7, an undrained stress controlled cyclic test from a normal consolidation at 200kPa for a medium dense sample ($v = 1.8$). Three key characteristics are:

- After 11 cycles, the test enters a phase of liquefaction with characteristic butterfly-shaped loops in the $p - q$ space, and large shear strain developing.
- The pore pressure build-up (the p relaxation) with cycles is important on the first cycle, then progressively diminish with cycles, until rapidly increasing over the course of a few cycles from p~100kPa.
- there is no ratcheting of strain for this symmetric test.

Figure 57 presents an undrained cyclic strain controlled test (TCUE9) which was preceded by a drained cycle. In each cycle, the additional pore pressure build-up diminishes, and after a few cycles, the cycle amplitude in shear stress diminishes with each cycle.

Figure 58 illustrates two undrained monotonic tests preceded by preloading, and a virgin undrained monotonic test (with no preloading) for comparison (blue curve). The three tests are on loose sand (v_0~1.94).

The test represented by the green curves is preceded by an isotropic loading such that the overconsolidation ratio is $OCR = 8/3$. In the following undrained test, there is no pore pressure build-up during the first stage of the test, and the shear stress at which the behaviour softens is higher than in the virgin test.

The test represented in red curves is preceded by a drained shear preloading. After the drained shear preloading, the stress path of the undrained test in $p - q$ space is extremely modified, with no pore pressure build-up, and instead a stress path curved towards higher p values that is close to the drained path. Until the shear stress level reaches the maximal stress level of the drained preloading, the behaviour is very stiff, and is immediately softer as it reaches this threshold.

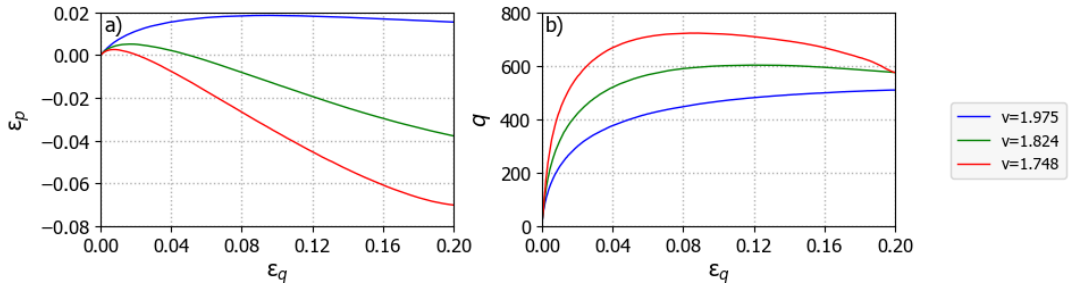


Figure 54 Drained tests (a) volumetric strain function of shear strain; b) shear stress function of shear strain)

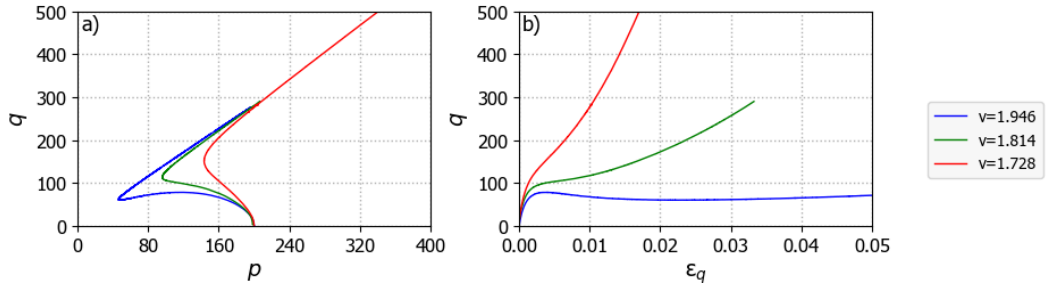


Figure 55 Undrained tests (a) shear stress function of volumetric stress; b) shear stress function of shear strain)

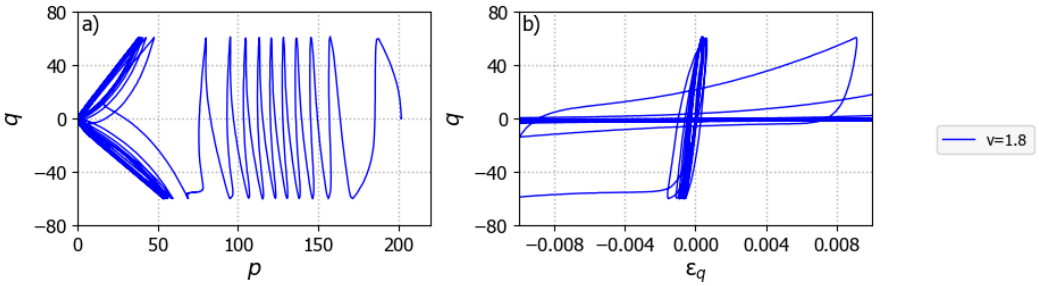


Figure 56 Undrained cyclic stress controlled test (a) shear stress function of volumetric stress; b) shear stress function of shear strain)

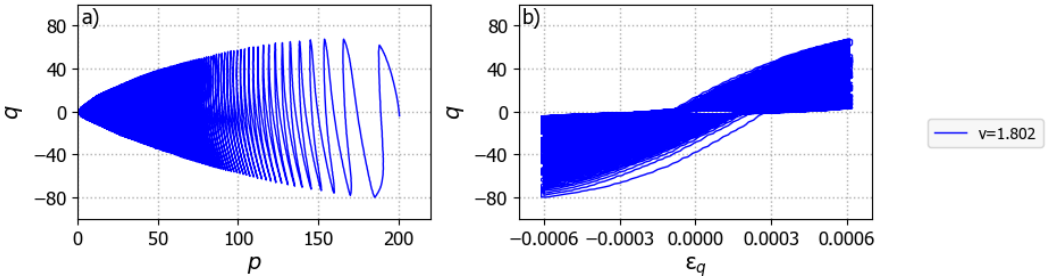


Figure 57 Undrained cyclic strain controlled test (a) shear stress function of volumetric stress; b) shear stress function of shear strain)

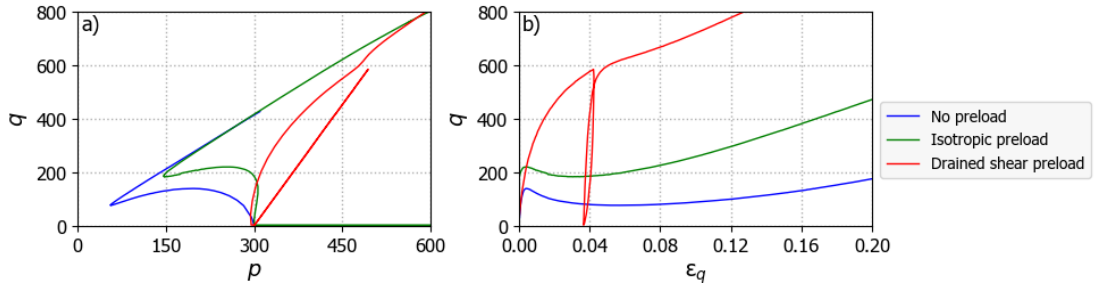


Figure 58 Undrained tests with preloading (a) shear stress function of volumetric stress; b) shear stress function of shear strain)

3.2.2. A frictional model with perfect plasticity and no volumetric plasticity

This model is abbreviated as Hyper_fric.

3.2.2.1. Theory

One of the major forces governing the behaviour of sand is friction (cf. Chapter 2). This guides the first step of the model construction with a simple frictional model, which is also the basis of the model developed by Houlsby (1992) and Houlsby and Mortara (2004) and is documented in Houlsby and Puzrin (2006) and Houlsby (2023).

This frictional model includes linear elasticity, and plastic shear strain, but no plastic volumetric strain. In consequence, the Gibbs energy function can be written:

$$g = -\frac{p^2}{2K} - \frac{q^2}{6G} - q\alpha_q \qquad \textit{Eq. 30}$$

The first term arises from the volumetric elasticity, the second from the shear elasticity, and the third from the shear plasticity.

The dissipation associated to a frictional model is proportional to the frictional force multiplied by the plastic shear strain rate:

$$d = Mp\left|\dot{\alpha}_q\right| \qquad \textit{Eq. 31}$$

In this expression, Mp is the frictional force, $\dot{\alpha}_q$ is the plastic shear strain. The dissipation is positive for any shear direction which explains the absolute value. The mechanical behaviour of the whole model can be deduced from Eq. 30 and Eq. 31 in the hyperplastic framework. First, the calculation of the volumetric strain is:

$$\epsilon_p = -\partial g/\partial p = p/K \qquad \textit{Eq. 32}$$

This means that the volumetric strain is purely elastic and proportional to the mean effective pressure via the bulk modulus. Second, the calculation of the deviatoric strain is:

$$\epsilon_q = -\partial g/\partial q = q/3G + \alpha_q \qquad \textit{Eq. 33}$$

This indicates that the shear strain has a plastic component (α_q), while its elastic component ($\epsilon_q - \alpha_q$) is proportional to the shear stress via the shear modulus.

From the dissipation function, the generalised shear stress is calculated:

$$\chi_q = \partial d/\partial \dot{\alpha}_q = MpS\left(\dot{\alpha}_q\right) \qquad \textit{Eq. 34}$$

Because Mp is positive, $S\left(\chi_q\right) = S\left(\dot{\alpha}_q\right)$ (where S is the signum function), thus, for $\dot{\alpha}_q \neq 0$:

$$\left|\chi_q\right| = Mp \qquad \textit{Eq. 35}$$

Therefore the subtraction of these two terms is equal to zero, and a yield surface expression is derived:

$$y = |\chi_q| - Mp = 0 \qquad \textit{Eq. 36}$$

In $p - q$ space, this yield function describes a wedge of slope M as presented in Figure 59.

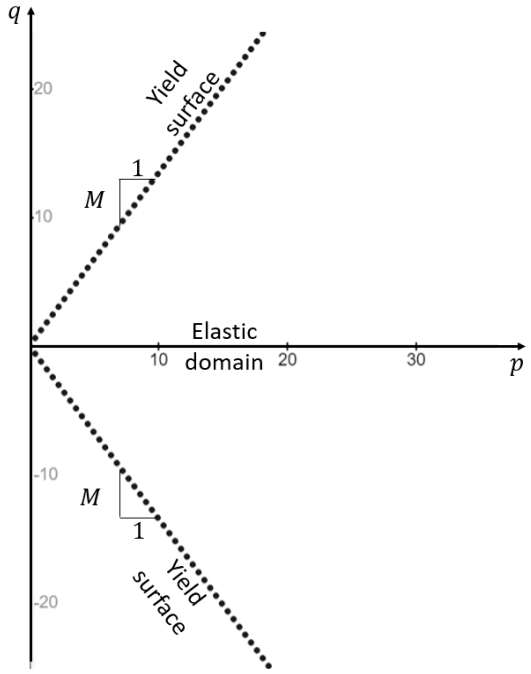


Figure 59 Representation of the yield surface and elastic domain for the simple frictional model

Inside this wedge, the behaviour is purely elastic with $\epsilon_p = p/K$ [Eq. 37] and $\dot{\epsilon}_q = \dot{q}/3G$ [Eq. 38], while upon reaching the yield surface ($\chi_q = \overline{\chi_q} = -\partial g/\partial \alpha_q = q = \pm Mp$ [Eq. 39]) the shear behaviour becomes perfectly plastic with $\epsilon_q = \frac{q}{3G} + \alpha_q$ [Eq. 40].

A summary of Hyper_fric is as follows:

Gibbs energy function: $g = -\frac{p^2}{2K} - \frac{q^2}{6G} - q\alpha_q$	*Eq. 41*
Dissipation function: $d = Mp\lvert\dot{\alpha_q}\rvert$	*Eq. 42*
Alternative to the dissipation function, yield function: $y = \lvert\chi_q\rvert - Mp$	*Eq. 43*

3.2.2.2. Analysis of the tests results

Figure 60 to Figure 64 attempt to respectively model Figure 54 to Figure 58 of Wichtmann tests using Hyper_fric.

This frictional model only allows to distinguish two phases: one elastic, and one perfectly plastic only in shear. This is largely insufficient to describe the behaviour of sand even under monotonic loading. The exclusion of plastic volumetric behaviour from the model has several consequences:

- for drained loading represented in Figure 60, the volumetric behaviour is contractive during the elastic phase and isochoric during the plastic phase. Thus, the model is not able to represent the characteristic dilation associated to dense sand.
- for undrained loading, represented in Figure 61, the absence of p variation is explained by the absence of plastic volumetric behaviour ($dp = Kd\epsilon_p^e = -Kd\epsilon_p^p = 0$ [Eq. 44]).

The absence of density dependence implies that the model does not distinguish between loose and dense sand.

For the undrained cyclic tests, the successive loadings are elastic and lay one over another with no p decrease and no reduction of the secant stiffness (cf. Figure 62 and Figure 63). These loadings are purely elastic because the loadings amplitudes are too low to reach the yield surface. In Figure 63, the X-shape in $p - q$ space is due to a first drained cycle (which has a 3/1 slope), followed by the undrained cycles (which are vertical).

The isotropic preloading has no impact on the subsequent undrained loading as it is purely elastic. The drained preloading to $\epsilon_q = 0.04$ goes perfectly plastic and thus accumulates plastic strain before the reloading as shown in Figure 64.

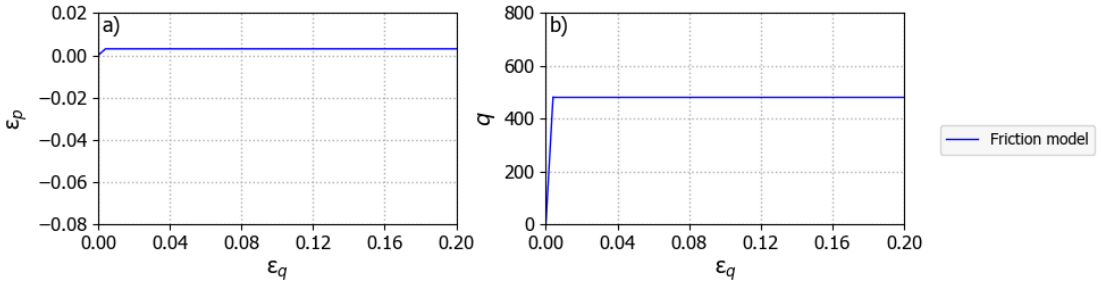


Figure 60 Drained tests (a) volumetric strain function of shear strain; b) shear stress function of shear strain)

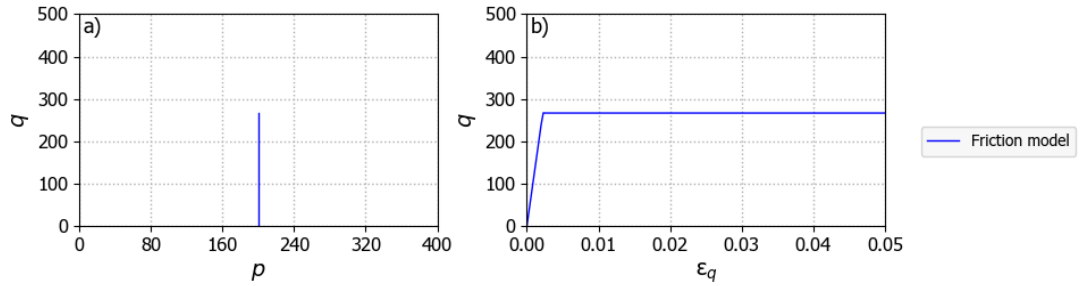


Figure 61 Undrained tests (a) shear stress function of volumetric stress; b) shear stress function of shear strain)

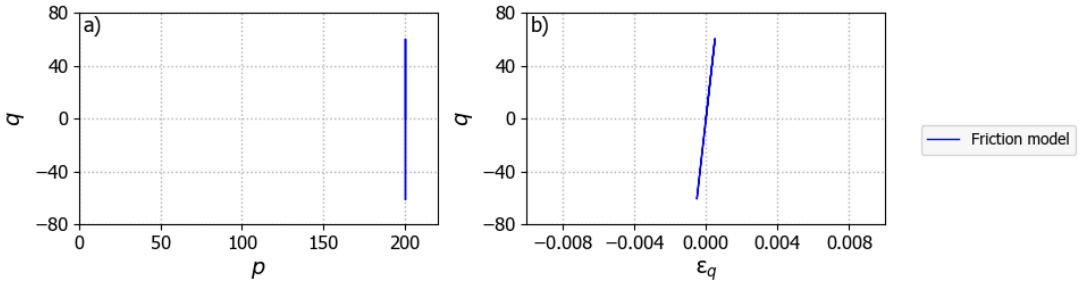


Figure 62 Undrained cyclic stress controlled test (a) shear stress function of volumetric stress; b) shear stress function of shear strain)

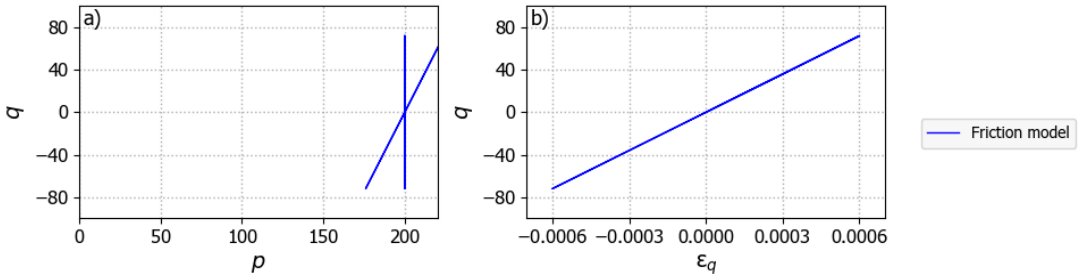


Figure 63 Undrained cyclic strain controlled test (a) shear stress function of volumetric stress; b) shear stress function of shear strain)

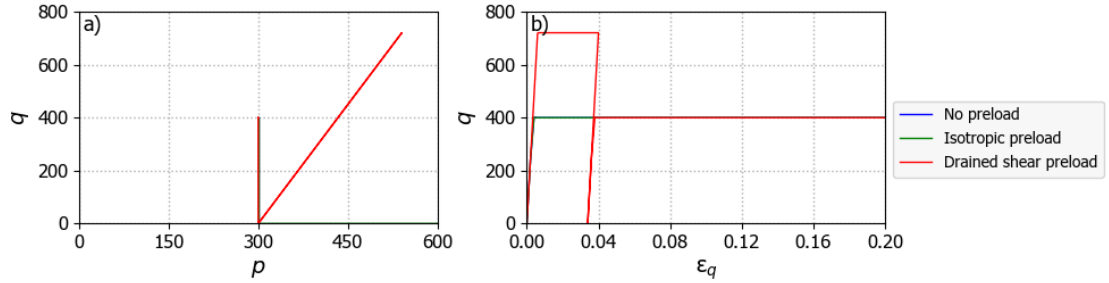


Figure 64 Undrained test with preloading (a) shear stress function of volumetric stress; b) shear stress function of shear strain)

3.2.3. Dilation constraint

This model is abbreviated as Hyper_fixed_dil.

3.2.3.1. Theory

Hyperplasticity allows an easy introduction of plastic volumetric strain. The energy function is modified such that volumetric plastic strain (α_p) is taken into account in Eq. 45. Eq. 46 gives the differential of the energy function by the mean effective pressure, which gives the volumetric strain, where the first term is the elastic term and the second the plastic term.

$$g = -\frac{p^2}{2K} - \frac{q^2}{6G} - q\alpha_q - p\alpha_p \qquad \textit{Eq. 45}$$

$$-\frac{\partial g}{\partial p} = \epsilon_{\mathrm{p}} = \frac{\mathrm{p}}{\mathrm{K}} + \alpha_p = \epsilon_p^e + \epsilon_p^p \qquad \textit{Eq. 46}$$

Dilation is introduced thanks to the constraint C_d. The plastic volumetric strain rate ($\dot{\alpha_p}$) is made dependent of the plastic shear strain rate via Eq. 47, leading to the dilation ratio in Eq. 48:

$$C_d = \dot{\alpha_p} + \beta\left|\dot{\alpha_q}\right| = 0 \qquad \textit{Eq. 47}$$

$$d_r = \frac{\dot{\alpha_p}}{\dot{\alpha_q}} = -\beta S(\dot{\alpha_q}) \qquad \textit{Eq. 48}$$

$S(\dot{\alpha_q})$ allows to obtain the same dilation when shearing in one direction or the other. The contractive-positive convention implies that a positive β leads to dilation, and a negative value leads to contraction.

The constraint equation is added to the dissipation equation which is still positive ($C_d = 0$):

$$d^* = Mp\left|\dot{\alpha_q}\right| + \Lambda_d C_d \qquad \textit{Eq. 49}$$

The general stresses obtained from the energy function then are:

$$\overline{\chi_p} = -\frac{\partial g}{\partial \alpha_p} = p \qquad \textit{Eq. 50}$$

$$\overline{\chi_q} = -\frac{\partial g}{\partial \alpha_q} = q \qquad \textit{Eq. 51}$$

And the general stresses obtained from the dissipation function are:

$$\chi_p = \frac{\partial d^*}{\partial \dot{\alpha_p}} = \Lambda_d \qquad \textit{Eq. 52}$$

$$\chi_q = \frac{\partial d^*}{\partial \dot{\alpha_q}} = \mathrm{MpS}\left(\dot{\alpha}_{\mathrm{q}}\right) + \Lambda_{\mathrm{d}}\beta S\left(\dot{\alpha_q}\right) \qquad \textit{Eq. 53}$$

Thus from the equation of χ_q, a yield surface function can be obtained:

$$y = \left|\chi_q\right| - Mp - \beta\chi_p = 0 \qquad \textit{Eq. 54}$$

From this yield surface equation, it can be observed that the constraint introduced to control the dilation rate also has a direct impact on the capacity:

- with no dilation constraint, plasticity is reached when $\left|\chi_q\right| = |q| = Mp$ [Eq. 55].
- with the dilation constraint, plasticity is reached when $|q| = (M + \beta)p$ [Eq. 56] which is inferior to Mp for a contraction, and superior to Mp for a dilation.

A summary of Hyper_fixed_dil is as follows:

Gibbs energy function: $g = -\frac{p^2}{2K} - \frac{q^2}{6G} - q\alpha_q - p\alpha_p$	*Eq. 57*
Dissipation function: $d = Mp\lvert\dot{\alpha_q}\rvert + \Lambda_d C_d$	*Eq. 58*
where the dilation constraint is: $C_d = \dot{\alpha_p} + \beta\lvert\dot{\alpha_q}\rvert = 0$	*Eq. 59*
Alternative to the dissipation function and constraint, yield function: $y = \lvert\chi_q\rvert - Mp - \beta\chi_p$	*Eq. 60*

3.2.3.2. Analysis of test results

Figure 65 to Figure 69 attempt to respectively model Figure 54 to Figure 58 of Wichtmann tests using Hyper_fixed_dil. The tests were run with three different β values (0 in green, -0.3 contractive blue, 0.3 dilative red).

In the drained monotonic test, see Figure 65, the dilation constraint captures the wanted dilation rate and the modified capacity $q = (M + \beta)p$. In contrast to the data, the capacities do not converge after large strain and instead stay constant at $q = (M + \beta)p$. Also, there are still only two phases, first elastic, and second perfectly plastic in the shear stress-strain space, while the data shows a progressive plasticity and a softening.

In the undrained monotonic tests, Figure 66, the strength at yield now is $q = (M + \beta)p$. Upon yielding, in the $p - q$ space, p either falls towards 0 in a contractive case, or goes towards increasing p and q for a dilative case, while it stays at $q = Mp$ for the neutral case. In both contractive and dilative cases, the curves follow the yield surface which has a slope $M + \beta$. To understand the preceding result, one can study the variation of p in the model:

$$dp = Kd\epsilon_p^e = K(d\epsilon_p - d\alpha_p) \qquad \textit{Eq. 61}$$

$d\epsilon_p = 0$ because the test is undrained, while the plastic volumetric strain can be expressed as a function of the plastic deviatoric strain via the constraint equation:

$$dp = -Kd\alpha_p = K\beta\lvert d\alpha_q\rvert \qquad \textit{Eq. 62}$$

This is such that if β is negative (contractive case) the mean effective pressure (p) is going to decrease, while if β is positive (dilative case) the mean effective pressure increases.

The cyclic undrained responses, Figure 67 and Figure 68, are still elastic. The pre-loaded tests, Figure 69, go plastic and have positive shear strain-shear stress slopes because $\beta = 0.3$.

Improvements of Hyper_fixed_dil from Hyper_fric:

A dilation rate (β) can be dictated.

It is accompanied by a modification of the yield surface, thus of the capacity, in agreement with observations.

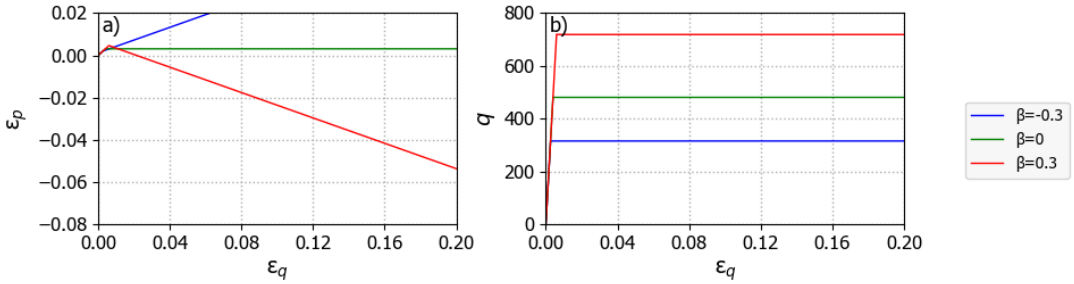


Figure 65 Drained tests (left: volumetric strain function of shear strain; right: shear stress function of shear strain)

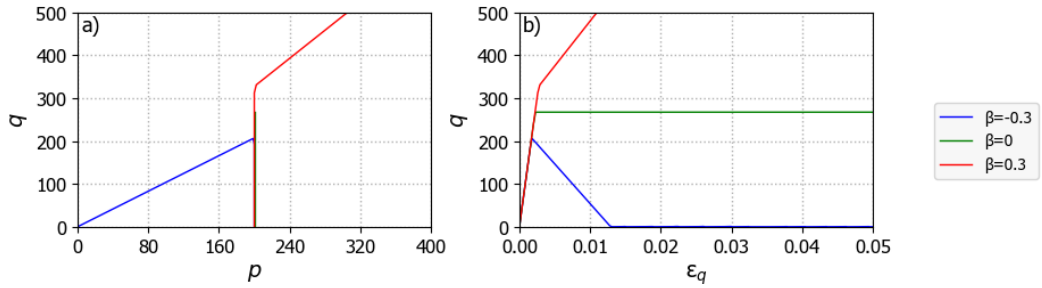


Figure 66 Undrained tests (left: shear stress function of volumetric stress; right: shear stress function of shear strain)

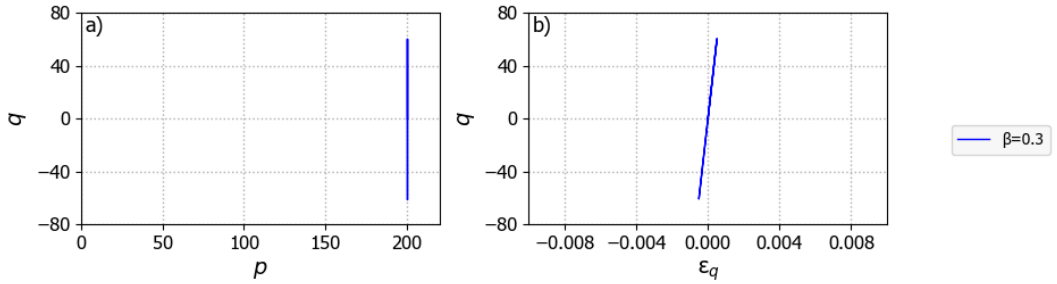


Figure 67 Undrained cyclic stress controlled test (left: shear stress function of volumetric stress; right: shear stress function of shear strain)

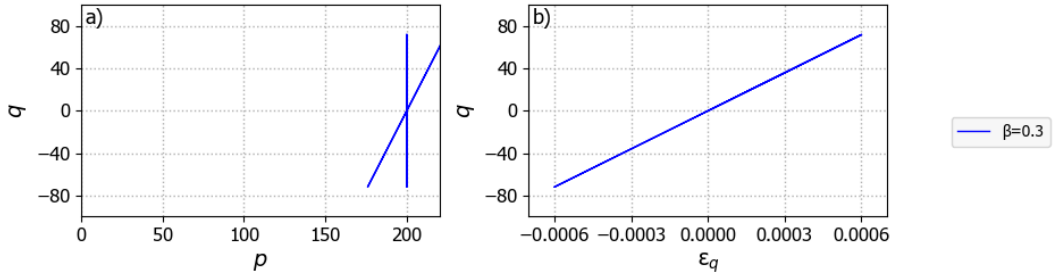


Figure 68 Undrained cyclic strain controlled test (left: shear stress function of volumetric stress; right: shear stress function of shear strain)

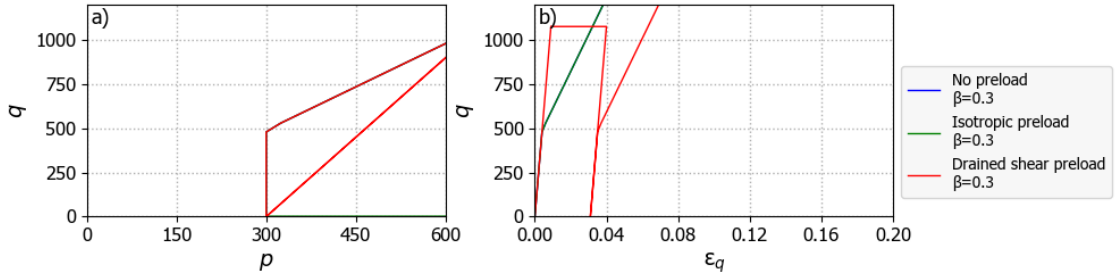


Figure 69 Undrained test with preloading (left: shear stress function of volumetric stress; right: shear stress function of shear strain) change from original scale

3.2.4. Asymmetrisation of the yield surface

The following model is abbreviated by Hyper_fixed_dil_asym.

3.2.4.1. Theory

The triaxial test is asymmetric by nature. In compression, the major principal stress is in the vertical direction while the minor principal stresses are both horizontal directions. While in extension, the situation reverses with major principal stresses in both horizontal directions and the vertical stress being the unique minor principal stress.

This asymmetry results in different behaviours. In Figure 70, the asymptotes in the $q - p$ space have different slopes in compression and extension.

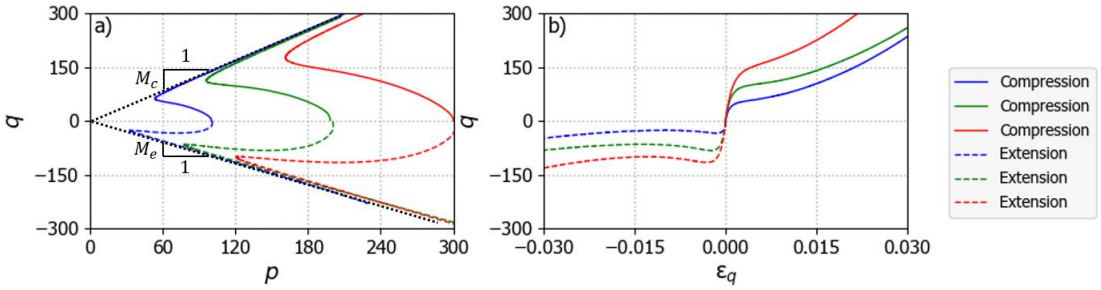


Figure 70 Undrained test on medium dense sand in compression and extension by Wichtmann (2021)

Houlsby and Mortara (2004) distinguish the behaviour in compression and extension through different critical stress ratio: M_c in compression, and M_e in extension. Here a new formulation emanates from the three-dimensional development (Chapter 2.3.3.2) which uses the Matsuoka-Nakai yield criterion (Matsuoka and Nakai (1974)).

In the triaxial space, this criterion takes the form (noting that $\sigma_1 = p + \frac{2}{3}q$ and $\sigma_3 = p - q/3$):

$$y = q^2 - 4\mu^2\left(p + \frac{2}{3}q\right)\left(p - \frac{q}{3}\right) = 0 \qquad \textit{Eq. 63}$$

Where $\mu = \tan\varphi$ and φ is the frictional angle, while $M_c = 6\sin\varphi\,/(3 - \sin\varphi)$ [Eq. 64] and $M_e = 6\sin\varphi\,/(3 + \sin\varphi)$ [Eq. 65].

Writing this expression to obtain zero dilation in hyperplastic terms can take the following form:

$$y = \chi_q^2 - 4\mu^2\left(p + \frac{2}{3}q\right)\left(p - \frac{q}{3}\right) = 0 \qquad \textit{Eq. 66}$$

Indeed, the dilation rate is:

$$d_r = \frac{\dot{\alpha_p}}{\dot{\alpha_q}} = \frac{\frac{\partial y}{\partial \chi_p}}{\frac{\partial y}{\partial \chi_q}} = \frac{0}{2\chi_q} = 0 \qquad \textit{Eq. 67}$$

This yield function can be obtained from the dissipation function:

$$d = 2\mu\sqrt{\left(p+\frac{2}{3}q\right)\left(p-\frac{q}{3}\right)}\left|\dot{\alpha}_q\right| \qquad \textit{Eq. 68}$$

The dilation constraint $C_d = \dot{\alpha}_p + \beta\left|\dot{\alpha}_q\right| = 0$ [Eq. 69] can be added:

$$d^* = 2\mu\sqrt{\left(p+\frac{2}{3}q\right)\left(p-\frac{q}{3}\right)}\left|\dot{\alpha}_q\right| + \Lambda_d\left(\dot{\alpha}_p + \beta\left|\dot{\alpha}_q\right|\right) \qquad \textit{Eq. 70}$$

The value of Λ_d is obtained by differentiating by the rate of plastic volumetric strain:

$$\chi_p = \frac{\partial d^*}{\partial \dot{\alpha}_p} = \Lambda_d \qquad \textit{Eq. 71}$$

The generalised shear stress can then be obtained:

$$\chi_q = \frac{\partial d^*}{\partial \dot{\alpha}_q} = 2\mu\sqrt{\left(p+\frac{2}{3}q\right)\left(p-\frac{q}{3}\right)}S(\chi_q) + \beta S(\chi_q)\chi_p \qquad \textit{Eq. 72}$$

From the expression of the generalised shear stress, a yield function can be established:

$$y = \left(\chi_q - \beta S(\chi_q)\chi_p\right)^2 - 4\mu^2\left(p+\frac{2}{3}q\right)\left(p-\frac{q}{3}\right) = 0 \qquad \textit{Eq. 73}$$

This version of the model conserves the dilation ratio, however the stress ratio at yield differs from the model by Houlsby and Mortara (2004) (noted HM), where the stress ratio at yield is:

$$\frac{q}{p}_{HM} = 6\mu\frac{\mu \pm 3\sqrt{1+\mu^2}}{9+8\mu^2} \pm \beta = M_{c/e} \pm \beta \qquad \textit{Eq. 74}$$

Here, solving the yield equation for the stress ratio $\frac{q}{p}$, noting that $\chi_q = q$ and $\chi_p = p$, leads to:

$$\frac{q}{p} = 6\mu\frac{\mu \pm \frac{3}{2}\frac{\beta}{\mu} \pm 3\sqrt{1+\mu^2 \pm \frac{\beta}{3} \mp \frac{2}{9}\beta^2}}{(9+8\mu^2)} \qquad \textit{Eq. 75}$$

This complicated stress ratio still provides an additional strength in the dilative phase of a test, and it allows one to clearly distinguish the compression and extension cases ($\pm$ in Eq. 74 and Eq. 75 correspond to a $+$ for compression and $-$ for extension, and reverse for $\mp$).

A summary of Hyper_fixed_dil_asym is as follows:

Gibbs energy function: $g = -\frac{p^2}{2K} - \frac{q^2}{6G} - q\alpha_q - p\alpha_p$	*Eq. 76*
Dissipation function: $d^* = 2\mu\sqrt{\left(p+\frac{2}{3}q\right)\left(p-\frac{q}{3}\right)}\left\|\dot{\alpha}_q\right\| + \Lambda_d C_d$	*Eq. 77*
where the dilation constraint is: $C_d = \dot{\alpha}_p + \beta\left\|\dot{\alpha}_q\right\| = 0$	*Eq. 78*
Alternative to the dissipation function and constraint, yield function: $y = \left(\chi_q - \beta S(\chi_q)\chi_p\right)^2 - 4\mu^2\left(p+\frac{2}{3}q\right)\left(p-\frac{q}{3}\right)$	*Eq. 79*

3.2.4.2. Analysis of test results

Figure 71 shows the differences between compression and extension for undrained tests with the model:

- a different stress ratio ($|q/p|$) at yield, here approximately $|q/p| \approx 1.583$ in compression, and $|q/p| \approx 1.095$ in extension.
- a different shear stress-shear strain slope once plastic, with $\approx 20.4MPa$ in compression, and $\approx 14.8MPa$ in extension.

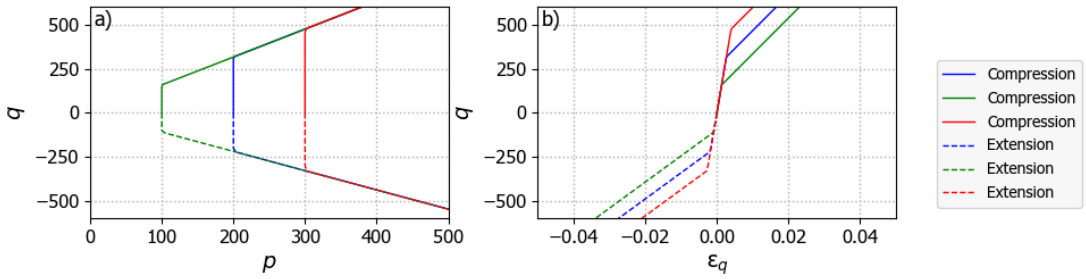


Figure 71 Monotonic undrained test in extension and compression with the model for $\beta = 0.3$

Figure 72 compares the results of the previous model (solid lines) to the new model (dashed lines) for drained monotonic tests in compression. The modification has little impact on the volumetric behaviour. As expected, the capacity is slightly modified when $\beta \neq 0$, still giving an additional strength for a dilative test (red), and less strength for a contractive test (blue).

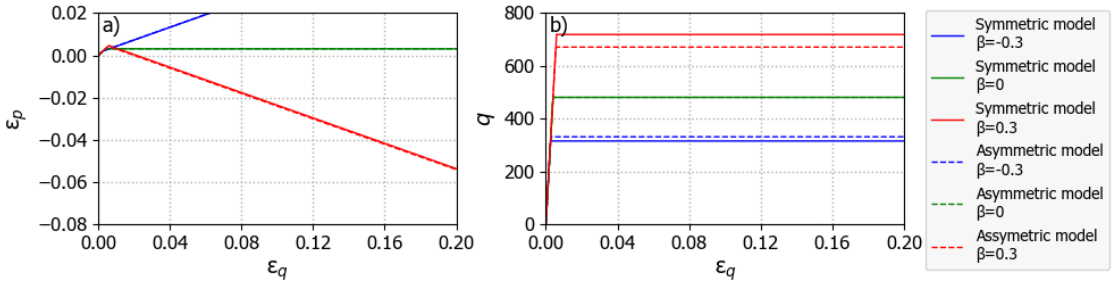


Figure 72 Monotonic drained tests comparison between previous (dashed) and new formulation (solid)

The comparisons with the tests by Wichtmann are not given here as they only differ slightly from the previous model.

Improvements brought by Hyper_fixed_dil_asym compared to Hyper_fixed_dil:

A distinction between compression and extension, compatible with the 3D development.

3.2.5. Introducing density dependence

This model is abbreviated by Hyper_vdep_dil.

3.2.5.1. Theory

The volumetric behaviour of sand is linked to its density. Based on Houlsby (1992), the dilation can be made a function of the distance of the current specific volume (v) to the critical state specific volume (Γ), with the maximal dilation rate (β_{max}) taking place at the densest specific volume possible (Δ):

$$\beta = \beta_{max}\frac{\ln(v)-\ln(\Gamma)}{\ln(\Delta)-\ln(\Gamma)} \qquad \textit{Eq. 80}$$

This expression delivers a maximal dilation rate $d_r = \beta_{max}$ [Eq. 81] at the densest state, then a smaller dilation rate the looser the sample is, no plastic volumetric strain at critical state, and contraction for looser than critical samples. The use of $(\ln(v)-\ln(\Gamma))/(\ln(\Delta)-\ln(\Gamma))$ is an alternative to other modelling strategies such as the index introduced by Basset and Wroth (1965), the state index used by Ishihara *et al.* (1975) ($I_s = (e_0-e)/(e_0-e_c)$ [Eq. 82]), or the state parameter used by Been and Jefferies (1985) ($\psi = e - e_c$ [Eq. 83]) and used for example in Sanisand (Dafalias and Manzari, 2004). All these options allow the current state to be located relative to the critical state via the void ratio or specific volume.

The dilation rate will evolve during a drained test because the specific volume is a function of volumetric strain:

$$\beta = \beta_{max}\frac{\ln(v)-\ln(\Gamma)}{\ln(\Delta)-\ln(\Gamma)} = \beta_{max}\frac{\ln(v_0 e^{-\epsilon_p})-\ln(\Gamma)}{\ln(\Delta)-\ln(\Gamma)} = \beta_{max}\frac{\ln(v_0)-\epsilon_p-\ln(\Gamma)}{\ln(\Delta)-\ln(\Gamma)} \qquad \textit{Eq. 84}$$

For example, for a dense sample, initially the dilation will be important, thus the specific volume will increase. This will in turn diminish the dilation ratio (β), thus the dilation, until the critical state is reached. In the shear stress-strain space, this means the model will soften.

Hyper_vdep_dil is summarised by:

Gibbs energy function: $g = -\frac{p^2}{2K} - \frac{q^2}{6G} - q\alpha_q - p\alpha_p$	*Eq. 85*
Dissipation function: $d^* = 2\mu\sqrt{\left(p+\frac{2}{3}q\right)\left(p-\frac{q}{3}\right)}\left\|\dot{\alpha_q}\right\| + \Lambda_d C_d$	*Eq. 86*
where the dilation constraint is: $C_d = \dot{\alpha_p} + \beta\left\|\dot{\alpha_q}\right\| = 0$	*Eq. 87*
Where $\beta = \beta_{max}\frac{\ln(v)-\ln(\Gamma)}{\ln(\Delta)-\ln(\Gamma)} = \beta_{max}\frac{\ln(v_0)-\epsilon_p-\ln(\Gamma)}{\ln(\Delta)-\ln(\Gamma)}$	*Eq. 88*
Alternative to the dissipation function and constraint, yield function: $y = \left(\chi_q - \beta S(\chi_q)\chi_p\right)^2 - 4\mu^2\left(p+\frac{2}{3}q\right)\left(p-\frac{q}{3}\right)$	*Eq. 89*

3.2.5.2. Analysis of test results

Figure 73 to Figure 77 attempt to respectively model Figure 54 to Figure 58 of Wichtmann tests using Hyper_vdep_dil. Note the change of scale in Figure 73, Figure 74 and Figure 77.

In the tests presented here, the critical state specific volume is set to $\Gamma = 1.98$, and $\Delta = 1.677$ for the densest state. Tests are run with the original Wichtmann specific volumes such that all samples are denser than critical. In Figure 74 representing undrained tests, this explains why none of the stress path collapses towards $p = 0$.

The variation of β across initial densities allows one to capture:

- more dilation the denser the sample initially is in drained tests, as seen in Figure 73,
- larger additional strength the denser the sample is in drained tests, as seen in Figure 73,
- steeper shear stress-strain asymptotes the denser the sample is in undrained tests, shown in Figure 74.

The embedded volumetric variation in the model allows one to capture:

- softening once the yield surface is reached in the drained tests, as shown in Figure 73,
- convergence towards a critical state for drained tests. The beginnings of the shear stress-strain curves convergence can be seen in Figure 73.

A major characteristic that is still not captured by the model is the initial compression in the drained monotonic tests (alternatively, the initial pore pressure build-up in the undrained tests), which should be the clearest in the $p - q$ space for undrained tests with an initial curvature of the stress path towards lower p that is not observed in Figure 74.

The model still presents an abrupt transition from a linear elastic behaviour to a plastic behaviour that is not representative of soils.

In Figure 75 and Figure 76, cyclic tests only present elastic "loops", and the appropriate behaviour is not yet captured at all.

In Figure 77, which represents the preloaded undrained tests, a slight softening is observed during the drained preloading, but the behaviour has globally not evolved from the previous step.

Improvements brought by Hyper_vdep_dil from Hyper_fixed_dil_asym :
Density dependence of dilation.
Embedded volumetric/density change, and, as a consequence, softening in drained tests.

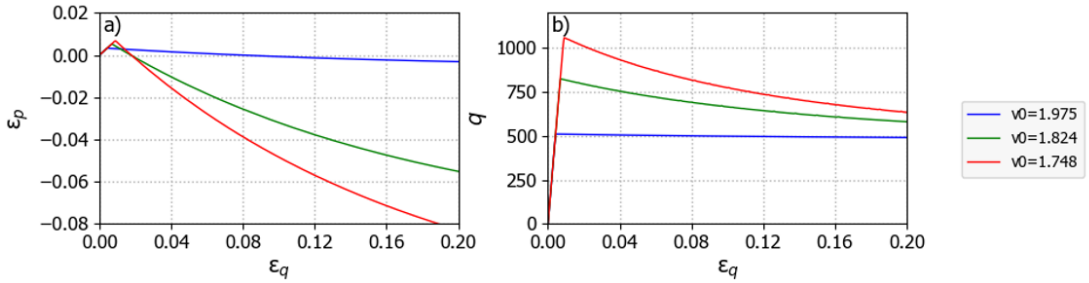


Figure 73 Drained tests (left: volumetric strain function of shear strain; right: shear stress function of shear strain) change from original scale

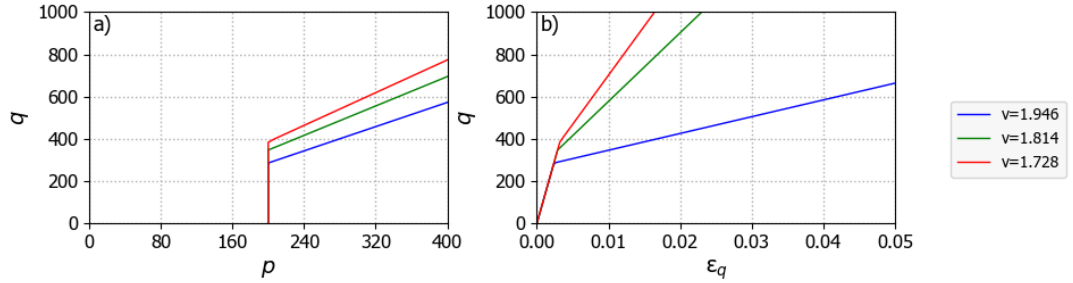


Figure 74 Undrained tests (left: shear stress function of volumetric stress; right: shear stress function of shear strain) change from original scale

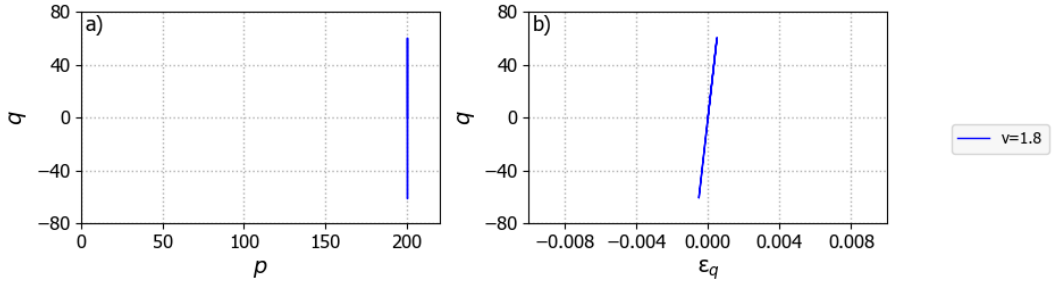


Figure 75 Undrained cyclic stress controlled test (left: shear stress function of volumetric stress; right: shear stress function of shear strain)

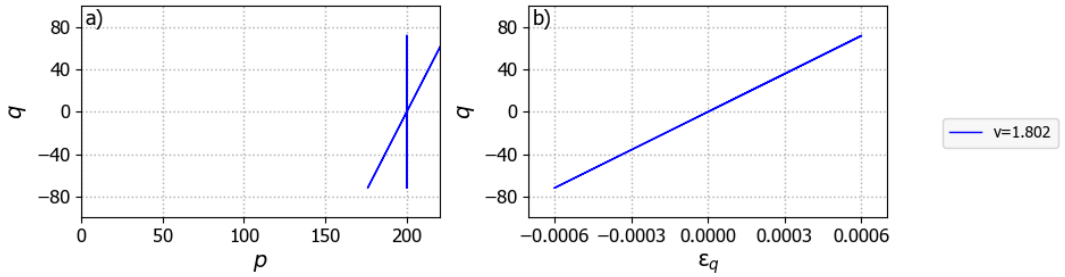


Figure 76 Undrained cyclic strain controlled test (left: shear stress function of volumetric stress; right: shear stress function of shear strain)

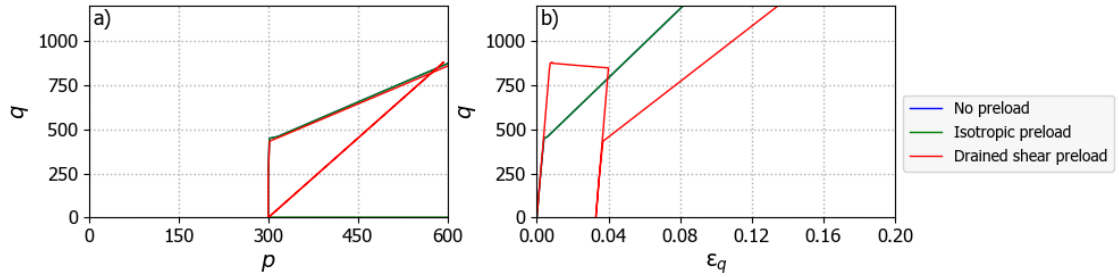


Figure 77 Undrained test with preloading (left: shear stress function of volumetric stress; right: shear stress function of shear strain) change from original scale

3.2.6. Anisotropy and its impact on volumetric strain

This model is abbreviated by Hyper_ani.

3.2.6.1. Experimental observations and theory

The left graph of Figure 78 presents two yield surfaces, with $\beta = 0$ (dotted black) and with $\beta = 0.7$ (solid blue). The current formulation, for $\beta > 0$, gives an extra-strength in both extension and compression.

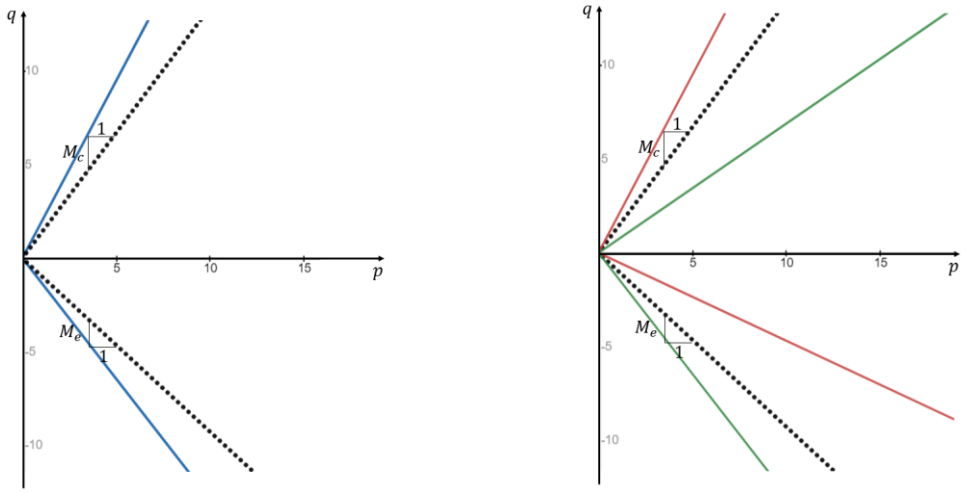


Figure 78 Yield surfaces in p-q space, former formulation on the left, new formulation on the right (a=0 dotted black, a=1 red, a=-1 green)

Houlsby (1992) has proposed to make dilation, and the associated extra-strength, a function of anisotropy. The objective is twofold: to have an initially null dilation developing with the anisotropy of the sample; to have contraction upon reversal of the loading.

From a physical point of view, the first objective would mean that there is initially no dilation for an isotropic sample. But as the sample is sheared and develops anisotropy (grains aligning in one preferred direction), grains start to override each other leading to more and more dilation.

For the second objective, tests show that upon unloading, a sample that was dilating on the loading will initially contract before dilating again, which can be understood as grains falling back in place after the dilative phase, leading to contraction, before a new dilative mechanism takes place. This last phenomenon can be observed in cyclic tests on sand, such as the one in Figure 79 by Pradhan *et al.* (1989), where a dilative phase is followed by a contractive phase upon load reversal, which itself turns into a dilative phase when the shearing continues in the same direction.

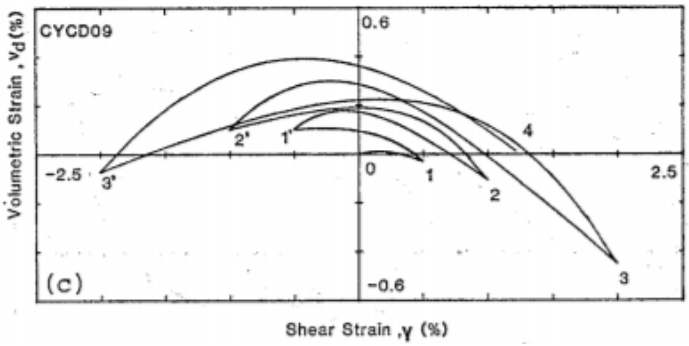


Figure 79 Results of cyclic triaxial drained test on dense Toyoura sand by Pradhan (1989)

In hyperplasticity, this phenomenon is captured with a new internal variable: the scalar a denoting the degree of anisotropy in compression ($0 < a < 1$) or in extension ($-1 < a < 0$), and being null for an isotropic state (Houlsby (1992)).

This scalar can be introduced in the dilation constraint equation:

$$C_d = \dot{\alpha_p} + a\beta\dot{\alpha_q} = 0 \qquad \textit{Eq. 90}$$

For $\beta > 0$:

- if a is null, then there is no volumetric strain.
- if $a > 0$, anisotropy has developed in the compression direction, then there is dilation if the loading continues in the compression direction ($\dot{\alpha_q} > 0$), and there is contraction if there is a load reversal towards extension ($\dot{\alpha_q} < 0$).
- if $a < 0$, the situation is the exact opposite from $a > 0$.

The cases $a = 0$ (dotted black), $a = 1$ (solid red) with extra strength in the compression direction and lower strength in the extension direction, and $a = -1$ (solid green) with the opposite, are illustrated in the right graph of Figure 78.

The introduction of anisotropy induces the following modification of the yield equation:

$$y = \left(\chi_q - a\beta\chi_p\right)^2 - 4\mu^2\left(p + \frac{2}{3}q\right)\left(p - \frac{q}{3}\right) \qquad \textit{Eq. 91}$$

3.2.6.2. Hysteretic anisotropic law

The variation of the anisotropy index (a) can be controlled by a constraint equation proposed by Houlsby (1992):

$$C_a = \dot{a} - A\left(1 - aS\left(\dot{\alpha_q}\right)\right)\dot{\alpha_q} = 0 \qquad \textit{Eq. 92}$$

The anisotropy rate parameter (A) controls how fast the scalar a develops with plastic shear strain. Figure 80 illustrates the evolution of the anisotropy with the plastic shear strain (α_q) for $A = 100$.

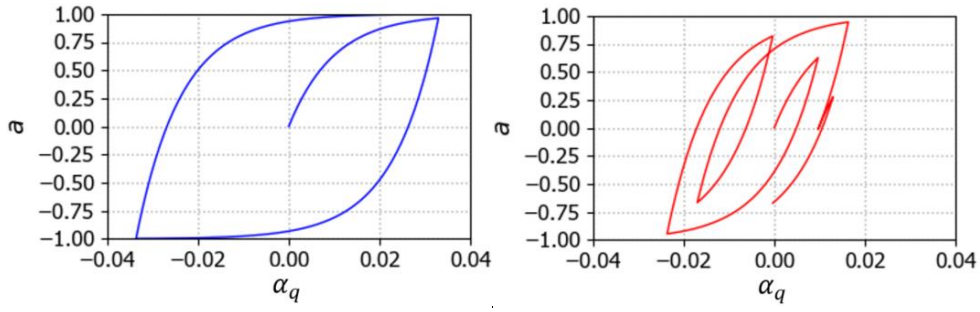


Figure 80 Development of anisotropy with the plastic shear strain in the model for different strain paths

This constraint equation implies a hysteretic development of the anisotropy scalar (a). Making anisotropy a hysteretic process is desirable: when the sample is sheared to a large strain in one direction, anisotropy develops and saturates (here with $a = 1 - e^{-A\alpha_q}$ during a virgin compressive loading), and upon load reversal it seems logical for the sample to necessitate a different amount of strain in the opposite direction to go back to an isotropic state.

The anisotropy constraint equation is added to the dissipation function:

$$d^* = 2\mu\sqrt{\left(p + \frac{2}{3}q\right)\left(p - \frac{q}{3}\right)}|\dot{\alpha}_q| + \Lambda_d(\dot{\alpha}_p + \beta|\dot{\alpha}_q|) + \Lambda_a\left(\dot{a} - A(\dot{\alpha}_q - a|\dot{\alpha}_q|)\right) \qquad \textit{Eq. 93}$$

This translates in the yield function to:

$$y = \left(\chi_q + A\left(1 - aS(\chi_q)\right)\chi_a - a\beta\chi_p\right)^2 - 4\mu^2\left(p + \frac{2}{3}q\right)\left(p - \frac{q}{3}\right) \qquad \textit{Eq. 94}$$

Where χ_a is the conjugate generalised stress to the internal variable a. This new term in the yield function allows the variation of a to be properly integrated into the formulation, but does not modify the value of the yield function. Indeed $\chi_a = \partial g/\partial a = 0$ because the unchanged energy function does not have any term in a.

3.2.6.3. Alternative integrable anisotropic law

The hysteretic law, Eq. 92, implies a rapid decrease of the anisotropy scalar (a) upon load reversal, as can be observed in Figure 80. However, Wichtmann's undrained cyclic strain controlled tests with large strain (Wichtmann and Triantafyllidis (2016b) show that, for dense samples, a large rate of pore pressure build-up is observed upon load reversal and is maintained for a large amount of strain. For example, Figure 81 presents the first two cycles of TCUE17 in which are circled the transition points from pore pressure build-up (equivalent to contraction in drained tests) to dissipation of pore pressure (equivalent to dilation in drained tests). In part b) of the figure, which represents shear stress as a function of shear strain, these transitions take place close to zero shear strain.

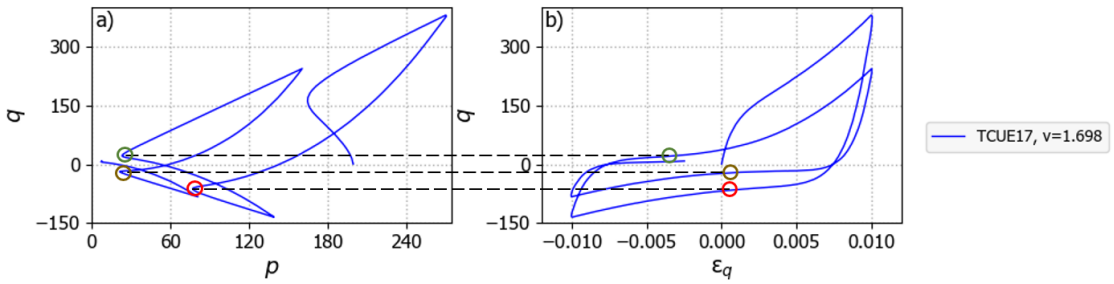


Figure 81 Truncated cyclic undrained strain controlled test on dense sand TCU17 by Wichtmann (2021)

Interpreting this result via the anisotropic concept presented before would mean that $|a|$ would have decreased back from its peak value to zero within approximately the same shear strain amount that was required to develop the anisotropy on loading. Thus, the anisotropy scalar can rather be represented by an integrable anisotropic law such as:

$$C_a = \dot{a} - A(1 - |a|)\dot{\alpha_q} = 0 \qquad \textit{Eq. 95}$$

This delivers the following expression for the anisotropy scalar:

$$a = \left(1 - e^{-A|\alpha_q|}\right) S(\alpha_q) \qquad \textit{Eq. 96}$$

Figure 82 presents the evolution of a for the same strain paths as Figure 80.

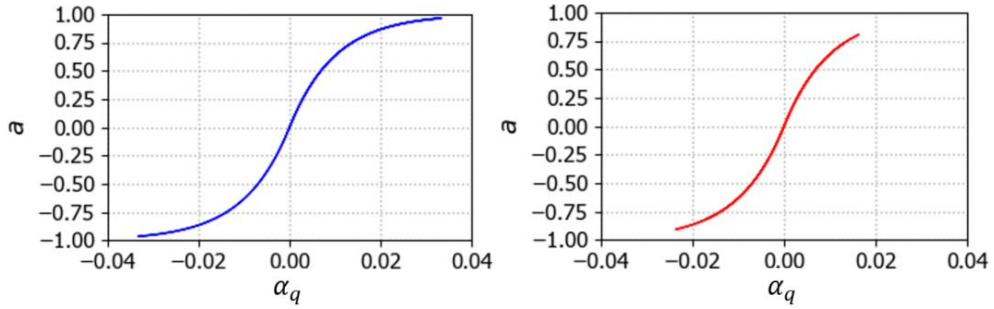


Figure 82 Anisotropy evolution with the integrable law

This anisotropy law translates in the yield function to:

$$y = \left(\chi_q + A(1 - |a|)\chi_a - a\beta\chi_p\right)^2 - 4\mu^2\left(p + \frac{2}{3}q\right)\left(p - \frac{q}{3}\right) \qquad \textit{Eq. 97}$$

3.2.6.4. Alternative hybrid anisotropic law

Because Figure 81 shows that the transition from contraction to dilation, and vice-versa, happens before reaching zero shear strain, and because of the previously explained reasons that have led Houlsby (1992) to retain a hysteretical law, the use of a hysteretical law in which the anisotropy does not dissipate as quickly as in the original hysteretic law appears judicious. Such a behaviour can be represented by mixing the original hysteretic law and the integrable law via a coefficient $f_a \in [0,1]$. The constraint equation becomes:

$$C_a = \dot{a} - A\left(1 - a((1 - f_a)S(a) + f_a S(\dot{\alpha_q})\right)\dot{\alpha_q} = 0 \qquad \textit{Eq. 98}$$

Which can also be written as:

$$C_a = \dot{a} - A\left((1 - |a|) + f_a a\left(S(a) - S(\dot{\alpha}_q)\right)\right)\dot{\alpha}_q = 0 \qquad \textit{Eq. 99}$$

When $f_a = 1$, this law becomes the original hysteretic law, and when $f_a = 0$, this law becomes the integrated law.

For $f_a = 0.05$ the anisotropy develops as represented in Figure 83. Hysteresis develops, but upon load reversal, the evolution of a is much slower than in the initial hysteretic law.

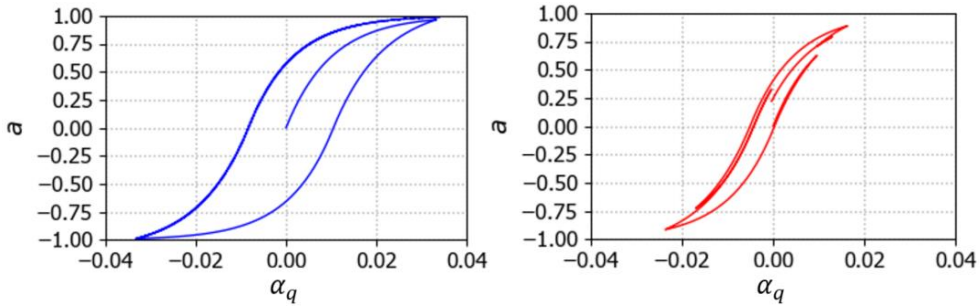


Figure 83 Anisotropy evolution with the hybrid law for f_a = 0.95

3.2.6.5. Choice of the anisotropy law for the base-model

For the sake of simplicity of the model, and because it will be shown in Chapter 5 to give good results, the integrable anisotropy law has been selected for the base-model. The addition of the mixing parameter f_a is avoided.

3.2.6.6. Density dependence of the anisotropy parameter

Based on the drained data by Wichtmann and Triantafyllidis (2016a), it appears that the amount of shear strain at which the peak capacity is reached depends on the density. Figure 84 presents five drained tests at different densities for the same starting effective mean pressure of $p_0 = 200kPa$. The shear strain at which peak capacity is reached increases with increasing specific volumes.

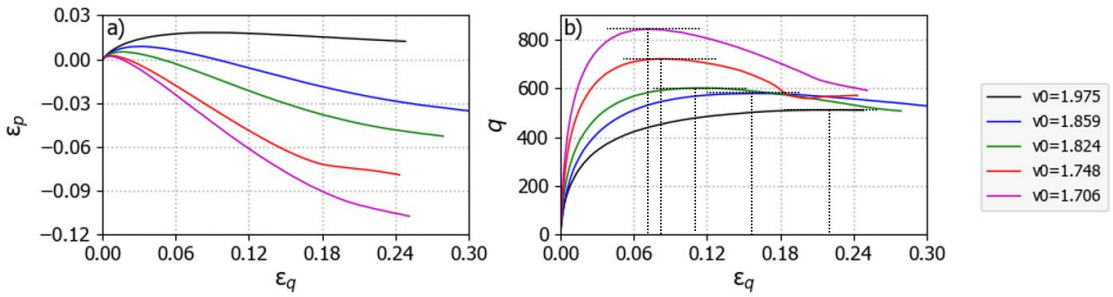


Figure 84 Drained tests on variable densities for a starting pressure of p_0 = 200kPa by Wichtmann (2021)

Figure 85 presents the shear strain at which peak capacity is reached as a function of initial specific volume for all drained tests conducted by Wichtmann.

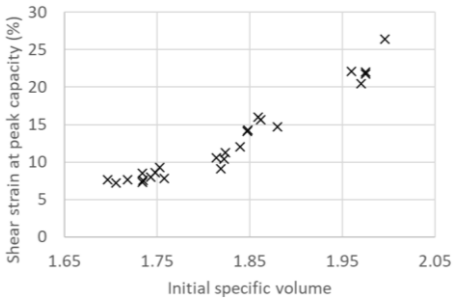


Figure 85 Shear strain at peak capacity against initial specific volume for drained tests by Wichtmann (2021) ($p_0 \in [50kPa, 400kPa]$)

In the theory outlined so far, it is not easy to draw a conclusion about the shear strain at peak capacity, because peak capacity is not reached for a precise value of a. Indeed, the increase of capacity with the increase of a via the dilation mechanism is counterbalanced by the softening taking place as the sample density decreases.

Supposing that all tests reach the peak capacity for the same degree of anisotropy, and neglecting the elastic strain, Eq. 96 entails that the anisotropy parameter (A) is proportional to the inverse of the shear strain at peak capacity $\left(A \propto 1/\epsilon_{q_{peak}}\right)$.

Figure 86 represents the inverse of the shear strain at peak capacity against initial relative density for the drained tests by Wichtmann. Here, the relative density is defined by:

$$D_{r_0} = \frac{ln(v_0) - ln(B)}{ln(\Delta) - ln(B)} \qquad \textit{Eq. 100}$$

Where Δ is, as previously defined, the densest specific volume at a reference pressure, and B is the loosest specific volume at a reference pressure. Here $\Delta = 1.677$ and $B = 2.054$ were adopted in accordance with the data by Wichtmann and Triantafyllidis (2016a).

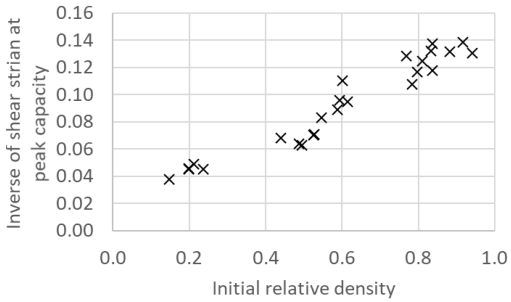


Figure 86 Inverse of the shear strain at peak capacity against initial relative density for drained tests by Wichtmann (2021) ($p_0 \in [50kPa, 400kPa]$)

In conclusion, the relation between relative density and the anisotropy parameter can be approximated by:

$$A = A_{max} \frac{ln(v) - ln(B)}{ln(\Delta) - ln(B)} \qquad \textit{Eq. 101}$$

Where A_{max} is the anisotropy rate development parameter in the densest state.

Hyper_ani is summarised by:

Gibbs energy function: $g = -\frac{p^2}{2K} - \frac{q^2}{6G} - q\alpha_q - p\alpha_p$ *Eq. 102*

Dissipation function: $d^* = 2\mu\sqrt{\left(p + \frac{2}{3}q\right)\left(p - \frac{q}{3}\right)}\left|\dot{\alpha_q}\right| + \Lambda_d C_d + \Lambda_a C_a$ *Eq. 103*

where the dilation constraint is: $C_d = \dot{\alpha_p} + a\beta\dot{\alpha_q} = 0$ *Eq. 104*

and the anisotropy constraint is: $C_a = \dot{a} - A(1 - |a|)\dot{\alpha_q} = 0$ *Eq. 105*

Where $\beta = \beta_{max}\frac{\ln(v) - \ln(\Gamma)}{\ln(\Delta) - \ln(\Gamma)} = \beta_{max}\frac{\ln(v_0) - \epsilon_p - \ln(\Gamma)}{\ln(\Delta) - \ln(\Gamma)}$ *Eq. 106*

Where $A = A_{max}\frac{\ln(v) - \ln(B)}{\ln(\Delta) - \ln(B)} = A_{max}\frac{\ln(v_0) - \epsilon_p - \ln(B)}{\ln(\Delta) - \ln(B)}$ *Eq. 107*

Alternative to the dissipation function and constraints, yield function:

$y = \left(\chi_q + A(1 - |a|)\chi_a - a\beta\chi_p\right)^2 - 4\mu^2\left(p + \frac{2}{3}q\right)\left(p - \frac{q}{3}\right)$ *Eq. 108*

3.2.6.7. Analysis of test results

Figure 90 to Figure 94 attempt to model Wichtmann tests using Hyper_ani.

The anisotropy built into the model makes it possible to control when the dilation is maximal. In the right part of Figure 90, where drained tests are presented, all tests yield at the same stress (because $a = 0$ initially), then harden until maximal dilation is reached, and finally soften similarly to the previous model. This transition better represents data than the previously displayed sharp transition from elastic to softening plastic at maximum dilation.

The parameter A_{max} allows one to control how fast this maximal dilation is reached. Figure 87 presents drained results for the medium dense case with different values of A_{max}. The larger A_{max} is, the quicker peak capacity is reached and the higher it is. It is higher because the sample is denser at this point than in other tests with lower A_{max}: despite the dilation being larger quicker, the volumetric change of the sample at this point is lower than for lower A_{max}, as shown by the dashed lines in Figure 87. Thus, the higher A_{max} is, the higher β is at maximum dilation.

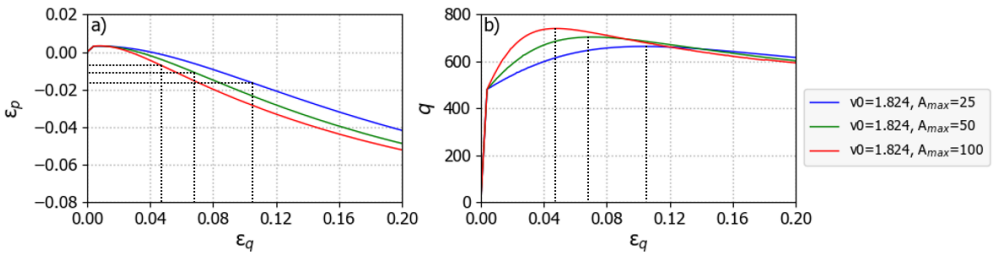


Figure 87 Influence of the value of A_{max} in a drained test

In Figure 90, the density dependence of A means that the medium dense sample (green curve) reaches its maximum capacity later than the dense sample (red curve) while the loose sample demonstrates little increase in capacity because of the density dependence of dilation.

For the undrained monotonic response, Figure 91, the first phase is still purely elastic, but all tests now yield at the same point independent of density (because $a = 0$ for all tests at this point), and then their asymptote in shear stress as a function of shear strain is reached progressively.

The cyclic undrained responses, Figure 92 and Figure 93, are unaffected as the stress levels reached are still inside the elastic domain.

The preloading has little influence on the selected test, as observed in Figure 94. The drained shear preloading is elastic-plastic, such that a develops. But these tests model loose samples, such that β is small, which implies that the drained shear preloading has little impact on the subsequent undrained loading. For a drained shear preload on a denser sample, however, there is a visible difference. In Figure 88, the strength at yield is higher after the preloading, and the shear stress as a function of shear strain slope is steeper after the preloading.

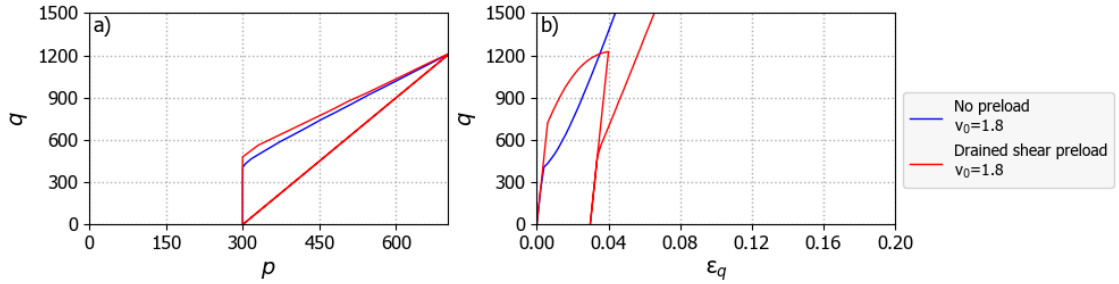


Figure 88 Undrained test with preloading of a dense sample

The plastic contraction upon load reversal after plastic dilation is captured as shown by Figure 89. More precisely, upon load reversal, first there is an elastic phase with the stress point being located inside the yield surface wedge (cf. Figure 78), before reaching the opposite side of the yield surface where it initially contracts before dilating after an amount of shear determined by the value of A. The purely hysteretic anisotropy law gives the result on the left (a), while the purely integrable anisotropy law gives the result to the right (b).

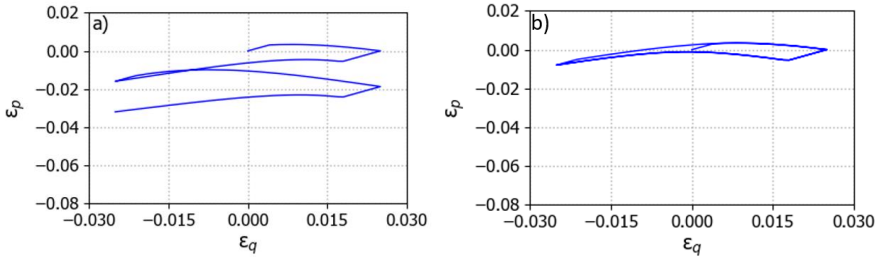


Figure 89 Drained cyclic loading with (a) purely hysteretic law, b) purely integrable law)

Improvements brought by Hyper_ani compared to Hyper_vdep_dil:

The plastic shear amount at which dilation is maximal is adjustable.

Upon load reversal after a dilative phase, contraction ensues.

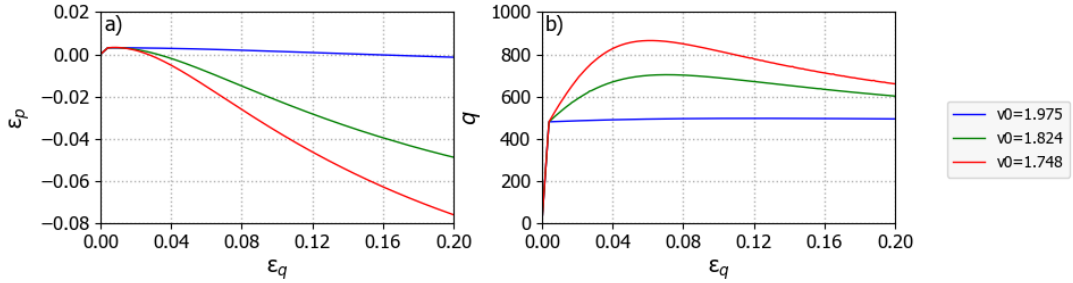


Figure 90 Drained tests (a) volumetric strain function of shear strain; b) shear stress function of shear strain) change from original scale

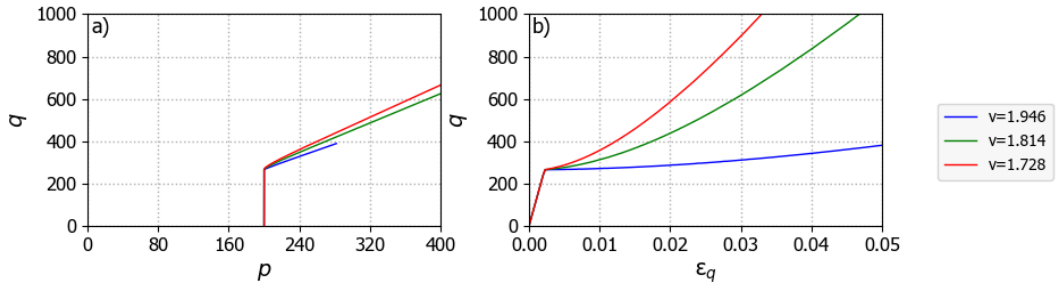


Figure 91 Undrained tests (a) shear stress function of volumetric stress; b) shear stress function of shear strain) change from original scale

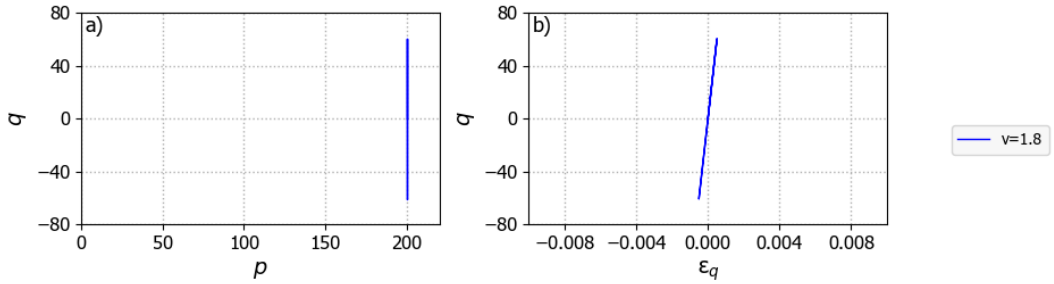


Figure 92 Undrained cyclic stress controlled test (a) shear stress function of volumetric stress; b) shear stress function of shear strain)

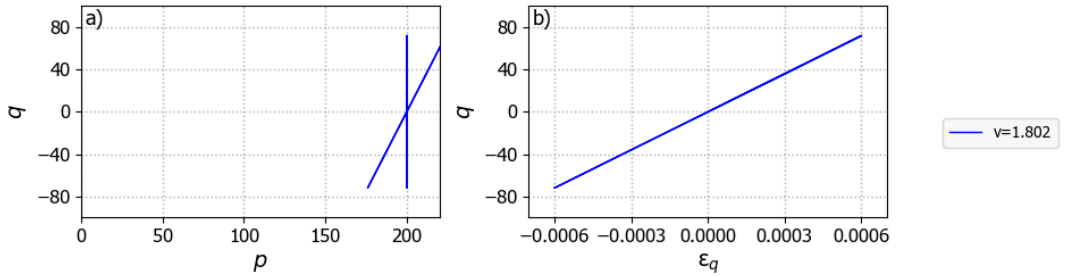


Figure 93 Undrained cyclic strain controlled test (a) shear stress function of volumetric stress; b) shear stress function of shear strain)

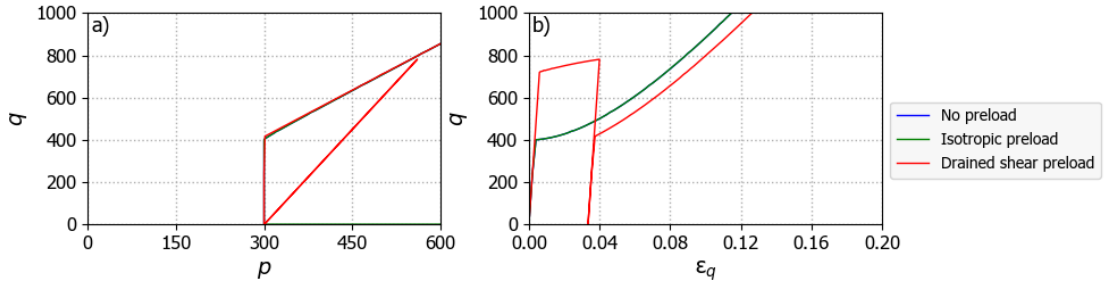


Figure 94 Undrained test with preloading (a) shear stress function of volumetric stress; b) shear stress function of shear strain) change from original scale

3.2.7. Non-linear elasticity

This model is abbreviated by Hyper_ani_nlel.

3.2.7.1. Isotropic tests observations

Upon isotropic loading, a sample contracts. This contraction is partly plastic. In Figure 95, isotropic loading tests with partial unloadings by Wichtmann and Triantafyllidis (2016b) demonstrate this behaviour. In Figure 95, the unloading-reloadings are non-linear elastic, while the isotropic loading beyond the current consolidation pressure is elasto-plastic.

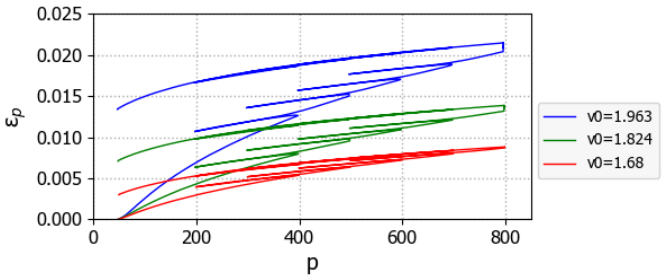


Figure 95 Isotropic tests (TCUI4,5,6 by Wichtmann (2021)) with unloading and reloading cycles

However, the yield surface presented so far is a wedge in $p - q$ space, with the entire inner zone being the elastic domain. This means that upon isotropic loading, the stress path will be purely linear-elastic, as shown in Figure 96 where the curves are superimposed because the elasticity does not vary with density in the model.

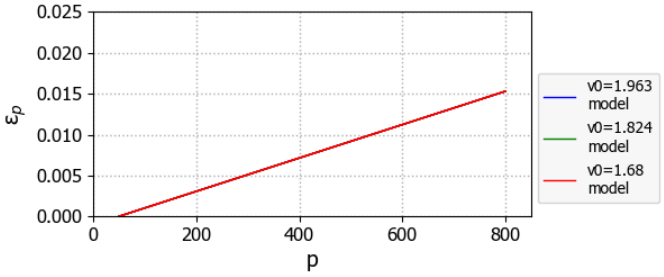


Figure 96 Isotropic loading and unloading with linear elasticity

For the model to reproduce the sand behaviour shown in Figure 95, the model needs to include non-linear elasticity, as well as a new plastic mechanism generating volumetric plastic strain upon isotropic loading (presented in section 3.2.8).

3.2.7.2. Non-linear elasticity implementation

In Houlsby *et al.* (2019), a non-linear elastic Gibbs energy function is given:

$$g = -\frac{p_r}{k_r(1-m)(2-m)}\left(\frac{p_0}{p_r}\right)^{2-m} \qquad \textit{Eq. 109}$$

$$p_0^2 = p^2 + \frac{k_r(1-m)}{3g_r}\,q^2 \qquad \textit{Eq. 110}$$

With $p_r = 100kPa$ a reference pressure, and where $G/p_r = g_r(p/p_r)^m$ [Eq. 111] and $K/p_r = k_r(p/p_r)^m$ [Eq. 112] on the isotropic axis, where m is the pressure index of non-linear elasticity.

Non-linear elasticity is included in the Gibbs energy function of the model by replacing the linear elastic term by the non-linear elastic term:

$$g = -\frac{p_r}{k_r(1-m)(2-m)}\left(\frac{p_0}{p_r}\right)^{2-m} - q\alpha_q - p\alpha_p \qquad \textit{Eq. 113}$$

This formulation allows to represent, in Figure 97, an adequate non-linear unloading.

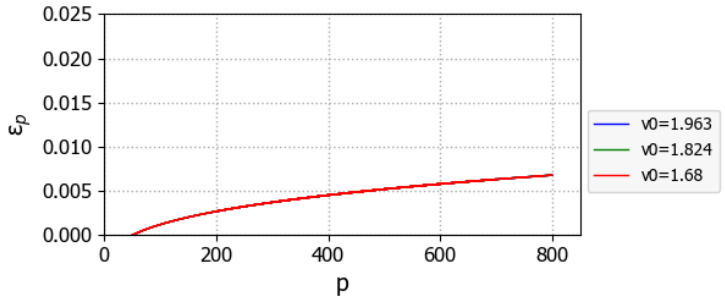


Figure 97 Isotropic loading and unloading with non-linear elasticity

Nevertheless, the curves for the different densities are still only non-linear elastic and the same for all densities, such that the loadings and unloadings at all densities are the same, hence their superimposition in Figure 97.

Hyper_ani_nlel is summarised by:

Gibbs energy function: $g = -\frac{p_r}{k_r(1-m)(2-m)}\left(\frac{p_0}{p_r}\right)^{2-m} - q\alpha_q - p\alpha_p$ *Eq. 114*

where: $p_0^2 = p^2 + \frac{k_r(1-m)}{3g_r}q^2$ with $p_r = 100kPa$ *Eq. 115*

Dissipation function: $d^* = 2\mu\sqrt{\left(p+\frac{2}{3}q\right)\left(p-\frac{q}{3}\right)}\left|\dot{\alpha_q}\right| + \Lambda_d C_d + \Lambda_a C_a$ *Eq. 116*

where the dilation constraint is: $C_d = \dot{\alpha_p} + a\beta\dot{\alpha_q} = 0$ *Eq. 117*

and the anisotropy constraint is: $C_a = \dot{a} - A(1-|a|)\dot{\alpha_q} = 0$ *Eq. 118*

Where $\beta = \beta_{max}\frac{\ln(v)-\ln(\Gamma)}{\ln(\Delta)-\ln(\Gamma)} = \beta_{max}\frac{\ln(v_0)-\epsilon_p-\ln(\Gamma)}{\ln(\Delta)-\ln(\Gamma)}$ *Eq. 119*

Where $A = A_{max}\frac{\ln(v)-\ln(B)}{\ln(\Delta)-\ln(B)} = A_{max}\frac{\ln(v_0)-\epsilon_p-\ln(B)}{\ln(\Delta)-\ln(B)}$ *Eq. 120*

Alternative to the dissipation function and constraints, yield function:

$$y = \left(\chi_q + A(1-|a|)\chi_a - a\beta\chi_p\right)^2 - 4\mu^2\left(p+\frac{2}{3}q\right)\left(p-\frac{q}{3}\right) \qquad \textit{Eq. 121}$$

3.2.7.3. Analysis of test results

Figure 98 to Figure 102 attempt to respectively model Figure 54 to Figure 58 of Wichtmann tests using Hyper_ani_nlel.

For the drained tests, Figure 98, the only noticeable difference is in the elastic loading which is now slightly stiffer because the reference shear modulus G was kept constant at $p_r = 100$kPa, which means that it is greater than before for the consolidation pressure of these tests $p_0 = 200$kPa.

The undrained monotonic tests, Figure 99, show a large difference in stress space, with the elastic loading curving to the right rather than previously being vertical. This is due to the adoption of the new non-linear elastic formula, Eq. 113, which brings non-diagonal terms in the elastic compliance matrix:

$$C^e = -\frac{\partial^2 g}{\partial \sigma^2} = -\begin{bmatrix} \frac{\partial^2 g}{\partial p^2} & \frac{\partial^2 g}{\partial p \partial q} \\ \frac{\partial^2 g}{\partial q \partial p} & \frac{\partial^2 g}{\partial q^2} \end{bmatrix} \qquad \textit{Eq. 122}$$

The off-diagonal terms are non-null, which translates to a coupling between shear and volumetric terms, such that the evolution of q during an undrained test implies a variation in p. This curvature of the elastic loading is also found in all other undrained tests in Figure 100, Figure 101, and Figure 102.

Noticeably, it is the first step in which the preloaded tests display an elastic behaviour similar to the one observed in the tests by Wichtmann.

Improvements brought by Hyper_ani_nlel compared to Hyper_ani:

The elastic parameters now depend on the effective mean pressure and deviatoric stress, allowing to capture a realistic elastic behaviour such as on isotropic unloadings, and overconsolidated undrained reloadings.

The undrained elastic loadings are curved in stress space because of the coupling between elastic shear and volumetric terms.

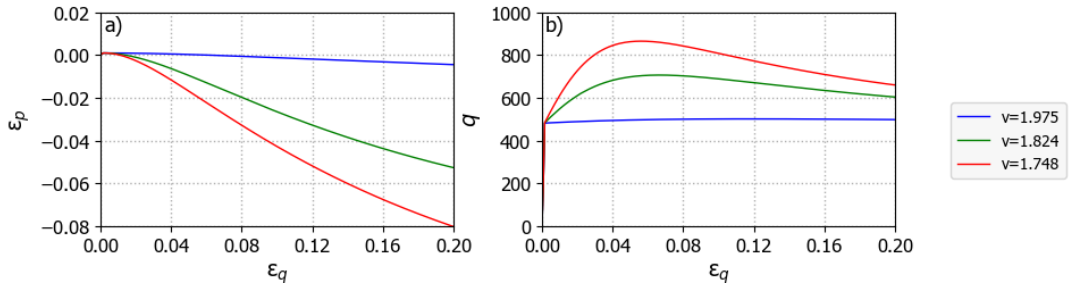


Figure 98 Drained tests (a) volumetric strain function of shear strain; b) shear stress function of shear strain) change from original scale

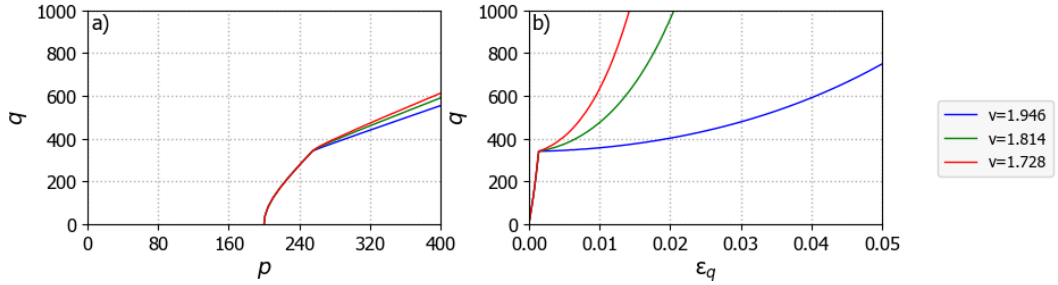


Figure 99 Undrained tests (a) shear stress function of volumetric stress; b) shear stress function of shear strain) change from original scale

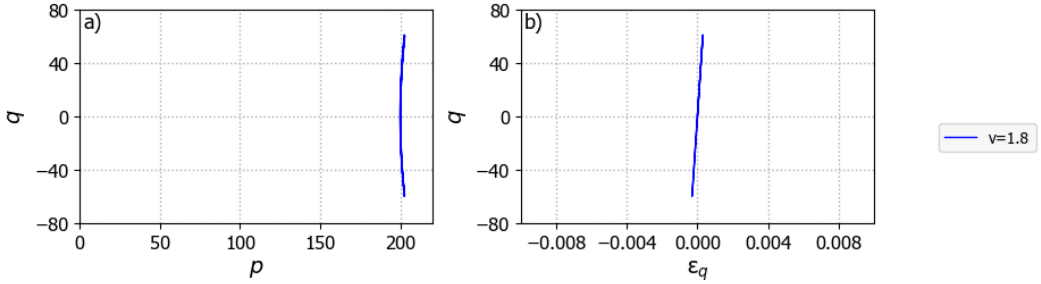


Figure 100 Undrained cyclic stress controlled test (a) shear stress function of volumetric stress; b) shear stress function of shear strain)

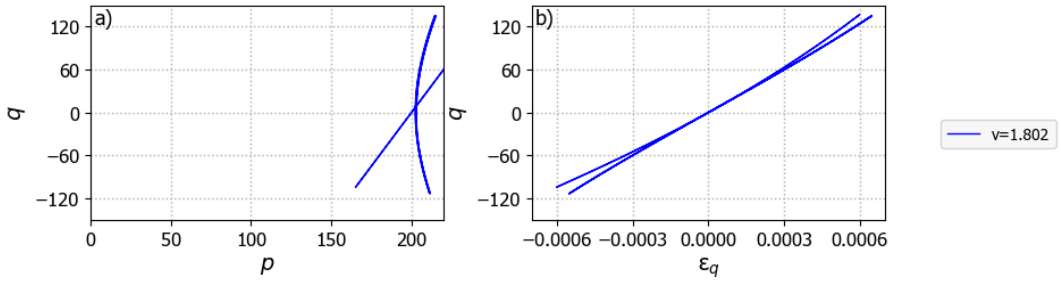


Figure 101 Undrained cyclic strain controlled test (a) shear stress function of volumetric stress; b) shear stress function of shear strain) change from original scale

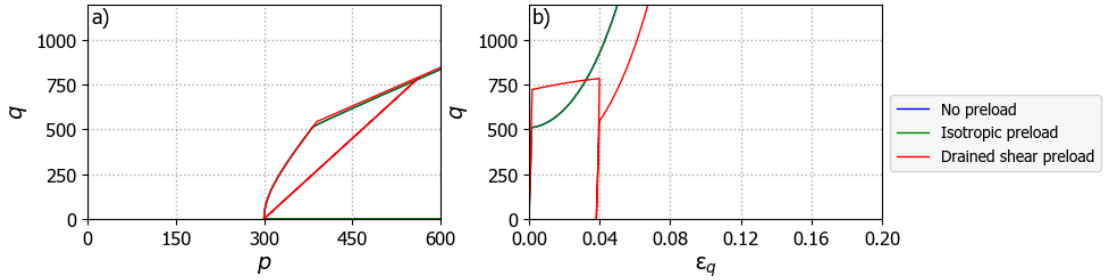


Figure 102 Undrained test with preloading (a) shear stress function of volumetric stress; b) shear stress function of shear strain) change from original scale

3.2.8. Consolidation plasticity

The model hereafter is abbreviated by Hyper_pc.

In order to enforce a plastic mechanism active upon isotropic loading, a yield surface cutting the isotropic stress axis should be implemented. In its most simple form, this yield surface should take the shape of a cap and cut the axis at a consolidation pressure p_c, which should correspond to the maximum isotropic stress encountered during loading.

3.2.8.1. Yield surface form

Multiple yield surface forms are possible: a vertical yield surface at p_c, an elliptical yield surface centred in $p = 0$ and of horizontal axis length $2p_c$, or an ellipse centred in $p = p_c/2$ and of horizontal axis length p_c such as the Modified Cam Clay model (Roscoe and Burland, 1968). These different options are sketched along with the current conical yield surface in the triaxial stress space in Figure 103.

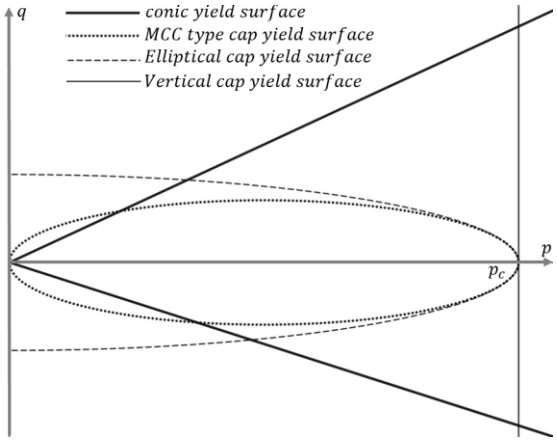


Figure 103 Current conic yield surface and cap yield surface options in the triaxial stress space

These different options would work for the sole purpose of representing the plastic consolidation mechanism, but the monotonic undrained tests on sand provide more information on the shape of the required cap yield surface. In Figure 104, which presents undrained monotonic tests by Wichtmann (2021), the initial stress path in $p - q$ space is a rounded pore pressure build-up with increase in shear stress. This suggests that the capping mechanism should be rounded.

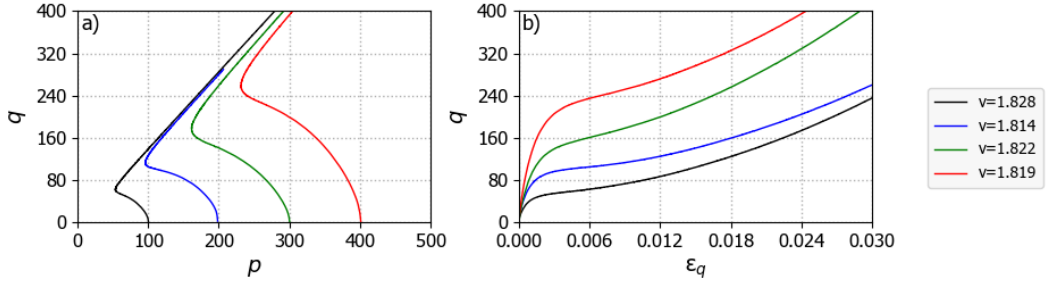


Figure 104 Monotonic undrained tests on medium dense sand by Wichtmann (2021)

3.2.8.1.1. An additional yield surface for the consolidation mechanism

In consequence, a number of model versions have been experimented with elliptical yield surfaces in addition to the original conic yield surface. Adding such a yield surface to capture the consolidation mechanism means that the model can become very versatile, as each yield surface behaviour can be adapted to fit its purpose, but the model also becomes more complex.

For example, it is necessary to include contraction in the conic yield surface, such as in Houlsby (1992) and Houlsby and Mortara (2004), because the cap only influences the behaviour when it is active, implying that there is no contractive contribution of the cap at low p/p_c ratios. However, contraction at such ratios is necessary to model the progressive pore pressure build-up in undrained cyclic tests such as the one shown in Figure 105.

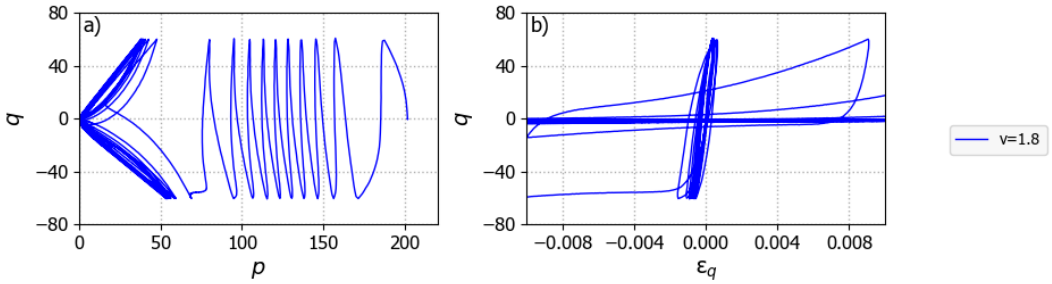


Figure 105 Undrained cyclic stress controlled test TCUI7 from Wichtmann (2021)

Also, the cap's behaviour versatility may come at the cost of either additional parameters, to rule its shape or hardening, or a complex coupling with the conic yield surface. The subsequent extension to a multi-surface model in 3.2.10 eventually implies the use of multiple caps, thus increasing the number of parameters even further, and complicating the coupling.

3.2.8.1.2. Combining the conical yield surface with the cap

To avoid including contraction into the conic yield surfaces, an option is to extend the influence of the cap further than its normal reach by using a combination technique such as in Houlsby and Richards (2023). The yield surface could take the form for the previously defined model combined with an elliptical cap centred in $(p, q) = (0,0)$ and of aspect ratio B:

$$y = \left(\left(\frac{\left(\chi_q + A(1-|a|)\chi_a - a\beta\chi_p\right)^2}{4\mu^2\left(p+\frac{2}{3}q\right)\left(p-\frac{q}{3}\right)} \right)^{n_C} + \left(\left(\frac{\chi_p}{p_c}\right)^2 + \left(\frac{\chi_q}{Bp_c}\right)^2 \right)^{n_C} \right)^{\frac{1}{n_C}} - 1 = 0 \quad \textit{Eq. 123}$$

Where $\left(\chi_q + A(1-|a|)\chi_a - a\beta\chi_p\right)^2/\left(4\mu^2(p+2q/3)(p-\mathrm{q}/3)\right)$ is the square of the gauge function for the conic yield surface, $\left(\chi_p/p_c\right)^2 + \left(\chi_q/Bp_c\right)^2$ is the square of the gauge function for the cap yield surface, and n_C the combination power. The larger n_C is, the more

independent the mechanisms are. Figure 106 illustrate the combination of the yield surfaces with $n_c = 1$ in red, and $n_c = 4$ in blue. Selecting a low n_c allows the cap to influence lower mean effective pressures.

This family of options were not extensively explored because of the success in the implementation of the hybrid option presented hereafter. However, the author encourages further exploration of this option.

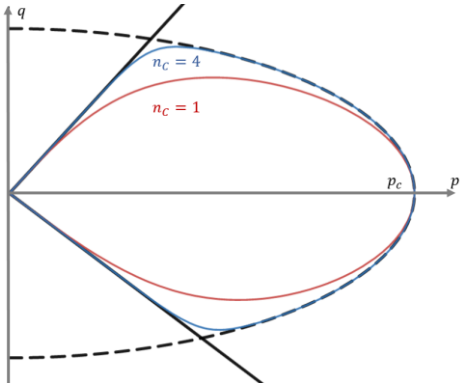


Figure 106 Merging of a conic yield surface (solid black) and of an elliptical yield surface (dashed black)

3.2.8.1.3. Hybrid solution

A solution to limit the number of surfaces and parameters is to integrate a pressure dependent contraction into the wedges, but differently from Houlsby (1992) and Houlsby and Mortara (2004).

This contraction can be added to the model through another internal variable (α_{pc}). This modifies the expression of the Gibbs energy function (formerly **Eq. 114**) to:

$$g = -\frac{p_r}{k_r(1-m)(2-m)}\left(\frac{p_0}{p_r}\right)^{2-m} - q\alpha_q - p(\alpha_p + \alpha_{pc}) \qquad \textit{Eq. 124}$$

Such that the volumetric strain becomes: $\epsilon_p = -\frac{\partial g}{\partial p} = \epsilon_p^e + (\alpha_p + \alpha_{pc})$ [Eq. 125].

The generalised stress conjugate of α_{pc} is χ_{pc}. A yield surface expression which achieves the wanted fusion is:

$$y = \left(\chi_q + A\left(1 - aS(\chi_q)\right)\chi_a - a\beta\chi_p\right)^2 - 4\mu^2\left(1 - \left(\frac{\chi_{pc}}{p_c}\right)^r\right)\left(p + \frac{2}{3}q\right)\left(p - \frac{q}{3}\right) = 0 \qquad \textit{Eq. 126}$$

The parameter r is a shape factor which controls both the shape of the yield surface, as represented in Figure 107, and the amount of plastic volumetric strain born from this plastic mechanism: $\alpha_{pc} \propto r\frac{\chi_{pc}{}^{r-1}}{p_c^r}$.

This shape of yield surface can be found in existing models such as the 2007 version of SANISAND (Taiebat *et al.*, 2007) or the constitutive anamnesis model by Tafili *et al.* (2021).

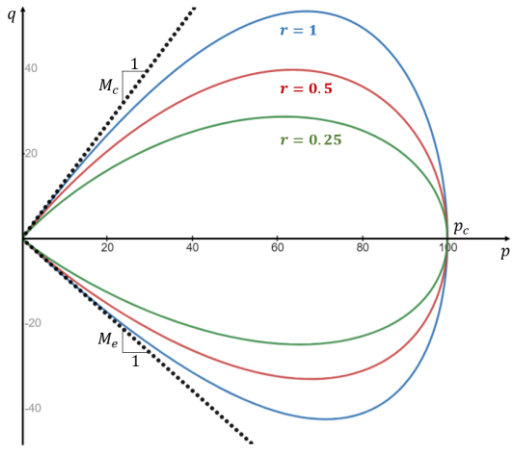


Figure 107 Influence of the shape factor r on the shape of the yield function

This yield surface (Eq. 126) is presented in blue in Figure 108 for $r = 1$, $\beta = 0.7$ and three values of the anisotropy scalar $a = 0$, $a = 1$ and $a = -1$. These shapes resemble experimental yield curves obtained by Yasufuku (1991) for anisotropic consolidation.

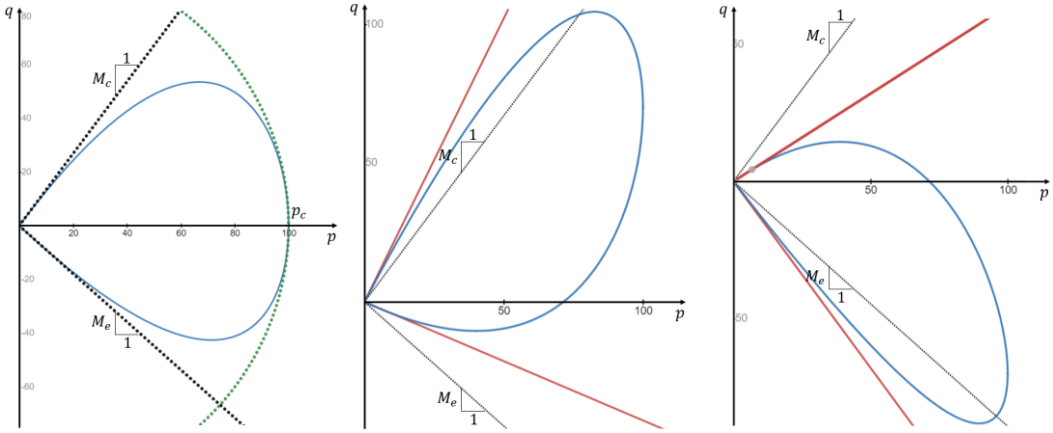


Figure 108 Left: capping in $p - q$ space with a circle (green), and hybrid solution for a=0 (blue). Middle: hybrid solution (blue) with a=1 and β=0.7. Right: hybrid solution (blue) with a=-1 and β=0.7

An interesting remark by Houlsby (2022) about the yield formulation in Eq. 126 is that it can be written in the form:

$$y = \left(\left(\frac{\chi_q + A\left(1 - aS(\chi_q)\right)\chi_a - a\beta\chi_p}{2\mu\sqrt{\left(p + \frac{2}{3}q\right)\left(p - \frac{q}{3}\right)}} \right)^2 + \left(\frac{\chi_{pc}}{p_c}\right)^r \right)^{\frac{1}{2}} - 1 = 0 \qquad \textit{Eq. 127}$$

This form is closely related to the combination technique evoked in 3.2.8.1.2. Here, instead of an ellipse, a vertical yield surface cutting the isotropic axis at p_c $\left(\chi_{pc}/p_c - 1 = 0 \ \ [\text{Eq. } 128]\right)$ is combined to the conic yield surface. Also, instead of using the same exponent n_c, as in Eq. 123 for example, two different exponents are used. In HySand, the parameter r will often take values below 0.5, which effectively means that the influence of the vertical yield surface, and by extension of the contraction born from the consolidation mechanism, extends to low p values.

The equivalent dissipation for this hybrid form can be, for $f_d \in [0,1]$:

$$d^* = \sqrt{f_d}\sqrt{4\mu^2\left(p+\frac{2}{3}q\right)\left(p-\frac{q}{3}\right)}\left|\dot{\alpha}_q\right| + (1-f_d)^{\frac{1}{r}}p_c\dot{\alpha}_{pc} + \Lambda_d C_d + \Lambda_a C_a \qquad \textit{Eq. 129}$$

This hybrid form has been selected for the base model.

3.2.8.2. Consolidation pressure evolution

Independently of the yield surface form, the consolidation pressure p_c must evolve with the new plastic volumetric strain α_{p_c}.

In critical state soil mechanics (e.g. Wood (1991)), a logarithmic relation is often assumed between the specific volume and the mean effective pressure, such as shown in Figure 109.

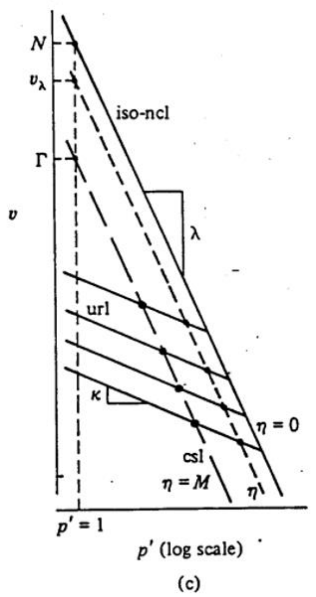


Figure 109 Normal consolidation line, critical state line, and elastic unloading lines (from Wood (1991)) Vertical axis specific volume (v), log-scale horizontal axis effective mean pressure (p'), Γ critical state line, N and λ normal consolidation line and its slope, κ slope of elastic line

The linear relation is sometimes assumed between the logarithm of the specific volume and the logarithm of the mean effective pressure (e.g. Butterfield, 1979). This implies a linear relation between the volumetric strain (because $\epsilon_p = -\ln(v/v_0)$) and the logarithm of the pressure. Such a relation has already been implemented in hyperplasticity by Houlsby (2023) and used by Simonin *et al.* (2023) where the consolidation pressure evolves with the law:

$$p_c = p_{c0}e^{\frac{\alpha_{pc}}{\lambda}} \qquad \textit{Eq. 130}$$

Where p_{c0} is the initial consolidation pressure and λ the slope of the normal consolidation line.

Figure 110 represents the volumetric strain against the pressure in a log-scale for an isotropic test on loose sand by Wichtmann (2021).

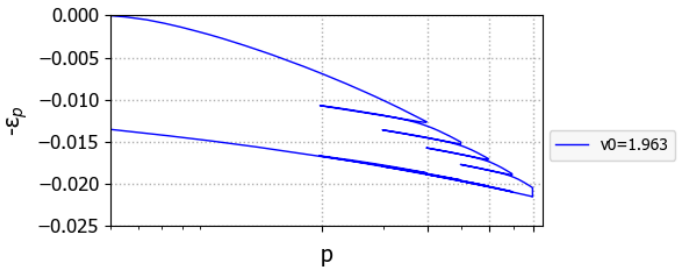


Figure 110 Representation of isotropic test on loose sand by Wichtmann (2021)

Both the elasto-plastic loading and elastic unloading are not linear. The elastic part has already been treated in 3.2.7. Houlsby (1992) proposes the following alternative power relation between the specific volume and the pressure with updated notations:

$$\ln(v) = \ln(v_0) - \frac{\lambda}{(1-m)}\left(\left(\frac{p}{p_r}\right)^{1-m} - 1\right) \qquad \textit{Eq. 131}$$

This relation adopts the same exponent as for the non-linear elasticity. Wichtmann's data on loose sand (2016a) is pictured in Figure 111 with $m = 0.7$.

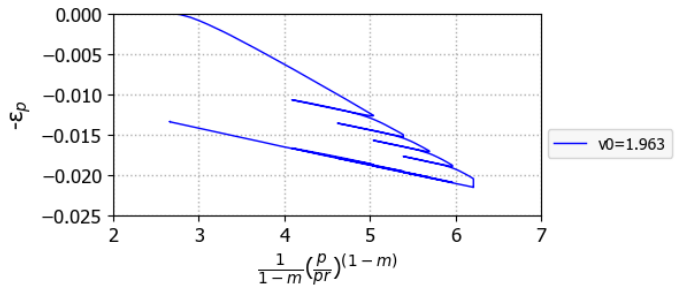


Figure 111 Second representation of isotropic test on loose sand by Wichtmann (2021)

Based on the comparison of Figure 110 and Figure 111, Eq. 131 appears to give the best approximation. For an even better approximation, one could consider different power exponents for the non-linear elasticity (m_1) and for the consolidation (m_2). However, one sole parameter m was considered sufficient for the base model.

Translating Eq. 131 for the evolution of the consolidation pressure gives:

$$p_c = p_{c0}\left(1 + \frac{(1-m)}{\lambda - 1/k_r}\alpha_{p_c}\right)^{\frac{1}{1-m}} \qquad \textit{Eq. 132}$$

For an isotropic normally consolidated test, the initial consolidation pressure (p_{c0}) should be the initial mean effective stress. But for the sake of numerical stability, p_{c0} is initialised slightly higher than the initial mean effective pressure (p_0): $p_{c0} = p_0 + 0.1$kPa.

Using the updated energy function in Eq. 124, the updated hybrid yield function in Eq. 126, and the evolution law of the consolidation pressure Eq. 132, along with adequate m and λ's, a good approximation of isotropic tests can be obtained as represented in Figure 112.

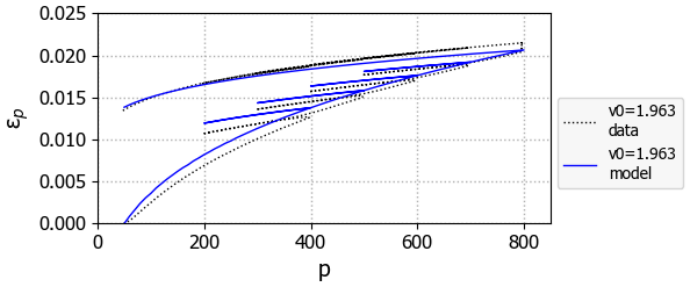


Figure 112 Loose isotropic test: data and model

Figure 95 shows that the accumulation of plastic volumetric strain largely varies with density: the larger the specific volume, the larger the accumulated plastic strain. This means that the slope of the normal consolidation lines (λ) should vary with density. As will be shown in Chapter 4, a power relation between the slope ratio and the specific volume could be used. However, for the simplicity of the model and to obtain closed-formed solutions in the following paragraph (3.2.9), the following relation is adopted:

$$\lambda = \lambda_B - (\lambda_B - \lambda_\Delta)\frac{\ln(v) - \ln(B)}{\ln(\Delta) - \ln(B)} \qquad \textit{Eq. 133}$$

Where λ_B is the slope ratio at the loosest state, and λ_Δ the slope ratio at the densest state.

3.2.8.3. Summary of the model

The model now comprises the hybrid yield formulation presented in Eq. 126, the consolidation pressure evolution law given in Eq. 132, and the variation of normal consolidation lines slopes given in Eq. 133. The shape of the yield surface in an anisotropic state is density dependent, with a larger shearing of the shape the denser the sample is, as shown in Figure 113.

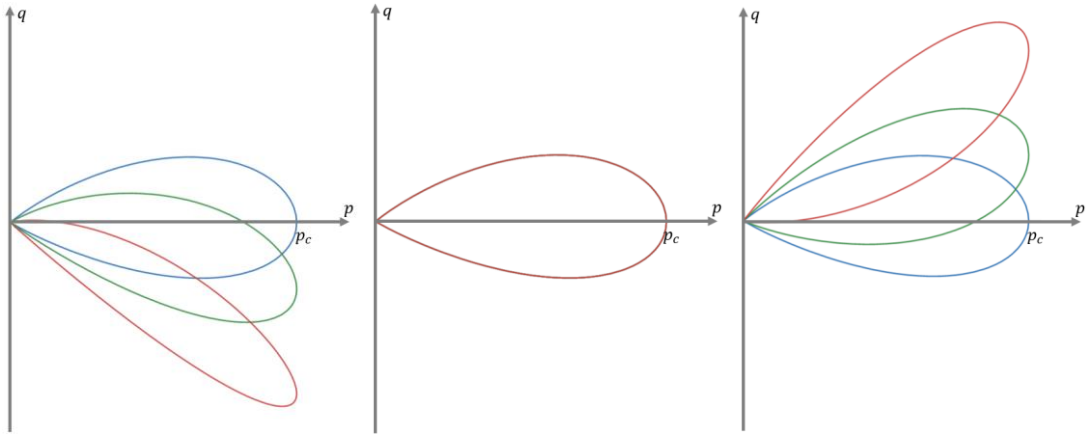


Figure 113 Yield surface shape for critical state (blue), medium (green) and densest (red) in triaxial stress space, for $a = -1,0,1$ from left to right

Hyper_pc is summarised by:

$$\text{Gibbs energy function: } g = -\frac{p_r}{k_r(1-m)(2-m)}\left(\frac{p_0}{p_r}\right)^{2-m} - q\alpha_q - p(\alpha_p + \alpha_{pc}) \quad \text{Eq. 134}$$

$$\text{where: } p_0^2 = p^2 + \frac{k_r(1-m)}{3g_r}\,q^2 \text{ with } p_r = 100kPa \quad \text{Eq. 135}$$

$$\text{Yield function:}$$

$$y = \left(\chi_q + A(1-|a|)\chi_a - a\beta\chi_p\right)^2 - 4\mu^2\left(1-\left(\frac{\chi_{pc}}{p_c}\right)^r\right)\left(p+\frac{2}{3}q\right)\left(p-\frac{q}{3}\right) \quad \text{Eq. 136}$$

$$\text{where } \beta = \beta_{max}\frac{\ln(v)-\ln(\Gamma)}{\ln(\Delta)-\ln(\Gamma)} = \beta_{max}\frac{\ln(v_0)-\epsilon_p-\ln(\Gamma)}{\ln(\Delta)-\ln(\Gamma)} \quad \text{Eq. 137}$$

$$\text{Where } A = A_{max}\frac{\ln(v)-\ln(B)}{\ln(\Delta)-\ln(B)} = A_{max}\frac{\ln(v_0)-\epsilon_p-\ln(B)}{\ln(\Delta)-\ln(B)} \quad \text{Eq. 138}$$

$$\text{and } p_c = p_{c0}\left(1+\frac{(1-m)}{\lambda-1/k_r}\alpha_{p_c}\right)^{\frac{1}{1-m}} \quad \text{Eq. 139}$$

$$\text{With } \lambda = \lambda_B - (\lambda_B-\lambda_\Delta)\frac{\ln(v)-\ln(B)}{\ln(\Delta)-\ln(B)} = \lambda_B - (\lambda_B-\lambda_\Delta)\frac{\ln(v_0)-\epsilon_p-\ln(B)}{\ln(\Delta)-\ln(B)} \quad \text{Eq. 140}$$

3.2.8.4. Analysis of test results

Unlike Hyper_ani and previous models which mostly modelled a change in behaviour upon a change in stress ratio (q/p) because of their conic nature, the foremost goal of Hyper_ani_nlel and Hyper_pc is to capture the behaviour of sand upon changes in the mean effective pressure. Figure 114 demonstrates that this was achieved for isotropic tests.

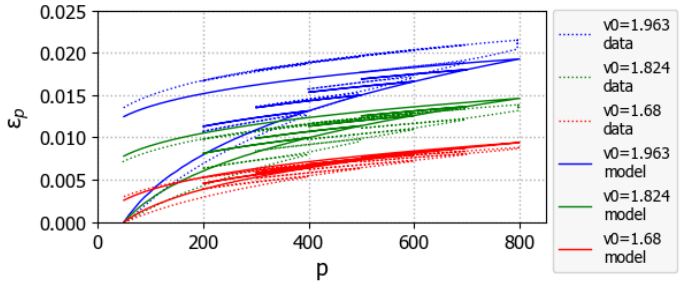


Figure 114 Isotropic tests data against simulation

If an additional vertical yield surface at p_c had been used instead of the hybrid solution, it would have had effects on the drained tests, with additional contraction, but no large impact on the undrained tests, and no impact overall at low p/p_c. However, because this vertical yield surface has been tightly linked to the conic yield surface thanks to Eq. 126, its effects reach much further.

Figure 115 to Figure 119 attempt to respectively model Figure 54 to Figure 58 of Wichtmann tests using Hyper_pc. The effect of the new yield surface form and of the additional volumetric plastic mechanism is very important on drained tests, Figure 115. Indeed, the behaviour is initially plastic. The stiffness is thus controlled on the one hand by the evolution of the consolidation pressure, and on the other hand by the development of anisotropy and dilation, both of which depend on density (via λ for the consolidation pressure). This explains the difference between

tests. The density dependence of λ also implies that the initial contraction is density dependent, such that looser tests display more contraction initially.

The new formulation also permits to capture the initial pore pressure build-up in undrained tests. In Figure 116, the undrained monotonic tests display a pore pressure build-up which increases with the specific volume as in Wichtmann's test. The density dependence of the slope ratio λ, the dilation β, and the anisotropy rate A explain this phenomenon.

The cyclic stress controlled test, Figure 117, is not fully elastic anymore. Because of the closure of the yield surface at p_c, the initial loading is plastic, such that pore pressure builds up. During this initial loading, the consolidation pressure increases, and anisotropy develops. During the second half cycle (decreasing q), because the yield surface has sheared with anisotropy, it is encountered again at the end of the half-cycle. However, the behaviour becomes elastic in the following cycles because compressive or extensive shear stresses of the same magnitude will not reach the yield surface anymore because of how much the consolidation pressure has increased.

The case of the strain controlled test, Figure 118, is different: the loading is partially plastic for the first few cycles. With cycles, the consolidation pressure increases. But, because the test is strain controlled and because the elastic loading is stiffer than the plastic loading, the loading goes towards larger stress ratios $|q/p|$, leading to additional elasto-plastic cycles and pore pressure build-up.

The new formulation plays a key role in modelling pre-loaded tests shown in Figure 119. An over-consolidated sample, green curve, therefore starts with an accordingly large consolidation pressure, which results in an initially elastic loading. This is followed by a contractive behaviour, because no anisotropy has developed during the isotropic consolidation. As anisotropy develops, the behaviour becomes dilative. The pre-shearing of a sample, red curve, implies both an increase of the consolidation pressure, and a development of the anisotropy in the shearing direction. For the subsequent undrained loading in the same shearing direction, it entails an initial elastic phase, followed by a shorter and less intense plastic contractive phase.

Improvements brought by Hyper_pc compared to Hyper_ani_nlel:
Changes in mean effective pressure provoke plastic loadings via the consolidation mechanism.
Pressure dependent isotropic contraction is included.
A normally consolidated test will immediately be plastic and contractive.
Pre-loaded samples will initially behave elastically.

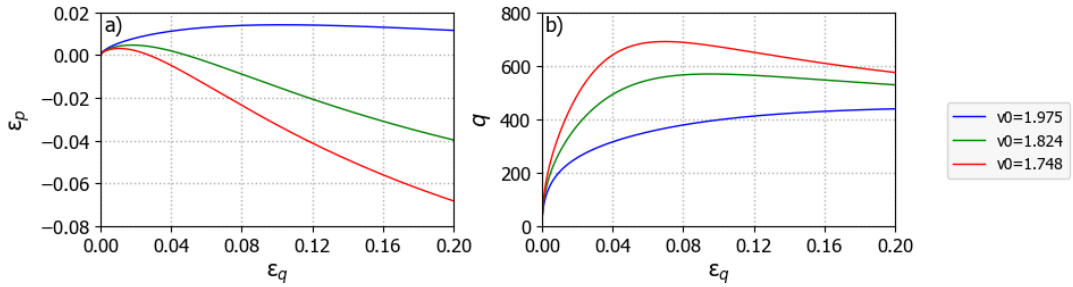


Figure 115 Drained tests (a) volumetric strain function of shear strain; b) shear stress function of shear strain)

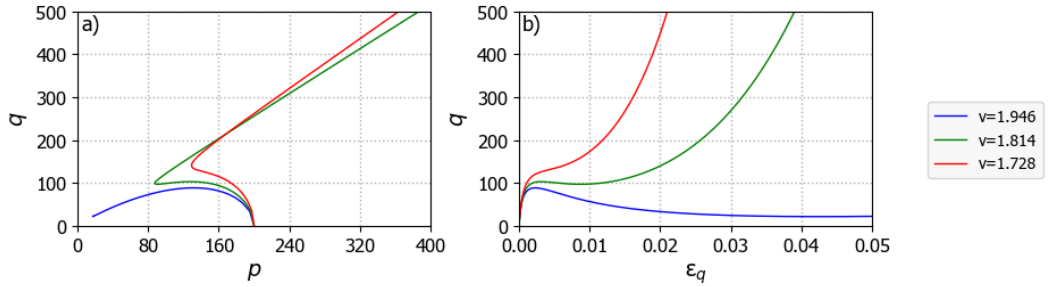


Figure 116 Undrained tests (a) shear stress function of volumetric stress; b) shear stress function of shear strain)

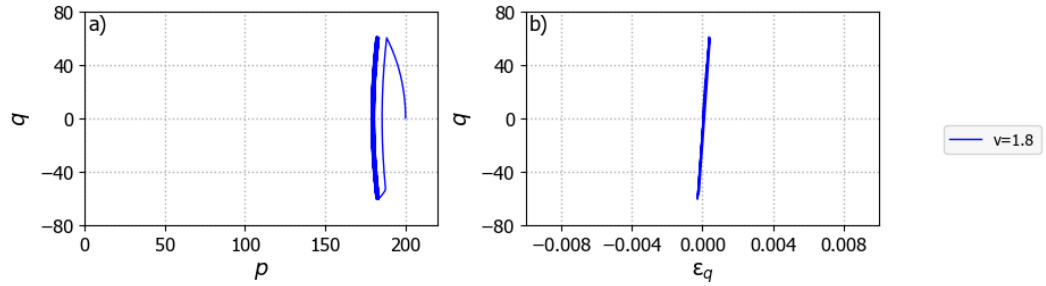


Figure 117 Undrained cyclic stress controlled test (a) shear stress function of volumetric stress; b) shear stress function of shear strain)

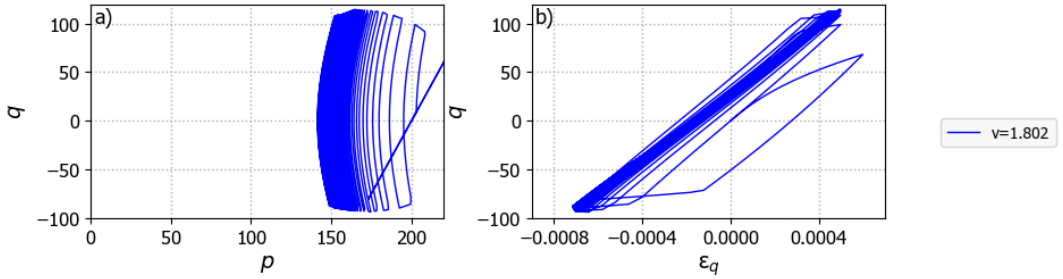


Figure 118 Undrained cyclic strain controlled test (a) shear stress function of volumetric stress; b) shear stress function of shear strain) change from original scale

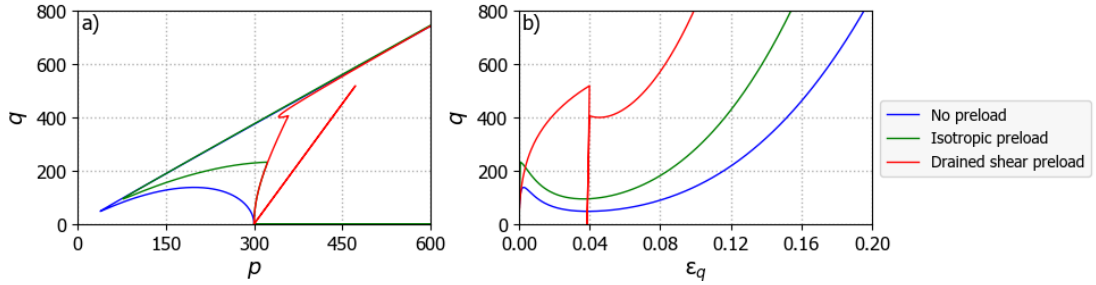


Figure 119 Undrained test with preloading (a) shear stress function of volumetric stress; b) shear stress function of shear strain)

3.2.9. Base monotonic model with updated density dependence

The model presented hereafter is abbreviated by HySand_base_mono.

3.2.9.1. State of the density dependence in the model

In the model, the dilation ratio (Eq. 141), the normal consolidation slope (Eq. 142), and the anisotropy rate development parameter (Eq. 143) depend on the specific volume:

$$\beta = \beta_{max}\frac{\ln(v)-\ln(\Gamma)}{\ln(\Delta)-\ln(\Gamma)} = \beta_{max}\frac{\ln(v_0)-\epsilon_p-\ln(\Gamma)}{\ln(\Delta)-\ln(\Gamma)} \qquad \textit{Eq. 141}$$

$$\lambda = \lambda_{\mathrm{B}} - (\lambda_{\mathrm{B}}-\lambda_{\Delta})\frac{\ln(v)-\ln(\mathrm{B})}{\ln(\Delta)-\ln(\mathrm{B})} = \lambda_{\mathrm{B}} - (\lambda_{\mathrm{B}}-\lambda_{\Delta})\frac{\ln(v_0)-\epsilon_p-\ln(\mathrm{B})}{\ln(\Delta)-\ln(\mathrm{B})} \qquad \textit{Eq. 142}$$

$$A = A_{max}\frac{\ln(v)-\ln(B)}{\ln(\Delta)-\ln(B)} = A_{max}\frac{\ln(v_0)-\epsilon_p-\ln(B)}{\ln(\Delta)-\ln(B)} \qquad \textit{Eq. 143}$$

Such that the denser a sample is, the more dilatant it is, the less contraction it produces with consolidation, and the quicker anisotropy develops.

These three quantities (β, λ, A) thus depend on the distance between the current specific volume and the critical/loosest state specific volume at a reference pressure, divided by the distance between the specific volumes at densest and critical/loosest states at a reference pressure.

Figure 120 is constructed by plotting the logarithm of specific volumes, loosest (blue), critical state (black), medium dense representing the current test (green), and densest state (red), against the relative non-linear pressure $\frac{1}{1-m}\left(\frac{p}{p_r}\right)^{1-m}$.

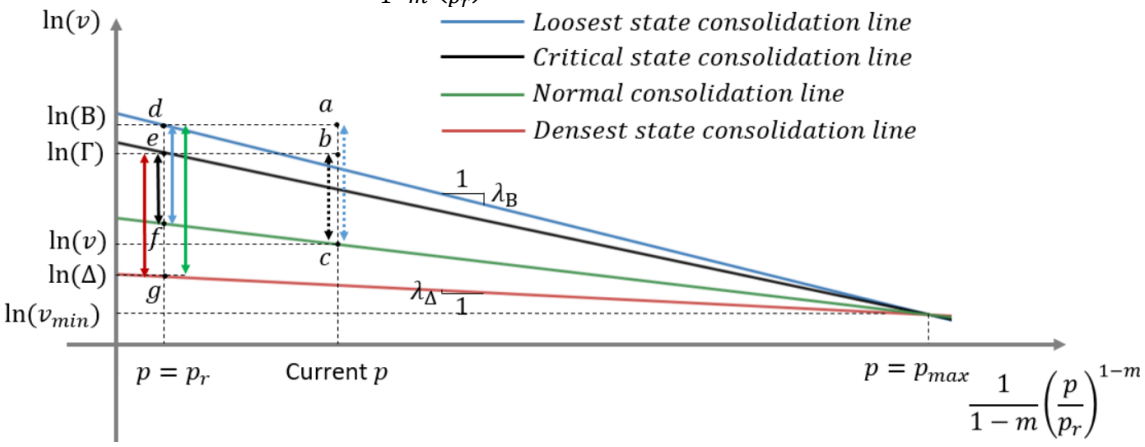


Figure 120 Relative density measurement

In the model defined so far, the ratio of distance used are the one represented in dotted black divided by the red one ($bc/eg = (\ln v - \ln \Gamma)/(\ln \Delta - \ln \Gamma)$), and the dotted blue one divided by the green one ($ac/dg = (\ln v - \ln \mathrm{B})/(\ln \Delta - \ln \mathrm{B})$). This mixes specific volumes at different states and means that two tests which would have the same specific volumes at very

different pressures would deliver the same relative distances. However, for two samples of same specific volume, the one under a higher pressure should be relatively looser.

3.2.9.2. New relative density measurement

To correct this problem, two equivalent solutions are either to compare the current specific volume to the corresponding loosest, critical, and densest state at the same pressure, or to compare the specific volume the sample would have at the reference pressure (v_λ) to the loosest (B), critical (Γ), and densest state (Δ) specific volumes at reference pressure.

The second option was selected. It is similar to Houlsby (1992) and Houlsby and Mortara (2004), or more generally to critical state soil mechanics (e.g. Wood, 1991), but differs because the normal consolidation line slopes depend on density in this model.

In Figure 120, the suggested correction corresponds to the division of the distance in solid black by the one in red ($ef/eg = (\ln v_\lambda - \ln \Gamma)/(\ln \Delta - \ln \Gamma)$), and the one in solid blue by the one in green ($df/dg = (\ln v_\lambda - \ln \mathrm{B})/(\ln \Delta - \ln \mathrm{B})$).

Because the normal consolidation line slope depends linearly on the logarithm of the specific volume, all consolidation lines meet at a common (p_{max}, v_{min}) point. This allows to determine the expression of the corresponding specific volume (v_λ) at the reference pressure.

It is such that:

$$\frac{\ln v_\lambda - \ln \mathrm{B}}{\ln \Delta - \ln \mathrm{B}} = \frac{(\ln v_0 - \epsilon_p) + \frac{\lambda_\mathrm{B}}{1-m}\left(\left(\frac{p}{p_r}\right)^{1-m} - 1\right) - \ln \mathrm{B}}{\ln \Delta + \frac{\lambda_\mathrm{B} - \lambda_\Delta}{1-m}\left(\left(\frac{p}{p_r}\right)^{1-m} - 1\right) - \ln \mathrm{B}} \qquad \textit{Eq. 144}$$

And more generally:

$$\ln v_\lambda = \ln \mathrm{B} - \ln\left(\frac{\mathrm{B}}{\Delta}\right) \frac{(\ln v_0 - \epsilon_p) + \frac{\lambda_\mathrm{B}}{1-m}\left(\left(\frac{p}{p_r}\right)^{1-m} - 1\right) - \ln \mathrm{B}}{\ln \Delta + \frac{\lambda_\mathrm{B} - \lambda_\Delta}{1-m}\left(\left(\frac{p}{p_r}\right)^{1-m} - 1\right) - \ln \mathrm{B}} \qquad \textit{Eq. 145}$$

The model with updated density dependence is the base triaxial monotonic model. It captures monotonic loading of sand across densities as will be shown in next paragraph.

This model employs 12 parameters shown in Table 3.

k_r	g_r	m	φ_c	β_{max}	B	Γ	Δ	λ_B	λ_Δ	$\mathrm{A_{max}}$	r

Table 3 Parameters of the base monotonic model

HySand_base_mono is summarised by:

$$\text{Gibbs energy function: } g = -\frac{p_r}{k_r(1-m)(2-m)}\left(\frac{p_0}{p_r}\right)^{2-m} - q\alpha_q - p(\alpha_p + \alpha_{pc}) \quad \textit{Eq. 146}$$

$$\text{where: } p_0^2 = p^2 + \frac{k_r(1-m)}{3g_r}\,q^2 \text{ with } p_r = 100kPa \quad \textit{Eq. 147}$$

Yield function:

$$y = \left(\chi_q + A(1-|a|)\chi_a - a\beta\chi_p\right)^2 - 4\mu^2\left(1-\left(\frac{\chi_{pc}}{p_c}\right)^r\right)\left(p+\frac{2}{3}q\right)\left(p-\frac{q}{3}\right) \quad \textit{Eq. 148}$$

$$\text{where } \beta = \beta_{max}\frac{\ln(v_\lambda)-\ln(\Gamma)}{\ln(\Delta)-\ln(\Gamma)} \quad \textit{Eq. 149}$$

$$\text{Where } A = A_{max}\frac{\ln(v_\lambda)-\ln(B)}{\ln(\Delta)-\ln(B)} \quad \textit{Eq. 150}$$

$$\text{and } p_c = p_{c0}\left(1+\frac{(1-m)}{\lambda-1/k_r}\alpha_{p_c}\right)^{\frac{1}{1-m}} \quad \textit{Eq. 151}$$

$$\text{With } \lambda = \lambda_B - (\lambda_B - \lambda_\Delta)\frac{\ln(v_\lambda)-\ln(B)}{\ln(\Delta)-\ln(B)} \quad \textit{Eq. 152}$$

$$\ln v_\lambda = \ln B - \ln\left(\frac{B}{\Delta}\right)\frac{(\ln v_0 - \epsilon_p) + \frac{\lambda_B}{1-m}\left(\left(\frac{p}{p_r}\right)^{1-m}-1\right) - \ln B}{\ln\Delta + \frac{\lambda_B-\lambda_\Delta}{1-m}\left(\left(\frac{p}{p_r}\right)^{1-m}-1\right) - \ln B} \quad \textit{Eq. 153}$$

3.2.9.3. Analysis of test results against former model

In Figure 122 to Figure 126, the results of HySand_base_mono are shown in solid lines, while the results of HySand_pc are shown in dashed lines.

The difference in the results between the two models is little for these tests since the tests are conducted at pressures close to the reference pressure $p_r = 100$kPa. However, one can observe that the new base monotonic model leads to less strength and dilation, which is expected as the re-evaluated distance from the critical state line or loosest state line is less than in previous steps.

If the test is conducted on normally consolidated samples at higher pressure, the difference is more noticeable, such as in Figure 121 which represents drained tests on medium dense sand normally consolidated at 500 kPa.

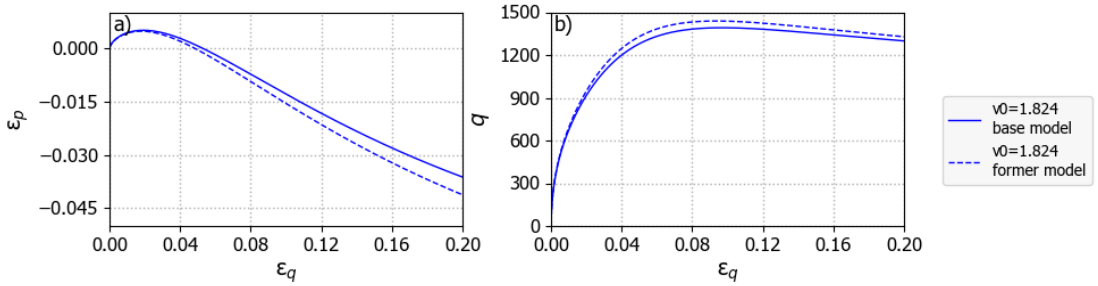


Figure 121 Monotonic results on medium dense sand normally consolidated at 500kPa

Improvements brought by HySand_base_mono compared to Hyper_pc:
Adequate measure of the relative density at a reference pressure.

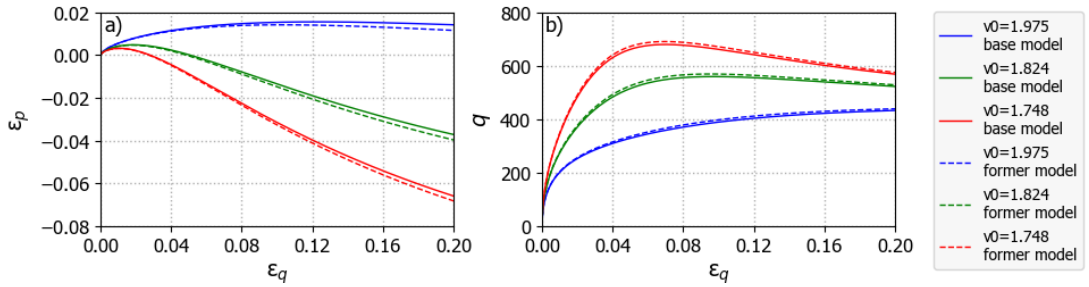


Figure 122 Drained tests (a) volumetric strain function of shear strain; b) shear stress function of shear strain)

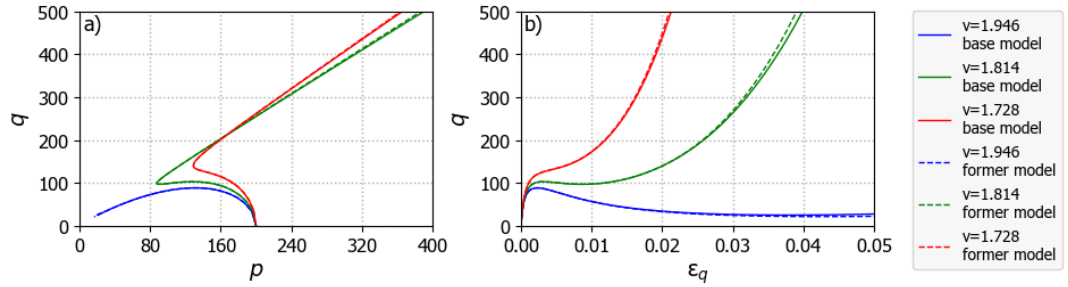


Figure 123 Undrained tests (a) shear stress function of volumetric stress; b) shear stress function of shear strain)

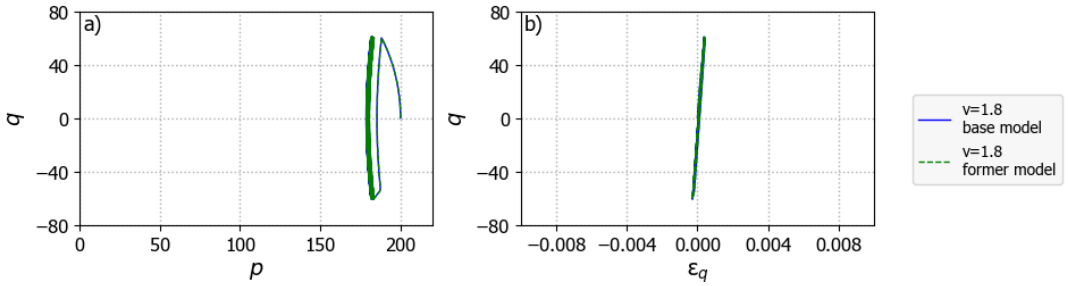


Figure 124 Undrained cyclic stress controlled test (a) shear stress function of volumetric stress; b) shear stress function of shear strain)

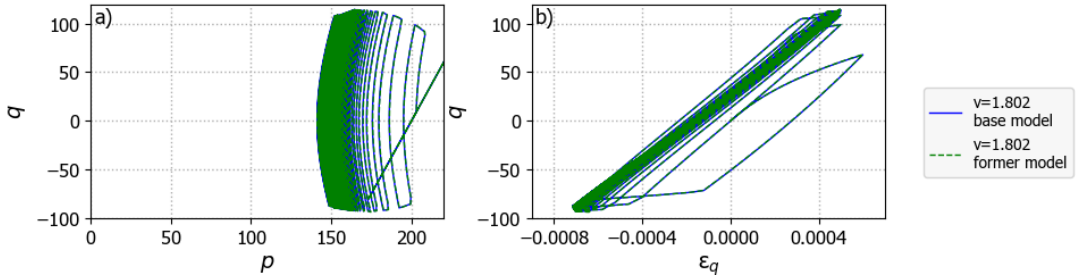


Figure 125 Undrained cyclic strain controlled test (a) shear stress function of volumetric stress; b) shear stress function of shear strain) change from original scale

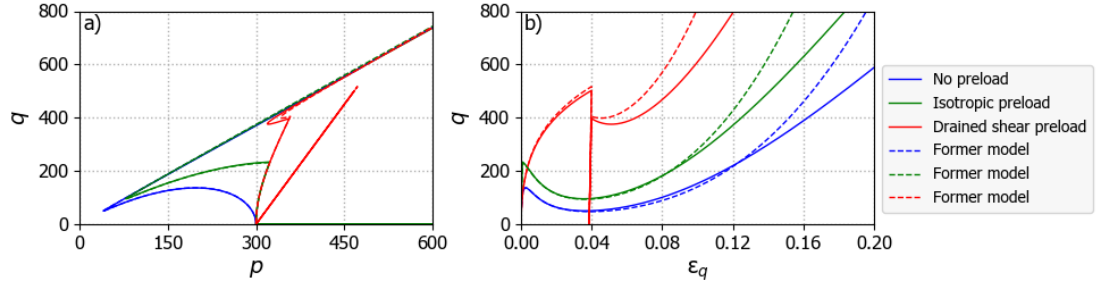


Figure 126 Undrained test with preloading (a) shear stress function of volumetric stress; b) shear stress function of shear strain)

3.2.9.4. Analysis of test results against monotonic data

This new model is called the base monotonic model because it is able to capture the behaviour of sand under monotonic loading across densities. This is shown in Figure 127 and Figure 128 where the model results are solid curves, and the data is in dotted curves.

These figures are produced with the parameters presented in Table 4.

k_r	g_r	m	φ_c	β_{max}	B	Γ	Δ	λ_B	λ_Δ	A_{max}	r
516	400	0.7	33.1	1.0	2.054	1.98	1.677	0.0053	0.0027	60	0.45

Table 4 Parameters of the base monotonic model for Wichtmann data

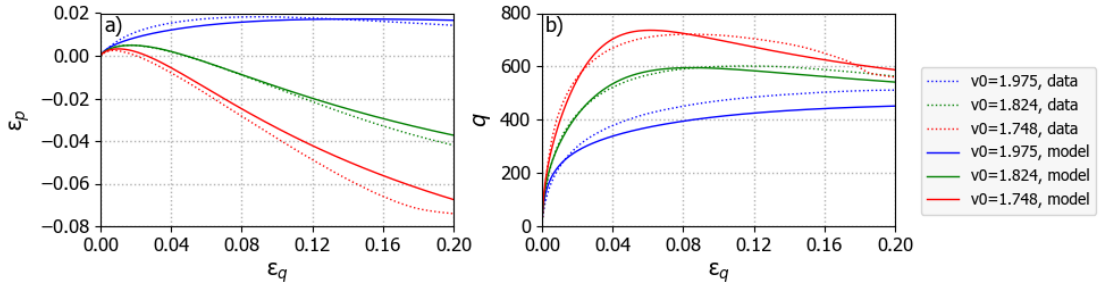


Figure 127 Comparison of the results of the base monotonic model with data for monotonic drained tests

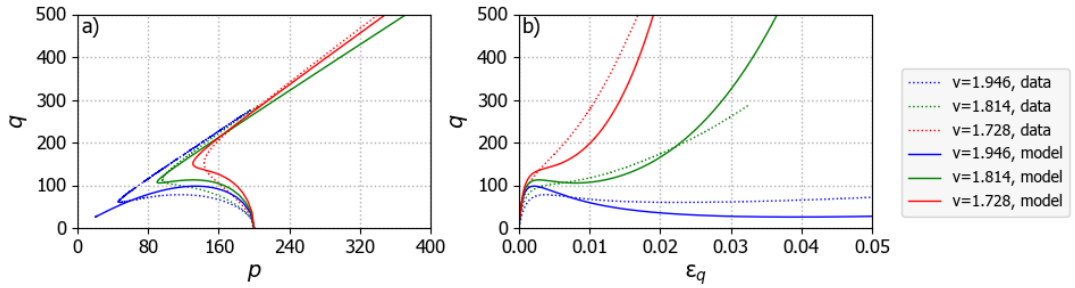


Figure 128 Comparison of the results of the base monotonic model with data for monotonic undrained tests

The simulated tests compare well to the data, with capacities, stiffness and dilation being well captured across densities for the drained tests. Furthermore, pore pressure build-up and shear stress function of shear strain are well captured in undrained tests.

3.2.10. General base model: Multi-surface

The following model is abbreviated by HySand_base.

The model developed so far is able to simulate monotonic tests. However, it cannot properly capture cyclic loading. This poor performance emerges from the yield surface being pushed away (consolidated) during the first cycles, such that further cycles with the same amplitude do not reach it. Houlsby and Mortara (2004) proposed to use a multi-surface plasticity approach to capture small strain stiffness and cyclic loading. The problem here is slightly different because monotonic normally consolidated loadings demonstrate plasticity from their initiation, contrary to the model by Houlsby and Mortara (2004). Nonetheless, multi-surface plasticity is still essential for the objective of capturing cyclic loading.

3.2.10.1. Mapping the stress space with multiple yield surfaces

Multi-surface plasticity, like bounding surface plasticity or hypoplasticity, is intended to allow development of models in which the transition from elasticity to plasticity is progressive. The choice of multi-surface plasticity is explained in Chapter 2.

In order to accommodate multiple yield surfaces with multiple consolidation pressures, the following energy function is adopted:

$$g = -\frac{p_r}{k_r(1-m)(2-m)}\left(\frac{p_0}{p_r}\right)^{2-m} - q\frac{1}{N}\sum_{n=1}^{N}\alpha_q^{(n)} - p\frac{1}{N}\sum_{n=1}^{N}\left(\alpha_p^{(n)} + \alpha_{pc}^{(n)}\right) \qquad \textit{Eq. 154}$$

It comprises N shear plastic strain variables, N volumetric plastic strain variables, and N consolidation plastic strain variables.

3.2.10.1.1. Selected option: Multi-friction and multiple consolidation pressures

Here, a mapping of the stress space can be obtained through the following formula for the nth surface out of a total of N surfaces:

$$y^{(n)} = \left(N\chi_q^{(n)} + A\left(1 - aS\left(\chi_q^{(n)}\right)\right)\chi_a - a\beta^{(n)}N\chi_p^{(n)}\right)^2 - 4\left(\frac{n}{N}\mu\right)^2\left(1 - \left(\frac{N\chi_{pc}^{(n)}}{p_c^{(n)}}\right)^r\right)\left(p + \frac{2}{3}q\right)\left(p - \frac{q}{3}\right) = 0 \qquad \textit{Eq. 155}$$

Each yield surface has its own friction $(n/N \times \mu)$, which enables to map the stress space, and its own dilation ratio ($\beta^{(n)}$):

$$\beta^{(n)} = \frac{\mathrm{n}}{\mathrm{N}}\beta = \frac{n}{N}\beta_{max}\frac{\ln v_\lambda - \ln \Gamma}{\ln \Delta - \ln \Gamma} \qquad \textit{Eq. 156}$$

Factoring the dilation by n/N is required to model initially anisotropic state (e.g. section 5.2.1). For an isotropically consolidated test, the factor n/N guarantees that even for an initial anisotropic state ($a_0 \neq 0$), part of the isotropic axis will lie inside all yield surfaces. Without the factor, it would not be the case for the inner yield surfaces with a large initial anisotropy value.

Each yield surface also has its own independent consolidation pressure:

$$p_c^{(n)} = p_{c0}\left(1 + \frac{(1-m)}{\lambda - 1/k_r}\alpha_{p_c}^{(n)}\right)^{\frac{1}{1-m}} \qquad \textit{Eq. 157}$$

Here, it is not possible to have the same consolidation pressure for all surfaces because plastic multipliers cannot be determined for one common consolidation pressure in isotropic loading.

In Figure 129, the black and blue solid curves illustrate the mapping of the stress space by five yield surfaces in their initial isotropic configuration, with same initial consolidation pressures.

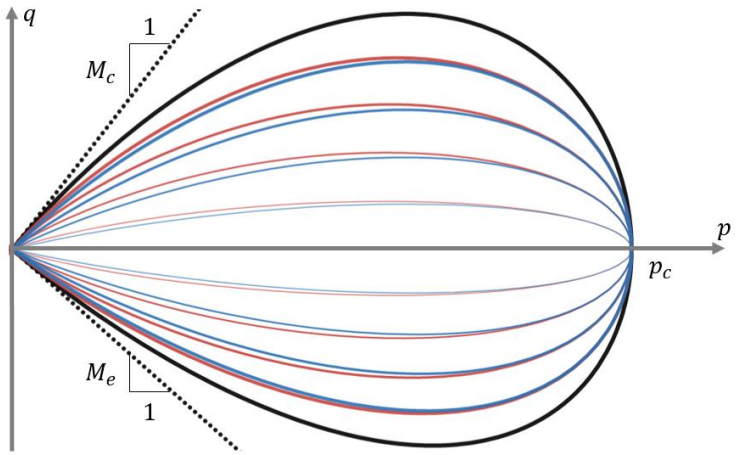


Figure 129 Yield surfaces in stress space: for a=0, with outer yield surface (black), inner multi-friction yield surfaces (blue), and inner multi consolidation exponents yield surfaces (red)

In this model, all surfaces contribute to the development of a global anisotropy a.

3.2.10.1.2. Alternative: Multiple consolidation pressures and multiple interaction exponents

As explained in 3.2.8.1.3, the one surface model can be seen as a combination of a frictional yield surface with exponent 2, and a vertical consolidation yield surface with exponent r. An option that has not been thoroughly explored, because the first presented option gave good results, is to keep the same friction (μ) for all surfaces, but to reduce the exponent r for the inner yield surfaces. This would imply a greater influence of the consolidation mechanism in inner yield surfaces.

This could for example take the following form:

$$y^{(n)} = \left(N\chi_q^{(n)} + A\left(1 - aS\left(\chi_q^{(n)}\right)\right)\chi_a - a\beta^{(n)}N\chi_p^{(n)}\right)^2 - 4\mu^2\left(1 - \left(\frac{N\chi_{pc}^{(n)}}{p_c^{(n)}}\right)^{\left(\frac{n}{N}\right)^2 r}\right)\left(p + \frac{2}{3}q\right)\left(p - \frac{q}{3}\right) \quad \textit{Eq. 158}$$

With the squared (n/N) factor in front of r to better map low shear stresses.

The initial isotropic yield surfaces of this option are represented in red in Figure 129. There is only slight difference at lower pressures between the yield shapes of the two options.

3.2.10.1.3. Alternative: One consolidation pressure and multiple friction ratios

Another interesting option that has not been explored would have been to only use one consolidation yield surface with the combination technique evoked in 3.2.8.1.3, but applied to N frictional surfaces, thanks to the following expression:

$$\mathrm{y} = \sqrt{\sum_{n=1}^{N}\left(\frac{\left(N\chi_q^{(n)} + A\left(1 - aS\left(\chi_q^{(n)}\right)\right)\chi_a - a\beta^{(n)}N\chi_p^{(n)}\right)}{2\left(\frac{\mathrm{n}}{\mathrm{N}}\right)\mu\sqrt{\left(p + \frac{2}{3}q\right)\left(p - \frac{q}{3}\right)}}\right)^2 + \left(\frac{\chi_{\mathrm{p_c}}}{p_c}\right)^r - 1} \quad \textit{Eq. 159}$$

Note that for this option, the energy function only requires one plastic consolidation variable.

3.2.10.2. Hardening of inner yield surfaces

After a full anisotropy development, all yield surfaces should reach maximal stress ratios $|q/p|_{max}$ of $M_c + \beta$ in compression, or $M_e + \beta$ in extension. However, with the model so far described, inner yield surfaces only reach stress ratios of $(n/N)M_c + \beta^{(n)}$ in compression, and $(n/N)M_e + \beta^{(n)}$ in extension. This is illustrated in Figure 130 for $a = 1$ and $a = -1$ in the unlikely event that consolidation pressures stay equal.

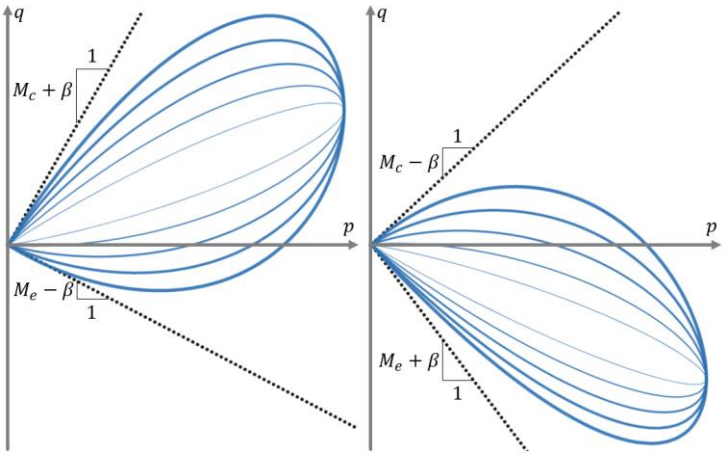


Figure 130 Anisotropic yield surfaces with same consolidation pressures for $a = 1$ on the left and $a = -1$ on the right

In order for the inner yield surfaces to reach the necessary stress ratios, hardening of these yield surfaces should be implemented. Furthermore, the value of the hardening modulus ($H^{(n)}$) of each yield surface is what defines its "degree of plasticity": how much plastic strain this yield surface will generate.

This hardening can take multiple forms, as discussed hereafter.

3.2.10.2.1. Kinematic hardening via the Gibbs energy function

In Houlsby and Mortara (2004) and Simonin *et al.* (2023), the Gibbs energy introduces kinematic hardening:

$$g = -\frac{p_r}{k_r(1-m)(2-m)}\left(\frac{p_0}{p_r}\right)^{2-m} - q\frac{1}{N}\sum_{n=1}^{N}\alpha_q^{(n)} - p\frac{1}{N}\sum_{n=1}^{N}\left(\alpha_p^{(n)} + \alpha_{pc}^{(n)}\right) + \frac{1}{N}\sum_{n=1}^{N}\frac{3}{2}H^{(n)}\alpha_q^{(n)^2} \qquad \textit{Eq. 160}$$

Such that the shear generalised stress is:

$$\chi_q^{(n)} = -\frac{\partial g}{\partial \alpha_q^{(n)}} = \frac{q - 3H^{(n)}\alpha_q^{(n)}}{\mathrm{N}} \qquad \textit{Eq. 161}$$

The medium axis of the inner yield surfaces would then translate in stress space. This is represented with realistic values for a drained loading in Figure 131.

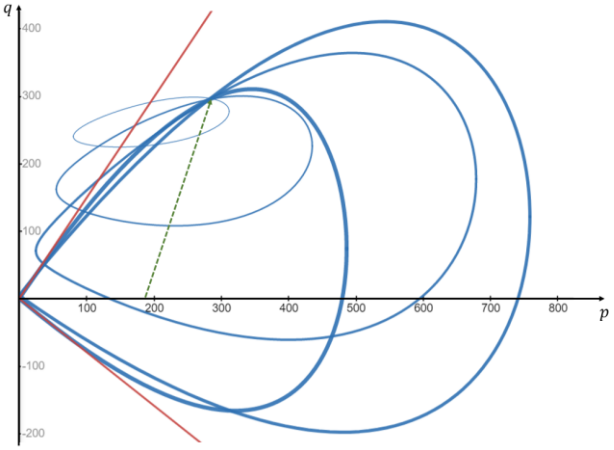


Figure 131 Yield surfaces translation with kinematic hardening during a drained test (dashed green stress path)

Such hardening provokes a complicated mapping of the stress space which seems unnatural for a frictional phenomenon.

3.2.10.2.2. Shear hardening via the Gibbs energy function

A more natural hardening for a frictional material would be a shear hardening mechanism which could be introduced in the Gibbs energy function as follows:

$$g = -\frac{p_r}{k_r(1-m)(2-m)}\left(\frac{p_0}{p_r}\right)^{2-m} - q\frac{1}{N}\sum_{n=1}^{N}\alpha_q^{(n)} - p\frac{1}{N}\sum_{n=1}^{N}\left(\alpha_p^{(n)} + \alpha_{pc}^{(n)}\right) + p\frac{1}{N}\sum_{n=1}^{N}\frac{3}{2}H^{(n)}\alpha_q^{(n)^2} \qquad \textit{Eq. 162}$$

Such that the shear generalised stress is:

$$\chi_q^{(n)} = -\frac{\partial g}{\partial \alpha_q^{(n)}} = \frac{q - 3H^{(n)}\alpha_q^{(n)} p}{\mathrm{N}} \qquad \textit{Eq. 163}$$

However, a major disadvantage of this formulation is the loss of the meaning of $\alpha_p^{(n)} + \alpha_{pc}^{(n)}$ and $\alpha_q^{(n)}$, which were, so far, pure volumetric plastic strain and pure shear plastic strain respectively.

Indeed the plastic volumetric strain in this formulation is:

$$\begin{aligned} \epsilon_p^p &= -\frac{\partial g}{\partial p} - \frac{\partial \left(\frac{p_r}{k_r(1-m)(2-m)} \left(\frac{p_0}{p_r}\right)^{2-m} \right)}{\partial p} \\ \leftrightarrow \epsilon_p^p &= \frac{1}{N}\sum_{n=1}^{N} \left(\alpha_p^{(n)} + \alpha_{pc}^{(n)} \right) - \frac{1}{N}\sum_{n=1}^{N} \frac{3}{2} H^{(n)} {\alpha_q^{(n)}}^2 \end{aligned} \qquad \textit{Eq. 164}$$

The plastic volumetric strain thus comprises a term in ${\alpha_q^{(n)}}^2$, which entails that for any plastic shear hardening, dilative plastic volumetric strain is created via this term. This is an unwanted by-product which implies that dilation would be created even for loose samples. For this reason, this formulation is abandoned.

3.2.10.2.3. Selected option: Hardening via the yield equations

Shear hardening is however desirable. Another way to introduce it is via the yield formulation. This avoids the change of definition of the plastic volumetric strain in the Gibbs energy function.

The yield surfaces, in their normalised form, are written:

$$y^{(n)} = \frac{\left(N\chi_q^{(n)} - h_n\left(p, q, \alpha_q^{(n)}\right) - a\beta^{(n)} N\chi_p^{(n)} + A(1-|a|)\chi_a \right)^2}{4\left(\frac{n}{N}\mu\right)^2 \left(p + \frac{2}{3}q\right)\left(p - \frac{q}{3}\right)} + \left(\frac{N\chi_{pc}^{(n)}}{p_c^{(n)}} \right)^r - 1 = 0 \qquad \textit{Eq. 165}$$

Where the hardening function in its base version is linear in $\alpha_q^{(n)}$:

$$h_n\left(p, q, \alpha_q^{(n)}\right) = 3H^{(n)}\alpha_q^{(n)} p \qquad \textit{Eq. 166}$$

Figure 132 represents the yield surfaces during a drained test.

With this formulation, one should be careful to not break the convexity of yield surfaces in generalised stress space, or equivalently the positivity of the dissipation. The positivity of the dissipation is demonstrated in Annex.

This option, which allows shear hardening without undesirable side effects, has been selected.

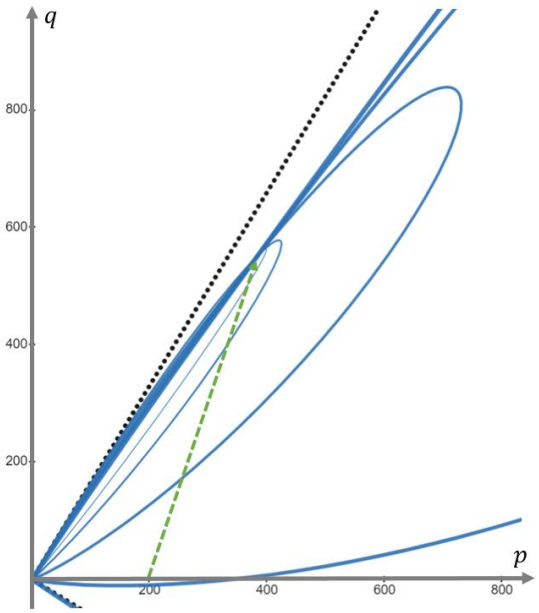


Figure 132 Yield surfaces shearing after realistic drained loading (stress path = green dashed line)

3.2.10.2.4. Plastic moduli

The two parameters formulation by Houlsby and Mortara (2004) has been retained:

$$H^{(n)} = h\left(1 - \frac{n}{N}\right)^{b} \qquad \textit{Eq. 167}$$

A low value of $b \in]0,2]$ means that plastic moduli have the same order of magnitude across surfaces. A higher value of b signifies that plastic moduli of the inner surfaces are high, while the plastic moduli near the outermost surface are very low, leading to a model showing little plasticity until close to the outermost surface. Values of b of 3 or 4 have been found to give good predictions for the Wichtmann database.

Analysis of the series of undrained stress-controlled tests by Wichtmann and Triantafyllidis (2016a) has shown that the plastic moduli ($H^{(n)}$) should be density dependent in order to predict the number of cycles to liquefaction across density. The power exponent b can be kept constant. However, h should be varied across densities, with lower values for looser samples. The model uses the same log-linear variation as for the anisotropy rate development parameter:

$$h = h_0 \frac{\ln(v_\lambda) - \ln(\mathrm{B})}{\ln(\Delta) - \ln(\mathrm{B})} \qquad \textit{Eq. 168}$$

The denser the sample, the less plastic the inner surfaces are. Indeed, the denser the sample, the larger h is, the higher the shearing is for an identical plastic strain quantity.

HySand_base is summarised by:

Gibbs energy function:

$$g = -\frac{p_r}{k_r(1-m)(2-m)}\left(\frac{p_0}{p_r}\right)^{2-m} - q\frac{1}{N}\sum_{n=1}^{N}\alpha_q^{(n)} - p\frac{1}{N}\sum_{n=1}^{N}(\alpha_p^{(n)} + \alpha_{pc}^{(n)}) \quad \textit{Eq. 169}$$

$$\text{where: } p_0^2 = p^2 + \frac{k_r(1-m)}{3g_r}\,q^2 \text{ with } p_r = 100kPa \quad \textit{Eq. 170}$$

Yield functions:

$$y^{(n)} = \frac{\left(N\chi_q^{(n)} - h_n\left(p,q,\alpha_q^{(n)}\right) - a\beta^{(n)}N\chi_p^{(n)} + A(1-|a|)\chi_a\right)^2}{4\left(\frac{n}{N}\mu\right)^2\left(p+\frac{2}{3}q\right)\left(p-\frac{q}{3}\right)} + \left(\frac{N\chi_{pc}^{(n)}}{p_c^{(n)}}\right)^r - 1 \quad \textit{Eq. 171}$$

$$\text{where } h_n\left(p,q,\alpha_q^{(n)}\right) = 3H^{(n)}\alpha_q^{(n)}p \quad \textit{Eq. 172}$$

$$\text{for which } H^{(n)} = h\left(1-\frac{n}{N}\right)^b \quad \textit{Eq. 173}$$

$$\text{in which } h = h_0\frac{\ln v_\lambda - \ln \mathrm{B}}{\ln \Delta - \ln \mathrm{B}} \quad \textit{Eq. 174}$$

$$\text{and } \beta^{(n)} = \frac{n}{N}\beta_{max}\frac{\ln v_\lambda - \ln \Gamma}{\ln \Delta - \ln \Gamma} \quad \textit{Eq. 175}$$

$$\text{and } A = A_{max}\frac{\ln v_\lambda - \ln B}{\ln \Delta - \ln B} \quad \textit{Eq. 176}$$

$$\text{and } p_c^{(n)} = p_{c0}\left(1+\frac{(1-m)}{\lambda - 1/k_r}\alpha_{p_c^{(n)}}\right)^{\frac{1}{1-m}} \quad \textit{Eq. 177}$$

$$\text{With } \lambda = \lambda_{\mathrm{B}} - (\lambda_{\mathrm{B}} - \lambda_{\Delta})\frac{\ln v_\lambda - \ln \mathrm{B}}{\ln \Delta - \ln \mathrm{B}} \quad \textit{Eq. 178}$$

$$\ln v_\lambda = \ln \mathrm{B} - \ln\left(\frac{\mathrm{B}}{\Delta}\right)\frac{(\ln v_0 - \epsilon_p) + \frac{\lambda_{\mathrm{B}}}{1-m}\left(\left(\frac{p}{p_r}\right)^{1-m} - 1\right) - \ln \mathrm{B}}{\ln \Delta + \frac{\lambda_{\mathrm{B}} - \lambda_{\Delta}}{1-m}\left(\left(\frac{p}{p_r}\right)^{1-m} - 1\right) - \ln \mathrm{B}} \quad \textit{Eq. 179}$$

This model thus employs the 14 parameters presented in Table 5

k_r	g_r	m	φ_c	β_{max}	B	Γ	Δ	λ_{B}	λ_{Δ}	$\mathrm{A_{max}}$	$\mathrm{h_0}$	b	r

Table 5 List of the parameters of the base model

3.2.10.3. Analysis of test results

In Figure 133 to Figure 137, the original data by Wichtmann (dotted curves) is compared to the base model results (solid curves) for $N = 10$ surface and with the parameters given in Table 6.

k_r	g_r	m	φ_c	β_{max}	B	Γ	Δ	λ_B	λ_Δ	A_{max}	h_0	b	r
516	400	0.7	33.1	1.0	2.054	1.98	1.677	0.0053	0.0027	40	750	3	0.3

Table 6 Base model parameters calibrated to Wichtmann's data

All tests are well reproduced with the base model. Only two divergences clearly appear:

- in the stress controlled undrained cyclic test, Figure 135, the progressive pore pressure build-up and the small strain behaviour is well reproduced. However, the liquefied behaviour is not well depicted, with an insufficient pore pressure build-up upon load reversal.
- in the pre-sheared monotonic undrained test, red curve in Figure 137, the modelled undrained reloading stress path is less curved towards higher mean effective stress than the data, and, in consequence, it goes plastic at a lower stress than in the data.

The implementation of multi-surface plasticity has a major impact on the cyclic tests. In Figure 135, which presents the stress controlled cyclic undrained test, the stress path still encounters some inner yield surfaces after the first cycle thanks to the mapping of the stress space with multiple hardening surfaces. This allows pore pressure build-up to progressively slow down, until pore pressure build-up accelerates again (at ~100kPa in the simulation). This subsequent acceleration emerges because the stress path reaches the narrow wedge end of outer surfaces, leading to more plastic deformation, thus to more pressure build-up. The model is capable of predicting the number of cycles until liquefaction but is not capable of simulating the liquefied behaviour itself. Here, the liquefaction criteria for the model is either reaching a shear strain of 2.5%, or a locking of stress loops at low p.

In Figure 136, the 50 first strain controlled cycles have been plotted for the data and the model. The model results and the data compare very well in the rate of pore pressure build-up and in the mobilised stress ratios.

Improvements brought by HySand_base compared to HySand_base_mono:

Former elastic loadings are now progressively plastic. This is essential to capture the cyclic tests.

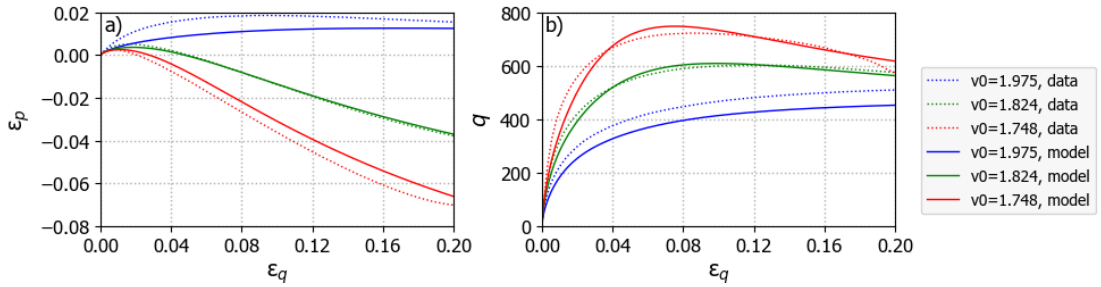


Figure 133 Drained tests (a) volumetric strain function of shear strain; b) shear stress function of shear strain)

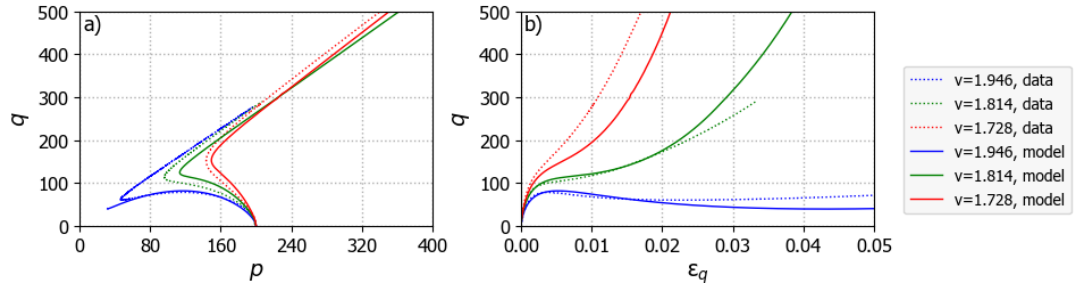


Figure 134 Undrained tests (a) shear stress function of volumetric stress; b) shear stress function of shear strain)

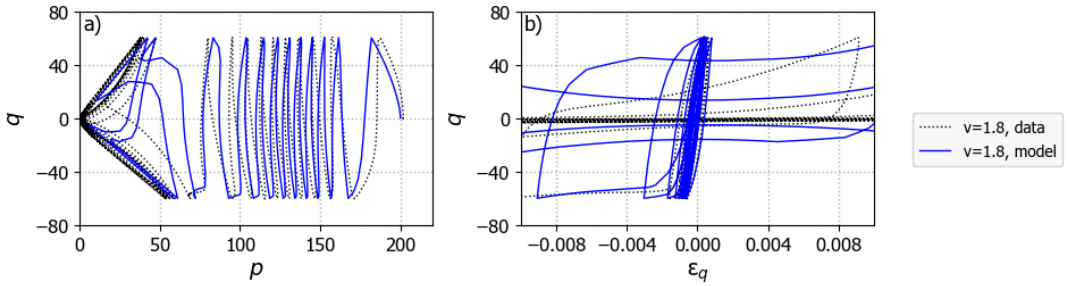


Figure 135 Undrained cyclic stress controlled test (a) shear stress function of volumetric stress; b) shear stress function of shear strain)

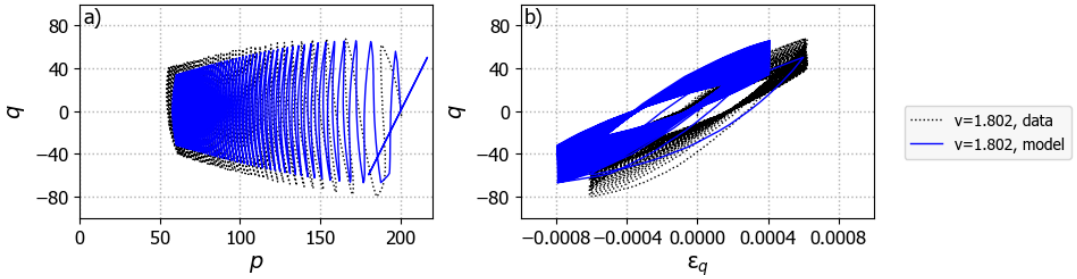


Figure 136 Undrained cyclic strain controlled test (a): shear stress function of volumetric stress; b) shear stress function of shear strain)

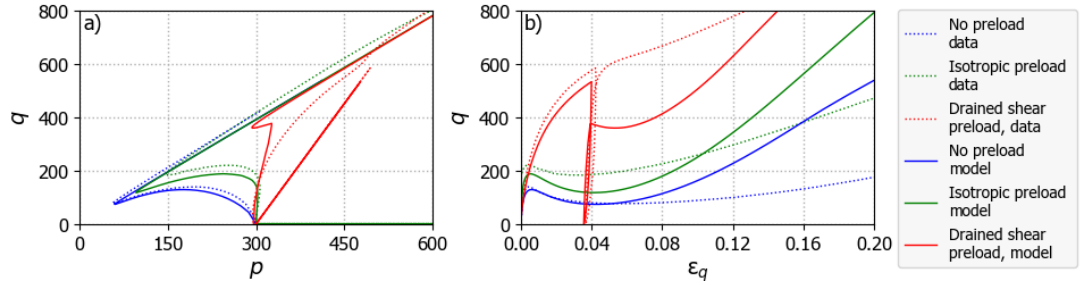


Figure 137 Undrained test with preloading (a): shear stress function of volumetric stress; b) shear stress function of shear strain)

3.2.11. Options for more advanced models

HySand_base has been judged the best compromise between simplicity, physical soundness, and quality of results, which will be further displayed and discussed in Chapter 5.

However, the results could be improved at the expense of making the model more complex. It could for example better capture the plastic volumetric behaviour upon load reversal (thus better capturing the liquefaction phase), or better capture the variation with density of the number of undrained cycles to liquefaction.

The main points of modification identified by the author are:

- the form in which parameters depend on density and pressure.
- the distinction between power exponents for volumetric non-linear elasticity, shear non-linear elasticity, and consolidation plasticity.
- the anisotropy law.
- the hardening law.
- the dilation law.

3.2.11.1. Density dependence

3.2.11.1.1. A non-linear density dependence

In HySand_base, the anisotropy, the dilation, the hardening, and the consolidation already depend on the density. However, only log-linear relations to the relative density of the sample are considered. Non-linear dependence could be considered.

For example the density dependence of anisotropy and hardening could follow:

$$A = A_{max}\left(\frac{\ln(v_\lambda) - \ln(B)}{\ln(\Delta) - \ln(B)}\right)^{A_v} \quad \textit{Eq. 180} \qquad h = h_0\left(\frac{\ln(v_\lambda) - \ln(\mathrm{B})}{\ln(\Delta) - \ln(\mathrm{B})}\right)^{A_v} \quad \textit{Eq. 181}$$

This modification allows additional control of the density dependence of anisotropy and hardening, but at the cost of an additional parameter A_v.

3.2.11.1.2. Density dependence of additional parameters

Further quantities could also be made dependent on density. For example, in Chapter 4, it is shown that the dimensionless bulk modulus (k_r) and the power exponent for non-linear elasticity (m) seem to depend on density.

The density dependence of these two parameters is not represented in HySand_base because the relative amplitude of the variation of these parameters with density is small compared to the other modelled dependence, and because accounting for it would require additional parameters.

3.2.11.2. Pressure dependence

In the used benchmark tests, there were drained and undrained tests with different densities. However, none was presenting different initial consolidation pressures. Figure 138 displays a comparison between data by Wichtmann and model results for normally consolidated drained tests at different initial consolidation pressures.

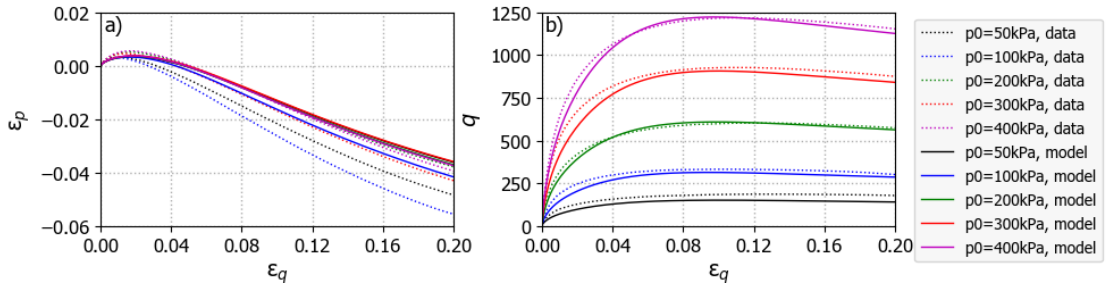


Figure 138 Normally consolidated drained tests on medium dense samples for different initial consolidation pressures

HySand_base performs well. However, observations on the ensemble of drained tests by Wichtmann indicate that the lower the initial consolidation pressure, the quicker dilation develops. This could be reproduced by making the anisotropy development pressure dependent such as:

$$A = A_{max}\frac{\ln(v_\lambda) - \ln(B)}{\ln(\Delta) - \ln(B)}\left(\frac{p}{p_r}\right)^{-A_p} \qquad \textit{Eq. 182}$$

Figure 139 displays results for $A_p = 0.5$ and an adequately modified A_{max} ($A_{max} = 150$, with other parameters given in Table 6). The improvement in the results resides in the better captured evolution of stiffness across initial pressures, and the dilation rate development across initial pressures.

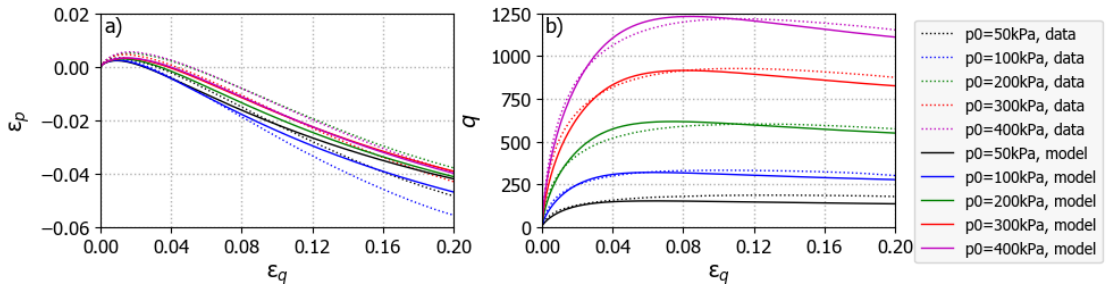


Figure 139 Normally consolidated drained tests on medium dense samples for different initial consolidation pressures for a modified anisotropy rate development parameter

This improvement would also come at the cost of an additional parameter: A_p.

3.2.11.3. Power exponent for non-linear elasticity and consolidation

In HySand_base, one power exponent (m) is used for non-linear elasticity, both volumetric and deviatoric, and for consolidation. Three independent exponents could beneficiate the modelling, but it would be at the cost of two additional parameters and additional calibration effort.

3.2.11.4. Anisotropy law

In 3.2.6, the choice of the integrable anisotropy law is guided by observations on cyclic tests, and by the simplicity of such a law.

As discussed however, a hysteretic law is desirable. It could take the form of the hybrid law:

$$C_a = \dot{a} - A\left((1-|a|) - (1-f_a)a\left(S(a) - S\left(\dot{\alpha_q}\right)\right)\right)\dot{\alpha_q} = 0 \qquad \textit{Eq. 183}$$

This would also add a parameter: f_a.

3.2.11.5. Hardening law

The current hardening law is linear with the plastic shear strain. This means that at any point in the loading, the rate at which one surface hardens is the same. This could easily be modified in the formulation if the need arises.

3.2.11.6. Dilation law

In Chapter 5, it is shown that cyclic undrained simulations with HySand_base do not demonstrate enough pore pressure build-up on load reversal after large shear straining in one direction. Equivalently, it is also shown that drained tests do not demonstrate enough contraction upon unloading after large shear straining. This indicates that the contraction dictated by the dilation law (Eq. 90) is not sufficient upon load reversal.

Houlsby (1992) and Houlsby and Mortara (2004) introduce an additional constant isotropic contraction in the dilation constraint written as:

$$C_d = \dot{\alpha_p} + a\beta_d\dot{\alpha_q} + \beta_c\left|\dot{\alpha_q}\right| = 0 \qquad \textit{Eq. 184}$$

Where $\beta_c < 0$ is a density dependent contraction ratio, and β_d is the dilation ratio. However, this leads to too large pore pressure build-up during cyclic strain-controlled undrained tests with small strain, which is why this option was discarded.

Another option to add contraction upon load reversal is the implementation of an anisotropy dependent contraction, modifying the dilation constraint to:

$$C_d = \dot{\alpha_p} + a\beta_d\dot{\alpha_q} + |a|\beta_c\left|\dot{\alpha_q}\right| = 0 \qquad \textit{Eq. 185}$$

Where β_d would be a modified dilation ratio with $\beta_d = \beta - \beta_c$ in order to compensate the contraction and conserve the meaning of the dilation ratio β.

For an isotropic state ($a = 0$), Eq. 185 would eliminate the undesirable contraction. But once the anisotropy has developed ($a \neq 0$), Eq. 185 implies an additional contraction upon load reversal. A potentially welcome by-product of Eq. 185 is the narrowing of the yield surface(s) with anisotropy development, which could lead to a better simulation of the butterfly-shaped liquefaction in cyclic stress-controlled undrained tests.

Figure 140 to Figure 144 present simulations with such a modified HySand model, with a contraction value $\beta_c = -0.4$. Figure 140 and Figure 141 present the simulation of two cyclic stress-controlled undrained tests on medium dense and dense sand, which can be compared to Figure 254 and Figure 255 (section 5.1.7.1). The addition of the anisotropic contraction seems to modify only the last few cycles, as large strains and thus anisotropy then develop. During these last few cycles, more pore pressure build-up is generated on load reversal, such that liquefaction is reached even for the simulation of the dense sample. The addition of the anisotropic contraction thus allows better modelling of the later cycles, reaching liquefaction, but still not simulating the cyclic mobility phase.

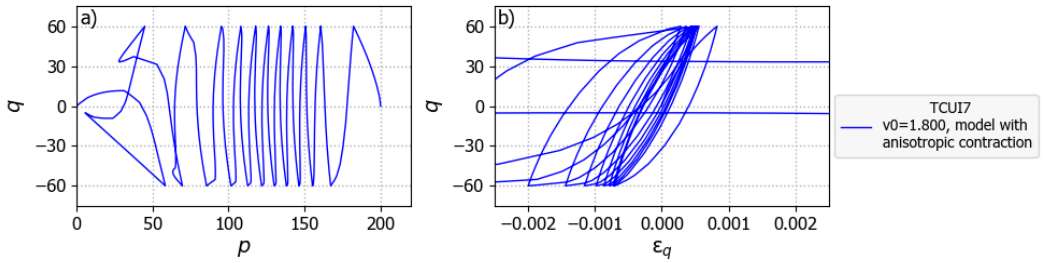


Figure 140 Simulation of TCUI7, cyclic stress-controlled undrained test on medium dense sand

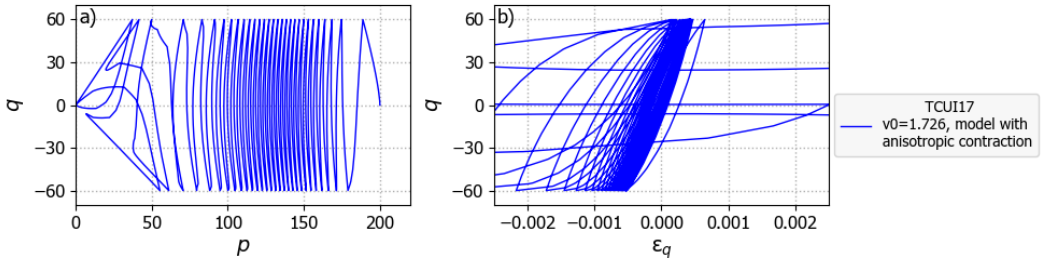


Figure 141 Simulation of TCUI17, cyclic stress-controlled undrainted test on dense sand

Data and simulation of a drained test on medium dense sand with unloads and reloads is shown in Figure 142. The addition of the anisotropic contraction allows to simulate the important contraction upon load reversal, which is not present in HySand_base (see Figure 281 in 5.1.9), as well as to represent better the unload-reload loops in the deviatoric stress-strain plane.

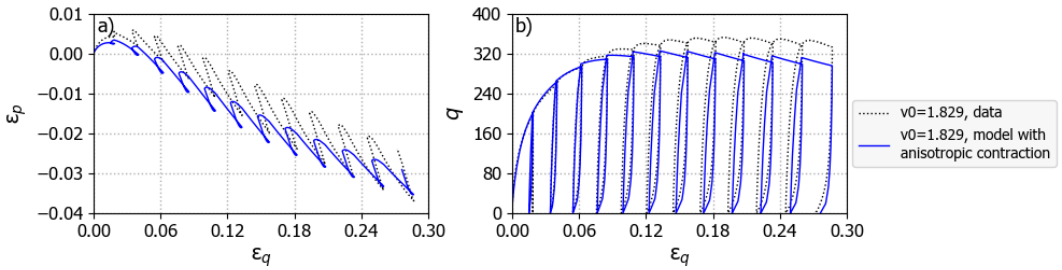


Figure 142 Drained tests with unloads and reloads

As will be discussed in section 5.4, a common limitation of many advanced consitutitve models is the inability to model correctly cyclic strain-controlled undrained test on dense sand. Some models do not capture the liquefaction that occurs in the data, while others do but fail to capture the progressive build-up of pore pressure. While HySand_base does not reach liquefaction (see Figure 377), the model with additional anisotropic contraction does (see Figure 143), with a progressive pore pressure build-up as observed in the data (see Figure 375).

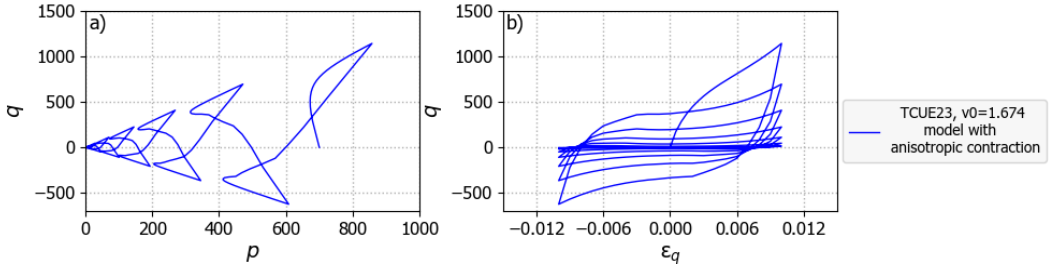


Figure 143 Simulation of TCUE23, cyclic strain-controlled undrained test on dense sand

Figure 144 presents the simulation of the undrained test TCUA2. This should be compared to Figure 263 and Figure 269 of section 5.1.7.2. The stress path is better predicted thanks to the additional anisotropic contraction/pore pressure build-up. However, the ratcheting does not slow down as it should, leading to a growing overestimation with growing number of cycles.

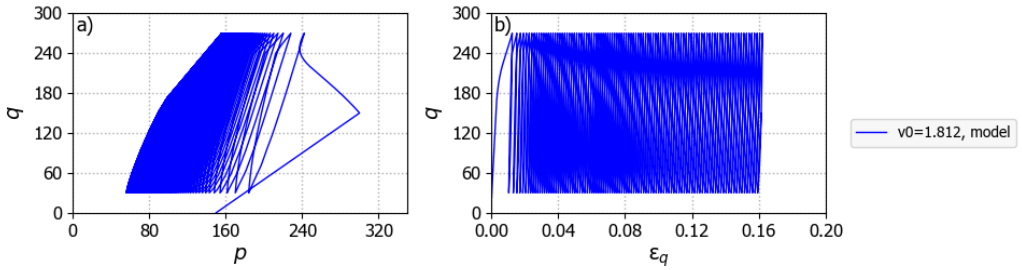


Figure 144 Simulation with a model with additional anisotropy of an undrained stress-controlled one-way test

The addition of the anisotropic contraction brings both local improvements and deterioriations to the modelling. Addition of the anisotropic contraction thus seems promising, but further work is necessary to study thoroughly its impact, as well as to correct the poor ratcheting performance which is essential in the context of the design of OWTs foundations.

3.3. Generalising to 3D

The following paragraphs explain how HySand_base that was developed in triaxial space has been generalised to three dimension for each feature of the model.

3.3.1. Non-linear elasticity in 3D

Houlsby *et al.* (2019) give the formulation for the Gibbs energy function of non-linear elasticity in three dimensions:

$$g = -\frac{p_r}{k_r(1-m)(2-m)}\left(\frac{p_0}{p_r}\right)^{2-m} \quad \textit{Eq. 186} \qquad p_0^2 = \frac{\sigma_{ii}\sigma_{jj}}{9} + \frac{k_r(1-m)}{2g_r}\sigma'_{ij}\sigma'_{ji} \quad \textit{Eq. 187}$$

Where σ'_{ij} is the deviator of σ_{ij}, and where the symmetric part of this tensor is not used (in contrast to the original paper). In the 3D formulation of the model, only the expression of p_0 is modified from the triaxial model.

3.3.2. Matusoka-Nakai yield criterion

The formulation of the dissipation and yield surfaces in triaxial space have been modified from the formulation by Houlsby (1992) and Houlsby and Mortara (2004) (cf. 3.2.4) in order to be compatible with the Matsuoka-Nakai yield criterion (Matsuoka and Nakai (1974)). The expression of the yield criterion in principal stresses in 3D is:

$$y_\sigma = \frac{(\sigma_1-\sigma_2)^2}{4\mu^2\sigma_1\sigma_2} + \frac{(\sigma_2-\sigma_3)^2}{4\mu^2\sigma_2\sigma_3} + \frac{(\sigma_3-\sigma_1)^2}{4\mu^2\sigma_3\sigma_1} - 2 = 0 \qquad \textit{Eq. 188}$$

Similarly to the triaxial case, the initial model should be purely frictional, which is achieved with:

$$y = \frac{(\chi_1-\chi_2)^2}{4\mu^2\sigma_1\sigma_2} + \frac{(\chi_2-\chi_3)^2}{4\mu^2\sigma_2\sigma_3} + \frac{(\chi_3-\chi_1)^2}{4\mu^2\sigma_3\sigma_1} - 2 = 0 \qquad \textit{Eq. 189}$$

The formulation of the criterion in general stress is:

$$\begin{aligned} y_\sigma = &-\sigma_{ii}\sigma_{jj}\sigma_{kk} + 4\sigma_{ii}\sigma_{jk}\sigma_{kj} - 3\sigma_{ij}\sigma_{jk}\sigma_{ki} \\ &-\frac{4}{3}\mu^2\left(\sigma_{ii}\sigma_{jj}\sigma_{kk} - 3\sigma_{ii}\sigma_{jk}\sigma_{kj} + 2\sigma_{ij}\sigma_{jk}\sigma_{ki}\right) \end{aligned} \qquad \textit{Eq. 190}$$

No volumetric strain should be produced, and the expression should devolve to the triaxial formulation. This can be achieved with the formula given by Houlsby (2021):

$$\begin{aligned} y = &-\sigma_{ii}\chi_{jj}\chi_{kk} + 2\sigma_{ii}\chi_{jk}\chi_{kj} + 2\chi_{ii}\sigma_{jk}\chi_{kj} - 3\sigma_{ij}\chi_{jk}\chi_{ki} \\ &-\frac{4}{3}\mu^2\left(\sigma_{ii}\sigma_{jj}\sigma_{kk} - 3\sigma_{ii}\sigma_{jk}\sigma_{kj} + 2\sigma_{ij}\sigma_{jk}\sigma_{ki}\right) \end{aligned} \qquad \textit{Eq. 191}$$

Eq. 191 differs from the triaxial expression by a factor σ_{ii}.

Noting that the general form only depends on the deviator of χ, it can also be written:

$$y = 2\sigma_{ii}\chi'_{jk}\chi'_{kj} - 3\sigma_{ij}\chi'_{jk}\chi'_{ki} - \frac{4}{3}\mu^2\left(\sigma_{ii}\sigma_{jj}\sigma_{kk} - 3\sigma_{ii}\sigma_{jk}\sigma_{kj} + 2\sigma_{ij}\sigma_{jk}\sigma_{ki}\right) = 0 \qquad \textit{Eq. 192}$$

Which can be written in invariant form as:

$$y = 4I_{1\sigma}J_{2\chi} - 3tr\left(\sigma\chi'^{2}\right) - 8\mu^{2}I_{3\sigma} = 0 \qquad \textit{Eq. 193}$$

This yield surface does not produce any volumetric strain and is an open cone in stress space.

Because the model now produces plastic strain, the Gibbs energy function now becomes:

$$g = -\frac{p_r}{k_r(1-n)(2-n)}\left(\frac{p_0}{p_r}\right)^{2-n} - \sigma_{ij}\alpha_{ij} \qquad \textit{Eq. 194}$$

The following three paragraphs propose a method to integrate anisotropy, dilation, and contraction based on the triaxial development.

3.3.3. Generalisation of anisotropy

In the triaxial case, the anisotropy is recorded with a scalar (a) which increases when the sample is sheared in compression ($a \to 1$), and decreases when the sample is sheared in extension ($a \to -1$). In order to obtain an equivalent behaviour in 3D, the anisotropy can be monitored through a tensor $\boldsymbol{a} = a_{ij}$. Houlsby (1992) proposes for the anisotropy constraint (in updated notation):

$$C_a = \dot{a}_{\mathrm{ij}} - A\left(\dot{\alpha}'_{ij} - a_{ij}\sqrt{\dot{\alpha}'_{kl}\dot{\alpha}'_{lk}}\right) = \dot{a}_{\mathrm{ij}} - A\left(\dot{\alpha}'_{ij} - a_{ij}\sqrt{2J_{2\dot{\alpha}}}\right) = 0 \qquad \textit{Eq. 195}$$

Eq. 195 corresponds to the hysteretic law that has been abandoned in favour of the integrable law. Houlsby (2021) proposes to arbitrarily define the triaxial value of the scalar as a function of the tensorial form by $a^2 = tr(\boldsymbol{a}^2) = 2J_{2a}$. This results in $a = \sqrt{2/3}(a_{11} - a_{33})$ in triaxial conditions. Noting that because $\boldsymbol{a}$ is purely deviatoric $a_{11} + 2a_{33} = 0$, this leads in triaxial condition to $a = \sqrt{3/2}a_{11}$. In coherence with the triaxial formulation, Eq. 195 leads to the following asymptotic values of a_{ij} in Voigt notation in the triaxial case:

$$a_{ij} = \left[\pm\sqrt{\frac{2}{3}}, \mp\sqrt{\frac{1}{6}}, \mp\sqrt{\frac{1}{6}}, 0,0,0\right]$$

The constraint equation is modified from Houlsby (1992) with the addition of a factor $\sqrt{2/3}$ and the adaptation to the integrable anisotropy law, in order to be coherent with the triaxial case:

$$C_{a_{ij}} = \dot{a}_{\mathrm{ij}} - \sqrt{\frac{2}{3}}A\left(1 - \sqrt{2J_{2\mathrm{a}}}\right)\dot{\alpha}'_{ij} \qquad \textit{Eq. 196}$$

Indeed, if Eq. 196 was written:

$$C_a = \dot{a}_{\mathrm{ij}} - A_{3d}\left(1 - \sqrt{2J_{2\mathrm{a}}}\right)\dot{\alpha}'_{ij} = 0 \qquad \textit{Eq. 197}$$

It would give the following increment of triaxial a in the triaxial case:

$$da = \sqrt{\frac{2}{3}}(da_{11} - da_{33}) = \sqrt{\frac{2}{3}}A_{3d}\left(1 - \sqrt{\frac{2}{3}}|a_{11} - a_{33}|\right)(d\alpha'_{11} - d\alpha'_{33}) \qquad \textit{Eq. 198}$$

Which gives, noting that $\alpha'_{11} = \frac{2}{3}\alpha_{11} - \frac{2}{3}\alpha_{33} = \alpha_q$ and $\alpha'_{33} = -\frac{\alpha_q}{2}$:

$$da = \sqrt{\frac{2}{3}}A_{3d}(1 - |a|)\left(d\alpha_q + \frac{d\alpha_q}{2}\right) = \sqrt{\frac{3}{2}}A_{3d}(1 - |a|)d\alpha_q \qquad \textit{Eq. 199}$$

To retain coherence with the triaxial equation, $A_{3d} = \sqrt{\frac{2}{3}}A$, leading to Eq. 196.

In a similar way to the triaxial case, this constraint equation can be integrated into the yield surface expression. The resulting yield equation is:

$$y = 4I_{1\sigma}J_{2X} - 3tr(\sigma \mathrm{X}^2) - 8\mu^2 I_{3\sigma} = 0 \qquad \textit{Eq. 200}$$

Where $\mathrm{X} = \chi' + \sqrt{2/3}A\left(1 - \sqrt{2J_{2a}}\right)\chi'_a$ [Eq. 201] with χ'_a the deviator of the generalised stress associated to the internal variable a_{ij}.

3.3.4. Generalisation of dilation

In triaxial space, dilation was integrated through the following transformation of the yield function:

$$y = \chi_q^2 - 4\mu^2\left(p + \frac{2}{3}q\right)\left(p - \frac{q}{3}\right) \qquad \textit{Eq. 202}$$

$$\downarrow$$

$$y = \left(\chi_q - a\beta\chi_p\right)^2 - 4\mu^2\left(p + \frac{2}{3}q\right)\left(p - \frac{q}{3}\right) \qquad \textit{Eq. 203}$$

The generalised shear stress (χ_q) was replaced by $\chi_q - a\beta\chi_p$. In a similar manner, the deviatoric part of the generalised stress (χ'_{ij}) can be replaced by $\chi'_{ij} - \sqrt{2/3}a_{ij}\beta(\chi_{kk}/3)$. Here a is replaced by a_{ij}, while the $\sqrt{2/3}$ factor ensures consistency with the triaxial formulation. The volumetric generalised stress χ_p is replaced by its direct equivalent in 3D which is $tr(\chi)/3 = \chi_{kk}/3$.

The yield equation is still Eq. 200, but X_{ij} is now:

$$\mathrm{X_{ij}} = \chi'_{ij} - \sqrt{\frac{2}{3}}a_{ij}\beta\frac{\chi_{kk}}{3} + \sqrt{\frac{2}{3}}A\left(1 - \sqrt{2J_{2a}}\right)\chi'_a \qquad \textit{Eq. 204}$$

3.3.5. Generalisation of consolidation

In the triaxial case the integration of the contraction implied the following transformation:

$$y = \left(\chi_q + A(1-|a|)\chi_a - a\beta\chi_p\right)^2 - 4\mu^2\left(p + \frac{2}{3}q\right)\left(p - \frac{q}{3}\right) \quad \textit{Eq. 205}$$

$$\downarrow$$

$$y = \left(\chi_q + A(1-|a|)\chi_a - a\beta\chi_p\right)^2 - 4\mu^2\left(1 - \left(\frac{\chi_{pc}}{p_c}\right)^r\right)\left(p + \frac{2}{3}q\right)\left(p - \frac{q}{3}\right) \quad \textit{Eq. 206}$$

The consolidation can be generalised in the same manner in 3D leading to:

$$y = 4I_{1\sigma}J_{2\mathrm{X}} - 3tr(\sigma \mathrm{X}^2) - 8\mu^2\left(1 - \left(\frac{\chi_{pc}}{p_c}\right)^r\right)I_{3\sigma} = 0 \quad \textit{Eq. 207}$$

$$\mathrm{X_{ij}} = \chi'_{ij} - \sqrt{\frac{2}{3}}a_{ij}\beta\frac{\chi_{kk}}{3} + \sqrt{\frac{2}{3}}A\left(1 - \sqrt{2J_{2a}}\right)\chi'_a \quad \textit{Eq. 208}$$

The conjugate of the generalised consolidation pressure stress χ_{pc} is α_{pc}, and the associated stress is $\frac{tr(\sigma)}{3} = \frac{I_{1\sigma}}{3}$. This appears in the Gibbs energy function under the form:

$$g = -\frac{p_r}{k_r(1-n)(2-n)}\left(\frac{p_0}{p_r}\right)^{2-n} - \sigma_{ij}\alpha_{ij} - \frac{I_{1\sigma}}{3}\alpha_{pc} \quad \textit{Eq. 209}$$

Eq. 207 can be normalised, resulting in the normalised yield expression:

$$y = \frac{4I_{1\sigma}J_{2\mathrm{X}} - 3tr(\sigma \mathrm{X}^2)}{8\mu^2 I_{3\sigma}} + \left(\frac{\chi_{pc}}{p_c}\right)^r - 1 = 0 \quad \textit{Eq. 210}$$

3.3.6. Translation to multi-surface

Finally the model is transformed into a multi surface model, mapping the stress space by dividing the friction ratio (μ), using multiple consolidation pressures and hardening in the yield expression:

$$y = \frac{4I_{1\sigma}J_{2\mathrm{X}^{(n)}} - 3tr\left(\sigma \mathrm{X}^{(n)^2}\right)}{8\left(\frac{n}{N}\mu\right)^2 I_{3\sigma}} + \left(\frac{N\chi_{pc}^{(n)}}{p_c^{(n)}}\right)^r - 1 = 0 \quad \textit{Eq. 211}$$

$$\mathrm{X_{ij}^{(n)}} = N\chi_{ij}^{(n)'} - h_n\left(\alpha'_{ij}, \sigma\right) - \sqrt{\frac{2}{3}}a_{ij}\beta^{(n)}N\frac{\chi_{kk}^{(n)}}{3} + \sqrt{\frac{2}{3}}A\left(1 - \sqrt{2J_{2a}}\right)\chi'_a \quad \textit{Eq. 212}$$

The Gibbs energy function is also modified in consequence:

$$g = -\frac{p_r}{k_r(1-n)(2-n)}\left(\frac{p_0}{p_r}\right)^{2-n} - \frac{1}{N}\sigma_{ij}\sum_{n=1}^{N}\alpha_{ij}^{(n)} - \frac{1}{\mathrm{N}}\frac{I_{1\sigma}}{3}\sum_{n=1}^{N}\alpha_{pc}^{(n)} \quad \textit{Eq. 213}$$

The hardening function is also modified:

$$h_n\left(\alpha'^{(n)}_{ij}, \sigma\right) = 2H^{(n)}\,\alpha'^{(n)}_{ij}\frac{I_{1\sigma}}{3} = \frac{2}{3}H^{(n)}\alpha'^{(n)}_{ij}I_{1\sigma} \quad \textit{Eq. 214}$$

In Eq. 214, the factor three in front of the hardening modulus in Eq. 172 is replaced by a factor two, and the mean effective pressure is replaced by the average of the principal stresses.

3.3.7. Comparing 2D and 3D results

Figure 145 presents a drained test on medium dense sand with the triaxial and generalised base models. Triaxial tests conducted with the base generalised model perfectly match the results of the base triaxial model, proving the coherence of the recasting in 3D of the triaxial model.

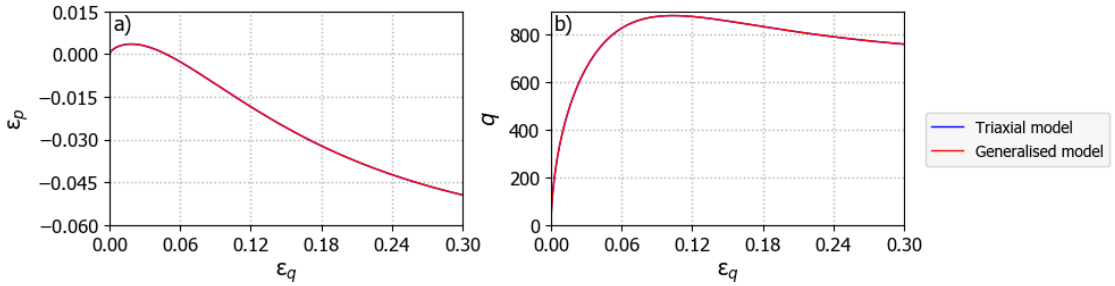


Figure 145 Comparison for a drained test on medium dense sand

Generalised base model defined by:

Gibbs energy function:

$$g = -\frac{p_r}{k_r(1-m)(2-m)}\left(\frac{p_0}{p_r}\right)^{2-m} - \frac{1}{N}\sigma_{ij}\sum_{n=1}^{N}\alpha_{ij}^{(n)} - \frac{1}{N}\frac{I_{1\sigma}}{3}\sum_{n=1}^{N}\alpha_{pc}^{(n)} \quad \text{Eq. 215}$$

$$\text{where: } p_0^2 = \frac{\sigma_{ii}\sigma_{jj}}{9} + \frac{k_r(1-m)}{2g_r}\sigma'_{ij}\sigma'_{ji} \text{ with } p_r = 100kPa \quad \text{Eq. 216}$$

Normalised yield functions:

$$y^{(n)} = \frac{4I_{1\sigma}J_{2X^{(n)}} - 3tr\left(\sigma X^{(n)^2}\right)}{8\left(\frac{n}{N}\mu\right)^2 I_{3\sigma}} + \left(\frac{N\chi_{pc}^{(n)}}{p_c^{(n)}}\right)^r - 1 \quad \text{Eq. 217}$$

Where:

$$X_{ij}^{(n)} = N\chi_{ij}^{(n)'} - h_n\left(\alpha_{ij}'^{(n)}, \sigma\right) - \sqrt{\frac{2}{3}}a_{ij}\beta^{(n)}\frac{N\chi_{kk}^{(n)}}{3} + \sqrt{\frac{2}{3}}A\left(1-\sqrt{2J_{2a}}\right)\chi'_a \quad \text{Eq. 218}$$

$$\text{where } h_n\left(\alpha_{ij}'^{(n)}, \sigma\right) = 2H^{(n)}\alpha_{ij}'^{(n)}\frac{I_{1\sigma}}{3} \quad \text{Eq. 219}$$

$$\text{for which } H^{(n)} = h\left(1-\frac{n}{N}\right)^b \quad \text{Eq. 220}$$

$$\text{in which } h = h_0\frac{\ln(v_\lambda)-\ln(\mathrm{B})}{\ln(\Delta)-\ln(\mathrm{B})} \quad \text{Eq. 221}$$

$$\text{and } \beta^{(n)} = \frac{n}{N}\beta_{max}\frac{\ln(v_\lambda)-\ln(\Gamma)}{\ln(\Delta)-\ln(\Gamma)} \quad \text{Eq. 222}$$

$$\text{and } A = A_{max}\frac{\ln(v_\lambda)-\ln(B)}{\ln(\Delta)-\ln(B)} \quad \text{Eq. 223}$$

$$\text{and } p_c^{(n)} = p_{c0}\left(1+\frac{(1-m)}{\lambda-1/k_r}\alpha_{p_c^{(n)}}\right)^{\frac{1}{1-m}} \quad \text{Eq. 224}$$

$$\text{With } \lambda = \lambda_B - (\lambda_B - \lambda_\Delta)\frac{\ln(v_\lambda)-\ln(\mathrm{B})}{\ln(\Delta)-\ln(\mathrm{B})} \quad \text{Eq. 225}$$

$$ln(v_\lambda) = \ln(\mathrm{B}) - \ln\left(\frac{\mathrm{B}}{\Delta}\right)\frac{(ln(v_0)-I_{1\epsilon}) + \frac{\lambda_B}{1-m}\left(\left(\frac{\frac{I_{1\sigma}}{3}}{p_r}\right)^{1-m}-1\right) - ln(\mathrm{B})}{ln(\Delta) + \frac{\lambda_B-\lambda_\Delta}{1-m}\left(\left(\frac{\frac{I_{1\sigma}}{3}}{p_r}\right)^{1-m}-1\right) - ln(\mathrm{B})} \quad \text{Eq. 226}$$

3.4. Numerical implementation

In the preceding paragraphs, all results from the model were calculated with the HyperDrive framework developed by Houlsby (2023). In running a model, three files are used:

- the data file, or a python script, indicates the model to use and its parameters, the type of test to run, and the size of increments.
- the model file contains the energy function and its derivatives, and the yield function and its derivatives.
- the incremental engine uses the derivatives contained in the model file to calculate the strain and stress increments of the test indicated by the data file or the python script.

The incremental engine allows calculation of stress and strain increments for different formulations (f or g with y), controls (stress, strain or general), and dimensions (one, two, and three [in Mandel notation]).

The example of general control for a Gibbs energy function with yield surfaces formulation ($g-y$ formulation) for a rate independent model is used to illustrate the calculation process.

For a given general control statement:

$$S_{ij}\delta\sigma_j + E_{ij}\delta\epsilon_j = T_i\delta t \qquad \textit{Eq. 227}$$

In the triaxial case, the control statement for a drained strain controlled triaxial test is:

$$\begin{bmatrix}3 & -1\\ 0 & 0\end{bmatrix}\begin{bmatrix}\delta p\\ \delta q\end{bmatrix} + \begin{bmatrix}0 & 0\\ 0 & 1\end{bmatrix}\begin{bmatrix}\delta\epsilon_p\\ \delta\epsilon_q\end{bmatrix} = \begin{bmatrix}0\\ 1\end{bmatrix}\delta t \qquad \textit{Eq. 228}$$

While for an undrained strain controlled test, it is:

$$\begin{bmatrix}0 & 0\\ 0 & 0\end{bmatrix}\begin{bmatrix}\delta p\\ \delta q\end{bmatrix} + \begin{bmatrix}1 & 0\\ 0 & 1\end{bmatrix}\begin{bmatrix}\delta\epsilon_p\\ \delta\epsilon_q\end{bmatrix} = \begin{bmatrix}0\\ 1\end{bmatrix}\delta t \qquad \textit{Eq. 229}$$

Using $\epsilon{=}-\partial g/\partial\sigma$, the control statement can be written:

$$S_{ij}\delta\sigma_j + E_{ij}\left(-\frac{\partial^2 g}{\partial\sigma_j\partial\sigma_k}\delta\sigma_k - \frac{\partial^2 g}{\partial\sigma_j\partial\alpha_k^{(m)}}\delta\alpha_k^{(m)}\right) = T_i\delta t \qquad \textit{Eq. 230}$$

Which can be arranged to:

$$\left(S_{ik} - E_{ij}\frac{\partial^2 g}{\partial\sigma_j\partial\sigma_k}\right)\delta\sigma_k = T_i\delta t + E_{ij}\frac{\partial^2 g}{\partial\sigma_j\partial\alpha_k^{(m)}}\delta\alpha_k^{(m)} \qquad \textit{Eq. 231}$$

Noting $Q_{ik} = \left(S_{ik} - E_{ij}\frac{\partial^2 g}{\partial\sigma_j\partial\sigma_k}\right)^{-1}$ [Eq. 232], the stress increment is equal to:

$$\delta\sigma_l = Q_{li}\left(T_i\delta t + E_{ij}\frac{\partial^2 g}{\partial\sigma_j\partial\alpha_k^{(m)}}\delta\alpha_k^{(m)}\right) \qquad \textit{Eq. 233}$$

The plastic calculation process for one yield surface is activated if the yield value for this surface is superior to a "small" negative value (-10^{-5} is used in HyperDrive). The consistency condition used in HyperDrive is not exact, but uses an equality to a small negative term $-a_c y_0^{(p)}$ where $a_c \in]0,1[$ is an acceleration parameter, and $y_0^{(p)}$ is the current value of the yield function. Thus, the yield value will exponentially decrease to 0 over the next increments if the current value of the yield function is positive (because of an overshoot). This technique avoids the calculation of the step size to perfectly land on the yield surface, and gives good results.

The consistency condition for surface p is:

$$\delta y^{(p)} = -a_c y_0^{(p)} = \frac{\partial y^{(p)}}{\partial \epsilon_i}\delta\epsilon_i + \frac{\partial y^{(p)}}{\partial \sigma_i}\delta\sigma_i + \frac{\partial y^{(p)}}{\partial \alpha_i^{(m)}}\delta\alpha_i^{(m)} + \frac{\partial y^{(p)}}{\partial \chi_i^{(m)}}\delta\chi_i^{(m)} \qquad \textit{Eq. 234}$$

Noting that $\chi_i^{(m)} = -\partial g/\partial \alpha_i^{(m)}$ [Eq. 235], the consistency condition can be written in term of stress and internal variable increments, leading to Eq. 240, which can be rewritten in Eq. 241, and noting that the stress increment can then be replaced with the control statement variables (Eq. 233) it leads to Eq. 242. Eq. 242 can be rewritten as Eq. 243.

Noting that the flow rule in hyperplasticity is:

$$\delta\alpha_i^{(m)} = \mathrm{L}^{(q)}\frac{\partial y^{(q)}}{\partial \chi_i^{(m)}} \qquad \textit{Eq. 236}$$

Injecting Eq. 243 into Eq. 236, the plastic multipliers can be found by solving Eq. 244.

Once the plastic multipliers are solved, all increments are calculated:

$$\delta\alpha_i^{(m)} = \mathrm{L}^{(p)}\frac{\partial y^{(p)}}{\partial \chi_i^{(m)}} \qquad \textit{Eq. 237}$$

$$\delta\sigma_l = Q_{li}\left(T_i\delta t + E_{ij}\frac{\partial^2 g}{\partial\sigma_j\partial\alpha_k^{(n)}}\delta\alpha_k^{(n)}\right) \qquad \textit{Eq. 238}$$

$$\delta\epsilon_j = -\frac{\partial^2 g}{\partial\sigma_j\partial\sigma_k}\delta\sigma_k - \frac{\partial^2 g}{\partial\sigma_j\partial\alpha_k^{(n)}}\delta\alpha_k^{(n)} \qquad \textit{Eq. 239}$$

This explicit numerical scheme does not vary with the model or the test, so that the user needs to input only the model and data files.

The hyperplastic engine (HyperDrive) along with example files, and a documentation, can be downloaded from Houlsby (2023).

$$\delta y^{(p)} = -a_c y_0^{(p)} = \frac{\partial y^{(p)}}{\partial \epsilon_i}\left(-\frac{\partial^2 g}{\partial \sigma_i \partial \sigma_j}\delta\sigma_j - \frac{\partial^2 g}{\partial \sigma_i \partial \alpha_j^{(n)}}\delta\alpha_j^{(n)}\right) + \frac{\partial y^{(p)}}{\partial \sigma_i}\delta\sigma_i + \frac{\partial y^{(p)}}{\partial \alpha_i^{(m)}}\delta\alpha_i^{(m)} + \frac{\partial y^{(p)}}{\partial \chi_i^{(m)}}\left(-\frac{\partial^2 g}{\partial \alpha_i^{(m)} \partial \sigma_j}\delta\sigma_j - \frac{\partial^2 g}{\partial \alpha_i^{(m)} \partial \alpha_j^{(n)}}\delta\alpha_j^{(n)}\right) \quad \textit{Eq. 240}$$

$$-a_c y_0^{(p)} = \left(-\frac{\partial y^{(p)}}{\partial \epsilon_i}\frac{\partial^2 g}{\partial \sigma_i \partial \sigma_j} + \frac{\partial y^{(p)}}{\partial \sigma_j} - \frac{\partial^2 g}{\partial \alpha_i^{(m)} \partial \sigma_j}\frac{\partial y^{(p)}}{\partial \chi_i^{(m)}}\right)\delta\sigma_j + \left(-\frac{\partial y^{(p)}}{\partial \epsilon_i}\frac{\partial^2 g}{\partial \sigma_i \partial \alpha_j^{(n)}} + \frac{\partial y^{(p)}}{\partial \alpha_j^{(n)}} - \frac{\partial^2 g}{\partial \alpha_i^{(m)} \partial \alpha_j^{(n)}}\frac{\partial y^{(p)}}{\partial \chi_i^{(m)}}\right)\delta\alpha_j^{(n)} \quad \textit{Eq. 241}$$

$$-a_c y_0^{(p)} = \left(-\frac{\partial y^{(p)}}{\partial \epsilon_i}\frac{\partial^2 g}{\partial \sigma_i \partial \sigma_j} + \frac{\partial y^{(p)}}{\partial \sigma_j} - \frac{\partial^2 g}{\partial \alpha_i^{(m)} \partial \sigma_j}\frac{\partial y^{(p)}}{\partial \chi_i^{(m)}}\right)Q_{jr}\left(T_r\delta t + E_{rl}\frac{\partial^2 g}{\partial \sigma_l \partial \alpha_k^{(m)}}\delta\alpha_k^{(m)}\right) + \left(-\frac{\partial y^{(p)}}{\partial \epsilon_i}\frac{\partial^2 g}{\partial \sigma_i \partial \alpha_j^{(n)}} + \frac{\partial y^{(p)}}{\partial \alpha_j^{(n)}} - \frac{\partial^2 g}{\partial \alpha_i^{(m)} \partial \alpha_j^{(n)}}\frac{\partial y^{(p)}}{\partial \chi_i^{(m)}}\right)\delta\alpha_j^{(n)} \quad \textit{Eq. 242}$$

$$-a_c y_0^{(p)} = \left(-\frac{\partial y^{(p)}}{\partial \epsilon_i}\frac{\partial^2 g}{\partial \sigma_i \partial \sigma_j} + \frac{\partial y^{(p)}}{\partial \sigma_j} - \frac{\partial^2 g}{\partial \alpha_i^{(m)} \partial \sigma_j}\frac{\partial y^{(p)}}{\partial \chi_i^{(m)}}\right)Q_{jr}T_r\delta t + \left(-\frac{\partial y^{(p)}}{\partial \epsilon_i}\frac{\partial^2 g}{\partial \sigma_i \partial \alpha_k^{(n)}} + \frac{\partial y^{(p)}}{\partial \alpha_k^{(n)}} - \frac{\partial^2 g}{\partial \alpha_i^{(m)} \partial \alpha_k^{(n)}}\frac{\partial y^{(p)}}{\partial \chi_i^{(m)}} + \left(-\frac{\partial y^{(p)}}{\partial \epsilon_i}\frac{\partial^2 g}{\partial \sigma_i \partial \sigma_j} + \frac{\partial y^{(p)}}{\partial \sigma_j} - \frac{\partial^2 g}{\partial \alpha_i^{(m)} \partial \sigma_j}\frac{\partial y^{(p)}}{\partial \chi_i^{(m)}}\right)Q_{jr}E_{rl}\frac{\partial^2 g}{\partial \sigma_l \partial \alpha_k^{(n)}}\right)\delta\alpha_k^{(n)} \quad \textit{Eq. 243}$$

$$\left(\frac{\partial y^{(p)}}{\partial \epsilon_i}\frac{\partial^2 g}{\partial \sigma_i \partial \alpha_k^{(n)}} - \frac{\partial y^{(p)}}{\partial \alpha_k^{(n)}} + \frac{\partial^2 g}{\partial \alpha_i^{(m)} \partial \alpha_k^{(n)}}\frac{\partial y^{(p)}}{\partial \chi_i^{(m)}} + \left(\frac{\partial y^{(p)}}{\partial \epsilon_i}\frac{\partial^2 g}{\partial \sigma_i \partial \sigma_j} - \frac{\partial y^{(p)}}{\partial \sigma_j} + \frac{\partial^2 g}{\partial \alpha_i^{(m)} \partial \sigma_j}\frac{\partial y^{(p)}}{\partial \chi_i^{(m)}}\right)Q_{jr}E_{rl}\frac{\partial^2 g}{\partial \sigma_l \partial \alpha_k^{(n)}}\right)\mathrm{L}^{(q)}\frac{\partial y^{(q)}}{\partial \chi_k^{(n)}} = a_c y_0^{(p)} + \left(-\frac{\partial y^{(p)}}{\partial \epsilon_i}\frac{\partial^2 g}{\partial \sigma_i \partial \sigma_j} + \frac{\partial y^{(p)}}{\partial \sigma_j} - \frac{\partial^2 g}{\partial \alpha_i^{(m)} \partial \sigma_j}\frac{\partial y^{(p)}}{\partial \chi_i^{(m)}}\right)Q_{jr}T_r\delta t \quad \textit{Eq. 244}$$

Chapter 4 Calibration process for the base model

HySand_base is presented in Chapter 3. Its construction has been explained, and the trade-off between simplicity of formulation and quality of prediction demonstrated.

HySand_base can produce good quality results, as Chapter 5 later shows, provided that its 14 parameters are well chosen for the sand for which behaviour is to be predicted. In order to ensure the model can withstand future use, a rigorous and systematic calibration process is described in the following. In a first part, the influence of the variation of parameters is displayed. A final table summarises the effects of the variation of each parameter. In a second part, the calibration process is explained. In a third part, an optimisation process is described. The optimisation process can replace the most tedious part of the calibration process.

All tests in this chapter are conducted with $N = 10$ surfaces.

4.1. Sensitivity study: Impact of the variation of parameters

In this section, monotonic drained and undrained tests are performed for each parameter presented in Table 7. These results are represented with green curves in the following figures.

k_r	g_r	m	φ_c	β_{max}	B	Γ	Δ	λ_B	λ_Δ	A_{max}	h_0	b	r
490	417	0.72	33.9	0.98	2.054	1.97	1.677	0.0057	0.0026	46	987	3.4	0.28

Table 7 Standard parameters for the sensitivity study

The tests are also conducted with variations of each parameter to highlight their respective roles.

In monotonic drained results (simulation of TMD13), the following are monitored: end of test capacity, peak capacity, shear strain at peak capacity, secant stiffness (at 1% shear strain), and maximum dilation ratio. In monotonic undrained results (simulation of TMU2), the following are monitored: pore-pressure build-up, stress ratio asymptote, shear stress-strain asymptote.

Cyclic stress-controlled tests (simulation of TCUI12 and 13) are also run to monitor the effects of the varying parameters on: the rate at which pore pressure builds-up, the secant stiffness, the mean effective pressure at which large pore pressure build-up leads to liquefaction.

The characteristic specific volumes (B, Γ, and Δ) are not varied. Their variation would mean a change in the relative density, and thus a previously studied change in β_{max}, A_{max}, and λ.

Note that k_r and g_r were varied individually for the sake of the study, without guaranteeing reasonable values of Poisson's ratio.

4.1.1. Effects of the variation of parameters on monotonic tests

The magnitude of variation of each parameter was selected to cover a sensible range.

4.1.1.1. Dimensionless bulk modulus: k_r

The variation of the dimensionless bulk modulus does not affect much the drained test, Figure 146, but influences the pore-pressure build-up in the undrained test, Figure 147. Indeed, a higher k_r means that the plastic volumetric strain is converted into a higher amount of pore pressure.

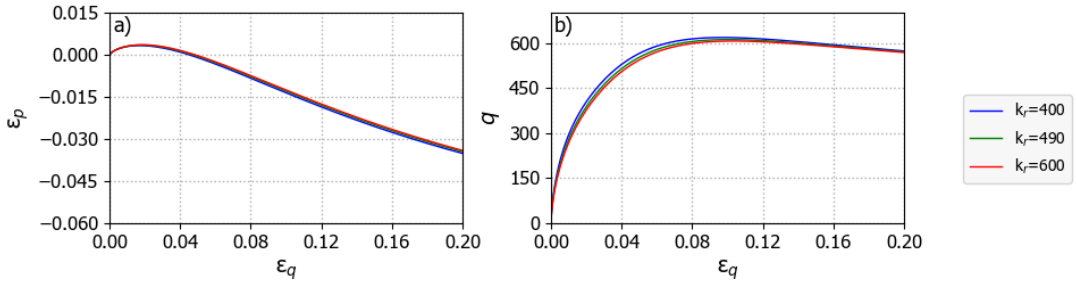


Figure 146 Drained monotonic test with variation of the dimensionless bulk modulus

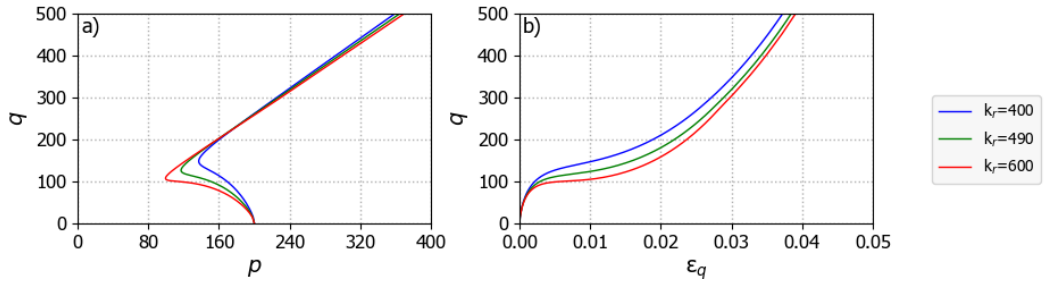


Figure 147 Undrained monotonic test with variation of the dimensionless bulk modulus

4.1.1.2. Dimensionless shear modulus: g_r

The variation of the dimensionless shear modulus has little impact on the monotonic tests in Figure 148 and Figure 149, because the simulations are plastic except at very small strain.

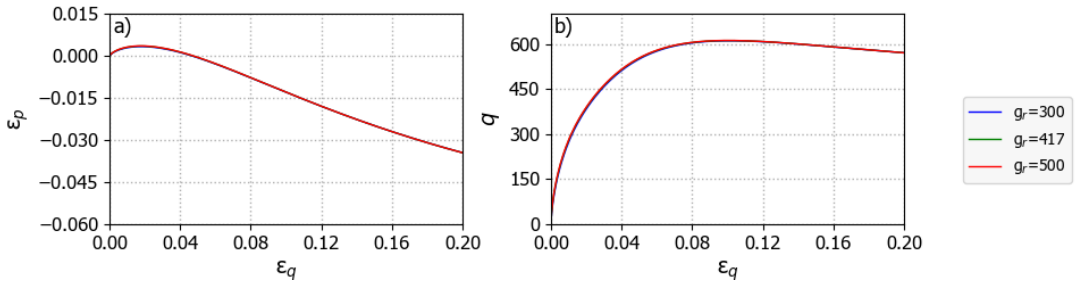


Figure 148 Drained monotonic test with variation of the dimensionless shear modulus

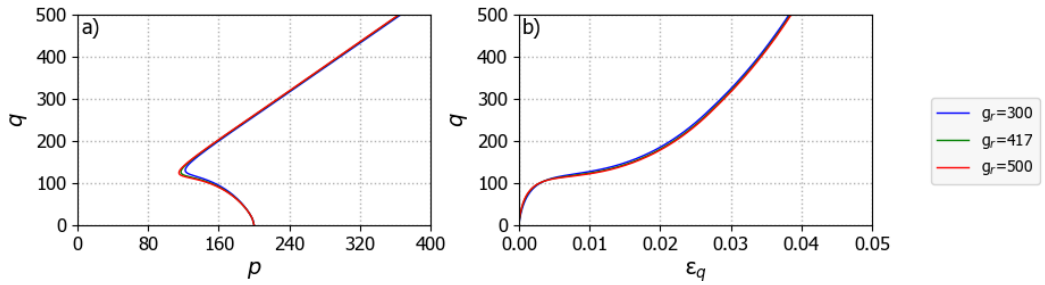


Figure 149 Undrained monotonic test with variation of the dimensionless shear modulus

4.1.1.3. Non-linear elasticity pressure exponent: m

The non-linear elasticity pressure exponent is varied, but initial bulk (K) and shear (G) moduli for the tests are kept constant by changing k_r and g_r.

The variation of m implies a significant change in the drained behaviour, Figure 150, with an increased capacity and a faster dilation development for an increased m.

In the undrained test, Figure 151, the increase leads to a steeper shear stress-strain asymptote.

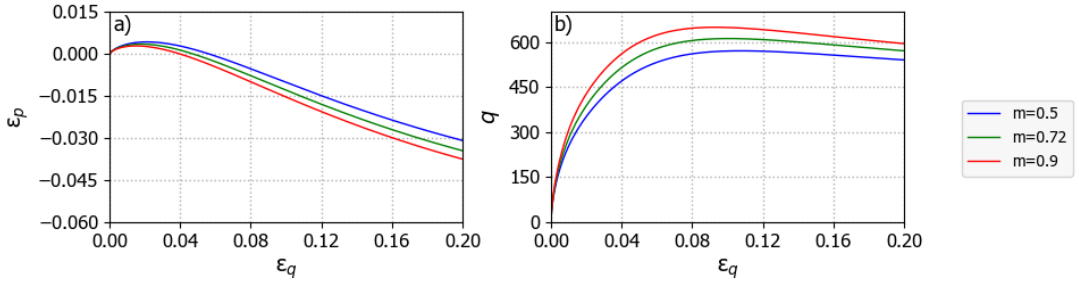


Figure 150 Drained monotonic test with variation of the non-linear elasticity power exponent

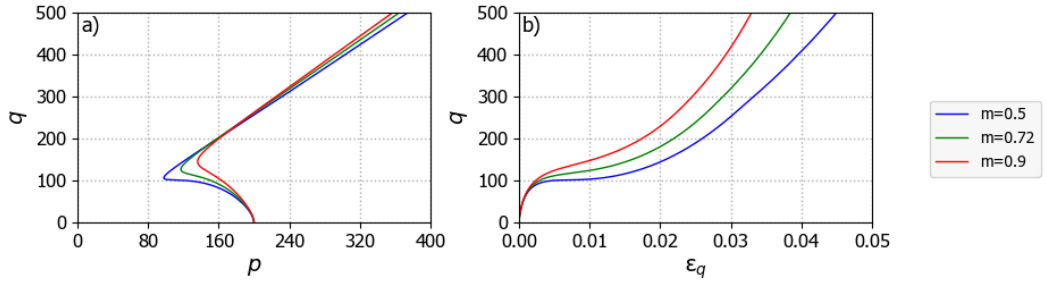


Figure 151 Undrained monotonic test with variation of the non-linear elasticity power exponent

4.1.1.4. Critical state friction angle: φ_c

As expected, increasing the critical state friction angle increases the friction ratio and capacity in the drained test, Figure 152, and the asymptotic stress ratio in the undrained test, Figure 153.

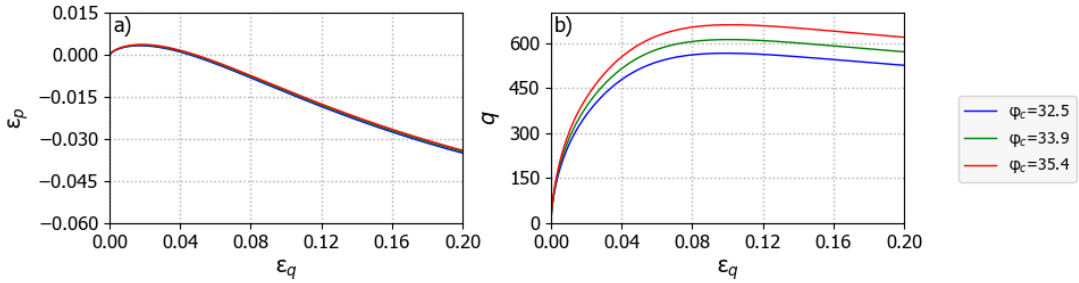


Figure 152 Drained monotonic test with variation of the critical state friction angle

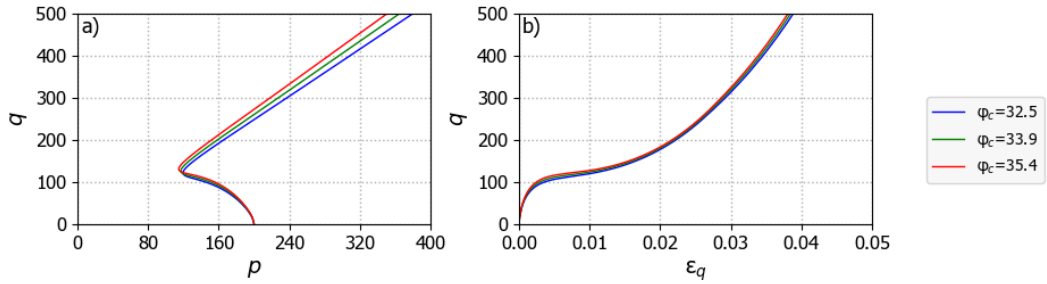


Figure 153 Undrained monotonic test with variation of the critical state friction angle

4.1.1.5. Maximum dilation ratio: β_{max}

Increased maximum dilation ratio leads to larger dilation and higher peak capacity in the drained test, Figure 154, and steeper shear stress-strain asymptote in the undrained test, Figure 155.

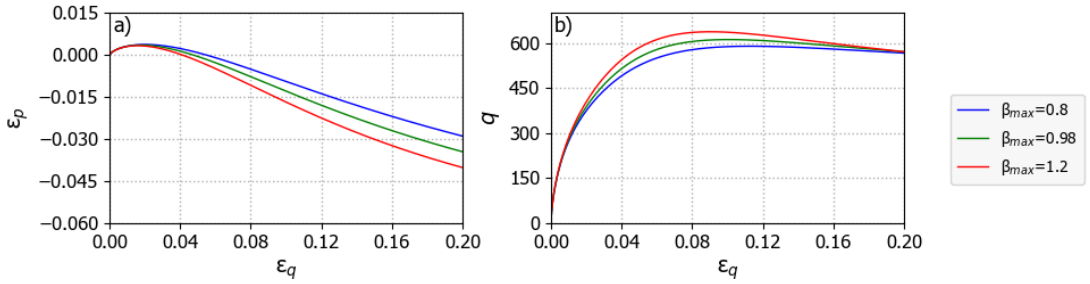


Figure 154 Drained monotonic test with variation of the maximum dilation ratio

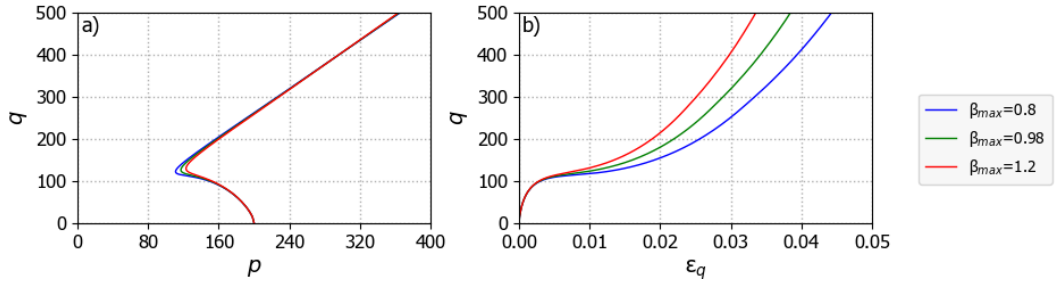


Figure 155 Undrained monotonic test with variation of the maximum dilation ratio

4.1.1.6. Normal consolidation line slopes: λ_Δ and λ_B

The consolidation slopes of the densest and loosest states were proportionally varied to obtain the same proportional variation in the normal consolidation slope of the test. In the drained test, Figure 156, the capacity and the initial contractive phase increase with a higher λ. In the undrained test, Figure 157, the pore pressure build-up increases with a higher λ, while the shear stress-strain asymptote decreases.

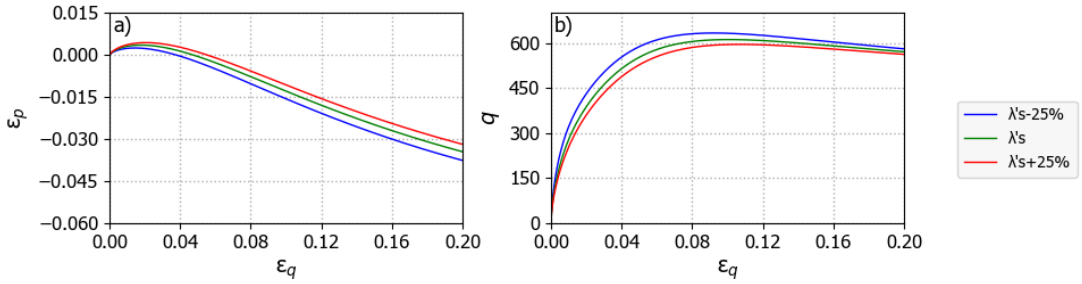


Figure 156 Drained monotonic test with variation of the consolidation slopes

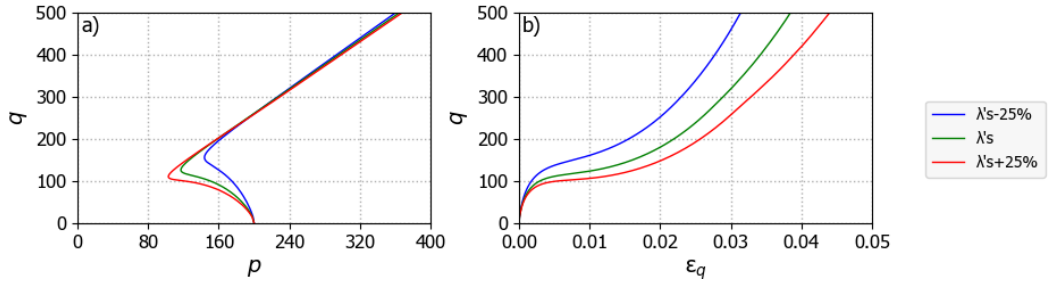


Figure 157 Undrained monotonic test with variation of the consolidation slopes

4.1.1.7. Anisotropy rate development parameter: A_{max}

Increasing the anisotropy rate development parameter leads to a faster development of dilation in the drained test, Figure 158. In the undrained test, Figure 159, it leads to slightly lower pore pressure build-up and a quicker development of the shear stress-strain asymptote.

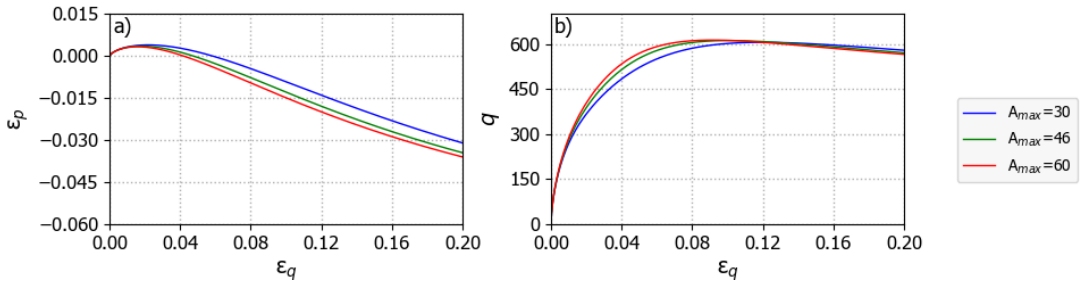


Figure 158 Drained monotonic test with variation of the maximum rate development parameter

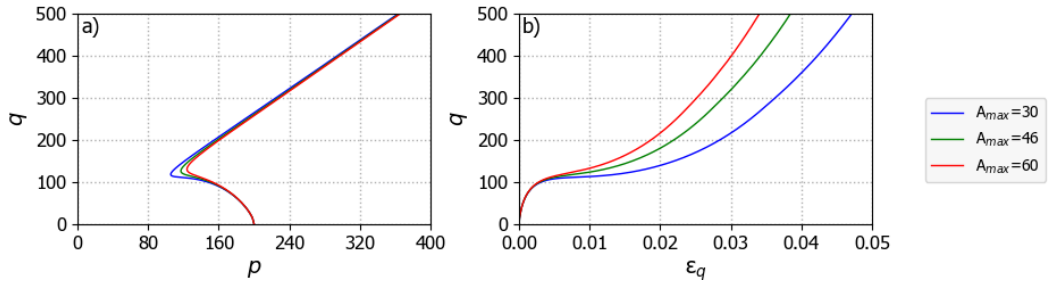


Figure 159 Undrained monotonic test with variation of the maximum rate development parameter

4.1.1.8. Consolidation power exponent: r

The increase of the consolidation power exponent implies an increase of capacity in a drained test, Figure 160, because the yield surface is wider at higher pressures. Similarly, the capacity and the stress ratio asymptote increase with a higher r in the undrained test, Figure 161.

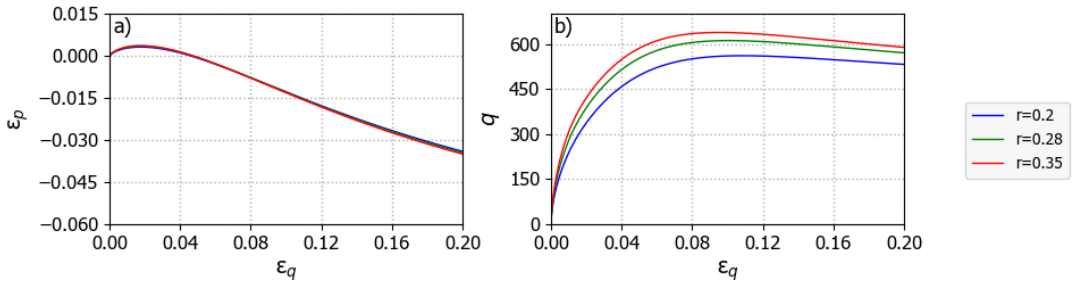


Figure 160 Drained monotonic test with variation of the consolidation exponent

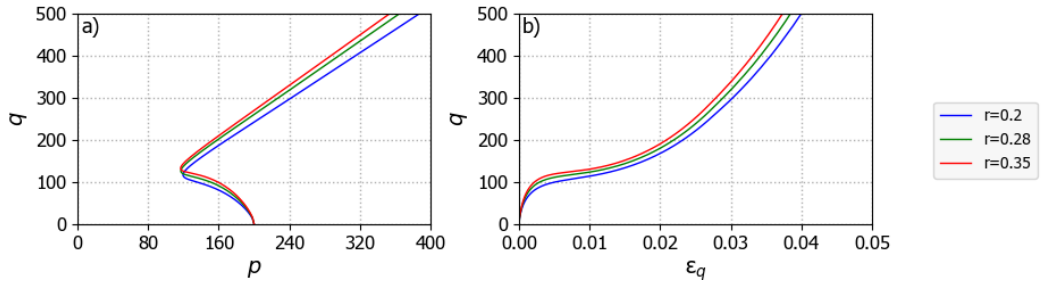


Figure 161 Undrained monotonic test with variation of the consolidation exponent

4.1.1.9. Hardening factor: h_0

The variation of the hardening factor has little impact on the monotonic tests. Monotonic behaviour is mainly controlled by the outter yield surfaces.

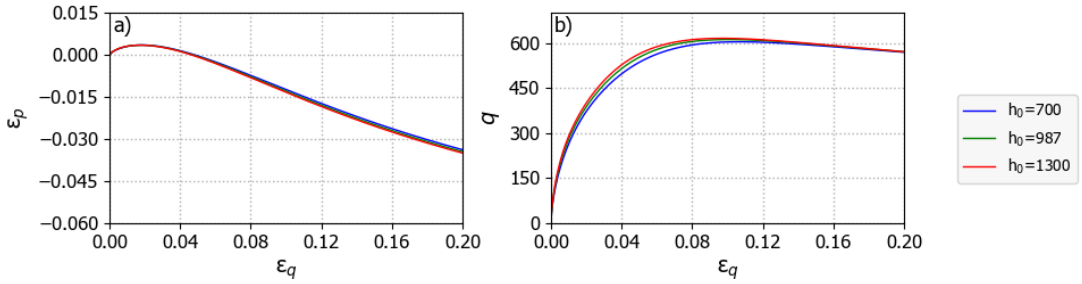


Figure 162 Drained monotonic test with variation of the shear hardening base modulus

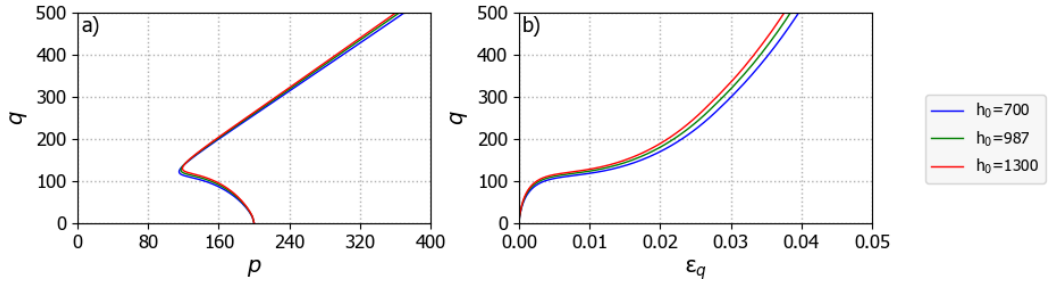


Figure 163 Undrained monotonic test with variation of the shear hardening base modulus

4.1.1.10. Hardening exponent: b

The increase of the hardening exponent leads to a decrease of capacity in both the drained and undrained tests, Figure 164 and Figure 165. This is due to the slower evolution of the yield surfaces close to the outer surface. Note that while varying h_0 by 30%, as in last paragraph, makes $H^{(n)}$'s vary by 30%, varying b by ~15% implies a much larger variation of the hardening moduli of the most outter yield surfaces.

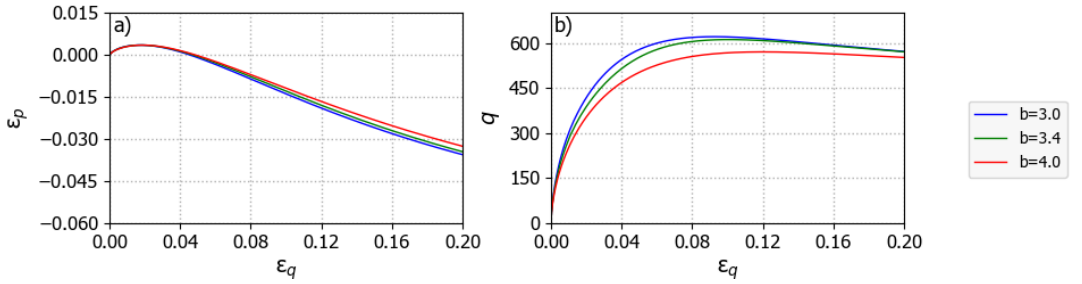


Figure 164 Drained monotonic test with variation of the shear hardening exponent

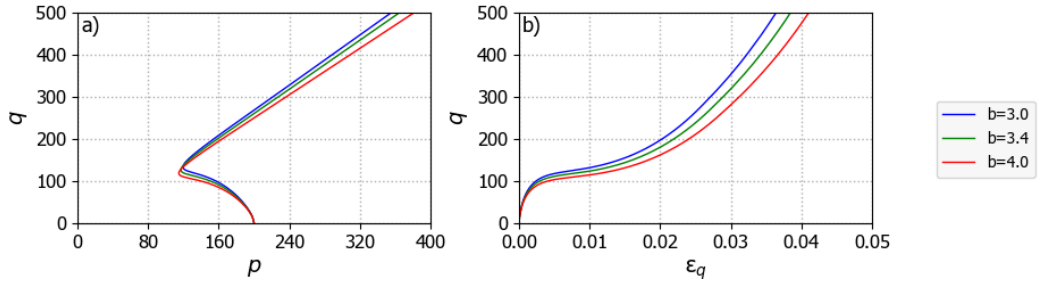


Figure 165 Undrained monotonic test with variation of the shear hardening exponent

4.1.2. Effects of the variation of parameters on cyclic undrained tests

For cyclic stress-controlled undrained tests, the focus is on the number of cycles to liquefaction, the secant stiffness, as well as the ratio of the number of cycles to liquefaction between two tests with different amplitudes (TCUI13 and TCUI12 of Wichtmann data, Figure 166 and Figure 167).

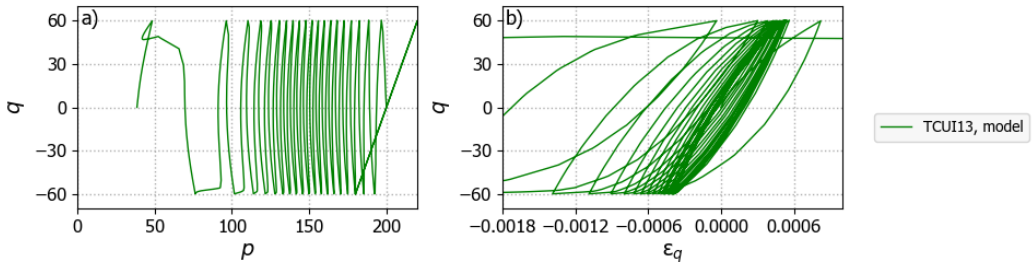


Figure 166 Simulated TCUI13 with standard parameters

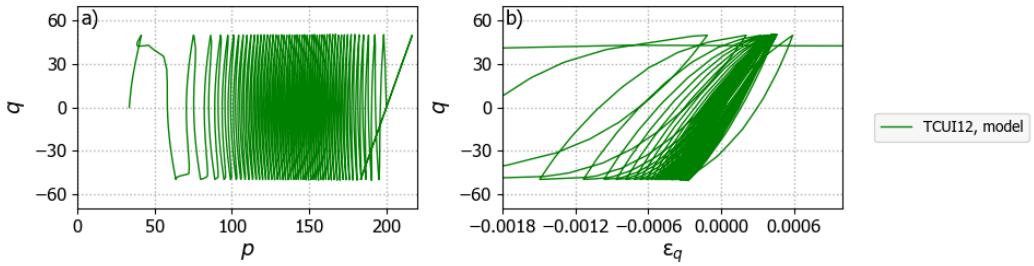


Figure 167 Simulated TCUI12 with standard parameters

The number of cycles to liquefaction for the larger amplitude is $N_{liq} = 19$, and for the lower amplitude $N_{liq} = 51$, leading to a ratio of 2.7. Note that the criterion used to stop the test is that $p < p_0/4$ at $q = 0$ during a cycle. This criterion was chosen to avoid the slower calculation of the cycle during which HySand_base reaches liquefaction or locks in stress space.

By zooming in on a few cycles (Figure 168, Figure 169), secant stiffness and damping can be observed better.

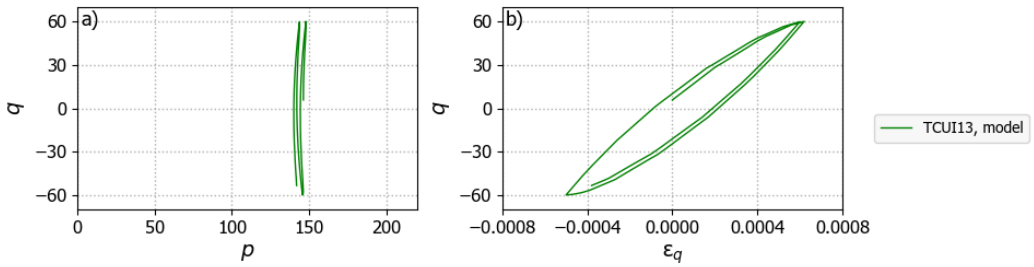


Figure 168 Isolation of a few cycles in the simulated TCUI13

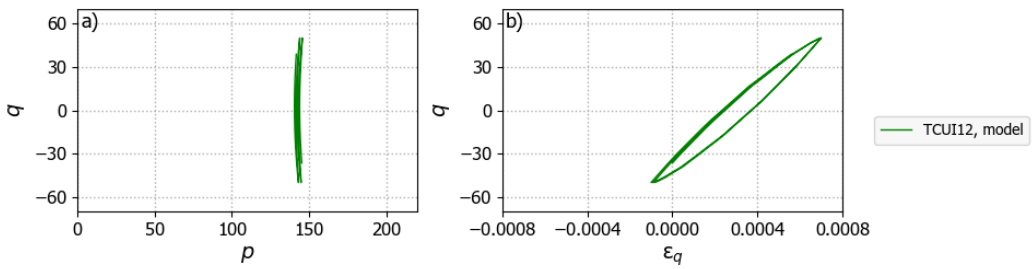


Figure 169 Isolation of a few cycles in the simulated TCUI12

4.1.2.1. Dimensionless bulk modulus: k_r

With $k_r = 600$ instead of $k_r = 490$, Figure 170 to Figure 172 are obtained.

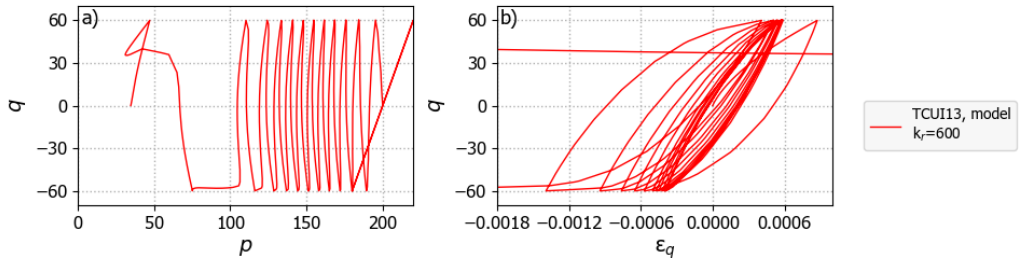


Figure 170 Simulated TCUI13

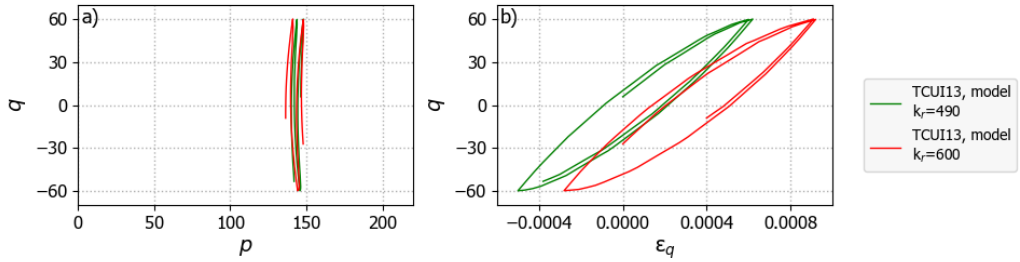


Figure 171 Isolation on a few cycles of TCUI13 with variable k_r

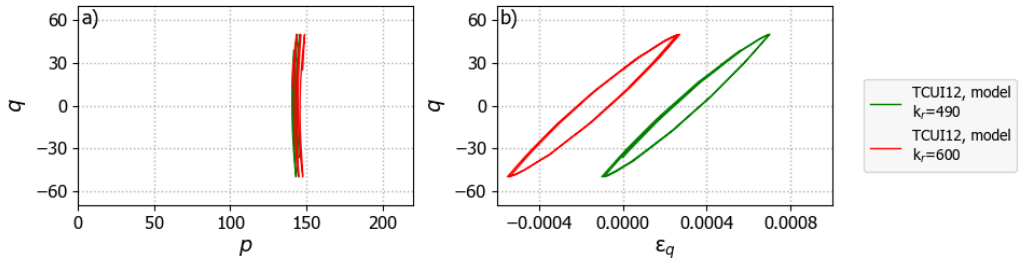


Figure 172 Isolation on a few cycles of TCUI12 with variable k_r

The number of cycles to liquefaction decreases to 11 for the larger amplitude, and 30 for the lower amplitude. Indeed, an increased bulk modulus leads to a stronger pore pressure build-up because the volumetric plastic strain is multiplied by the bulk modulus to obtain this pore pressure build-up. Secant stiffness and the N_{liq} ratio (2.7) do not change significantly.

4.1.2.2. Dimensionless shear modulus: g_r

With $g_r = 500$ instead of $g_r = 417$, Figure 173 to Figure 175 are obtained.

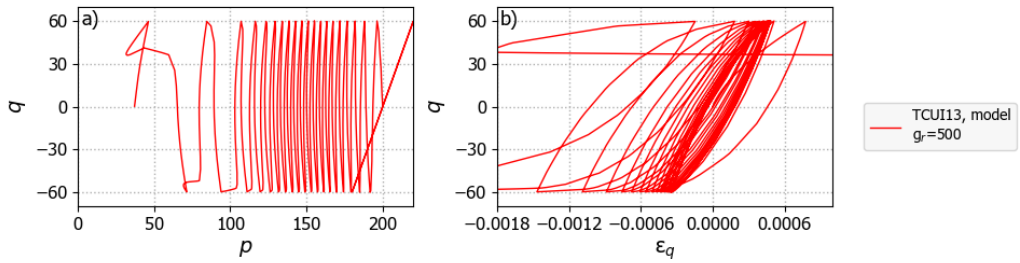


Figure 173 Simulated TCUI13

The variation of g_r has no impact on the number of cycles to liquefaction: $N_{liq} = 19$ for the larger amplitude, and $N_{liq} = 51$ for the lower amplitude, giving a ratio of 2.7.

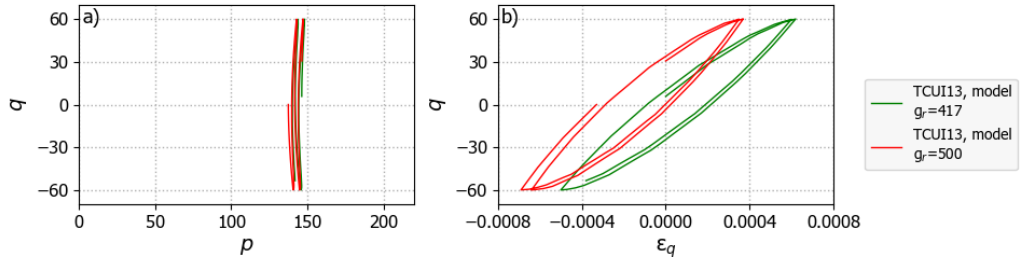


Figure 174 Isolation on a few cycles of TCUI13 with variable g_r

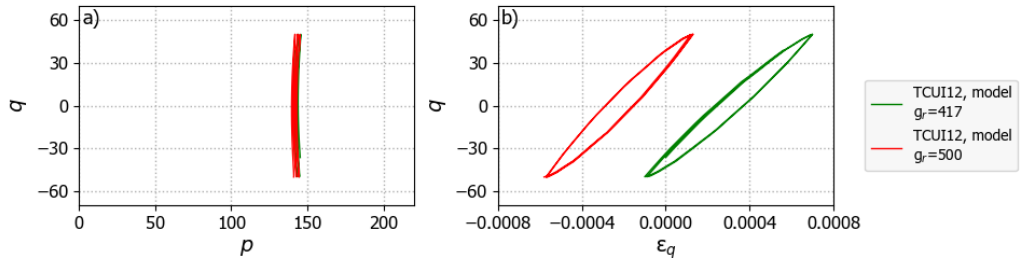


Figure 175 Isolation on a few cycles of TCUI12 with variable g_r

Naturally, the increase in the dimensionless shear modulus leads to an increase of secant stiffness.

4.1.2.3. Non-linear elasticity pressure exponent: m

With $m = 0.9$, but keeping constant initial K and G, thus updating to $k_r = 433$ and $g_r = 368$, Figure 176 to Figure 178 are obtained.

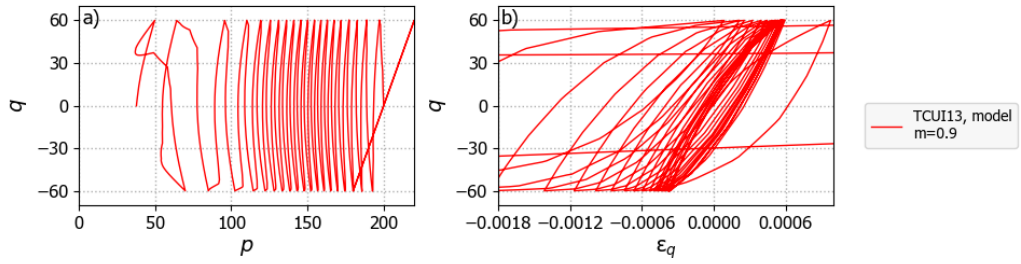


Figure 176 Simulated TCUI13

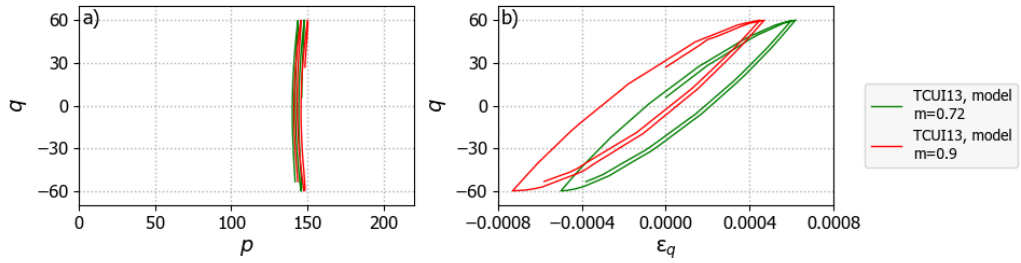


Figure 177 Isolation on a few cycles of TCUI13 with variable m

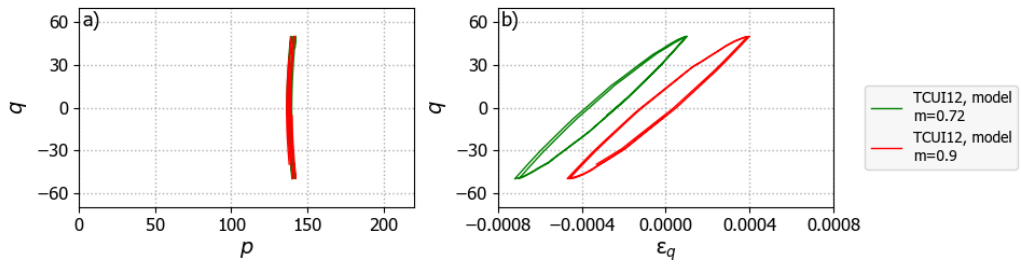


Figure 178 Isolation on a few cycles of TCUI12 with variable m

The increase in the non-linear elastic exponent m, while maintaining equivalent initial bulk and shear moduli, has little impact on the number of cycles necessary to reach liquefaction: for the larger amplitude $N_{liq} = 19$, and for the lower amplitude $N_{liq} = 50$, leading to a ratio of 2.6.

A larger m implies a greater reduction of K with pressure, thus leading to less pore pressure build-up at lower pressure, as can be observed in Figure 176. Similarly, despite an identical initial G, the shear modulus at lower mean effective stress is lower, leading to lower secant stiffnesses.

4.1.2.4. Critical state friction angle: φ_c

Testing for $\varphi_c = 35.4$ instead of $\varphi_c = 33.9$ is shown in Figure 179 to Figure 181.

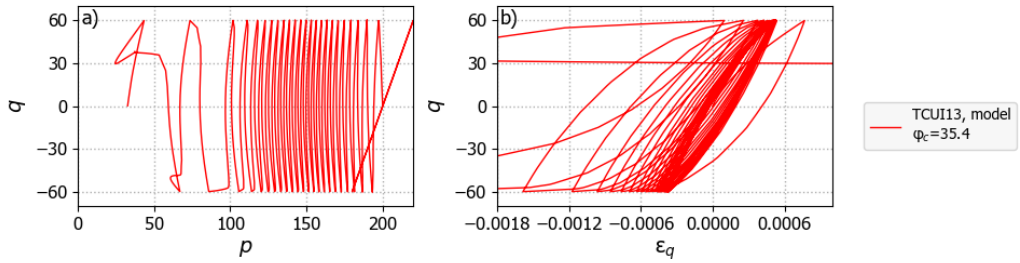


Figure 179 Simulated TCUI13

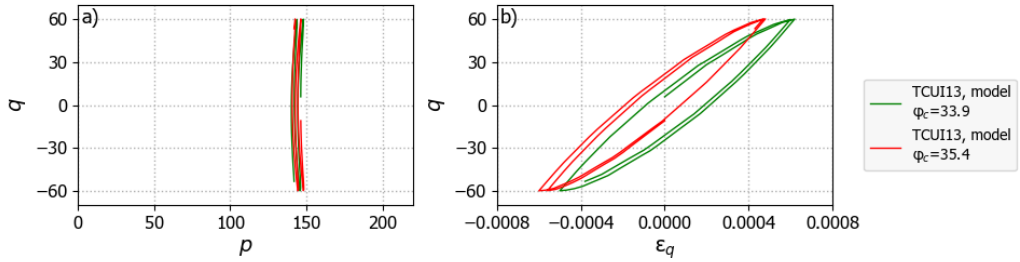


Figure 180 Isolation on a few cycles of TCUI13 with variable φ_c

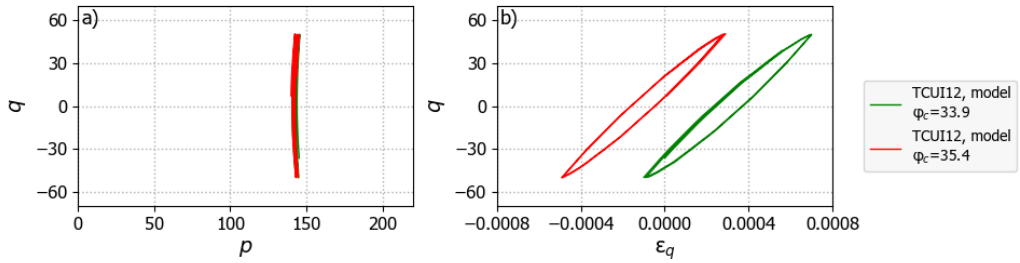


Figure 181 Isolation on a few cycles of TCUI12 with variable φ_c

A larger critical friction angle leads to wider yield surfaces, hence less plastic strain, hence less pore pressure build-up, hence more cycles before liquefaction: for the larger amplitude $N_{liq} = 23$, and for the lower amplitude $N_{liq} = 59$, leading to a ratio of 2.6. However, this is mainly observed at low mean effective stresses, because near $p = p_c$ the shape of the yield surfaces is more influenced by the consolidation exponent r than by the critical friction angle. This explains the only slightly stiffer responses in Figure 180 and Figure 181 for cycles at high mean effective stresses.

4.1.2.5. Maximum dilation ratio: β_{max}

With $\beta_{max} = 1.2$ instead of $\beta_{max} = 0.98$, Figure 182 to Figure 184 are obtained.

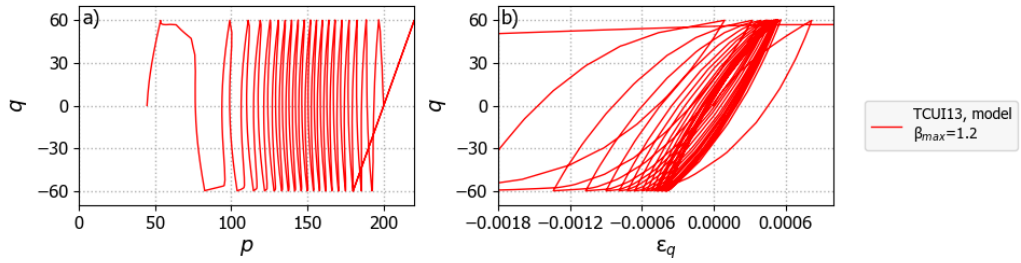


Figure 182 Simulated TCUI13

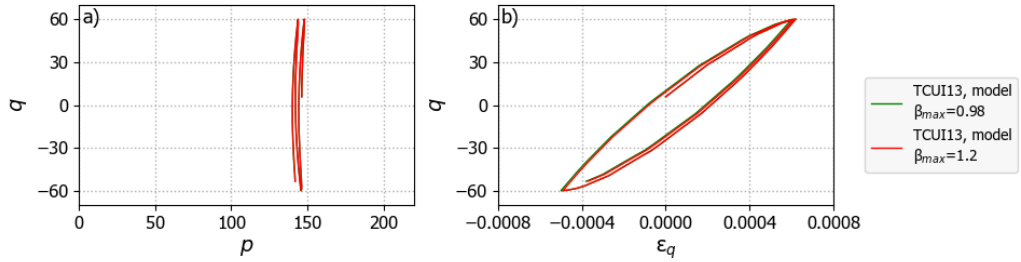


Figure 183 Isolation on a few cycles of TCUI13 with variable β_{max}

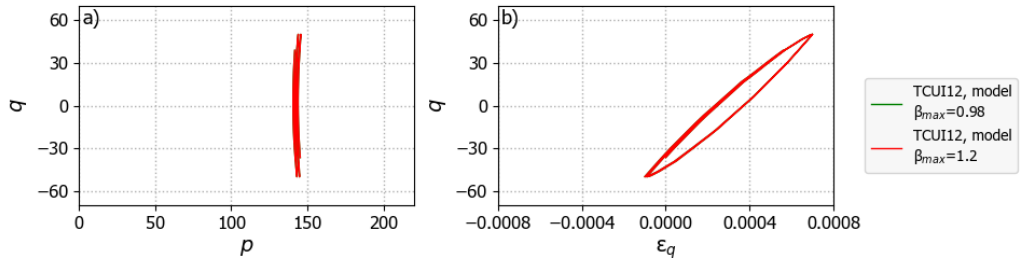


Figure 184 Isolation on a few cycles of TCUI12 with variable β_{max}

Variation of the maximum dilation ratio has no impact on the monitored metrics: for the larger amplitude $N_{liq} = 19$, and for the lower amplitude $N_{liq} = 51$, leading to a ratio of 2.7.

4.1.2.6. Normal consolidation line slopes: λ_Δ and λ_B

With $\lambda_\Delta = 0.0033$ and $\lambda_B = 0.0071$, instead of $\lambda_\Delta = 0.0026$ and $\lambda_B = 0.0057$, Figure 185 to Figure 187 are obtained.

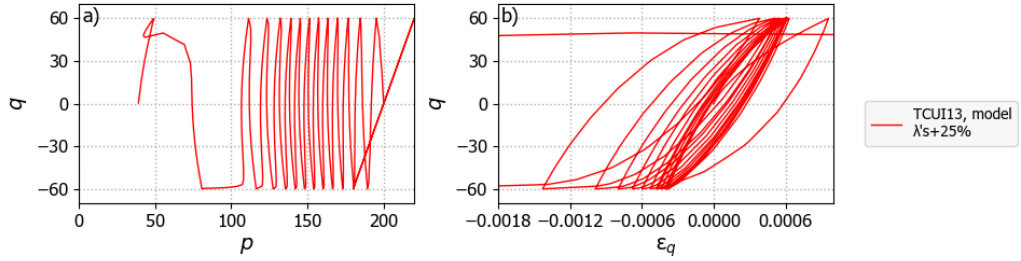


Figure 185 Simulated TCUI13

A steeper consolidation slope leads to a greater contraction. This explains the reduction in the number of cycles required to reach liquefaction: 12 for the larger amplitude, and 34 for the lower amplitude, leading to a ratio of 2.8. The increase in λ also implies a reduction in secant stiffness.

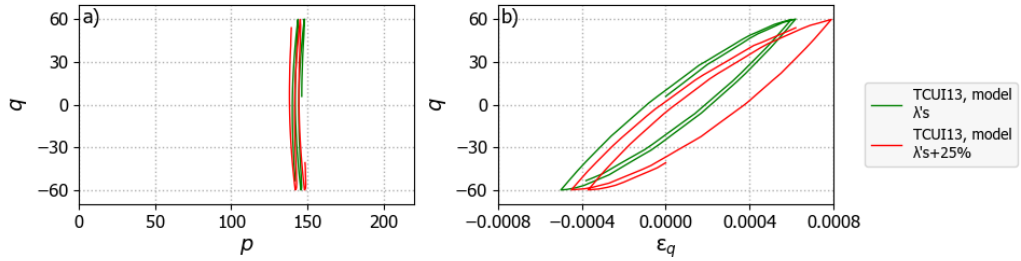


Figure 186 Isolation on a few cycles of TCUI13 with variable λ_B and λ_Δ

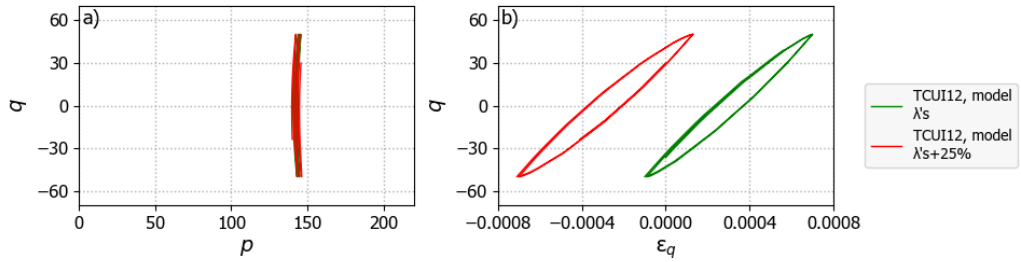


Figure 187 Isolation on a few cycles of TCUI12 with variable λ_B and λ_Δ

4.1.2.7. Anisotropy rate development parameter: A_{max}

With $A_{max} = 60$ instead of $A_{max} = 46$, Figure 188 to Figure 190 are obtained.

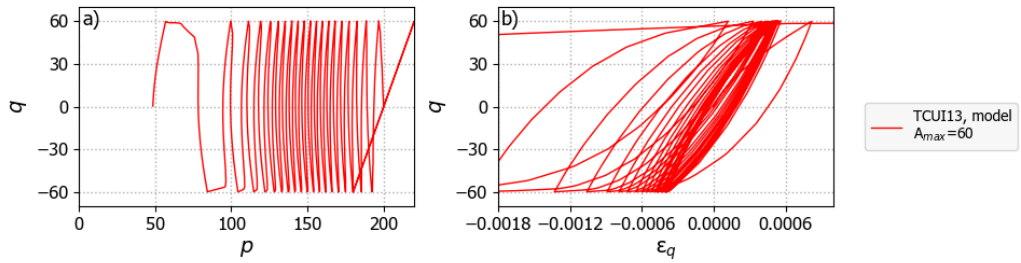


Figure 188 Simulated TCUI13

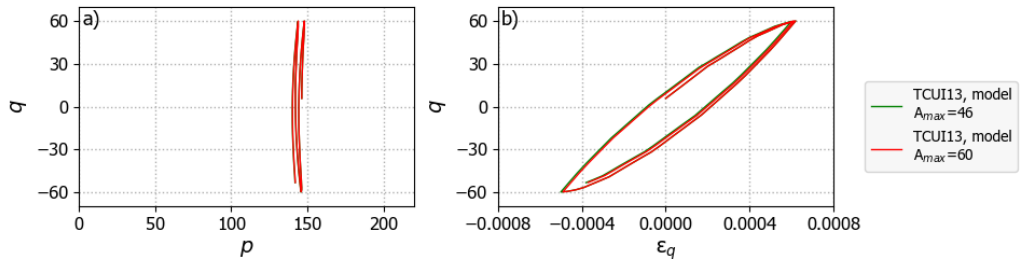


Figure 189 Isolation on a few cycles of TCUI13 with variable A_{max}

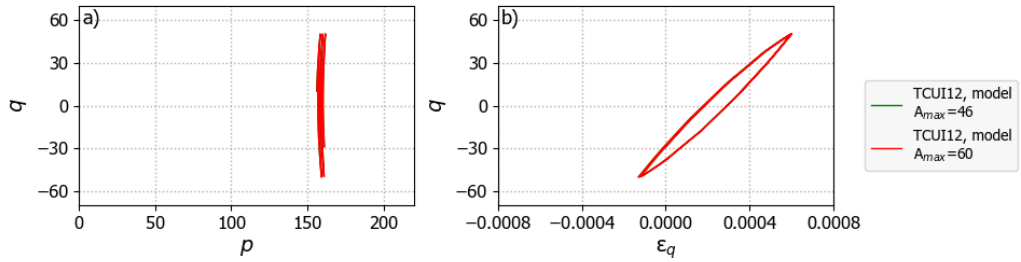


Figure 190 Isolation on a few cycles of TCUI12 with variable A_{max}

The variation of A_{max} has very little impact on the monitored metrics: for the larger amplitude $N_{liq} = 19$, and for the lower amplitude $N_{liq} = 52$, leading to a ratio of 2.7.

4.1.2.8. Consolidation power exponent: r

With $r = 0.35$ instead of $r = 0.28$, Figure 191 to Figure 193 are obtained.

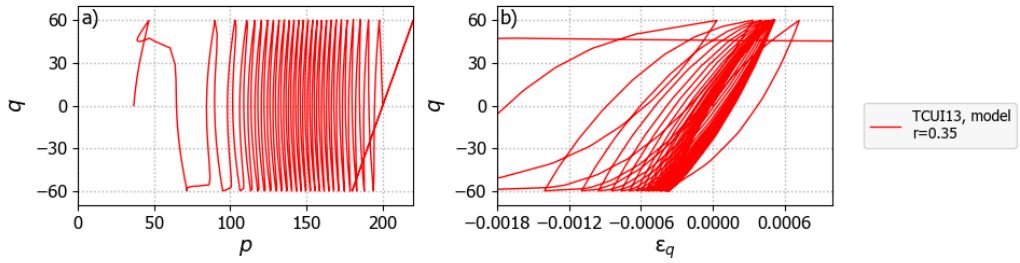


Figure 191 Simulated TCUI13

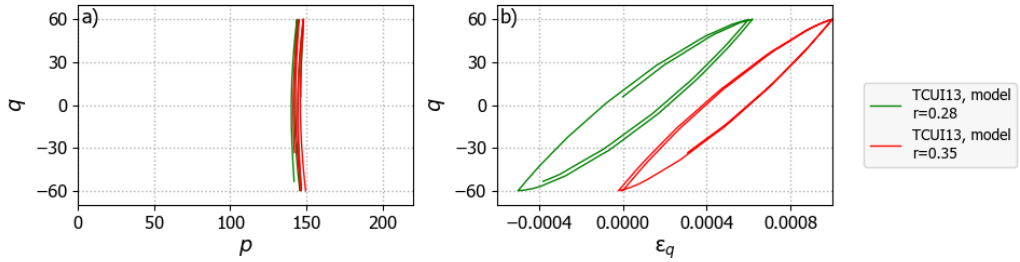


Figure 192 Isolation on a few cycles of TCUI13 with variable r

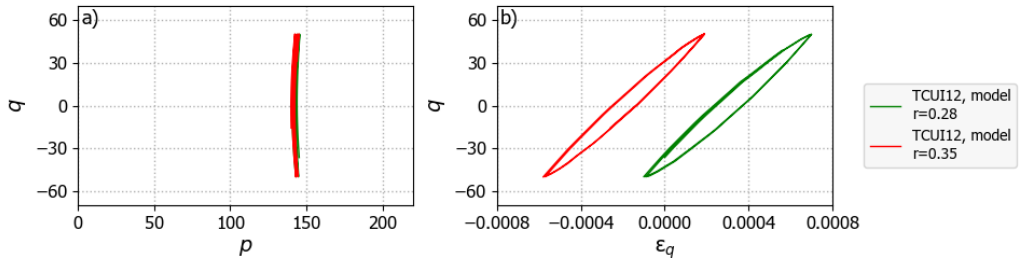


Figure 193 Isolation on a few cycles of TCUI12 with variable r

For the larger amplitude $N_{liq} = 26$, and for the lower amplitude $N_{liq} = 66$, a ratio of 2.5.

Increasing the consolidation exponent r widens the yield surface (see Figure 107). As a result, less plastic strain is produced, which leads to a higher secant stiffness, and a higher number of cycles needed to reach liquefaction.

4.1.2.9. Hardening factor: h_0

With $h_0 = 1300$ instead of $h_0 = 987$, Figure 194 to Figure 196 are obtained.

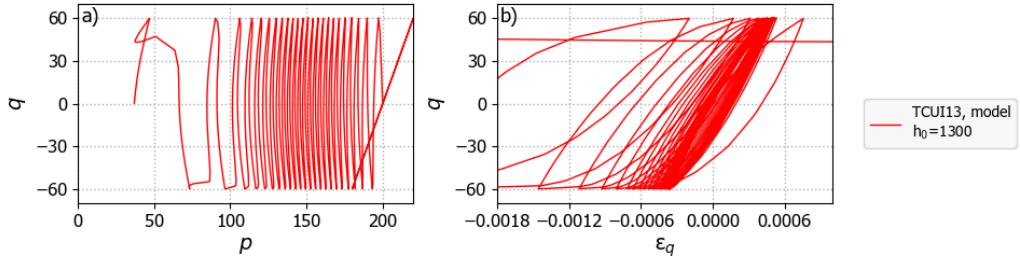


Figure 194 Simulated TCUI13

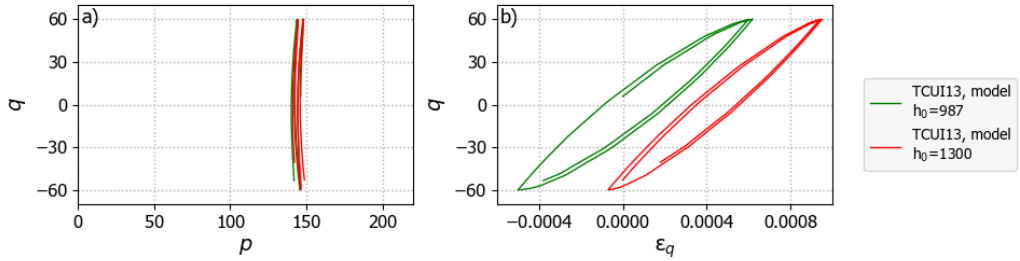


Figure 195 Isolation on a few cycles of TCUI13 with variable h_0

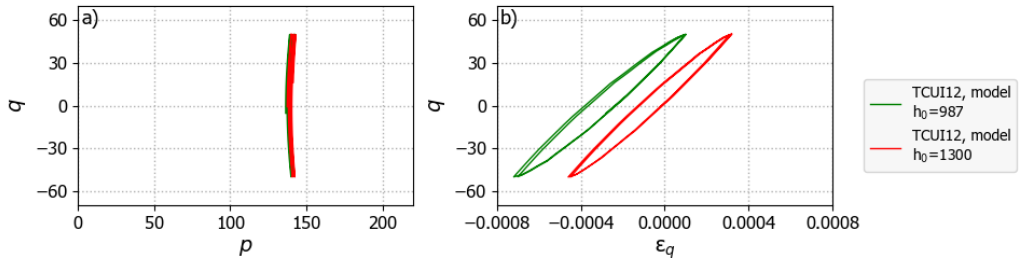


Figure 196 Isolation on a few cycles of TCUI12 with variable h_0

An increased hardening factor leads to less plastic strain, thus higher secant stiffness, and a higher number of cycles to liquefaction: for the larger amplitude $N_{liq} = 23$, and for the lower amplitude $N_{liq} = 60$. The ratio between the two tests is marginally affected, with a decrease to 2.6.

4.1.2.10. Hardening exponent: *b*

With $b = 4$ instead of $b = 3.4$, Figure 197 to Figure 199 are obtained.

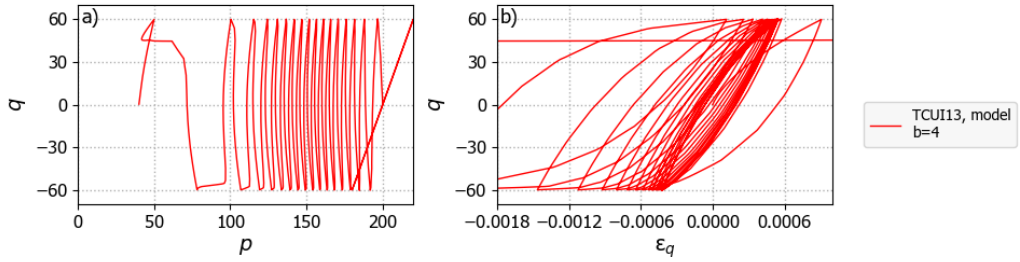


Figure 197 Simulated TCUI13

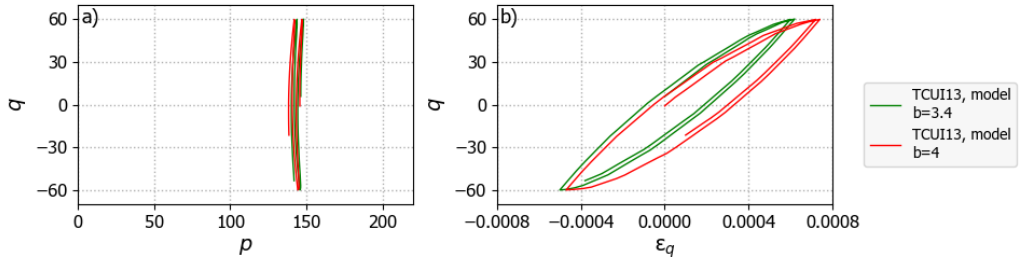


Figure 198 Isolation on a few cycles of TCUI13 with variable b

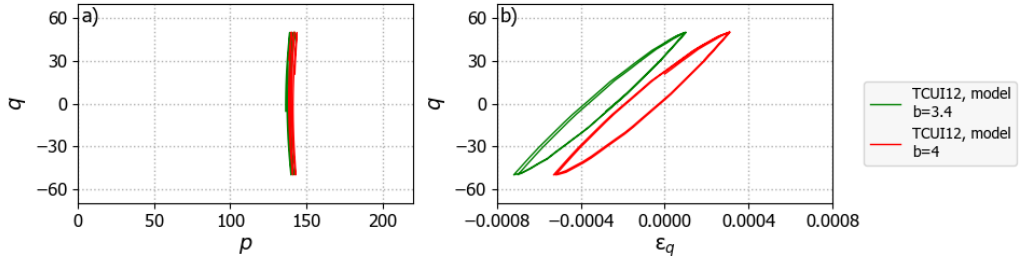


Figure 199 Isolation on a few cycles of TCUI12 with variable b

Increasing the hardening exponent while maintaining a constant hardening factor leads to lower plastic moduli. In turn, this leads to more plastic strain, thus lower secant stiffness, and fewer cycles needed to reach liquefaction: 16 for the larger amplitude, and 45 for the lower amplitude. The ratio of number of cycles to liquefaction between the two tests increases with increasing b, but only to a limited extent. This is shown for a broader range of b in Table 8.

b	1	2	3	4	5	6
N_{liq} larger amplitude	46	30	22	16	13	10
N_{liq} lower amplitude	90	71	56	45	36	29
Ratio	2.0	2.4	2.5	2.8	2.8	2.9

Table 8 Number of cycles to liquefaction for different values of the hardening exponent.

4.1.3. Summary

Table 9 is a summary of the effects of the variation of each parameter on the tests. The plus signs imply a positive interaction between the increase of the parameter and the increase of the effect. The number of signs symbolise the intensity of the impact of the variation.

	Monotonic drained test					Mono. undrained test				Cyclic stress-controlled tests		
	End of test capacity	Peak capacity	Shear strain at peak capacity	Secant stiffness (1% shear)	Maximum dilation ratio	Maximum pore pressure build-up	Stress ratio asymptote in $p-q$ space	Slope of shear stress-strain asymptotes	Stiffness before softening	Number of cycles to liquefaction	Secant stiffness	Ratio low amplitude N_{liq} to high amp N_{liq}
k_r	0	0	0	0	0	++	-	+	0	--	0	0
g_r	0	0	0	0	0	-	0	0	0	0	+	0
m	++	++	-	0	0	0	+	+	0	-	++	0
φ_c	+++	+++	0	+	0	0	++	0	0	++	0	0
$\lambda's$	-	-	+	0	0	++	0	--	0	--	0	0
β_{max}	0	+++	-	0	+++	-	0	+++	0	0	0	0
A_{max}	0	+	--	0	0	-	0	++	0	0	0	0
r	+++	+++	0	+++	0	0	++	0	+	+++	++	-
h_0	0	+	0	+	0	0	+	0	+	++	++	0
b	-	--	0	--	0	0	--	0	-	-	-	+

Table 9 Influence of parameters on the sand behaviour

4.2. Initialisation of tests

Initially, all internal variables of HySand_base ($\alpha_q^{(n)}$, $\alpha_p^{(n)}$, $\alpha_{p_c}^{(n)}$), except for the anisotropy scalar (a), are set to zero, mainly because it is impossible to measure them.

4.2.1. Isotropic fabric

In this thesis, the vast majority of tests are assumed to have an initially isotropic fabric, with the exception of the tests on Adamidis data (see section 5.2). In the case of an assumed initial isotropy of the fabric, the initial value of the anisotropic scalar (a_0) is assumed to be null.

In the case of an initial isotropic stress state ($q_0 = 0$), the simulation starts from the initial stress state and specific volume (v_0) of the test, and the initial consolidation pressure (p_{c_0}) is set slightly higher than the initial mean effective stress ($p_{c_0} = p_0 + 0.1$kPa) to avoid numerical issues.

In the case of an initial anisotropic stress state ($p_0 \geq 0, q_0 \neq 0$), the simulation cannot start from the initial stress state of the test. Indeed, this stress state could be located outside a number of the yield surfaces, which initial configuration is shown in Figure 129. Instead, if $q_0 < p_0$, the test is started from an isotropic state ($p_0 - q_0, 0$) which guarantees to be inside all yield surfaces, and a drained loading of slope $dq/dp = 1$ is used to reach the desired "initial state". Note that the initial specific volume should be adjusted to take into account the initial drained loading. If $q_0 > p_0$, a steeper slope should be used for the drained loading.

4.2.2. Anisotropic fabric

As encountered in section 5.2, sands can initially present an anisotropic fabric, and this will often be the case in the field because of its deposition history. It is however difficult to measure and quantify anisotropy in the laboratory, even more in-situ, and no clear mechanism has been designed yet to set the initial anisotropy scalar (a_0) based on experimental observations. Measurement of the shear wave velocity (Mital *et al.* (2020), Gu *et al.* (2023)) could be an interesting lead. In section 5.2, each a_0 is chosen to best reproduce the experiments.

4.2.3. Overconsolidated sample

For an isotropically overconsolidated sample, p_{c_0} is initialised at the overconsolidation pressure. However, for anisotropically overconsolidated sample, the anisotropic overconsolidation has to be simulated with an initial drained loading-unloading to the wanted value. Care should be given to obtain the wanted initial specific volume after this loading-unloading drained cycle.

4.3. Calibration process

The following calibration process should be conducted in the order presented. Note that the calibration steps up to 4.3.4.1 should be performed in all cases. However, the final determination of β_{max}, A_{max}, r, h_0, and b can either be done by a trial-and-error process, or with the optimisation process presented in 4.4.

The tests required for this calibration procedure are as follows: the determination of the densest and loosest packing of the sand, three isotropic tests with different densities, three monotonic drained tests with different densities brought to large strains to approach critical state, and two cyclic stress controlled undrained tests with the same density but different amplitudes. Figure 200 represents each required test and the associated parameters calibrated from the tests.

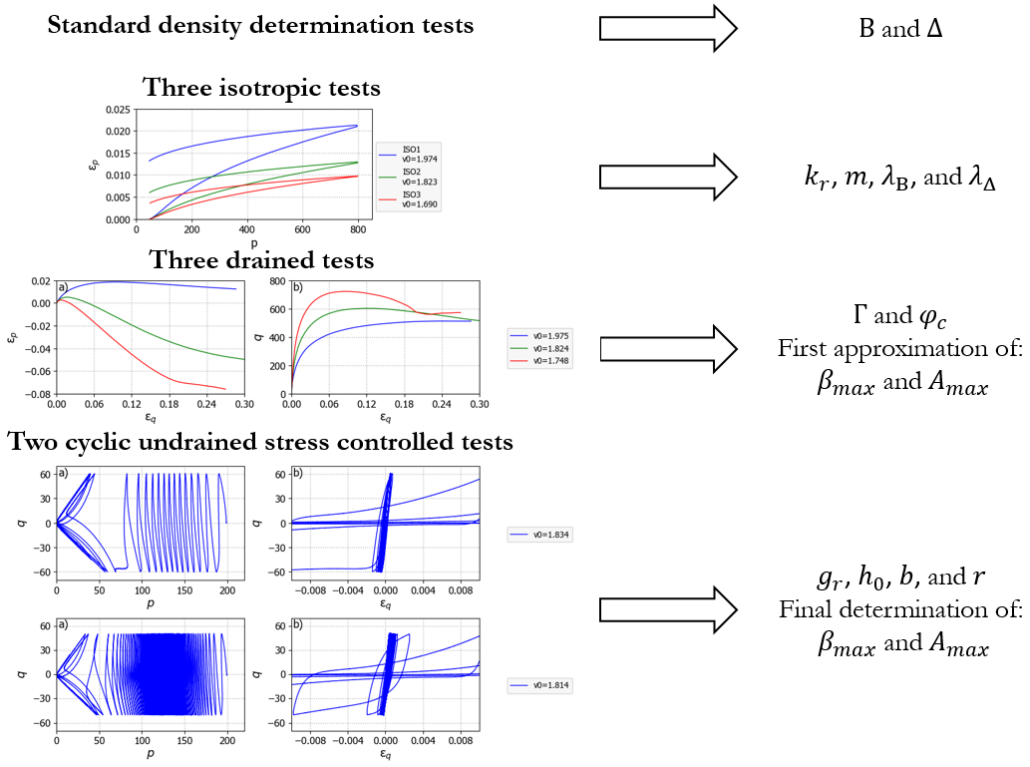


Figure 200 Tests used for the calibration process and associated calibrated parameters

The case of Karlsruhe fine sand is used as an example for this calibration procedure.

Note that for sand, especially offshore, it is not possible to retrieve and test in the laboratory undisturbed samples, meaning that field properties cannot be perfectly measured in the laboratory. Nonetheless, laboratory testing is necessary in the calibration of HySand_base, and best effort should be made to maximise the representativeness of the field conditions during the reconstitution of the specimen, such that air or water pluviation are recommended for free falling sand through air or water (Wichtmann, 2016).

4.3.1. Characteristic specific volumes: Δ and B

In HySand, the densest (Δ), loosest (B), and critical state (Γ) specific volumes at a reference pressure allow control of the dilation, the anisotropy rate development, the hardening, and the consolidation for the current void ratio (v) and stress state.

Minimum (Δ) and maximum (B) specific volumes can be determined from standard tests according to DIN 18126. In the case of the Karlsruhe fine sand studied by Wichtmann (2021), the densest specific volume is $\boldsymbol{\Delta = 1.677}$, while the loosest is $\boldsymbol{B = 2.054}$.

4.3.2. Isotropic tests: k_r, m, λ_B, λ_Δ

Three isotropic tests should be conducted on normally consolidated samples to cover the range of densities of the sand. These isotropic tests should start at a low effective mean pressure, load to a high p, and unload to the starting p again. These low and high p values should cover the range that will be used with the model, for example: 0kPa to 1000kPa for an offshore wind turbine problem requiring a 3D FEA spanning from the surface to 100m deep (three times the embedded length of a typical monopile).

From Wichtmann (2021), three isotropic tests, ISO1, 2, and 3, shown in Figure 201 are used.

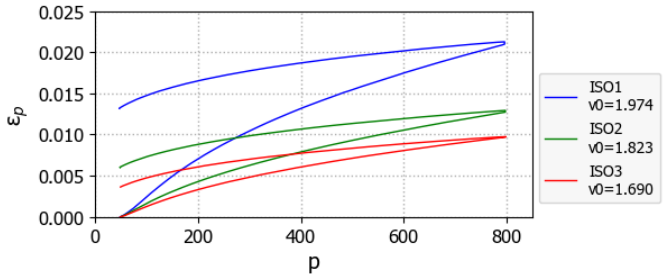


Figure 201 Truncated isotropic tests by Wichtmann (2021): ISO1, ISO2, ISO3

λ, the normal consolidation slope, determines the amount of plastic volumetric strain during the isotropic loading (the distance between the loading and unloading branches in Figure 202). The elastic parameters have an influence on the unloading branch, with k_r directing the overall slope and m the curvature of the slope.

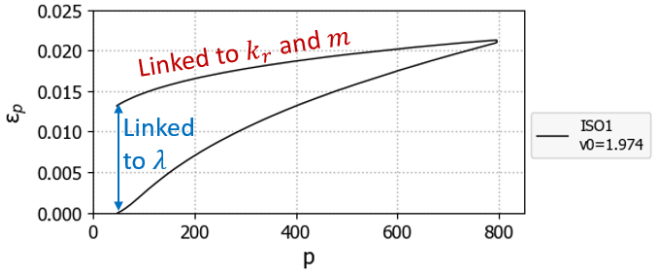


Figure 202 Influence of elastic and plastic parameters on isotropic loading

For isotropic loading, noting that $\alpha_p^{(n)} = 0$ (because no $\alpha_q^{(n)}$ is created during the isotropic loading), the volumetric strain is:

$$\epsilon_p = -\frac{\partial g}{\partial p} = \frac{1}{(1-\mathrm{m})\mathrm{k_r}}\left(\frac{p}{p_r}\right)^{1-m} + \frac{1}{N}\sum_{n=1}^{N}\alpha_{pc}^{(n)} \qquad \textit{Eq. 245}$$

The plastic consolidation strain $\alpha_{pc}^{(n)}$ and the local consolidation pressure $p_c^{(n)}$ are related through:

$$p_c^{(\mathrm{n})} = p_{c0}\left(1 + \frac{(1-m)}{\lambda - 1/k_r}\alpha_{p_c}^{(n)}\right)^{\frac{1}{1-m}} \qquad \textit{Eq. 246}$$

$$\leftrightarrow\ \alpha_{pc}^{(n)} = \frac{\lambda - 1/k_r}{1-m}\left(\left(\frac{p_c^{(n)}}{p_{c0}}\right)^{1-m} - 1\right) \qquad \textit{Eq. 247}$$

Replacing $\alpha_{pc}^{(n)}$ by its expression in Eq. 247 into Eq. 132 leads to the volumetric strain:

$$\epsilon_p = \frac{1}{(1-\mathrm{m})\mathrm{k_r}}\left(\frac{p}{p_r}\right)^{1-m} + \frac{\lambda - 1/k_r}{1-m}\frac{1}{N}\sum_{n=1}^{N}\left(\left(\frac{p_c^{(n)}}{p_{c0}}\right)^{1-m} - 1\right) \qquad \textit{Eq. 248}$$

In an isotropic test, all local consolidation pressures ($p_c^{(n)}$) are equal, such that:

$$\epsilon_p = \frac{1}{(1-\mathrm{m})\mathrm{k_r}}\left(\frac{p}{p_r}\right)^{1-m} + \frac{\lambda - 1/k_r}{1-m}\left(\left(\frac{p_c^{(n)}}{p_{c0}}\right)^{1-m} - 1\right) \qquad \textit{Eq. 249}$$

During virgin isotropic loading $p_c^{(n)} = p$, and during the unloading $p_c^{(n)} = p_{max}$ where p_{max} is the maximal mean effective stress reached during the test.

This means that during unloading, the volumetric strain is:

$$\epsilon_p = \frac{1}{(1-\mathrm{m})\mathrm{k_r}}\left(\frac{p}{p_r}\right)^{1-m} + \frac{\lambda - 1/k_r}{1-m}\left(\left(\frac{p_{max}}{p_{c0}}\right)^{1-m} - 1\right) \qquad \textit{Eq. 250}$$

Taking the logarithm of Eq. 250 and noting C_0 a constant encompassing all terms that do not depend on p, one can write:

$$\ln \epsilon_p = (1-m)\ln p + C_0 \qquad \textit{Eq. 251}$$

Plotting $\ln(\epsilon_p)$ as a function of $\ln(p)$ permits determination of the non-linear elastic pressure exponent (m) via the measure of the slope of the unloading, equal to $(1-m)$ (c.f. Figure 203).

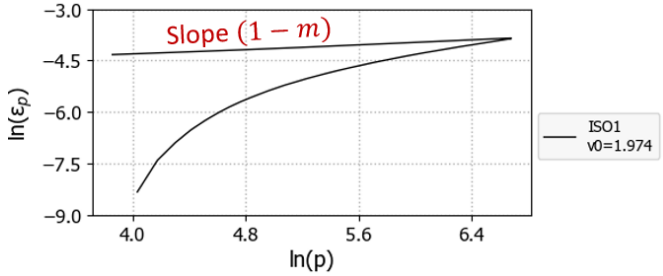


Figure 203 Isotropic test plotted with log of volumetric strain function of log of mean effective pressure

The values of m for ISO1,2 and 3 by Wichtmann are shown in Table 10.

v_0	1.975	1.824	1.69
m	0.83	0.73	0.65

Table 10 Variation of the power exponent for non-linear elasticity with density

In HySand_base, the variation of m is not taken into account, such that the value for the average value for the three tests is taken: $\boldsymbol{m = 0.73}$.

Once m is identified, one can plot the loading-unloading in $\epsilon_p - p^{1-m}/(1-m)$ space. According to Eq. 249, the loading has a slope λ/p_{c0}^{1-m} , and the unloading a slope $1/(k_r p_r^{1-m})$ (c.f. Figure 204).

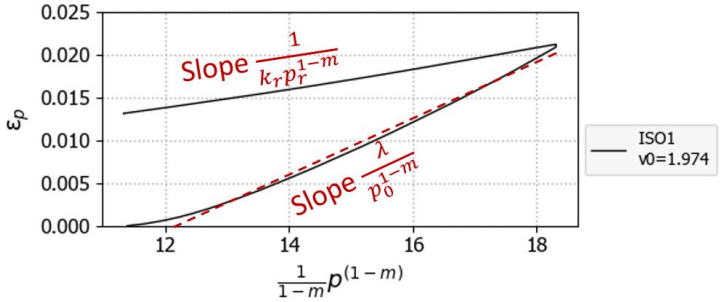


Figure 204 Isotropic test with volumetric strain as a function of mean effective pressure power (1-m)

Note that the average m should be used, and not individual density dependent ones. In Figure 204, the loading slope is not perfectly linear, leading to an overestimate of the plastic strain generation at low pressures, and an underestimate at high pressures with HySand_base.

In Table 11, the values of k_r and λ obtained for Wichtmann data for $m = 0.73$ are presented.

v_0	1.975	1.824	1.69
k_r	424	499	557
λ	0.0053	0.0032	0.0024

Table 11 Parameters obtained from the calibration on isotropic tests

In HySand_base, only the variation of the normal consolidation slope with density is taken into account. The average value of the dimensionless bulk modulus is selected: $\boldsymbol{k_r = 493}$.

In HySand base, the variation of λ with relative density to the loosest state is:

$$\lambda = \lambda_B - (\lambda_B - \lambda_\Delta)\frac{\ln(v_\lambda) - \ln(B)}{\ln(\Delta) - \ln(B)} \qquad \textit{Eq. 252}$$

The values of normal consolidation slopes are plotted against the initial relative density in Figure 205. Although the variation of λ with initial relative density is not perfectly linear for the data, it can be approximated by a linear relation which has the advantages described in Chapter 3. For this linear relation, one should take care not to take just the linear interpolation of the obtained data points as this would cause too important an underestimation for the densest case. In the

case of the Wichtmann data, the values obtained by linear interpolation are $\boldsymbol{\lambda_B = 0.0059}$, and $\lambda_\Delta = 0.0021$. However, after simulation of the three tests, the densest slope value is adjusted to $\boldsymbol{\lambda_\Delta = 0.0025}$.

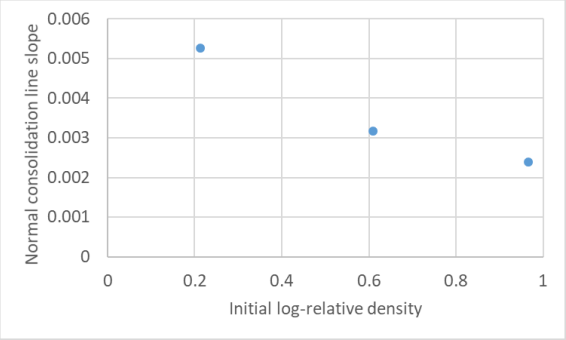


Figure 205 Normal consolidation slopes as a function of initial log-relative density

4.3.3. Drained tests: Γ, φ_c, β_{LB}, A_{max}

Three drained tests on normal consolidated samples (at one p_0 of interest, e.g. 200kPa) of different densities should be conducted to large strains (>20%). For example, in the Wichtmann database, the tests TMD3, 13 and 23 can be used.

4.3.3.1. Critical state specific volume: Γ

To determine Γ, two quantities are needed: the asymptotic specific volume (at which there is no more dilation), and the effective mean pressure at which this happens. Tests TMD3, 13, and 23 are represented in Figure 206.

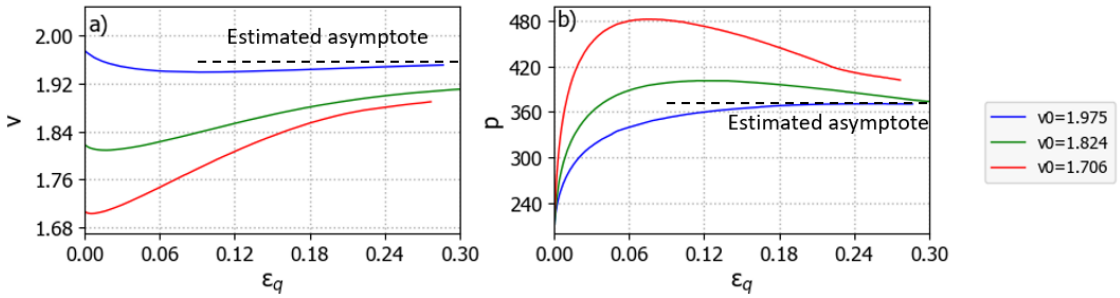


Figure 206 Drained tests TMD3, 13 and 23, estimation of asymptotic specific volume and mean effective pressure

For the Wichtmann data, the specific volume seems to converge to $v \approx 1.96$ at a pressure of $p \approx 400$kPa. This method is not precise because the specific volumes have not fully stabilised. To calculate Γ at the reference pressure, Eq. 253 is used:

$$ln(v_\lambda) = \ln(\mathrm{B}) - \ln\left(\frac{\mathrm{B}}{\Delta}\right)\frac{\ln(v) + \frac{\lambda_\mathrm{B}}{1-m}\left(\left(\frac{p}{p_r}\right)^{1-m} - 1\right) - ln(\mathrm{B})}{ln(\Delta) + \frac{\lambda_\mathrm{B} - \lambda_\Delta}{1-m}\left(\left(\frac{p}{p_r}\right)^{1-m} - 1\right) - ln(\mathrm{B})} \qquad \textit{Eq. 253}$$

Such that in the case of Wichtmann data, the critical state specific volume is $\boldsymbol{\Gamma = 1.97}$.

4.3.3.2. Critical state friction angle: φ_c

The critical state friction angle is related to the critical stress ratio in compression $M_c = 6\sin\varphi_c/(3-\sin\varphi_c)$. φ_c is thus determined based on the estimated asymptotic deviatoric stress q reached at large strains in the three drained tests.

The right hand graph of Figure 207 shows the shear stress function of shear strain for the drained tests by Wichtmann.

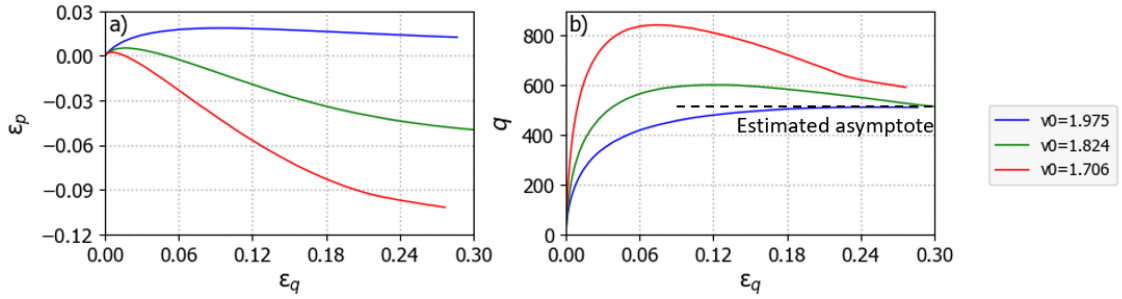


Figure 207 Drained tests TMD3, 13 and 23, estimation of asymptotic shear stress

The asymptotic deviatoric stress is estimated to be $q = 505kPa$, for an asymptotic effective mean pressure of p =368.3kPa, leading to $M_c = 1.37$. The critical state friction angle for the Wichtmann data thus is $\boldsymbol{\varphi_c = 33.9°}$, which is in the range expected for a silica sand.

4.3.3.3. Lower bound of the maximum dilation ratio: $\beta_{max_{LB}}$

The development of α_p is ruled by the dilation constraint such that:

$$\frac{\dot{\alpha}_p}{\dot{\alpha}_q} = \beta = \beta_{max}\frac{\ln(v_\lambda)-\ln(\Gamma)}{\ln(\Delta)-\ln(\Gamma)} \qquad \textit{Eq. 254}$$

$$ln(v_\lambda) = \ln(\mathrm{B}) - \ln\left(\frac{\mathrm{B}}{\Delta}\right)\frac{ln(v)+\frac{\lambda_\mathrm{B}}{1-m}\left(\left(\frac{p}{p_r}\right)^{1-m}-1\right)-ln(\mathrm{B})}{ln(\Delta)+\frac{\lambda_\mathrm{B}-\lambda_\Delta}{1-m}\left(\left(\frac{p}{p_r}\right)^{1-m}-1\right)-ln(\mathrm{B})} \qquad \textit{Eq. 255}$$

By observing the dilation ratios in drained tests, a lower bound for β_{max} can be determined. However, it is insufficient to determine β_{max} precisely because the volumetric strain also varies with the consolidation strain.

Using the two drained tests on medium dense and dense samples, looking at the volumetric strain as a function of the deviatoric strain, one can deduce the maximal dilation ratios experienced by the samples.

In the left part of Figure 208, volumetric strain as a function of shear strain is pictured for Wichtmann tests.

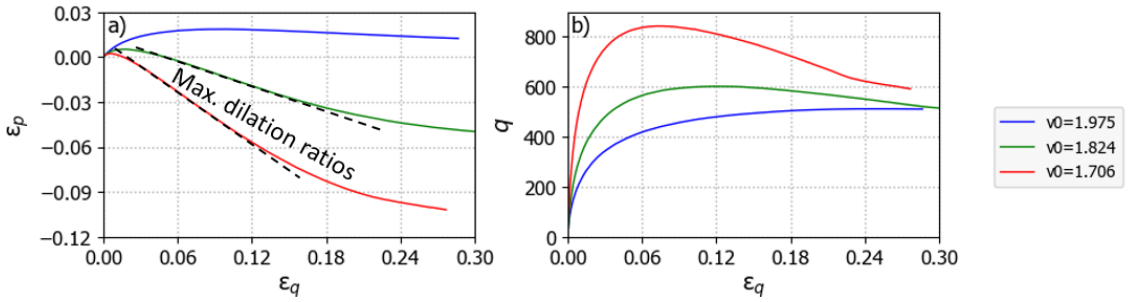


Figure 208 Drained tests TMD3, 13 and 23, estimation of maximal dilation ratios

The dilation ratios should be calculated, and the local value of the specific volume and current mean effective stress should be measured. Using Eq. 254, the lower bound of β_{max} can then be calculated for each test.

In the case of Wichtmann data, the slope for the medium dense and dense samples are respectively $\beta = 0.31$ and $\beta = 0.61$, at specific volumes and mean effective stress of $v = 1.844$ and p=400kPa, and $v = 1.746$ and p=480kPa at the local maxima.

Estimations of the maximum dilation ratio for the medium dense sample and the dense sample are $\beta_{max} > 0.8$ for medium dense and $\beta_{max} > 0.82$. In conclusion, a lower bound for the maximum dilation ratio is $\beta_{LB} = 0.8$.

An accurate value of β_{max} can only be determined later in the calibration process by trial and error or by an optimisation routine.

4.3.3.4. Anisotropy rate development parameter: A_{max}

Using the previously determined parameters completed by the draft parameters given in Table 12, a first approximation of the anisotropy rate development parameter can be made by trial and error.

k_r	g_r	m	φ_c	β_{max}	B	Γ	Δ	λ_B	λ_Δ	A_{max}	h_0	b	r
493	400	0.73	33.9	0.8	2.054	1.97	1.677	0.0059	0.0025	100	1000	3	0.3

Table 12 Parameters calibrated so far (dark background), and dummy parameters (white background)

For the densest drained test, these values deliver the simulation shown in Figure 209.

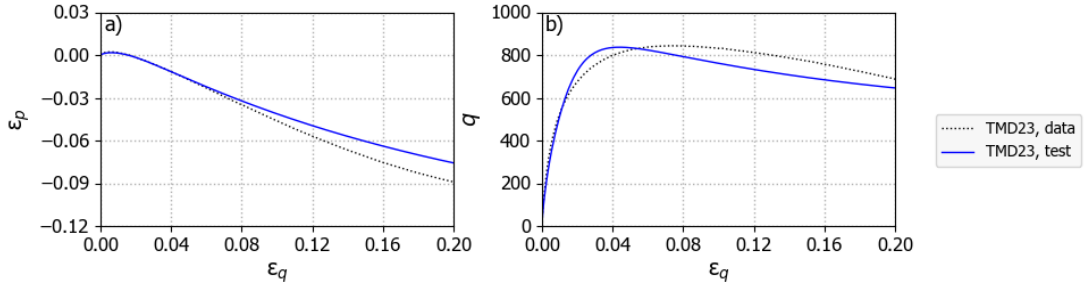


Figure 209 First simulation of TMD23 with non-calibrated parameters

The greater the anisotropy rate development parameter, the quicker the transition from contraction to dilation, and the quicker the peak capacity is reached. In Figure 209, the transition is too fast such that the peak capacity of the simulation is too early compared to the data. Adjusting A_{max} to 40 leads to a better prediction of the shear strain at peak capacity ($\epsilon_q \approx 7\%$), shown in Figure 210

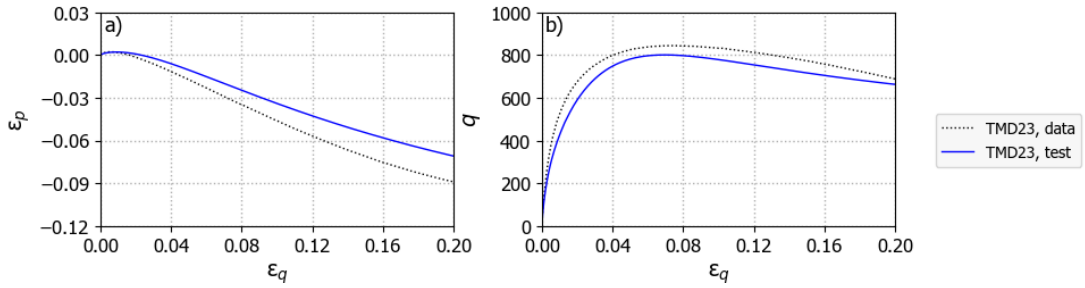


Figure 210 First simulation of TMD23 with non-calibrated parameters

However, as expected, using the lower bound for β_{max} leads to a lower dilation as well as a lower peak capacity than the data.

$A_{max} = 40$ is, however, a good first approximation for the rest of the calibration.

4.3.4. Undrained cyclic tests: g_r, h_0, b and r

Two undrained cyclic stress controlled tests should be conducted: both at the same density, but with different amplitudes. Ideally the first test should take approximately 10 cycles to liquefy, and the second approximately five times more.

For example, calibration on Wichtmann data can be done using the tests TCUI13 and TCUI12 on medium dense sand normally consolidated at p_0=200kPa, including a first drained cycle, with amplitudes of 60kPa and 50 kPa respectively, which liquefy after 15 and 77 cycles respectively.

Note that it is not necessary to start the test with an initial drained cycle.

4.3.4.1. Dimensionless shear modulus: g_r

The shear modulus can be studied using advanced laboratory techniques (bender elements, resonant column, etc.), but it can also be calibrated by observing the shear stress-strain behaviour for very small strain after load reversal. By isolating a few cycles of one of the two tests, and plotting the shear stress against the shear strain, one can measure the slope upon load reversal (taking care to ignore the corner of the cycles where the data is less trustworthy), as in Figure 211. Despite the simplicity of such a technique, it should be noted that this might lead to lower values than ones found by bender elements or in-situ measurements

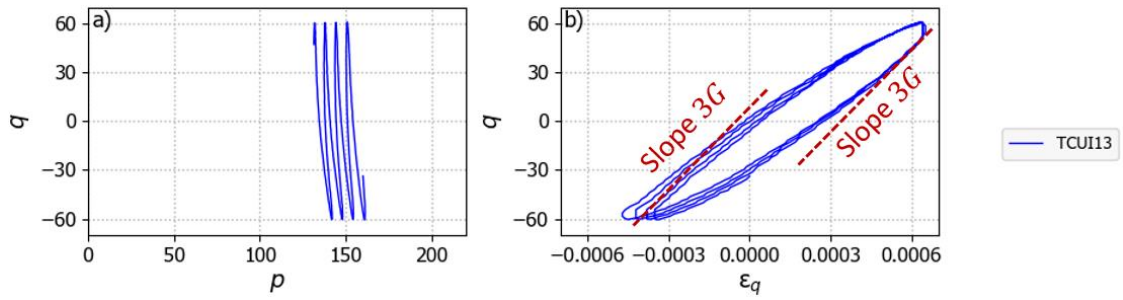


Figure 211 Zoom on a few cycles of TCUI13 and measure of the elastic unloading slope

This slope is of $3G = 168000$kPa in the case of Wichtmann data, and is taken for cycles at around $p = 150$kPa. One can approximate the shear modulus with the following expression, disregarding the coupling terms with q:

$$\frac{G}{p_r} = g_r \left(\frac{p}{p_r}\right)^m \qquad \textit{Eq. 256}$$

Eq. 256 leads to $\boldsymbol{g_r = 417}$, and an equivalent Poisson ratio $v_{PR} = 0.17$, which is in the expected range for a silica sand.

Properly accounting for the coupling terms, the expression would be:

$$\frac{1}{3G} = \frac{1}{3g_r p_r}\left(\frac{p^2}{p_r^2} + \frac{k_r(1-m)q^2}{3g_r p_r^2}\right)^{-\frac{m}{2}} - \frac{mk_r(1-m)q^2}{(3g_r)^2 p_r^3}\left(\frac{p^2}{p_r^2} + \frac{k_r(1-m)q^2}{3g_r p_r^2}\right)^{-\frac{m}{2}-1} \qquad \textit{Eq. 257}$$

Which leads to $g_r = 410$, such that Eq. 256 is a good approximation for cyclic loadings at low stress ratios ($q_{max}/p_0 < 0.5$).

4.3.4.2. Shear hardening and consolidation exponent: h_0, b, and r

It is possible to determine the shear hardening parameters (h_0 and b) and the consolidation exponent (r), as well as to refine the determination of the maximum dilation ratio (β_{max}) and the anisotropy rate development parameter (A_{max}) through a series of trial and error simulations of the two cyclic tests and the drained test on medium dense sand.

The guideline for this trial and error scheme is as follows.

4.3.4.2.1. Trial and error guideline

First, using the parameters determined so far and the dummy parameters $h_0 = 1000$, $b = 3$ and $r = 0.3$, one should run the simulation of the cyclic test with the largest amplitude.

Second, study the secant stiffness after a few cycles of the test. h_0 should then be adjusted to obtain an adequate stiffness: increase h_0 if the stiffness is too low, and decrease it if the stiffness is too high.

Third, once the secant stiffness is adjusted, the number of cycles to liquefaction should be observed. If it is too low, r should be increased; if it is too large, r should be decreased. Noting that r has an influence on secant stiffness (a lower r leads to a lower stiffness), h_0 should be adjusted to counterbalance the variation. At the end of this step, the cyclic test with the larger amplitude should be well represented.

Fourth, the drained test should be run with the updated parameters. A_{max} and β_{max} can then be adjusted to fit the drained test. This should have little impact on the cyclic test previously calibrated.

Fifth, the second cyclic test (with lower amplitude should be simulated).

The ratio of cycles to liquefaction between the larger and lower amplitude might be inaccurate. However, this ratio is only marginally affected by the variation of parameters (c.f. Table 9).

An optional sixth step: the shear hardening exponent b can be changed to slightly improve the ratio of the number of cycles to liquefaction between the two different amplitudes. However, this implies a recalibration of h_0, r, A_{max} and β_{max} because the modification of b has a large impact on both the monotonic and cyclic tests. Otherwise, the shear hardening exponent can be kept at $b = 3$.

4.3.4.2.2. Trial and error example for Wichtmann data

k_r	g_r	m	φ_c	β_{max}	B	Γ	Δ	λ_B	λ_Δ	A_{max}	h_0	b	r
493	417	0.73	33.9	0.8	2.054	1.97	1.677	0.0059	0.0025	40	*1000*	*3*	*0.3*

Table 13 Parameters calibrated so far (grey backgrounds), and dummy parameters (white background)

First, using the parameters determined so far and the dummy parameters presented in Table 13, a simulation of test TCUI13 (blue) and the test data (dotted black) are represented in Figure 212.

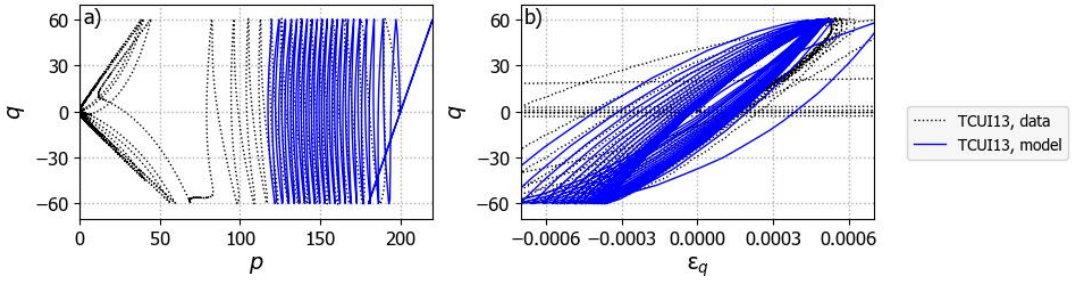


Figure 212 TCUI13, data and

Second, as the simulated TCUI13 has too high secant stiffness, h_0 should be lowered. $h_0 = 750$ leads to an adequate secant stiffness, as shown in Figure 213 for a few cycles, but the numbers of cycles required to reach liquefaction is too high: 20 rather than 15 as shown in Figure 214.

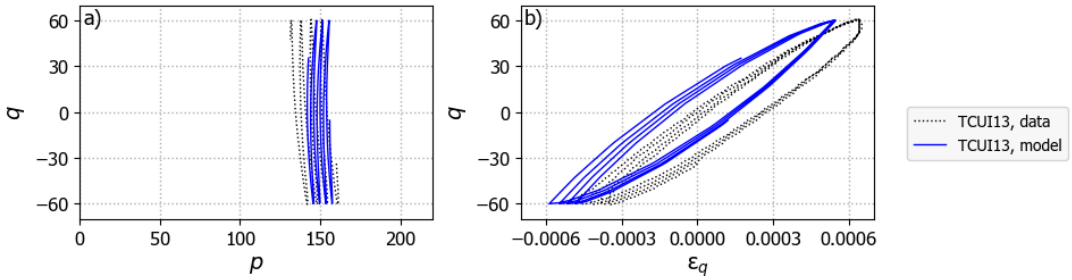


Figure 213 Modelling of TCUI13 with calibrated h_0 for the secant stiffness, zoom on a few cycles

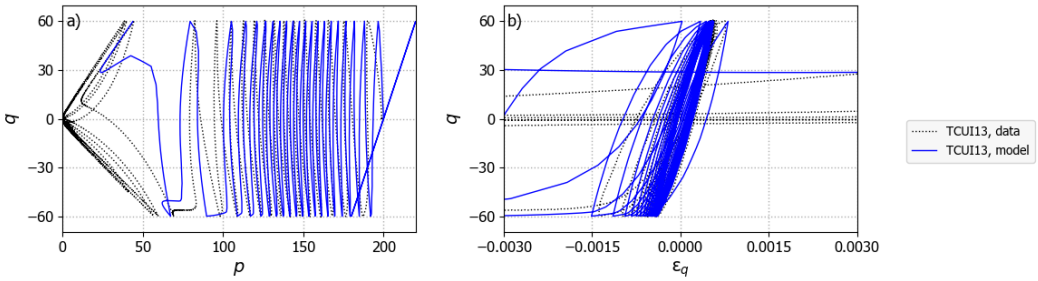


Figure 214 Modelling of TCUI13 with calibrated h_0 for the secant stiffness

In order to better capture the number of cycles to liquefaction, an iterative process where both r, in order to model well the pore pressure build-up, and h_0, to maintain a good secant stiffness, are varied, is used. For Wichtmann data, this iteration process leads to $r = 0.25$ and $h_0 = 900$, which gives the result displayed in Figure 215, where the secant stiffness is well captured, and the number of cycles to liquefaction is 17 rather than 15.

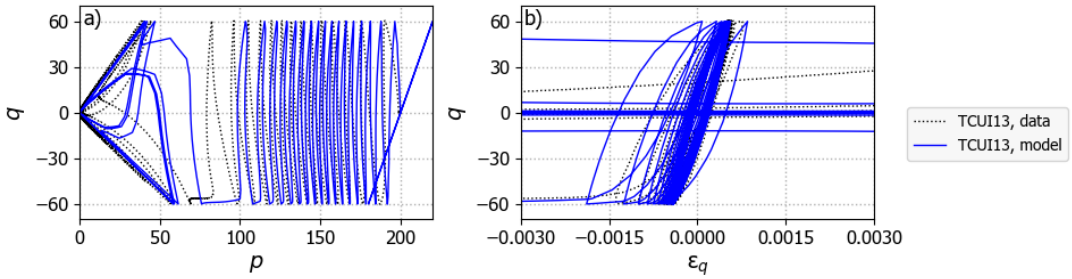


Figure 215 Modelled TCUI13 with calibrated h_0 and r to match number of cycles and secant stiffness

Fourth, the drained test on medium dense sand is simulated (c.f. Figure 216).

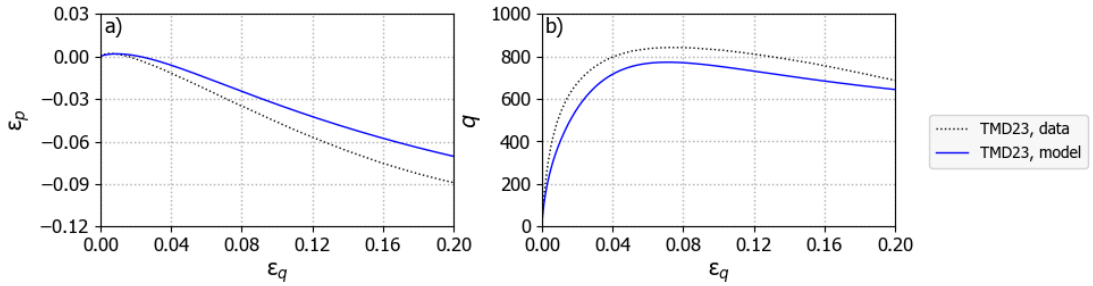


Figure 216 Simulated TMD13 after adjustment of h_0 and r

The anisotropy rate parameter and dilation are adjusted to improve the modelling of the drained test. Values $A_{max} = 35$ and $\beta_{max} = 1.05$ lead to the simulated behaviour in Figure 217.

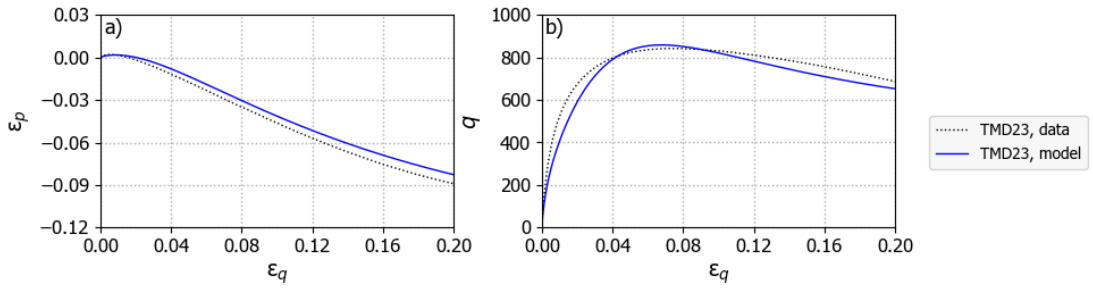


Figure 217 Simulated TMD13 after adjustment of A_{max} and β_{max}

As expected, the cyclic result is only slightly affected (c.f. Figure 218).

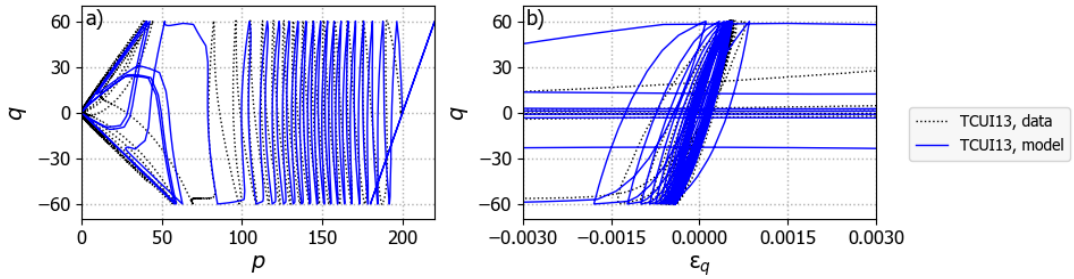


Figure 218 Simulated TCUI13 after adjustment of A_{max} and β_{max}

Fifth, the lower amplitude cyclic test is simulated. It is shown in Figure 219.

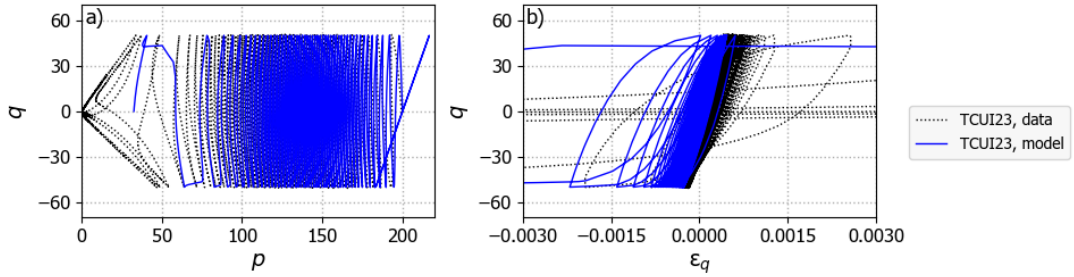


Figure 219 Simulated TCUI12 after adjustment of A_{max} and β_{max}

The simulated number of cycles to liquefaction is 51, rather than 77 for the data. The final optional step is not taken.

The obtained parameters are presented in Table 14.

k_r	g_r	m	φ_c	β_{max}	B	Γ	Δ	λ_B	λ_Δ	A_{max}	h_0	b	r
493	417	0.73	33.9	1.05	2.054	1.97	1.677	0.0059	0.0025	35	900	3	0.25

Table 14 Parameters calibrated with the trial and error method

The optimisation routine presented hereafter allows the variation of the shear hardening exponent (b), and avoids the trial and error process.

4.4. Optimisation routine

A first approximation of the maximum dilation ratio (β_{max}) and of the anisotropy rate parameter (A_{max}) can be obtained from monotonic data. The determination of the shear hardening parameters (h_0 and b) and of the consolidation exponent (r) is tedious as the three parameters are tightly intertwined and have counterbalancing effects on both cyclic and monotonic loadings (c.f. Table 9).

To achieve the calibration, an optimisation process can be used. This optimisation process uses the data of three of the previously mentioned tests on medium dense sand:

- one monotonic drained test.
- the two isotropic cyclic stress controlled undrained tests with different cyclic amplitudes.

The use of these three tests allows exploration of the whole strain range, which is essential for the determination of the hardening parameters across the yield surfaces.

The goal of the process is to optimise the five parameters β_{max}, A_{max}, r, h_0 and b. To do so, a differential evolution algorithm (Storn and Price, 1997), followed by an additional Basin-Hopping algorithm (Wales and Dove, 1997) are used in Python. Differential evolution is a global optimisation algorithm that first simulates an initial population of tests, then mutates this population by mixing the candidates, and retains the new trial candidate if it is better than the original candidate. Differential evolution is stochastic and does not use gradient methods. Basin-hopping is also a global optimisation algorithm, but with an additional local minimisation scheme which allows refinement of the minimum in an identified basin. The basin-hopping algorithm cannot be the only algorithm used because it requires too many iterations for this problem. Using the differential evolution algorithm first allows identification of one promising basin in which the basin-hopping algorithm can be run in order to optimise the minimum of this basin. The advantage of basin-hopping compared to another local minimum optimiser is that, if run for long enough, it will run trials outside of the explored basin, eventually allowing identification of a better global optimum.

The function used to evaluate the candidates is an error function f_{err} defined hereafter.

4.4.1. Error function f_{err}

The case of Wichtmann's data is taken as an example. Monotonic drained TMD13 ($v_0 = 1.824$ and $p_0 = 200$kPa), cyclic stress controlled undrained with initial drained cycle TCUI13 ($p_0 = 200kPa$ and $q_c = 60$kPa, liquefying after 15 cycles), and cyclic stress controlled undrained with initial drained cycle TCUI12 ($p_0 = 200$kPa and $q_c = 50$kPa, liquefying after 77 cycles), are used.

4.4.1.1. Drained test

For the drained test, Figure 220, points on the shear stress/strain (graph on the left) and on the volumetric/shear strain curves (graph on the right) are used. The data points used for the evaluation of the error are highlighted. For the shear stress/strain curve, the eight points span the first 20% of shear strain. For the volumetric/shear strain, three points are used: the point at which volumetric strain is null, two points at shear strain 10% and 20%.

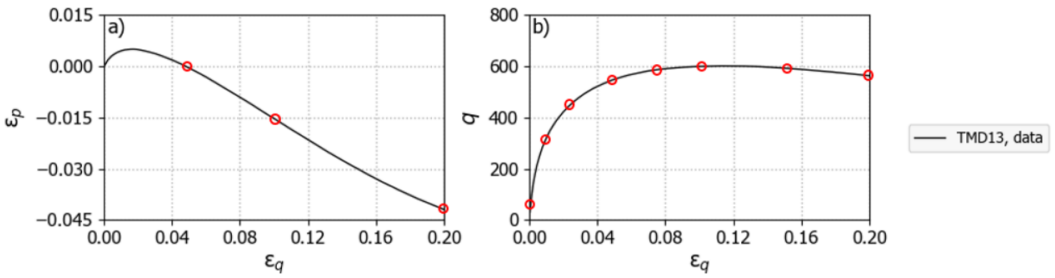


Figure 220 Data points for TMD13

Table 15 summarises the data points for TMD13, where the subscript d stands for data.

ϵ_{q_d}	0.001	0.01	0.025	0.049	0.05	0.075	0.1	0.15	0.2
q_d (kPa)	65	317	452		546	585	599	597	574
ϵ_{p_d}				0			-0.014		-0.038

Table 15 Data points of TMD13 used for the optimisation routine

The evaluation of the error on the drained test (TMD_{err}) takes the following form, where the subscript m stands for the model results:

$$TMD_{err} = \frac{1}{1+w}\left(\frac{1}{11}\left(2\times\sum_{n=1}^{3}\left(1-\left|\frac{q_m^{(n)}}{q_d^{(n)}}\right|\right)+\sum_{n=4}^{8}\left(1-\left|\frac{q_m^{(n)}}{q_d^{(n)}}\right|\right)\right)\right.$$
$$\left. + w\frac{1}{3}\left(\sum_{n=1}^{2}\left(1-\left|\frac{\epsilon_{p_m}^{(n)}}{\epsilon_{p_d}^{(n)}}\right|\right)+\left(1-\left|\frac{\epsilon_{q_m}(\epsilon_p=0)}{\epsilon_{q_d}(\epsilon_p=0)}\right|\right)\right)\right) \qquad \textit{Eq. 258}$$

The weight w allows more or less importance to be given to the dilation or to the strength and stiffness. The choice made for Wichtmann data in Eq. 258 is $w = 0.3$. The double weight on the first three shear stress measures gives more weight to the initial stiffness, which could also be done by taking more measured points at low strains.

4.4.1.2. Cyclic stress controlled undrained tests

The evaluation of the error for the cyclic stress controlled tests uses four data points per test:

- the number of cycles to liquefaction N_{liq} (15 for TCUI13, and 77 for TCUI12).
- the mean effective stress ($p_{N_{liq}}$) before liquefaction (at cycle $N_{liq} - 1$ and at $q = 0$) (75kPa after 14 cycles for TCUI13, and 50kPa after 76 cycles for TCUI12).
- the pore pressure build-up ($u_{30\%}$) after a number of cycles approximatively equal to a third of N_{liq} (50kPa after 5 cycles for TCUI13, and 62kPa after 25 cycles for TCUI12).
- the secant stiffness ($3g_{sec}$) on a cycle after approximately a third of N_{liq} (120 MPa at the 5th cycle for TCUI13, and 137MPa at the 25th for TCUI12).

These quantities are represented in Figure 221 and Figure 222.

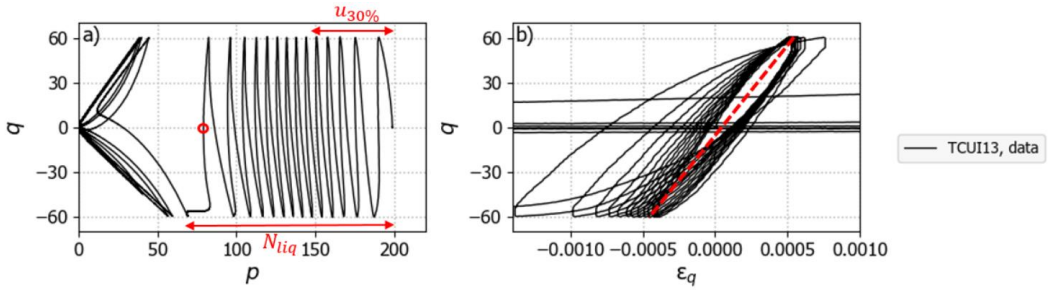


Figure 221 Data points for TCUI13

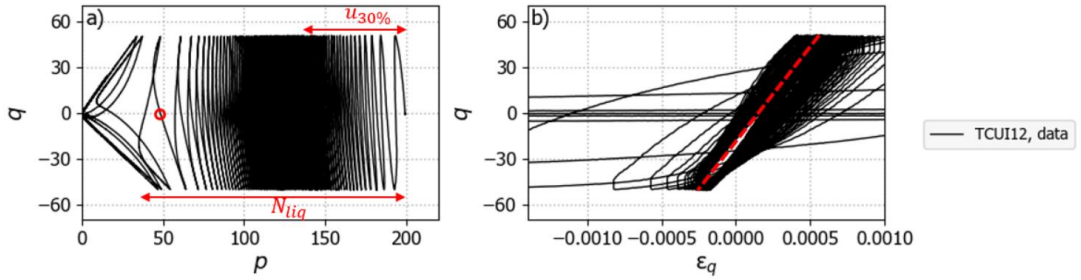


Figure 222 Data points for TCUI12

For the error evaluation, three cases are considered:

- case (1): the number of cycles needed to reach liquefaction is lower than approximately a third of the data number (5 for TCUI13, 30 for TCUI12);
- case (2): the number of cycles simulated reaches a cap value (20 for TCUI13, 100 for TCUI12) without reaching liquefaction;
- case (3): the situation between the two first cases, where liquefaction is reached before the cycles' cap value, but not in too few cycles.

In case (1), the error is only based on the number of cycles needed to reach liquefaction:

$$TCUI_{err} = 1 - \frac{N_{liq}{}_m}{N_{liq}{}_d} \qquad \textit{Eq. 259}$$

In case (2), the error is the normalised difference between the mean effective pressure reached in the cycle before liquefaction (($p_{N_{liq}}$ reached at cycle number $N_{liq} - 1$) of the data, and the mean effective pressure at the same cycle number of the simulation:

$$TCUI_{err} = 1 - \frac{p_{N_{liq}}{}_m}{p_{N_{liq}}{}_d} \qquad \textit{Eq. 260}$$

In case (3), the error is a combination of the number of cycles needed to reach liquefaction (N_{liq}), the error in mean effective pressure after a third of cycles to liquefaction ($u_{30\%}$), and the error of the secant stiffness (g_{sec}):

$$TCUI_{err} = \frac{1}{2.5}\left(\left(1 - \frac{N_{liq}{}_m}{N_{liq}{}_d}\right) + \frac{1}{2}\left(1 - \frac{u_{30\%m}}{u_{30\%d}}\right) + \left(1 - \frac{g_{sec}{}_m}{g_{sec}{}_d}\right)\right) \qquad \textit{Eq. 261}$$

The weight on the measure of pore pressure build-up is halved to stress the importance of capturing the number of cycles to liquefaction and the secant stiffness.

Errors are obtained for both cyclic tests and are noted $TCUI_{err}{}_a$ (for TCUI13 in the case of Wichtmann data) and $TCUI_{err}{}_b$ (for TCUI12 in the case of Wichtmann data).

4.4.1.3. Global error measure

The global error measure (f_{err}) is the square root of the weighted sum of squared errors:

$$f_{err} = \frac{1}{2}\sqrt{2(TMD_{err})^2 + \left(TCUI_{err}{}_a\right)^2 + \left(TCUI_{err}{}_b\right)^2} \qquad \textit{Eq. 262}$$

Here, the error on the monotonic drained test has the same weight as the sum of errors on the cyclic undrained tests. This is to counterbalance the small strain measurements (mainly the cyclic test), with the large strain measurements (mainly the drained test). The square root of the sum of squares allows prioritising homogenously low errors for the three tests.

4.4.2. Running the optimisation routine

4.4.2.1. Increment sizes

For the different tests, increment sizes should be chosen to provide sufficiently accurate results within a reasonable time for the optimisation.

For the drained test, the loading is initially stress-controlled to $q = 0.01$ with forty increments.

It is then followed by strain-controlled increments with sizes indicated in Table 16.

Starting strain	~0	0.002	0.005	0.01
Ending strain	0.002	0.005	0.01	0.2
Increment size	0.00005	0.000075	0.000125	0.00025

Table 16 Increment size for the drained test

Such a test with N =10 surfaces takes less than 3s to run in HyperDrive on a laptop with 8GB RAM.

For stress-controlled cyclic undrained tests, the numerical control of the model is in fact strain-controlled. This avoids issues just before liquefaction, where a test can show absolute shear stress decrease due to a contractive mechanism during the quarter-cycle where the absolute shear stress is only supposed to increase.

The balance between the increment size and the simulation time is essential here since the tests take longer to run than the drained test. Larger strain increments will lead to underestimation of the number of cycles to liquefaction. For example, for the simulation of TCUI12, a simulation with a strain increment size of 5×10^{-7} (size for which convergence of results is observe) leads to N_{liq}=60 cycles and takes 12min to calculate, whereas a simulation with 100 times larger increments only takes five seconds to run but predicts N_{liq}=32 cycles. An acceptable compromise is an increment size of 5×10^{-6} which takes 45s to run and delivers a N_{liq} with less than 10% error.

In conclusion, an increment strain size of 5×10^{-6} is used to simulate TCUI12, and an increment strain size of 1×10^{-5} is used to simulate TCUI13.

The simulation of TMD13, TCUI13 and TCUI12 takes on average one minute. Several hours are thus required to run a significant number of simulations leading to an adequate set of parameters.

4.4.2.2. Parameters range

4.4.2.2.1. Maximal dilation ratio: β_{max}

The lower bound of the maximal dilation ratio (β_{LB} is determined from the drained tests as indicated in 4.3.3.3. The advised range is as $\beta_{max} \in [\beta_{LB}, 1.5 \times \beta_{LB}]$. For Wichtmann data, the range of dilation ratios explored is $\beta_{max} \in [0.8,1.2]$.

4.4.2.2.2. Anisotropy rate development parameter: A_{max}

The anisotropy rate development parameter determined in 4.3.3.4 is a good approximation of the parameter, but the dilative behaviour is influenced by the variation of β_{max} and r, and to a lesser extent by the variation of h_0 and b.

The advised range is $A_{max} \in [0.5A_0, 1.5A_0]$ where A_0 is the one determined in 4.3.3.4. For Wichtmann data, this leads to the range $A_{max} \in [20,60]$.

4.4.2.2.3. Consolidation power exponent: r

The advised range for the consolidation power exponent is $r \in [0.15,0.4]$.

4.4.2.2.4. Shear hardening parameters: h_0 and b

The advised ranges for the shear hardening parameters are $h_0 \in [500,1500]$ and $b \in [2,5]$.

4.4.2.3. Results of the optimisation for Wichtmann data

4.4.2.3.1. Differential evolution

Running the differential evolution algorithm for a day, and more than 1000 simulations for an initial population of 350, leads to the minimal value $f_{err} = 11.7\%$, where $TMD_{err} = 7.1\%$, $TCUI_{err_a} = 11.6\%$ and $TCUI_{err_b} = 17.6\%$, with the parameters presented in Table 17.

k_r	g_r	m	φ_c	β_{max}	B	Γ	Δ	λ_B	λ_Δ	A_{max}	h_0	b	r
493	417	0.73	33.9	1.04	2.054	1.97	1.677	0.0059	0.0025	38.5	1448	2.92	0.194

Table 17 Optimised parameters after the differential evolution

The results for TMD13, TCUI13 and TCUI12 are shown in Figure 223, Figure 224, and Figure 225.

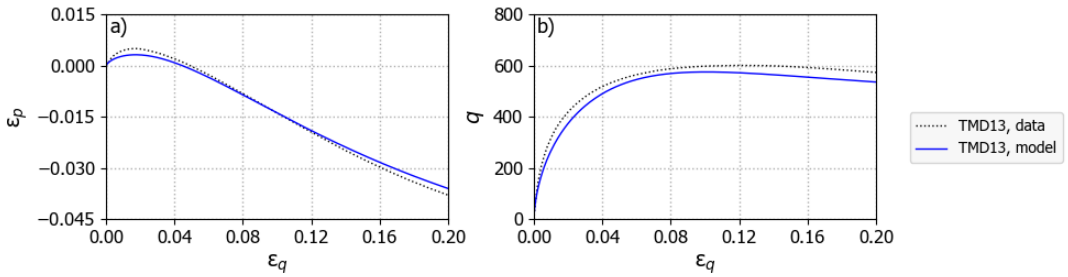


Figure 223 Drained test TMD13, data and simulation after optimisation of parameters

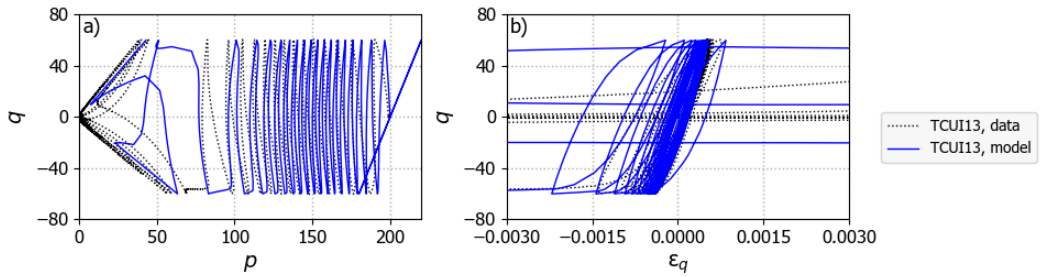


Figure 224 Undrained cyclic test TCUI13, data and simulation after optimisation of parameters

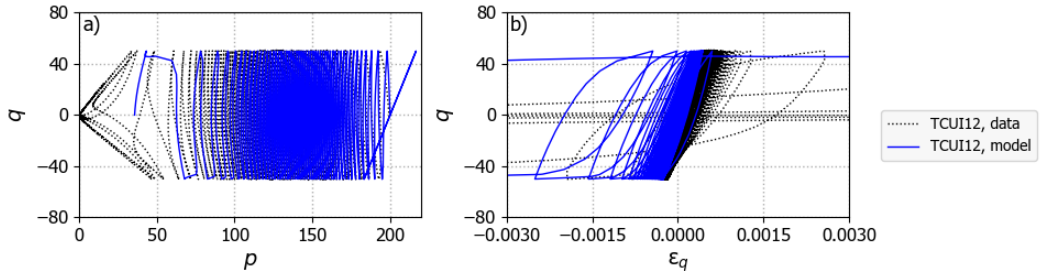


Figure 225 Undrained cyclic test TCUI12, data and simulation after optimisation of parameters

The simulated number of cycles to liquefaction for TCUI13 is 17 (instead of 15), and 51 for TCUI12 (instead of 77) for the increment sizes given in 4.4.2.1. An isolation of a few cycles allows a better observation of the simulated secant stiffness in comparison to the data for TCUI13 and TCUI12 in Figure 226 and Figure 227.

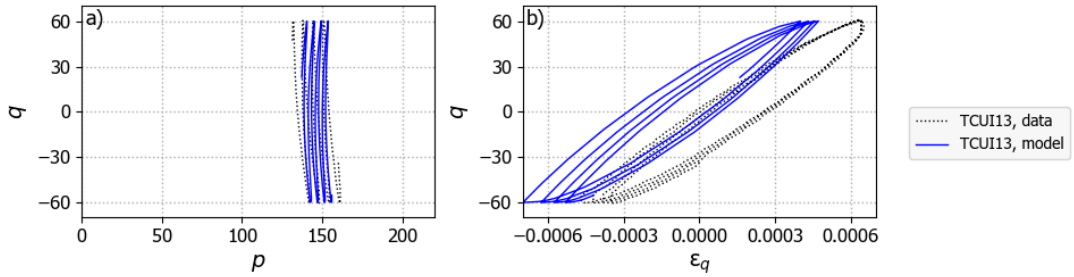


Figure 226 Isolation of the 5th cycle of TCUI13 for the data and the simulation

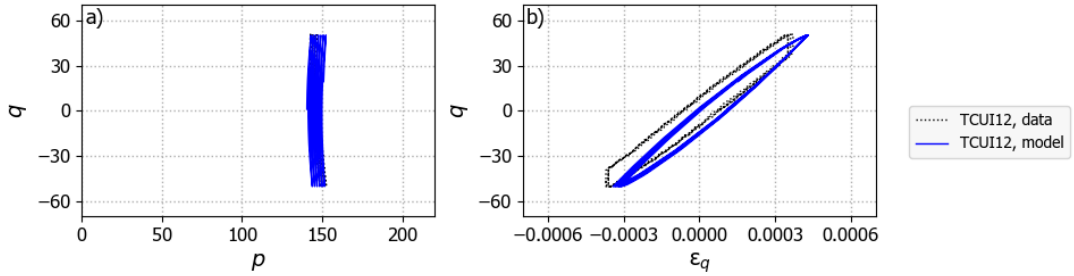


Figure 227 Isolation of the 25th cycle of TCUI12 for the data and the simulation

The secant stiffness is well captured by the model.

4.4.2.3.2. Basin-hopping

Running the basin-hopping mechanism with the optimised values given by the differential evolution mechanism as initial values lead to the parameters obtained in Table 18, for error values of: $f_{err} = 11.4\%$, where $TMD_{err} = 6.5\%$, $TCUI_{err_a} = 6.7\%$ and $TCUI_{err_b} = 19.7\%$

k_r	g_r	m	φ_c	β_{max}	B	Γ	Δ	λ_B	λ_Δ	A_{max}	h_0	b	r
493	**417**	**0.73**	**33.9**	**1.09**	**2.054**	**1.97**	**1.677**	**0.0059**	**0.0025**	**34.3**	**1216**	**3.00**	**0.206**

Table 18 Final optimised parameters

The results for TMD13, TCUI13 and TCUI12 are shown in Figure 228, Figure 229, and Figure 230.

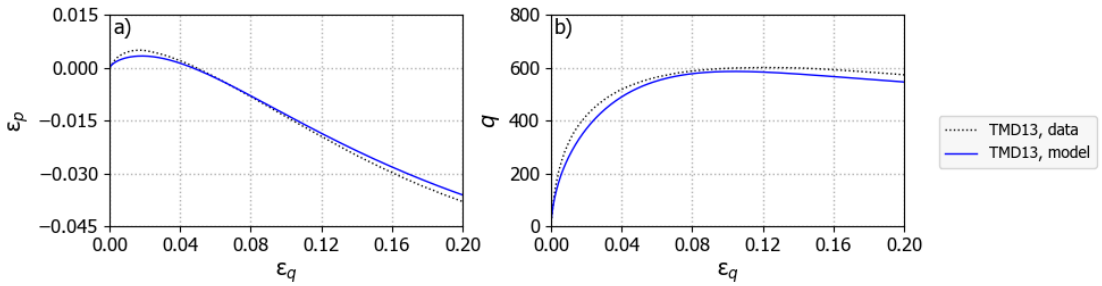


Figure 228 Drained test TMD13, data and simulation after optimisation of parameters

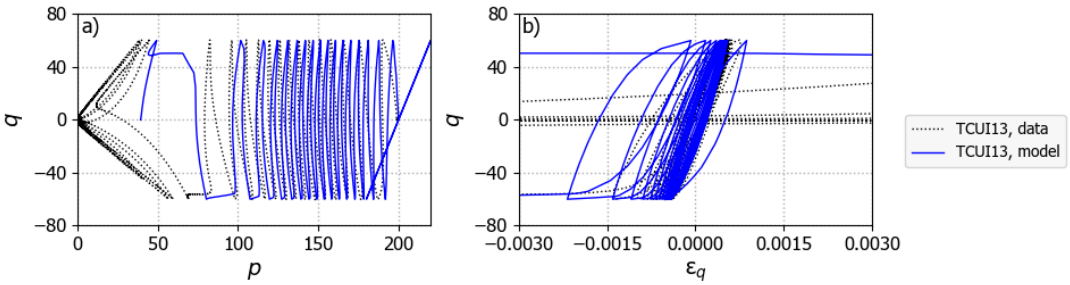


Figure 229 Undrained cyclic test TCUI13, data and simulation after optimisation of parameters

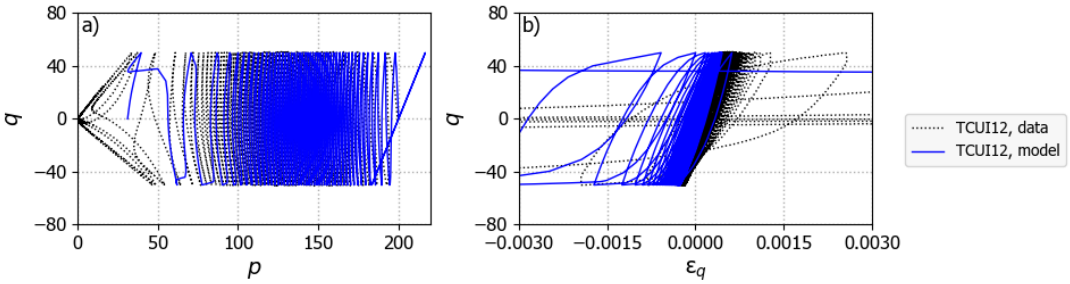


Figure 230 Undrained cyclic test TCUI12, data and simulation after optimisation of parameters

The simulated number of cycles to liquefaction for TCUI13 is 16 (instead of 15), and 48 for TCUI12 (instead of 77) for the increment sizes given in 4.4.2.1. An isolation of a few cycles allows a better observation of the simulated secant stiffness in comparison to the data for TCUI13 and TCUI12 in Figure 226 and Figure 227.

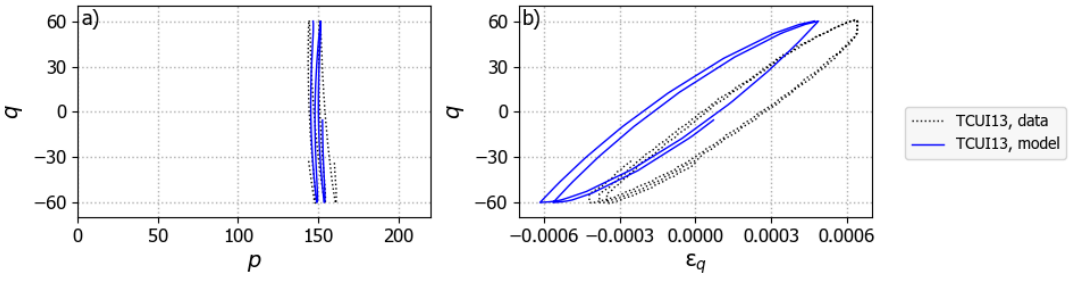


Figure 231 Isolation of the 5th cycle of TCUI13 for the data and the simulation

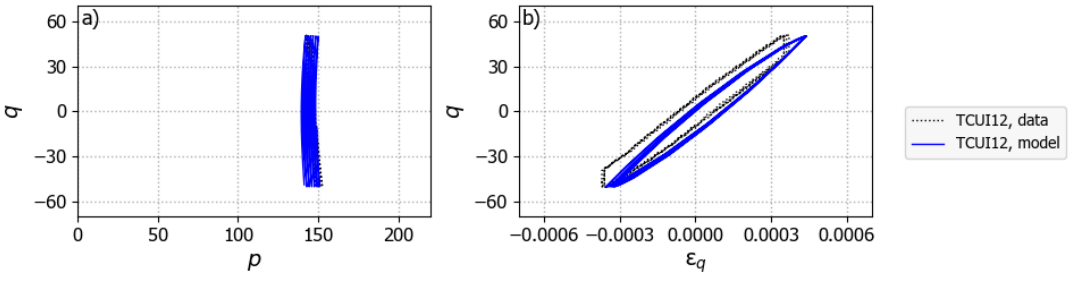


Figure 232 Isolation of the 25th cycle of TCUI12 for the data and the simulation

The secant stiffness is well captured by the model.

4.4.3. Alternative use of the optimisation routine

The optimisation routine is also a useful tool for the development of new model features. Indeed, running the optimisation process for different models allows one to estimate quantitatively the contribution of a new feature. This is especially practical for hyperplasticity, in which the mathematical structure makes addition of new features very easy. This method has been used during the development of HySand_base.

4.5. Conclusion of the calibration process

A rigorous calibration process has been presented and illustrated for Wichtmann data on Karlsruhe fine sand in this chapter.

The calibration requires the determination of the minimum and maximum specific volumes of the sand, three isotropic tests, three drained tests, and two undrained cyclic stress-controlled tests.

These eight triaxial tests, of which only two are cyclic tests, and additional specific volumes determination, allow a precise calibration of the fourteen parameters of HySand_base.

Of these fourteen parameters, nine ($\Delta, \mathrm{B}, \Gamma, k_r, g_r, m, \lambda_\mathrm{B}, \lambda_\Delta$, and φ_c) are easily and quickly determined. The five remaining parameters (β_{max}, A_{max}, h_0, b, and r) require either a trial and error process where one monotonic drained test and one cyclic undrained stress-controlled test are iteratively run, or an optimisation routine combining global and local optimisation of a function evaluating the error of the modelling for a monotonic drained test and two cyclic undrained stress-controlled tests.

In Chapter 5, the parameters obtained with the optimisation routine are used to evaluate the model against the whole database by Wichtmann.

Chapter 5 HySand_base results

HySand_base has been presented in Chapter 3, and its calibration process has been explained in Chapter 4.

This chapter highlights the strengths and weaknesses of this base model. To do this, a large number of triaxial tests are simulated with an adequate calibration:

- the complete database by Wichtmann (2021) on Karlsruhe fine sand for which the model was calibrated in Chapter 4.
- part of the database by Adamidis (2022) on Hostun sand.

A number of qualitative comparisons are also presented for other triaxial tests of interest with other sands:

- Hostun sand, for which the calibrated parameters for Adamidis data are used, with the effect of pre-loading on undrained test.
- Fuji river sand, with the effects of pre-cyclic undrained loading and pre-consolidation on subsequent cyclic undrained loading.
- Toyoura sand, with drained cyclic loading.

The model results are also critically analysed within the scope of the characteristic limitations of constitutive models for cyclic loading identified by Duque *et al.* (2022). The model is thus compared to the most advanced models currently available.

Finally, the robustness of the model is tested with a one hour pseudo-random series loading representative of a storm loading on an offshore wind turbine.

5.1. Simulation of the Wichtmann database

All tests available in the database on Karlsruhe fine sand by Wichtmann (2021) have been simulated with HySand_base with the calibrated parameters presented in Table 18 for $N = 10$ surfaces. This includes, for a variety of sand density and initial consolidation pressures, isotropic, oedometric, monotonic drained and undrained, cyclic stress-controlled undrained with isotropic or anisotropic consolidation, cyclic strain-controlled, drained with unloading and reloading, and some other original tests. HySand_base is evaluated for these tests by analysing its capacity to capture characteristic behaviours displayed by the sand both qualitatively and quantitatively.

5.1.1. Critical state line

Figure 233 presents on the left (e, p) states at large strain (25%) for undrained and drained monotonic tests on Karlsruhe fine sand by Wichtmann (2016), and extrapolates a critical state represented by the black curve. On the right, the state curve obtained by Wichtmann (dashed black) can be compared to the one given by HySand_base calibrated for Karlsruhe fine sand.

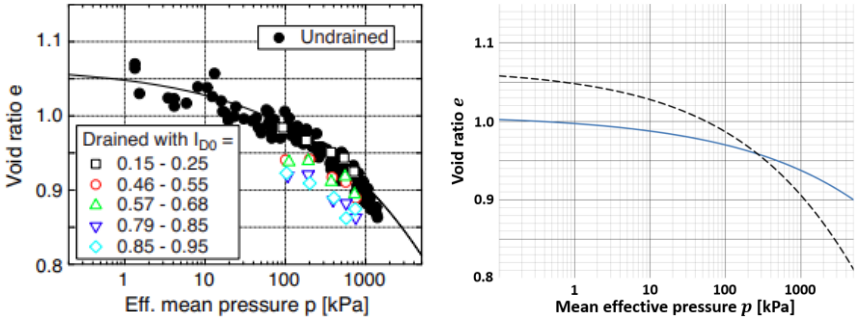


Figure 233 Critical state deduced from both drained and undrained tests (extract from Wichtmann 2016)

One can observe that the critical state line depicted by HySand_base is flatter in the $e - \ln(p)$ space than the one extrapolated by Wichtmann based on drained and undrained results. Nonetheless, the difference of void ratio in the range 1kPa to 1000kPa is inferior to 5%.

5.1.2. Stiffness degradation with strain

Figure 234 presents the degradation of shear stiffness with shear strain in HySand_base. This is based on the simulation of test TMD13 of the Wichtmann database with 10^{-7} strain increments.

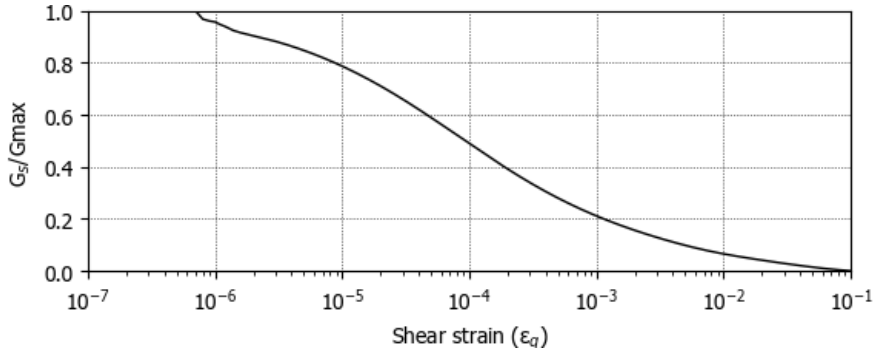


Figure 234 Modelled normalised shear stiffness degradation with shear strain, based on simulation of TMD13

This curve has an expected shape except for the non-smooth transition from the elastic plateau at very small strains, where G_s/G_{max}=1, to the progressive decrease of shear strain. This might be due to the progressive activation of a different number of surfaces at first.

5.1.3. Isotropic tests

In Figure 235, isotropic tests by Wichtmann and simulations with HySand_base are shown. Because they are part of the calibration process, these tests are well represented by the model.

However, for tests ISO1, 2 and 3, HySand_base is not able to capture the accumulation of volumetric strain after the first isotropic loading-unloading. Indeed, in HySand_base, after the first cycle, no further consolidation occurs such that the subsequent cycles are elastic.

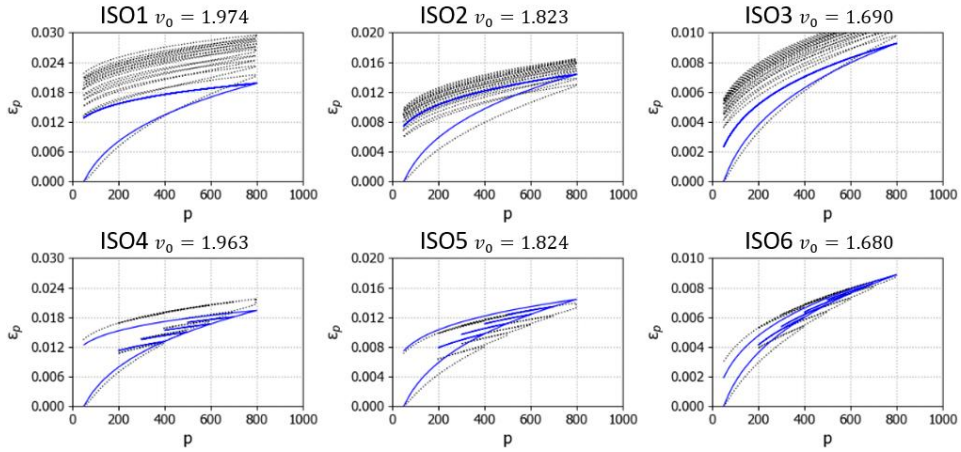


Figure 235 Isotropic tests by Wichtmann (dotted black) and simulation with HySand_base (blue)

5.1.4. Oedometric tests

If the initial consolidation pressure (p_{c0}) is initialised as for all other tests presented in this thesis ($p_{c0} = p_0 + 0.1$kPa), then the simulation of oedometric tests is poor at low stresses. This is shown for very loose sand in Figure 236. The void ratio decrease is far too important. This is due to the definition of the evolution law of the consolidation pressure (Eq. 132), in which the plastic strain produced is proportional to the many-fold increase of the consolidation pressure at the power ($1 - m$). This means that an increase of the consolidation pressure from 0.1kPa to 1kPa produces as much plastic strain as an increase from 100kPa to 1000kPa.

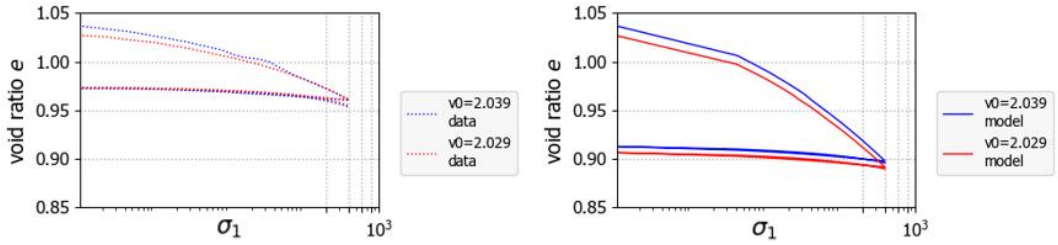


Figure 236 Oedometric tests, left: Wichtmann data, right: HySand_base for $p_{c0} = 0.2kPa$

In order to better model the oedometric behaviour to 800kPa, the initial consolidation pressure of HySand_base should be set to $p_{c0} = 5kPa$. The initial elastic behaviour better captures the evolution of void ratio/volumetric strain at low stresses than the consolidation mechanism. This is shown for the the oedometric tests by Wichtmann (OE1 to 12) in Figure 237 and Figure 238.

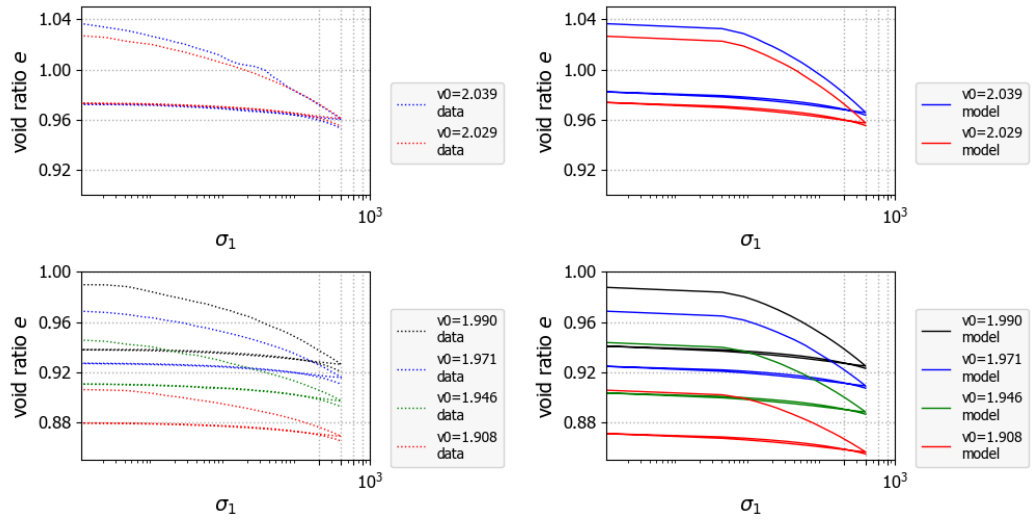


Figure 237 Oedometric tests on loose sand, left: Wichtmann data, right: HySand_base for $p_{c0} = 5kPa$

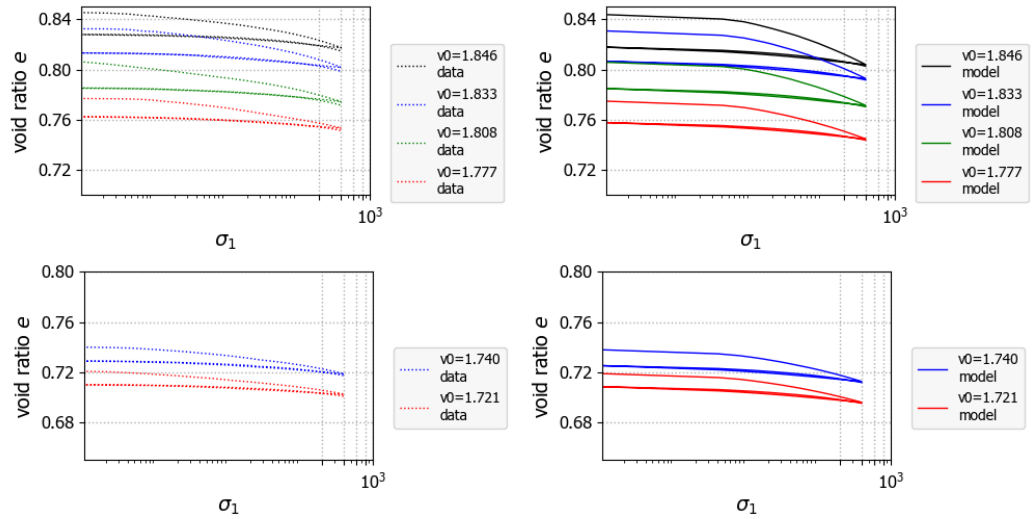


Figure 238 Oedometric tests on dense sand, left: Wichtmann data, left: HySand_base for $p_{c0} = 5kPa$

Data for Oedometric tests with progressive unloadings and reloadings are presented in Figure 239 along with simulations. HySand_base depicts well the tests, but it underpredicts the consolidation at low stress for loose sand, and overpredicts the consolidation for dense sand.

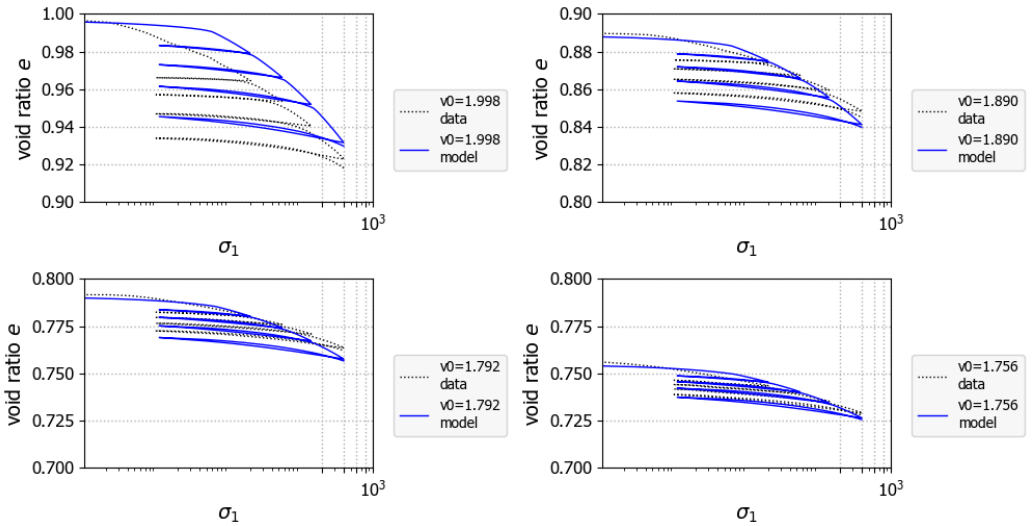


Figure 239 Cyclic oedometric tests, Wichtmann data (dotted black), and simulations with $p_{c0} = 5kPa$ *(blue)*

5.1.5. Monotonic drained tests

Wichtmann has conducted 25 normally consolidated drained tests on Karlsruhe fine sand for five groups of densities (very loose $v_0 \in [1.960,1.975]$, medium loose $v_0 \in [1.847,1.880]$, medium dense $v_0 \in [1.814,1.840]$, dense $v_0 \in [1.734,1.758]$, and very dense $v_0 \in [1.697,1.735]$), each at five different initial consolidation pressure ($p_0 \in \{50,100,200,300,400\}$[kPa]).

In the following, data by Wichtmann will be represented with dotted lines, while simulated behaviour with HySand_base will be represented with solid lines.

In Figure 240, tests TMD1 to TMD25 are plotted. Each figure represents tests with the same range of densities for different consolidation pressures.

HySand_base captures well the final capacity for all drained tests, except for the loosest one where it is underpredicted. This underprediction could come from the linear dependence of the base shear hardening factor (h_0) (c.f. Eq. 174) which implies $h_0 = 0$ for the loosest state. It might be beneficial to have $h_0 > 0$ for $v_\lambda = \mathrm{B}$.

The peak capacity is well captured across densities, except at low initial consolidation pressures where it is underpredicted, and for very loose samples where it is also underpredicted. Its increase with increasing initial consolidation pressure is well captured.

The secant stiffness at $\epsilon_q = 2\%$ seems to be well captured for high initial consolidation pressure ($p_0 \geq 200kPa$), but less well captured for lower initial consolidation where it is underpredicted. This underprediction is also visible for secant stiffness at $\epsilon_q = 0.5\%$. This is pictured for tests with $p_0 = 200kPa$ in Figure 241.

In parallel, while the maximum dilation ratios are all well captured, the speed at which dilation develops is also underpredicted for low initial consolidation pressures. This issue and the secant stiffness issue could both be improved by the dependence of the anisotropy rate development parameter (A) on mean effective stress, as discussed in Chapter 3.

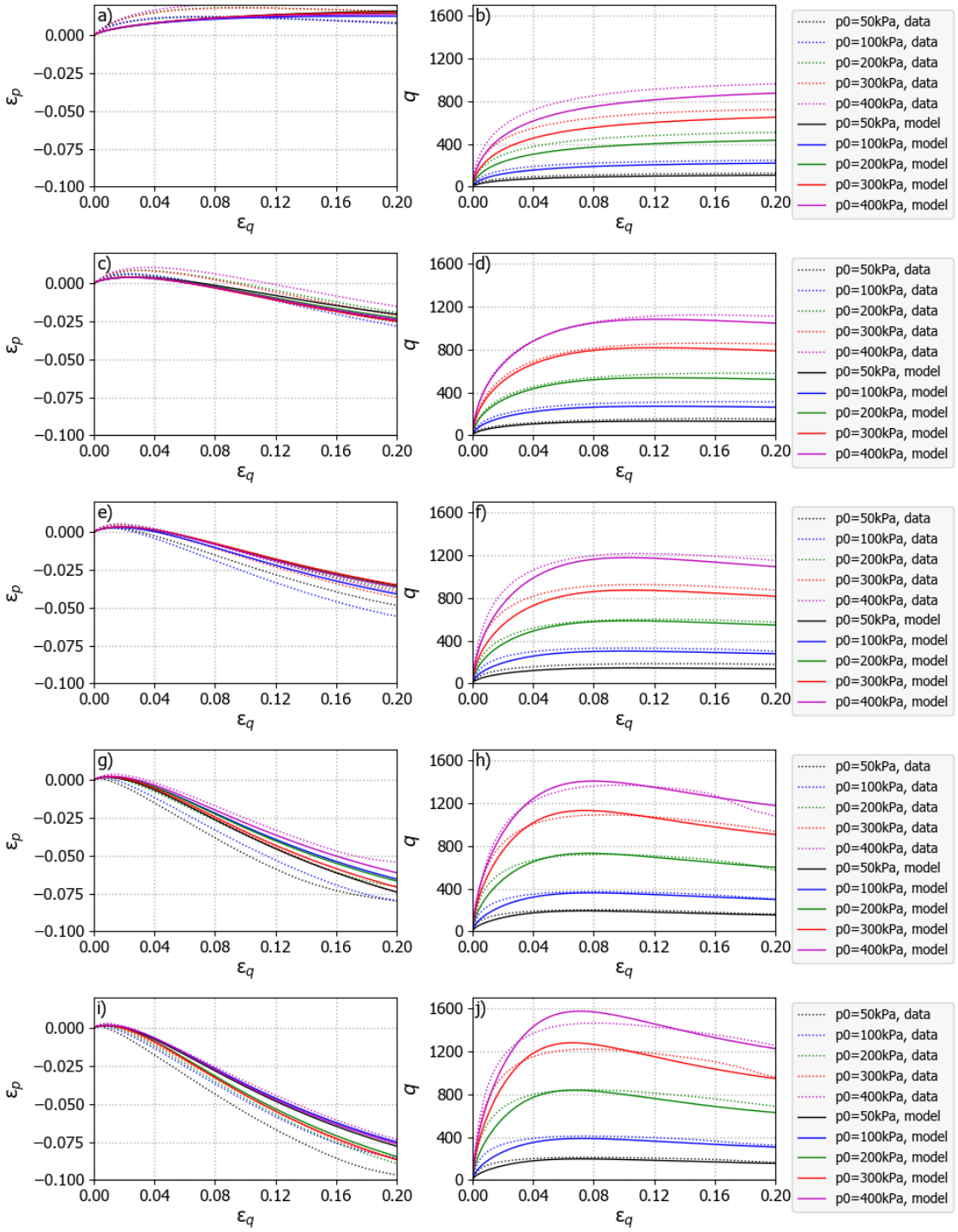


Figure 240 Drained tests on: a)b) loose ($v_0 \in [1.960,1.996]$), c)d) medium loose ($v_0 \in [1.847,1.880]$), e)f) medium dense ($v_0 \in [1.814,1.840]$), g)h) dense ($v_0 \in [1.734,1.758]$), i)j) very dense sand ($v_0 \in [1.697,1.735]$)

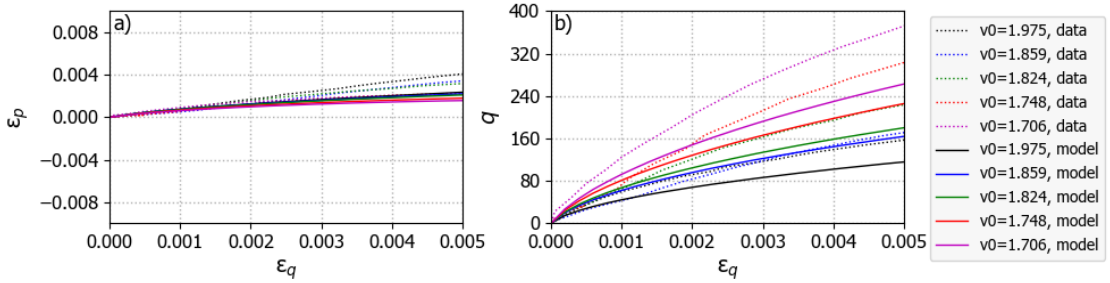


Figure 241 Drained tests with $p_0 = 200kPa$, zoom on first 0.5% deviatoric strains

5.1.6. Monotonic undrained tests

Wichtmann has conducted 12 monotonic normally consolidated undrained tests, including different densities, different initial consolidation pressures, in compression and in extension.

In the following, data is represented with dotted lines, and the simulated tests with solid lines.

5.1.6.1. Different densities

Figure 242 and Figure 243 present three tests in compression for different densities. In Figure 242, HySand_base is shown to depict well the capacity, the stiffness and the pore pressure build-up of the three tests. Small strain behaviour is well captured, as seen in Figure 243.

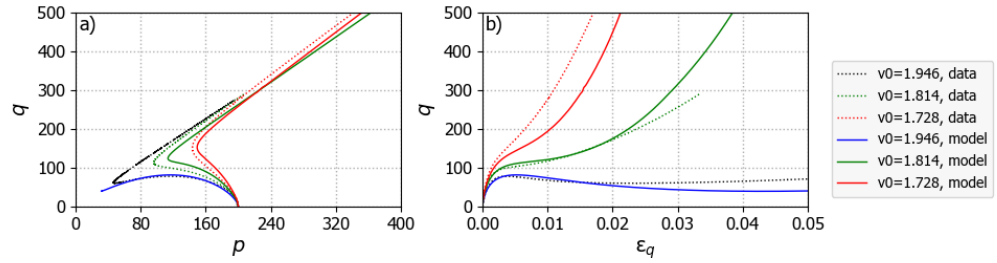


Figure 242 Monotonic undrained test TMU2,5,6 by Wichtmann, and simulations with HySand_base

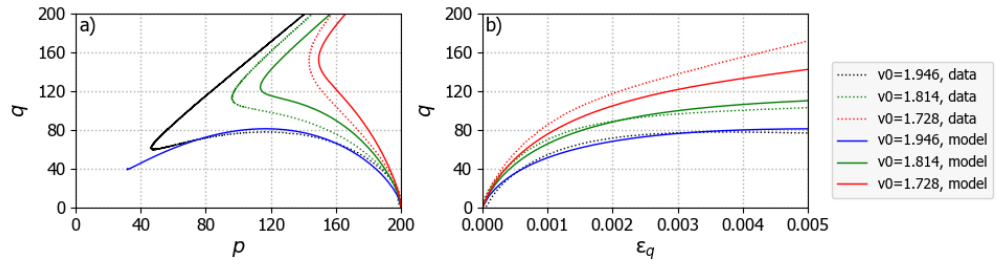


Figure 243 Zoom on monotonic undrained test TMU2,5,6 by Wichtmann, and simulations

Tests in extension (TMU8,11 and 12) are represented in Figure 244. The pore pressure build-up and the capacity and the stiffness before the dilative phase are well captured. The shear stress-strain asymptotes are however steeper in the simulation than in the data.

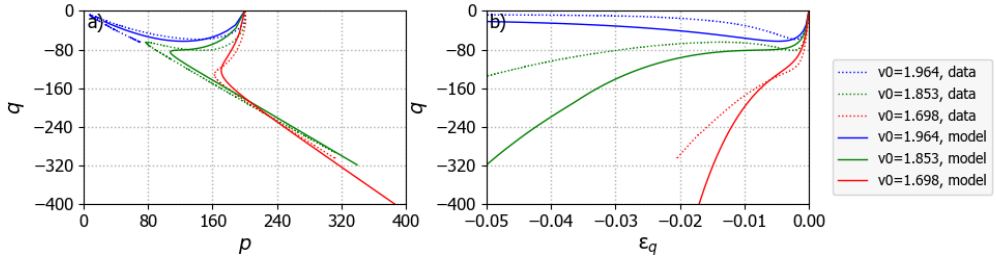


Figure 244 Monotonic undrained test TMU8,11,12 by Wichtmann, and simulations with HySand_base

5.1.6.2. Different consolidation pressures

Figure 245 and Figure 246 present tests on medium dense sand with different initial consolidation pressures. The behaviour is well captured by HySand_base, at the exception of the shear stress-strain asymptotes that are too steep, especially in the extension case.

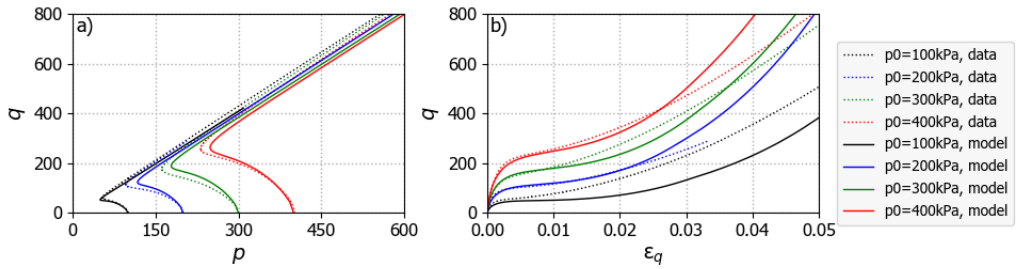


Figure 245 Monotonic undrained test TMU1,2,3,4 by Wichtmann, and simulations with HySand_base

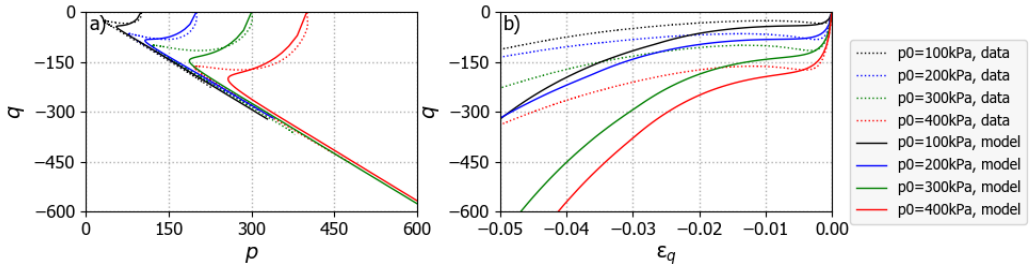


Figure 246 Monotonic undrained test TMU7,8,9,10 by Wichtmann, and simulations with HySand_base

5.1.6.3. Other preparation techniques

All tests presented so far, have been made on samples prepared by pluviating air-dried sand through a funnel. Wichtmann has also conducted undrained tests on loose samples prepared by moist tamping, which behave differently from the air-pluviated samples. These tests and simulation with HySand_base are represented in Figure 247 to Figure 249. Note that the test on very loose sand ($v_0 = 2.038$) with $p_0 = 500kPa$ cannot be run with HySand_base because this specific volume is not within the bound of HySand_base at $p_0 = 500kPa$. Indeed, the theoretical loosest specific volume at $p_0 = 500kPa$ is $v_0 = 2.030$ according to Eq. 179.

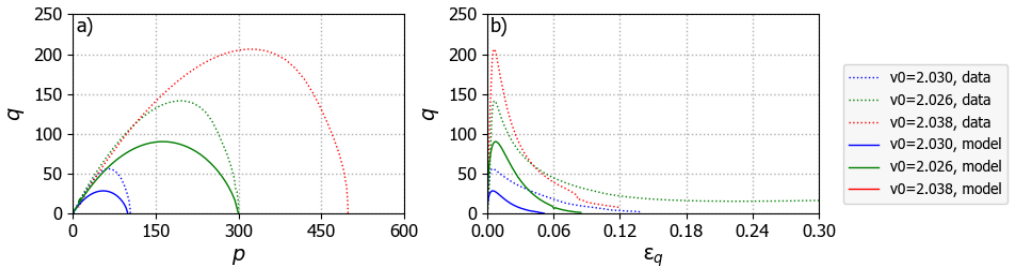


Figure 247 Test data for TMU-MT1,4,7 and simulation with calibrated HySand_base

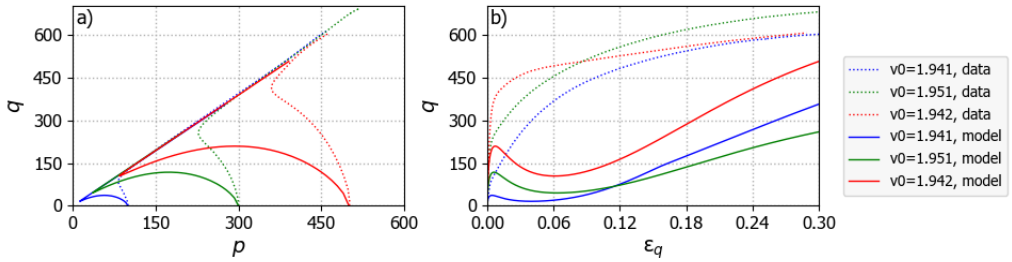


Figure 248 Test data for TMU-MT2,5,8 and simulation with calibrated HySand_base

Moist-tamping preparation apparently leads to less pore pressure build-up. HySand_base generates too much pore pressure, which leads to lower capacities before the dilative phase. Also,

in Figure 248 and Figure 249, as the samples are sheared to larger strains the stiffness decreases. On the contrary, the stiffness progressively increases with HySand_base.

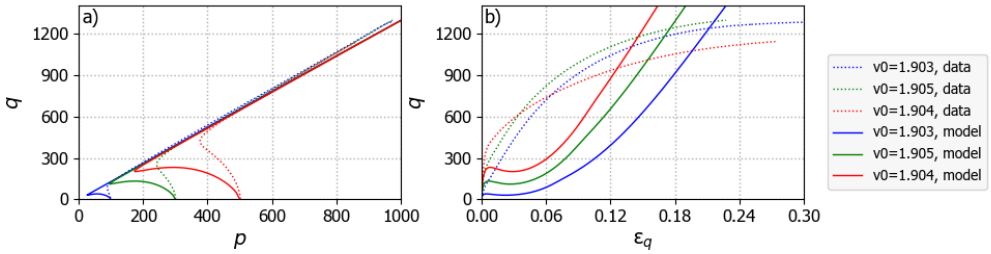


Figure 249 Test data for TMU-MT3,6,9 and simulation with calibrated HySand_base

In order to improve the simulation of the pore pressure build-up and by extension of the capacity before the dilative phase, the consolidation exponent (r) can be increased. Increasing r means that the consolidation provokes less contraction upon shearing at lower p. This increase could be justified to represent the impact of moist tamping on the crushing of the sand particles. Figure 250 to 250 present the data and simulation for $r = 1$. The simulation of the stress path is better. But the simulated strain asymptotes pictured in Figure 251 and Figure 252 are still wrong.

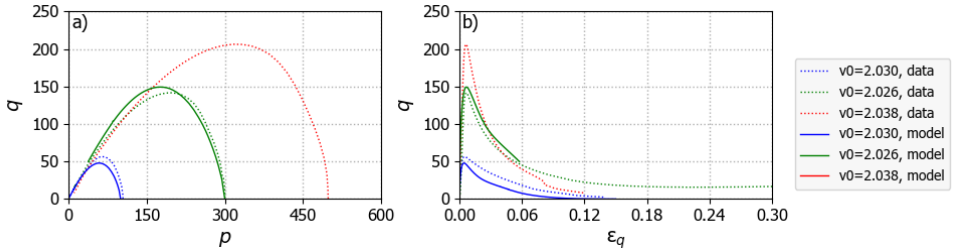


Figure 250 Test data for TMU-MT1,4,7 and simulation with calibrated HySand_base with $r = 1$

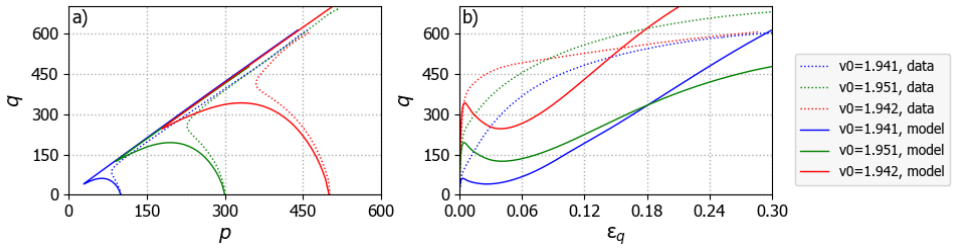


Figure 251 Test data for TMU-MT1,4,7 and simulation with calibrated HySand_base with $r = 1$

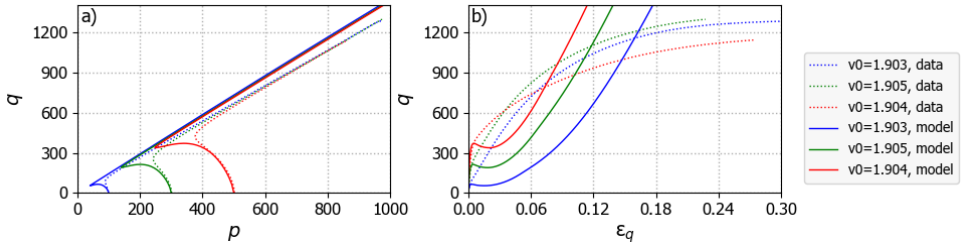


Figure 252 Test data for TMU-MT1,4,7 and simulation with calibrated HySand_base with $r = 1$

Thus, calibrated parameters are only suitable for tests conducted with the same preparation technique used for the calibration tests. It is therefore essential that the preparation technique is relevant to the application. Here, pluviation appears relevant for offshore sands.

5.1.7. Cyclic stress controlled tests

In the following, data by Wichtmann is pictured in black, and all simulations are pictured in blue.

5.1.7.1. Isotropic consolidation

In Figure 253 to Figure 255, tests without an initial drained cycle are represented. The criteria to stop the simulation is $|\epsilon_q| > 2.5\%$, except for the dense sand where it was stopped after 10 similar loops in stress space because shear strain saturates at approximately 1.5% in this case.

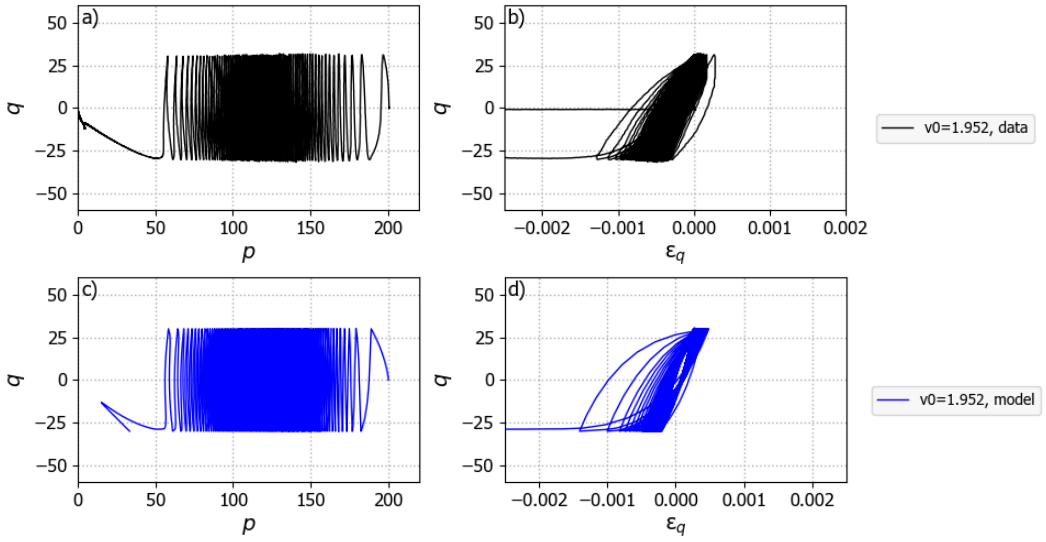


Figure 253 a)b) Test data of TCUI1, c)d) Simulation with HySand_base

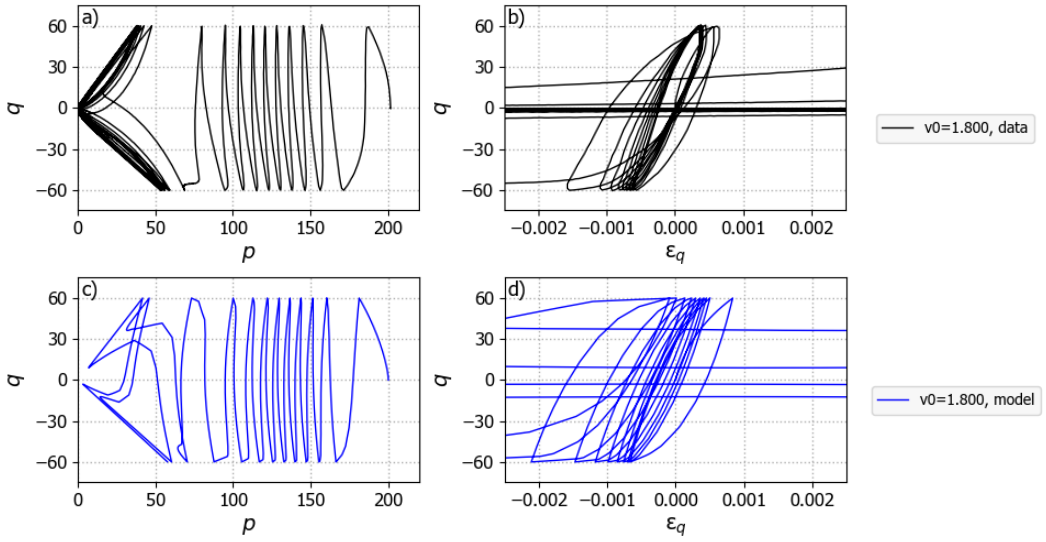


Figure 254 a)b) Test data of TCUI7, c)d) Simulation with HySand_base

The simulations of TCUI1,7 and 17 give an excellent depiction of the characteristic rate at which pore pressure builds-up: an initial important build-up on the first cycle, then a progressive slowdown until approximately 125kPa, before a new acceleration of the build-up before reaching liquefaction. The pick-up at low p is well captured for loose and medium dense sand, however, for the dense sand, the acceleration of pore pressure build-up appears too strong.

The stiffness of the loops is also well captured by HySand_base.

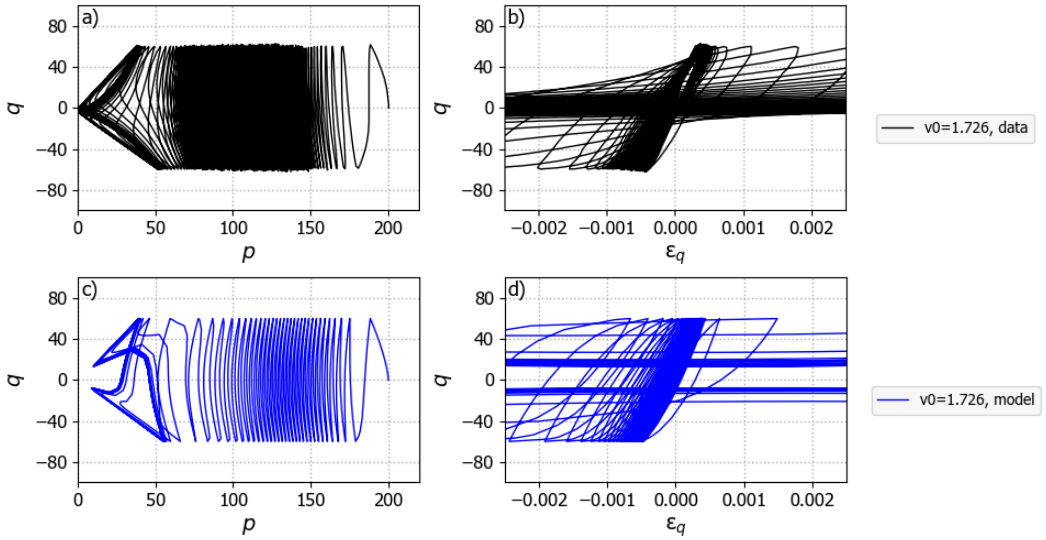


Figure 255 a)b) Test data of TCUI17, c)d) Simulation with HySand_base

The number of cycles to liquefaction (c.f. Table 19) is well approximated for tests TCUI1 and TCUI7, however, the comparison of the data and simulation in Figure 255 shows that HySand_base underpredicts the number of cycles to liquefaction of the dense test (TCUI17).

HySand_base does not capture the characteristic butterfly-shaped loops at low p. For medium dense and dense sand, HySand_base presents loops which do not reach $p = 0$. This could be because the contractive behaviour upon load reversal is not strong enough.

Most of the Wichtmann undrained cyclic stress-controlled tests are preceded by an initial drained test of same amplitude. Figure 256 to Figure 258 picture tests TCUI5, 13, and 21 with such an initial drained test, and same initial consolidation $p_0 = 200kPa$ and approximatively the same initial specific volume as tests TCUI1, 7 and 17.

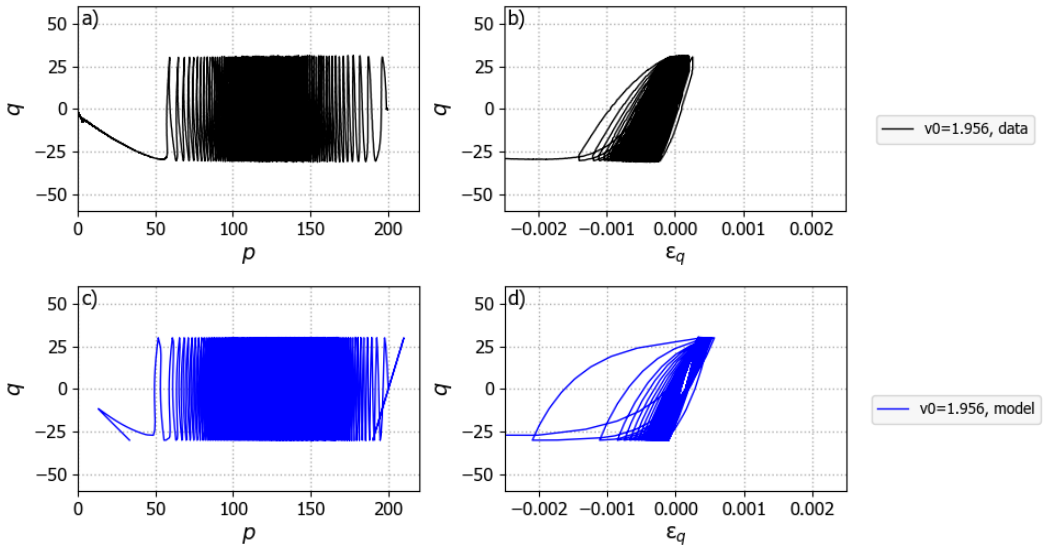


Figure 256 a)b) Test data of TCUI5 (first drained cycle is not pictured), c)d) simulation with HySand_base

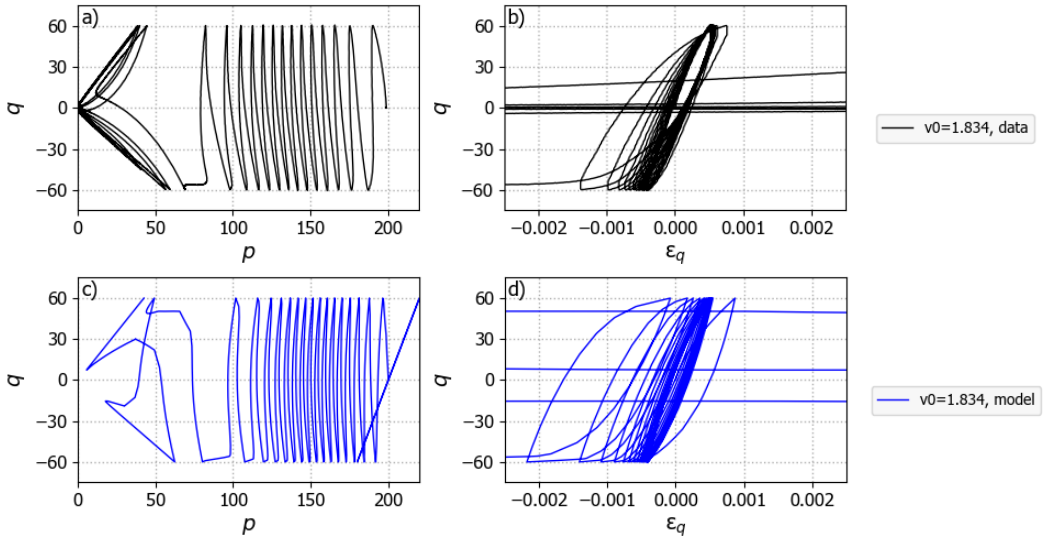


Figure 257 a)b) Test data of TCUI13 (first drained cycle is not pictured), c)d) Simulation with HySand_base

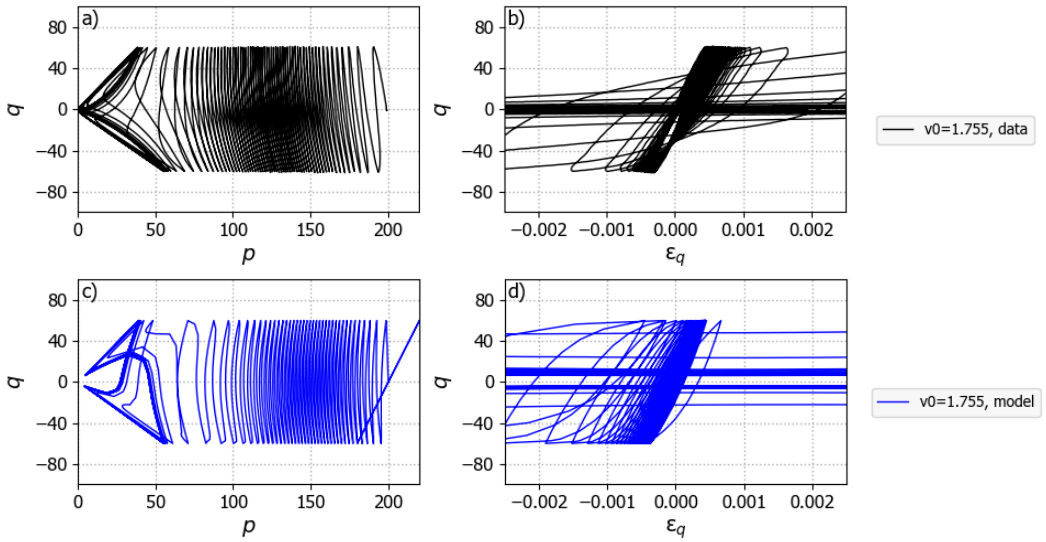


Figure 258 a)b) Test data of TCUI21 (first drained cycle is not pictured), c)d) Simulations with HySand_base

Two characteristic traits of the tests with an initial drained cycle compared to the tests without one are the decreased pore pressure build-up during the first cycles, and the higher numbers of cycles necessary to reach liquefaction (with an exception for TCUI21 with 61 cycles, compared to 185 cycles for TCUI17). These two phenomena are well captured by HySand_base because the first drained cycle pushes the consolidation pressures at which the yield surfaces close, leading to less consolidation-born contraction during the cyclic undrained loading.

All isotropically consolidated undrained cyclic stress-controlled tests by Wichtmann were simulated. Table 19 lists the number of cycles before liquefaction for the data (N_{liq} data) and the simulation (N_{liq} model). The criteria used for initial liquefaction of the simulations is the first encountered of shear strain larger than 2.5% or entering almost stationary stress loops.

Note that tests TCUI1, 7 and 17 are the only one without an initial drained cycle.

TCUI	1	2	3	4	5	6	7	8	9	10	11
v_0	1.952	1.962	1.95	1.963	1.956	1.964	1.8	1.822	1.799	1.826	1.843
p_0(kPa)	200	100	100	100	200	300	200	100	100	100	200
q_c/p_0	0.15	0.15	0.2	0.25	0.15	0.15	0.3	0.2	0.25	0.3	0.2
N_{liq} data	72	87	15	5	86	144	11	249	100	15	146
N_{liq} model	94	93	22	9	130	137	10	89	40	13	102
Error (%)	30	7	46	80	51	-5	-9	-74	-60	-13	-30
TCUI	12	13	14	15	16	17	18	19	20	21	22
v_0	1.814	1.834	1.847	1.809	1.817	1.726	1.76	1.762	1.757	1.755	1.745
p_0(kPa)	200	200	300	300	300	200	100	100	100	200	300
q_c/p_0	0.25	0.3	0.2	0.25	0.3	0.3	0.3	0.4	0.5	0.3	0.3
N_{liq} data	77	15	257	110	24	185	54	15	6	61	269
N_{liq} model	48	16	118	61	24	32	26	7	4	38	53
Error (%)	-38	7	-54	-45	0	-83	-52	-53	-50	-38	-80

Table 19 Summary of the undrained cyclic stress-controlled tests by Wichtmann

The evolution of the number of cycles required to reach liquefaction with variation of density and amplitude is well captured qualitatively. A comparison with other advanced constitutive models is undertaken later in the chapter (5.4.3). Figure 259 presents a graphical comparison of the numbers of cycles required to reach liquefaction by the model against the data.

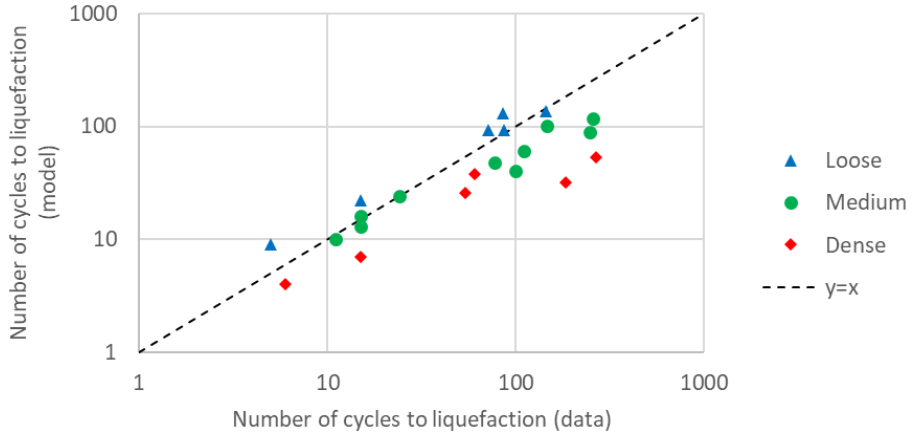


Figure 259 Number of cycles to liquefaction for isotropic consolidated cyclic stress-controlled tests: data vs model

On average, simulations of loose sand tests overpredict (+35%) the number of cycles to initial liquefaction, while they underpredict it (-32%) for medium dense sand, and dense sand (-59%). Thus, on average, the pore pressure build-up is too large for dense samples, and not large enough for loose samples. Equivalently it means that contraction is too strong for dense samples, and too weak for loose samples. Two situations can arise: first, the shear strain and the volumetric strain can both be poorly predicted; second, the shear strain can be well predicted but the volumetric strain poorly.

To examine the issue, one can zoom on a few cycle of tests on dense sand (Figure 260) and loose sand (Figure 261) to compare the shear stiffness of the data and of the simulations.

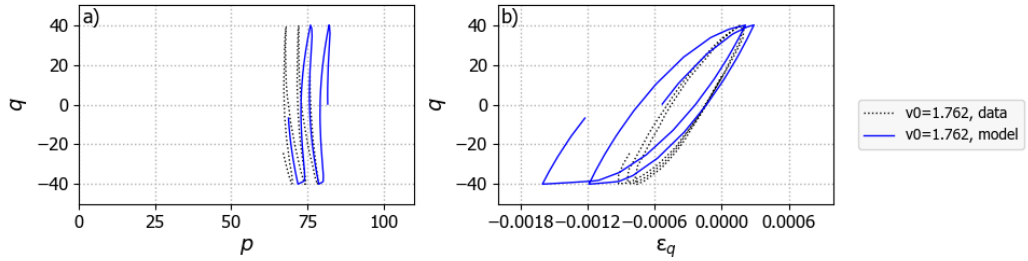


Figure 260 Zoom on a few cycles of TCUI19

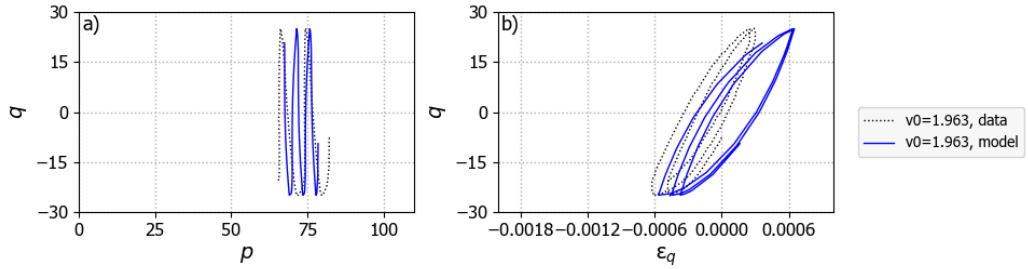


Figure 261 Zoom on a few cycles of TCUI4

For test TCUI19, the simulated secant stiffness is too low, such that an increase of the shear hardening moduli $H^{(n)}$ for denser samples could be appropriate. This would provide a stiffer response, which would lead to less plastic contraction, and thus to less pore pressure build-up.

For test TCUI4, the secant stiffness is also too low. Increasing the stiffness would lead to even less pore pressure build-up, such that an increase of the shear hardening moduli does not appear to be a good solution. To increase the pore pressure build-up, a lower r would be required, while the shear hardening moduli would have to be increased in order to predict the stiffness well.

5.1.7.2. Anisotropic consolidation

For all simulations, except for TCUA12, the initial anisotropic stress (p_0, q_0) is reached via a ramp of slope one in stress space: the simulation starts at $(p_0 - q_0, 0)$ and then a drained loading is used to reach the test initial condition (p_0, q_0). This is not pictured in the following figures to allow a better comparison with the data. For TCUA12, a ramp of slope 2 is used. Table 20 presents the properties of these tests.

TCUA	1	2	3	4	5	6	7	8	9	10
v_0	1.945	1.812	1.727	1.817	1.820	1.825	1.916	1.732	1.841	1.806
p_0 [kPa]	300	300	300	300	300	300	300	300	100	200
q_0/p_0	0.5	0.5	0.5	0.5	0.5	0.5	0.5	0.5	0.75	0.75
q_c/p_0	0.4	0.4	0.4	0.2	0.3	0.4	0.4	0.4	0.25	0.25
TCUA	11	12	13	14	15	16	17	18	19	
v_0	1.819	1.827	1.814	1.840	1.808	1.844	1.810	1.824	1.808	
p_0 [kPa]	300	200	200	200	200	200	200	200	200	
q_0/p_0	0.75	1.0	0.75	0.5	0.3	0.25	-0.25	-0.25	-0.5	
q_c/p_0	0.25	0.3	0.3	0.3	0.3	0.3	0.3	0.2	0.2	

Table 20 Summary of cyclic stress-controlled undrained tests with anisotropic consolidation by Wichtmann

Figure 262 to Figure 264 present three tests without a prior drained cycle for different initial densities. Note that for the other simulations (TCUA4 to 19), the initial drained loading is simulated with HySand_base, but this is not pictured to allow a better comparison with the data.

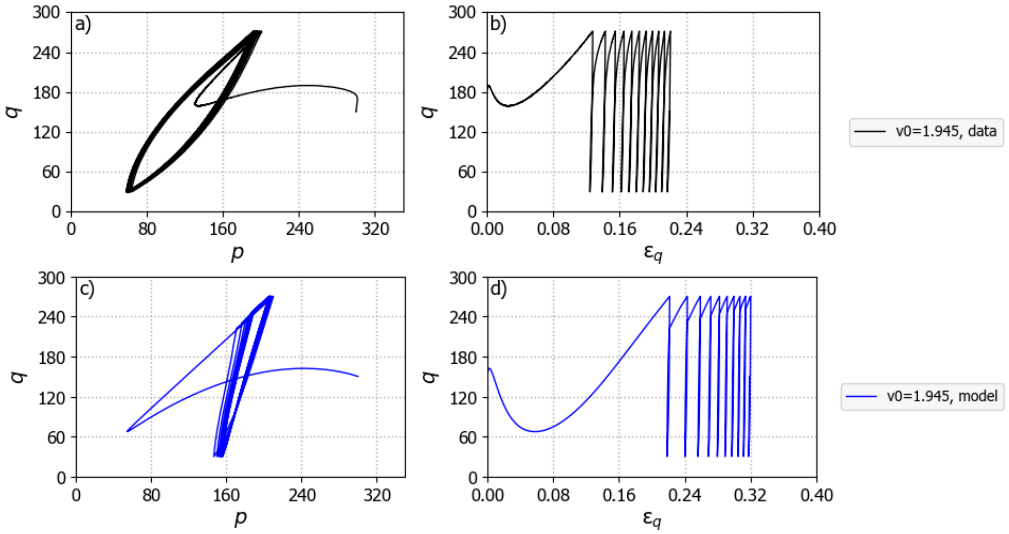


Figure 262 a)b)Test data of TCUA1, c)d) Simulation with HySand_base

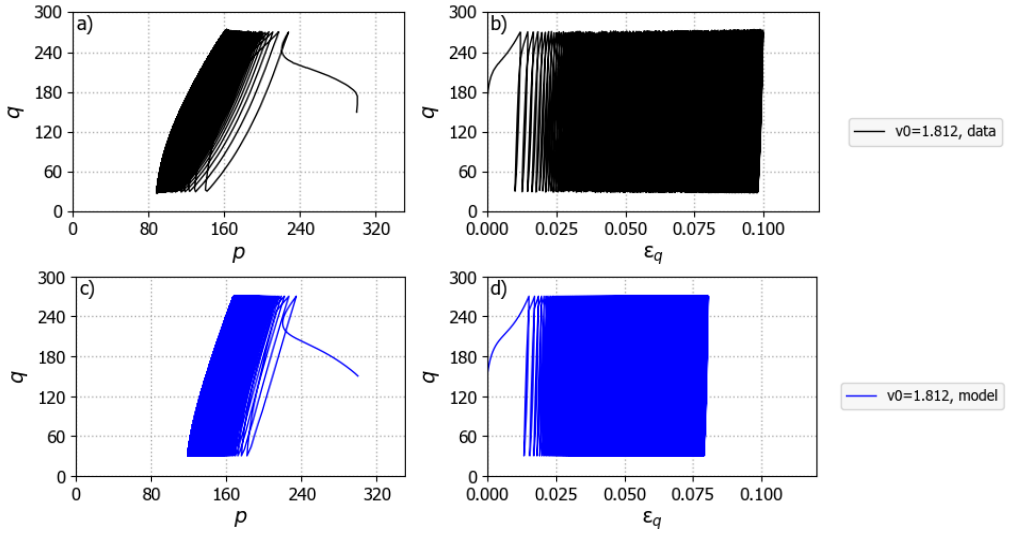


Figure 263 a)b) Test data of TCUA2, c)d) Simulation with HySand_base

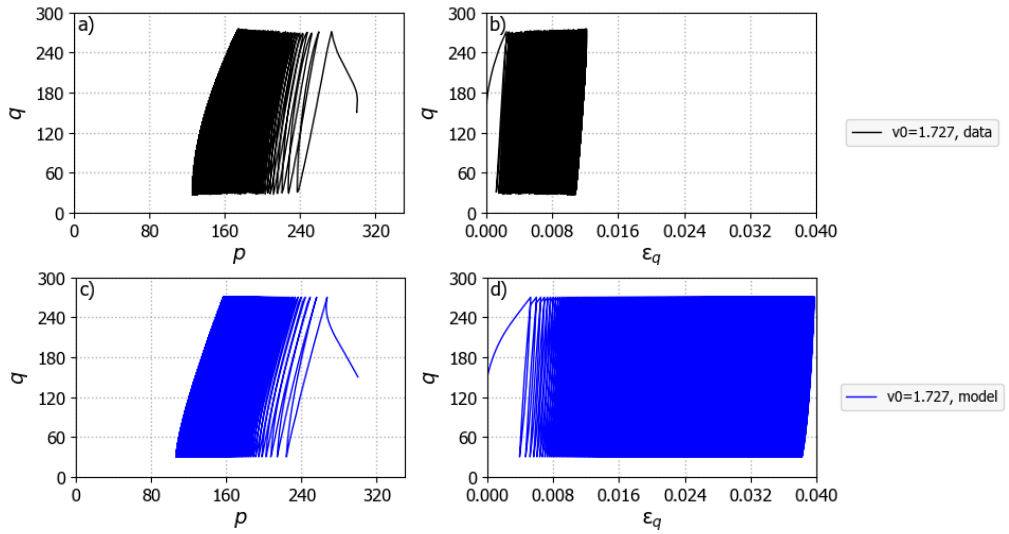


Figure 264 a)b) Test data for TCUA3, c)d) Simulation with HySand_base

HySand_base captures well the decrease in ratcheting the denser the sample is. It also captures well the progressive diminution of the ratcheting with cycles. As for other cyclic tests, HySand_base does not capture well the pore pressure build-up (the contraction) upon load reversal, for example in Figure 262 c), the simulated cycle is less inclined than the data.

Test TCUA4, shown in Figure 265, is conducted on medium dense sand, like TCUA2, but with a smaller cyclic amplitude, leading to less ratcheting. This is also captured by HySand_base.

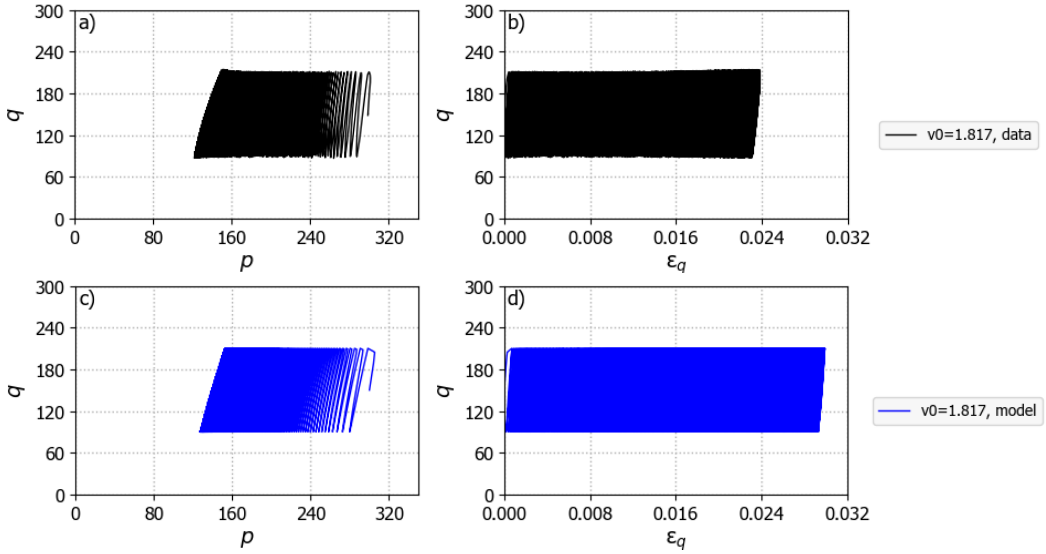


Figure 265 a)b) Test data for TCUA4, c)d) Simulation with HySand_base

Figure 266 shows test TCUA6 which is identical to test TCUA2 pictured in Figure 263 except for the initial drained cycle. The only noticeable impact of this difference is on the first few cycles after the drained cycle for which the pore pressure build-up and the deviatoric strain are smaller.

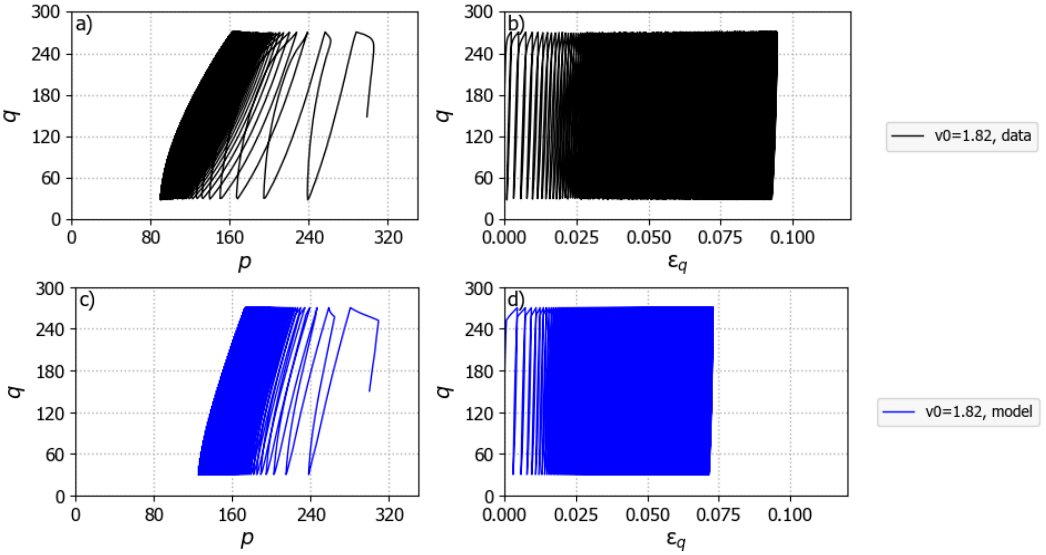


Figure 266 a)b) Test data of TCUA6, c)d) Simulation with HySand_base

In the previous figures of this section, only one-way tests have been shown. Such one way tests do not liquefy (reach $p = 0$), even when the loading reduces to $q = 0$, such as TCUA15 shown

in Figure 267. An interesting behaviour that is well captured by HySand_base for test TCUA15 is that initially the ratcheting rate is very small, before it increases, before slowing down again.

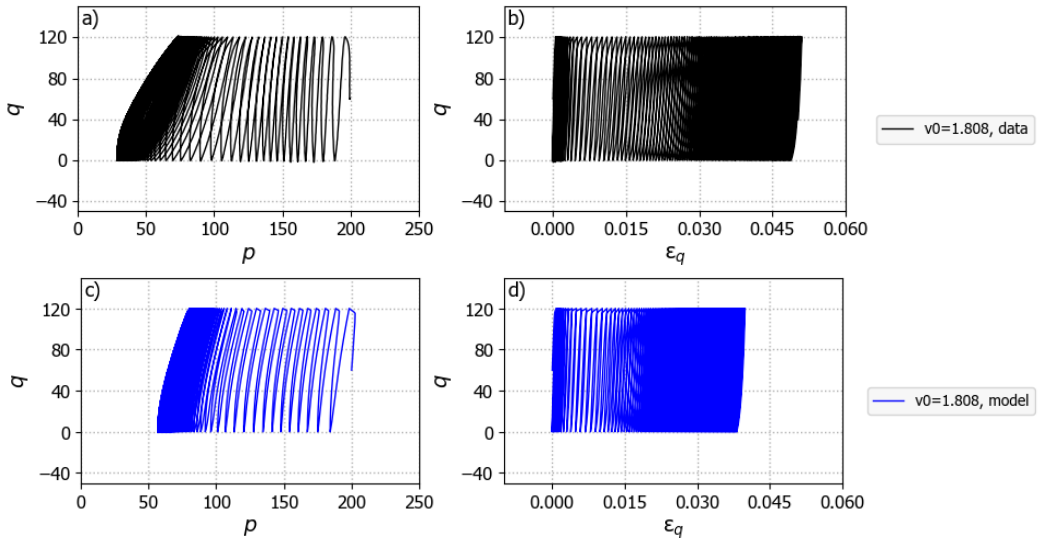


Figure 267 a)b) Test data of TCUA15, c)d) Simulation with HySand_base

According to the data by Wichtmann, partial two-way tests reach liquefaction, even with a much smaller amplitude on one side. Figure 268 pictures the data for such a test (TCUA17), as well as the simulation with HySand_base, which fails to capture this phenomenon. More generally, HySand_base seems not to capture so well the tests on the extension side.

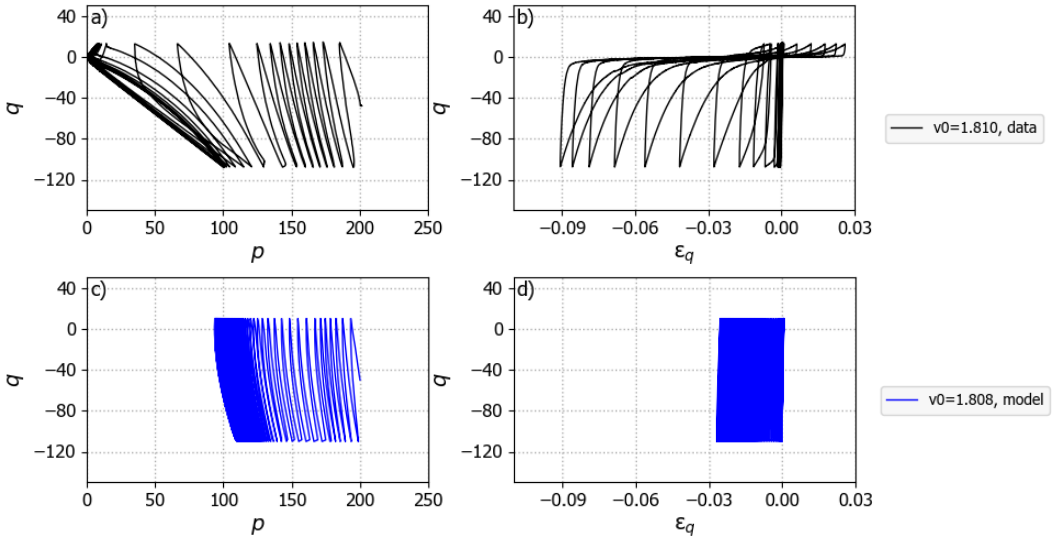


Figure 268 a)b) Test data of TCUA17, c)d) Simulation with HySand_base up to 100 cycles

Figure 262 to Figure 268 allow a qualitative comparison of the stress paths and the ratcheting. Ratcheting is an essential metric for offshore wind turbine foundations, and it is thus important that constitutive models simulate it well at the laboratory scale. In order to quantitatively compare the ratcheting between the data and the simulations, the ratcheting as a function of the cycle number is shown in Figure 269 for all TCUA tests except TCUA1.

The same number of cycles as in the experiment were simulated, except for tests TCUA7, 16, 17 and 18 where the simulation was pushed to 100 cycles.

As explained before, the tests on the extension side (TCUA17,18 and 19) are not so well simulated. Nonetheless, the ratcheting simulated for tests on the compression side matches the data well, with the exception of a few tests such as TCUA3, 8. In conclusion, HySand_base seems able to capture ratcheting for one-way cyclic tests on the compression side.

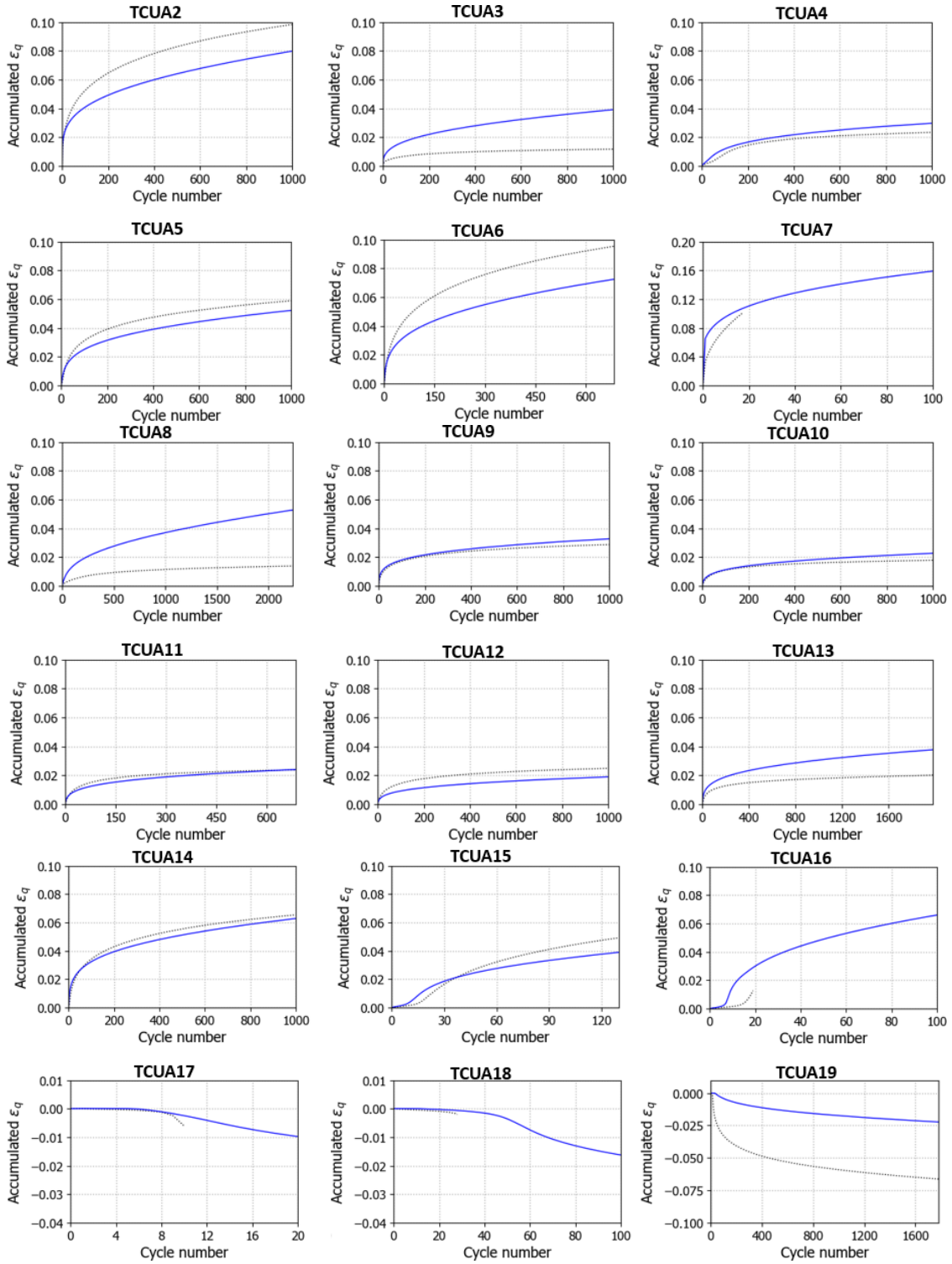


Figure 269 Ratcheting for TCUA tests: data (dotted black), simulation (blue)

5.1.8. Cyclic strain controlled tests

Wichtmann has conducted 23 cyclic strain-controlled tests, of which 14 have a small strain amplitude ($\leq 0.08\%$), and 9 a large strain amplitude ($\geq 0.5\%$). Some of these tests were conducted on anisotropically consolidated samples. In HySand_base, the anisotropic consolidation to (p_0, q_0) was modelled with a ramp of slope one in stress space starting from $(p_0 - q_0, 0)$, except for TCUE8, where a ramp of slope two was used. These ramps are not shown in the graphs, and care was taken to adjust the initial specific volume to compensate the densification due to the initial drained anisotropic consolidation.

In the following, all tests by Wichtmann are shown in black, while simulations are shown in blue.

5.1.8.1. Small strain

All small strain tests (except TCUE1 and 3), begin with an initial drained cycle, which is not pictured in the data, but is shown for the simulations. Table 21 summarises these tests.

TCUE	1	2	3	4	5	6	7	8	9	10	11	12	13	14
v_0	1.812	1.789	1.854	1.829	1.794	1.910	1.746	1.805	1.802	1.844	1.836	1.834	1.788	1.806
p_0 [kPa]	200	200	200	200	200	200	200	200	200	200	200	50	100	300
p_0/q_0	0.75	0.75	-0.5	0.75	0.75	0.75	0.75	1.15	0	-0.5	-0.75	0.75	0.75	0.75
$\epsilon_q^{amp} \times 10^{-4}$	6	6	6	4	8	6	6	6	6	6	6	6	6	6

Table 21 Summary of test TCUE1 to 14

Tests TCUE1 to 14 were simulated with HySand_base, stopping either after 100 cycles, or when the mean effective stress reached 5% of its initial value. Only the stress paths are pictured.

Figure 270 present tests TCUE1, 2 which shows that the first drained cycle leads to a reduction of pore pressure build-up during the first cycles, which is well captured by HySand_base.

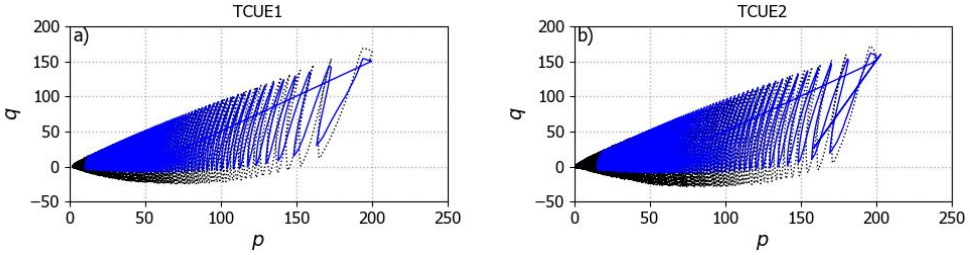


Figure 270 a) Test TCUE1, b) Test TCUE2, data and simulation

Figure 271 presents tests TCUE4 and 5, with different strain amplitudes. A larger amplitude leads to more pore pressure build-up, and a larger shear stress amplitude. The first phenomenon is well captured by the model, but the amplitude of shear stress is underpredicted for larger strains.

Figure 272 represents tests TCUE6 and 7, with different initial densities. The denser the sample is, the larger the shear stress amplitude is. This is qualitatively but not quantitatively captured.

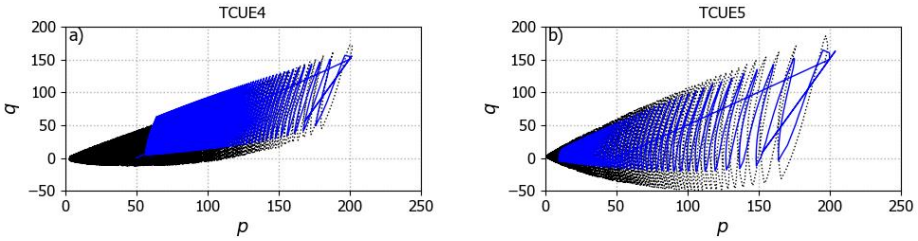


Figure 271 a) Test TCUE4, b) Test TCUE5, data and simulation

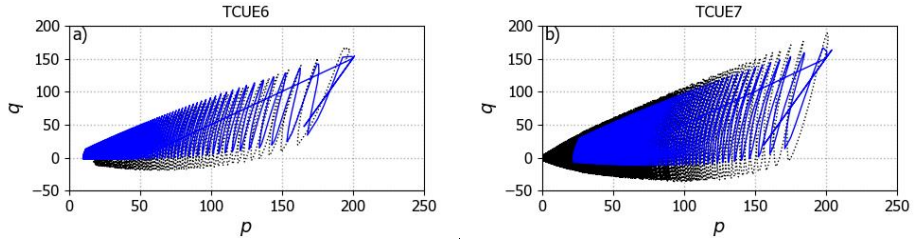


Figure 272 a) Test TCUE6, b) Test TCUE7, data and simulation

Figure 273 presents the well-modelled tests TCUI8 and 11, with different initial stress ratios.

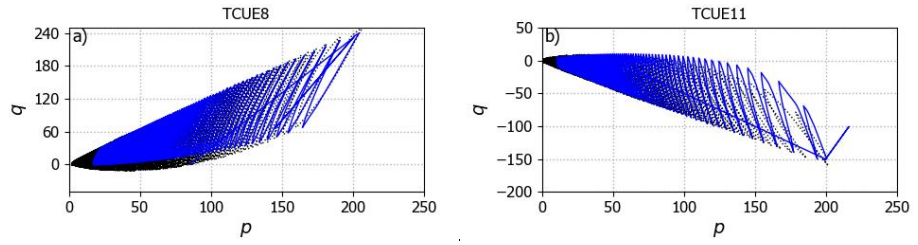


Figure 273 a) Test TCUE8, b) Test TCUE11, data and simulation

Figure 274 presents TCUE12 and 14, with different initial mean effective stresses. The prediction of the stress path of TCUE14 ($p_0 = 300$kPa) is better than for TCUE12 ($p_0 = 50kPa$). For TCUE12, HySand_base predicts too little stress amplitude, which would mean that the surfaces produce too much plasticity. At the same time, HySand_base predicts too little pore pressure build-up, hinting an underprediction of the bulk modulus at low mean effective stress.

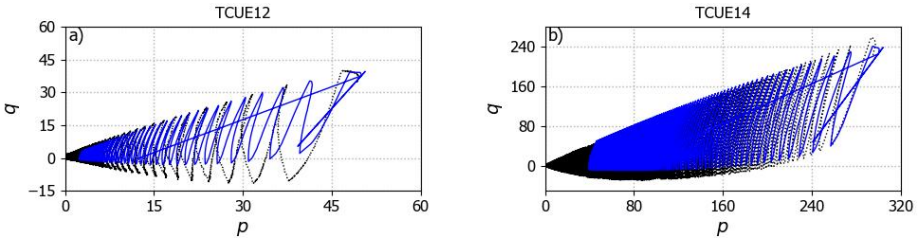


Figure 274 a) Test TCUE12, c)d) Test TCUI14, data and simulation

Figure 270 to 272 show that HySand_base models well the stress path, and that the rate at which pore pressure builds-up seems adequate. A better observation of the rate of pore pressure build-up is possible in Figure 275. For the test data, Wichtmann has monitored the average mean effective stress for each cycle. For the simulation, the value at the start of each cycle is monitored.The evolution of p for TCUE3, 6, 9, 10 and 13 is extremely well captured. For the other tests, HySand_base captures the trend well but overpredicts the rate at which p decreases.

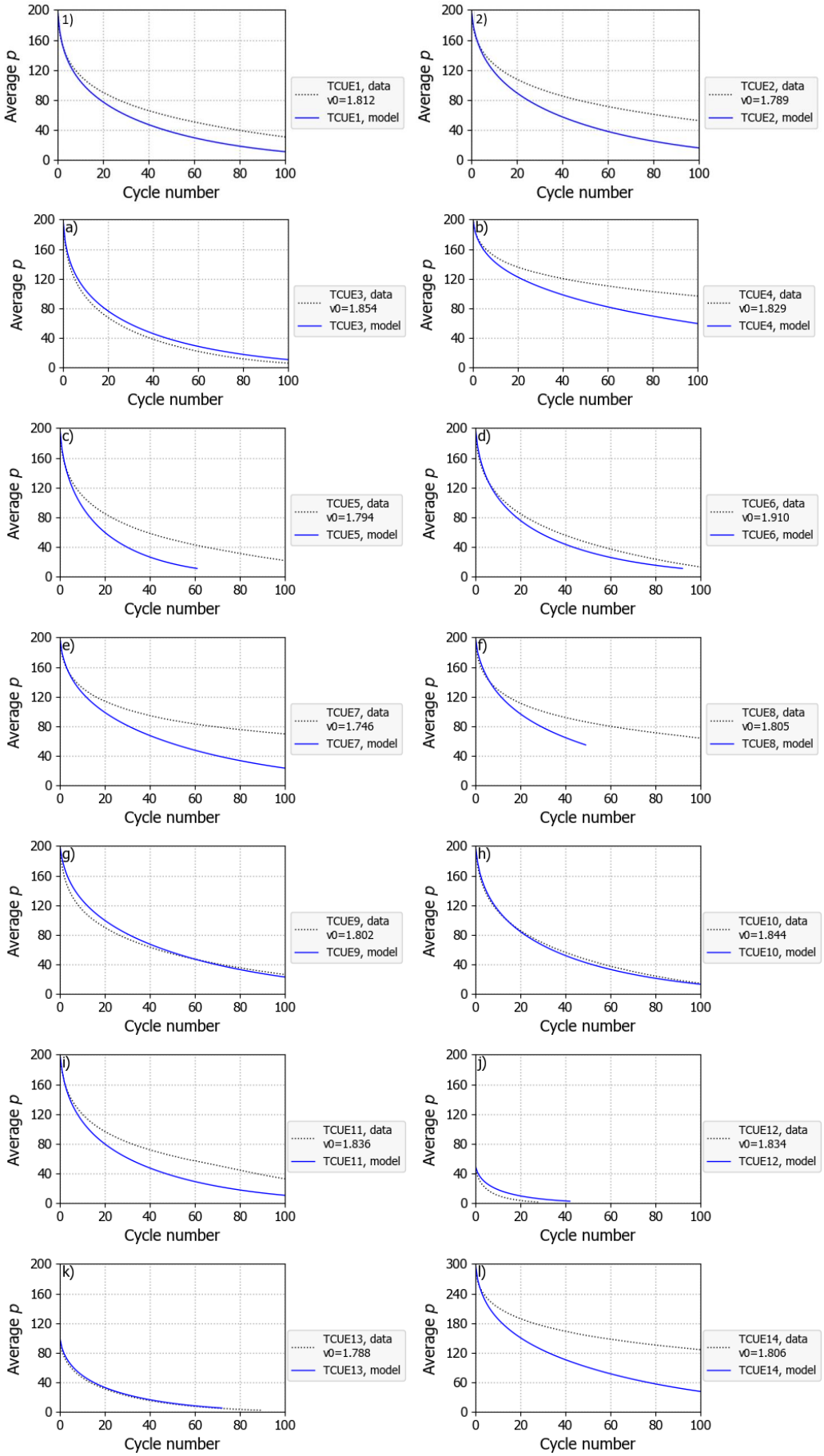


Figure 275 Average mean effective stress vs number of cycles 1) TCUE1, 2)TCUE2, a) TCUE3, b)TCUE4, c) TCUE5, d) TCUE6, e) TCUE7, f) TCUE8 , g) TCUE9, h) TCUE10 i)TCUE11, j) TCUE12, k) TCUE13, l)TCUE14 (with a change of scale)

5.1.8.2. Large strain

Table 22 summarises the properties of tests with large strain amplitudes.

TCUE	15	16	17	18	19	20	21	22	23
v_0	1.944	1.804	1.698	1.812	1.814	1.816	1.827	1.686	1.674
p_0 [kPa]	200	200	200	100	700	200	200	100	700
p_0/q_0	0	0	0	0	0	0	0.75	0	0
ϵ_q^{amp}(%)	1	1	1	1	1	0.5	1	1	1

Table 22 Properties of cyclic strain controlled tests with large strain amplitudes

Figure 276 presents tests TMCUE15, 16 and 17, with differential initial densities. HySand_base captures well the decrease of pore pressure build-up with increased density. However, the model does not capture well the large pore pressure build-up upon load reversal. This is especially problematic for dense sand (TMCUE17) where the simulation does not reach liquefaction.

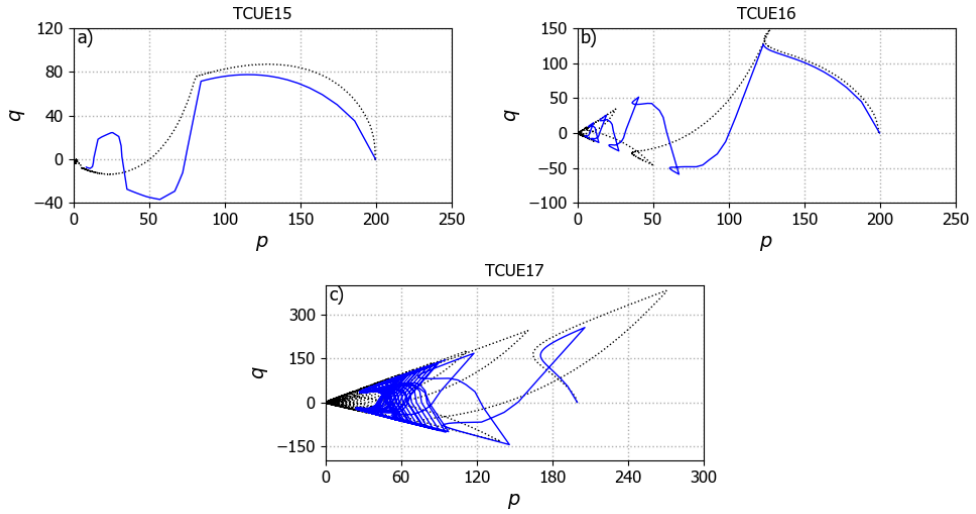


Figure 276 a) Test TCUE15, b) Test TCUE16, c) Test TCUE17, data and simulation

Figure 277 shows test TCUE20 (similar to TCUE16 but with a smaller amplitude). The model captures the absence of dilative phase, but overestimates the number of cycles to liquefaction.

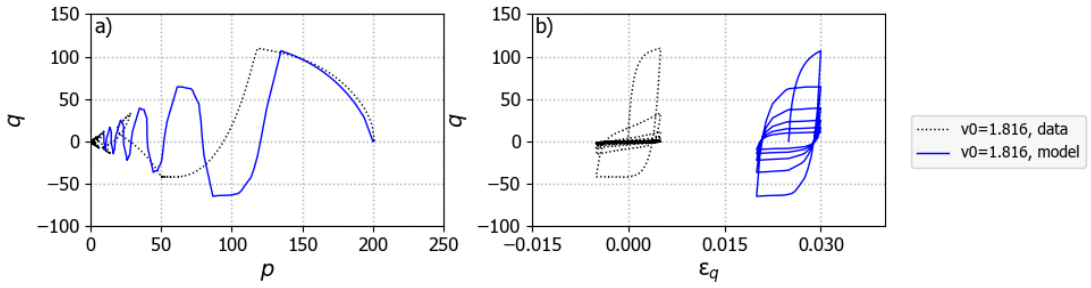


Figure 277 Test TCUE20, data and simulation

Figure 278 present tests with varying initial consolidation pressures: TCUE18, 19 for medium sand, and TCUE22 and 23 for dense sand. While the test data tends to show little difference for normalised stress paths between tests with different initial consolidation pressures, HySand_base tends to generate less contraction for higher consolidation pressures.

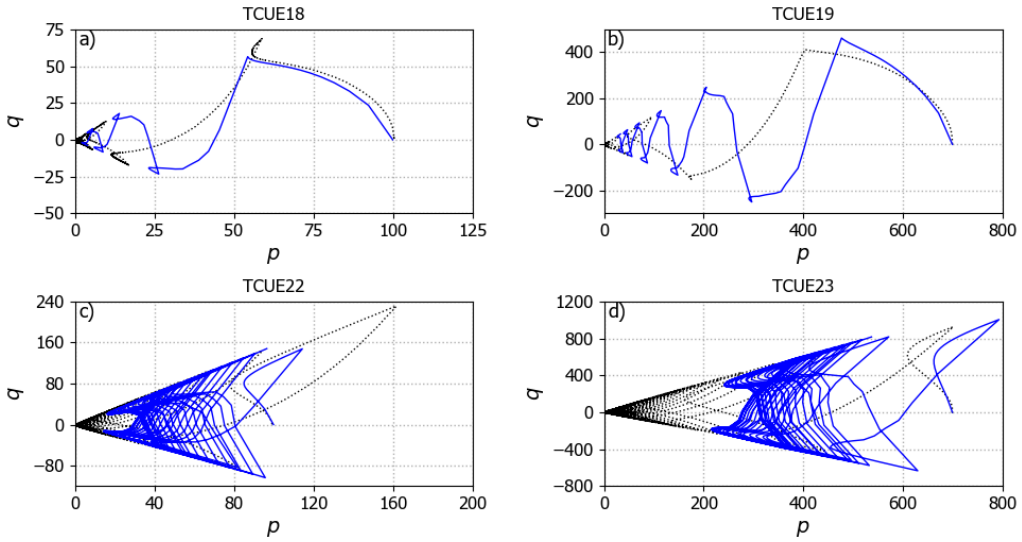


Figure 278 a) Test TCUE18, b) Test TCUE19, c) Test TCUE22, d) Test TCUE23, data and simulation

Figure 279 represents test TCUE21, with an initial anisotropic consolidation (simulated with a ramp of slope one from ($p_0 = 50$kPa,0). The first three-quarter of cycle are well pictured by HySand_base, but upon the reloading towards compression, almost no pore pressure build-up is simulated whereas the data shows a large pore pressure build-up.

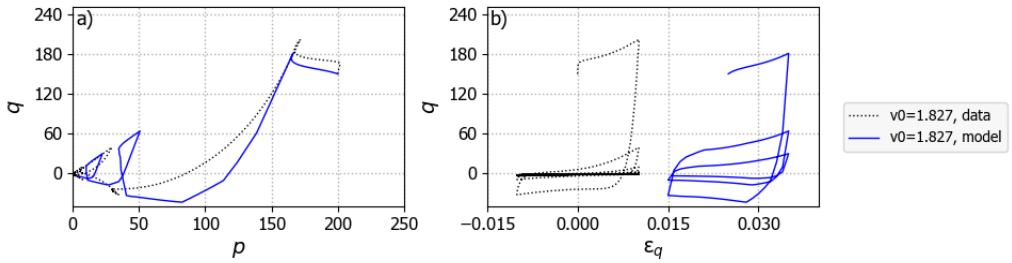


Figure 279 Test TCUE21, data and simulation

In conclusion, HySand_base captures well the trend of these large strain tests. However, it underestimates the pore pressure build-up (plastic contraction) upon load reversal.

5.1.9. Drained tests with unloading reloading

Wichtmann has conducted seven drained tests with unloadings and reloadings, with an initial mean effective stress $p_0 = 100$kPa, except TMCD6 ($p_0 = 200$kPa), and TMCD7 ($p_0 = 50$kPa). The data of these tests is presented along their simulation in Figure 280 to Figure 286.

HySand_base captures the monotonic backbone of the tests correctly. However, the unloading reloading cycles present two issues. First, HySand_base does not give rise to as much shear strain on unloading as in the data, such that HySand_base simulates much tighter hysteresis loops than in the data. Second, during the unloading-reloading, the data presents important variations of volumetric strain that are not captured by the model.

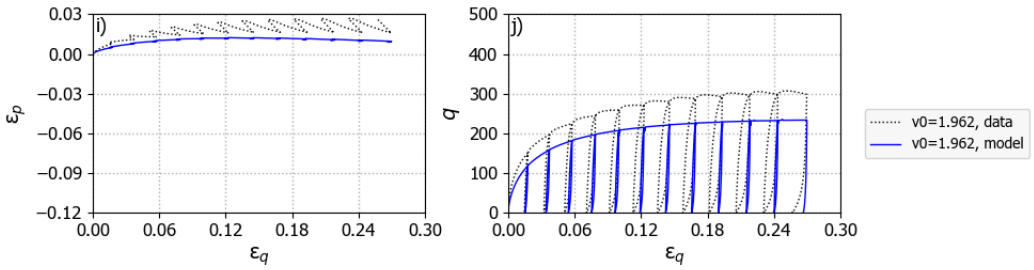


Figure 280 Test TMCD1

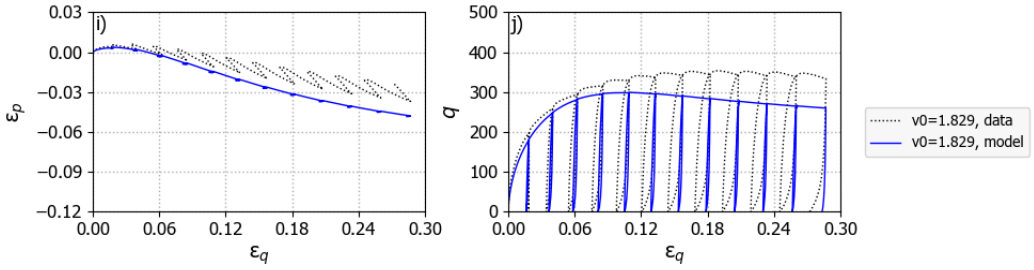


Figure 281 Test TMCD2

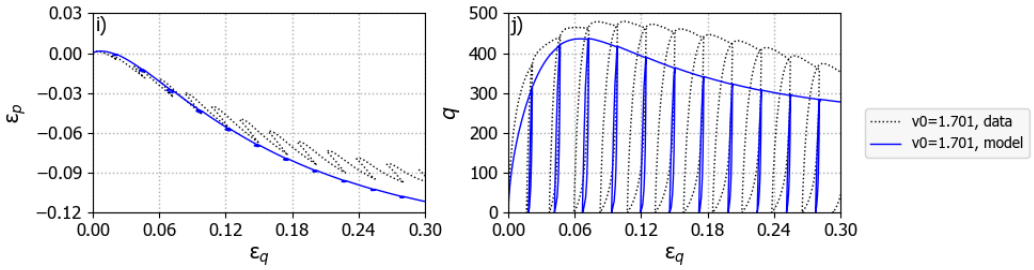


Figure 282 Test TMCD3

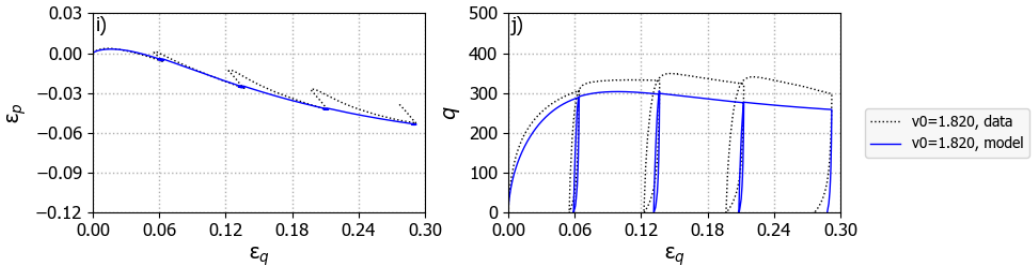


Figure 283 Test TMCD4

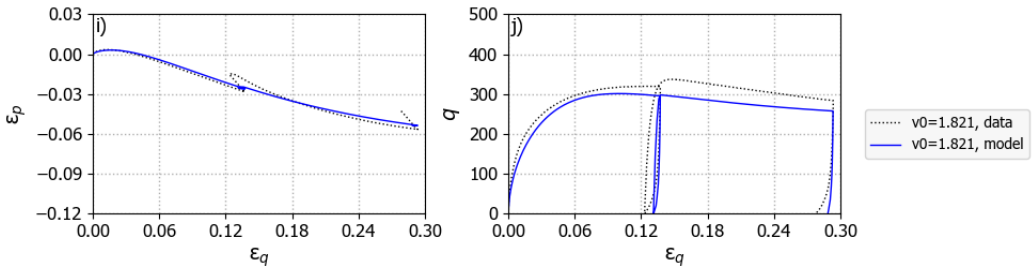


Figure 284 Test TMCD5

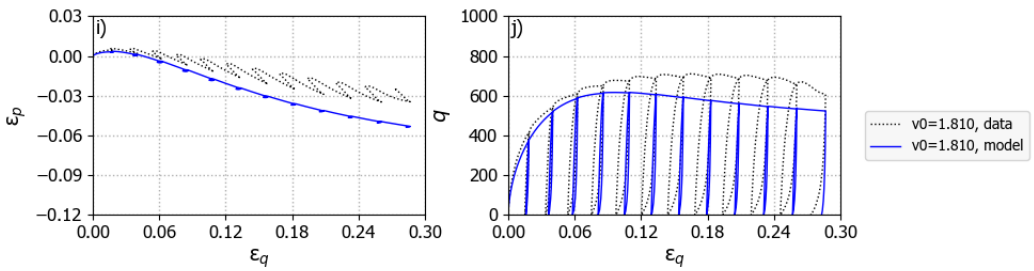


Figure 285 Test TMCD6

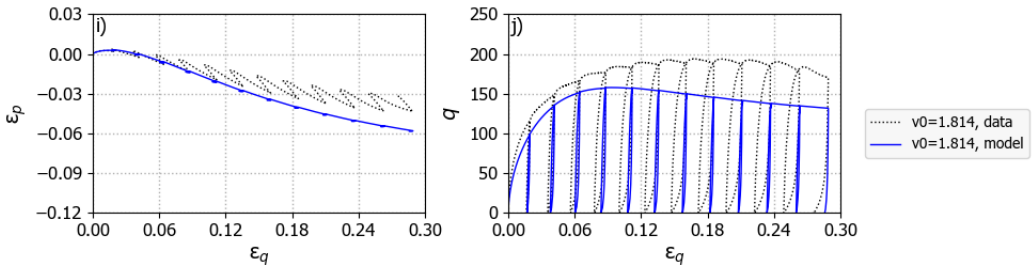


Figure 286 Test TMCD7

5.1.10. Special tests

5.1.10.1. Cyclic strain controlled tests with additional constant straining

Wichtmann has conducted four tests where, for cycle of 0.06% strain amplitude, a constant positive shear strain is added: 0.002% for TMCU1 (see Figure 287), 0.005% for TMCU2 (see Figure 288), 0.01% for TMCU3 (see Figure 289), 0.03% for TMCU4 (see Figure 290).

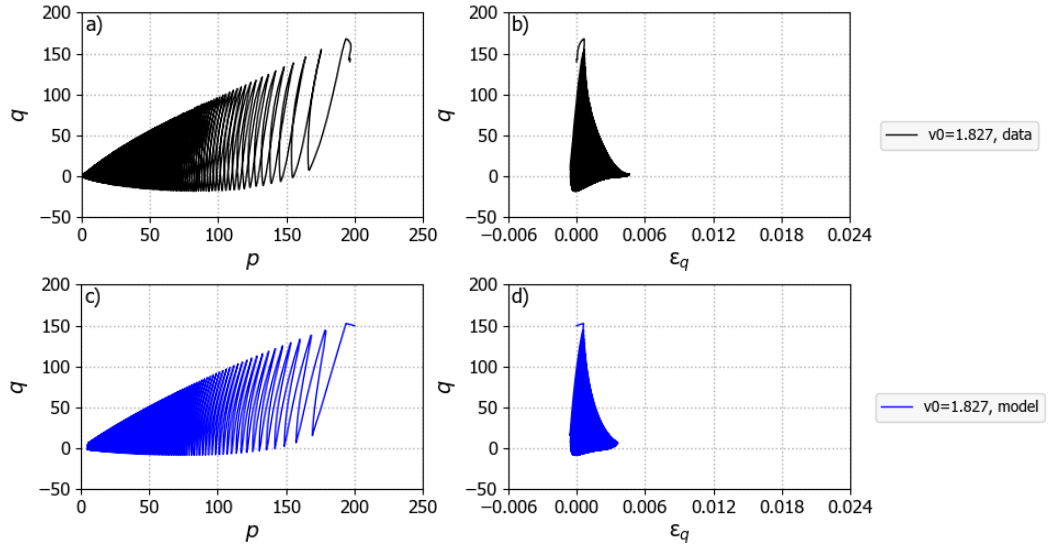


Figure 287 a)b) Test TMCU1, data by Wichtmann, c)d) Simulation with HySand_base

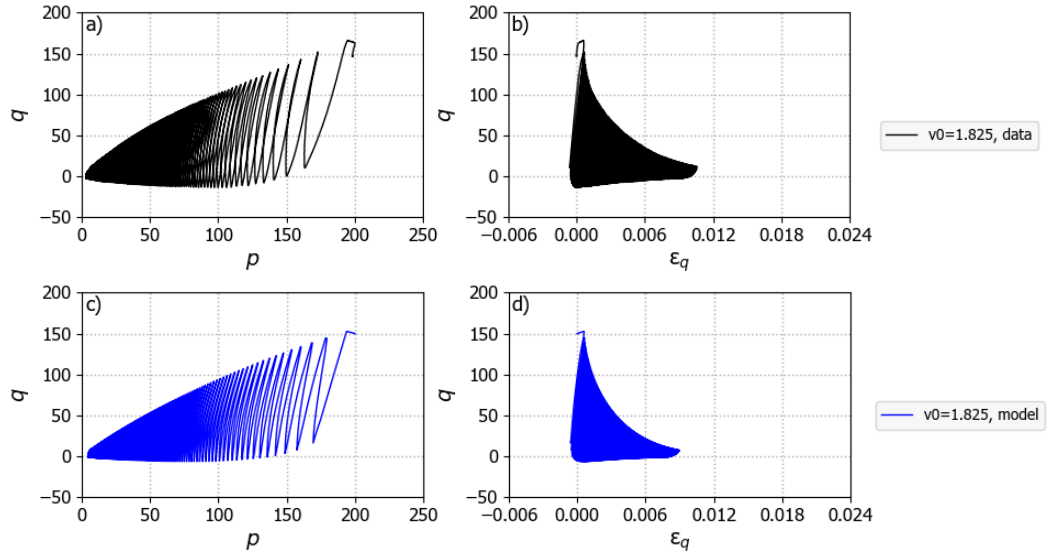


Figure 288 a)b) Test TMCU2, data by Wichtmann, c)d) Simulation with HySand_base

The strain accumulation for tests TMCU1 and TMCU2 is well captured by HySand_base.

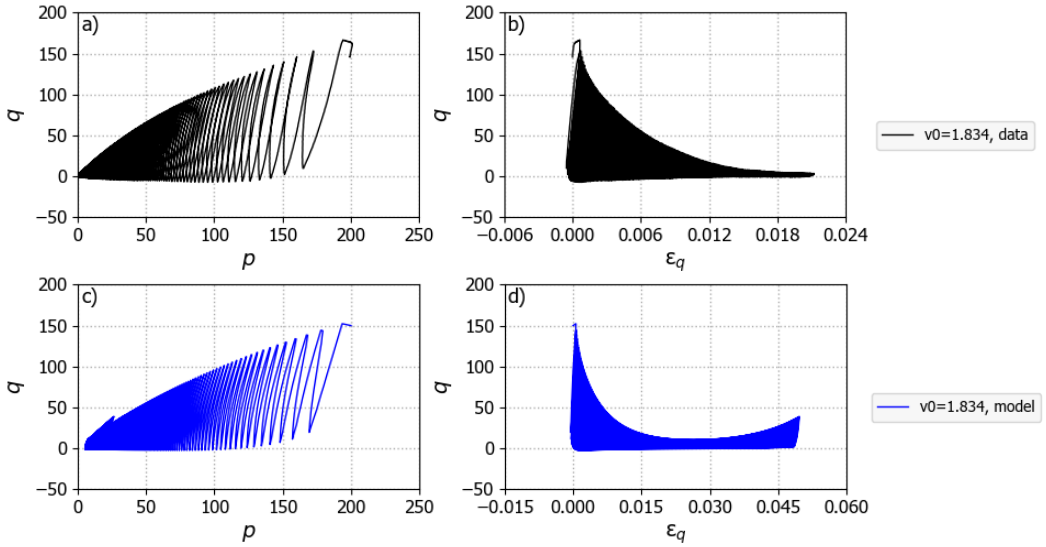


Figure 289 a)b) Test TMCU3, data by Wichtmann, c)d) Simulation with HySand_base for 500 cycles. Note the change of scale

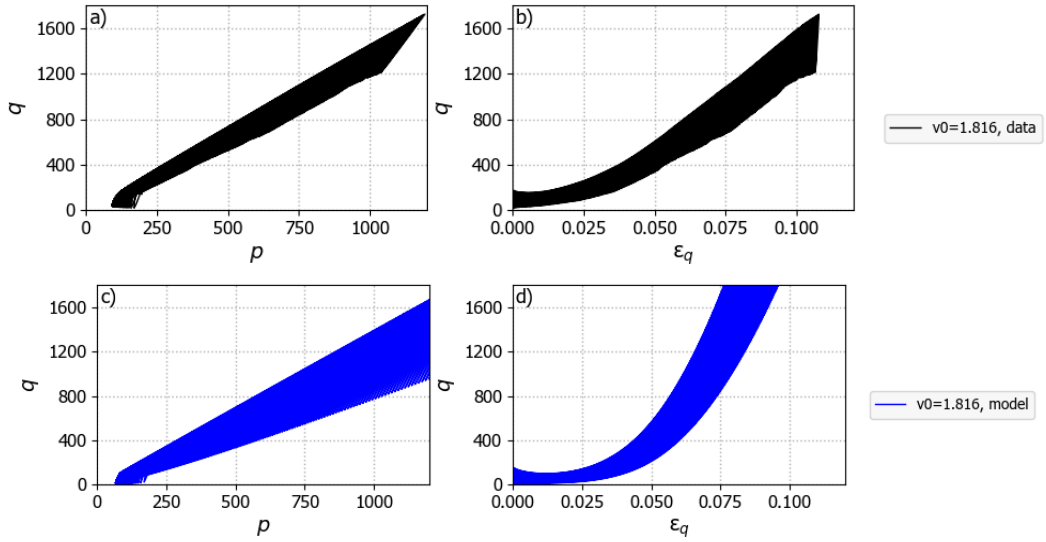


Figure 290 a)b) Test TMCU4, data by Wichtmann, c)d) Simulation with HySand_base up to 500 cycles

The simulation of test TMCU3 compares well to the data down to $p \approx 10$kPa. At this point, the pore pressure continues to build-up in the test data, whereas a dilatant phase starts for the simulation. This dilatancy is more visible for test TMCU4, both for the data and the simulation. During the dilatant phase, the test follows the same path as a monotonic undrained test in compression, but with superimposed cycles.

5.1.10.2. Monotonic undrained test after stress-controlled undrained cycles

Wichtmann has also conducted an undrained test to large strain after an undrained cyclic stress-controlled test brought close to liquefaction. The test shown in Figure 291 is well reproduced.

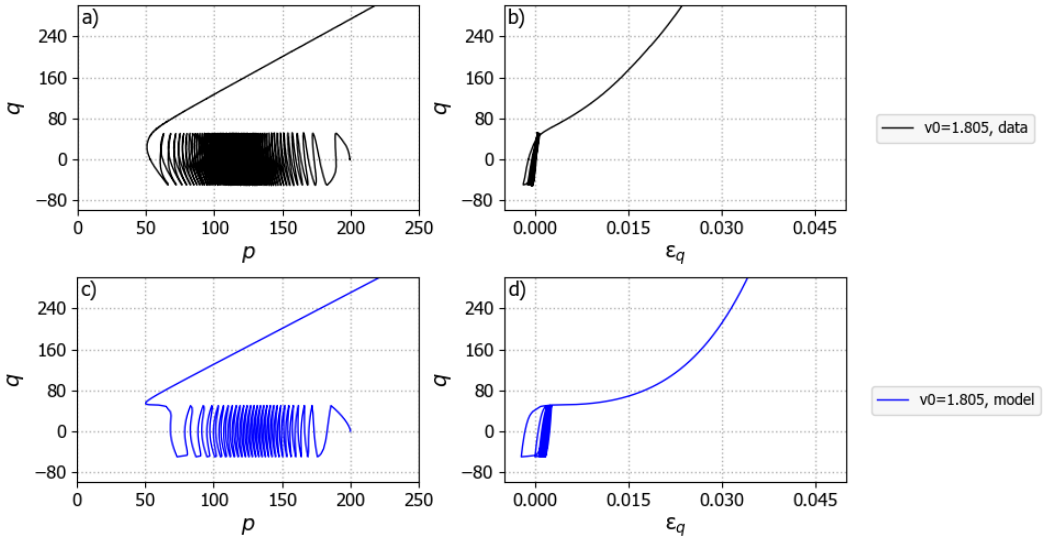


Figure 291 a)b) Test TMCU5, data by Wichtmann, c)d) Simulation with HySand_base

5.1.10.3. Complex undrained test

Figure 292 presents an undrained test with load to $q = 400$kPa, unload to $q = 50$kPa, reload to $q = 250$kPa, unload to $q = 0$kPa, before stress-controlled cycles of amplitude $q_a = 100$kPa.

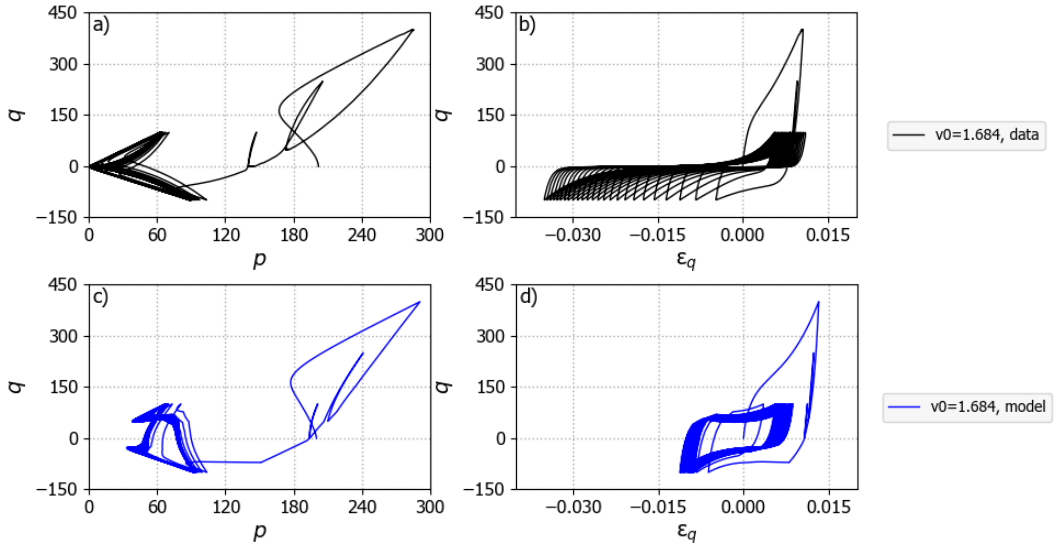


Figure 292 a)b) Test TMCU6 by Wichtmann, c)d) Simulation with HySand_base

Apart from the final cyclic mobility phase, the rest of the test is well captured by HySand_base.

5.1.11. Conclusions for Wichtmann data

Wichtmann has provided a very large and diverse database for air-pluviated samples of Karlsruhe fine sand which constitutes an excellent benchmark for constitutive models.

HySand_base performs well overall for all the tests of this database.

In isotropic tests and oedometric tests, the volumetric strain generation is well reproduced across densities. Importantly, the consolidation pressure should not be initialised below 5kPa to avoid an overestimation of the contraction at low stresses.

Both monotonic drained and undrained tests are well captured by HySand_base. Slight issues exist for the capacity of loose sand and for the stiffness of tests with low initial pressure. Both are underpredicted for drained tests. In undrained tests, the shear stress-strain asymptotes are too steep.

The few tests prepared by moist tamping (undrained monotonic tests) are poorly predicted by HySand_base.

Cyclic stress-controlled tests are also well represented by the model, with good prediction of the pore pressure build-up for both isotropic and anisotropic consolidation, as well as a good depiction of ratcheting for anisotropic consolidation, apart for tests in extension. However, HySand_base cannot reproduce the cyclic-mobility phase for medium dense and dense samples.

Cyclic (small) strain-controlled tests are very well simulated by the model with a good representation of the stress paths and of the rates of pore pressure build-up.

The simulation of cyclic (large) strain-controlled tests and drained tests with unloading-reloading loops, despite adequate overall simulation, face an issue: the lack of contraction or pore pressure build-up upon load reversal. This is also the source of the inability of HySand_base to model liquefaction.

Wichtmann has also conducted more original tests (combined cyclic and monotonic strain, complex stress paths) that are well reproduced by HySand.

5.2. Adamidis data

In Adamidis and Anastasopoulos (2022), a number of undrained cyclic stress-controlled tests have been conducted on Hostun sand. The specific feature of some of these tests is that a controlled inflow of water is delivered to the sample during the test.

5.2.1. Initial anisotropy of the samples

An important observation on the Adamidis dataset is that the samples seem initially anisotropic. This anisotropy can be presumed for drained tests such as the ones presented in Figure 293. In the development of HySand, it has been shown that the denser a sample is, the quicker anisotropy develops (c.f. Chapter 3). However, here, the difference is apparently too great, with the looser sample (blue curve) initially contracting for a much larger shear strain than the two other samples, and showing much lower stiffness. This could be explained by a much lower initial anisotropy (developed in extension) of the looser sample compared to the other two.

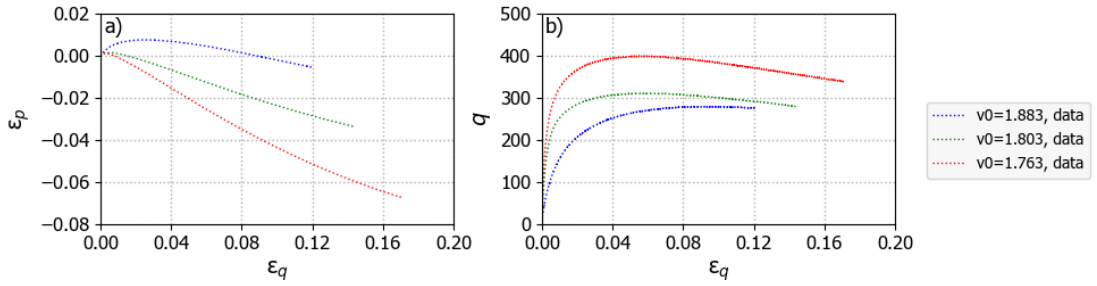


Figure 293 Drained tests on Hostun sand by Adamidis

The presence of initial anisotropy could also explain the asymmetry in cyclic stress controlled undrained tests, such as the one pictured in Figure 294. There is very little pore pressure build-up upon the first half-cycle on the compression side, but a very large one upon the rest of the cycle on the extension side. This can be modelled in HySand_base by an initial positive anisotropy (developed in compression → $a_0 > 0$).

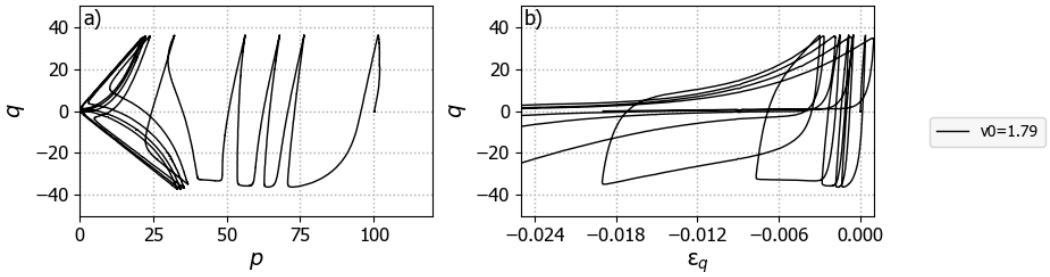


Figure 294 Undrained cyclic stress controlled test on medium dense sand by Adamidis

Unlike the Wichtmann dataset, where all tests were considered initially isotropic, it is important for the Adamidis dataset to estimate initial anisotropies ($a_0 \neq 0$) for some of the simulated tests.

5.2.2. Calibration

For the sake of calibration, Adamidis provided three isotropic tests and three drained tests. These were used in conjunction with cyclic stress-controlled undrained tests ICT65/100/30/0 and ICT65/100/36/0. The procedure described in Chapter 4, including the trial and error process rather than the optimisation, has been used to obtain the parameters presented in Table 23.

k_r	g_r	m	φ_c	β_{max}	B	Γ	Δ	λ_B	λ_Δ	A_{max}	h_0	b	r
351	610	0.74	34.4	1.15	2.049	1.95	1.671	0.0052	0.0028	50	1500	3	0.2

Table 23 Initial parameters for the calibration of shear hardening and consolidation parameters

5.2.3. Isotropic tests

Three isotropic tests, of the four provided by Adamidis (right-hand of Figure 295), were used for calibration. Simulations with HySand_base are presented in the right-hand of Figure 295. All tests show too much contraction at low mean effective stress, and too little contraction at high pressure. The linear variation with density of the normal consolidation slope is an approximation leading to too high values for medium dense samples, and too low values for loose samples.

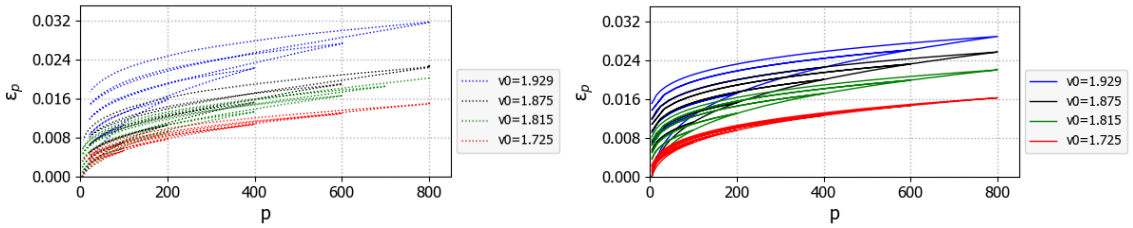


Figure 295 Isotropic tests on Hostun sand. Left: data by Adamidis; Right: simulation with HySand_base

5.2.4. Monotonic drained tests

The three drained tests presented in Figure 296 have been used in the calibration. Initial anisotropy values of $a_0 = -0.2$ for the loose sample, and $a_0 = 0.5$ for the two denser samples have been used. These initial anisotropy values are essential to be able to represent the differences in initial stiffness and rate of dilation development.

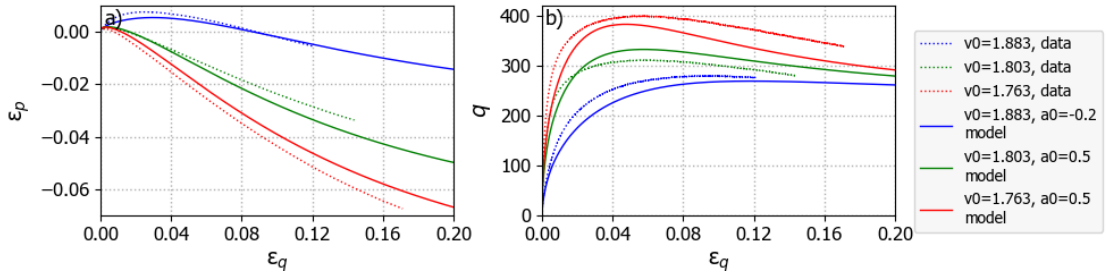


Figure 296 Drained tests with final calibrated parameters

5.2.5. Cyclic stress-controlled tests with no inflow

5.2.5.1. Loose sand

ICT40/100/28/0 is a cyclic stress-controlled test on loose sand. The data is represented in Figure 297, and the simulated behaviour with $a_0 = 0$ is represented in Figure 298.

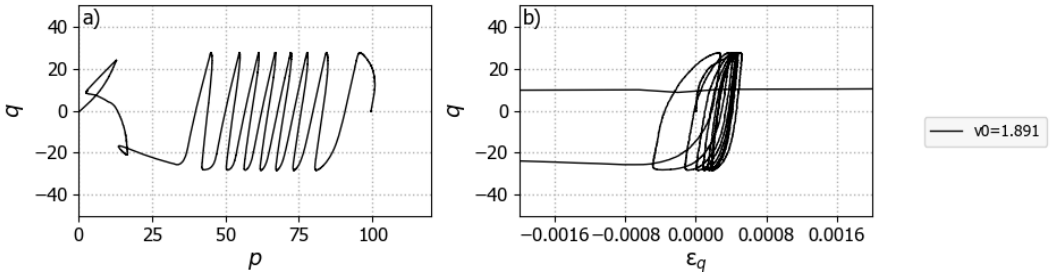


Figure 297 ICT40/100/28/0 by Adamidis

The number of cycles to liquefaction for the data is 8, while it is 21 for the simulation.

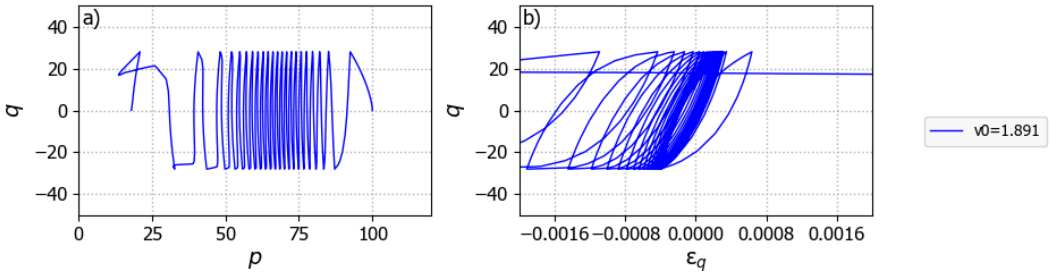


Figure 298 Simulated ICT40/100/28/0 with HySand_base

The secant stiffness is too low as seen in Figure 299.

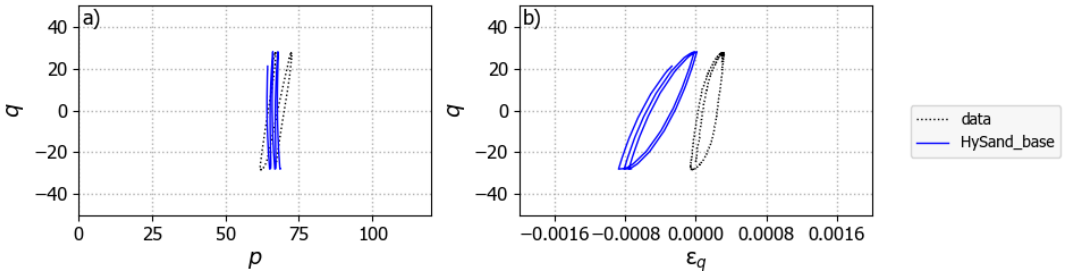


Figure 299 Zoom on a few cycles of ICT40/100/28/0

ICT40/100/20/0 is another test on loose sand pictured in Figure 300, with 99 cycles to liquefaction. It is well reproduced with HySand_base with initial anisotropy $a_0 = -0.2$, requiring 118 cycles to liquefy, pictured in Figure 301.

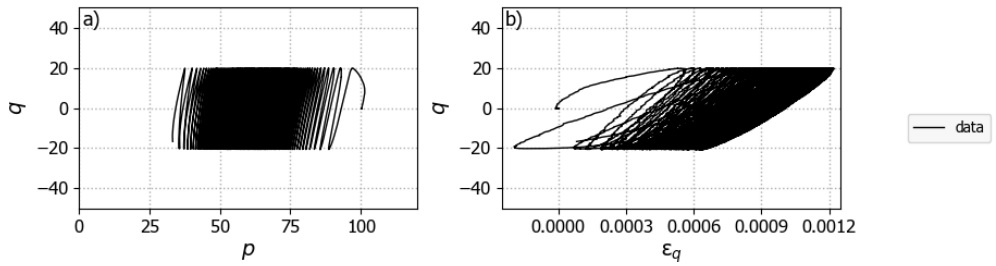


Figure 300 Test ICT40/100/20/0 on loose sand by Adamidis

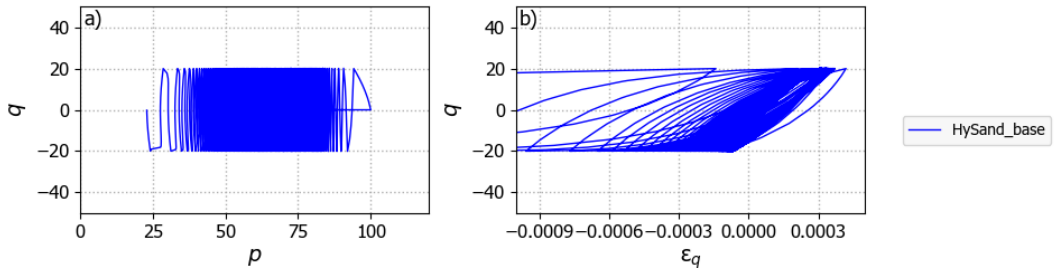


Figure 301 Simulation of ICT40/100/20/0 with HySand_base

The simulation with HySand_base in this case overestimates slightly the secant stiffness, as shown in Figure 302.

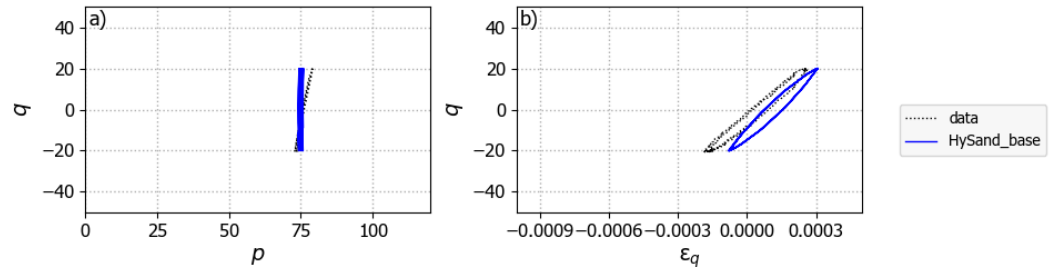


Figure 302 Zoom on a few cycles of ICT40/100/20/0

5.2.5.2. Medium dense sand

For medium dense sand, test ICT55/100/30/0 requires 19 cycles to reach liquefaction (c.f. Figure 303). Figure 304 presents the simulation of the test with HySand_base for $a_0 = 0.15$, which matches perfectly the number of cycles to liquefaction.

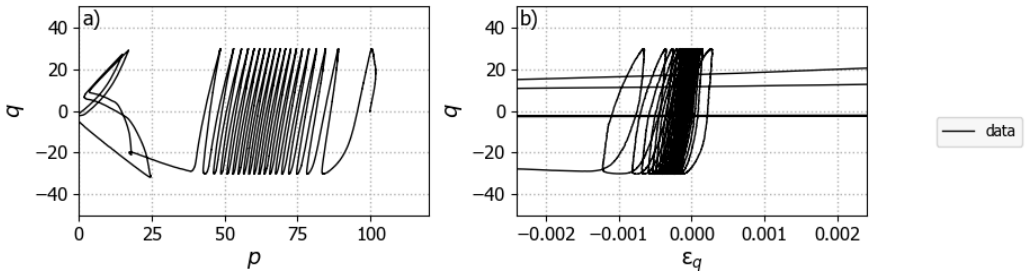


Figure 303 ICT55/100/30/0 by Adamidis

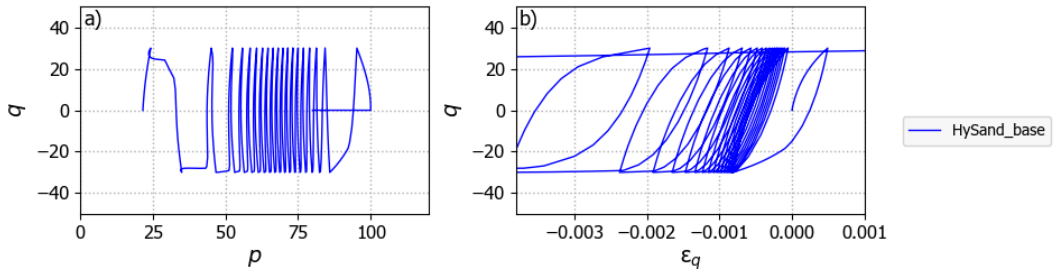


Figure 304 Simulation of ICT55/100/30/0 with HySand_base

The zoom on a few cycles of ICT55/100/30/0, shown in Figure 305, shows that the secant stiffness of the simulation is lower than for the data.

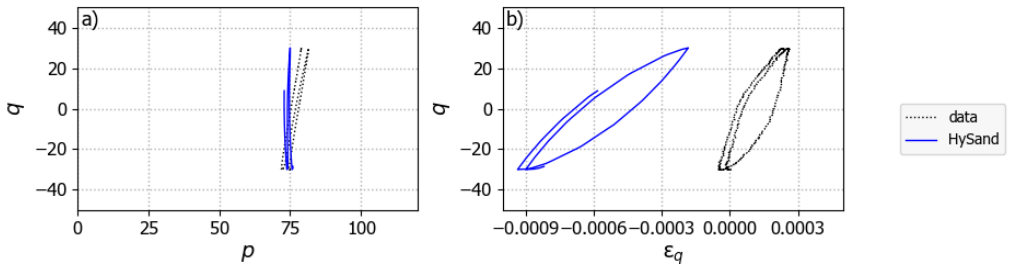


Figure 305 Zoom on a few cycles of ICT55/100/30/0

5.2.5.3. Dense sand

The two cyclic undrained stress-controlled tests on dense sand normally consolidated at $p_0 = 100$kPa used for the calibration, denoted ICT65/100/30/0 ($v_0 = 1.804$) and ICT65/100/36/0 ($v_0 = 1.793$), with cyclic amplitudes of 30kPa and 36kPa, require 40 and 5 cycles to liquefy respectively. These tests are pictured in Figure 306 and Figure 307. The asymmetry of the shear stress-strain response during the cyclic mobility-phase in Figure 306 and Figure 307 could be due to the initial anisotropy of the material.

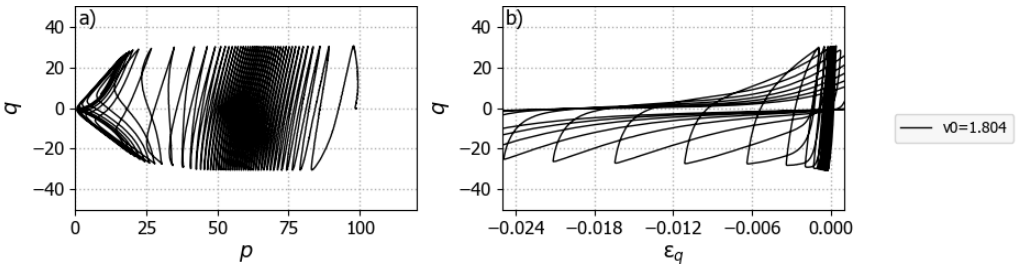


Figure 306 Test ICT65/100/30/0 by Adamidis

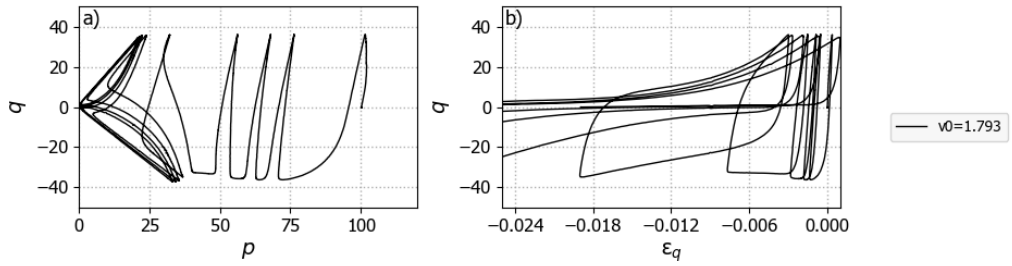


Figure 307 Test ICT65/100/36/0 by Adamidis

Simulations show good results in Figure 308 and Figure 309, with an adequate secant stiffness and number of cycles to liquefaction (50 for ICT65/100/30/0, and 4 for ICT65/100/36/0). An initial anisotropy of $a_0 = 0.35$ has been used for ICT65/100/36/0, which seems to capture the asymmetry of the stress-strain response during the cyclic-mobility phase.

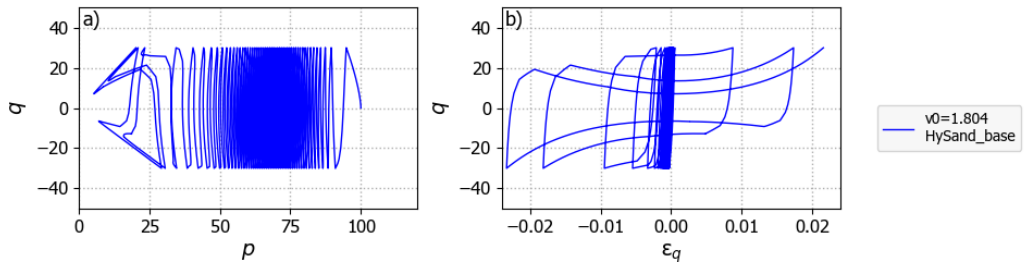


Figure 308 Simulation of ICT65/100/30/0

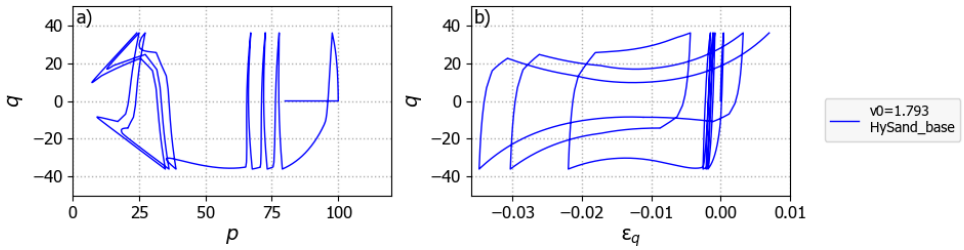


Figure 309 Simulation of ICT65/100/36/0

5.2.6. Cyclic stress-controlled tests with inflow

Apart from the simulations in the present section (5.2.6), all undrained cyclic stress-controlled tests are simulated via strain control with fixed-size increments of shear strain which change sign once the stress target is reached. This allows to deal with increments of stress of the opposite sign to the control, such as can be seen in the left graph of Figure 309 in the fourth cycle where there is a shear stress increase during the extension (for $\sim 35kPa < p < 65kPa$).

In the case of water inflow, general control is used to impose both the stress control and the volumetric strain control (simulating the water inflow). As a consequence, numerical issues arise, such as can be seen in the left graph of Figure 311 during the extension phase of the last cycle.

5.2.6.1. Loose sand

Test ICT40/100/20/5 by Adamidis is pictured in Figure 310. It is a test on loose sand with the same amplitude as ICT40/100/20/0, but with a water inflow leading to 0.04% volumetric strain per cycle. The water inflow brings down the number of cycles to liquefaction from 99 to 9.

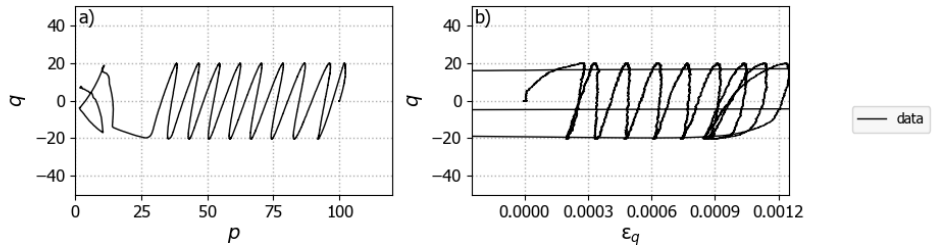


Figure 310 ICT40/100/20/5 by Adamidis

The simulation with HySand_base of ICT40/100/20/5 is pictured in Figure 311. The simulated number of cycles to liquefaction was 118 with no water inflow, and here it is 6, showing that HySand_base captures the effect of volume change very well.

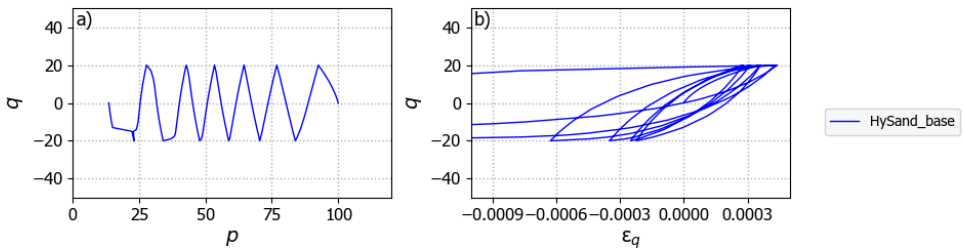


Figure 311 Simulation of ICT40/100/20/5

5.2.6.2. Medium dense sand

ICT55/100/30/5 is pictured in Figure 312. With a water inflow representing a volumetric strain of 0.04% per cycle, the numbers of cycles to liquefaction goes down from 19 to 4.

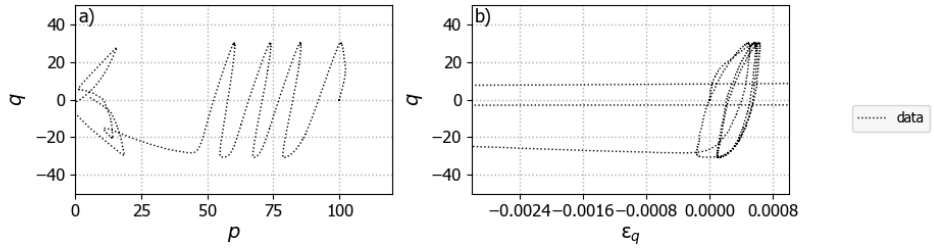


Figure 312 ICT55/100/30/5 by Adamidis

In the simulation of ICT55/100/30/5 (Figure 313), four cycles are required before liquefaction.

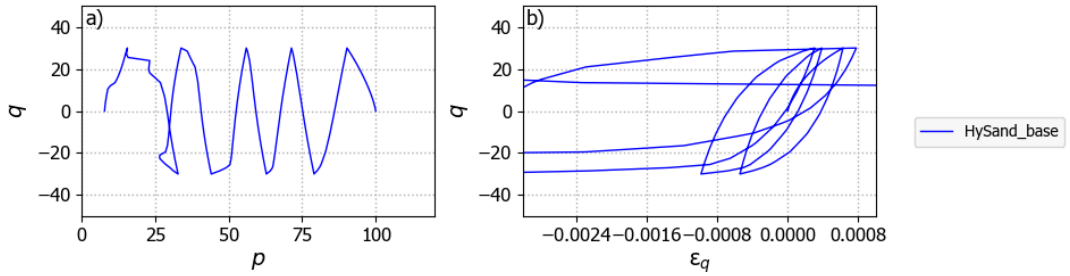


Figure 313 Simulation of ICT55/100/30/5

5.2.6.3. Dense sand

Test ICT65/100/30/5 is pictured in Figure 314, where there is a water inflow representing 0.03% of volumetric strain per cycle. It requires four cycles to liquefy, against 50 without water inflow.

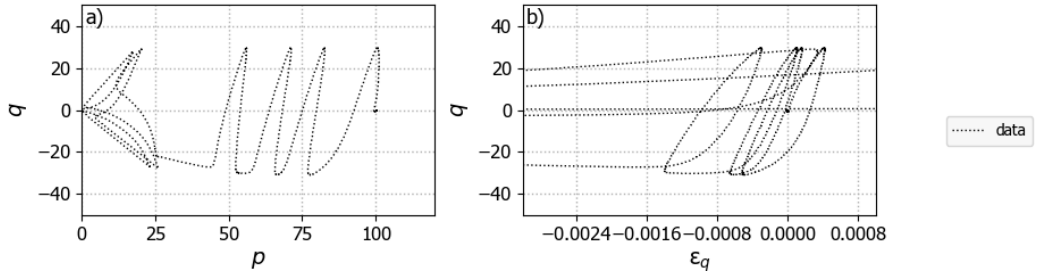


Figure 314 ICT65/100/30/5 by Adamidis

Figure 315 presents its simulation with $a_0 = 0.1$ (light initial anisotropy developed in compression). It requires five cycles to liquefy.

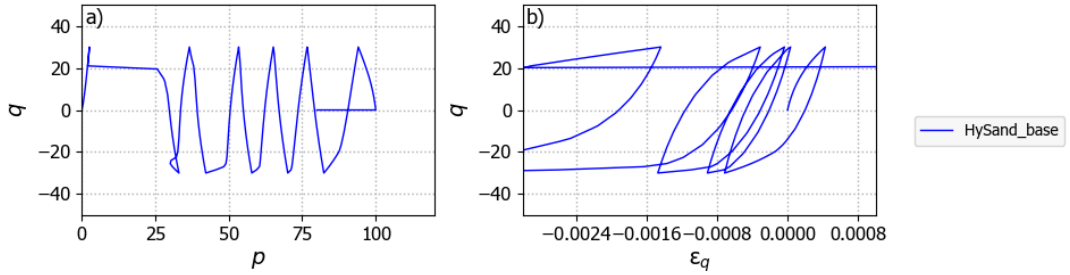


Figure 315 Simulation of ICT65/100/30/5

ICT65/100/30/15, shown in Figure 316, represents the same test with a greater water inflow (equivalent to 0.08% volumetric strain), and needs three cycles to liquefy.

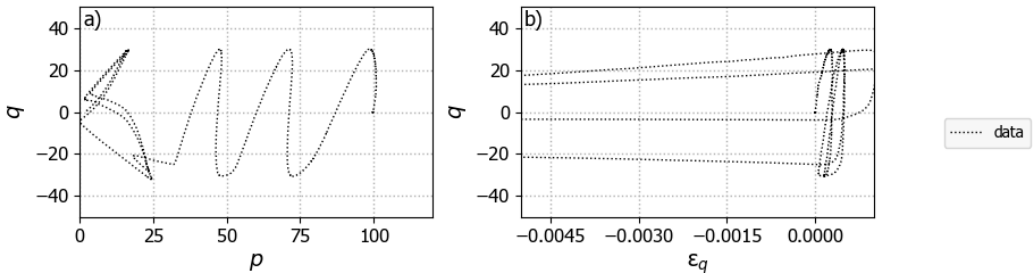


Figure 316 Test ICT65/100/30/15 by Adamidis

The simulation of ICT65/100/30/15 is pictured in Figure 317. It also needs three cycles to liquefy.

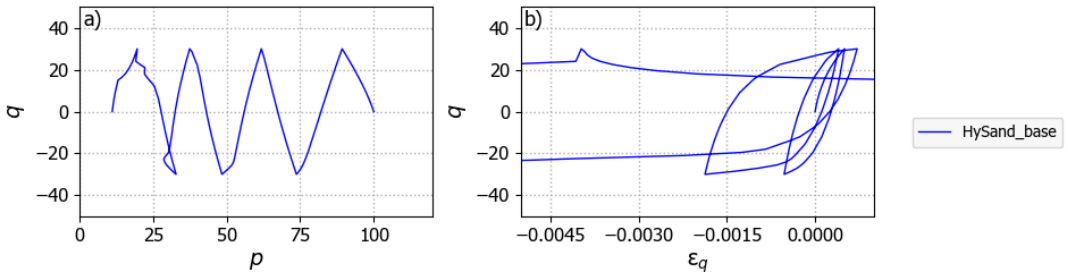


Figure 317 Simulation of ICT65/100/30/15

5.2.7. Conclusions for Adamidis data

HySand_base has been calibrated for Adamidis data, which is more complex to calibrate than Wichtmann data because of the initial anisotropic state of some samples.

The calibration leads to a good depiction of isotropic tests, despite an overprediction of the volumetric strain generation at low confining stresses.

Once adequate initial anisotropies are chosen, stiffness, capacity and dilation during drained tests are also well depicted with HySand_base.

The cyclic undrained stress-controlled key metrics are also well depicted: number of cycles to liquefaction, secant stiffness, and rate of pore pressure build-up.

The key interest of Adamidis' tests is the simulation of water inflow. The decrease of the number of cycles needed with different water inflows is well captured by the model both qualitatively and quantitatively. This last result underlines the quality of the depiction of evolution of the bulk modulus with pressure, which is essential to translate the additional plastic volumetric strain imposed by the water inflow into pore pressure build-up.

5.3. Other qualitative comparisons

A number of other interesting and original triaxial tests are available in the literature. Often, however, not enough data is available for the calibration of HySand_base. Nonetheless, it is possible to compare qualitatively simulations using approximate parameters.

5.3.1. Hostun sand

For the simulation of tests on Hostun sand at ENTPE (France), the calibrated parameters for Hostun sand used at ETH Zurich (Switzerland) by Adamidis and Anastasopoulos (2022) are used. These parameters are repeated in Table 24.

k_r	g_r	m	φ_c	β_{max}	B	Γ	Δ	λ_B	λ_Δ	A_{max}	h_0	b	r
351	*610*	0.74	34.4	1.15	2.051	1.95	1.671	0.0052	0.0028	50	*1500*	*3*	*0.2*

Table 24 Initial parameters for the calibration of shear hardening and consolidation parameters

5.3.1.1. Effect of anisotropic consolidation on the undrained behaviour of loose sand

Doanh *et al.* (1997) have conducted a series of monotonic undrained tests with anisotropic consolidation for which K_0=0.5 or 0.66 on very loose Hostun sand prepared by a modified moist tamping and undercompaction procedure. In these experiments, the consolidated state, isotropic or anisotropic, is reached from an isotropic starting point at 20kPa.

Figure 318 reproduces the results for isotropically consolidated samples by Doanh *et al.*

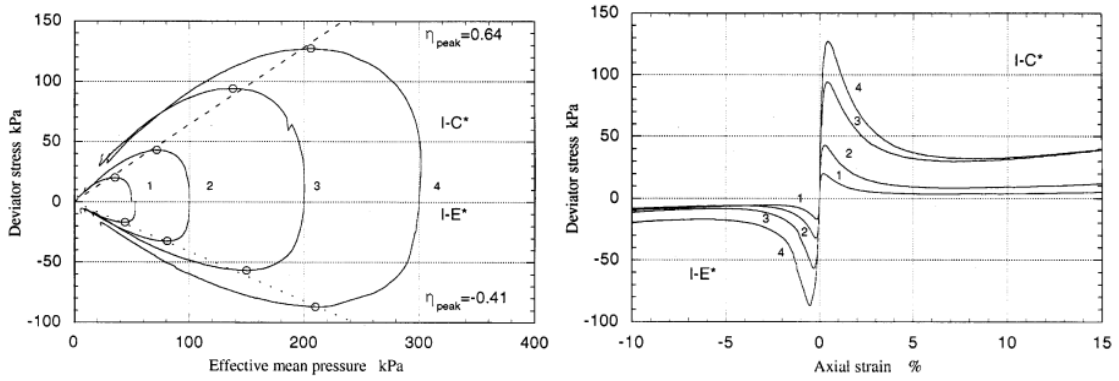


Figure 318 Isotropic consolidated monotonic undrained tests by Doanh (extracted from Doanh et al. (1997))

Figure 319 is the simulation of the same tests obtained with HySand_base. HySand_base reproduces well the stress paths and the peak capacity. However, it underestimates the end of test capacities. This disparity is not very big nor surprising if one considers that this Hostun sand does not have the exact same properties as the one tested by Adamidis.

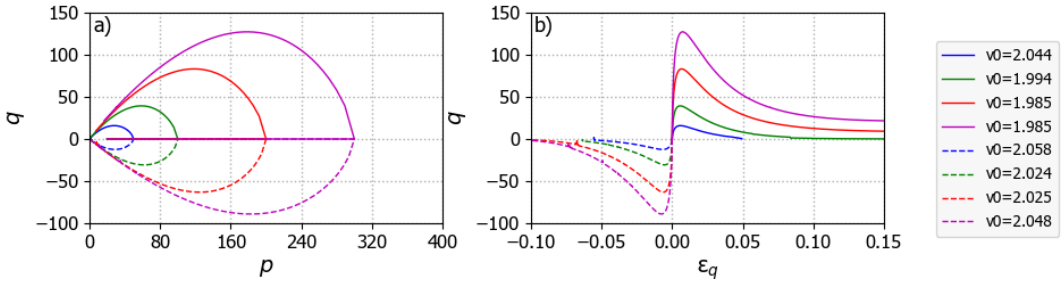


Figure 319 Simulations of isotropic consolidated tests with HySand_base

Figure 320 shows the tests on anisotropically consolidated samples with K_0=0.66.

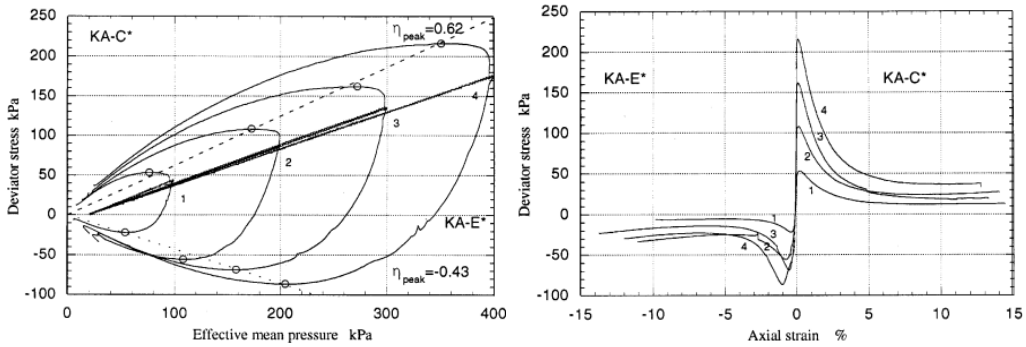


Figure 320 Tests by Doanh with K_0=0.66 (from Doanh (1997)

Figure 321 presents the simulation of the same tests with HySand_base.

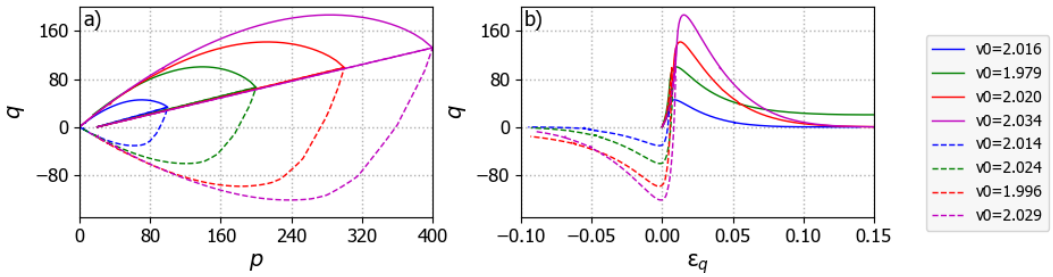


Figure 321 Simulation of the tests with K_0=0.66 (note the change of scale for q)

The simulated stress paths have an appropriate shape, but, under compressive undrained loading, the data initially shows no pore pressure build-up (vertical stress path) which is not reproduced by the model. The simulated stress-strain behaviour is also adequate, but the simulated maximum amplitudes of shear stress of the simulations are lower in compression and higher in extension than for the data.

Tests with $K_0 = 0.5$ show the same behaviour and are not reproduced here.

HySand appears able to reproduce well the monotonic undrained tests for both isotropically and anisotropically consolidated samples.

5.3.1.2. Effect of drained preloading on the undrained behaviour of loose sand

Gajo and Piffer (1999) have tested very loose Hostun sand prepared with the moist-tamping technique and preloaded with different drained paths.

5.3.1.2.1. Drained preloading of different amplitudes

Figure 322 presents monotonic undrained tests with drained preloading of different amplitudes.

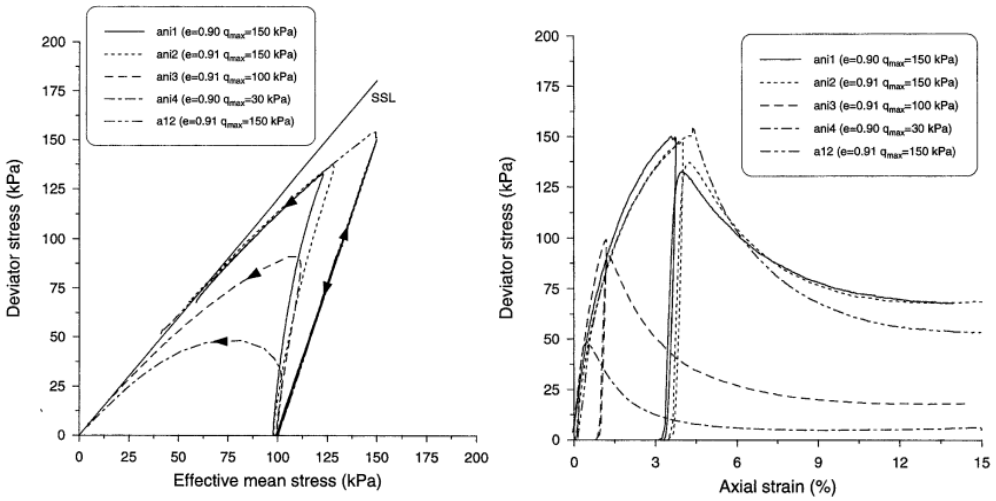


Figure 322 Monotonic undrained tests after drained preloading (from Gajo and Piffer (1999))

Figure 323 shows the simulation of a virgin loading and three tests with drained shear preloading (with maximum shear stresses of 30kPa, 100kPa, and 150kPa). The initial specific volume was re-adjusted to 1.95 rather than 1.9. This re-adjustment is also used in the following paragraphs.

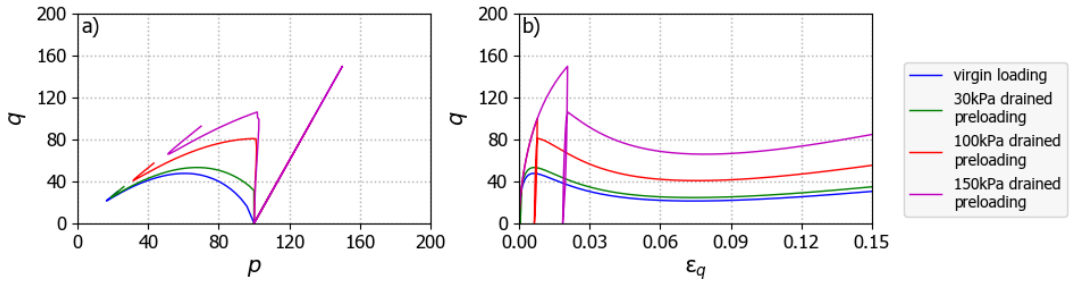


Figure 323 Simulations of drained preloaded tests with HySand_base with v_0=1.95

The tests are well reproduced with HySand, except that the elastic stress path is too vertical.

5.3.1.2.2. Drained preloading with different stress directions

Figure 324 presents other tests with drained preloading with different stress paths.

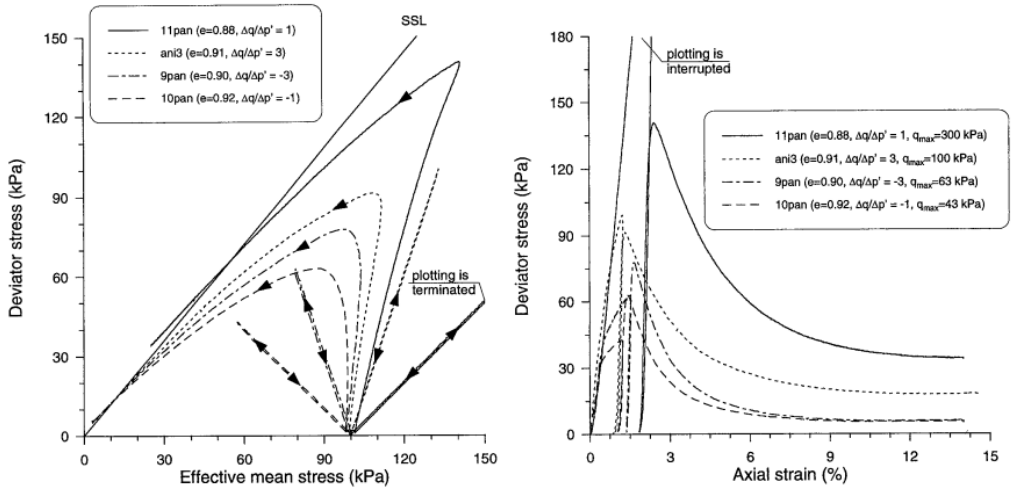


Figure 324 Undrained loading after different drained stress paths (from Gajo and Piffer (1999))

The simulated tests with HySand base are represented in Figure 325.

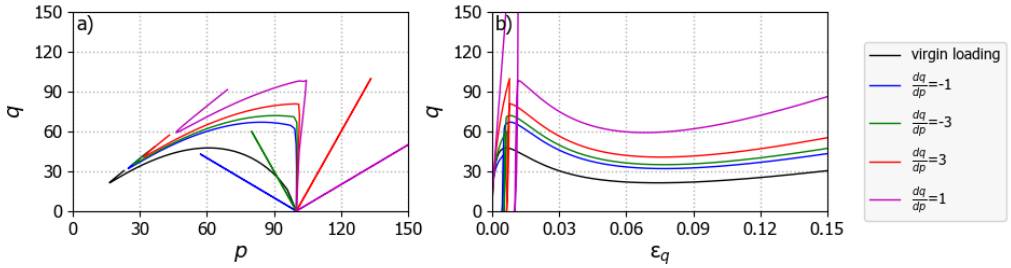


Figure 325 Simulation of the drained directional preloaded tests with HySand_base

The depiction of the tests by HySand_base is good, with increasing peak capacity with increasing dp/dq preloading ratio, and with undershooting (if $dp/dq > 0$ on preloading) or overshooting (if $dp/dq < 0$ on preloading) upon undrained reloading. What is not perfectly pictured by HySand_base is the curvature of the stress path upon the undrained reloading.

5.3.1.2.3. Influence of drained preloading in compression on tests in extension

Gajo and Piffer (1999) have also studied the influence of drained preloading in compression on a subsequent undrained loading in extension (c.f. Figure 326).

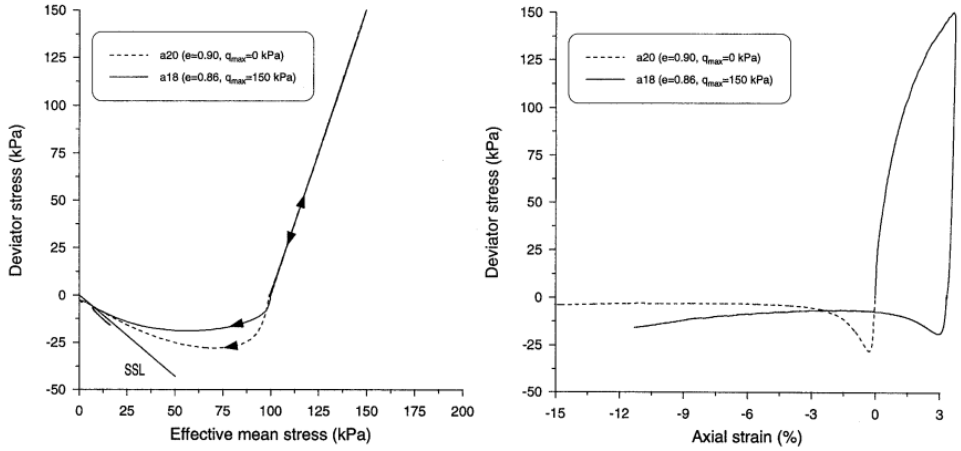


Figure 326 Virgin and drained shear preloaded undrained tests in extension (from Gajo and Piffer (1999))

Figure 327 presents the simulation with HySand_base. While in the data, the undrained loading following the drained preloading has a lower capacity than the virgin loading, the simulation with HySand_base shows the opposite behaviour. If one interprets the behaviour of HySand_base keeping in mind the multi-surface and consolidation mechanisms, it means that, despite the shearing of the surfaces towards the compression side, the consolidation pressure has grown so large that the stress path encounters the surfaces at lower shear stresses than for the virgin loading. To reproduce the phenomenon observed in the data, the shearing of the yield surfaces should dominate the development of the consolidation pressures in this case.

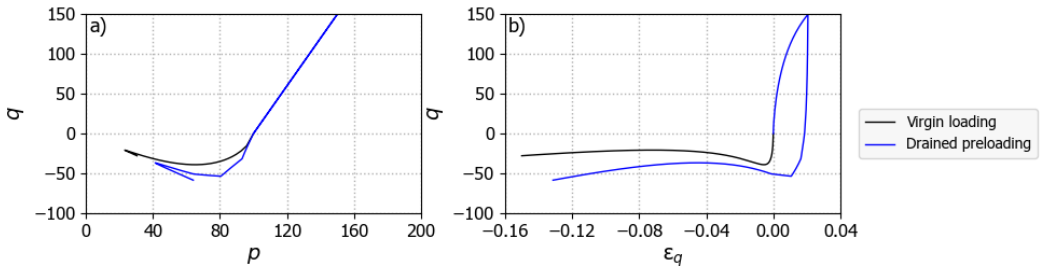


Figure 327 Simulation of undrained tests in extension with HySand_base

5.3.1.2.4. Drained preloading in extension

Figure 328 presents undrained loadings in compression and extension, without preloading or with a drained preloading in extension.

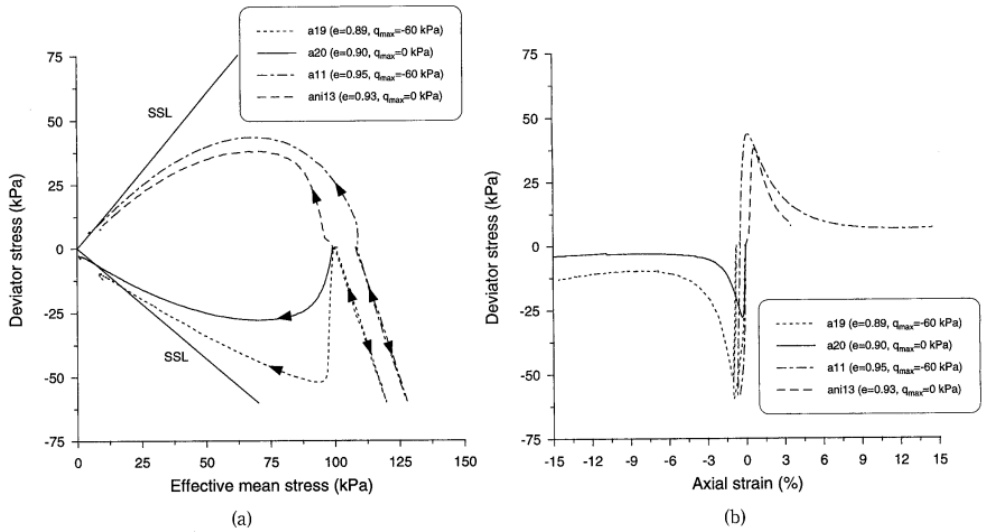


Figure 328 Influence of drained preloading in extension on undrained loading (from Gajo and Piffer (1999))

The simulation of the tests, shown in Figure 329, gives a good depiction of the data: larger capacities on reloading in both compression and extension, more pronounced in extension.

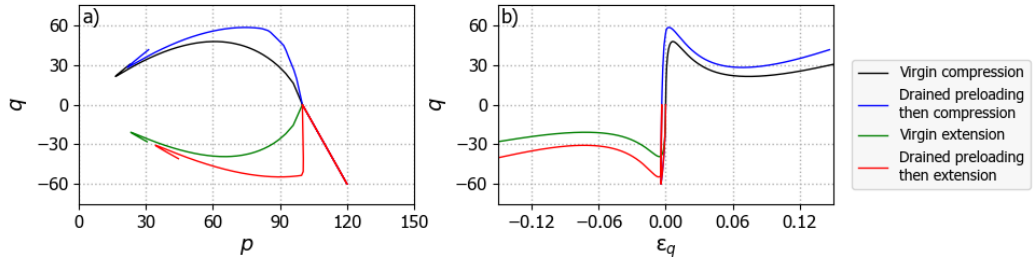


Figure 329 Simulation with HySand base of undrained tests after drained preloading in extension

5.3.1.2.5. Influence of drained preloading in compression and extension on subsequent undrained loading in compression

Figure 330 presents three undrained tests in compression: one without preloading, one with drained preloading in compression, and one with drained preloading in compression and then in extension.

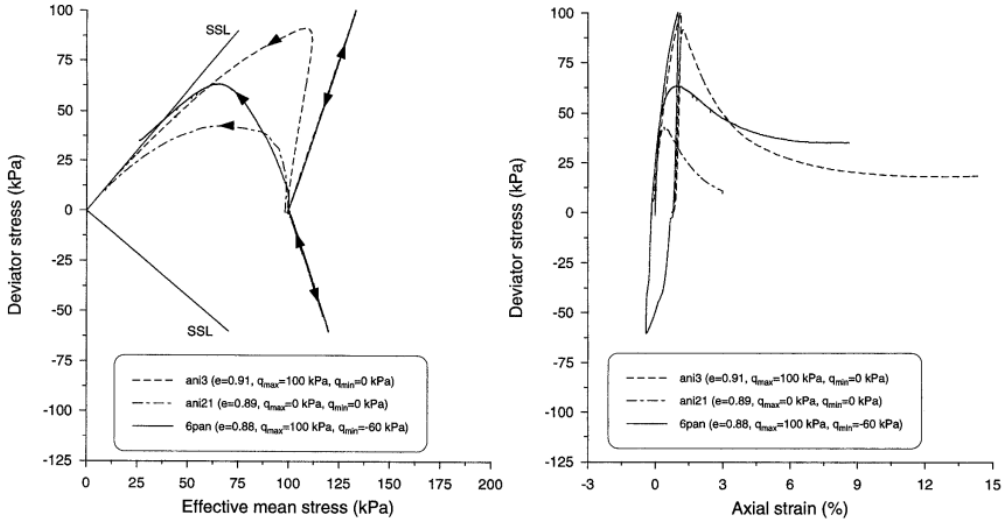


Figure 330 Drained preloading in compression, and compression then extension (from Gajo and Piffer (1999))

Simulated tests with HySand_base are shown in Figure 331. The simulation does depict the key phenomenon: the preloaded test in both compression and then extension lies, in stress space, in between the virgin loading and the preloaded in compression tests.

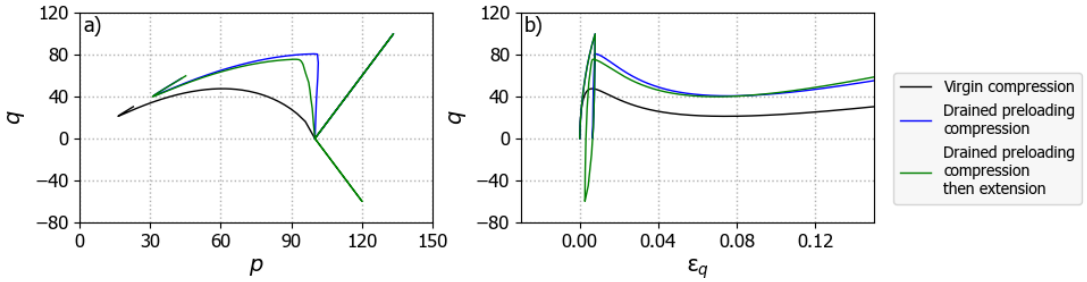


Figure 331 Simulation with HySand_base of undrained tests in compression after different drained preloadings

5.3.1.2.6. Influence of undrained preloading in compression on undrained loading

Figure 332 presents undrained tests by Gajo and Piffer after reconsolidation of undrained tests in compression until liquefaction.

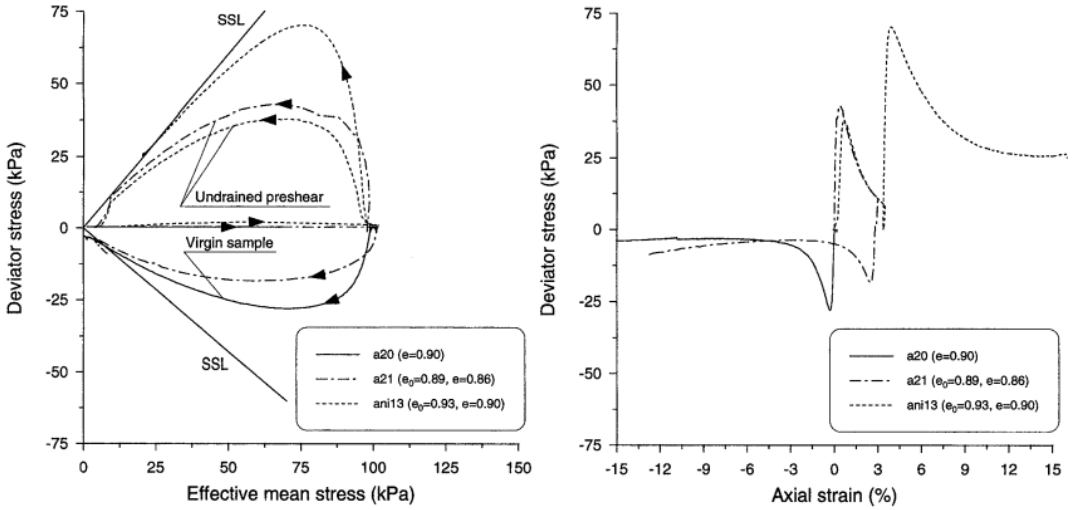


Figure 332 Undrained tests with undrained compression preloading (from Gajo and Piffer (1999))

The simulated tests, shown in Figure 333, are preloaded to a shear strain of 4%, then follow a stress path to $p = 5$kPa and $q = 0$kPa, before being reconsolidated to $p = 100$kPa. In the simulation, the reloading in compression shows more capacity than the virgin loading, as for the data. The simulation of the reloading in extension shows an increase of capacity, opposite to that observed in the data, one of the few occasions where the trend is not captured correctly.

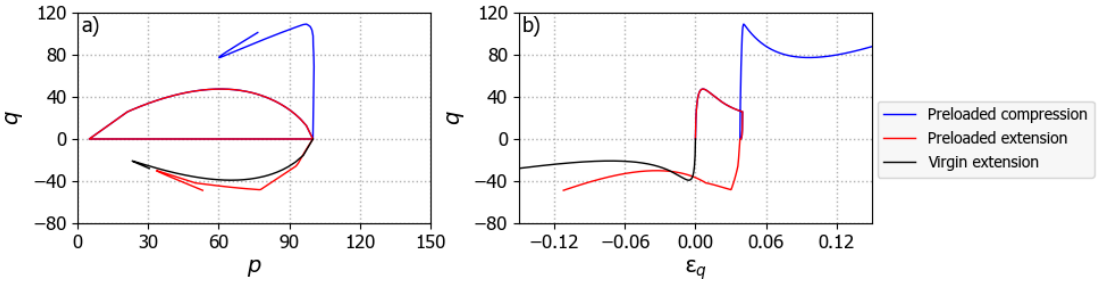


Figure 333 Simulated undrained tests after undrained preloading in compression

5.3.1.3. Comparison of undrained monotonic and cyclic stress paths

De Gennaro *et al.* (2004) have conducted tests on medium loose Hostun sand. Among these, comparisons between the monotonic undrained stress paths in compression and extension, with a cyclic two-way undrained stress path, shown on the left of Figure 334, are of special interest. One can observe that the sudden important pore pressure build-up on the extension side just before liquefaction of the cyclic test follows the stress path of the monotonic extension test. In the right-hand graph of Figure 334, HySand_base simulations with $v_0 = 1.94$ reproduce well this phenomenon.

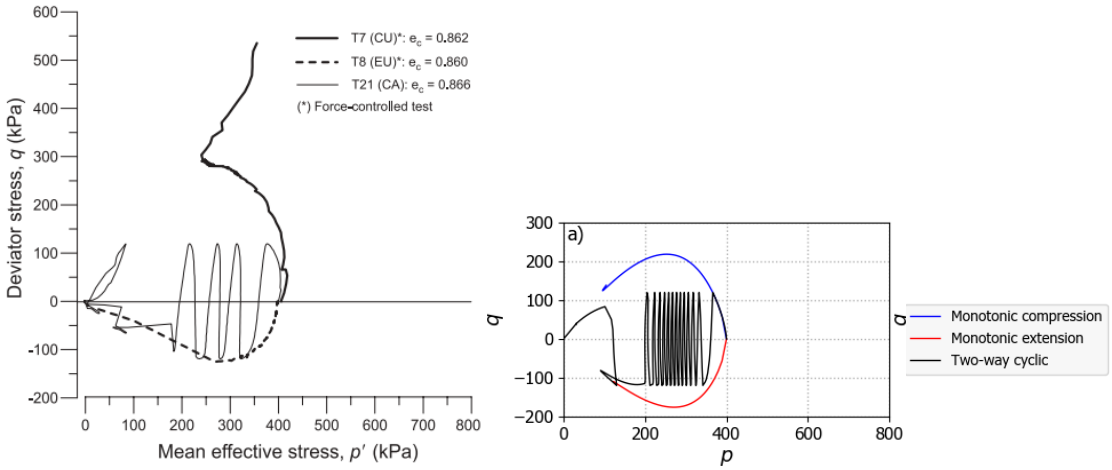


Figure 334 Left: Undrained tests on medium loose Hostun sand (from De Gennaro et al. (2004)); Right: simulation with HySand_base

5.3.1.4. Effect of isotropic and anisotropic overconsolidation

Finge *et al.* (2006) have studied the impact of isotropic and anisotropic overconsolidation on loose Hostun sand prepared with the moist tamping technique.

5.3.1.4.1. Isotropic consolidation

The impact of isotropic overconsolidation (ratios 1, 1.4, 2, 4, and 8) is presented in Figure 335.

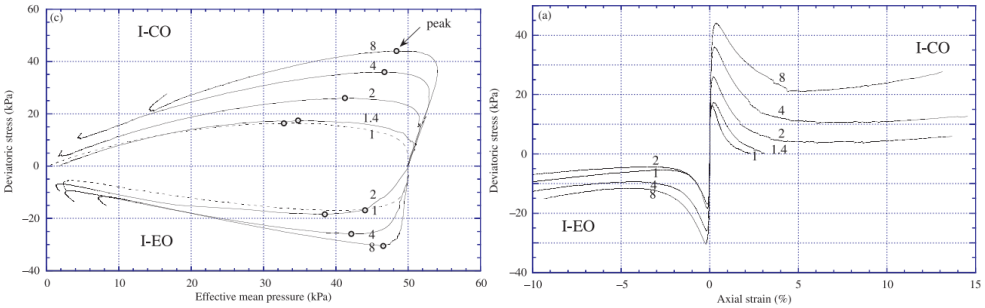


Figure 335 Undrained loadings with different OCR by Finge (2004)

HySand_base captures well the progressive increase of capacity with increasing OCR values, as shown in Figure 336 using $v_0 = 1.965$.

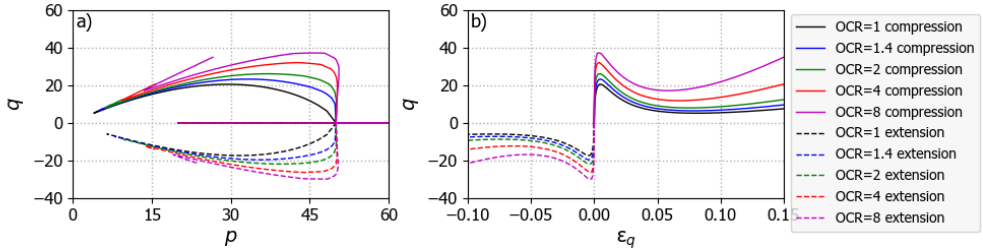


Figure 336 Simulations with HySand_base of overconsolidated undrained tests

5.3.1.4.2. Anisotropic consolidation

Anisotropic consolidation has been applied by Finge from a starting isotropic $p = 50$kPa. The results for $K_0 = 0.5$ are presented in Figure 337. Here the OCR levels (1, 2, 4, 8, 24) refer to the maximal mean effective stress reached during the consolidation divided by the initial 50kPa.

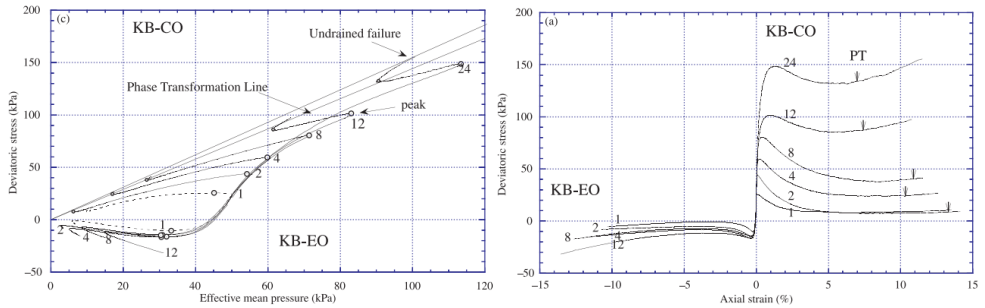


Figure 337 Anisotropically overconsolidated (K_0=0.5) undrained tests by Finge (2004)

The simulation of the tests (in Figure 338) depicts the tendencies observed for the data: increased capacity with increasing consolidation for tests in compression, and uniformly increased capacity for overconsolidated samples in extension. However, for tests in compression, the data shows a larger increase of capacity with overconsolidation because stress paths are more curved towards higher p than in HySand_base, leading to higher shear stresses at the end of what one can assume as their elastic phase. Overall the fitting of these tests is not good in quantitative terms.

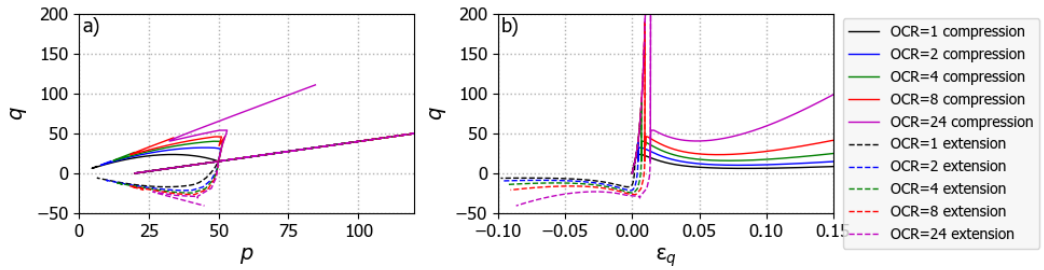


Figure 338 Simulation of anisotropically overconsolidated (K_0=0.5) undrained tests with HySand_base

5.3.1.5. Effect of drained preloading and reloading on undrained behaviour

Doanh *et al.*(2010) conducted undrained tests on loose Hostun sand (see Figure 339) prepared by moist tamping and preloaded in drained shear, before a complete or partial drained unloading.

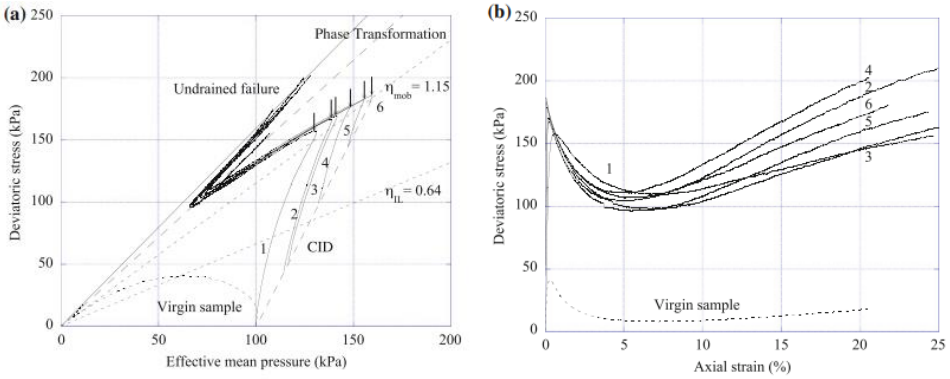


Figure 339 Undrained tests after drained preloading and partial unloading (from Doanh et al. (2010))

The simulation with HySand_base, shown in Figure 340, represents well the behaviour observed in the data: a stiff reloading (although too vertical in stress space for the simulation), a progressive increase in capacity with decreasing drained unloading, and overlayed stress paths during the contractive phase (pore pressure build-up) and dilative phase (pore pressure dissipation).

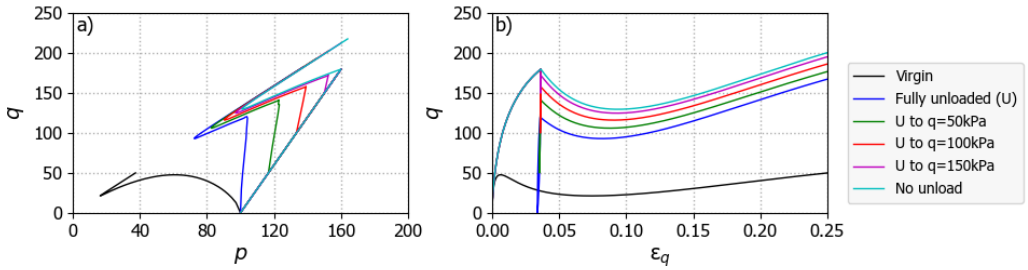


Figure 340 Simulated undrained tests after drained preloading and partial unloading with HySand_base

5.3.1.6. Summary of results for tests at ENTPE on Hostun sand

HySand_base is able to reproduce qualitatively the behaviour of undrained tests on Hostun sand which were preloaded in a variety of ways (isotropic and anisotropic consolidation, undrained and drained preloading in compression and extension with different directions of stress paths).

An aspect that HySand_base does not seem to reproduce well is the curvature of the stress path during the elastic reloading: HySand_base leads to undrained elastic stress paths which are too

vertical. Although the qualitative comparison is usually good, some effects are not well captured in quantitative terms: a specific calibration of material parameters may improve the comparison.

5.3.2. Fuji river sand

The Fuji river sand is a subangular sand with characteristic specific volumes $\Delta = 1.53$ and $B = 2.08$. "Saturated specimens were prepared in a loose state of packing by pouring freshly boiled sand into a split mold filled with de-aired water" (Ishihara, 1978). The calibration of properties for this sand could not be done. The parameters used are the ones for Hostun sand shown in Table 24, except for the characteristic specific volumes replaced by the above.

5.3.2.1. Effect of cyclic loading with small preshearing

Ishihara and Okada (1978a) compare two cyclic stress-controlled undrained tests: the first one normally consolidated, and the second one starting from the reconsolidation of the first one to the same initial mean effective stress. The two tests are shown in Figure 341.

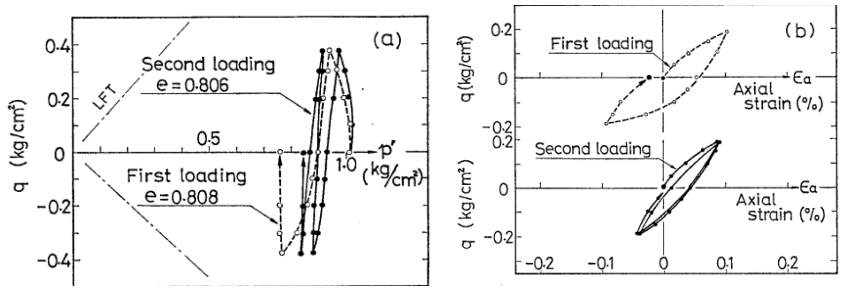


Figure 341 Undrained stress-controlled cyclic tests by Ishihara and Okada (1978a)

HySand_base (results in Figure 342) reproduces the characteristic behaviour shown in the data: less pore pressure build-up and stiffer response for second loading after reconsolidation.

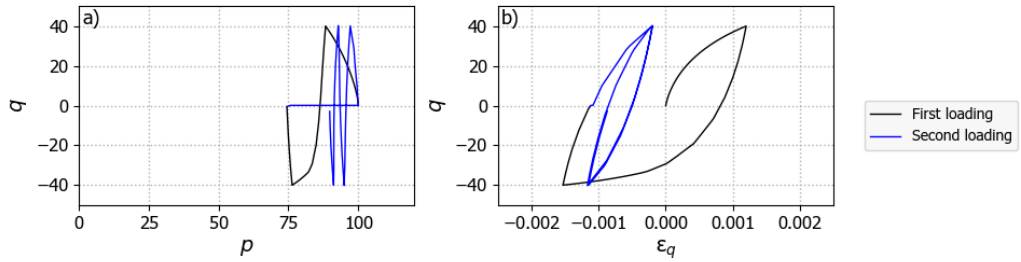


Figure 342 Simulation of undrained stress controlled cyclic tests with HySand_base

5.3.2.2. Effect of large preshearing on one side on subsequent cyclic loading

In the previous paragraph, the first cycle of loading only gives rise to low shear strains, and the behaviour is entirely contractive (only pore pressure build-up). Ishihara and Okada (1978a) remark that larger preshearing implies a different behaviour during the second loading, with a larger pore pressure build-up in the half cycle with the direction opposite to the one of the large

preshearing. This is illustrated in Figure 343 for large preshearing in the compression direction: upon reloading, the pore pressure build-up is reduced in the compression direction, but larger in the extension direction. HySand_base (see Figure 344) captures well this behaviour: almost no pore pressure generation and a very stiff response during the reloading in compression, but a large pore pressure build-up and a softer response in extension, and no pore pressure build-up on the final half cycle on the compression side.

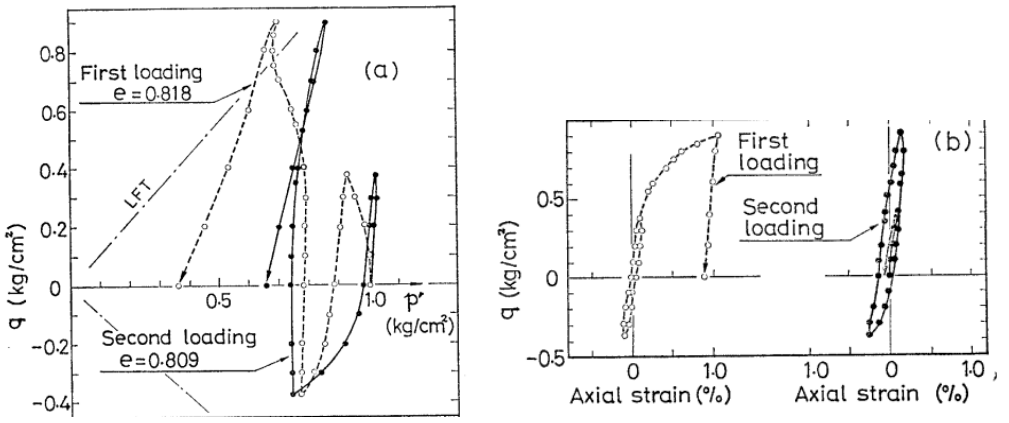


Figure 343 Undrained stress-controlled cyclic loading after large preshearing in the compression direction by Ishihara and Okada (1978a)

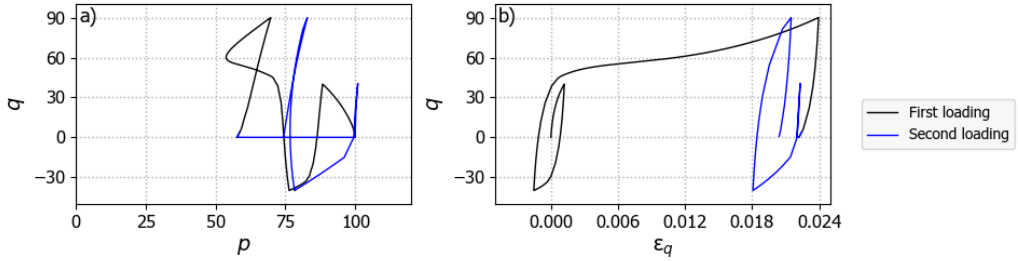


Figure 344 Simulation with HySand_base of an undrained test after large preshearing

5.3.2.3. Successive large shearing in different directions

Ishihara and Okada (1978a) have also conducted tests with successive large shearing in compression and extension pictured in Figure 345.

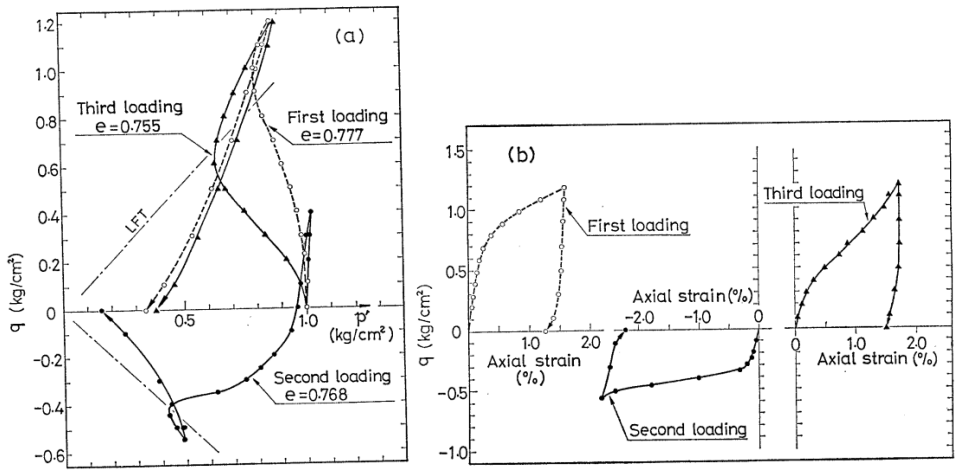


Figure 345 Successive large shearing in compression and extension by Ishihara and Okada (1978a)

The behaviour displayed during this test is well captured with HySand_base (see Figure 346): a large pore pressure build-up only in extension during the second loading, and a third loading resembling the first one but with a softer initial response with more pore pressure build-up.

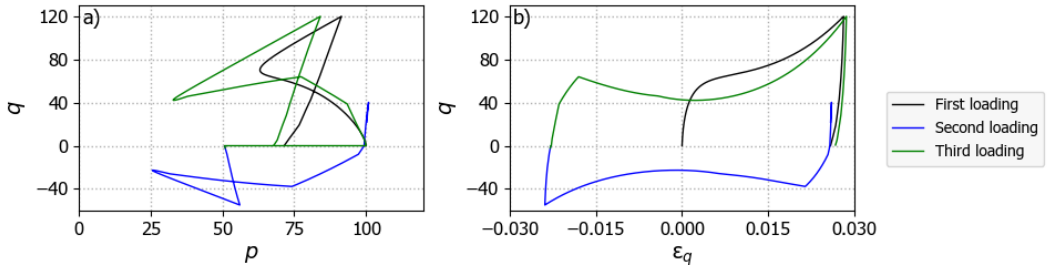


Figure 346 Simulation with HySand_base of large shearing in compression and extension

5.3.2.4. Overconsolidation to determine yield locus

Ishihara and Okada (1978b) have tried to determine yield loci for Fuji river sand. Running overconsolidated undrained tests, reproduced in Figure 347, Ishihara and Okada have tried to locate a transition from elastic to plastic behaviour.

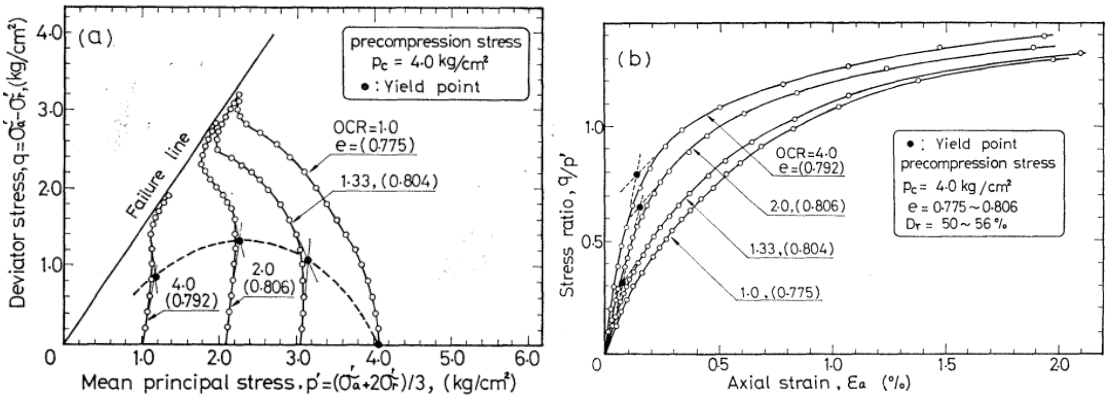


Figure 347 Overconsolidated tests on Fuji river sand by Ishihara and Okada (1978b)

The plastic nature and the presence of the consolidation mechanism of HySand_base lead to a good depiction of this transition from elasticity to plasticity, as shown in Figure 348. The stress paths against the stress ratio are also well depicted.

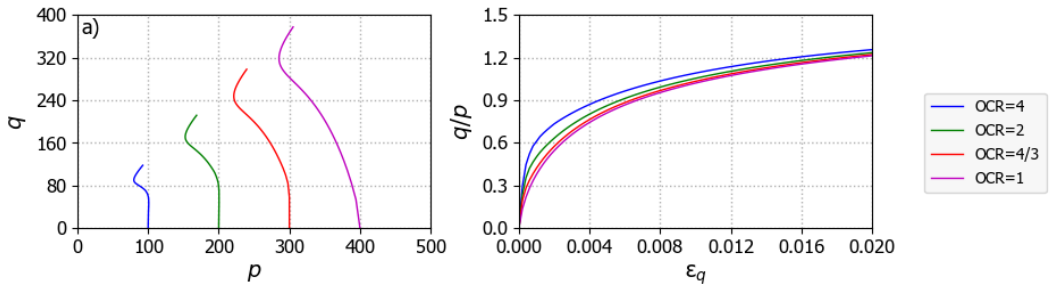


Figure 348 Simulation of overconsolidated tests with HySand_base

5.3.2.5. Impact of overconsolidation on cyclic stress-controlled loading

Ishihara and Okada (1978b) also show, see Figure 349 and Figure 350, that an increased overconsolidation ratio leads to less pore pressure build-up upon cycling, and a stiffer response.

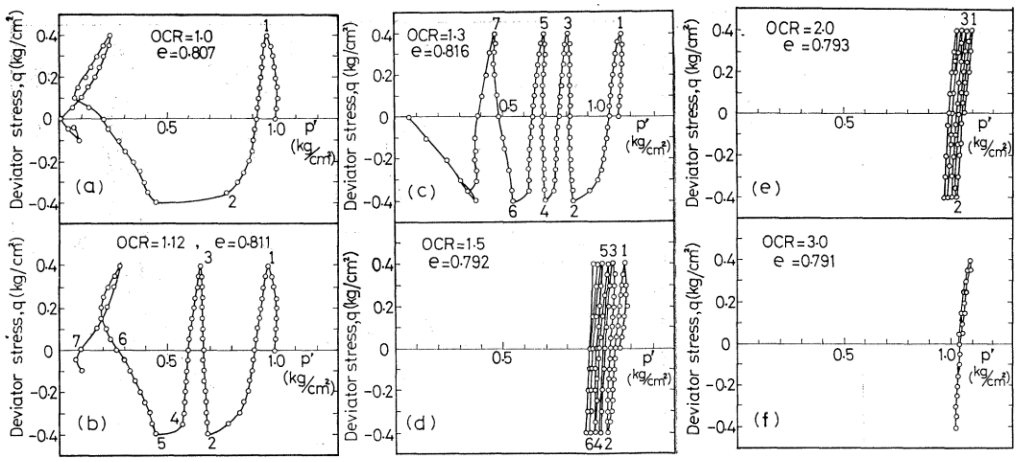


Figure 349 Overconsolidated cyclic undrained stress-controlled tests by Ishihara and Okada (1978b): part 1

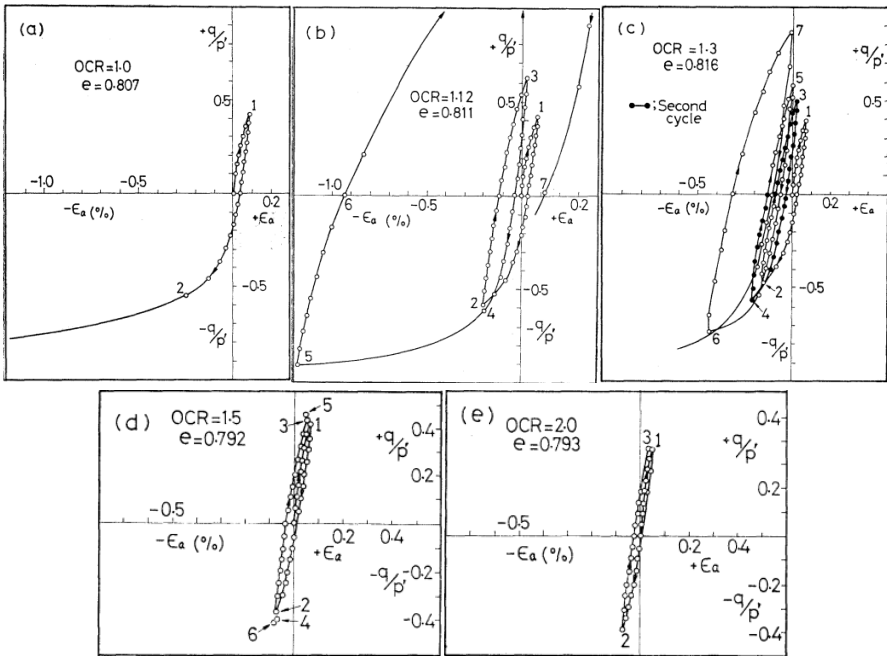


Figure 350 Overconsolidated cyclic undrained stress-controlled tests by Ishihara and Okada (1978b): part 2

Despite not perfectly capturing the number of cycles to liquefaction (presumably because it was not calibrated), HySand_base does represent the two phenomena cited above (see Figure 351 and Figure 352).

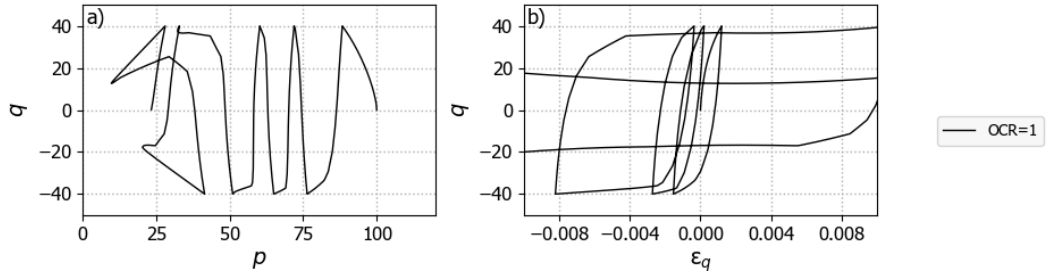


Figure 351 Simulations with HySand_base of a normally consolidated sample

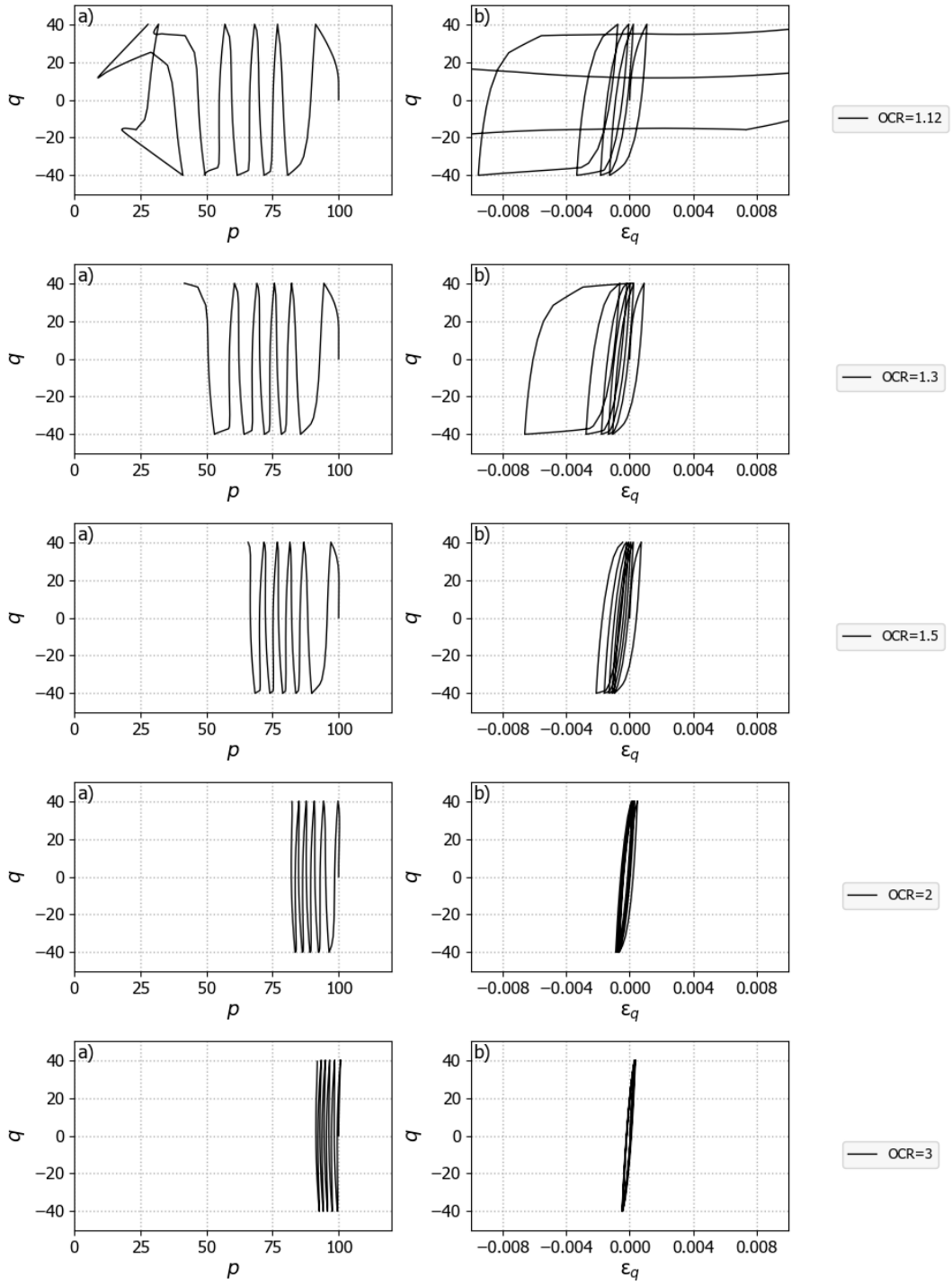


Figure 352 Simulations with HySand_base of overconsolidated samples

5.3.2.6. Summary of results of test on Fuji river sand

HySand_base appears to capture well the effect of preloading (small and large shearing, overconsolidation, undrained cycles) on subsequent cyclic undrained loading: overconsolidation and small shearing in cyclic loading lead to a stiffer response with less pore pressure build-up; large shearing in one direction (compression or extension) leads to a largely stiffer response and almost no pressure build-up in the same direction, but to a softer response and a large pore pressure build-up in the opposite direction.

5.3.3. Toyoura sand

5.3.3.1. Monotonic undrained and drained tests

In Verdugo and Ishihara (1996), the steady state of Toyoura sand is studied via monotonic drained and undrained tests. The characteristic volumes are $\mathrm{B} = 1.977$ and $\Delta = 1.597$. However, one of the drained test has a starting specific volume of $v_0 = 1.996$. The simulations with HySand_base are run with the parameters given in Table 24, modifying the characteristic specific volumes to $\mathrm{B} = 2.05, \Gamma = 1.91$ and $\Delta = 1.597$.

Verdugo and Ishihara obtained the undrained tests at different initial consolidation pressures and different initial specific volumes presented in Figure 353 to Figure 355.

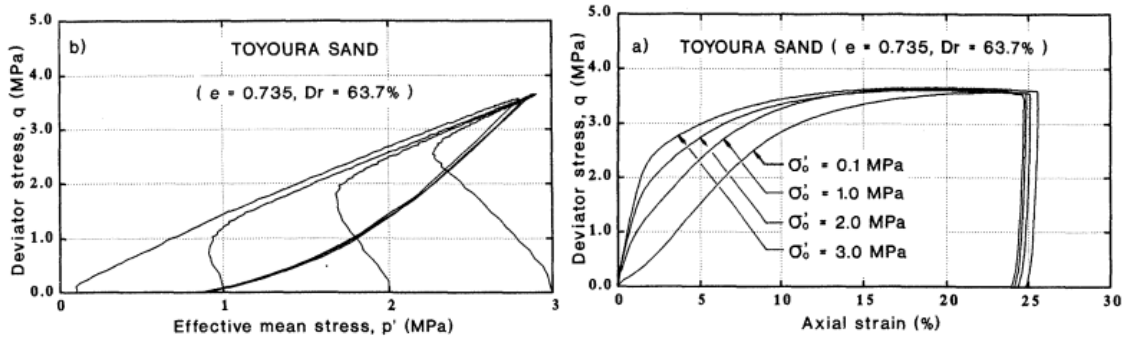


Figure 353 Undrained tests with $v_0 = 1.735$ by Verdugo (1996)

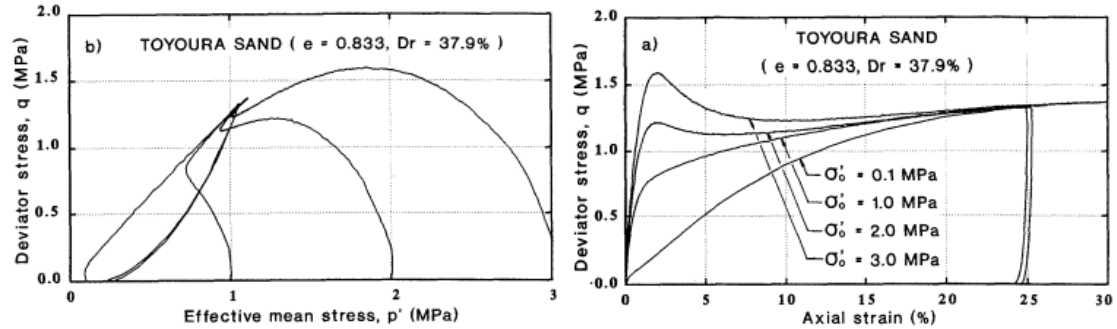


Figure 354 Undrained tests with $v_0 = 1.833$ by Verdugo (1996)

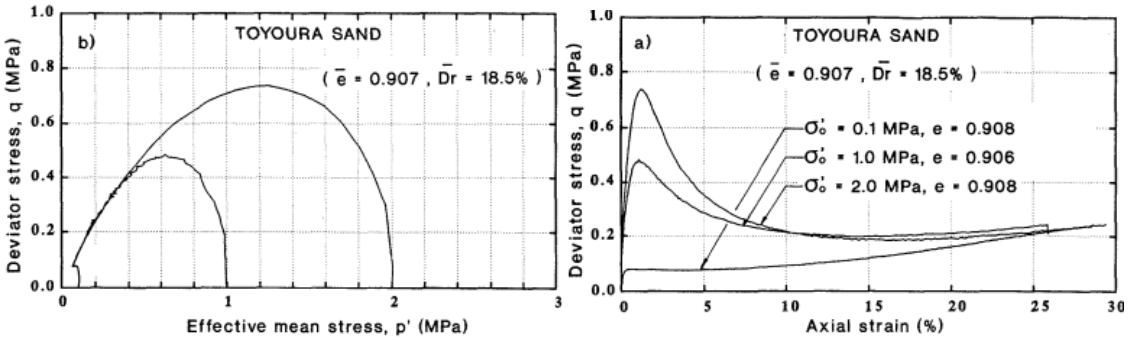


Figure 355 Undrained tests with $v_0 = 1.907$ by Verdugo (1996)

The simulations with HySand_base are shown in Figure 356 to Figure 358.

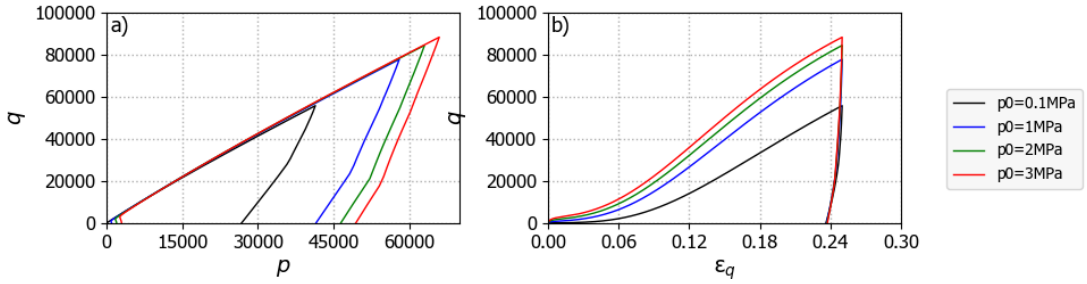


Figure 356 Simulation with HySand_base of undrained tests with $v_0 = 1.735$

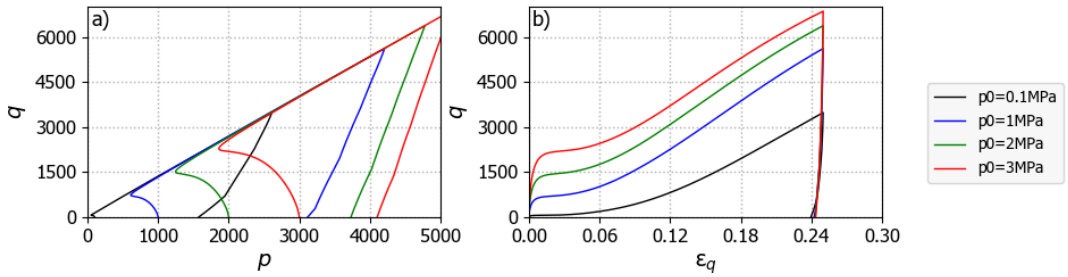


Figure 357 Simulation with HySand_base of undrained tests with $v_0 = 1.833$

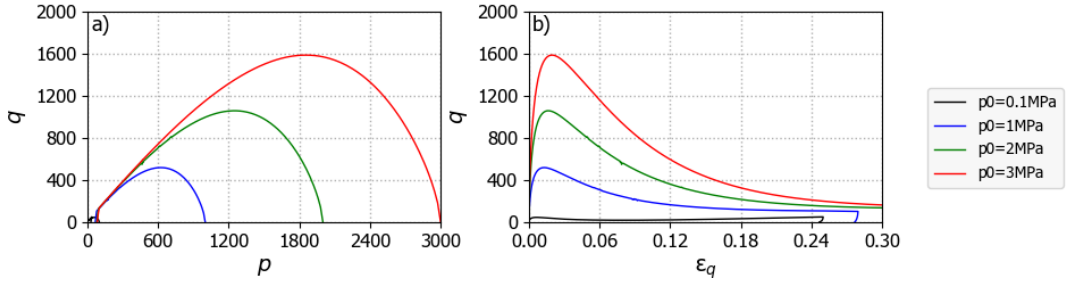


Figure 358 Simulation with HySand_base of undrained tests with $v_0 = 1.907$

While the test data shows a saturation of the shear capacity below 4MPa for the densest sample, and 1.5MPa for the medium dense sample, no such saturation is captured by HySand_base. In HySand_base, tests with initial low specific volumes will exhibit positive shear stress/strain asymptotes, and thus no saturation of the capacity.

Verdugo also conducted drained tests for different initial specific volumes and initial consolidation pressures. These are presented in Figure 359 and Figure 360.

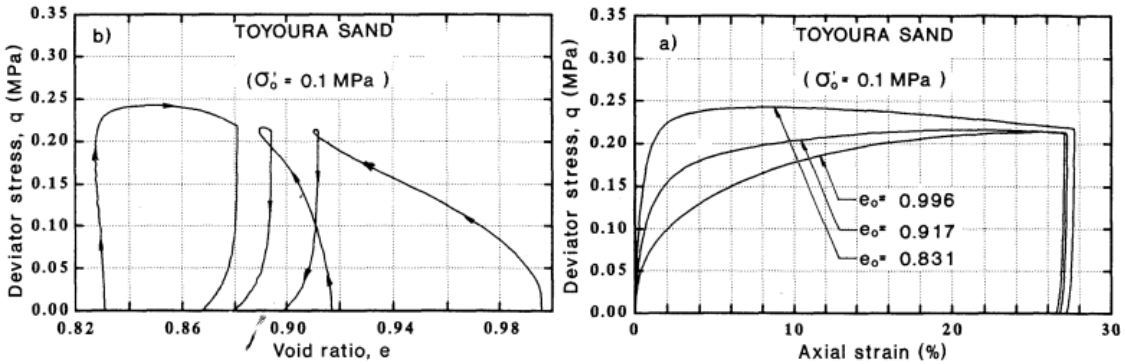


Figure 359 Drained tests on Toyoura sand with $p_0 = 100kPa$ *by Verdugo (1996)*

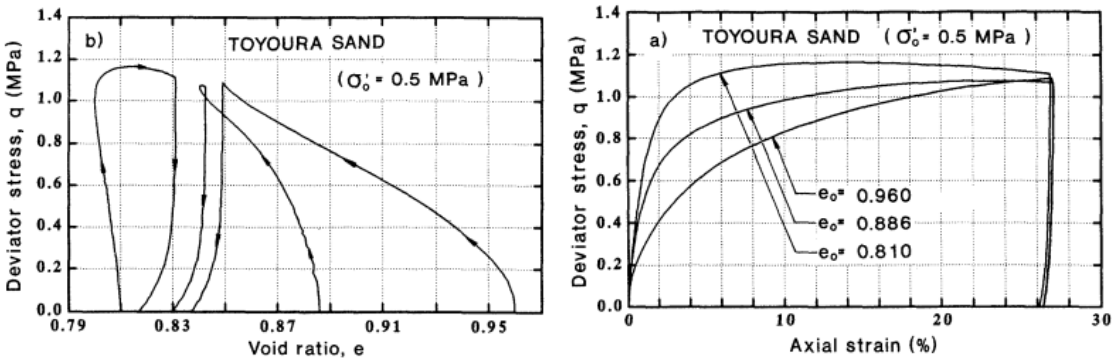


Figure 360 Drained tests on Toyoura sand with $p_0 = 500kPa$ by Verdugo (1996)

The simulations with HySand_base, Figure 361 and Figure 362, seem to reproduce well the behaviour observed in the data, with the exception of the evolution of the void ratio on unloading: in the simulation it almost does not change, whereas a significant reduction is observed in the data. This matches other observations of an insufficient contraction during load reversal.

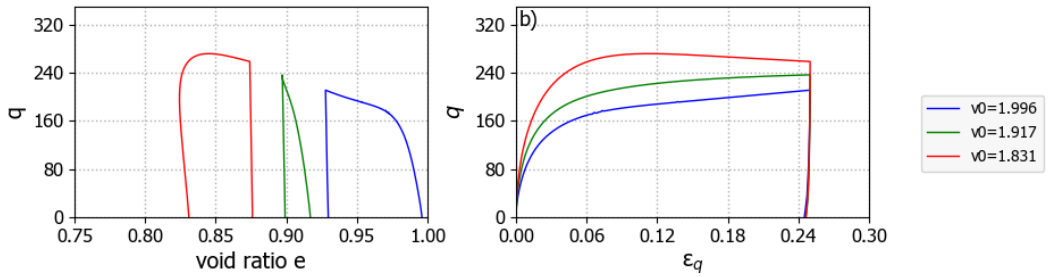


Figure 361 Simulation with HySand_base of drained tests with $p_0 = 100kPa$

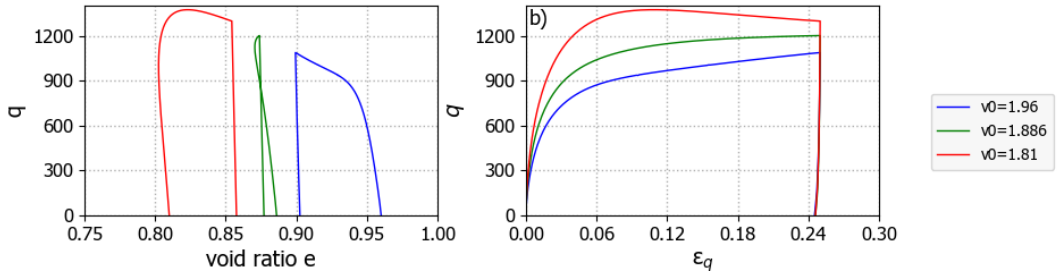


Figure 362 Simulation with HySand_base of drained tests with $p_0 = 500kPa$

5.3.3.2. Cyclic drained tests with increasing strain amplitude

Pradhan *et al.* (1989) have conducted drained cyclic tests with constant mean effective stress on loose and dense Toyoura sand prepared by air pluviation, shown in Figure 363 for which $B = 1.977$ and $\Delta = 1.605$.

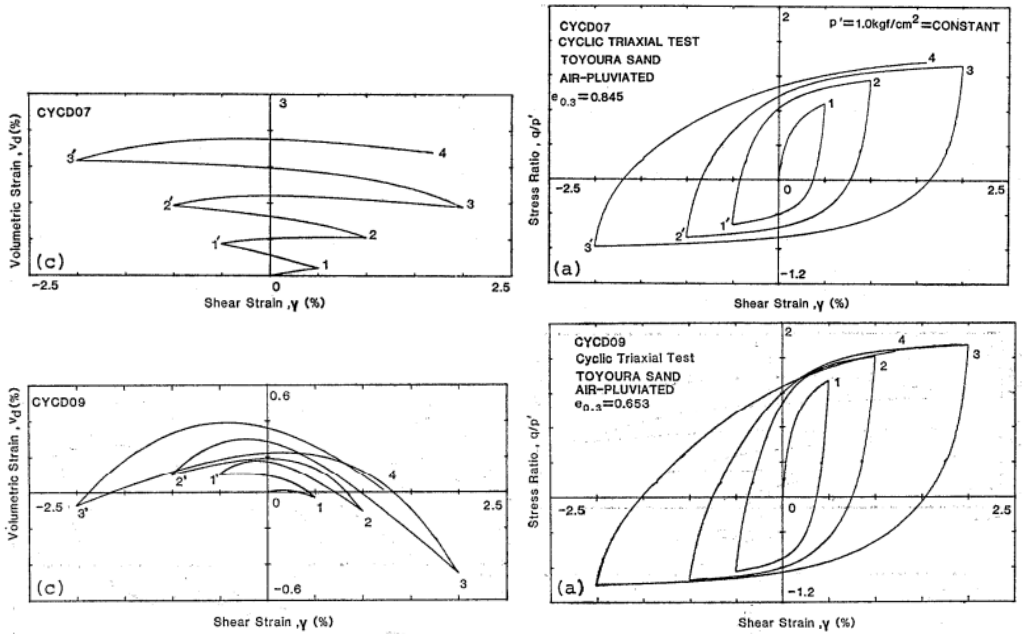


Figure 363 Drained cyclic test on loose (top) amd dense (bottom) Toyoura sand by Pradhan (1989)

These two tests are simulated with HySand_base, using the parameters presented in Table 24, simply updating B and Δ, as well as $\Gamma = 1.9$, and using the specific volumes of the tests: $v_0 = 1.845$ represented in Figure 364, and $v_0 = 1.653$ represented in Figure 365. The behaviour is qualitatively well represented by HySand_base: a progressive accumulation of contraction for the loose sample, and an approximate stalemate for the dense sand.

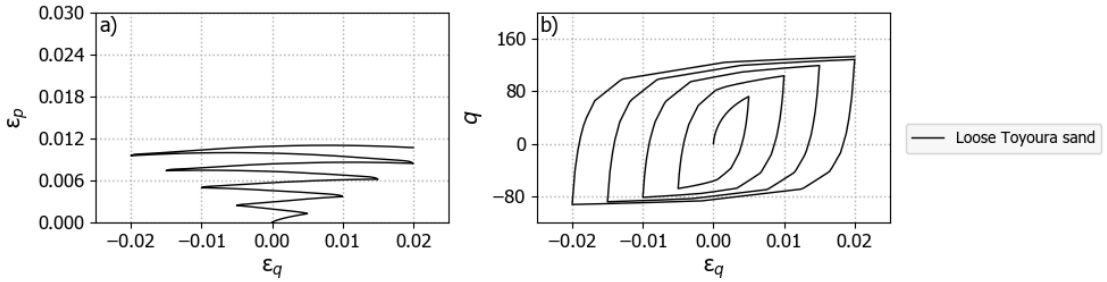


Figure 364 Simulation of drained cyclic test on loose sand with HySand_base

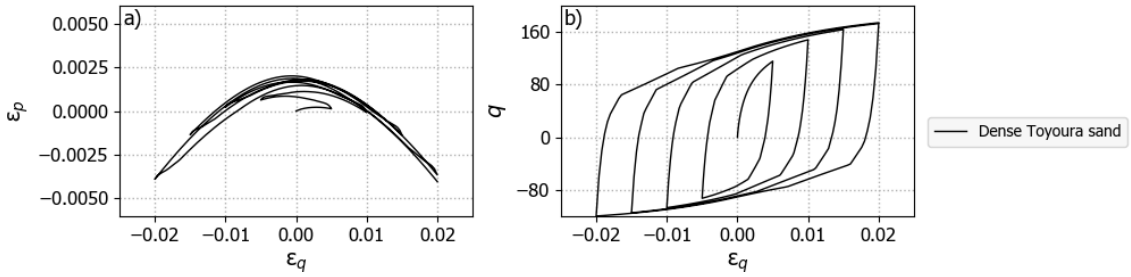


Figure 365 Simulation of drained cyclic test on dense sand with HySand_base

5.4. Characteristic limitations of constitutive models for cyclic loading of sand

The following paragraphs are based on the paper by Duque *et al.* (2022) where characteristic limitations of constitutive models for sand under cyclic loading are highlighted. Four constitutive models were studied: SANISAND DM04 (Dafalias and Manzari 2004), SANISAND MSf with memory surface and semifluidized state (Yang *et al.*, 2022), the hypoplastic with intergranular strain model HP+IS (von Wolffersdorff (1996) and Niemunis and Herle (1997)), and an enhanced hypoplastic model HP+ISA (Fuentes and Triantafyllidis (2015), Fuentes *et al.* (2020)).

The characteristic limitations of cyclic models highlighted by Duque are evaluated for HySand_base in the following paragraphs, and the results compared to data and existing models.

5.4.1. Overshooting after small unloading/reloading

Overshooting issues are often observed in models. For an undrained triaxial test, overshooting means, here, that small unloading-reloading steps during loading lead to higher stresses than those observed in the monotonic test.

To illustrate this, Duque evaluated the four models against tests on Toyoura sand by Ishihara (1996). In the monotonic test, an isotropic normally consolidated sample at 100kPa of relative density 16% was submitted to a drained loading up to $q = 80kPa$, before an undrained loading up to $\epsilon_1 = 20\%$. In the unloading-reloading test, instead of the monotonic loading to 20% strain, the loading goes up to 0.3% strain, then five unloading-reloading cycles of amplitude 0.03% are run, before a final reloading to 20%. Figure 366 presents the data on Toyoura sand.

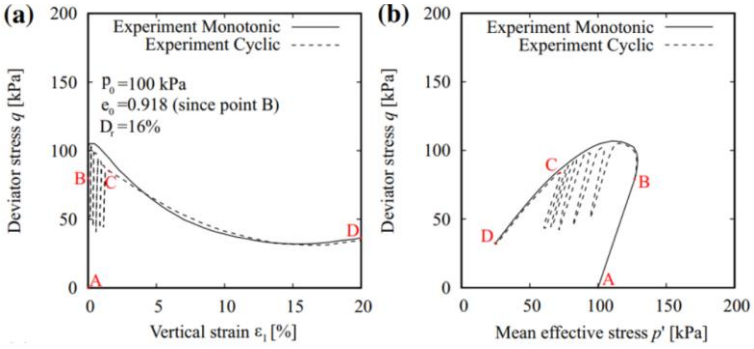


Figure 366 Undrained monotonic and "cyclic" tests on loose Toyoura sand

Figure 367 presents its simulation with the four advanced constitutive models. Three models, DM04, SANISAND-MSf, and HP+IS, show overshooting issues, with a very severe issue for the HP+IS model. The HP+ISA model shows the opposite problem: undershooting.

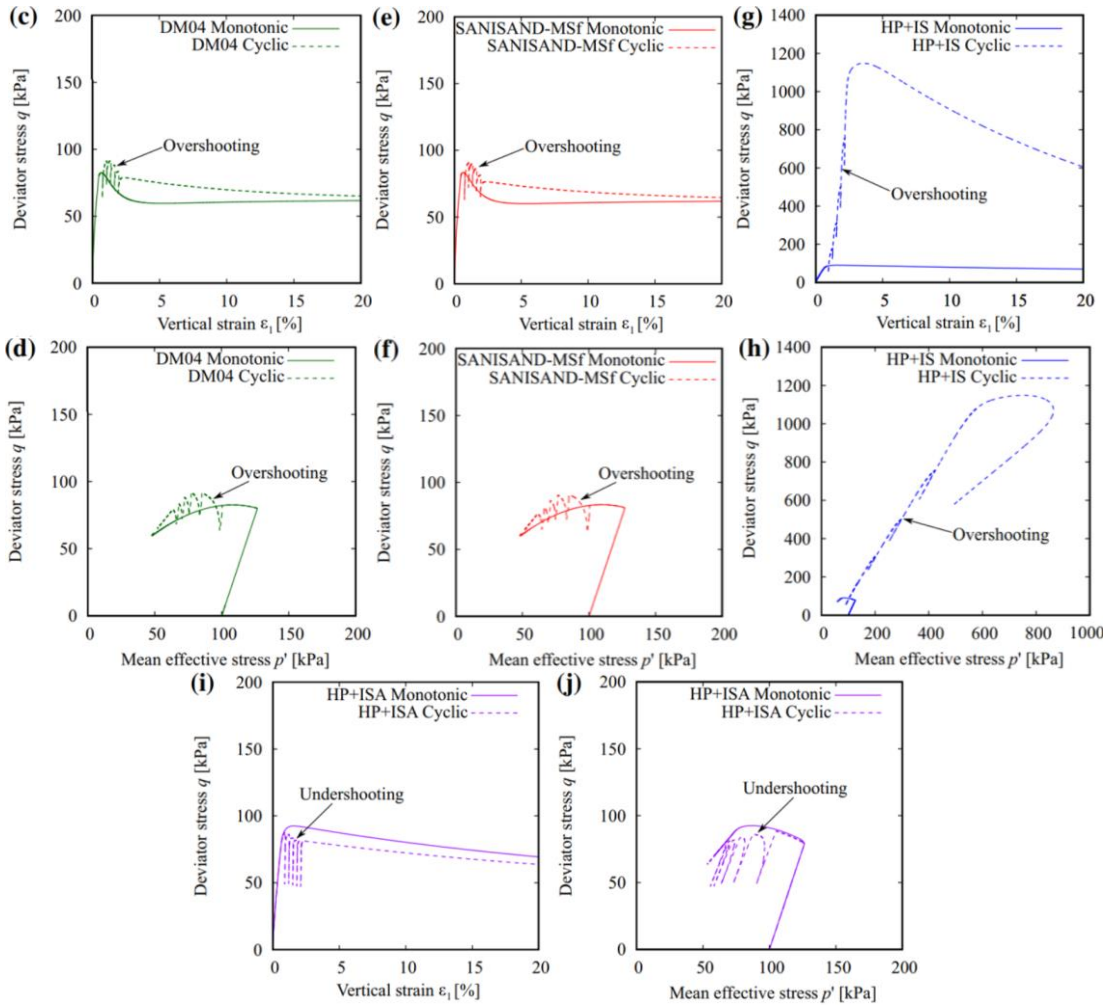


Figure 367 Simulation by Duque et al. (2022) of the tests on Toyoura sand

The base model is run with ten surfaces for this case. Instead of a proper calibration, solely the characteristic specific volumes are modified from the calibration in Chapter 4: $B = 1.977$, $\Gamma = 1.93$, and $\Delta = 1.597$. No over or under shooting is observed in the simulation shown in Figure 368. This behaviour comes from the multi-surface nature of the model: when a small unload-reload cycle takes place, most plastic surfaces stay in place such that the test backer-engages these yield surfaces at the same stress point after the unloading-reloading cycles. This is a fundamental feature of multi-surface models as opposed to boundary surface or hypoplastic models.

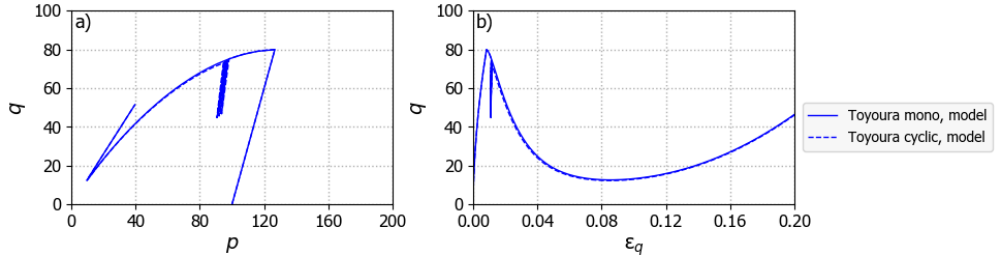


Figure 368 Simulation of the tests on Toyoura sand with HySand_base

Compared to the data, one can note that the base model builds-up less pore pressure during the unloading-reloading cycles.

5.4.2. Strain accumulation during cyclic mobility for a symmetric loading

A symmetric undrained stress controlled test leads to a cyclic mobility, a phase during which large strains develop, but without any overall accumulation of strain as shown in Figure 369 a)b).

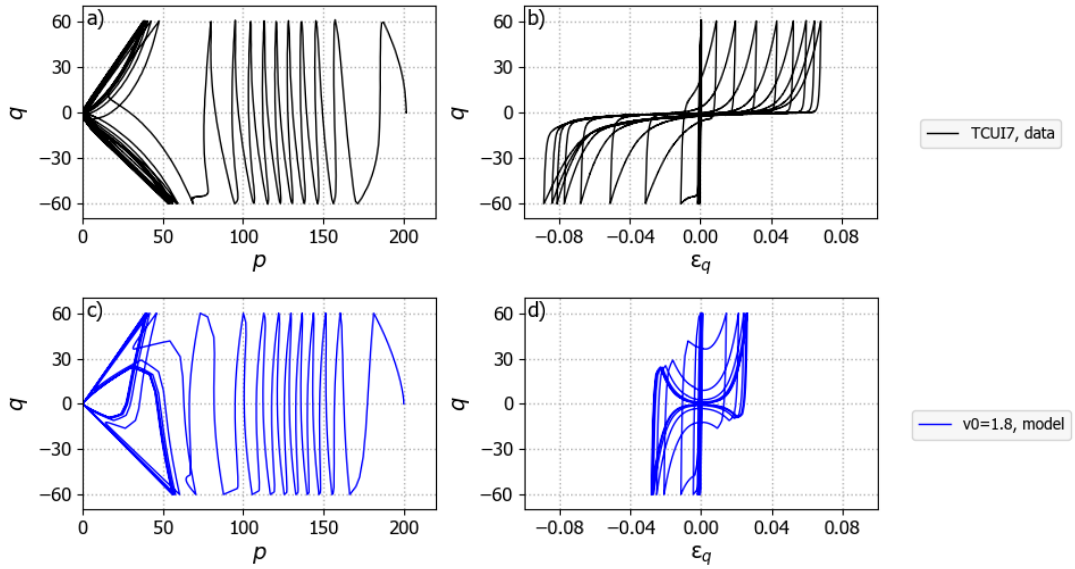


Figure 369 a)b) Test TCUI7 by Wichtmann on medium dense sand, c)d) simulation with HySand_base

However Duque shows that, of the four advanced models, three (DM04, HP+IS, and HP+ISA) produce negative shear strain accumulation, as seen in Figure 370.

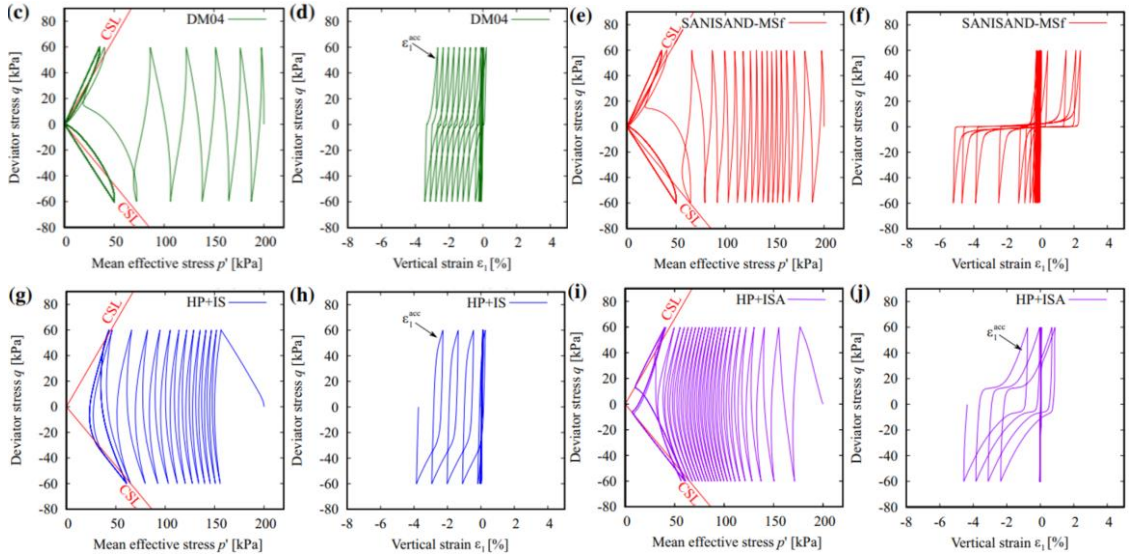


Figure 370 Simulation of TCUI7 tests with four advanced models by Duque (2022)

Figure 369 c)d) presents the simulation of TCUI7 with HySand_base calibrated in Chapter 4. It does not present any strain accumulation. One can also note in stress space the quality of the simulation of the progressive pore pressure build-up with cycles compared to other models. However, the butterfly-shaped cyclic mobility loops are not well captured by HySand_base.

5.4.3. Cyclic liquefaction strength curves

One of the most challenging phenomena to capture is the variation of the numbers of cycles to liquefaction across densities and across cyclic amplitudes. Tests TCUI1 to TCUI22 by Wichtmann and Triantafyllidis (2016a) are a good benchmarking tool for this phenomenon.

From the Wichtmann experiments, Duque *et al.* (2022) have extrapolated a power law relation between the number of cycles to liquefaction and the cyclic stress ratio (CSR: shear half amplitude divided by the initial mean effective stress). Here, such power laws are not used and the experimental and simulation data points are simply superimposed.

The definition for the initiation of liquefaction can vary. In the following, the number of cycles to liquefaction denotes the number of cycles to reach a pore pressure build-up of 95% of the initial mean effective stress. Note that the simulations with the HP+IS model never reach this definition and are thus not presented.

In Figure 371 to Figure 373, results of tests TCUI2,3,4,8,9,10,11,12,13,14,15,16,18,19 and 20 by Wichtmann and Triantafyllidis (2016a) are superimposed with the results of the advanced models by Duque *et al.*. The results of the different models by Duque *et al.* are for standardised initial densities (loose: $D_r = 26\%$, medium: $D_r = 63\%$, dense: $D_r = 81\%$) and for normally consolidated samples at $p = 100kPa$. Figure 371 to Figure 373 show that DM04 does not manage to capture the variation of number of cycles to liquefaction with the variation of CSR, while SANISAND-MSf and HP+ISA perform rather well.

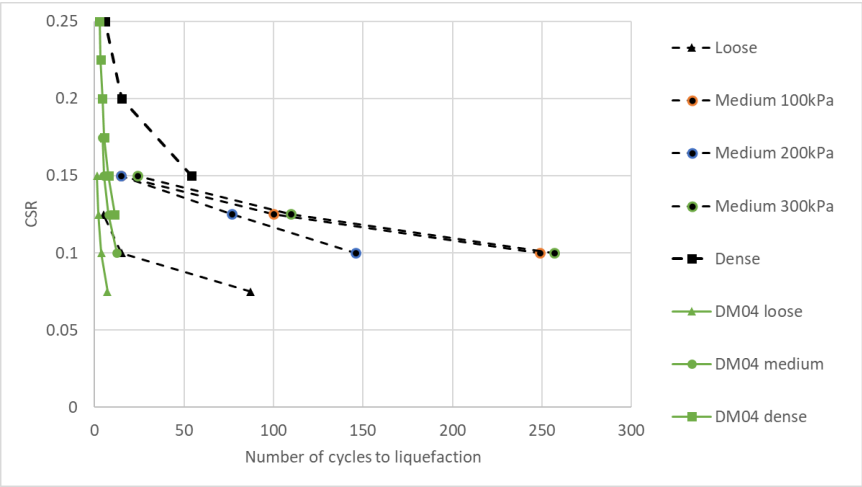


Figure 371 Data points for test by Wichtmann (black) and simulation results with DM04 (green)

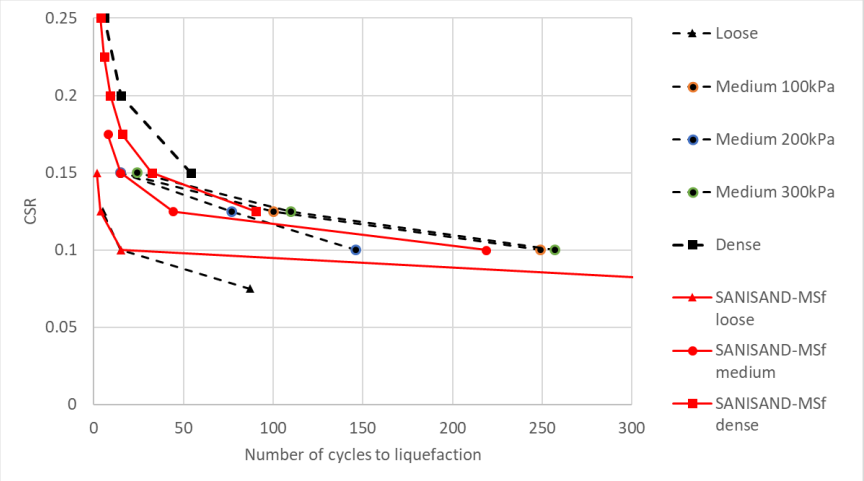


Figure 372 Data points for test by Wichtmann (black) and simulation results with SANISADN-MSf (red)

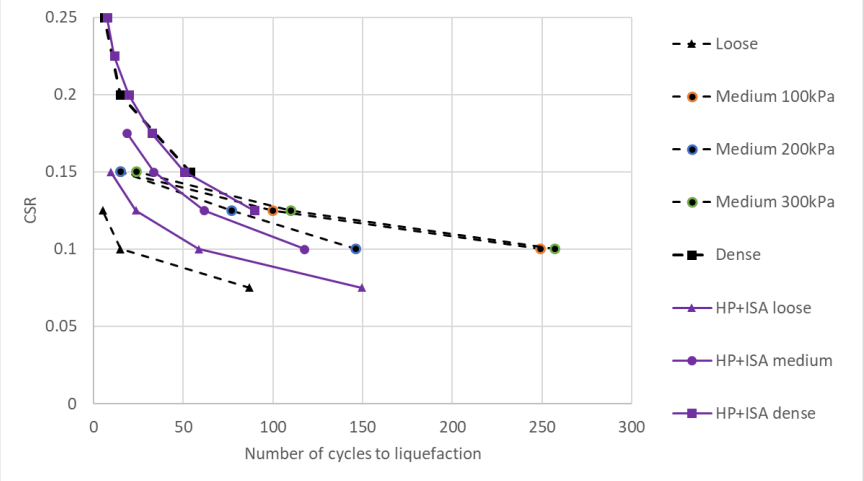


Figure 373 Data points for test by Wichtmann (black) and simulation results with HP+ISA (purple)

Figure 374 presents the results of the base model calibrated in Chapter 4 and the data for tests with an initial drained cycle TCUI2,3,4,8,9,10,11,12,13,14,15,16,18,19,20 by Wichtmann (2021). Contrarily to the simulation by Duque *et al.*, identical tests to Wichtmann are run (with the same initial specific volume and consolidation pressures), and with a first drained cycle.

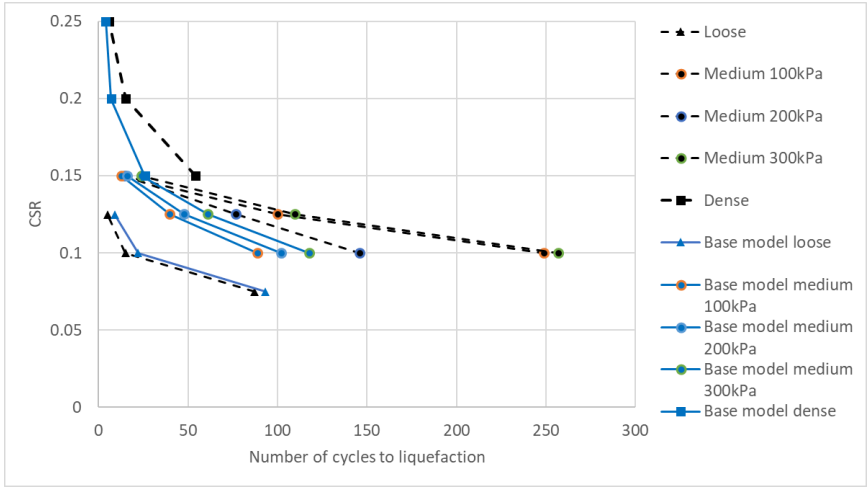


Figure 374 CSR against number of cycles to liquefaction (black: data, blue: HySand_base)

Figure 374 shows that the base model performs well across densities and CSR's.

5.4.4. Dense sample liquefaction in undrained cyclic strain controlled tests

Another limitation identified by Duque *et al.* is the ability of the models to simulate undrained cyclic strain-controlled tests for large strain. Specifically, Duque *et al.* identify a weakness of the two hypoplastic models: their inability to reach liquefaction for dense samples.

Test TCUE23 by Wichtmann and Triantafyllidis (2016b) on dense sand is shown in Figure 375. Pore pressure progressively builds-up with cycles until liquefaction is reached.

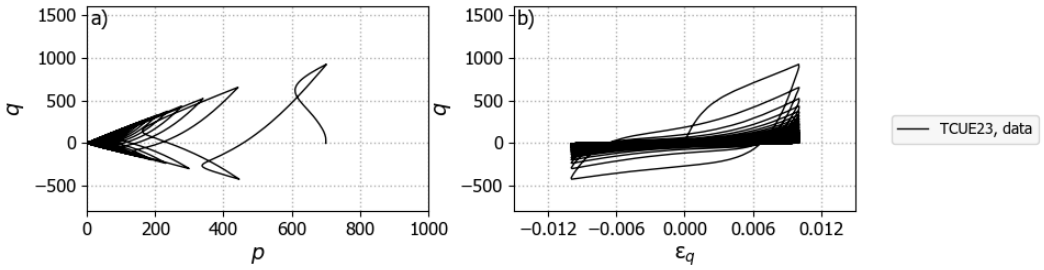


Figure 375 Strain controlled undrained test TCUE23 by Wichtmann(2021)

In Figure 376, simulations by Duque *et al.* are presented. Both SANISAND models reach liquefaction on the first cycle. The hypoplastic models do not reach liquefaction, with a locking of the cycles away from $p = 0$. For all four models, the secant stiffness does not decrease sufficiently with cycles compared to the data where it progressively decreases until reaching zero.

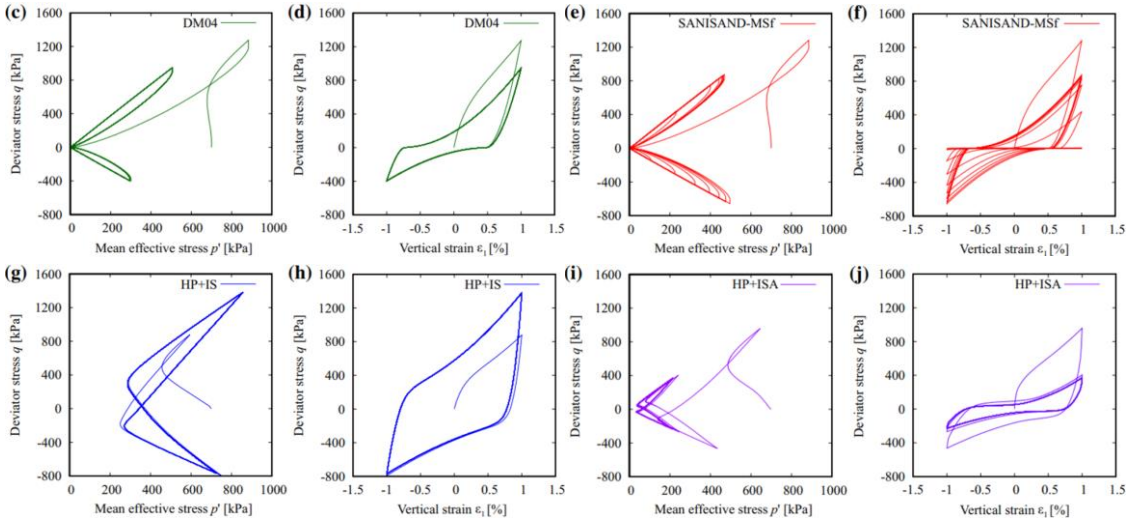


Figure 376 Simulations of TCUE23 by Duque (2022)

Figure 377 presents the simulation of TCUE23 with HySand_base calibrated in Chapter 4. The base model does not lead to liquefaction. Once again the contraction on load reversal is insufficient in HySand_base which, as a consequence, shows this limitation.

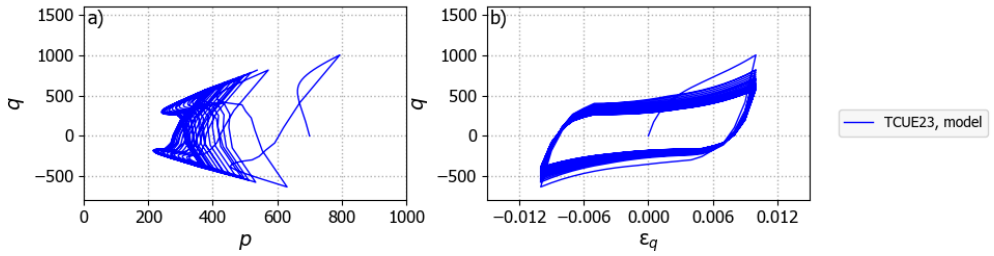


Figure 377 Simulation of TCUE23 with HySand_base

5.4.5. Accumulation of strain on small closed loop cycles

Poblete *et al.* (2016) have run closed looped cycles in $p - q$ space on Karlsruhe fine sand. The variation of the triaxial stresses describe an ellipse in stress space, with the following formulation:

$$p = 200 + \frac{20}{\sqrt{3}} \sin\left(\frac{2\pi}{200} t\right) \qquad \textit{Eq. 263}$$

$$q = 100 + 20\sqrt{3/2} \cos\left(\frac{2\pi}{200} t\right) \qquad \textit{Eq. 264}$$

The initial conditions of the test are $p = 200$kPa, $q = 124.5$kPa and $v_0 = 1.857$. With HySand_base, an initial drained triaxial loading from the isotropic line at $p = 158.5$kPa is considered. Figure 378 presents the results of the test by Poblete (2016). There is almost no strain accumulation, with a slow decrease of the void ratio, and quasi-elastic cycles.

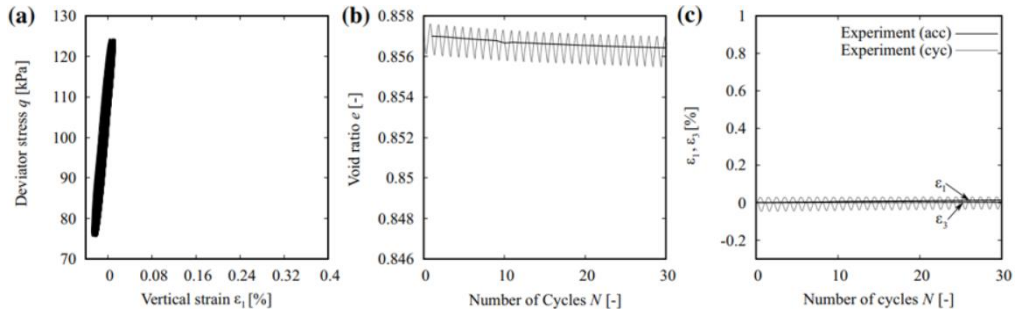


Figure 378 Stress loops tests by Poblete (2016), figure from Duque (2022)

Figure 379 presents the results of the simulation with the base model. The base model predicts well the test: no accumulation of vertical strain, and a slow decrease of the void ratio. However, the cyclic variation of strain and void ratio lacks amplitude compared to the data.

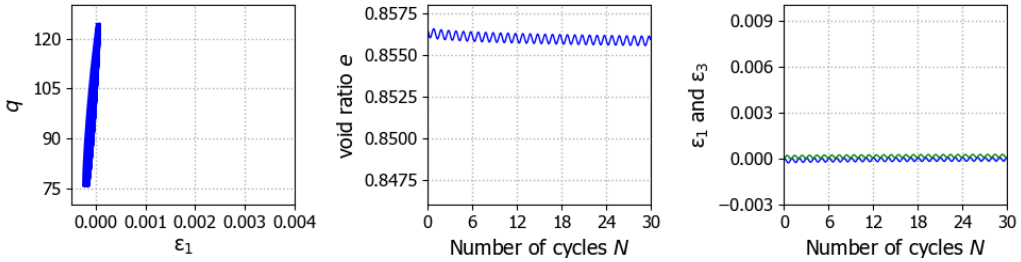


Figure 379 Simulation with HySand_base of the test by Poblete (2016)

The main fault of the two SANISAND models and of the HP+IS model is the accumulation of vertical strain during the loading, (c.f. Figure 380).

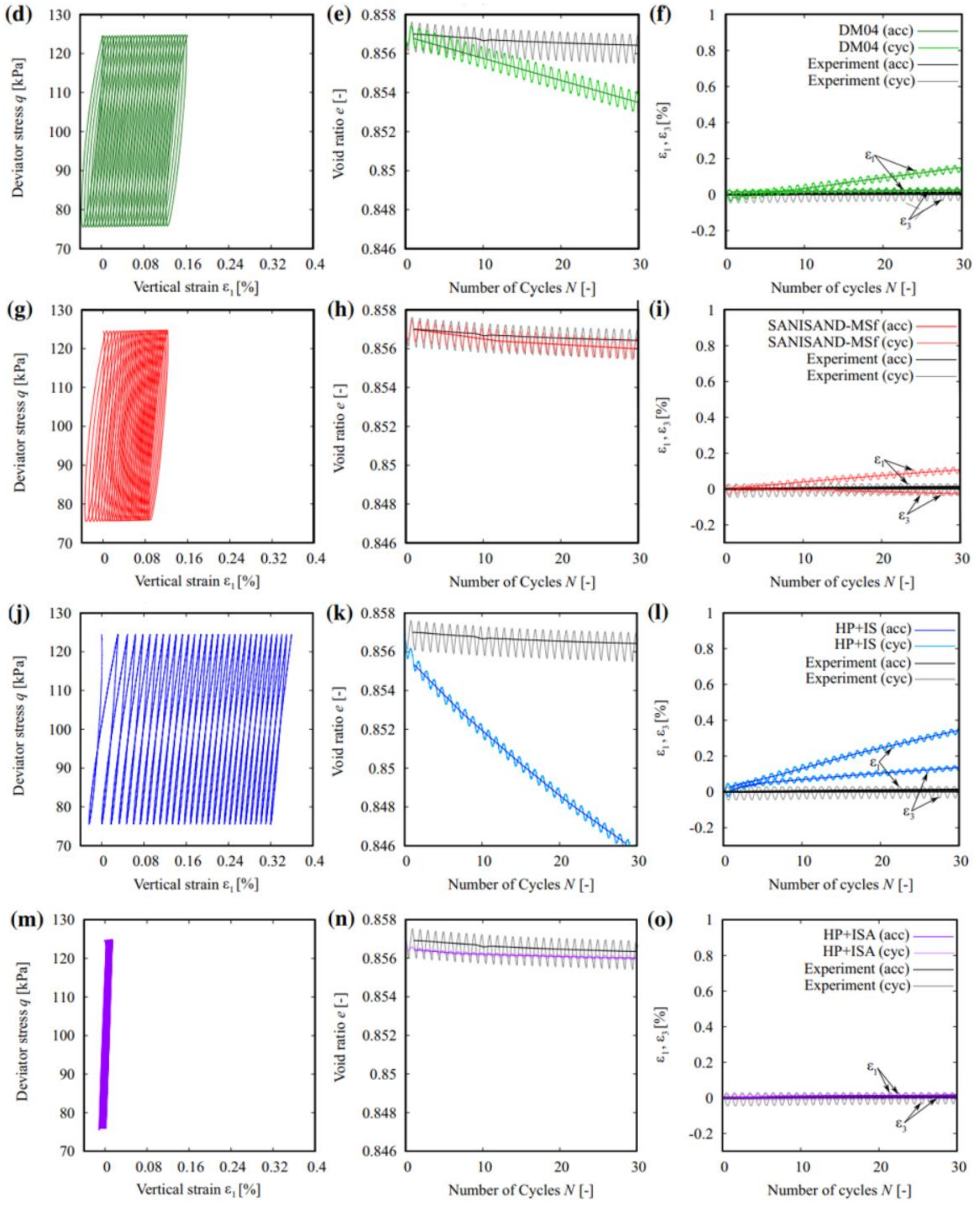


Figure 380 Results of the simulation of Poblete test by Duque (2022)

5.4.6. Oedometric stiffness and over/undershooting

Duque *et al.* (2022) highlight two common limitations of constitutive models when predicting oedemetric tests with unloadings and reloadings: a poor depiction of the oedometric stiffness, and over or undershooting problems after unloading/reloading loops.

Figure 381 presents the result of OEC2, a cyclic oedometric test on medium dense Karlsruhe fine sand by Wichtmann and Triantafyllidis (2016b).

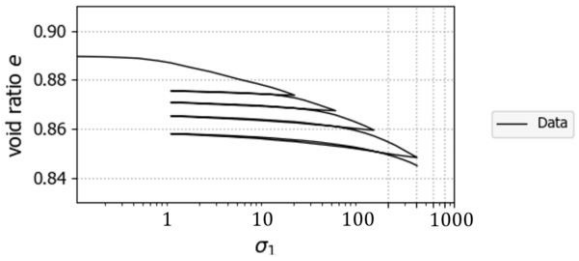


Figure 381 Test OEC2 on medium dense sand by Wichtmann (2021)

Figure 382 presents simulations of OEC2, along the simulation of a monotonic oedometric test, by Duque *et al.* (2022). Both SANISAND models present an oedemetric stiffness inferior to the data and an undershooting of the reloadings compared to the monotonic test. Both hypoplastic models lead to a better estimate of the oedometric stiffness, but present overshooting for the first three reloadings, and undershooting for the final reloading.

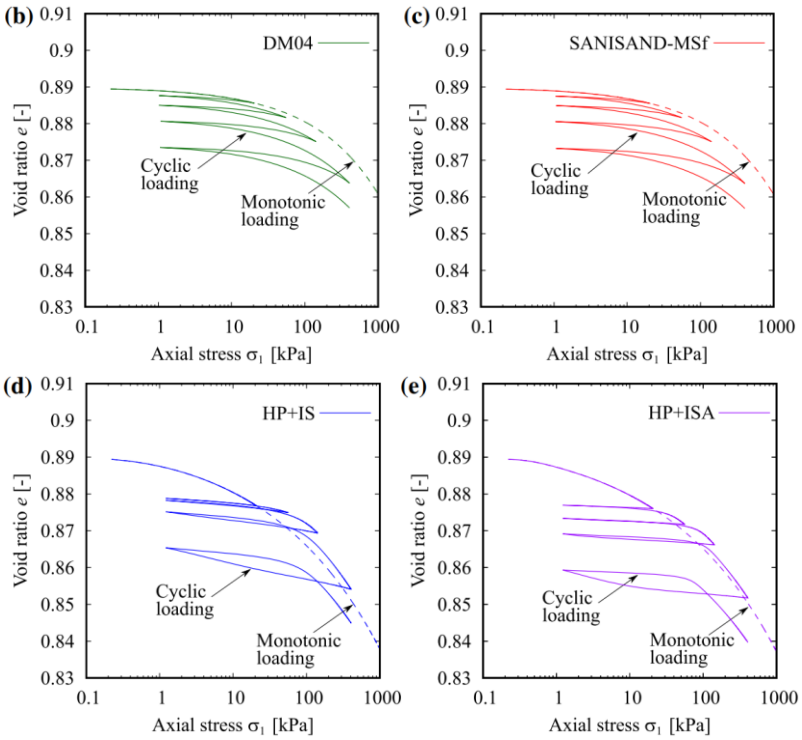


Figure 382 Simulations of test OEC2 with four advanced constitutive models by Duque (2022)

Simulation with HySand_base is represented in Figure 383 for an initial consolidation pressure of 0.2kPa. The reloading behaviour does not show any over or undershooting, but the oedometric stiffness is too low.

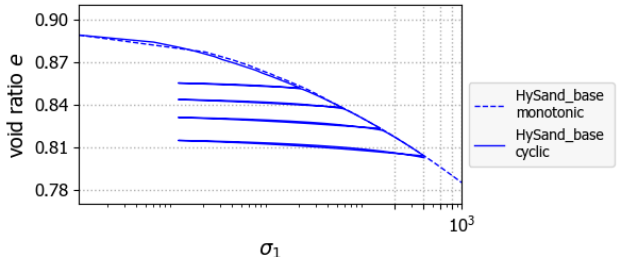


Figure 383 Simulation of test OEC2 with HySand_base and $p_{c0} = 0.2kPa$ (change of void ratio scale)

Similarly to paragraph 5.1.4 of this chapter, the poor simulation of the oedometric stiffness is principally due to the quick densification in the first few kPa of the simulation. While the data shows a decrease of the void ratio (e) from 0.89 to 0.88 in the first 10kPa of the test, the simulation shows a decrease to $e = 0.86$. If the initial consolidation pressure is taken as $p_{c0} = 5kPa$, then HySand_base simulates well the oedometric stiffness (see Figure 384).

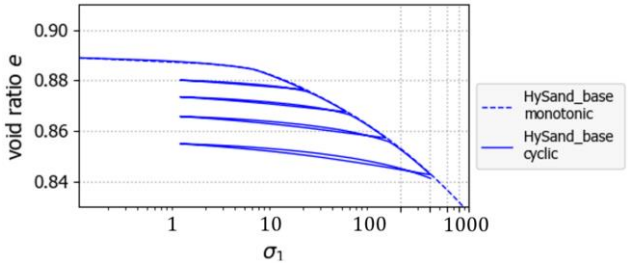


Figure 384 Simulation of test OEC2 with HySand_base and $p_{c0} = 5kPa$

5.4.7. Influence of preloading

Outside of the laboratory, before a loading of interest, sand has inevitably sustained the loading history of the site. For an offshore wind turbine founded on a monopile, the sand around the monopile sustains millions of cycles over its lifetime, with different directions, different speeds and intensities (leading to drained or partially undrained loadings). One of the most important features of a constitutive model for sand thus is to be able to simulate preloaded tests. Wichtmann (2016) has conducted undrained tests on loose Karlsruhe fine sand, of which one virgin loading, one after an isotropic loading, and another after a drained preloading. The results of these tests are shown in Figure 385. After the isotropic preloading, the capacity is increased, and there is no initial pore pressure build-up. After the shear preloading, the loading is initially elastic, before a plastic phase with pore pressure dissipation, and the capacity is largely increased.

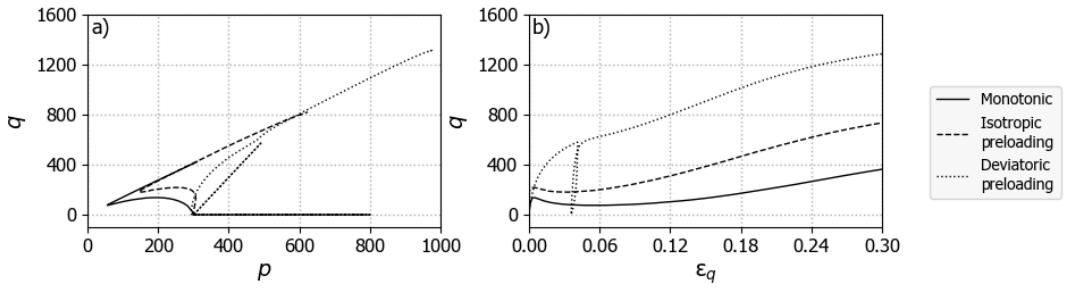


Figure 385 Preloaded undrained tests on loose sand by Wichtmann (2016)

Duque *et al.* show that the four advanced constitutive models struggle to capture the effect of preloading (see Figure 386). The isotropic loading has almost no influence on the SANISAND models. The shear preloading has no influence on pore pressure build-up for the DM04 model and an insufficient influence for the MSf model, and the two models present an undershooting problem on reloading. In the case of the two hypoplastic models, the preloading effects are not well represented, with the exception of the shear preloading with HP+IS which is accounted for, apart for the undershooting on reload.

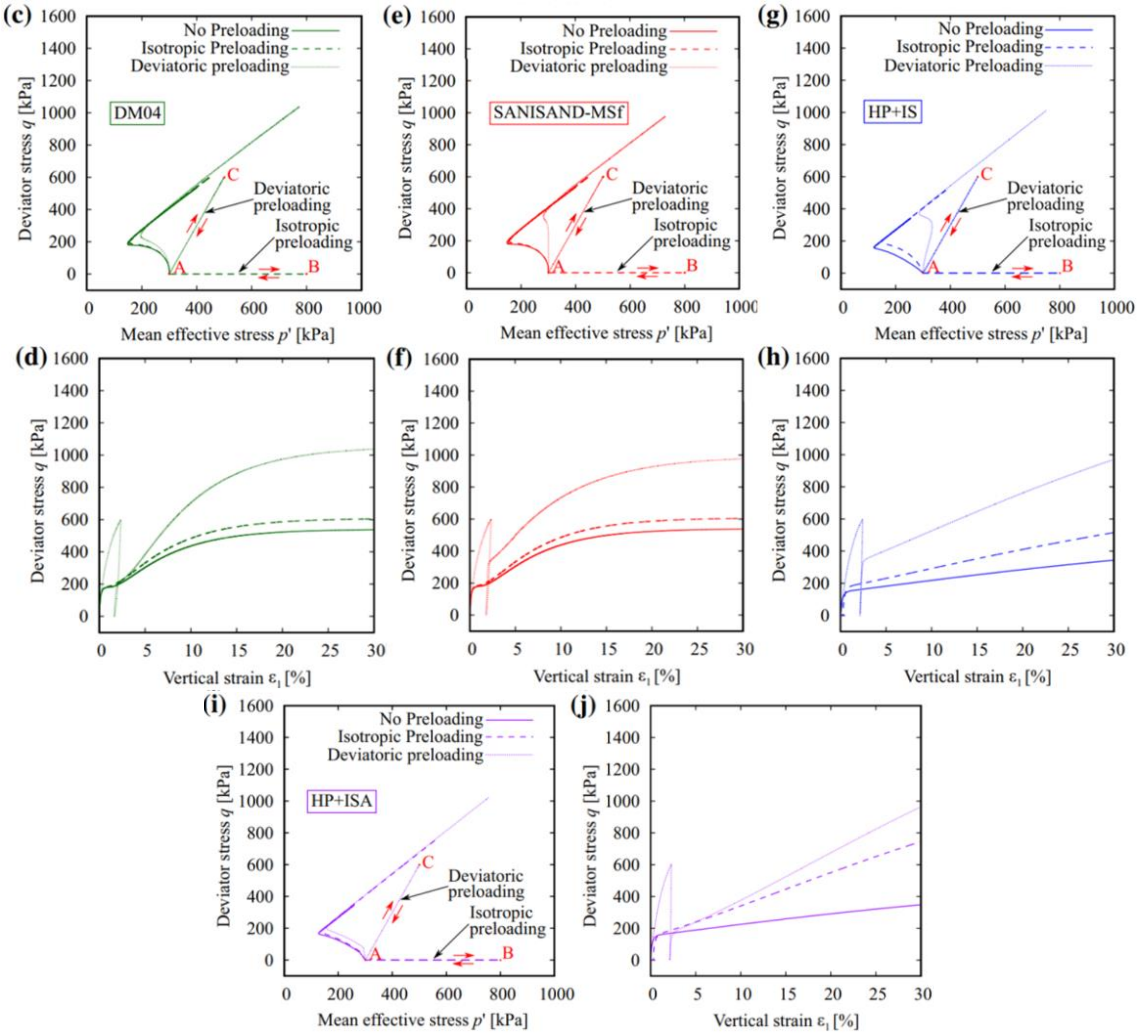


Figure 386 Simulations of preloaded tests by Duque (2022)

HySand_base leads to better predictions than the other four models. However, the pore pressure build-up is too important after the isotropic loading, and a short pore pressure build-up phase follows the shear preloading rather than the pore pressure dissipation observed for Wichtmann data.

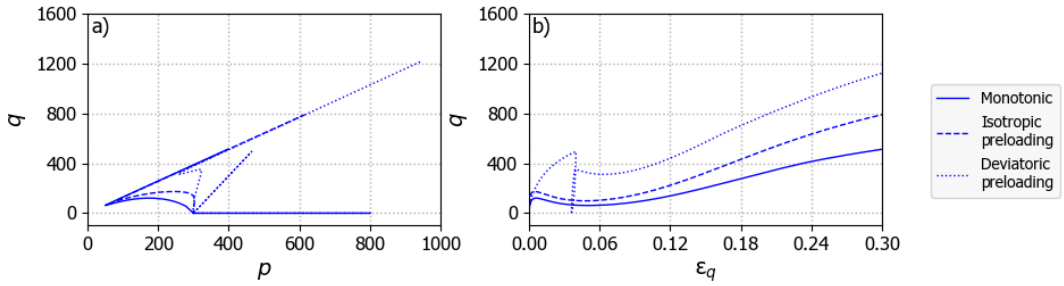


Figure 387 Simulation with the base model of preloaded tests

5.4.8. Conclusion

HySand_base does not exhibit most of the characteristic limitations highlighted by Duque *et al.* In particular, HySand_base leads to no over or undershooting on unloading-reloading cycles, nor does it lead to unwanted ratcheting. HySand_base depicts the progressive build-up of pore pressure in undrained tests better than the models studied by Duque, except that mean effective stress does not reach zero during cyclic strain-controlled tests on dense samples with large strains. HySand_base also gives good prediction of the number of cycles to liquefaction as a function of CSR across densities, and predicts well preloaded tests.

However, HySand_base is not capable of reproducing well the cyclic mobility phase in stress-controlled cyclic tests. Also, the initial consolidation pressure should not be set too low (<5kPa) in order to prevent an over-prediction of densification for normally consolidated samples at very low stresses.

In conclusion, HySand_base does not face most of the characteristic limitations its most advanced bounding surface and hypoplastic counterparts exhibit.

5.5. Storm data series

The development of HySand models is motivated by the design of OWTs monopile foundations. These monopiles sustain pseudo-random loading born from the wind and waves. It is thus important to demonstrate that HySand_base is able to model pseudo-random loadings with robustness. To this effect, the simulation of a pseudo-random time series representing one hour of loading of an OWT (Qiu (2023)) is used. This time series contains the normalised variation of horizontal forces applied to the OWT for over 360,000 time steps, representing 323 loading cycles and approximately an hour of storm loading.

This time series is used for a drained (at constant p) triaxial test with $p_0 = 100$kPa and $v_0 = 1.8$ and the calibrated parameters of Table 18, where the normalised amplitude of the time series is multiplied by 100kPa to obtain the applied variation of shear stress pictured in Figure 388.

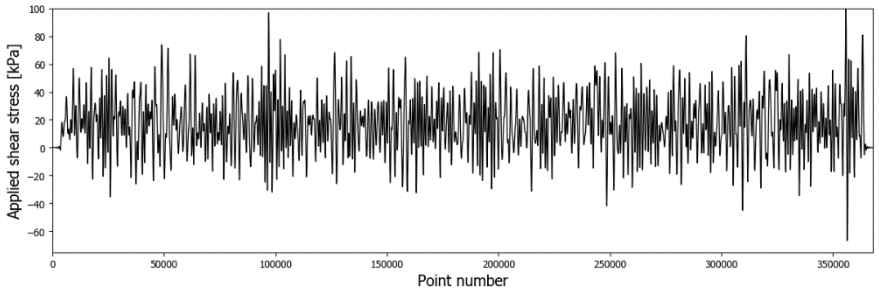


Figure 388 Variation of shear stress for the simulation of the storm loading with HySand_base

The results of the simulation are shown in Figure 389. This triaxial test is not representative of the behaviour of the whole foundation, nonetheless, the triaxial simulation highlights important characteristics of sand behaviour around a monopile: large deformations are only born from cycles with large amplitude; these large deformations seem to hit and follow a backbone curve. The backbone curve is the stress-strain curve that is obtained during a monotonic test under the same conditions.

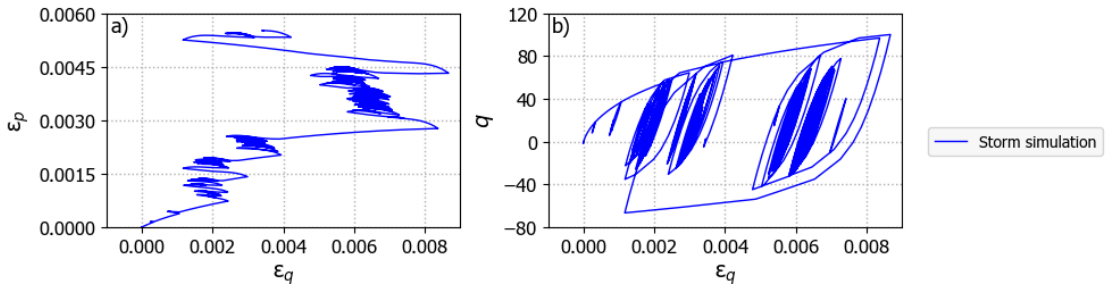


Figure 389 Results of the simulation of a storm loading with HySand_base

This simulation demonstrates the robustness of HySand_base which is able to run 323 pseudo-random cycles without demonstrating any aberrant behaviour.

5.6. Conclusions on HySand_base performance

The results displayed in this chapter show that HySand_base performs well for all types of triaxial tests, covering the entire density range that the sand under study can take, and pressures from a few kPa to almost 1MPa.

HySand_base does not face some common limitations of other advanced models: unwanted ratcheting, nor under or overshooting.

It is important to note that, in this chapter, HySand_base has been evaluated against triaxial tests. HySand_base is generalised to three dimensions. It would thus be important in the future to evaluate HySand_base against other laboratory tests (true triaxial, shear, torsional) or simple geotechnical problems (settlement of a footing, for example).

5.6.1. Tests summary

The following is a test-by-test summary of the capacity of HySand_base to capture characteristic behaviour of sand.

5.6.1.1. Isotropic tests

HySand_base captures well the quantity of volumetric strain generated up to 800kPa across densities for a single load-reload, or for a load with intermediate unloads.

HySand_base cannot model further generation of volumetric strain upon cyclic isotropic loading.

Note that modelling across densities could be improved if the normal consolidation line slope (λ) dependence on density was non-linear, and if the dimensionless bulk modulus (k_r) and the pressure exponent for non-linear elasticity (m) were made density dependent.

5.6.1.2. Oedometric tests

To avoid overestimating the consolidation at low stresses, HySand_base should not be initialised below 5kPa.

HySand_base performs well across densities and produces no over or undershooting upon cyclic loading, unlike other advanced models.

5.6.1.3. Monotonic drained test

HySand_base performs well across densities and initial consolidation pressures, capturing the variation of peak capacity, dilation and stiffness.

However, the model underpredicts the capacity of loose samples, and underpredicts the secant stiffness at low strains (<2%) at low initial consolidation pressures.

5.6.1.4. Monotonic undrained tests

5.6.1.4.1. Normally consolidated tests

HySand_base captures very well the pore pressure build-up, the stiffness, and the capacity under 3% strain for undrained tests across densities and initial consolidation pressures. However, the steepness of the shear stress-strain slope for denser than critical samples is overestimated at strains over 3%, such that capacity is overestimated besides this strain, especially for tests in extension.

HySand_base has been developed based on air-pluviation tests. It does not model well undrained tests of samples prepared by moist-tamping, especially not the saturation of the capacity. An improved modelling might be achieved by recalibration of parameters for this preparation method.

HySand_base seems to predict well both isotropically and anisotropically consolidated tests.

5.6.1.4.2. Preloaded tests

The influence of a variety of preloadings on undrained tests in compression and extension have been studied: drained with full or partial unloading and with a variety of stress paths, monotonic undrained in compression or extension, isotropic and anisotropic overconsolidation.

All of these tests are well modelled by HySand_base. The only notable issue is that the elastic reloading of HySand_base is too vertical in stress space, instead of curving toward higher mean effective stresses. This often implies an underprediction of the shear stress at which HySand_base turns plastic again, and thus of the capacity.

5.6.1.5. Cyclic stress controlled tests

5.6.1.5.1. Normal and isotropic consolidation, two-way tests

HySand_base predicts extremely well the rate of pore pressure development. It also captures well the influence of a change in amplitude or in initial density: a smaller amplitude or a denser sample imply less pore pressure build-up and higher secant stiffness.

HySand_base gives good predictions for the number of cycles required to reach liquefaction, but tends to overestimate the number of cycles needed for loose sand, and underestimate it for dense

sand. Compared to other advanced models such as SANISAND MSf or hypoplasticity + ISA, HySand_base predicts the number of cycles to liquefaction at least as well as these models.

However, HySand_base does not allow capture of the cyclic mobility phase for medium and dense sand. This is due to the lack of pore pressure build-up upon load reversal once large strains develop.

Contrarily to other advanced models, HySand_base does not generate unwanted ratcheting upon symmetric loading.

5.6.1.5.2. Normal and anisotropic consolidation, one-way and partial two-way cycles

HySand_base predicts well the stress path and the ratcheting of anisotropically consolidated samples submitted to one-way loading in compression.

However, because of the same lack of pore pressure build-up upon load reversal, the locked stress paths of the one-way tests are too vertical, and the partially two-way tests do not reach liquefaction as they should.

HySand_base does not seem to perform well for the few tests in extension of the database.

5.6.1.5.3. Preloaded two-way tests

Tests with cyclic stress-controlled preloading to small or large strains, and isotropic preloading, are well depicted by HySand_base: cyclic stress-controlled with small straining and isotropic preloading both imply less pore pressure build-up and a stiffer response during the subsequent loading; cyclic stress-controlled preloading with large straining in one direction implies a stiff response and little pore pressure build-up on the same side upon reloading, but a softer response and large pore pressure build-up on the opposite side.

5.6.1.5.4. Two-way tests with water inflow

Work on the Adamidis database has showed that HySand_base captures well the impact of water inflow on cyclic stress-controlled loading, with fewer cycles required to reach liquefaction the larger the water inflow.

5.6.1.6. Cyclic strain-controlled tests

5.6.1.6.1. Small strains

HySand_base performs well for strain-controlled tests with small strains ($\leq 0.08\%$): the stress path for isotropically and anisotropically consolidated samples is well depicted with an initial widening before a narrowing towards low mean effective stresses; the progressive pore pressure build-up with cycle is also well depicted.

5.6.1.6.2. Large strains

HySand_base captures the good trend for large strains ($> 0.5\%$), with looser samples producing more pore pressure build-up. However, because it does not capture well the large pore pressure build-up which takes place upon load reversal, HySand_base overpredicts the required number of cycles to liquefaction. Especially, HySand_base cannot model the liquefaction observed in the data for dense sand, but can for loose and medium dense sand.

5.6.2. Initial anisotropy

An important quality of HySand_base is the possibility to model initially anisotropic samples. Without this possibility, it would be impossible to reproduce some tests by Adamidis, for example.

5.6.3. Perspectives

The quality of the performance of HySand_base for this large set of tests should allow a confident future use of the model. This use will be facilitated by the implementation of HySand_base in finite element software, which is presented in Chapter 6.

Chapter 6 Implementation of HySand into finite element codes

As reported in this thesis so far, the family of HySand models has been implemented in Python in triaxial space or in three dimensional space. The HyperDrive calculations in Python model a single integration point, which is sufficient to model an idealised small-scale test such as a triaxial test. However, for HySand to be of use to the geotechnical community, it needs to be applicable to geotechnical problems on a larger scale. The implementation of HySand into a finite element software is therefore essential.

Thanks to a joint effort of Houlsby (principal architect of the Fortran interface), Saberi (focus on the implementation in Abaqus), and the author (focus on the implementation in PLAXIS 3D), any rate independent hyperplastic model expressed in g-y form can be used in PLAXIS 3D and Abaqus.

In the first part of this chapter, the implementation scheme for any hyperplastic model is briefly explained. Results in PLAXIS are presented in the following parts: a single element triaxial test, a multi-element triaxial test, a cavity expansion problem, and a circular footing problem.

6.1. Implementation scheme

The interface code (Hyper_FEA, coded in Fortran) between hyperplastic models and PLAXIS and Abaqus has mainly been developed by Houlsby. An explanation of its use can be found in Houlsby *et al.* (2023). A brief summary is given here.

6.1.1. Inputs and outputs

In order to interface with a finite element software, Hyper_FEA will receive as inputs the current state of stress, the current state variables, and the proposed strain increments. State variables are essential for Hyper_FEA to store the hyperplastic internal variables. Hyper_FEA then needs to return an updated state of stress, updated state variables, and the tangential stiffness matrix.

6.1.2. Structure of Hyper_FEA

Hyper_FEA is composed of four files, as follows. H_first contains standard functions evaluating tensor invariants and quantities, and their derivatives.

H_second contains matrix utilities (mainly to invert matrices), conversion utilities (to translate between the hyperplastic format [Mandel xx, yy, yz, xz, xy] and the Abaqus format [Voigt xx, yy,

zz, xy, xz, yz] or the PLAXIS format [Voigt xx, yy, zz, xy, yz, zx]), and the hyperplastic calculations (a stress update routine and a stiffness matrix calculation routine explained in Houlsby (2023)).

A model file contains the derivatives of the Gibbs energy function, the yield function and its derivatives, the definition of the model properties, a setup routine to initialise state variables, and an update routine.

An interface file, either with PLAXIS (User_Mod) or with Abaqus (UMAT), allows declaration of the number of state variables, initialising these state variables, and declaring the form of the stiffness matrix (asymmetric in the case of HySand_base). It also contains the necessary interface to retrieve the inputs from the software, to send them to be processed by the calculation routines, and finally to send the output to the graphical interface software.

6.1.3. Implementation of a specific model

To use a specific model, only the model file should be modified. In the model file, the parameters of the model, the setup routine, the derivatives of the Gibbs energy function, the yield functions and their derivatives, and the update routine should be defined for the required three-dimensional constitutive model. For HySand_base, this represents ≈250 lines of code.

6.1.4. Numerical scheme

The explicit numerical scheme, contained in H_second, is very similar to HyperDrive presented in 3.4, but it is done in strain control in FEA. Two differences can be highlighter:

First, the size of the strain increment is dictated by the software, and it is then divided in substeps in the scheme. The number of substeps is the norm of the increment of strain in entry divided by a critical strain, which in the case of HySand_base is taken as 5% of μ/g_r plus one.

Second, it is necessary to calculate the stiffness matrix. Rewriting Eq. 241 at yield ($y_0^{(p)} = 0$) and using Eq. 237 for the plastic flow, one can write:

$$L^{(q)} = (A^{pq})^{-1} B_j^p \delta\sigma_j \qquad \textit{Eq. 265}$$

$$A^{pq} = -\left(-\frac{\partial y^{(p)}}{\partial \epsilon_i} \frac{\partial^2 g}{\partial \sigma_i \partial \alpha_j^{(n)}} + \frac{\partial y^{(p)}}{\partial \alpha_j^{(n)}} - \frac{\partial^2 g}{\partial \alpha_i^{(m)} \partial \alpha_j^{(n)}} \frac{\partial y^{(p)}}{\partial \chi_i^{(m)}} \right) \frac{\partial y^{(q)}}{\partial \chi_j^{(n)}} \qquad \textit{Eq. 266}$$

$$B_j^p = \left(-\frac{\partial y^{(p)}}{\partial \epsilon_i} \frac{\partial^2 g}{\partial \sigma_i \partial \sigma_j} + \frac{\partial y^{(p)}}{\partial \sigma_j} - \frac{\partial^2 g}{\partial \alpha_i^{(m)} \partial \sigma_j} \frac{\partial y^{(p)}}{\partial \chi_i^{(m)}} \right) \qquad \textit{Eq. 267}$$

At yield, combining Eq. 237, Eq. 239, and Eq. 265, one obtains the following:

$$\delta\epsilon_i = \left(-\frac{\partial^2 g}{\partial\sigma_i \partial\sigma_j} - \frac{\partial^2 g}{\partial\sigma_i \partial\alpha_k^{(m)}} \frac{\partial y^{(q)}}{\partial\chi_k^{(m)}} (A^{pq})^{-1} B_j^p \right) \delta\sigma_j \qquad \textit{Eq. 268}$$

The bracket is inverted to obtain the elasto-plastic stiffness matrix.

6.1.5. Use in PLAXIS

Houlsby *et al.* (2023) detail how to use Hyper_FEA. In summary, for PLAXIS, a dynamic link library (dll) must be generated for the four files of Hyper_FEA. This dll should be placed in the udsm folder inside the PLAXIS folder of the computer. In PLAXIS, the created constitutive model can then be used for a new material set. In the "General" tab, of the new material set, "User defined" should be selected. Then in the "Parameters" tab, the appropriate .dll and model in the .dll should be selected, before setting the model parameters.

6.2. Triaxial tests in PLAXIS

In PLAXIS, SoilTest allows simulation of laboratory tests by using a constitutive model on one element. Its results are thus a good benchmark to validate the constitutive model implemented in the Hyper_FEA suite (Fortran) against the version developed in the HyperDrive suite (Python).

To test the good operation of Hyper_FEA for a multi-element finite element problem, a triaxial test is simulated with 87 10-node tetrahedral elements. Note that 10-node tetrahedral elements are the only available elements in PLAXIS 3D. The test simulates an 8th of the triaxial test via symmetries.

6.2.1. Drained test TMD7

A drained test, simulating TMD7 by Wichtmann ($v_0 = 1.862$, $p_0 = 100$kPa), using HySand_base with $p_{c0} = 110$kPa and $N = 3$ yield surfaces, is run in HyperDrive, SoilTest and for the 87 elements 1m³ cube represented in Figure 390.

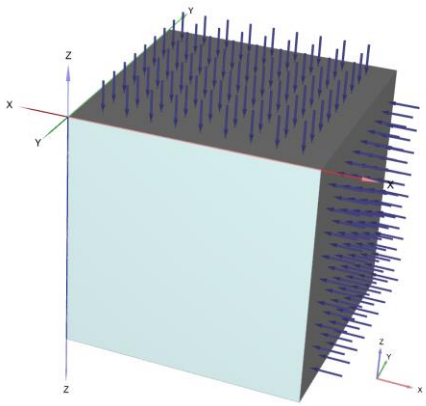


Figure 390 87 elements 1/8th of triaxial test

The 87 elements model is initialised via the field stress procedure and with no self-weight, then 100kPa pressures are applied to the three free boundaries, before a displacement control is applied to the top face.

The results of HyperDrive, SoilTest, and the 87 elements FEA simulations, Figure 391, agree for both the shear stress function of axial strain, and the volumetric strain function of axial strain. For the 87 elements problem, the shear stress is taken as the global vertical force recorded by PLAXIS, the axial strain is the relative imposed displacement of the top face, and the minor strain is the relative displacement measured at point (1,0,-1) (c.f. Figure 391).

These results show that Hyper_FEA is able to implement HySand_base for PLAXIS.

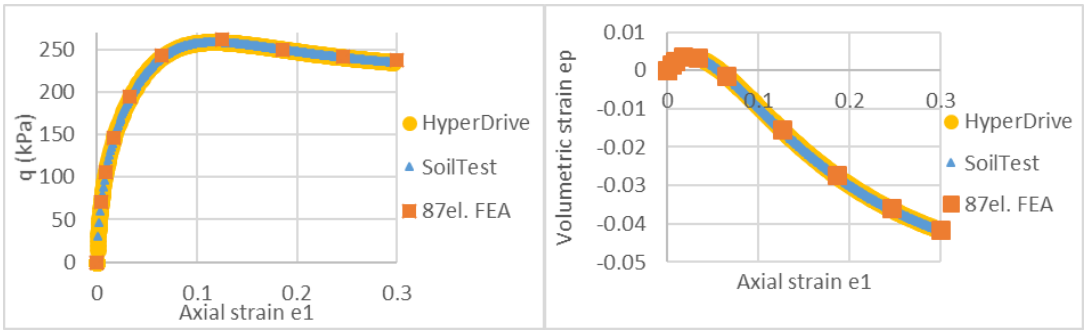


Figure 391 Results of HyperDrive and PLAXIS for the simulation of TMD7 by Wichtmann

6.2.2. Undrained test: TMU2

The test TMU2 by Wichtmann ($v_0 = 1.814$, $p_0 = 200$kPa) was run with $p_{c0} = 1.1p_0$ and for three surfaces ($N = 3$) in HyperDrive, SoilTest, and for the 87 elements cube (measuring the excess pore pressure in the cube). The results are shown in Figure 392.

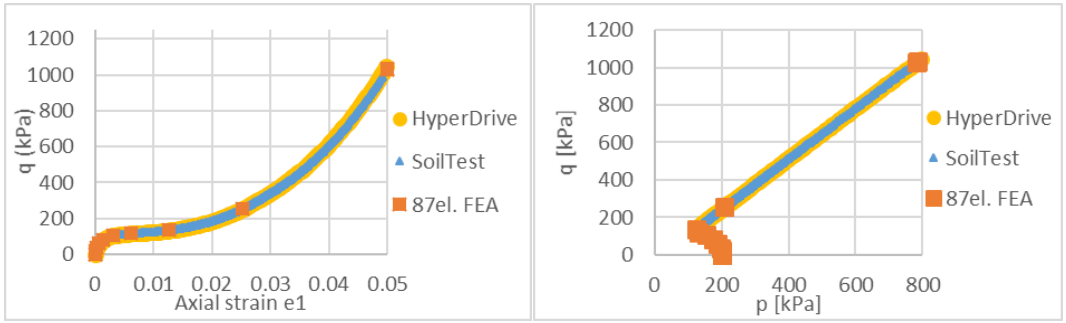


Figure 392 Results of HyperDrive and PLAXIS for the simulation of TMU2 by Wichtmann

The results from HyperDrive, SoilTest and 87 elements problem again match very well.

6.3. Cavity expansion

In a triaxial test, only the axial stress is varied. To demonstrate further the capacities of Hyper_FEA and HySand_base, a drained cavity expansion model, where both the radial and hoop stress vary, is modelled.

The circular cavity has a 1m radius, and the region of soil modelled with 1082 elements has a 20m radius. Because of symmetries, only a quarter of the problem could have been modelled, but half is modelled here such that the model can also be used for lateral displacement of the cavity (not presented herein). The upper and lower faces are normally fixed, the outer circular boundary is fully fixed, and the inner circular boundary is initially fully fixed. The problem is initialised with a field stress of 100kPa, then an inner pressure of 100kPa is applied at the cavity walls, then the inner circular boundary is freed from its displacement constraints and the cavity is expanded with force control. HySand_base was used with $v_0 \in [1.7, 2.05]$ and the calibrated parameters for Wichtmann data base (c.f. Table 18). This problem is illustrated in Figure 393.

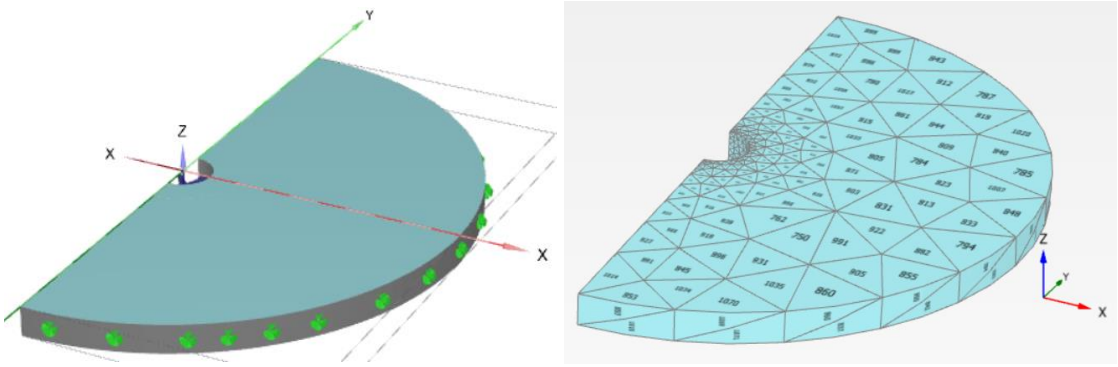


Figure 393 Cavity expansion problem in PLAXIS

Figure 394 presents the pressure function of the radial displacement at the cavity walls. The implementation of HySand_base in Hyper_FEA is robust. But, the denser the sample is initially, the sooner the calculation fails to complete, probably as a result of lack of convergence. This result could be due to the increased softening with density. The fact that analyses of dense sands with softening and non-associated flow present difficulties for FEA is well-recognised.

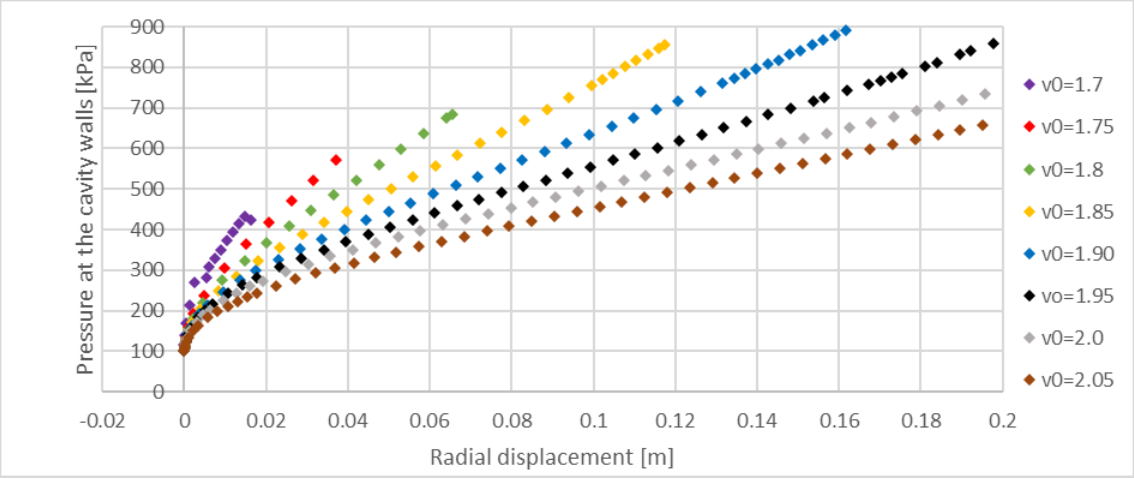


Figure 394 Cavity expansion results with HySand_base: pressure in the cavity function of the radial displacement

6.4. Circular footing

The robustness of the implementation of HySand_base with Hyper_FEA has now been demonstrated for problems where stresses vary in one or two dimensions. Modelling the settlement of a circular footing, a true three dimensional problem, represents a new degree of complexity.

A quarter of the problem is represented, exploiting the symmetries, with a circular footing of 1m radius in a region of soil of 10m radius and 10m depth, and with normal fixities for the lateral limits and full fixities for the bottom surface, resulting in a total of 4854 elements. This is represented in Figure 395.

Unfortunately, the model is unstable at low mean effective stress currently. This is potentially due to two main reasons: first, in the model, if $I_1(\sigma) \leq 0$ or if $I_3(\sigma) = 0$ numerical issues arise; second, the yield surfaces are not well defined for $I_1(\sigma) < 0$ with zones where $y^{(n)} < 0$ which should not be explored.

In consequence, at this stage, to run a circular footing problem, an additional heavy layer should be placed on top of the HySand_base material layer during the initial phase, which uses the K_0 procedure. An additional one metre layer of elastic material with a weight of 100kN/m³ is used. During the second phase, this additional layer is deleted and replaced by a 100kPa overburden pressure. In the third phase, a homogenous vertical displacement is imposed to the surface representing the location of the footing (c.f. Figure 395).

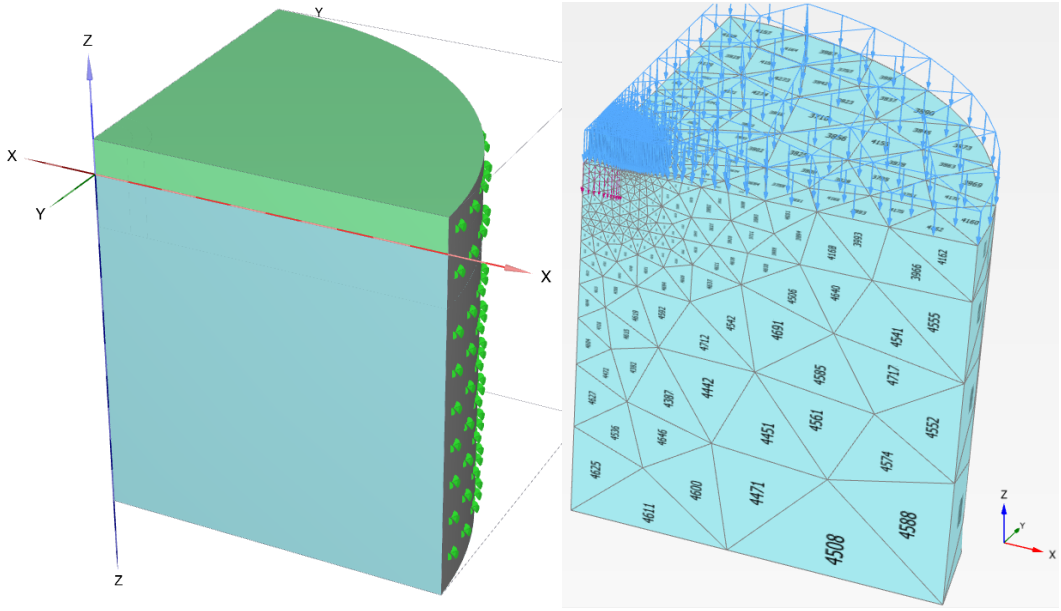


Figure 395 Circular footing problem in PLAXIS

Figure 396 presents the settlement of the footing under vertical force for an initial specific volume $v_0 = 1.9$. The calculation is stopped at 2.7cm because it cannot be carried further. Indeed, zones of very low mean effective stresses appear (at 2.7cm displacement, the lowest is $p = 3.6$kPa), such that carrying the calculations further causes the process to terminate.

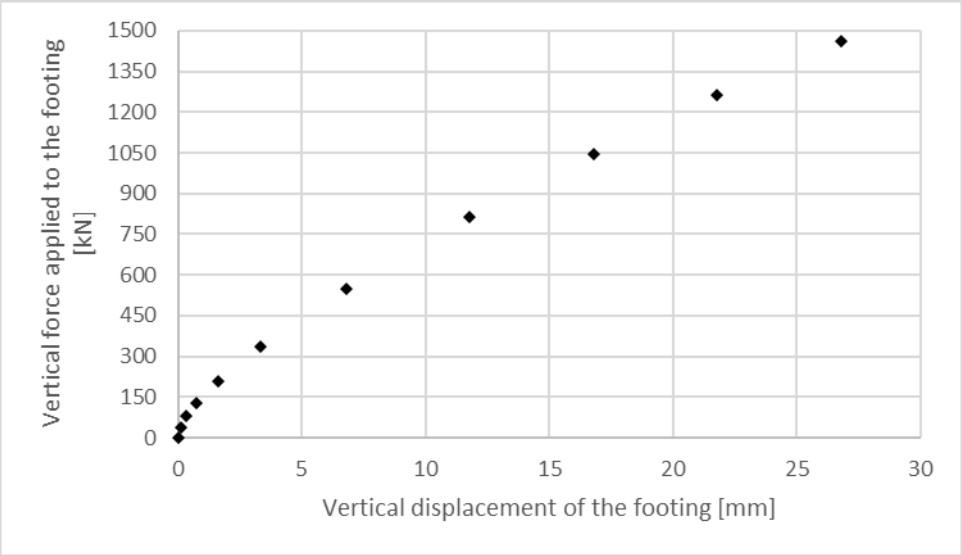


Figure 396 Settlement of the circular footing under vertical force for $v_0 = 1.9$

6.5. Conclusions on the finite element implementation

Rate independent constitutive models expressed in $g - y$ form in hyperplasticity can be implemented in Hyper_FEA and used in PLAXIS and Abaqus.

HySand_base has been implemented, with the parameters calibrated for Wichtmann's database, and tested for increasingly complex boundary value problems in PLAXIS.

Results of HySand_base for drained and undrained triaxial tests with HyperDrive, SoilTest and an 87 elements 3D simulation in PLAXIS compare very well.

HySand_base has been used with a variety of initial densities for a cavity expansion problem. The cavity could be expanded to a variable extent before the calculation collapsed depending on the initial density (1.6cm for $v_0 = 1.7$ to more than 35cm for $v_0 = 2.05$). This could be due to the increasing softening of HySand_base with density.

Finally, HySand_base was used for a circular footing settlement simulation. This problem showed that the implementation of HySand_base still needs to be made more robust: the calculation currently terminates when low mean effective stresses are encountered.

Chapter 7 Conclusions

7.1. Introduction

This thesis has examined the constitutive modelling of sand under cyclic loading. The complexity of sand behaviour has been explored, and the importance of its memory highlighted. Different modelling strategies have been presented, and current advanced constitutive models have been shown to be insufficient to model sand under cyclic loading.

This analysis points out the necessity to develop a new constitutive model. The theoretical framework of multi-surface plasticity has been chosen because of its capacity to model the memory of the material. The hyperplastic framework is used to ensure a sound and flexible development, and a thermodynamically admissible formulation. The construction in triaxial space of a simple but versatile model, HySand_base, is presented, starting from a basic frictional model, and progressively adding key features to capture the behaviour of sand in a framework compatible with critical state soil mechanics: non-linear elasticity, a Matsuoka-Nakai yield surface shape, an anisotropy development law, a density and anisotropy dependent dilation, and a consolidation mechanism leading to contraction. This model is generalised in three-dimensions.

A precise and concise calibration process for HySand_base is presented and used as an example for Karlsruhe fine sand. This process necessitates the determination of the minimum and maximum specific volumes of the sand, along with three isotropic tests, three monotonic drained tests, and two cyclic stress-controlled undrained tests in order to determine the 14 parameters of the model.

A large number of simulations have been run for a variety of sands and triaxial tests in order to explore the qualities and the defaults of HySand_base. Properly calibrated models are used for Karlsruhe fine sand and Hostun sand for a large database of tests, and qualitative comparisons with a focus on preloaded tests are led for data on Hostun, Fuji river and Toyoura sand. HySand_base is also compared to other advanced constitutive models.

Finally, HySand_base has been implemented in finite element software, and results in PLAXIS for simple boundary value problems have been shown.

7.2. Key contributions

Highlighting the key phenomena of sand behaviour

In Chapters 2 and 5, the key mechanisms governing the mechanical behaviour of clean saturated sand have been highlighted in a literature review. Very well-known phenomena have been recalled, such as the density dependence of dilation. More complex phenomena displayed during cyclic loading have also been emphasised, such as the complex evolution of the rate of pore pressure build-up during undrained loading. Finally, the impacts of different types of preloadings on subsequent tests have been synthetized, thus emphasising the role of memory for sand behaviour, which has led to the natural adoption of multisurface plasticity for its modelling.

Versatility of the hyperplastic framework for constitutive model development

In Chapter 3, the hyperplastic framework has been presented, and an advanced constitutive model has been progressively built. This progressive and modular construction demonstrates the quality of the hyperplastic framework to develop complex constitutive models. As demonstrated by this chapter, the different key mechanisms that have been built into the model can very clearly be distinguished, easily included or removed, which guarantees the possibility to easily modify the model as needed. The formulation is contained in only two equations from which the whole constitutive behaviour can be deduced in a systematic way. Finally, the rigorous development in hyperplasticity of the model ensures its compliance with thermodynamics.

HySand_base: a constitutive model for sand under cyclic loading

The main contribution of this thesis is the development of the HySand models family presented in Chapter 3. HySand_base is a compromise between simplicity of formulation and ability to capture the complex behaviour of sand under cyclic loading. This compromise results in a 14 parameter effective stress hyperplastic model which comprises different mechanisms:

- non-linear elasticity.
- a frictional base (shear plasticity), with Matsuoka-Nakai type yield surfaces shape.
- a density and anisotropy dependent plastic volumetric mechanism for dilation.
- an anisotropy development law based on the development of plastic shear strain.
- a density dependent plastic volumetric mechanism for consolidation.
- a multisurface framework with density dependent shear hardening.

Calibration routine for HySand_base

In Chapter 4, a precise calibration process is presented to determine the 14 parameters of HySand_base. The calibration of HySand_base necessitates the determination of the maximum and minimum specific volume of the studied sand, and eight triaxial tests:

- three isotropic tests to characterise the consolidation behaviour and the volumetric elasticity.
- three drained tests to characterise the critical state, the anisotropy rate development, and the maximum dilation ratio.
- two cyclic stress-controlled undrained tests to characterise the shear elasticity, the hardening parameters.

The final part of the calibration process can either be done by trial and error, or via an optimisation routine.

Validation of HySand_base

In Chapter 5, numerous triaxial tests conducted in different universities on various sands have been simulated in order to assess the performance of HySand_base over a large range of behaviour: tests that are fully/partially/un-drained, monotonic/cyclic, normally/over consolidated, iso/aniso-tropically consolidated, virgin/preloaded, symmetric/asymmetric, strain/stress-controlled.

This is especially important for offshore geotechnics, where different drainaige conditions can be encountered, where the foundation sustains millions of cycles of varying amplitude and average, and where a dominant direction of loading is likely.

Implementation into finite element commercial software

The final step of this thesis, the implementation of HySand_base in PLAXIS, has been presented in Chapter 6. This is part of a larger effort with Guy Houlsby and Miad Saberi to develop an interface between rate-independent hyperplastic models expressed in $g - y$ form and finite element software (so far Abaqus and PLAXIS).

7.3. Implications for design

Constitutive model for finite element modelling with cyclic loading

The design under serviceability and fatigue limit state of OWTs foundations requires the modelling of the foundation under cyclic loading. Such modelling can be undertaken with the finite element method which requires an adequate constitutive model for the soil surrounding the monopile. Adequate constitutive models for cyclic loading of sand have been lacking, but HySand_base fills this gap.

Importance of previous history and current state of sand

This thesis has demonstrated the importance of the current state of the sand (density, anisotropy, stresses), as well as of the history of previous loading, in modelling triaxial tests. This will also inevitably be true at the larger foundation scale. It is thus essential to conduct extensive test campaigns to characterise the soil, and to take into account the geotechnical history of the soil when modelling. At any stage of the modelling, it appears crucial to evaluate the effects of the geological history on the anisotropy of the sand, and the effects of the installation method of the monopile. While modelling cycles during the lifetime of the monopile, it is also critical to account for the past cyclic history of the monopile.

Importance of considering the drainage condition

This thesis has also shown that the behaviour of sand highly depends on the drainage conditions during the loading. It is thus decisive to assess the drainage conditions during the modelling of the foundation. Once assessed, HySand_base is able to account for these drainage conditions for the modelling of the sand behaviour.

7.4. Future work

Dissemination of the research

This thesis is currently the most complete presentation of the HySand family of models. During its construction, different development versions of models of the HySand family have been presented to the geotechnical community in different conferences (EMMC 2022, JNGG 2022, IACMAG 2022) and in smaller seminars. It is now essential to publish the final outcomes of the research for it to be available to the wider geotechnical community.

Perspectives for the improvement of the model

HySand_base has been proven to be an excellent compromise between simplicity and its capacity to model the behaviour of sand. Potential improvements are, however, possible, and modifications easy to undertake because of the modular nature of the hyperplastic framework. In this thesis, new potential explorations for HySand have been discussed. The inclusion of anisotropy dependent contraction to improve the modelling of the important contraction/ pore pressure build-up upon load reversal after large straining in one direction appears important. Also, recasting of HySand_base into a unique yield surface model, as in Houlsby and Richards (2023), while keeping the multi-surface spirit of the model (see 3.2.10.1.3) seems promising.

Further testing of the model

HySand_base has been validated against a wide range of triaxial data.

HySand_base being generalised to three-dimensions and implemented in FE software, it is possible to simulate a wider range of laboratory, model and full scale tests. This will be essential to validate HySand_base in other stress conditions.

Further implementation efforts in FE

Chapter 6 has shown numerical limitations of the current implementation of HySand_base in 3D FEA. In order to model more complex geotechnical problems, the numerical implementation of HySand_base has to be improved. It will also be interesting to widen the compatibility of Hyper_FEA to further software, including open source packages, such as Opensees or MOOSE.

Use of HySand_base in model scale and large scale simulations of monopiles

The development of HySand_base is part of the PICASO project. HySand_base will play a key role in the modelling of the upcoming large scale testing of monopiles in sand.

Modelling large number of cycles

OWTs sustain millions of load cycles during their lifetime. The full history of these cycles cannot be modelled with FEA because of the computation and time cost of such endeavour. Methods should thus be used to distinguish the cycles that need to be modelled with FEA, and the bridges needed between the modelled cycles.

An existing method is the use of an explicit model, such as the high-cycle accumulation model for sand (Niemunis *et al.*, 2005), which alternates between the simulation of cycles with a constitutive model, and the extrapolation of large numbers of cycles based on the intermediate simulations. The HARM framework, developed by Houlsby, Abadie *et al.* (2017), with the possibility to accelerate the ratcheting in order to represent the effects of a large number of cycles with the simulation of only a few cycles is also an interesting perspective.

This coupled implementation should then be evaluated for its capacity to capture key phenomena of offshore geotechnics such as the evolution of ratcheting, stiffness, capacity, and damping.

7.5. Overview

The design under monotonic loading of monopile foundations for OWTs has been optimised thanks to the PISA project. Because of this optimisation, the increasing size of monopiles, and the deeper waters in which they are being installed, cyclic loading has become a key consideration for the design of new monopiles. However, no adequate design method has yet been developed for such design.

Based on previous research efforts, the University of Oxford and Ørsted are developing a research program, the PICASO project, with the objective of developing such design method. The work presented in this thesis is an integral part of this project.

The development of HySand_base, a new constitutive model in effective stress for sand under cyclic loading, and its implementation in finite element analysis software are of essence for the adequate modelling of monopiles founded in sand submitted to cyclic loading. The simulations led with HySand_base should prove essential for future design methods of monopiles under cyclic loading.

References

Abadie, C.N. (2015). "Cyclic Lateral Loading of Monopile Foundations in Cohesionless Soils". DPhil thesis, University of Oxford.

Adamidis, O. and Madabhushi, S.P.G. (2018). "Experimental investigation of drainage during earthquake-induced liquefaction". *Géotechnique* 68.8, pp. 655–665. DOI: 10.1680/jgeot.16.P.090.

Adamidis, O. and Anastasopoulos, I. (2022). "Cyclic liquefaction resistance of sand under a constant inflow rate". *Géotechnique (Ahead of print)*. DOI: 10.1680/jgeot.21.00082.

Andò, E., Viggiani, G., Hall, S., Desrues, J. (2013). "Experimental micro-mechanics of granular media studied by x-ray tomography: Recent results and challenges". *Géotechnique Letters* 3. pp. 142–146. DOI: 10.1680/geolett.13.00036.

API (2011). *Geotechnical and Foundation Design Considerations ANSI/API RP 2GEO*. 1st Ed.

Aubry, D., Hujeux, J.C., Lassoudiere, F., Meimon, Y. (1982). "A double memory model with multiple mechanisms for cyclic soil behaviour". *Int. Symp. Num. Models in Geomech*. Zurich, Switzerland, pp. 3–13.

Been, K., and Jefferies, M. G. (1985) "A state parameter for sands" *Géotechnique* 35.2, pp. 99–112. DOI: 10.1680/geot.1985.35.2.99.

Bhattacharya, S. (2019) *Design of foundations for offshore wind turbines*. Wiley, Hoboken, NJ, USA.

Boulanger, R. W., and Ziotopoulou, K. (2013). "Formulation of a sand plasticity plane-strain model for earthquake engineering applications." *Journal of Soil Dynamics and Earthquake Engineering* 53, pp. 254–267, DOI: 10.1016/j.soildyn.2013.07.006.

Burd, H.J., Taborda, D.M.G., Zdravković, L., Abadie, C.N., Byrne, B.W., Houlsby, G.T., Gavin, K.G., Igoe, D.J.P, Jardine, R.J., Martin, C.M., McAdam, R.A., Pedro, A.M.G, Potts, D.M. (2020a). "PISA design model for monopiles for offshore wind turbines: application to a marine sand" *Géotechnique* 70.11, pp. 1048–1066. DOI: 10.1680/jgeot.18.P.277.

Burd, H.J., Abadie, C.N., Byrne, B.W., Houlsby, G.T, Martin, C.M., McAdam, R.A., Jardine, R.J., Pedro, A.M.G., Potts, D.M., Taborda, D.M.G, Zdravković, L., Pacheco Andrade, M. (2020b). "Application of the PISA design model to monopiles embedded in layered soils" *Géotechnique* 70.11, pp. 1067–1082 DOI: 10.1680/jgeot.20.PISA.009.

Butterfield, R. (1979). "A natural compression law for soils (an advance on e-log p')" *Géotechnique* 29.4, pp. 469–480. DOI: 10.1680/geot.1979.29.4.469.

Byrne, B.W. and Houlsby, G.T. (2004). "Foundations for offshore wind turbines" *Philosophical transactions. Series A, Mathematical, physical, and engineering sciences*. 361. 2909-30. DOI: 10.1098/rsta.2003.1286.

Byrne, B.W. and Houlsby, G.T. (2006). "Assessing novel foundation options for offshore wind turbines" In *The World Maritime Technology Conference (WMTC 2006)*. London, UK.

Byrne, B. W., McAdam, R. A., Burd, H. J., Houlsby, G. T., Martin, C. M., Beuckelaers, W. J. A. P., Zdravković, L., Taborda, D. M. G., Potts, D. M., Jardine, R. J., Ushev, E., Liu, T., Abadias, D., Gavin, K., Igoe, D., Doherty, P., Skov Gretlund, J., Pache, S., and Plummer, M. A. L. (2017). "PISA: New design method for offshore wind turbine monopiles". *Proceedings of the 8th International Conference on Offshore Site Investigation and Geotechnics (SUT OSIG)*. London, UK, pp. 142–161.

Byrne, B.W. (2020). "Editorial: geotechnical design for offshore wind turbine monopiles" *Géotechnique* 70.11, pp. 943–944. DOI: 10.1680/jgeot.2020.70.11.943.

Byrne, B.W., Houlsby, G.T., Burd, H.J., Gavin, K.G., Igoe, D.J.P., Jardine, R.J., Martin, C.M., McAdam, R.A., Potts, D.M., Taborda, D.M.G., Zdravković, L. (2020a). "PISA design model for monopiles for offshore wind turbines: application to a stiff glacial clay till" *Géotechnique* 70.11, pp. 1030–1047. DOI: 10.1680/jgeot.18.P.255.

Byrne, B.W., Aghakouchak, A., Buckley, R.M., Burd, H.J., Gengenbach, J., Houlsby, G.T., McAdam, R.A., Martin, C.M., Schranz, F., Sheil, B.B., Suryasentana, S.K. (2020b) "PICASO: Cyclic Lateral Loading of Offshore Wind Turbine Monopiles" In Z. Westgate (Ed.), *International Symposium on Frontiers in Offshore Geotechnics: ISFOG2020*

Cheng, Z. and Detournay, C., (2021). "Formulation, validation and application of a practice-oriented two-surface plasticity sand model" *Computers and Geotechnics* 132, DOI: 10.1016/j.compgeo.2020.103984.

Chiaro, G., Silva, L., Kiyota, T., Koseki, J. (2011). "An elasto-plastic model to describe the undrained cyclic behavior of saturated sand with initial static shear" In: *5th International Symposium on Deformation Characteristics of Geomaterials* 2, pp. 1026–1033. Hanrimwon Co., Ltd.

Coleman, B. D. (1964). "Thermodynamics of materials with memory" *Arch. Rational Mech. Anal.* 17, pp. 1-46.

Collins, I. F. and Houlsby, G. T. (1997). "Application of thermomechanical principles to modelling of geotechnical materials" *Proc. R. Soc. London Ser. A* 453, pp. 1975–2001.

Corti, R. (2016). *Hardening memory surface constitutive model for granular soils under cyclic loading*. Ph.D. thesis, University of Bristol.

Cox, W. R., Reese, L. C., Grubbs, B. R. (1974). "Field Testing of Laterally Loaded Piles In Sand". *Proceedings of the Offshore Technology Conference (OTC*). Houston, Texas, pp. 459–464. DOI: 10.4043/2079-MS.

Cundall, P.A. and Strack, O.D.L. (1979). "A discrete numerical model for granular assemblies" *Géotechnique* 29.1, pp. 47–65. DOI: 10.1680/geot.1979.29.1.47.

Dafalias, Y.F. and Herrmann, L.R. (1980). "A bounding surface soil plasticity model". In: Balkema, A.A., *Proceedings of the International Symposium on Soils under Cyclic and Transient*, pp. 335–345.

Dafalias, Y. F. and Manzari, M. T. (2004). "Simple plasticity sand model accounting for fabric change effects" *Journal of Engineering Mechanics* 130.6, pp. 622–634. DOI: 10.1061/%28ASCE%290733-9399%282004%29130%3A6%28622%29.

Dang, H., Gobbi, S., Reiffsteck, P., Lenti, L. (2020). "The effect of isotropic preloading on static liquefaction of sandy soils" In *4th International Conference on Geotechnics for Sustainable Infrastructure Development,* Hanoi, VIETNAM*,* 2019-11-28*, Lecture Notes in Civil Engineering* 62*,* pp. 971–976. DOI: 10.1007/978-981-15-2184-3_127.

De Gennaro, V., Canou, J., Dupla, J.C., Benahmed, N. (2004). "Influence of loading path on the undrained behaviour of a medium loose sand" *Canadian Geotechnical Journal* 41.1, pp. 166–180. DOI: 10.1139/t03-082

Desrues, J., and Chambon, R. (1993). "A new rate type Constitutive Model for Geomaterials: CloE." In: D. Kolymbas (editor) *Modern Approaches to Plasticity*, Elsevier.

Desrues, J., Viggiani, G. (2004). "Strain localization in sand: An overview of the experimental results obtained in Grenoble using stereophotogrammetry". *International Journal for Numerical and Analytical Methods in Geomechanics* 28, pp. 279–321. DOI: 10.1002/nag.338.

DIN 18126: *Bestimmung der Dichte nichtbindiger Böden bei lockerster und dichtester*. Lagerung, 1996.

DNV GL (2016). *Support structures for wind turbines DNVGL-ST-0126*.

Doanh, T., Ibraim, E., Matiotti, R. (1997). "Undrained instability of very loose hostun sand in triaxial compression and extension. part 1: experimental observations" *Mechanics of cohesive frictional materials* 2.1, pp. 47–70. DOI: 10.1002/(SICI)1099-1484(199701)2:1<47::AID-CFM26>3.0.CO;2-9

Doanh, T., Finge, Z., Dubujet, P. (2006). "Undrained anisotropy of Hostun RF loose sand: New experimental investigations" *Canadian Geotechnical Journal* 43, pp. 1195–1212. DOI: 10.1139/t06-068.

Doanh, T., Dubujet, P., Touron, G. (2010). "Exploring the undrained induced anisotropy of Hostun RF loose sand" *Acta Geotech*. 5, pp. 239–256. DOI: 10.1007/s11440-010-0128-x.

Doherty, P. and Gavin, K (2012). "Laterally loaded monopile design for offshore wind farms". *Proceedings of the Institution of Civil Engineers - Energy* 165.1, pp. 7–17. DOI: 10.1680/ener.11.00003.

Duque, J., Yang, M., Fuentes, W., Mašín, D., Taiebat, M. (2022). "Characteristic limitations of advanced plasticity and hypoplasticity models for cyclic loading of sands" *Acta Geotechnica* 17. DOI: 10.1007/s11440-021-01418-z.

Dutch Ministry of Foreign Affairs (2022) *China offshore wind.* https://www.rvo.nl/sites/default/files/2022/03/Rapport-Offshore-wind-China.pdf [Accessed 26/01/2023]

Elgamal, A., Yang, Z., Parra, E. (2002) "Computational modeling of cyclic mobility and post-liquefaction site response" *Soil Dynamics and Earthquake Engineering* 22.4, pp. 259–271. DOI: 10.1016/S0267-7261(02)00022-2.

European Comission (2020). *Communication de la commission au parlement européen, au conseil, au comité économique et social européen et au comité des régions* https://eur-lex.europa.eu/legal-content/FR/TXT/PDF/?uri=CELEX:52020DC0741&from=FR [Accessed 26/01/2023]

Finge, Z., Doanh, T., Dubujet, P. (2006). "Undrained anisotropy of Hostun RF loose sand: new experimental investigations" *Canadian Geotechnical Journal* 43.11, pp. 1195–1212. DOI: 10.1139/t06-068

Fuentes, W., and Triantafyllidis, Th. (2015a). "ISA model: A constitutive model for soils with yield surface in the intergranular strain space" *Int. J. Numer. Anal. Meth. Geomech*. 39, pp. 1235–1254. DOI: 10.1002/nag.2370.

Fuentes, W. and Triantafyllidis, T. (2015b). "ISA: A constitutive model for deposited sand" In: Schanz, T., Hettler, A. (eds*) Aktuelle Forschung in der Bodenmechanik 2015*. Springer Vieweg, Berlin, Heidelberg. DOI: 10.1007/978-3-662-45991-1_10

Fuentes, W., Wichtmann, T., Gil, M., Lascarro, C. (2020). "ISA-Hypoplasticity accounting for cyclic mobility effects for liquefaction analysis" *Acta Geotech* 15, pp. 1513–1531. DOI: 10.1007/s11440-019-00846-2

Gajo, A., and Piffer, L. (1999) "The Effects of Preloading History on the Undrained Behaviour of Saturated Loose Sand" *Soils and Foundations* 39.6, pp. 43–53. DOI: 10.3208/sandf.39.6_43

Germain, P., Nguyen,Q.S., Suquet, P. (1983). "Continuum thermodynamics" *Trans. ASME J. Appl. Mech.* 50.4B, pp. 1010–1020. DOI: 10.1115/1.3167184.

Grandas Tavera, C.E., Triantafyllidis, T., Knittel, L. (2020). "A Constitutive Model with a Historiotropic Yield Surface for Sands" In: Triantafyllidis, T. (eds) *Recent Developments of Soil Mechanics and Geotechnics in Theory and Practice. Lecture Notes in Applied and Computational Mechanics* 91. Springer, Cham. pp. 33-43. DOI: 10.1007/978-3-030-28516-6_2

Gu, X., Liang, X., Hu, J. (2023). "Quantifying fabric anisotropy of granular materials using wave velocity anisotropy: A numerical investigation". *Géotechnique*. 35.1. DOI : 10.1680/jgeot.22.00314.

Halphen, B., and Nguyen, Q. (1975). "Sur les Matériaux Standard Généralisés" *Journal de Mécanique* 14. pp. 39–63.

Hirai, H. (1987). "An elastoplastic constitutive model for cyclic behaviour of sands" *Int. J. Numer. Anal. Meth. Geomech.* 11, pp. 503–520. DOI: 10.1002/nag.1610110506

Houlsby, G. T. (1981). *Study of plasticity theories and their applicability to soils*. Doctoral thesis, University of Cambridge. DOI: 10.17863/CAM.14121

Houlsby, G.T. (1985) "The choice of framework for theoretical models for soils" *Discussion, Proceedings of the 11th International Conference on Soil Mechanics and Foundation Engineering*, San Francisco, USA, 12-16 August 1985, Vol. 5, p. 2624, ISBN 90-6191-565-1.

Houlsby, G.T. (1992) "Interpretation of Dilation as a Kinematic Constraint" *Proceedings of the Workshop on Modern Approaches to Plasticity*, Horton, Greece, June 12–16 1992, ISBN 0-444-89970-7, pp. 19-38.

Houlsby, G.T. (2021). *Matsuoka notes*. Private communication

Houlsby, G.T. (2022). Personal Communication.

Houlsby, G.T. (2023). https://hyperplasticity.wordpress.com. Website with lecture slides on hyperplasticity, HyperDrive documentation, and link to related github repository. [Last accessed 18/02/2023]

Houlsby, G.T., and Mortara, G. (2004). "A continuous hyperplasticity model for sands under cyclic loading" *Proceedings of the International Conference on Cyclic Behaviour of Soils and Liquefaction Phenomena*, Bochum, Germany, 31 March - 2 April 2004, pp. 21–26. DOI: 10.1201/9781439833452.ch3.

Houlsby, G.T., Puzrin, A.M. (2006). *Principles of Hyperplasticity*. ISBN 978-1-84628-239-3. Berlin: Springer.

Houlsby, G.T., Abadie, C.N., Beuckelaers, W., Byrne, B.W. (2017). "A model for nonlinear hysteretic and ratcheting behaviour" *International Journal of Solids and Structures* 120, pp. 67–80 DOI: 10.1016/j.ijsolstr.2017.04.031.

Houlsby, G.T., Amorosi, A., Rollo, F. (2019). "Non-linear anisotropic hyperelasticity for granular materials" *Computers and Geotechnics* 115. DOI: 10.1016/j.compgeo.2019.103167.

Houlsby, G.T., Richards, I.A. (2023). "Multi-surface and bounding surface models in hyperplasticity" *Computers and Geotechnics* 156, Article 105143. DOI: 10.1016/j.compgeo.2022.105143.

Houlsby, G.T, Simonin, L.E.J, Saberi, M. (2023). *Hyper_FEA*. Internal document.

Imam, R., Morgenstern, N., Robertson, P., Chan, D. (2011). "A critical-state constitutive model for liquefiable sand" *Canadian Geotechnical Journal* 42, pp. 830–855. DOI: 10.1139/t05-014.

Ishihara, K., Tatsuoka, F., Yasuda, S. (1975). "Undrained deformation and liquefaction of sand under cyclic stresses" *Soils Found.* 15.1, pp. 29–44. DOI: 10.3208/sandf1972.15.29.

Ishihara, K., and Okada, S. (1978a). Effects of stress history on cyclic behaviour of sand" *Soil and Foundations* 18.4, pp. 31–45. DOI: 10.3208/sandf1972.18.4_31.

Ishihara, K., and Okada, S. (1978b). "Yielding of Overconsolidated Sand and Liquefaction Model under Cyclic Stresses" *Soils and Foundations* 18.1, pp. 57–72. DOI: 10.3208/sandf1972.18.57.

Ishihara, K., and Okada, S. (1982). "Effects of large preshearing on cyclic behaviour of sand" *Soils and Foundations* 22.3, pp. 109–125. DOI: 10.3208/sandf1972.22.3_109.

Ishihara, K. (1996). *Soil behaviour in earthquake geotechnics*. Oxford University Press, New York

Iwan, W. D. (1967). "On a class of models for the yielding behavior of continuous and composite systems" *Journal of Applied Mechanics* 34.3, pp. 612–617. DOI: 10.1115/1.3607751.

Jefferies, M. G. (1993). "Nor-Sand: a simle critical state model for sand" *Géotechnique* 43.1, pp. 91–103. DOI: 10.1680/geot.1993.43.1.91.

Jefferies, M.G., and Shuttle, D.A. (2005). "NorSand: Features, calibration and use" In: *Soil Constitutive Models: Evaluation, Selection, and Calibration*, Geo-Frontiers Congress 2005, January 24-26 2005, Austin, Texas, USA, pp. 204–236. DOI: 10.1061/40771%28169%299

Kallehave, D., Byrne, B.W., LeBlanc Thilsted, C., and Mikkelsen, K.K. (2015). "Optimization of monopiles for offshore wind turbines" *Phil. Trans. R. Soc. A.* 373 : 20140100. DOI: 10.1098/rsta.2014.0100.

Kolymbas, D. and Herle, I. (2005). "Hypoplasticity as a constitutive framework for granular soils" *Geo-Frontiers Congress 2005*, January 24-26 2005, Austin, Texas, USA. DOI: 10.1061/40771%28169%2911.

Kolymbas, D. (2015). "Introduction to barodesy" *Géotechnique* 65.1, pp. 52–65. DOI: 10.1680/geot.14.P.151.

Krabbenhoft, K. (2019). *Data driven constitutive modelling of geomaterials*. Presentation given at the Univesity of Oxford. 4th of June 2019.

Li, S., Zhang, Y., Jostad, H.P. (2019). "Drainage conditions around monopiles in sand" *Applied Ocean Research* 86, pp. 111–116. ISSN 0141-1187. DOI: 10.1016/j.apor.2019.01.024.

Liu, H., Abell, J., Diambra, A., Pisanò, F. (2018). "Modelling the cyclic ratcheting of sands through memory-enhanced bounding surface plasticity" *Géotechnique* 69.9, pp. 1–57. DOI: 10.1680/jgeot.17.p.307.

Manceau, S., McLean, R., Sia, A., and Soares, M. (2019). "Application of the Findings of the PISA Joint Industry Project in the Design of Monopile Foundations for a North Sea Wind Farm". *Proceedings of the Offshore Technology Conference (OTC)*. Houston, Texas, May 2019. DOI: 10.4043/29557-MS.

Matlock, H. (1970). "Correlations for design of laterally loaded pilesin soft clay" *Proceedings of the 2nd annual offshore technology conference*, Houston, TX, USA, vol. 1, paper no. OTC 1204, pp. 577–594. DOI: 10.4043/1204-MS

Manzari, M.T., Dafalias , Y.F. (1997). "A critical state two-surface plasticity model for sands" *Géotechnique* 47.2, pp. 255–272. DOI: 10.1680/geot.1997.47.2.255.

Masing, G. (1926). "Eigenspannungen und verfestigung beim messing (Self stretching and hardening for brass)" *Proc. 2nd Int. Congress for Applied Mechanics*, Zurich, Switzerland, pp. 332–335 (in German).

Matsuoka, H., and Nakai, T. (1974). "Stress-deformation and strength characteristics of soil under three different principal stresses". *Proceedings of JSCE* 232, pp. 59–74. DOI: 10.2208/jscej1969.1974.232_59.

McAdam, R., Byrne, B., Houlsby, G., Beuckelaers, W., Burd, H., Gavin, K., Igoe, D., Jardine, R., Martin, C., Wood, A., Potts, D., Skov Gretlund, J., Taborda, D.M.G., Zdravkovic, L. (2019). "Monotonic laterally loaded pile testing in a dense marine sand at Dunkirk" *Géotechnique* 70.11, pp. 1–34. DOI: 10.1680/jgeot.18.pisa.004.

Ministère de l'écologie français (2022). *Eolien en mer*. https://www.ecologie.gouv.fr/eolien-en-mer-0 [Accessed 26/01/2023]

Mital, U., Kawamoto, R. & Andrade, J.E. (2020). "Effect of fabric on shear wave velocity in granular soils". *Acta Geotech.* 15, pp. 1189–1203. DOI : 10.1007/s11440-019-00766-1.

Moreau, J. J. (1970). "Sur les lois de frottement, de plasticité et de viscosité" *C. R. Acad. Sc.*, t. 271, Paris, France, Sptember 28 1970, pp. 608-611.

Moreau, J. J. (1971) "Fonctions de résistance et Fonctions de dissipation" and "Rafle par un convexe variable" *Seminaire d'Analyse convexe*, Montpellier, France, 1971.

Mróz, Z. (1967). "On the description of anisotropic work hardening" *Journal of the Mechanics and Physics of Solids* 15, pp. 163–175. DOI: 10.1016/0022-5096(67)90030-0.

Mróz, Z. (1969). "An attempt to describe the behavior of metals under cyclic loads using a more general workhardening model" *Acta Mech.* 7, pp. 199–212. DOI: 10.1007/BF01176668.

Mróz, Z. and Pietruszczak, S. (1983). "A constitutive model for sand with anisotropic hardening rule" *Int. J. Numer. Anal. Meth. Geomech.* 7, pp. 305–320. DOI: 10.1002/nag.1610070304.

Mróz Z. (1998) "Elastoplastic and viscoplastic constitutive models for granular materials" In: *Behaviour of granular materials*, Cambou B (ed.). *CISM courses and Lectures* 385, pp. 269–337. DOI: 10.1007/978-3-7091-2526-7_6.

Nardelli, V. and Coop, M.R. (2019). "The Experimental Contact Behaviour of Sands: Normal and Tangential Loading" *Géotechnique* 69.8, pp. 672–686. DOI: 10.1680/jgeot.17.P.167

Niemunis, A. and Herle I. (1997). "Hypoplastic model for cohesionless soils with elastic strain range" *Mechanics of Cohesive-Frictional Materials* 2, pp. 279–299. DOI: 10.1002/(SICI)1099-1484(199710)2:4<279::AID-CFM29>3.0.CO;2-8

Niemunis, A., Wichtmann, T., Triantafyllidis, Th. (2005). "A high-cycle accumulation model for sand" *Computers and Geotechnics* 32.4, pp. 245–263. DOI: 10.1002/bate.200590128.

Oka, F., Yashima, A., Shibata, T. *et al.* (1994). "FEM-FDM coupled liquefaction analysis of a porous soil using an elasto-plastic model" *Appl. Sci. Res.* 52, pp. 209–245. DOI: 10.1007/BF00853951.

Papadimitriou, A., and Bouckovalas, G. (2001). "Plasticity Model for Sand under Small and Large Cyclic Strains" *Soil Dynamics and Earthquake Engineering* 22, pp. 191–204. DOI: 10.1016/S0267-7261(02)00009-X.

Pastor, M., Zienkiewicz, O.C., Leung, K.H. (1985). "Simple model for transient soil loading in earthquake analysis. II. Non-associative models for sands" *International Journal for Numerical and Analytical Methods in Geomechanics* 9.5, pp. 477–498. DOI: 10.1002/nag.1610090505.

Pestana, J.M. and Whittle, A.J. (1999). "Formulation of a unified constitutive model for clays and sands" *Int. J. Numer. Anal. Meth. Geomech.* 23, pp. 1215–1243. DOI: 10.1002/(SICI)1096-9853(199910)23:12<1215::AID-NAG29>3.0.CO;2-F

Petalas, A.L., Dafalias, Y.F., Papadimitriou, A.G., (2020). "SANISAND-F: Sand constitutive model with evolving fabric anisotropy" *International Journal of Solids and Structures* 188–189, pp. 12–31. DOI: 10.1016/j.ijsolstr.2019.09.005.

PLAXIS (2020). *Material Models Manual.* Accessed on 05.01.2023 from https://communities.bentley.com/

Poblete, M., Fuentes, W., Triantafyllidis, T. (2016). "On the simulation of multidimensional cyclic loading with intergranular strain" *Acta Geotechnica* 11.6, pp. 1263–1285. DOI: 10.1007/s11440-016-0492-2.

Pradhan, T.B.S, Tatsuoka, F.,Sato, Y. (1989). "Experimental Stress-Dilatancy Relations of Sand Subjected to Cyclic Loading" *Soils and Foundations* 29.1, pp. 45–64. DOI: 10.3208/sandf1972.29.45.

Prévost, J.H. (1977). "Mathematical modelling of monotonic and cyclic undrained clay behaviour" *International Journal for Numerical and Analytical Methods in Geomechanics* 1.2, pp. 195–216. DOI: 10.1002/nag.1610010206.

Prévost, J.H. (1978a). "Anisotropic Undrained Stress-Strain Behavior of Clays" *Journal of Geotechnical Engineering-Asce* 104 (GT8, Proc. Paper 13942), pp. 1075–1090. DOI: 10.1061/AJGEB6.0000679.

Prévost, J.H. (1978b). "Plasticity Theory for Soil Stress-Strain Behavior" *Journal of Engineering Mechanics-Asce. 104* (EM5, Proc. Paper 14069), pp. 1177–1194. DOI: 10.1061/JMCEA3.0002411.

Prévost, J.H. (1982). "Two-Surface vs. Multi-Surface Plasticity Theories" *International Journal for Numerical and Analytical Methods in Geomechanics* 6, pp. 323–338. DOI: 10.1002/nag.1610060305.

Prévost, J.-H. (1985). "A simple plasticity theory for frictional cohesionless soils" *Soil Dyn Earthq Eng* 4.1, pp. 9–17. DOI: 10.1016/0261-7277(85)90030-0

Qiu, Z. (2023). *Cyclic simple shear testing of Cowden till.* DPhil Thesis. University of Oxford.

Reese, L. C., Cox, W. R., Koop, F. D. (1974). "Analysis of Laterally Loaded Piles in Sand" *Proceedings of the Offshore Technology Conference (OTC)*. Houston, Texas, pp. 473–483. DOI: 10.4043/2080-MS.

Richards, I.A., Byrne, B.W., Houlsby, G.T. (2019). "Monopile rotation under complex cyclic lateral loading in sand" *Géotechnique* 70.10, pp. 1–44. DOI: 10.1680/jgeot.18.p.302.

Roscoe, K.H. and Burland, J.B. (1968) "On the generalised stress-strain behaviour of 'wet' clay", in *Engineering Plasticity*, papers for a conference in Cambridge, March, ed. Heyman, J. and Leckie, F.A., CUP, pp 535–609.

Simonin, L.E.J., Houlsby, G.T., Byrne, B.W. (2023). "HySand: A New Constitutive Model for Sand Under Cyclic Loading" In: Barla, M., Di Donna, A., Sterpi, D., Insana, A. (eds) *Challenges and Innovations in Geomechanics. IACMAG 2022. Lecture Notes in Civil Engineering* 288. Springer, Cham. DOI: 10.1007/978-3-031-12851-6_18.

Storn, R., and Price, K. (1997). "Differential Evolution - a Simple and Efficient Heuristic for Global Optimization over Continuous Spaces" *Journal of Global Optimization* 11, pp. 341 – 359. DOI: 10.1023/a:1008202821328

Suquet, P. (n.d.) *Rupture et Plasticité, chapter 7.* Course at ENSTA ParisTech.

Taborda, D. M. G., Zdravković, L., Kontoe, S., Potts, D. M. (2014). "Computational study on the modification of a bounding surface plasticity model for sands" *Comput. Geotech.* 59, pp. 145–160. DOI: 10.1016/j.compgeo.2014.03.005

Taborda, D. M. G., Zdravković, L., Potts, D. M., Burd, H. J.,Byrne, B. W., Gavin, K. G., Houlsby, G. T., Jardine, R. J.,Liu, T., Martin, C. M., McAdam, R. A. (2020). "Finite element modelling of laterally loaded piles in a dense marine sand at Dunkirk". *Géotechnique* 70.11, pp. 1014–1029. DOI: 10.1680/jgeot.18.PISA.006.

Tafili, M., Wichtmann, T., Triantafyllidis, T. (2021). "Experimental investigation and constitutive modeling of the behaviour of highly plastic Lower Rhine clay under monotonic and cyclic loading" *Can. Geotech. J.* 58.9, pp. 1396–1410. DOI: 10.1139/cgj-2020-0012.

Taiebat, M., Dafalias, Y. (2008). "SANISAND: simple anisotropic sand plasticity model" *International Journal for Numerical and Analytical Methods in Geomechanics* 32, pp. 915–948. DOI: 10.1002/nag.651.

Truesdell, C. (1955). "Hypo-elasticity" *J. Rational Mech. Anal.* 4, pp. 83–133. Springer-Verlag.

Tsetas, A., Tsouvalas, A., Gómez, S.S., Pisanò, F., Kementzetzidis, E., Molenkamp, T., Elkadi, A.S.K, Metrikine, A.V. (2023). "Gentle Driving of Piles (GDP) at a sandy site combining axial and torsional vibrations: Part I - installation tests" *Ocean Engineering* 270. DOI: 10.1016/j.oceaneng.2022.113453.

United Kingdom government (2022). *British energy security strategy*. https://www.gov.uk/government/publications/british-energy-security-strategy/british-energy-security-strategy [Accessed 26/01/2023]

Verdugo, R., Ishihara, K. (1996). "The Steady State of Sandy Soils" *Soils and Foundations* 36.2, pp. 81–91. DOI: 10.3208/sandf.36.2_81.

von Wolffersdorff, P.-A. (1996). "A hypoplastic relation for granular materials with a predefined limit state surface" *Mech Cohes Frict Mater* 1.3, pp. 251–271. DOI: 10.1002/(SICI)1099-1484(199607)1:3<251::AID-CFM13>3.0.CO;2-3

Wales, D. J., and Doye, J.P.K. (1997). "Global Optimization by Basin-Hopping and the Lowest Energy Structures of Lennard-Jones Clusters Containing up to 110 Atoms" *Journal of Physical Chemistry A* 101.28, 5111-5116. DOI: 10.1021/jp970984n.

Wang Z, Dafalias Y, Shen C (1990). "Bounding surface hypoplasticity model for sand" *J Eng Mech* 116.5, pp. 983–1001. DOI: 10.1061/%28ASCE%290733-9399%281990%29116%3A5%28983%29.

Wichtmann, T. (2016). *Soil behaviour under cyclic loading - experimental observations, constitutive description and applications*. Habilitation thesis. Ruhr-Universität Bochum.

Wichtmann, T., and Triantafyllidis, T. (2016a). "An experimental data base for the development, calibration and verification of constitutive models for sand with focus to cyclic loading. Part I - tests with monotonic loading and stress cycles" *Acta Geotechnica* 11. pp. 739–761. DOI: 10.1007/s11440-015-0402-z

Wichtmann, T., and Triantafyllidis, T. (2016b). "An experimental data base for the development, calibration and verification of constitutive models for sand with focus to cyclic loading. Part II - tests with strain cycles and combined loading" *Acta Geotechnica* 11, pp. 763–774. DOI: 10.1007/s11440-015-0412-x.

Wichtmann, T. (2021). http://www.torsten-wichtmann.de. Website with an important database of cyclic triaxial tests and other laboratory tests. [Data downloaded in November 2019]

Wind Europe (2021a). *Wind energy in Europe: 2021 Statistics and the outlook for 2022-2026*. https://windeurope.org/intelligence-platform/product/wind-energy-in-europe-2021-statistics-and-the-outlook-for-2022-2026/ [Accessed 25/01/2023]

Wind Europe (2021b) *Offshore wind in Europe—key trends and statistics 2020*.

Wood, D. (1991). *Soil Behaviour and Critical State Soil Mechanics*. Cambridge: Cambridge University Press.

Wroth, C.P., and Basset, R.H. (1965) "A Stress–Strain Relationship for the Shearing Behaviour of a Sand" *Géotechnique* 15.1, pp. 32–56. DOI: 10.1680/geot.1965.15.1.32.

Wu, W. and Bauer, E. (1994). "A simple hypoplastic constitutive model for sand" *Int. J. Numer. Anal. Meth. Geomech.* 18, pp. 833–862. DOI: 10.1002/nag.1610181203.

Yang, Z., Elgamal, A., Parra, E. (2003). "Computational model for cyclic mobility and associated shear deformation" *J Geotech Geoenviron Eng* 129.12, pp. 1119–1127. DOI: 10.1061/%28ASCE%291090-0241%282003%29129%3A12%281119%29

Yang, M., Taiebat, M., Dafalias, Y.F. (2022). "SANISAND-MSf: a sand plasticity model with memory surface and semifluidised state" *Géotechnique* 72.3, pp. 227–246. DOI: 10.1680/jgeot.19.P.363.

Yasufuku, N., Murata, H., Hyodo, M. (1991). "Yield characteristics of anisotropically consolidated sand under low and high stresses" *Soils and Foundations* 31.1, pp. 95-109. DOI: 10.3208/sandf1972.31.95.

Zdravković, L., Taborda, D. M. G., Potts, D. M., Abadias, D.,Burd, H. J., Byrne, B. W., Gavin, K. G., Houlsby, G. T.,Jardine, R. J., Martin, C. M., McAdam, R. A., Ushev, E.(2020). "Finite element modelling of laterally loaded piles in a stiff glacial clay till at Cowden" *Géotechnique* 70.11, pp. 999–1013. DOI: 10.1680/jgeot.18.PISA.005.

Zhang, J.-M., and Wang, G. (2012). "Large post-liquefaction deformation of sand, part I: physical mechanism, constitutive description and numerical algorithm" *Acta Geotechnica* 7.2, pp. 69–113. DOI: 10.1007/s11440-011-0150-7

Ziegler, H. (1963). "Some extremum principles in irreversible thermodynamics with application to continuum mechanics" *Progress in Solid Mechanics*, tome IV, Noth Holland, Amsterdam.

Ziegler, H. (1977). (2nd Edition 1983) *An Introduction to Thermomechanics*, North Holland, Amsterdam, 355pp.

Annex

Positivity of dissipation for shear hardening directly included in the yield function

For HySand_base, the dissipation including shear hardening can take the form:

$$Nd^{(n)} = \left(1-\frac{\mathrm{n}}{\mathrm{N}}\right)\sqrt{4\left(\frac{n}{N}\mu\right)^2\left(p+\frac{2}{3}q\right)\left(p-\frac{q}{3}\right)}\left|\dot{\alpha}_q^{(n)}\right| + \left(1-\left(1-\frac{\mathrm{n}}{\mathrm{N}}\right)^2\right)^{\frac{1}{r}} p_c^{(n)}\dot{\alpha}_{pc}^{(n)} \quad \text{Eq. 269}$$
$$+3H^{(n)}p\alpha_q^{(n)}\dot{\alpha}_q^{(n)} + \Lambda_d^{(n)}\left(\dot{\alpha_p}^{(\mathrm{n})} + a\beta^{(n)}\dot{\alpha_q}^{(n)}\right) + \Lambda_a\left(\dot{a} - A(1-|a|)\dot{\alpha_q}^{(n)}\right)$$

Differentiating Eq. 269 by $\dot{\alpha_p}^{(n)}$ leads to:

$$N\chi_p^{(n)} = \Lambda_d^{(n)} \quad \text{Eq. 270}$$

Differentiating Eq. 269 by $\dot{a}$ and equalling it to the differentiation of g (Eq. 169) by a leads to:

$$0 = \overline{\chi_a} = \chi_a = \frac{1}{\mathrm{N}}\Lambda_{\mathrm{a}} \quad \text{Eq. 271}$$

Differentiating Eq. 269 by $\dot{\alpha}_q^{(n)}$ and using Eq. 270 ($\Lambda_d^{(n)} = \chi_p^{(n)}$) and Eq. 271 ($\Lambda_a = 0$) gives:

$$N\chi_q^{(n)} - 3H^{(n)}p\alpha_q^{(n)} - a\beta^{(n)}N\chi_{\mathrm{p}}^{(\mathrm{n})} = \left(1-\frac{\mathrm{n}}{\mathrm{N}}\right)\sqrt{4\left(\frac{n}{N}\mu\right)^2\left(p+\frac{2}{3}q\right)\left(p-\frac{q}{3}\right)}S(\chi_q^{(n)}) \quad \text{Eq. 272}$$

$$\leftrightarrow \frac{\left(N\chi_q^{(n)} - 3H^{(n)}p\alpha_q^{(n)} - a\beta^{(n)}N\chi_{\mathrm{p}}^{(\mathrm{n})}\right)^2}{4\left(\frac{n}{N}\mu\right)^2\left(p+\frac{2}{3}q\right)\left(p-\frac{q}{3}\right)} = \left(1-\frac{\mathrm{n}}{\mathrm{N}}\right)^2 \quad \text{Eq. 273}$$

Differentiating Eq. 269 by $\dot{\alpha}_{pc}^{(n)}$:

$$\left(\frac{N\chi_{pc}^{(n)}}{p_c^{(n)}}\right)^r = 1-\left(1-\frac{\mathrm{n}}{\mathrm{N}}\right)^2 \quad \text{Eq. 274}$$

Summing Eq. 273 and Eq. 274 a yield surface can be derived:

$$y = \frac{\left(N\chi_q^{(n)} - 3H^{(n)}p\alpha_q^{(n)}\right)^2}{4\left(\frac{n}{N}\mu\right)^2\left(p+\frac{2}{3}q\right)\left(p-\frac{q}{3}\right)} + \left(\frac{N\chi_{pc}^{(n)}}{p_c^{(n)}}\right)^r - 1 = 0 \quad \text{Eq. 275}$$

Eq. 269 is thus equivalent to the yield surface in HySand_base. One now needs to check the positivity of the dissipation.

In Eq. 269 $(1-(1-n/N)^2)^{(1/\mathrm{r})}p_c^{(n)}\dot{\alpha}_{pc}^{(n)} > 0$ because all the terms are positive (α_{pc} and the consolidation pressure can only increase), and both the constraints are null by definition $\left(\dot{\alpha_p}^{(\mathrm{n})} + a\beta^{(n)}\dot{\alpha_q}^{(n)}\right) = 0$ and $\left(\dot{a} - A(1-|a|)\dot{\alpha_q}^{(n)}\right) = 0$.

One should thus demonstrate that:

$$\left(1-\frac{n}{N}\right)\sqrt{4\left(\frac{n}{N}\mu\right)^2\left(p+\frac{2}{3}q\right)\left(p-\frac{q}{3}\right)}\left|\dot{\alpha}_q^{(n)}\right| + 3H^{(n)}p\alpha_q^{(n)}\dot{\alpha}_q^{(n)} \geq 0 \quad \text{Eq. 276}$$

The hardening is limited by the outer yield surface which does not harden, such that:

$$\left|3pH^{(n)}\alpha_q^{(n)}\right| = 3pH^{(n)}\left|\alpha_q^{(n)}\right| < 2\left(1-\frac{n}{N}\right)\mu\sqrt{\left(p+\frac{2}{3}q\right)\left(p-\frac{q}{3}\right)} \quad \text{Eq. 277}$$

$$\rightarrow \quad \mu > \frac{3pH^{(n)}\left|\alpha_q^{(n)}\right|}{2\left(1-\frac{n}{N}\right)\sqrt{\left(p+\frac{2}{3}q\right)\left(p-\frac{q}{3}\right)}} \quad \text{Eq. 278}$$

The dissipation thus is positive.